FORMATION FLIGHT DESIGN USING NATURAL DYNAMICS FOR HALO
ORBITING AND EARTH ORBITING SPACECRAFT

A THESIS SUBMITTED TO
THE GRADUATE SCHOOL OF NATURAL AND APPLIED SCIENCES
OF
MIDDLE EAST TECHNICAL UNIVERSITY

BY

AYKUT KUTLU

IN PARTIAL FULFILLMENT OF THE REQUIREMENTS
FOR
THE DEGREE OF DOCTOR OF PHILOSOPHY
IN
AEROSPACE ENGINEERING

SEPTEMBER 2020

Approval of the thesis:

FORMATION FLIGHT DESIGN USING NATURAL DYNAMICS FOR HALO ORBITING AND EARTH ORBITING SPACECRAFT

submitted by **AYKUT KUTLU** in partial fulfillment of the requirements for the degree of **Doctor of Philosophy** in **Aerospace Engineering, Middle East Technical University** by,

Prof. Dr. Halil Kalıpçılar

Dean, Graduate School of **Natural and Applied Sciences**

Prof. Dr. İsmail H. Tuncer Ercan

Head of the Department, **Aerospace Engineering**

Prof. Dr. Ozan Tekinalp

Supervisor, **Aerospace Engineering, METU**

Examining Committee Members:

Prof. Dr. M. Kemal Özgören

Mechanical Engineering, METU

Prof. Dr. Ozan Tekinalp

Aerospace Engineering, METU

Assoc. Prof. Dr. Ali Türker Kutay

Aerospace Engineering, METU

Prof. Dr. Cengiz Hacızade

Aeronautical Engineering, ITU

Assist. Prof. Dr. Cuma Yarım

Astronautical Engineering, ITU

Date: 23.09.2020

I hereby declare that all information in this document has been obtained and presented in accordance with academic rules and ethical conduct. I also declare that, as required by these rules and conduct, I have fully cited and referenced all material and results that are not original to this work.

Name, Last name : Aykut Kutlu

Signature :

ABSTRACT

FORMATION FLIGHT DESIGN USING NATURAL DYNAMICS FOR HALO ORBITING AND EARTH ORBITING SPACECRAFT

Kutlu, Aykut
Doctor of Philosophy, Aerospace Engineering
Supervisor : Prof. Dr. Ozan Tekinalp

September 2020, 360 pages

This thesis presents the studies performed for spacecraft formation flight design and analyses. Two main design problems are addressed in this thesis: First the formation flight design of satellites flying near Sun-Earth collinear libration points; the second the formation flight design of satellites flying at Low Earth Orbit.

Thus, formation flight design near Sun-Earth L1 and L2 libration points is investigated first, where solar radiation pressure as well as the gravitational disturbances of the planets are taken into account, for different Julian dates. The periodicity of the relative motion in formation flight is taken as a design criterion and convenient initial conditions are computed for each deputy satellite for desired formation configuration. It is desired that the required formation is maintained without the need of any correction maneuvers for formation keeping.

In the second part, the method presented in this thesis for formation flight design is applied to Low Earth Orbit satellites. The results are also compared to the results obtained using current methods available in the literature. Results show that proposed method gives more consistent results and provides flexibility on the orbit

design for formation in terms of formation keeping and fuel consumption needs as compared with the currently available methods.

Finally, it can be stated that the trajectory and orbit computations done using the method presented in this thesis provide long term formation flight for space missions at L1, L2 libration points and for Low Earth Orbit missions. The main contribution of this method is the inclusion of all disturbancing forces acting on the satellite as a time variant discrete model. The initial conditions are found iteratively that ensures the periodic trajectory. Here, the usage of time variant discrete model to obtain periodic relative motion is a feature that distinguishes the current study from the existing methods in the literature.

ÖZ

DOĞAL DİNAMİK KULLANILARAK HALE YÖRÜNGEDE VE DÜNYA ETRAFINDA SEYIR EDEN UZAY ARAÇLARI İÇİN KOL UÇUŞU TASARIMI

Kutlu, Aykut
Doktora, Havacılık ve Uzay Mühendisliği
Tez Yöneticisi: Prof. Dr. Ozan Tekinalp

Eylül 2020, 360 sayfa

Bu tez çalışmasında uzay araçları kol uçuşu tasarımı ve analizleri üzerine yapılan çalışmalar sunulmaktadır. Tez iki ana bölümden oluşmaktadır. İlk ana kısım Güneş-Dünya eşdoğrusal sallantı noktaları civarında kol uçuşu tasarımı üzerinedir; ikinci ana kısım Dünya Alçak Yörünge uydularının kol uçuşunu incelemektedir.

İlk ana kısımda, güneş ışınım basıncı ile diğer gezegenlerin çekim kuvveti kaynaklı bozuntuları farklı Julian tarihler göz önüne alınarak L1 ve L2 Güneş-Dünya eşdoğrusal sallantı noktaları civarındaki kol uçuşu incelenmektedir. Formasyon uçuşundaki göreli hareketin periyodikliği bir tasarım kriteri olarak alınmaktadır ve her bir vekil uydunun uygun başlangıç koşulları istenen kol uçuşu konfigürasyonu için hesaplanmaktadır. Kol uçuşunun korunması için herhangi bir düzeltme manevrasına ihtiyaç duyulmadan hedeflenen uçuşun sürdürülmesi istenmektedir.

İkinci kısımda alçak Dünya Alçak Yörünge uyduları için mevcut yöntemler ile bu tezde sunulan yöntem kıyaslanmıştır. Sonuçlar kol uçuşu korunması ve yakıt tüketimi açısından bu tezde sunulan yöntemin uygun sonuçlar verdiğini ve yörünge tasarımında esneklik sağladığını göstermektedir.

Sonuç olarak, bu tezde sunulan yöntemin kullanımı ile tasarlanan uçuş yolu ve yörüngeler hem L1 ve L2 sallantı noktaları civarı uzay görevleri hem de Dünya Alçak Yörünge görevleri için uzun süreli kol uçuşu sağlamaktadır. L1 ve L2 durumları için, bu çalışmanın ana katkısı tüm bozuntu kaynaklarının zaman değişkenli ayrık modelde kullanımı ve böylece periyodik yörüngeyi garantileyen ilk koşulların bulunmasıdır. Dünya Alçak Yörünge durumunda, periyodik göreli hareket elde etmek için zaman değişkenli ayrık modelin kullanımı özelliği bu yöntemi diğer mevcut yöntemlerden ayıran bir özelliktir

Anahtar Kelimeler: Uzay aracı Kol Uçuşu, Güneş-Dünya Sallantı Noktaları, Lagrange Noktaları, Hale Yörünge, Dünya Alçak Yörünge

To my dear wife Esra and

our newborn little son Özgür Uras

ACKNOWLEDGMENTS

TABLE OF CONTENTS

CHAPTERS

LIST OF TABLES

LIST OF FIGURES

FIGURES

xxii

LIST OF ABBREVIATIONS

ABBREVIATIONS

CRTBP:	Circular Restricted Three-Body Problem
CW:	Clohessy-Wiltshire
DCM:	Direction Cosine Matrix
DDOR:	Delta Differenced One-Way Range
DSCOVR:	Deep Space Climate Observatory
ECEF:	Earth-Centered Earth Fixed
ECI:	Earth-Centered Inertial
EFF:	Enhanced Formation Flying
ESA:	European Space Agency
ETF:	Equilateral Triangle-shape Formation
FIR:	Far Infrared
FISICA:	Far Infrared Space Interferometer Critical Assessment
GMTI:	Ground Moving Target Indication
GROM:	Geometrical Relative Orbit Modeling
GSFC:	Goddard Space Flight Center
HEO:	High Earth Orbit
ICs	Initial Conditions
IR:	Infrared

ISF: Inclined Square-shape Formation

LEO: Low Earth Orbit

LVLH: Local Vertical Local Horizontal

NASA: National Aeronautics and Space Administration

NIR: Near Infrared

OPTICs: Optimal Initial Conditions

PCO: Projected Circular Orbit

PCO-ICs: Projected Circular Orbit- Initial Conditions

PCR3BP: Photogravitational Circular Restricted Three-Body Problem

RAAN: Right Ascension of Ascending Node

RTB: Restricted Three Body

RTBP: Restricted Three Body problem

SAR: Synthetic Aperture Radar

SF: Square-shape Formation

SRP: Solar Radiation Pressure

UAF: Uniformly Aligned Formation

VLBI: Very Long Baseline Interferometry

WMAP: Wilkonson Microwave Anisotropy Probe

LIST OF SYMBOLS

SYMBOLS

$\dot{\bar{r}}_{CoM}$:   Velocity matrix of the Center of Masses

$\dot{\bar{r}}_{k\_i}$: k^{th} component of the velocity vector of ith body

$X|_{orb}$:   X in orbital reference frame

$X|_{syn}$:   X in synodic reference frame

$\bar{c}_i$: i^{th} integration constant

$\vec{e}_i$ i^{th} unit vector

$\bar{r}_{CoM}$:   Position matrix of the Center of Masses

$\vec{r}_i$:   Position vector of ith body

$\bar{r}_{i\_cm}$:   Position matrix of ith body with respect to the center of mass

$\vec{r}_{ij}$:   Position vector from j^{th} body to i^{th} body

$\bar{r}_{ij}$:   Position matrix from j^{th} body to i^{th} body

$\bar{r}_{k\_i}$: k^{th} component of the position vector of ith body

$\bar{v}_{CoM}$:   Velocity matrix of the Center of Masses

$\bar{h}$:   Angular momentum in matrix form

$\widetilde{X}$:   Skew-symmetric matrix of X

C_R :   Spacecraft reflectivity

C_{orb}^{syn} :   Direction cosine matrix from orbital frame to synodic frame

D_f :   Differential variation of $f(X_{sub})$

P_{SR} :   Solar pressure

m_i :   Mass of the ith body

x_1 :   Distance between Sun and Center of Mass of Sun- Earth system

x_2 :   Distance between Earth and Center of Mass of Sun-Earth system

$\boldsymbol{F}_i$:   Force due to ith body

$\vec{\rho}$:   Vector of relative distance between two satellites

$\boldsymbol{\rho}_{ij}$:   Distance between ith and jth bodies

G: Universal gravitational constant

L1:   First Lagrange Point (Libration Point)

L2:   Second Lagrange Point (Libration Point)

T: Period

Φ :   State transition matrix

Ω: Angular velocity of orbital frame with respect to synodic frame

C :   Jacobi Constant

F :   State propagation matrix

S: Cross sectional area of the satellite exposed to the sun

T :   Kinetic energy

V :   Potential energy

X: State vector in matrix form

$au = R$:   Distance between Sun and Earth: Astronomic Unit

λ :   Eigenvalue

$\mu = mu$:   Mass ratio of second primary to total mass

τ :   Orbital Time

ω :   Angular velocity

CHAPTER 1

INTRODUCTION

1.1. Thesis motivation and definition of spacecraft formation flight

Mystery of deep space and the strong desire of the mankind to discover Earth-like planets trigger numerous innovations and the development of space technologies. In last few decades, especially in the last few years, studies on deep space mission have become even more popular due to number of related projects. In this way, many related subtopics appear such as interplanetary navigation, orbit design for long terms navigations in solar system and beyond. In addition, various innovative mission concepts, such as satellites flying in formation has attracted attention. Other mission driven technology development activities may be listed as follows: payload development to explore other planets and stars, development of sensors and actuators to fulfill more stringent mission requirements, design of specific experiments and equipment in order to collect data for the resistance of human being in space environments, studies on plant growing in space environment, etc. In this context, the studies presented in this thesis are on the formation flight design and analyses.

This thesis study is twofold: First main part is on the formation flight design near Sun-Earth collinear libration points L1 and L2; and the second main part examines the formation flight for Low Earth Orbit (LEO) satellites.

The most common definition for the satellite formation flying is the concept that multiple satellites can work together in a group to perform a specified mission. NASA's Goddard Space Flight Center (GSFC) defines the formation flight as, *"the tracking or maintenance of a desired relative separation, orientation or position between or among spacecraft"* [1]. Actually, spacecraft formation flying is

a specific case of more general category called, Distributed Space Systems, also defined by NASA GSFC as, "*an end-to-end system including two or more space vehicles and a cooperative infrastructure for science measurement, data acquisition, processing, analysis and distribution*" [1].

These definitions raise the question of what kind of advantages can be achieved with formation flying. Formation fleets may provide many advantages in terms of redundancy in case of any failure of one or more satellites, manufacturing lighter and smaller satellites, instead of utilizing one big satellite with huge observation payload, smaller satellites with smaller payloads, having more launcher possibility and less launcher cost, having stable and periodic relative motion between members of the fleet will not require frequent correction maneuvers, so this may increase lifetime of satellites as well as formation fleet.

1.2. Formation flying missions and literature review

The main motivation of the first main part of this thesis study is the existence of the many mission concepts that aim to study planet and star formations in order to detect Earth-like planets and to understand the conditions of early Earth-like planets. The common payload used for this kind of missions is Far-Infrared interferometer. In October 2014, FISICA published the report named "Far Infrared Space Interferometer Critical Assessment" report and the need of high resolution Far-IR is explained [2]. The technologic developments on Far-IR and optical/NIR (Near Infrared) are given in a white paper [3] and this white paper mentions how optical/NIR and Far-IR allow to watch the Universe, to understand the cosmology, to examine the origin of planetary systems and galaxy formation.

In recent years, numerous formations flying missions have been planned for the scientific objectives, such an imaging of extra-solar planets and lunar gravitometry. One of these projects is called DARWIN, is a European mission aims to characterize Earth-like planets. DARWIN constellation has three to four free-flying spacecraft

that will be at the second Lagrange point of the Earth-Sun system [4]. It is planed that one of the members of the fleet carry the optics for beam recombination and the other three members (or more) carry the large collector telescopes. DARWIN is a part of ESA's Cosmic Vision 2020 plan and the details on its mission is given in Ref.[5].

Three other concepts called respectively FIRIT, ESPRIT and TALC are the concepts presented for the subarcseconds far infrared observatory payload. Among these three concepts ESPRIT has a formation flight scheme. The trade-off report notices that ESPRIT has a loose formation flying constraints [3]. The wavelength range of the Far-Infrared Space Interferometer of the ESPRIT is 0.5 to 6 THz and the phenomena connected to star and planet formation are best studied in the far-infrared/Terahertz regime; 0.5 THz to several THz [6]. FIRIT is a spacecraft having two properties in payload, photometry and spectroscopy, in order to fulfill the mission requirements. Main goal is to observe star and planetary systems, the targets are given in Ref.[7]. Spacecraft contains one main module, called center hub, and two sub modules attached by booms at left and right of the satellite. Those attached booms carry two telescopes and the distance between submodules is 30 meters [8]. TALC is satellite having deployable mirror stacks forming an umbrella shape after deployment completed. Mirror stacks form a ring that is supported by the cables from the main hub of the satellite. Mechanical design is really a challenging topic. Trade off analyses and details are given Ref.[9].

The WIND spacecraft can be considered as one the first spacecraft sent to L1 Lissajous orbit and it was launched in 1994. WIND was initially in a Lunar orbit. Then its mission was extended, in November 1996, to be injected in to halo orbit about L1. WIND mission is to collect data from sun to investigate solar wind, solar dynamics. In 2014, its mission extended 10 years and WIND is really a venerable spacecraft since it keeps on performing its mission more than 20 years [10]. One of the most well-known of the satellites at point L1 is SOHO. SOHO is a joint project of ESA and NASA. Spacecraft's integration, testing work packages were on ESA responsibility. NASA was responsible for the launch and ground-segment services

as well as for in-flight operations following the launch on 2 December 1995 [11]. SOHO is in a quasi-periodic halo orbit around the Sun-Earth collinear point L1 which is a good position for the direct observation of the Sun. SOHO has a suite of 12 scientific instruments as payload. These payloads are imaging sensors used to study phenomena relating to the solar surface and atmosphere [12]. Science Program Committee (SPC) of ESA has declared that the operation of SOHO (additional operation of several satellites: Hinode, Hubble, IRIS, ExoMarsTGO) is extended up to 2022. Considering the launch date of SOHO, this lifetime is really an admirable duration [13]. An US satellite, WMAP (The Wilkonson Microwave Anisotropy Probe) observes deep space from an orbit about the L2 Sun-Earth Lagrange point. WMAP was launched in 2001, its lifetime was completed in 2010. Its mission was to measure the properties of the cosmic microwave background radiation of the universe [14]. WMAP team receives the fundamentals Physics Awards for detailed maps of the early universe [15]. GENESIS spacecraft was launched in August 2001. GENESIS navigates around L1 of Sun-Earth system. Its mission is to collect samples from solar winds and, that is the very interesting part, return them to Earth by its capsule for detailed analysis. However, unfortunately the parachute of the capsule failed to deploy on re-entry to Earth atmosphere and capsule crashed in the Utah desert in September 2004 [16]. TRIANA spacecraft originally planned to launch in 2002, with space shuttle. But, because of the budgetary problems, its launch is canceled. The budgetary priority was given to ISS and Hubble Space Telescope. Then, TRIANA was placed in storage at Goddard Spaceflight Center. In 2003, it renamed as DSCOVR (Deep Space Climate Observatory) and finally launched in November 2014 and it is positioned around L1 having a Lissajous orbit. DSCOVR delivers space weather measurements for the prediction of Sun activities [17].

Orbit design and orbit control near Sun-Earth libration points is also investigated by researchers. For example, paper by Folta and Beckman present a summary on the historical missions and the future planned missions [19]. It also gives a description of the numerical and dynamical orbit and trajectory design techniques for Sun-Earth libration points proposed for GSFC missions by emphasizing the critical role of

computing the libration trajectories. It is emphasized that the software must integrate spacecraft trajectories very accurately. This accuracy need force the model to include up to 100x100 Earth and lunar gravity potentials, solar radiation pressure, multiple 3rd-body perturbation effects [18]. For that reason, in this thesis solar pressure sourced disturbances and the gravitational effects of the solar system planets are added into the developed software model. Another challenging issue is the usage of the integrating method. In Ref. [19], it is stated that various high order variable or fixed step numerical integrators are incorporated in their software such as Runge Kutta, Cowell, and Bulirsch-Stoer. In this thesis 4th order Runge Kutta integration method is selected for simulations and analysis. It is seen that 4th order Runge Kutta is sufficient for computing trajectories since detailed maneuver performance are not studied in thesis context.

A detailed overview of formation flight concept for deep space explorations are given in Leitner's paper [20]. Formation flight technology needed to perform most challenging space missions and related projects are given in Leitner's study. It is emphasized that formation flying will be only solution to realize improvements in space-based telescopes and interferometer payloads in order to observe deep space with high resolution. Another comprehensive report on the missions at Sun-Earth libration points is prepared by G. Gomez et.al. [21]. Their study summarizes all the projects related to this topic and the main description on libration points, the dynamics, and new trends in mission design are commentated. The study of K. C. Howell and B. G. Marchand is on the formation keeping problem near the vicinity of the Sun–Earth libration points. The important parts of this study in terms of formation dynamics, part related to this thesis, it is the comments given for formation modeling. It is noticed that restricted three body problem is a good starting point for modeling. However more complete ephemeris model is needed to precisely determine the periodic orbits [22]. In line with this reccommendation, this thesis adds the ephemeris model on the periodic orbit computation, such that time dependent positions of the planets are recursively computed in simulation time. Furthermore, the solar radiation based disturbances are also added on the models as noticed in

Ref.[22]. So, this provides to obtain naturally existing formations near the libration points. The study performed by P. Chidambararaj, R.K. Sharma consider also the oblateness of Earth in the Halo orbit computations [23]. In this paper, the generation of Halo orbit in three-dimensional photogravitational restricted three-body problem is presented. Thus, the massive primary is considered as the source of radiation and the smaller primary is an oblate spheroid with its equatorial plane coincident with the plane of motion. In this paper, periodic solution of motion is given in terms a polynomial having sinusoidal functions. This analytical approach is not used in this thesis because this thesis uses the numerical method to obtain the satellite trajectory. Reference [23] presents the comparison of analytical and numerical solutions.

Most recent project on exoplanets exploration is called STARSHADES, with the mission to observe and characterize Earth-like exoplanets in the next decade. Main requirement is to precisely positioning in formation flight, the lateral formation sensing and control, is shared in the report released by California Institute of Technology in 2018 [24]. Technology Readiness Level (TRL) especially related to the formation keeping is reported. This report focuses specifically on lateral formation sensing and control technology. Formation flying behavior is given in the results parts of this reference. It is seen that this kind of relative motion is very similar to the examples given in this thesis.

One other approach used for Halo orbits design in libration points is the use of elliptic restricted three body problem instead of circular one. In that case the radius and the true anomaly of the elliptic motion of two primary bodies are needed to derive the equation of motion in the ER3BP; the details are given in [25].

The orbit determination for Sun-Earth libration points has a critical role on formation flight analyses and control. The results from NASA flight (ISEE-3, SOHO, ACE, and MAP) are collected in the paper prepared by NASA's Goddard Space Flight Center [26]. Standard method to determine the orbital position is based on standard range and Doppler measurement types from ground tracking sites of NASA. Different orbit determination options are available thanks to advanced technology.

For instance, including onboard navigation using onboard attitude sensor and the use of Very Long Baseline Interferometry (VLBI) measurement and Delta Differenced One-Way Range (DDOR). The results obtained using those measurements are presented in Ref.[26]. It is obvious that the main elements to obtain a good formation flight during the orbital navigation is to obtain an accurate relative position measurements between spacecraft. A method based on Laser ranging is presented in Ref.[18]. Here, extended Kalman filter algorithm is used with laser simulator. The paper stated that the relative distance measurement performance at millimeter levels for a distance of 10 km, and it is sub-millimeter levels for the distance less than 1 km.

There exists some studies on natural Halo orbit design and on relative trajectory design for formation flights. T. Luo, M.Xu and Y. Dong [27] proposes a numerical searching method based on Poincaré mappings to find natural formation flying on quasi-halo orbits in a Photogravitational Circular Restricted Three-Body Problem (PCR3BP). Their paper presents a relative trajectory for natural formation flying in PCR3BP both for typical and solar sail spacecraft. It also includes a control scheme since relative trajectory is considered unstable. Héritier and Howell [28] studied on the regions near the libration points for small distance and large distance formations. Their study is on the Sun-Earth L2 libration point; circular restricted three-body problem is used and low drift regions are investigated. They investigated the natural dynamics in a multi-body regime for formation flying applications in the collinear libration points [29]. The named article proposes a different dynamical model from Reference [28], where the position of the Sun and Earth is expressed as sinusoidal functions to define the relative equations of motion. Unlike, in this thesis satellite position and relative equations between chief and deputy satellites are written in nonlinear equations of motion forms; and the ephemeris model is used to add the planets disturbances depending on the planets position. K. Shahid and K. D. Kumar [30] present the use of solar radiation pressure for satellite formation reconfiguration at the L2 of Sun–Bary system. This paper is focused on the adaptive control techniques to obtain the desired formation where an elliptic restricted three-body

problem is used in modeling. Multi-tethered satellite formations using nonlinear coupling dynamics is studied by studied by Zhao and Cai [31]. A formation configuration having three satellites is examined and the stability of the tethered formation analyzed for Sun-Earth L2. Ilyin et al. [32], unlike other studies, they compute suitable solution to a circular restricted three-body problem as first step, than they convert this for a restricted four-body problem with real motion of the Sun, Earth, and Moon.

Some studies focused on the control of spacecraft formation flying near libration points. Formation flight reconfiguration near Sun-Earth libration points is investigated by Gong et.al.[33]. Reconfiguration is performed with impulsive maneuvers and genetic algorithm is adopted to optimize the fuel consumption. Another paper is on the use of the solar radiation pressure to maintain the formation schema near L2 Sun-Earth system. In another paper, authors propose to implement continuous low thrust using solar radiation pressure in order to reach tight formation flight [34]. Jung and Kim propose a control method called Hamiltonian structure preserving control to stabilize the motion of the satellite along the trajectory around libration point [35] and their numerical solution is used for Earth-Moon system's L2 halo orbit. Taberner and Masdemont propose a method based on finite elements for formation flight to calculate formation keeping maneuvers [36]. This technique includes optimal control and collision avoidance method. A new numerical algorithm for solving the periodic Riccati differential equation to implement continuous low-thrust to keep the formation near libration points of Sun-Earth system is proposed by Peng et al. [37]. Zhanga and Li studied station keeping strategies for the orbits near libration points. The interesting point is that there is no need the information of the nominal orbit to perform station keeping [38]. They demonstrated this method on Earth-Moon libration points. YunHe et al. use Floquet theory to design and control formation flying satellites near libration points [39]. An orbit control strategy based on an analytical method is proposed by Jing et.al. [40]. In the study they eliminated the dominant unstable components of libration point orbits. An analytical expression for nonlinear control force is derived on their article.

When such missions are examined, for the future, it is necessary to contemplate a formation flying satellite fleets that perform mission at L1 and L2, with many advantages such that redundancy, cost, mission lifetime that the formation flight fleets can provide. For the reasons mentioned above, the objective of the first main part of this thesis is to design a formation flight scheme near Sun-Earth collinear libration points L1 and L2.

The second main part of this thesis is dedicated to the formation flight design and analyses for the LEO satellites. The motivation source for this examination is the recent projected prepared for the Earth observation missions using formation flight concept. For LEO missions, like in the case of deep-space missions, the redundancy and cost advantages of the formation concept have forced the people work on it for LEO satellites.

For instance, TECHSAT-21 was a microsatellite cluster that was adaptable to perform a variety of missions and the initial focus of the TECHSAT-21 program was on Ground Moving Target Indication (GMTI) and Synthetic Aperture Radar (SAR) imaging [41]. Another mission called CLUSTER from ESA; it is a cluster structure containing four identical satellites having highly elliptical polar orbits around Earth (19000 km perigee and 119000 km apogee). Their mission is to measure the effects of the Sun particles to the Earth's magnetic field. They launched in August 2000 for nine years mission lifetime [42, 43]. Another example is PROBA low-cost satellites that are being used to validate new spacecraft technologies. PROBA-3 is ESA's first precision formation flying mission and launch date was planned at the 2020 but, as of 2018, the launch is delayed to the second quarter of 2021 [44]. The mission will demonstrate formation flying for a science experiment. The paired satellites will study the Sun's faint corona. Beside its scientific mission, the experiment will measure the performance of the precise positioning of the two spacecraft [45]. The GRACE is also a mission that uses formation flight technology planned by ESA and NASA. GRACE has two identical satellites orbiting around Earth. Its purpose is to provide measures in order to generate high accurate model of the Earth's gravitational field [46]. The orbit altitude was about 500 km and satellites are

launched at 2002 and the mission lifetime was 5 years, however it is expected to continue until 2015 [47], likely its mission ends at October 2017 [48].

NASA's First Autonomous formation flying mission has been successfully demonstrated by Earth Observing-1 (EO-1) satellite launched in November 2000. EO-1 mission is flying in formation with LANDSAT-7. Their payloads enable to study on climatic trends in the Earth's environment. EO-1 mission demonstrates Enhanced Formation Flying (EFF) developed by NASA's Goddard Space Flight Center (GSFC). EFF provide that satellites can keep their formation without human intervention. The EO-1 is located 1 minute behind of LANDSAT-7 in the same ground track, so the distance between them is approximately 450 km. EFF tests are performed from January 2001 through July 2001 and then in November 2001. The EO-1 EFF successfully accomplished with ten formation-flying maneuvers that are combination of reactionary, formation and an inclination maneuvers, and formation performance was within approximately 3 km [49]. The algorithm used for EFF is embedded on the spacecraft computer and it propose to save time in maneuver planning done on ground stations. Another study presents the simulation results of EFF integrated in an autonomous fuzzy logic control system called AutoCon [50]. AutoCon details and maneuver control algorithm description is given in [51]. The closed-loop control results of EFF in either constellation is also presented by David Folta using AutoCon and FreeFyler for simulations with various fidelity levels of modeling. However, the constellation members taken in this paper have all the same orbital plane, same inclination value (98.2 degree) and same altitude (705 km) [52]. In this kind of formation configuration, satellites share the same orbit with different phase angle. The method presented in this thesis provide to find a different orbit close to the chief satellite, it gives a deputy's trajectory around chief satellite with minimum maneuvers for formation corrections, see in section 8.

It is obvious that the fuel consumption is a critical issue for the LEO formation flying satellites in terms of mission and satellite's life time. Studies on low thrust implementation for LEO formation flight can be found in literature. For instance, Arnot and McInnes study proposes continuous low thrust provided by solar electric

propulsion, since the corrections needed for keeping formation are small. In Arnot and McInnes study, Clohessy-Wiltshire approximation of motion in a rotating frame is taken and Projected Circular Orbit concept is used [53]. Unlike this reference, this thesis use nonlinear relative equations of motion and it does not contain any constraint like usage of PCO or any other assumption, details given in section 8.3.

The formation flight mission analyses of the PROBA-3 are given in Ref.[54]. PROBA -3, having HEO orbit, it is planned to make scientific researches using a coronagraphic payload to observe the Sun corona. The configuration having two spacecraft, one carries the sun occulter and the other carries the coronagraph instrument [54]. The main spacecraft weighs 320 kg, and the second one is 180 kg. The relative distance of the two spacecraft is adjustable and it varies from 25 to 250 meters according to the focal length needs [45]. An overview of the PROBA-3 mission, with a more detailed description of the formation flying preliminary design and results, is given in Ref.[55]. Here the aim is to orient formation flying satellites toward Sun in order to examine the Sun corona. So, the formation is computed regarding to the Sun position with respect to the satellite's reference orbit. It may be possible to compute a variety of orbit for deputy satellite using the method given in this thesis, since circular orbit assumption in not done and the proposed method is based on the discrete dynamic, so it allows the usage for HEO orbits. Another example for formation flight around Earth is the TECHSAT-21, and its flight experiment demonstrates a formation of three microsatellites flying in formation. Each satellite is identical having 150 kg mass and 550 km orbit altitude. The satellites initially relatively positioned approximately 5 km to each other. Then, relative distance slowly decreased to 100-500m [56].

1.3. Original Contributions

The contributions of this thesis study are collected in two main groups. In the first part, formation flight fleets near Sun-Earth L1 and L2 points are examined. The formation flight design method presented in this thesis make it possible to construct a feasible formation while complying with the mission needs and payload capabilities. The contributions of this first part may be listed as follows:

- Adding the solar radiation perturbation as well as gravitational perturbations caused by the planets where the planets positions are computed for every sampling time in the simulation model, in discrete time, using ephemeris models for different Julian date intervals.

- The utilization of the periodicity of relative motion in formation flight and the computation of convenient initial velocity of each deputy to maintain the desired formation configuration (desired initial relative position).

- Derivation of the nonlinear relative equations of motion: Relative motion between chief and deputy satellites are written in nonlinear equations of motion forms.

- Determination of the optimum relative trajectory. In this vein,
  - First, planar formations are studied like equilateral triangle shape, square shape, inclined square shape. Optimum initial condition set is found that provide minimum deviation in relative motion.
  - Second, rectilinear formation is derived. Deputies are aligned and uniformly equally separated from each other. This linear formation configuration provides constant relative distances between successive deputies.

- Providing long-term natural formation flight: Computed initial conditions guarantee to keep the relative distance between satellites as required during an orbital period time without the need of any correction maneuver for keeping formation.

In the second part of this thesis formation flight design problem for LEO satellites is addressed. The formation design methods existing in the literature for LEO satellites are based on some assumptions and constraints like close formations, equal semimajor axis, projected motion (planar) and they are focused on initial position, without considering initial velocities. Consequently, the contiributions of this second part may be listed as follows:

- The usage of the nonlinear relative equations of motion: Nonlinear model does not contain any constraint like usage of projected circular orbit.
- The proposition of flexibility on formation design in terms of formation configuration: The method given in the first part is extended for LEO formation flight and successful formation flight results are obtained for different formation configurations.
- The use of time variant discrete model to obtain periodic relative motion is a feature that distinguishes it from the existing methods.
- Ensure the long-term formation flight without any design constraint: It is possible to obtain a formation for an arbitrary initial relative position having both azimuth and elevation angle.
- Profit from fuel consumption: This is certainly important for maintaining formation for extended durations.

1.4. Thesis organization

This thesis is organized into two main parts. First part contains the chapters written for the formation flight design near Sun-Earth collinear libration points, from Chapter 2 to Chapter 5. The second part is dedicated to the formation flight for design for LEO satellites between Chapter 6 and 9.

Specifically, Chapter 2 gives details on three body dynamics and libration points. Here, the aim is to set all the required sub-components in order to design orbits at

Lagrange points. For that reason, the explanation and simulations related to the three body dynamics are given. Restricted three body problem is explained and the general equations of motion are presented in order to demonstrate the consistency and the accuracy of the prepared codes, on the software structure. The libration points are also presented in this chapter with their stability characteristics. The zero velocity boundaries which are related to the energy level of the spacecraft are presented in this chapter.

Chapter 3 presents the orbit types and the methodology used to design Halo orbit. Here, the equations of motion for undisturbed and disturbed cases are given. The disturbance sources are examined. The effect of the solar system planets and the solar radiation pressure on the orbit stability are examined in details. A brief subchapter on the orbital correction maneuver in order to keep the Halo orbit is also presented.

The main goal, "formation flight design" is presented in Chapter 4. Here, the methodology used is examined. The effects of the selected formation scheme, the importance of the optimization parameters, etc. are explained. The relative equations of motion are derived in this chapter. Several formation clusters around L1 and L2 libration points are examined in detail. The relative distance behavior, the change of the relative distance regarding to the orbital period are presented and the importance of the selected initial conditions are demonstrated as well. Optimum formation clusters are presented in this chapter. Chapter 5 summarizes and concludes the results obtained for formation flight design for L1 and L2. The comments and important inferences are presented.

The second main part of thesis starts with Chapter 6. This chapter contains the relative motion modeling approaches for LEO formation flight. The following Chapter 7 presents the methods used in the literature for formation flight design. This Chapter also contains the method proposed in this thesis. Chapter 8 presents all the simulation results obtained by comparing the methods used for different desired formation schemes. Furthermore, the orbit correction maneuver budgets are also presented this chapter in order to give a performance index using formation flight

accuracy, endurance versus required correction, fuel consumption by comparing the existence method and proposed method in this thesis. The inferences on results obtained for LEO formation design are presented in Chapter 9. Finally, Chapter 10 summarizes the main results. Conclusions are presented and recommendations for the future work are also given.

CHAPTER 2

DYNAMIC MODELING

2.1. Three body problem

The motion of a system having N body can be described with Newton's laws of motion as;

$$\vec{F}_i = m_i \ddot{\vec{\rho}}_i = \sum_{j=1, j \neq i}^{N} G \frac{m_i m_j}{\left| \vec{\rho}_{ij} \right|^3} \vec{\rho}_{ij} \implies \ddot{\vec{\rho}}_i = \sum_{j=1, j \neq i}^{N} G \frac{m_j}{\left| \vec{\rho}_{ij} \right|^3} \vec{\rho}_{ij} \qquad \text{Eq. 2-1}$$

Here, $\vec{\rho}_{ij}$ is the distance between i$^{\text{th}}$ and j$^{\text{th}}$ bodies, G is the universal gravitational constant, m_i is the mass of i$^{\text{th}}$ the body. The three-body problem is a special case of the N body problem. The three-body problem determines the motion of three bodies according to the Newton's law of motion, for a given initial position and velocity set of each bodies.

As known, the general problem of the motion of three bodies, moving in the effect of their gravitational forces' interactions, cannot be solved in closed form [57]. However, there are ten constants, or said integrals of motion, along the solution trajectories [58]. It is possible to compute these ten constants for a given set of initial conditions and then, it is known that they will not change all later times.

Equations of Motion for a system having 3 bodies with respect to inertial frame can be written as follows. Let three bodies having masses m_1, m_2, m_3 and with position vectors $\vec{r_1}, \vec{r_2}, \vec{r_3}$.

$$\ddot{\vec{r}}_{1\_i} = \frac{Gm_2\vec{r}_{12}}{|\vec{r}_{12}|^3} + \frac{Gm_3\vec{r}_{13}}{|\vec{r}_{13}|^3}$$

$$\ddot{\vec{r}}_{2\_i} = \frac{Gm_1\vec{r}_{21}}{|\vec{r}_{21}|^3} + \frac{Gm_3\vec{r}_{23}}{|\vec{r}_{23}|^3} \qquad \text{Eq. 2-2}$$

$$\ddot{\vec{r}}_{3\_i} = \frac{Gm_1\vec{r}_{31}}{|\vec{r}_{31}|^3} + \frac{Gm_2\vec{r}_{32}}{|\vec{r}_{32}|^3}$$

It's useful to write the system in matrix form for numerical integrations used in the simulation. When the system is written as a first order differential equation set:

$$\dot{X} = \begin{bmatrix} \dot{\vec{r}}_{1\_i} \\ \dot{\vec{r}}_{2\_i} \\ \dot{\vec{r}}_{3\_i} \\ \ddot{\vec{r}}_{1\_i} \\ \ddot{\vec{r}}_{2\_i} \\ \ddot{\vec{r}}_{3\_i} \end{bmatrix} = \begin{bmatrix} \dot{\vec{r}}_{1\_i} \\ \dot{\vec{r}}_{2\_i} \\ \dot{\vec{r}}_{3\_i} \\ \dfrac{Gm_2\bar{r}_{12}}{|\bar{r}_{12}|^3} + \dfrac{Gm_3\bar{r}_{13}}{|\bar{r}_{13}|^3} \\ \dfrac{Gm_1\bar{r}_{21}}{|\bar{r}_{21}|^3} + \dfrac{Gm_3\bar{r}_{23}}{|\bar{r}_{23}|^3} \\ \dfrac{Gm_1\bar{r}_{31}}{|\bar{r}_{31}|^3} + \dfrac{Gm_2\bar{r}_{32}}{|\bar{r}_{32}|^3} \end{bmatrix} \qquad \text{Eq. 2-3}$$

Here, $\dot{X}$ can be called as the vector field for the Three-Body-Problem. The frame used in presented in Figure 2-1:
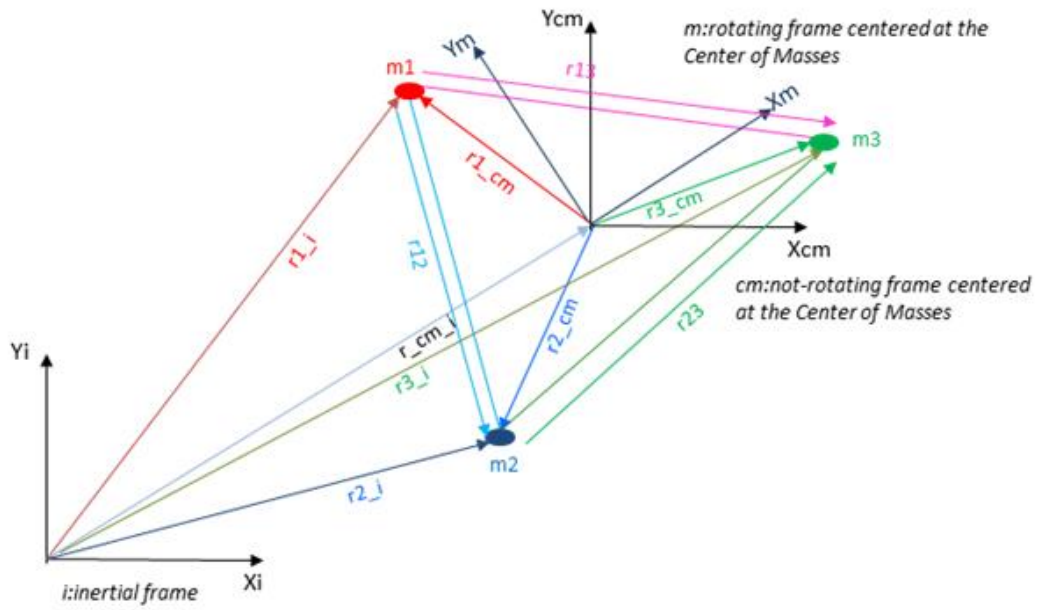
Figure 2-1. Frames used to describe the motion of the third body

Here, the relative position can be written as: $\vec{r}_{12} = \vec{r_2} - \vec{r_1}$; $\vec{r}_{13} = \vec{r_3} - \vec{r_1}$; $\vec{r}_{23} = \vec{r_3} - \vec{r_2}$. In matrix form $\bar{r}_{kl} = -\bar{r}_{lk}$; $|\bar{r}_{kl}|^3 = |\bar{r}_{lk}|^3$; $\bar{r}_{kl} = \bar{r}_{l\_cm} - \bar{r}_{k\_cm}$ or $\bar{r}_{kl} = \bar{r}_{l\_i} - \bar{r}_{k\_i}$. Here, subscript *i* denotes inertial frame, subscript *cm* represents the not-rotating frame fixed on the Center of Mass, and finally subscript *m* represents the rotating frame fixed to the Center of Mass as shown in the figure above. The position of the Center of Masses, $\bar{r}_{CoM}$, it is defined with respect to in inertial frame as:

$$\bar{r}_{CoM} = \frac{\bar{r}_1 . m_1 + \bar{r}_2 . m_2 + \bar{r}_3 . m_3}{m_1 + m_2 + m_3}$$

Eq. 2-4

The position of the bodies with respect to not-rotating frame:

$$\bar{r}_{1\_cm} = \bar{r}_{1\_i} - \bar{r}_{CoM}$$
$$\bar{r}_{2\_cm} = \bar{r}_{2\_i} - \bar{r}_{CoM} \qquad \text{Eq. 2-5}$$
$$\bar{r}_{3\_cm} = \bar{r}_{3\_i} - \bar{r}_{CoM}$$

The position of the bodies with respect to rotating frame:

$$\bar{r}_{1\_m} = Rot \cdot \bar{r}_{1\_om}$$
$$\bar{r}_{2\_m} = Rot \cdot \bar{r}_{2\_om} \qquad \text{Eq. 2-6}$$
$$\bar{r}_{3\_m} = Rot \cdot \bar{r}_{3\_om}$$

Here;

$$Rot = \begin{bmatrix} cos(\omega.t) & sin(\omega.t) & 0 \\ -sin(\omega.t) & cos(\omega.t) & 0 \\ 0 & 0 & 1 \end{bmatrix} \qquad \text{Eq. 2-7}$$

where, ω is the angular velocity of the frame centered at the center of three masses with respect to the inertial frame: $\omega = \sqrt{G \sum_{k=1}^{3} m_k / r^3}$

As reminded above, the integrals of motion can be computed along the solution trajectories and they will not change in time in undisturbed environment. The track of those constants behaves like an indicator and they give an idea about the accuracy of the numerical integration. If there is a drift from initial value, it means that numerical results are no longer valid. In a dynamical system point of view, non-changed integrals of motion provide a sub-trajectory (called manifold) and give information about the behaviors of the dynamics. These ten integrals of motion can be computed using conservation of the linear momentum, angular momentum and energy.

2.1.1. Conservation of the linear momentum

Conservation of the linear momentum states that center of the masses of the N body system moves with a constant velocity, so its acceleration is zeros [58]:

$$\ddot{\bar{r}}_{CoM} = 0 \qquad\qquad \text{Eq. 2-8}$$

Instantaneous position of the center of mass for the system having three particles is:

$$\bar{r}_{CoM} = \frac{1}{M} \sum_{k=1}^{N=3} m_k \bar{r}_k(t) \qquad\qquad \text{Eq. 2-9}$$

And where M is the total mass:

$$M = \sum_{k=1}^{N=3} m_k \qquad\qquad \text{Eq. 2-10}$$

First integration gives three constants of motion.

$$\dot{\bar{r}}_{CoM}(t) = \bar{v}_{CoM}(t) = \bar{c}_1 \qquad\qquad \text{Eq. 2-11}$$

$$\bar{c}_1 = \bar{v}_{CoM}(0) = \frac{1}{M} \sum_{k=1}^{N=3} \bar{v}_k(0) \qquad\qquad \text{Eq. 2-12}$$

Explicitly it can be written as:

$\frac{1}{M} \sum_{k=1}^{N=3} m_k \bar{v}_k(t) = \frac{1}{M} \sum_{k=1}^{N=3} m_k \bar{v}_k(0) = \bar{c}_1$ where $\bar{v}_k$ is the velocity vector having

three components as:

$$\bar{v}_k = [v_{xk} \quad v_{yk} \quad v_{zk}]^T$$

Second integration gives three more constants of motion:

$$\bar{r}_{CoM}(t) = \bar{c}_1 t + \bar{c}_2 \implies \bar{r}_{CoM}(t) - \bar{c}_1 t = \bar{c}_2 \qquad\qquad \text{Eq. 2-13}$$

$$\bar{r}_{CoM}(t) - \bar{v}_{CoM}(0)t = \bar{c}_2 = \frac{1}{M} \sum_{k=1}^{N=3} \bar{r}_k(0) \qquad\qquad \text{Eq. 2-14}$$

$$\bar{c}_2 = \frac{1}{M} \left[\sum_{k=1}^{N=3} m_k \bar{r}_k(t) - t \sum_{k=1}^{N=3} m_k \bar{v}_k(0) \right] = \frac{1}{M} \sum_{k=1}^{N=3} \bar{r}_k(0) \qquad\qquad \text{Eq. 2-15}$$

where velocity and position matrices having three components:

$$\bar{v}_k = [v_{xk} \quad v_{yk} \quad v_{zk}]^T \text{ and } \bar{r}_k = [r_{xk} \quad r_{yk} \quad r_{zk}]^T$$

Thus, conservation of the linear momentum provides six integrals of motion.

2.1.2. Conservation of the angular momentum

Conservation of the angular momentum provides three more constant. Angular momentum value is constant, the change of the angular momentum in time is zeros [57, 59]:

$$\dot{\bar{h}}(t) = 0 \qquad \text{Eq. 2-16}$$

Angular momentum of the system:

$$\bar{h}(t) = \sum_{k=1}^{N=3} \bar{h}_k(t) = \sum_{k=1}^{N=3} m_k(\bar{r}_k(t) \times \bar{v}_k(t))$$

$$= \sum_{k=1}^{N=3} m_k(\bar{r}_k(t) \times \dot{\bar{r}}_k(t)) \qquad \text{Eq. 2-17}$$

First integration of the angular momentum gives $\bar{h}(t) = \bar{c}_3$, and for initial time $\bar{c}_3 = \bar{h}(0)$. So, this equality gives three more constants. Three components of integral of motions:

$$\sum_{k=1}^{N=3} m_k \left[\bar{r}_{yk}(t) \bar{v}_{zk}(t) - \bar{r}_{zk}(t) \bar{v}_{yk}(t) \right] = h_x(0)$$

$$\sum_{k=1}^{N=3} m_k \left[\bar{r}_{zk}(t) \bar{v}_{xk}(t) - \bar{r}_{xk}(t) \bar{v}_{zk}(t) \right] = h_y(0) \qquad \text{Eq. 2-18}$$

$$\sum_{k=1}^{N=3} m_k \left[\bar{r}_{xk}(t) \bar{v}_{yk}(t) - \bar{r}_{yk}(t) \bar{v}_{xk}(t) \right] = h_z(0)$$

$$\bar{c}_3 = \bar{h}(0) = [h_x(0) \quad h_y(0) \quad h_z(0)]^T \qquad \text{Eq. 2-19}$$

2.1.3. Conservation of the energy

Conservation of the energy gives the last constant [58]. The dynamics of the particle is defined using Newton's second law:

$$m \frac{d^2}{dt^2} r = F(r) \qquad \text{Eq. 2-20}$$

Here, vector field is a function of the position of the body. Integrating this equality along the path for a time t=t$_f$ and by choosing arbitrary initial conditions such as $\bar{x}_0 = (\bar{r}_0, \dot{\bar{r}}_0)$

$$\int_{r(0)}^{r(T)} m\ddot{\bar{r}} \, dr = \int_0^{t_f} m\ddot{\bar{r}} \cdot \dot{\bar{r}} \, dt \qquad \text{Eq. 2-21}$$

where;

$$\ddot{\bar{r}} \cdot \dot{\bar{r}} = \frac{d}{dt} \frac{\left| \dot{\bar{r}} \right|^2}{2} \qquad \text{Eq. 2-22}$$

Then,

$$\int_{r(0)}^{r(t_f)} m\ddot{\bar{r}} \, dr = \int_0^{t_f} m\frac{d}{dt}\frac{|\dot{\bar{r}}|^2}{2} dt = m\frac{|v(t_f)|^2}{2} - m\frac{|v(0)|^2}{2} \Rightarrow \qquad \text{Eq. 2-23}$$

This relation gives the kinetic energy description. For three body system it can be rewritten as:

$$T(v) = \frac{1}{2}\sum_{k=1}^{N=3} m_k |v_k|^2 \qquad \text{Eq. 2-24}$$

Let take again the change of the kinetic energy with time can be rewritten as:

$$\left.\frac{dT}{dt}\right|_0^{t_f} = \int_0^{t_f} m\ddot{\bar{r}} \cdot \dot{r} \, dt = \int_{r(0)}^{r(t_f)} m\ddot{\bar{r}} \, dr = m\frac{|v(t_f)|^2}{2} - m\frac{|v(0)|^2}{2}$$

$$= \int_{r(0)}^{r(t_f)} F_k(r_k) \quad dr_k = f\big(r(t_f)\big) - f(r(0)) \qquad \text{Eq. 2-25}$$

Here, f is a potential function related to the position of the particle, called as potential energy. So, for three body system, we have:

$$\int_{r(0)}^{r(t_f)} F_k(r_k) \quad dr_k = \int_{r(0)}^{r(t_f)} \left(G \sum_{\substack{j=1 \\ j \neq k}}^{N=3} \frac{m_k m_j}{|\bar{r}_{kj}|^3} \bar{r}_{kj} \right) dr_k$$

$$= G \sum_{\substack{j=1 \\ j \neq k}}^{N=3} \int_{r(0)}^{r(t_f)} \left(\frac{m_k m_j}{|\bar{r}_{kj}|^3} \bar{r}_{kj} \right) dr_k \qquad \text{Eq. 2-26}$$

$$= -G\left[\frac{m_1 m_2}{|\bar{r}_{12}|^3}\dot{\bar{r}}_{12} \cdot \bar{r}_{12} + \frac{m_2 m_3}{|\bar{r}_{23}|^3}\dot{\bar{r}}_{23} \cdot \bar{r}_{23} + \frac{m_3 m_1}{|\bar{r}_{31}|^3}\dot{\bar{r}}_{31} \cdot \bar{r}_{31} \right]$$

$$-\frac{dV}{dt} = G\frac{d}{dt}\left[\frac{m_1 m_2}{|\bar{r}_{12}|} + \frac{m_2 m_3}{|\bar{r}_{23}|} + \frac{m_3 m_1}{|\bar{r}_{31}|} \right] \qquad \text{Eq. 2-27}$$

where the potential energy V of the three body system is:

$$V = -G\left[\frac{m_1 m_2}{|\bar{r}_{12}|} + \frac{m_2 m_3}{|\bar{r}_{23}|} + \frac{m_3 m_1}{|\bar{r}_{31}|}\right]$$

<div align="right">Eq. 2-28</div>

From the equation $\frac{dT}{dt}\Big|_0^{t_f} = \int_0^{t_f} m\ddot{\bar{r}} \cdot \dot{\bar{r}}\, dt$ it can be rewritten that the change on the kinetic energy is equal to the change on potential energy, so sum of their change in time are zeros:

$$\frac{dT}{dt} + \frac{dV}{dt} = 0$$

<div align="right">Eq. 2-29</div>

So total energy is constant: $T + V = c_4$

Finally putting all of this together gives the last the tenth integral of motion for the three-body system:

$$\sum_{k=1}^{N=3} m_k \frac{|v_k(t_f)|^2}{2} - \frac{1}{2}G\sum_{k=1}^{N=3} m_k \sum_{\substack{j=1 \\ j \neq k}}^{N=3} \frac{m_j}{|\bar{r}_{kj}(t_f)|}$$

$$= \sum_{k=1}^{N=3} m_k \frac{|v_k(0)|^2}{2} - \frac{1}{2}G\sum_{k=1}^{N=3} m_k \sum_{\substack{j=1 \\ j \neq k}}^{N=3} \frac{m_j}{|\bar{r}_{kj}(0)|}$$

<div align="right">Eq. 2-30</div>

Left Side, LS is:

$$LS = m_1 \frac{|v_1(t_f)|^2}{2} - \frac{1}{2}G\left[\frac{m_1 m_2}{|\bar{r}_{12}(t_f)|} + \frac{m_1 m_3}{|\bar{r}_{13}(t_f)|}\right] + m_2 \frac{|v_2(t_f)|^2}{2}$$

$$- \frac{1}{2}G\left[\frac{m_2 m_1}{|\bar{r}_{21}(t_f)|} + \frac{m_2 m_3}{|\bar{r}_{23}(t_f)|}\right]$$

<div align="right">Eq. 2-31</div>

$$+m_3 \frac{|v_3(t_f)|^2}{2} - \frac{1}{2}Gm_3\left[\frac{m_3 m_1}{|\bar{r}_{31}(t_f)|} + \frac{m_3 m_2}{|\bar{r}_{32}(t_f)|}\right]$$

$$LS = m_1 \frac{\left|v_1(t_f)\right|^2}{2} + m_2 \frac{\left|v_2(t_f)\right|^2}{2} + m_3 \frac{\left|v_3(t_f)\right|^2}{2}$$
$$- G\left[\frac{m_1 m_2}{\left|\bar{r}_{12}(t_f)\right|} + \frac{m_2 m_3}{\left|\bar{r}_{23}(t_f)\right|} + \frac{m_3 m_1}{\left|\bar{r}_{31}(t_f)\right|}\right]$$

Eq. 2-32

Same manner, right side, RS is:

$$RS = m_1 \frac{\left|v_1(0)\right|^2}{2} + m_2 \frac{\left|v_2(0)\right|^2}{2} + m_3 \frac{\left|v_3(0)\right|^2}{2}$$
$$- G\left[\frac{m_1 m_2}{\left|\bar{r}_{12}(0)\right|} + \frac{m_2 m_3}{\left|\bar{r}_{23}(0)\right|} + \frac{m_3 m_1}{\left|\bar{r}_{31}(0)\right|}\right]$$

Eq. 2-33

So;

$$LS = RS = c_4$$

Eq. 2-34

$$m_1 \frac{\left|v_1(t_f)\right|^2}{2} + m_2 \frac{\left|v_2(t_f)\right|^2}{2} + m_3 \frac{\left|v_3(t_f)\right|^2}{2}$$
$$- G\left[\frac{m_1 m_2}{\left|\bar{r}_{12}(t_f)\right|} + \frac{m_2 m_3}{\left|\bar{r}_{23}(t_f)\right|} + \frac{m_3 m_1}{\left|\bar{r}_{31}(t_f)\right|}\right] =$$
$$m_1 \frac{\left|v_1(0)\right|^2}{2} + m_2 \frac{\left|v_2(0)\right|^2}{2} + m_3 \frac{\left|v_3(0)\right|^2}{2}$$
$$- G\left[\frac{m_1 m_2}{\left|\bar{r}_{12}(0)\right|} + \frac{m_2 m_3}{\left|\bar{r}_{23}(0)\right|} + \frac{m_3 m_1}{\left|\bar{r}_{31}(0)\right|}\right] = c_4$$

Eq. 2-35

Finally, ten integrals of motion are obtained:

$$[\bar{c}_1 \quad \bar{c}_2 \quad \bar{c}_3 \quad c_4]^T$$
$$= [c_{11} \quad c_{12} \quad c_{13} \quad c_{21} \quad c_{22} \quad c_{23} \quad c_{31} \quad c_{32} \quad c_{33} \quad c_4]^T$$

Eq. 2-36

2.1.4. Simulation examples of three body dynamics

In this section, the simulation examples are presented using three body dynamics equations of motion given in the previous section. The main goal is to see the results of the simulation codes that are prepared and in this way; the simulation tool is presented and validated.

Here, dimensionless unit are used in order to see the effects of the mass distribution between three bodies. So, simulation time is taken $2\pi\ radian = 1\ revolution$, the angular rate will be $1\ radian/sec$, gravitational constant $G = 1$, and the masses are taken as the total mass is unit ($m_1 + m_2 + m_3 = 1$).

First, the motion of the three bodies having equal masses and having equal initial distances between them is simulated. Secondly the real mass values of the Sun, Earth+Moon system and satellite are given in order to simulate the motion of this Sun-Earth+Moon-Satellite three body system.

2.1.4.1. Case study I: Equal masses and equal distances

So, firstly let $m_1 = m_2 = m_3 = 1/3\ unit\ mass$ and $r_{12} = r_{13} = r_{23} = 1$ is unit distance. The distances between bodies and center of mass are defines as: $r_{1\_cm} = r_{2\_cm} = r_{3\_cm} = 1/\sqrt{3} = 0.5774$ unit.

Let's take initial positions for masses:

$$\bar{r}_{1\_cm\_t0} = \begin{bmatrix} 0 \\ 0.5774 \\ 0 \end{bmatrix};\ \bar{r}_{2\_cm\_t0} = \begin{bmatrix} -0.5 \\ -0.2887 \\ 0 \end{bmatrix};\ \bar{r}_{3\_cm\_t0} = \begin{bmatrix} 0.5 \\ -0.2887 \\ 0 \end{bmatrix}$$

Initial position for the center of mass $\bar{r}_{cm\_t0}$ and initial velocity $\bar{V}_{cm\_t0}$ for the center of mass, it is given in +X and +Y directions: a motion upwards will be obtained with a rotation ω around center of masses.

$$\bar{r}_{cm\_t0} = \begin{bmatrix} 0 \\ 0 \\ 0 \end{bmatrix};\ \bar{V}_{cm\_t0} = \begin{bmatrix} 0.5 \\ 1 \\ 0 \end{bmatrix}$$

The computed initial velocities of the masses for $\bar{V}_{cm\_t0}$ are:

$$\bar{v}_{1\_cm\_t0} = \begin{bmatrix} -0.0774 \\ 1 \\ 0 \end{bmatrix};\ \bar{v}_{2\_cm\_t0} = \begin{bmatrix} 0.7887 \\ 0.5 \\ 0 \end{bmatrix};\ \bar{v}_{3\_cm\_t0} = \begin{bmatrix} 0.7887 \\ 1.5 \\ 0 \end{bmatrix}$$

The trajectories obtained for each body and for the center of masses expressed in the inertial frame are seen in Figure 2-2. In Figure 2-3, these trajectories are given with respect to the not-rotating frame centered on the center of masses and rotating frame centered on the center of masses.
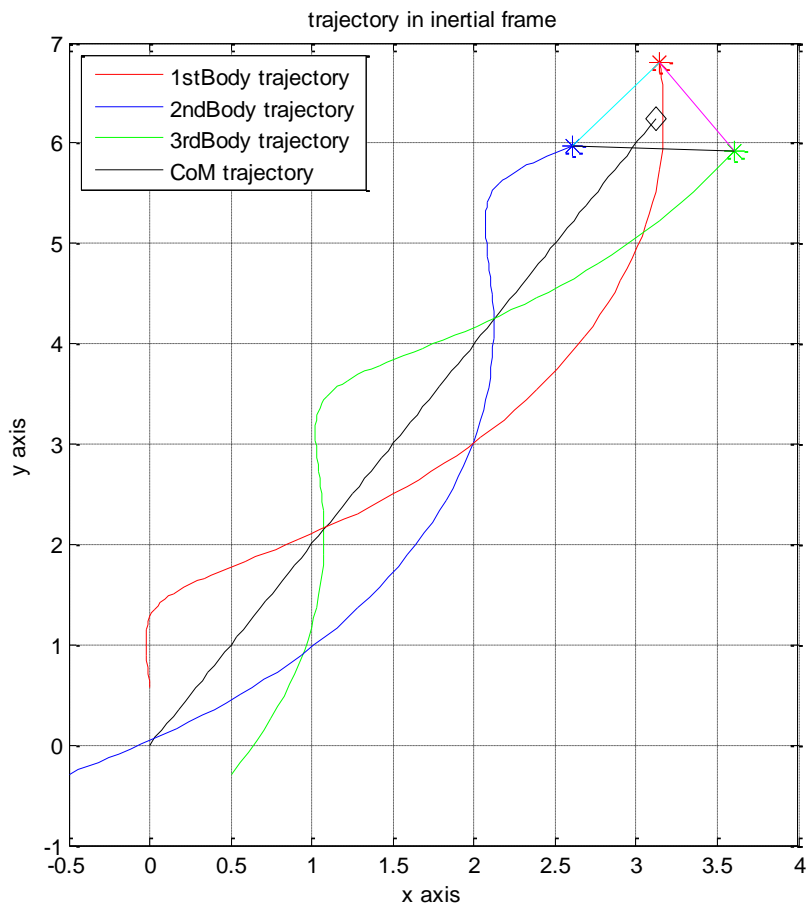
Figure 2-2. Trajectory of three bodies in inertial frame
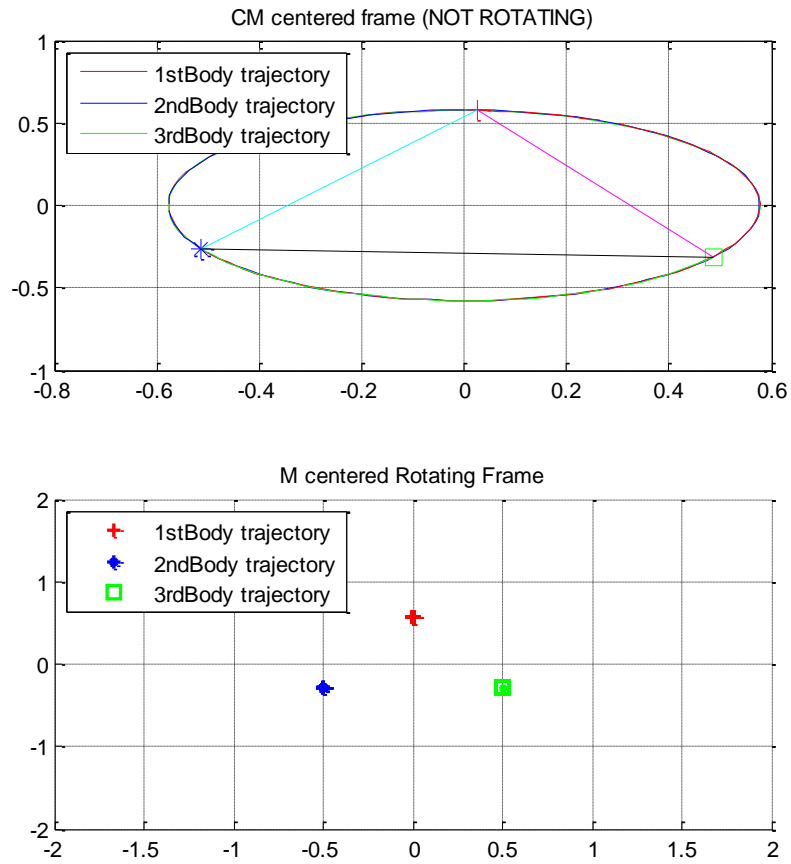
Figure 2-3. Trajectory of three bodies in not-rotating and rotating frame

The motion in inertial frame and not rotating frame will be similar when the initial velocity of the center of masses is given as zeros. Figure 2-4 and Figure 2-5 show this result:
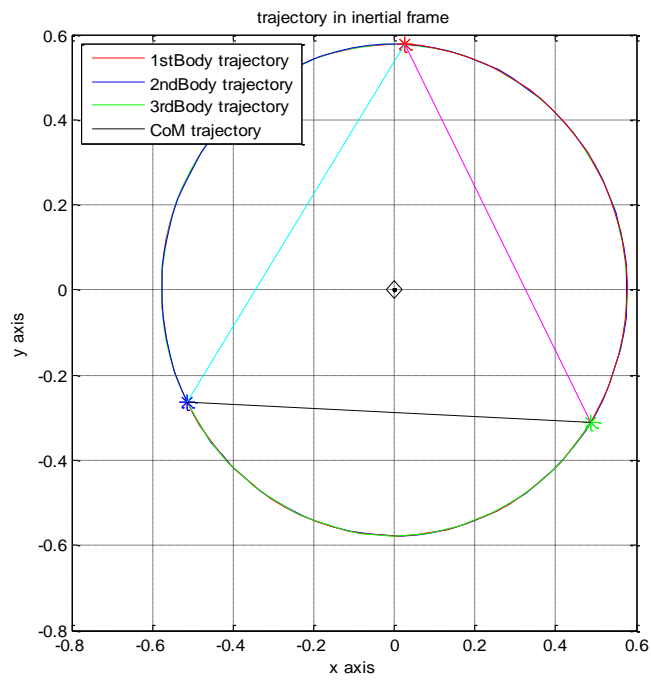
Figure 2-4. Trajectory of three bodies in inertial frame with not-moving CoM
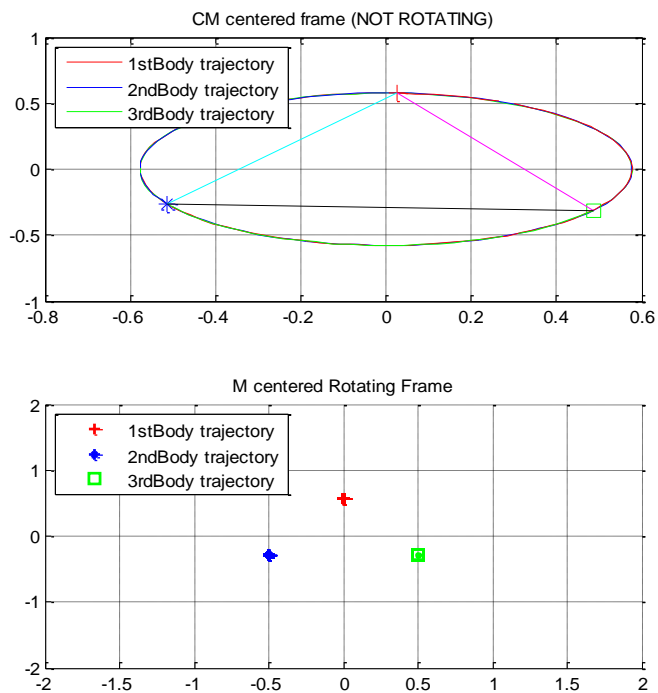
Figure 2-5. Three bodies in not-rotating and rotating frames, not-moving CoM

As mentioned at the beginning of this subsection, integrals of motion give an idea about the stability and/or accuracy of the integration computation. For instance, integration error accumulation become more pronounced after the third period when this simulation is run for a long time (See Figure 2-6). In these simulations fourth order Runge-Kutta method is used. The changes on the integral of motion for long term trajectories are shared on Figure 2-7 to Figure 2-9. Even so, it is seen that the changes on integrals of motion are in an acceptable range at first three periods. In this simulation sample time are taken as dt = 7.1677e-4 revolution, actually when it's thought that 1 revolution is a 1 year time, this sample time refers to the 1 hour, this comparison is given in order to describe the time values taken in the simulation.
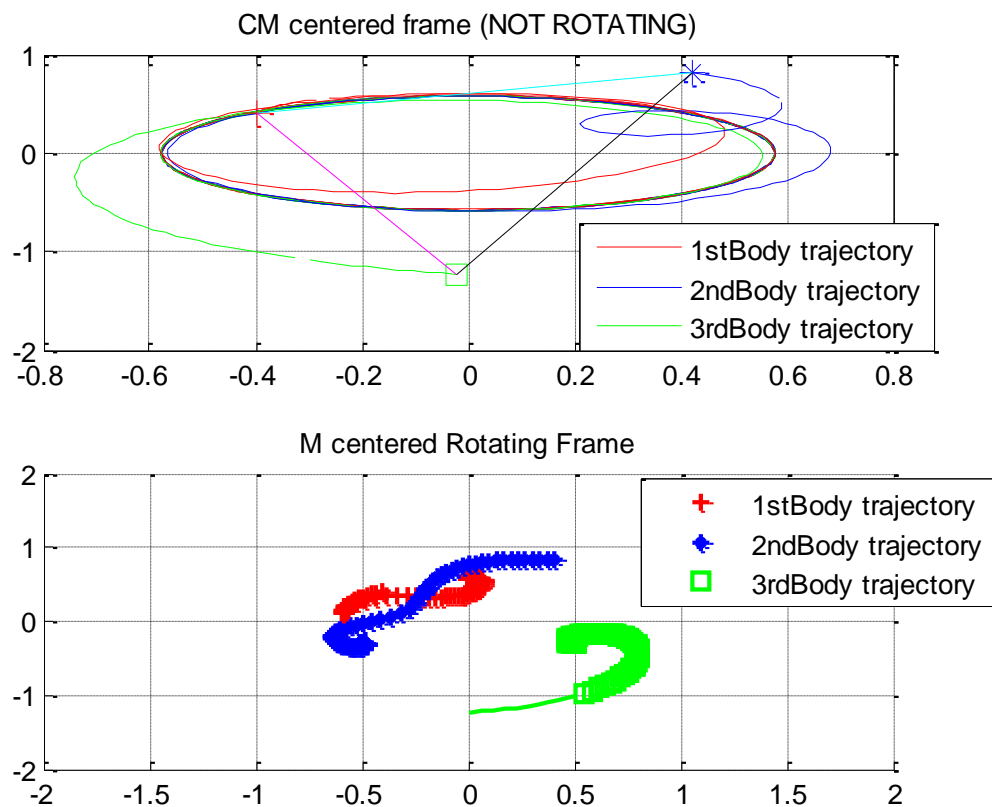
Figure 2-6. Long term trajectories in inertial frame (sampling time:1 hour)
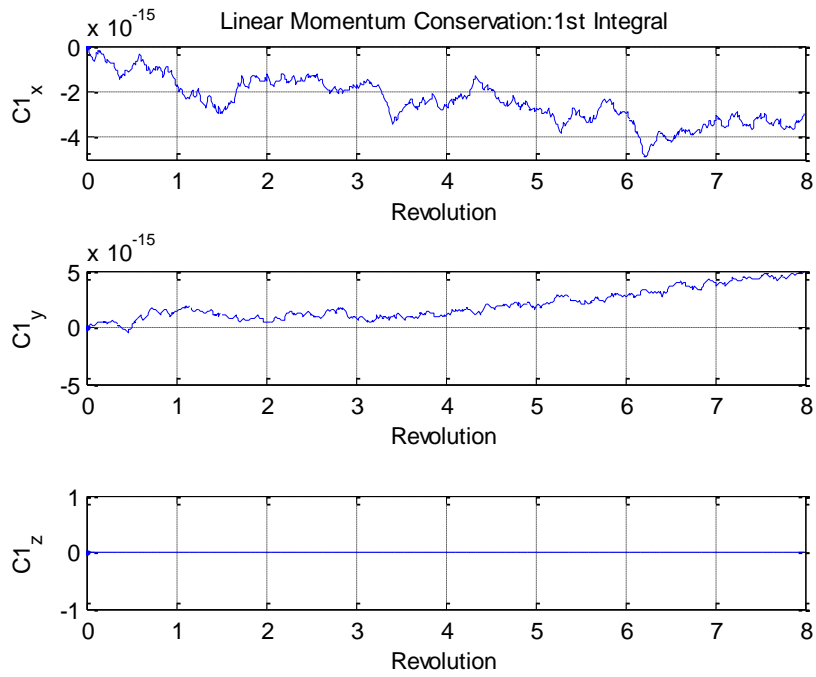
Figure 2-7. Linear momentum conservation 1st integral (sampling time: 1 hour)
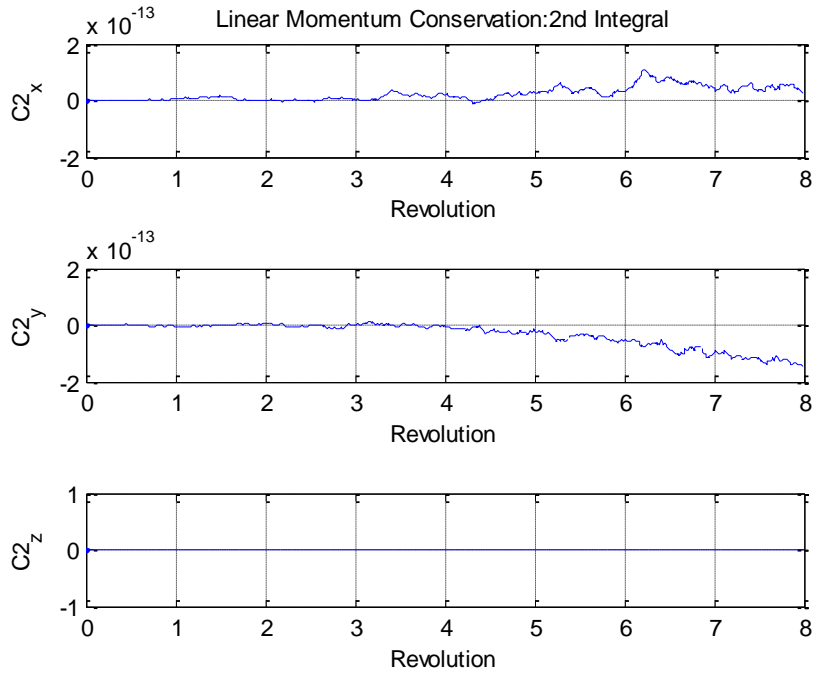
Figure 2-8. Linear momentum conservation 2nd integral (sampling time: 1 hour)

32
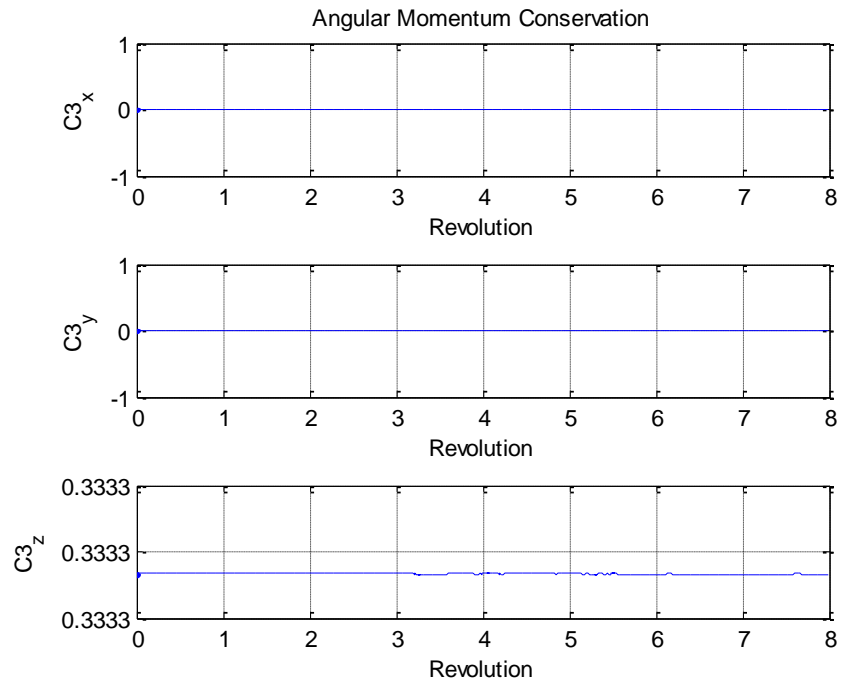
Figure 2-9. Angular momentum conservation (sampling time: 1 hour)
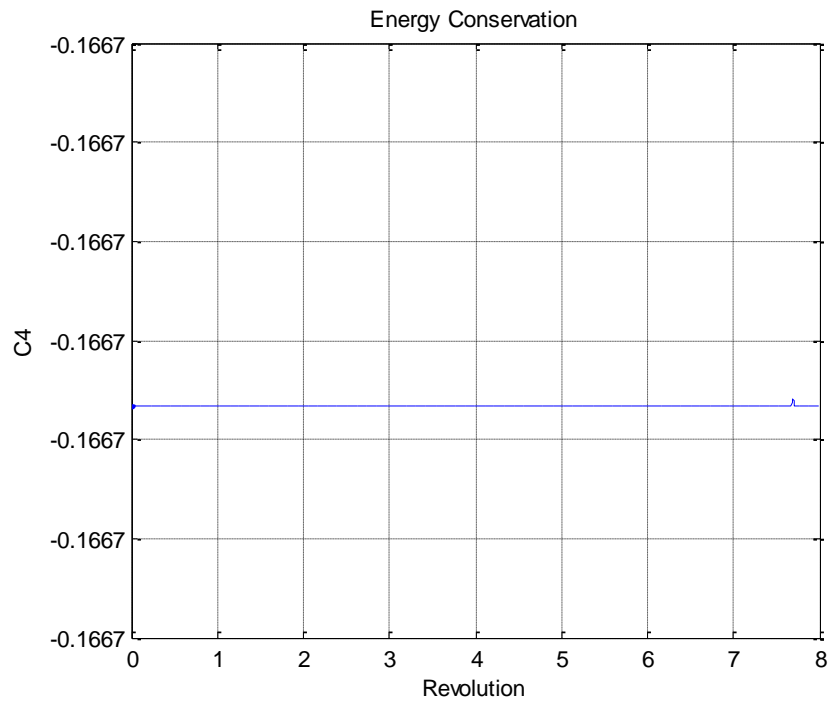
Figure 2-10. Energy conservation (sampling time: 1 hour)

Actually, the value of the sampling time also is critical. Regarding to the simulations run for the different sample times, it is seen that when a larger sampling time value is selected (i.e. dt=5 hours), the accuracy of the integration degrades but long time simulation results are more resistant (Figure 2-11), when a smaller sample time value is selected (i.e. dt=6 minutes), the accuracy obtained for each cycle of the first periods are more high, integrations are good but, decompositions starts suddenly and large divergence are seen at a long time simulation (Figure 2-13). In our case, it is seen that the second integrals of the linear momentum constants are more dominant, the constants which are related to the velocity (C2). For that reason, the C2's results and trajectories are given to show the sampling time value effect.

For a dt= 5 hours:
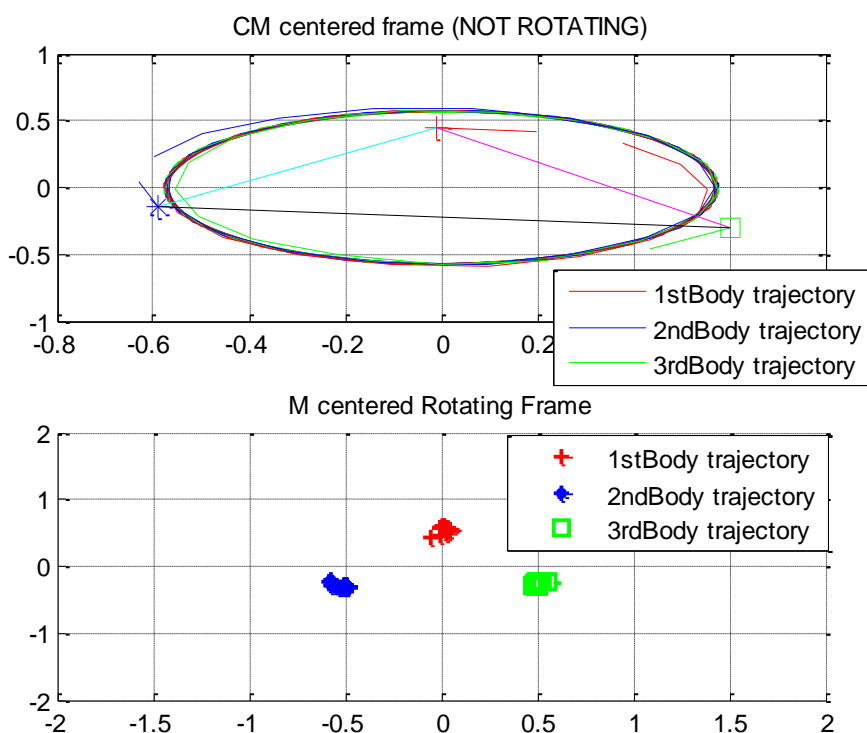
Figure 2-11. Long term trajectories in inertial frame (sampling time: 5 hours)
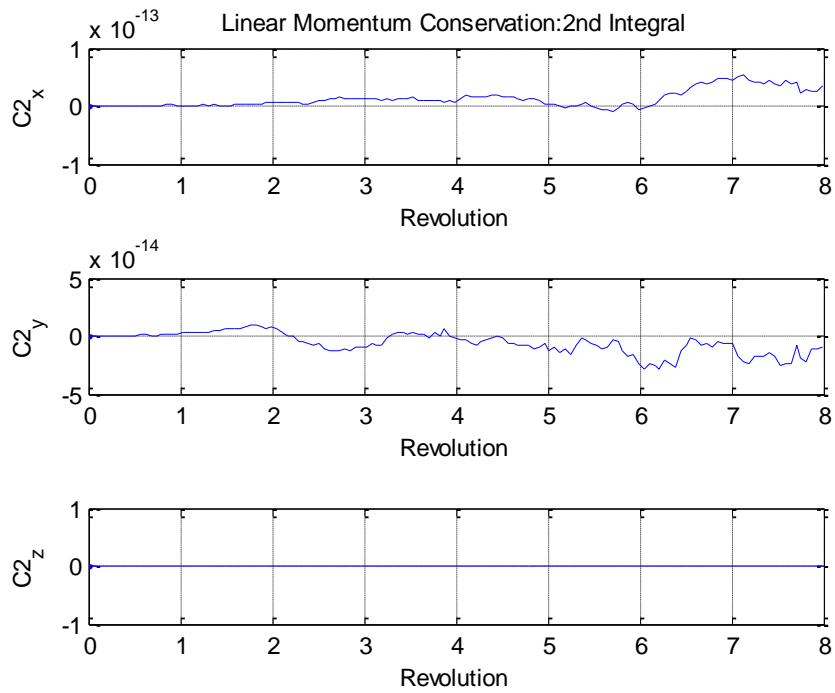
Figure 2-12. Linear momentum conservation 2nd integral (sampling time: 5 hr*s*)

For a dt= 1/10 hours=6 minutes:
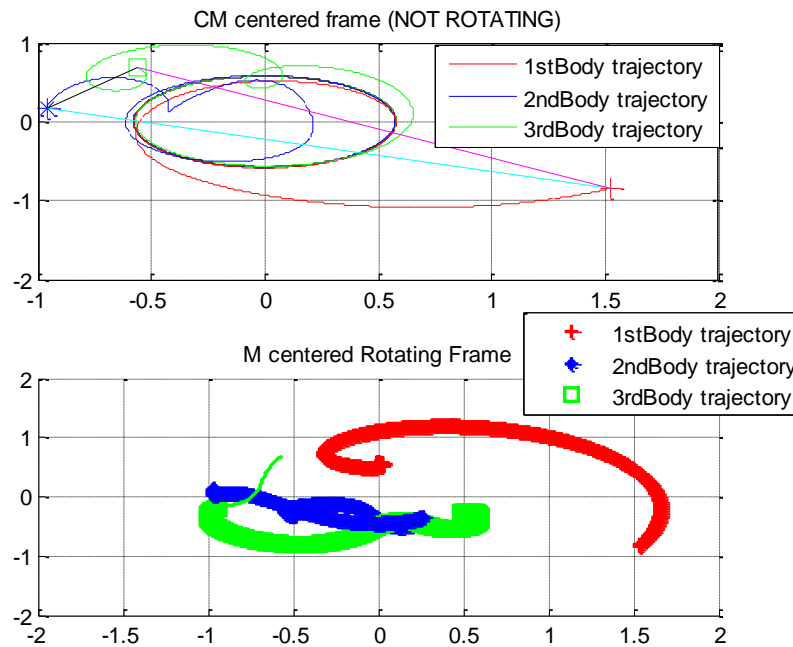
Figure 2-13. Long term trajectories in inertial frame (sampling time: 6 min)
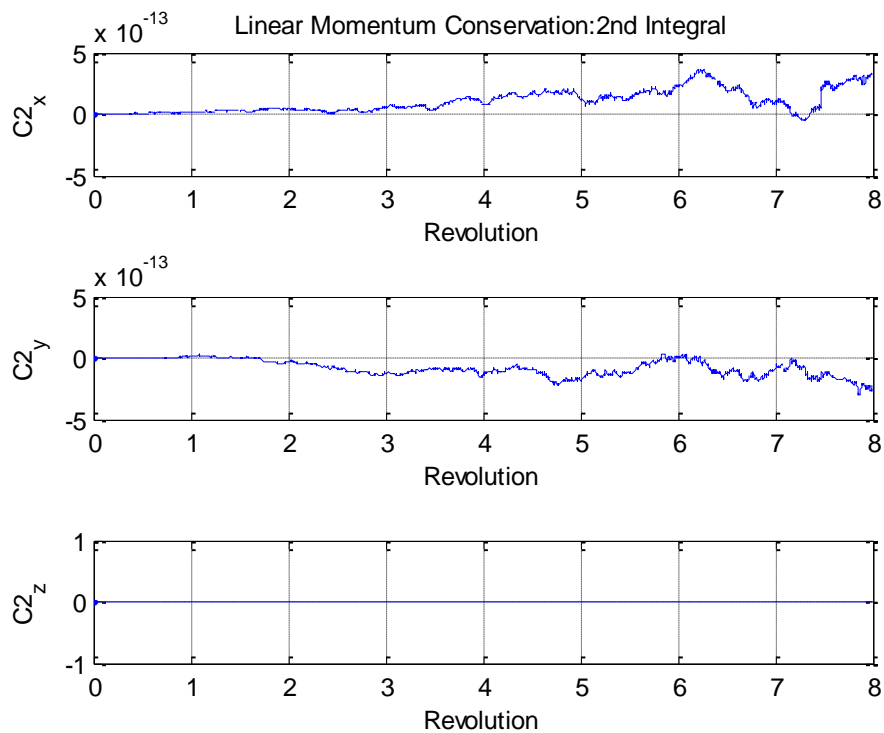
Figure 2-14. Linear momentum conservation 2nd integral (sampling time: 6 min.)

2.1.4.2. Case study II: Sun-Earth/Moon-Satellite simulation

Here, the real mass values of the satellite, Sun, Earth+Moon (considered together), are given in order to define the motion of these three bodies. Let describe the motion on rotating frame. Equations of motion expressed at this frame having origin at the center of masses, in vector form:

$$\ddot{\bar{r}}_{1cm} = \frac{Gm_2\bar{r}_{12}}{|\bar{r}_{12}|^3} + \frac{Gm_3\bar{r}_{13}}{|\bar{r}_{13}|^3} - \left(2\widetilde{\Omega}\,\dot{\bar{r}}_{1cm} + \dot{\widetilde{\Omega}}\,\bar{r}_{1cm} + \widetilde{\Omega}^2\bar{r}_{1cm}\right)$$

$$\ddot{\bar{r}}_{2cm} = \frac{Gm_1\bar{r}_{21}}{|\bar{r}_{21}|^3} + \frac{Gm_3\bar{r}_{23}}{|\bar{r}_{23}|^3} - \left(2\widetilde{\Omega}\,\dot{\bar{r}}_{2cm} + \dot{\widetilde{\Omega}}\,\bar{r}_{2cm} + \widetilde{\Omega}^2\bar{r}_{2cm}\right) \qquad \text{Eq. 2-37}$$

$$\ddot{\bar{r}}_{3cm} = \frac{Gm_1\bar{r}_{31}}{|\bar{r}_{31}|^3} + \frac{Gm_2\bar{r}_{32}}{|\bar{r}_{32}|^3} - \left(2\widetilde{\Omega}\,\dot{\bar{r}}_{3cm} + \dot{\widetilde{\Omega}}\,\bar{r}_{3cm} + \widetilde{\Omega}^2\bar{r}_{3cm}\right)$$

Here $\widetilde{\Omega}$ is the skew symmetric matrix containing angular rate of the frame centered at center of masses (non-rotating frame) with respect to inertial frame. So, now the motion can be defined in synodic frame using real mass values and distances of the Sun first body, Earth and Moon considered together as second body and Satellite is third body. The synodic reference frame is used, with its origin at the center-of-mass of the Sun and Earth+Moon (hereafter Earth-Moon pair is called as Bary) system, the x-axis passing through the Sun and the Bary, and oriented towards the Bary, and the z-axis perpendicular to the ecliptic plane [59]. The formal representation and the definition of the synodic frame is given in Appendix-A-ii.

So, the values taken are:

$\boldsymbol{m_{SUN}} = 1.9886294261178590 \times 10^{30}\ kg; \boldsymbol{m_{BARY}} = 6.045476730900739 \times 10^{24}\ kg$

$\boldsymbol{m_{SAT}} = 1.0\ \times 10^3\ kg;\ \boldsymbol{m_{TOTAL}} = 1.98863547655321 \times 10^{30}\ kg$

In the simulation, the total mass is taken as equal to 1, unit mass, so;

$m_{SUN\_unit} = 0.999996959987480;\ m_{BARY\_unit} = 3.040012519674380\text{e-}6$

$m_{SAT\_unit} = 5.028573684083036\text{e-}28;\ \ m_{TOTAL\_unit} = 1$

In this case, only rotational motion is considered and simulated to imitate the nature, for that reason initial translational velocities are given zeros for all of the bodies to obtain non-translating motion. The distance between two massive bodies is taken as unit distance, so let initial unit positions for bodies are to be:

37

$$\bar{r}_{1\_cm\_t0} = \begin{bmatrix} 0 \\ 0 \\ 0 \end{bmatrix}; \ \bar{r}_{2\_cm\_t0} = \begin{bmatrix} 1 \\ 0 \\ 0 \end{bmatrix}; \ \bar{r}_{3\_cm\_t0} = \begin{bmatrix} 0.992 \\ 0 \\ -0.001783 \end{bmatrix}$$

Trajectories obtained from simulation are presented in the following figures. Here, the results are obtained as expected: the orbital motion of the Bary around the center of masses (Figure 2-15) and the trajectory of the Sun around center of masses (Figure 2-16). The initial position of the satellite is near libration points between Sun and Bary, L1. According to its energy level its motion also is obtained as expected as seen in Figure 2-17. The details about the motions around libration points is discussed in details in the next chapters.
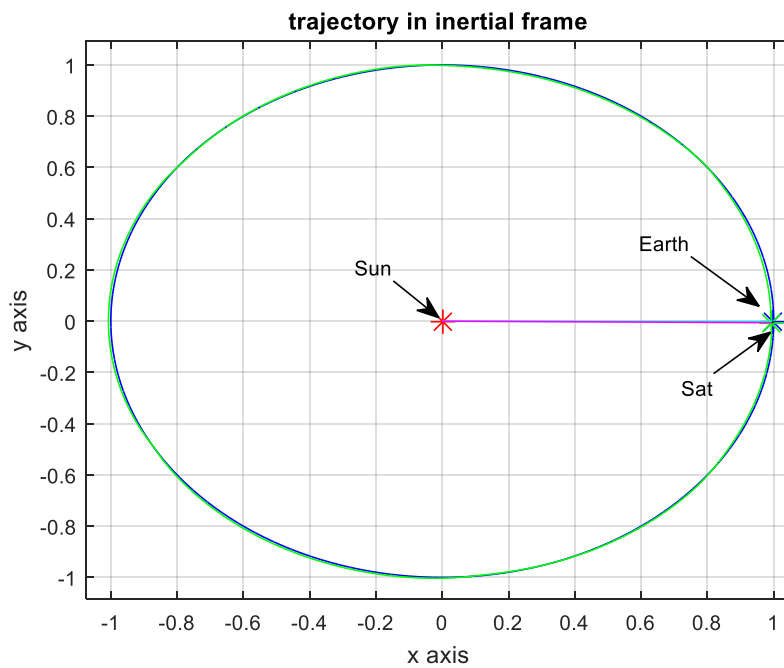
Figure 2-15. Trajectories for Sun-Earth-Satellite trio
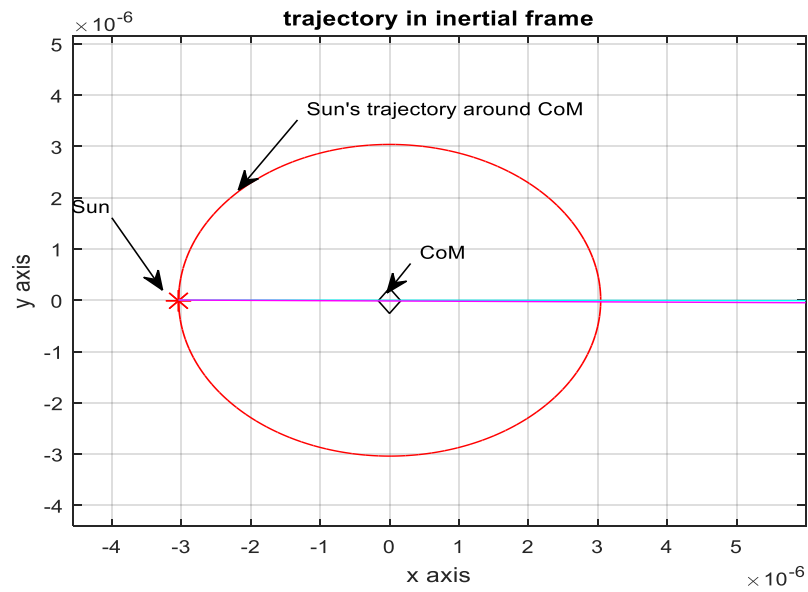
Figure 2-16. Trajectories of Sun around CoM
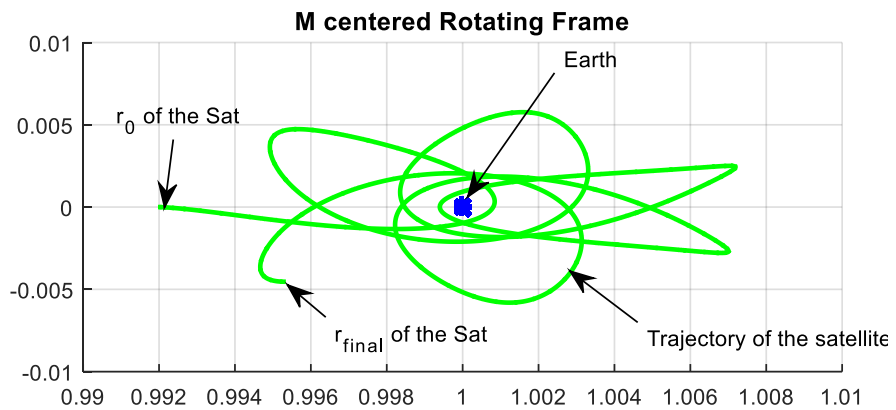
Figure 2-17. Trajectories of satellite around Earth

The simulation stability is checked by examining the propagation of linear momentum, angular momentum and energy. The results are presented in Figure 2-18.
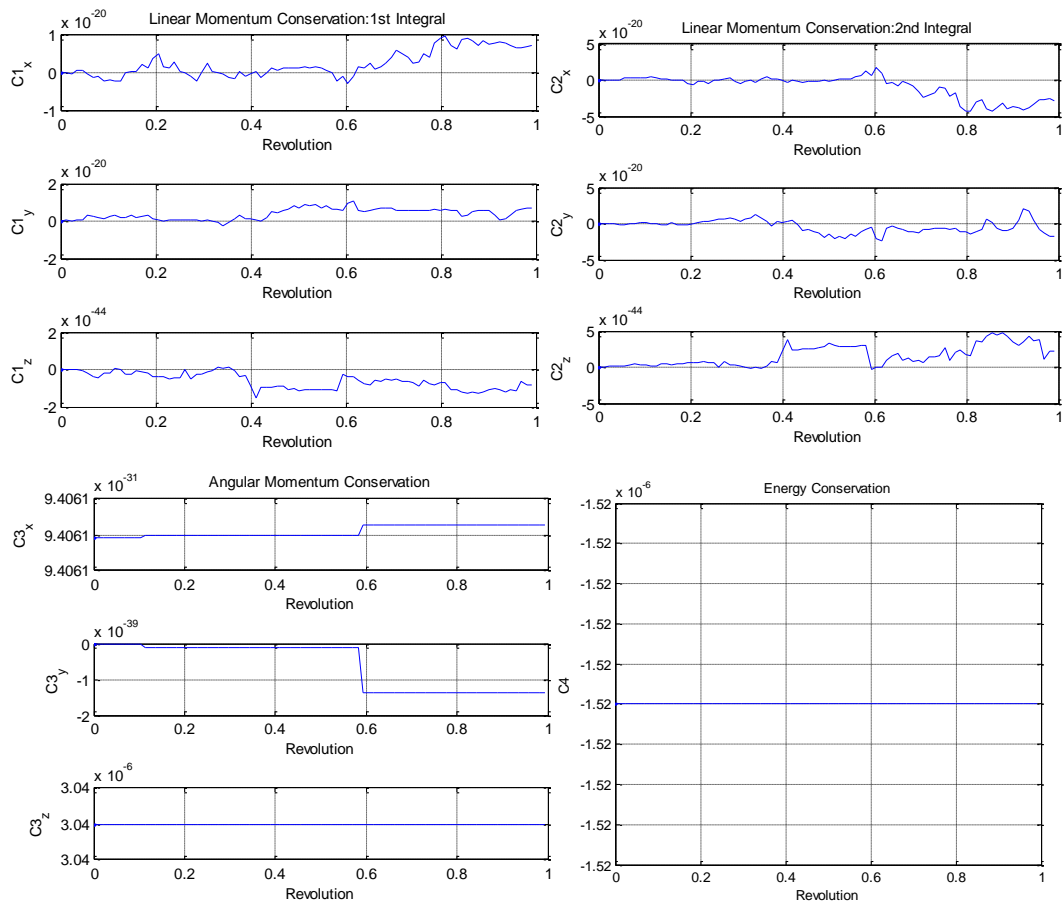
Figure 2-18. Integrals of motion

As may be observed from Figure 2-18, total linear momentum, total angular momentum and total energy are almost constant. This proves the accuracy of simulation. The trajectory of the third body is quite dependent on the initial conditions; the details about that subject are presented in Appendix-G through Poincare Maps.

2.2. Restricted three-body problem

The restricted three body problem is a simplified version and special case of the three-body problem: One of the bodies has negligible masses compared the two

others. In this case, the motion of two massive bodies, let's call them primaries, can be defined using two-body problem and the third body with negligible mass that navigates in the field of primaries. Practically it is reasonable to neglect the mass of the third body when this body is a satellite or an asteroid. For Sun-Earth system, or Sun-Jupiter, it is also seen that the motion of the planet around Sun is considered circular. So, in that case, the motion of the third body is studied using "circular restricted three body problem". The five equilibrium points of this system, called libration points or Lagrange points – details given in the next chapters – remain fix in the reference system which is rotating with primaries. For that reason, it is possible and useful for computations to use Synodic reference frame to study the motion [57, 61, 62].

2.2.1. Equations of Motion

Equations of motion for circular restricted three-body problem can be rewritten as follows. As the equations are expressed in the synodic reference frame, first the angular motion of this reference frame with respect to the inertial frame is computed. This is related to the primaries' mass and distance between them.

$$\boldsymbol{\omega} = \sqrt{\frac{G(m_1 + m_2)}{R^3}} \qquad \text{Eq. 2-38}$$

$$\begin{bmatrix} \ddot{x} \\ \ddot{y} \\ \ddot{z} \end{bmatrix} = \begin{bmatrix} \omega^2 x + 2\omega\dot{y} - \dfrac{Gm_1(x + x_1)}{r_1^3} - \dfrac{Gm_2(x - x_2)}{r_2^3} \\ \omega^2 y - 2\omega\dot{x} - \dfrac{Gm_1 y}{r_1^3} - \dfrac{Gm_2 y}{r_2^3} \\ -\dfrac{Gm_1 z}{r_1^3} - \dfrac{Gm_2 z}{r_2^3} \end{bmatrix} \qquad \text{Eq. 2-39}$$

where;

$$r_1 = \sqrt{(x + x_1)^2 + y^2 + z^2} \qquad\qquad \text{Eq. 2-40}$$

$$r_2 = \sqrt{(x - x_2)^2 + y^2 + z^2} \qquad\qquad \text{Eq. 2-41}$$

The description of the positions is presented in Figure 2-19:
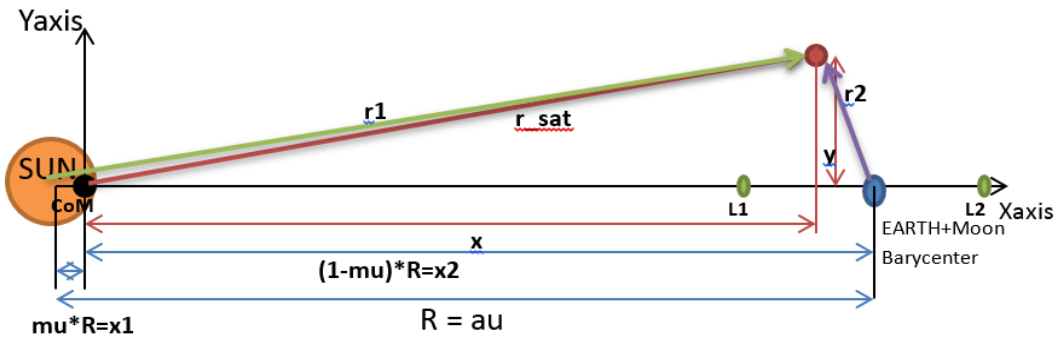
Figure 2-19. Representation of Sun-Bary-Spacecraft in synodic reference frame

2.2.2. Dimensionless Equations of Motion

It is also very useful for computations to write these equations with dimensionless parameters. To do it, conservation of linear momentum is used:

$$-m_1 x_1 + m_2 x_2 = 0 \Rightarrow x_1 = \frac{m_2}{m_1} x_2 \qquad\qquad \text{Eq. 2-42}$$

$$R = r_2 - r_1 = r_{12} = x_2 - (-x_1) = x_2 + x_1 \Rightarrow x_2 = r_{12} - x_1 \qquad \text{Eq. 2-43}$$

$$\Rightarrow x_1 = \frac{m_2}{m_1}(R - x_1) \Rightarrow x_1 = \left(\frac{m_2}{m_1 + m_2}\right) R \qquad\qquad \text{Eq. 2-44}$$

42

Let define:

$$\mu = \left(\frac{m_2}{m_1 + m_2}\right)$$

Eq. 2-45

So,

$$x_1 = \mu R$$

Eq. 2-46

$$x_2 = (1 - \mu)R$$

Eq. 2-47

and;

$$m_1 = m_2 \frac{1-\mu}{\mu}$$

Eq. 2-48

$$m_1 + m_2 = \frac{m_2}{\mu}$$

Eq. 2-49

$$\omega = \sqrt{\frac{G(m_1 + m_2)}{R^3}} \Rightarrow G = \frac{\omega^2 R^3 \mu}{m_2}$$

Eq. 2-50

First properties Eq. 2-46 and Eq. 2-47 are substituted in differential equations, so we get:

$$\begin{bmatrix} \ddot{x} \\ \ddot{y} \\ \ddot{z} \end{bmatrix} = \begin{bmatrix} \omega^2 x + 2\omega\dot{y} - \dfrac{Gm_1(x + \mu R)}{r_1^3} - \dfrac{Gm_2(x - (1 - \mu)R)}{r_2^3} \\ \omega^2 y - 2\omega\dot{x} - \dfrac{Gm_1 y}{r_1^3} - \dfrac{Gm_2 y}{r_2^3} \\ -\dfrac{Gm_1 z}{r_1^3} - \dfrac{Gm_2 z}{r_2^3} \end{bmatrix}$$

Eq. 2-51

Then properties Eq. 2-48 is substituted and x is divided by the distance between mass R (for Sun-Earth system, R is astronomic unit), so $x = \bar{x}R$, $y = \bar{y}R$, and $z = \bar{z}R$ here $\bar{x}$ is unit distance; then r_1 and r_2 became:

$$r_1 = \sqrt{[R(\bar{x} + \mu)]^2 + R^2\bar{y}^2 + R^2\bar{z}^2} = R\bar{r_1}$$

$$r_2 = \sqrt{\left[R(\bar{x} - (1 - \mu))\right]^2 + R^2\bar{y}^2 + R^2\bar{z}^2} = R\bar{r_2}$$

and $\dot{x} = \dot{\bar{x}}\omega R, \ \dot{y} = \dot{\bar{y}}\omega R$,

Then, differential equations are:

$$\ddot{x} = \omega^2\bar{x}R + 2\omega\dot{\bar{y}}\omega R - \frac{Gm_2R(\bar{x} + \mu)}{R^3\bar{r_1}^3}\left(\frac{1 - \mu}{\mu}\right)$$

$$- \frac{Gm_2R(\bar{x} - (1 - \mu))}{R^3\bar{r_2}^3}$$

$$\ddot{y} = \omega^2\bar{y}R - 2\omega\dot{\bar{x}}\omega R - \frac{Gm_2\bar{y}R}{R^3\bar{r_1}^3}\left(\frac{1 - \mu}{\mu}\right) - \frac{Gm_2\bar{y}R}{R^3\bar{r_2}^3}$$

$$\ddot{z} = -\frac{Gm_2\bar{z}R}{R^3\bar{r_1}^3}\left(\frac{1 - \mu}{\mu}\right) - \frac{Gm_2\bar{z}R}{R^3\bar{r_2}^3}$$

Finally, property Eq. 2-50 is substituted:

$$\ddot{x} = \omega^2\bar{x}R + 2\omega\dot{\bar{y}}\omega R - \left(\frac{\ddot{\omega}^2R^3\mu}{m_2}\right)\frac{m_2R(\bar{x} + \mu)}{R^3\bar{r_1}^3}\left(\frac{1 - \mu}{\mu}\right)$$

$$- \left(\frac{\omega^2R^3\mu}{m_2}\right)\frac{m_2R(\bar{x} - (1 - \mu))}{R^3\bar{r_2}^3}$$

$$\ddot{y} = \omega^2\bar{y}R - 2\omega\dot{\bar{x}}\omega R - \left(\frac{\omega^2R^3\mu}{m_2}\right)\frac{m_2\bar{y}R}{R^3\bar{r_1}^3}\left(\frac{1 - \mu}{\mu}\right)$$

$$- \left(\frac{\omega^2R^3\mu}{m_2}\right)\frac{m_2\bar{y}R}{R^3\bar{r_2}^3}$$

$$\ddot{z} = -\left(\frac{\omega^2R^3\mu}{m_2}\right)\frac{m_2\bar{z}R}{R^3\bar{r_1}^3}\left(\frac{1 - \mu}{\mu}\right) - \left(\frac{\omega^2R^3\mu}{m_2}\right)\frac{m_2\bar{z}R}{R^3\bar{r_2}^3}$$

So, the dimensionless accelerations are $\ddot{x} = \ddot{\bar{x}}\omega^2 R,\ \ddot{y} = \ddot{\bar{y}}\omega^2 R$,

When both left side and right side of the equations set divided by $\omega^2 R$:

$$\ddot{\bar{x}} = \bar{x} + 2\dot{\bar{y}} - \left(\frac{R^2\mu}{m_2}\right)\frac{m_2 R(\bar{x} + \mu)}{R^3 \bar{r}_1^3}\left(\frac{1 - \mu}{\mu}\right)$$
$$- \left(\frac{R^2\mu}{m_2}\right)\frac{m_2 R(\bar{x} - (1 - \mu))}{R^3 \bar{r}_2^3}$$

Eq. 2-56

$$\ddot{\bar{y}} = \bar{y} - 2\dot{\bar{x}} - \left(\frac{R^2\mu}{m_2}\right)\frac{m_2 \bar{y}R}{R^3 \bar{r}_1^3}\left(\frac{1 - \mu}{\mu}\right) - \left(\frac{R^2\mu}{m_2}\right)\frac{m_2 \bar{y}R}{R^3 \bar{r}_2^3}$$

$$\ddot{\bar{z}} = -\left(\frac{R^2\mu}{m_2}\right)\frac{m_2 \bar{z}R}{R^3 \bar{r}_1^3}\left(\frac{1 - \mu}{\mu}\right) - \left(\frac{R^2\mu}{m_2}\right)\frac{m_2 \bar{z}R}{R^3 \bar{r}_2^3}$$

After some simplifications, the dimensionless equations of motion set obtained are:

$$\begin{bmatrix}\ddot{\bar{x}} \\ \ddot{\bar{y}} \\ \ddot{\bar{z}}\end{bmatrix} = \begin{bmatrix}\bar{x} + 2\dot{\bar{y}} - \dfrac{(1 - \mu)(\bar{x} + \mu)}{\bar{r}_1^3} - \dfrac{\mu(\bar{x} - (1 - \mu))}{\bar{r}_2^3} \\ \bar{y} - 2\dot{\bar{x}} - \dfrac{(1 - \mu)\bar{y}}{\bar{r}_1^3} - \dfrac{\mu\bar{y}}{\bar{r}_2^3} \\ -\dfrac{(1 - \mu)\bar{z}}{\bar{r}_1^3} - \dfrac{\mu\bar{z}}{\bar{r}_2^3}\end{bmatrix}$$

Eq. 2-57

Here, it is important to note that in this equation set, disturbances are not considered in the motion, let it called this set as non-perturbed equation of motion. And this equation set is expressed in synodic reference frame having origin at the center of mass.

It may be useful also to express this equation set by taking L1 libration point (or L2) as center, when an orbit is designed near L1 (or L2). So, in that case, it is only needed to transport the frame with a distance of L1 (or L2) with respect to center of mass. As L1 and L2 are located on the x axis, only the x related parameters will be shifted. So, new sets obtained for L1 (or L2) originated reference frame are as follows:

$$
\begin{bmatrix} \ddot{\bar{x}} \\ \ddot{\bar{y}} \\ \ddot{\bar{z}} \end{bmatrix}
$$

$$
= \begin{bmatrix} (\bar{x} + L_x) + 2\dot{\bar{y}} - \dfrac{(1-\mu)(\bar{x} + L_x + \mu)}{\bar{r}_1^3} - \dfrac{\mu(\bar{x} + L_x - (1-\mu))}{\bar{r}_2^3} \\[2mm] \bar{y} - 2\dot{\bar{x}} - \dfrac{(1-\mu)\bar{y}}{\bar{r}_1^3} - \dfrac{\mu\bar{y}}{\bar{r}_2^3} \\[2mm] -\dfrac{(1-\mu)\bar{z}}{\bar{r}_1^3} - \dfrac{\mu\bar{z}}{\bar{r}_2^3} \end{bmatrix} \qquad \text{Eq. 2-58}
$$

here;

$$
\bar{r}_1 = \sqrt{(\bar{x} + L_x + \mu)^2 + \bar{y}^2 + \bar{z}^2} = \bar{r}_1 \qquad \text{Eq. 2-59}
$$

$$
\bar{r}_2 = \sqrt{(\bar{x} + L_x - (1-\mu))^2 + \bar{y}^2 + \bar{z}^2} \qquad \text{Eq. 2-60}
$$

where L_x is the x position of the collinear libration points with respect to the center of mass.

So, it is possible to define the shape of orbit of the third body (i.e. maximum and minimum distances from libration point, etc.) since the x, y, z positions are measured from the libration point considered.

2.2.3. Jacobi Integral

Jacobi Integral is also an important term used in circular restricted three-body problem. This is an additional integral of motion related to the energy. The equation given previous section can be rewritten in terms of potential energy, since gravitational forces and position of the body can be considered as the elements of the potential energy [60, 62]. So, let define:

$$U(x, y, z) = \frac{1}{2}(x^2 + y^2) + \frac{1 - \mu}{r_1} + \frac{\mu}{r_2} \qquad \text{Eq. 2-61}$$

and;

$$\begin{bmatrix} \ddot{x} \\ \ddot{y} \\ \ddot{z} \end{bmatrix} = \begin{bmatrix} 2\dot{y} + \dfrac{\partial U}{\partial x} \\ -2\dot{x} + \dfrac{\partial U}{\partial y} \\ \dfrac{\partial U}{\partial z} \end{bmatrix} \qquad \text{Eq. 2-62}$$

It is well known that the change of the potential energy in time is equal negatively to the change of the kinetic energy in time. Since the kinetic energy is related to the velocity square:

$$K = \frac{1}{2}(\dot{x}^2 + \dot{y}^2 + \dot{z}^2) \qquad \text{Eq. 2-63}$$

So;

$$\frac{d}{dt}\left[\frac{1}{2}(\dot{x}^2 + \dot{y}^2 + \dot{z}^2)\right] = \frac{dU}{dt} \qquad \text{Eq. 2-64}$$

Integrating this gives:

$$\left[\frac{1}{2}(\dot{x}^2 + \dot{y}^2 + \dot{z}^2)\right] + c_1 = U + c_2 \qquad \text{Eq. 2-65}$$

Let define that $c_2 - c_1 = -C/2$, so:

$$2U - (\dot{x}^2 + \dot{y}^2 + \dot{z}^2) = C \Longrightarrow$$

$$C = (x^2 + y^2) + 2\frac{1 - \mu}{r_1} + 2\frac{\mu}{r_2} - (\dot{x}^2 + \dot{y}^2 + \dot{z}^2) \qquad \text{Eq. 2-66}$$

This constant C is called as Jacobi Integral or Jacobi Energy since it is related to the total energy of the particle. This value is used to recognize some particles such

comets even after close encounters of them with planets (called Tisserand criterion). The value of the Jacobi Integral does not change even if orbital parameters of the comet substantially changed. Jacobi integral is also used to define spatial regions, called Hill's surfaces of zero velocity that gives the boundaries of the third body motion. This is described in detailed in the sub-chapter-2.4.

2.3. Libration points

For any two orbiting massive bodies about their center of masses, there exist five equilibrium (stationary) points where the force acting on a third body (having very small mass compared to the two others) is zeros. Those equilibrium points are called Lagrange points, after Joseph Lagrange, Italian-French mathematician, who discovered those stationary points while studying the restricted three-body problem. Restricted refers that one of the three bodies have very small and ignorable mass compared to two others. Since the net force is zeros at those points, when a particle is initially stay here, it remains here forever. In synodic coordinates, Lagrange points have zero velocity, it means that the attraction of the massive bodies is exactly canceled by the centrifugal force and they describe circular orbits. In particular, the position of the Lagrange points with respect to the two main bodies remains always the same. Today, it is well-known that, three-body problem cannot be solved in closed form and it has chaotic properties. Therefore, as Lagrange did, restricted approximation is a reasonable approach to obtain solution. It is clear that the two massive bodies are considered as Earth and Moon for space missions related to the Moon exploration. For deep space missions this set can be taken as Sun and the Earth-Moon barycenter or Sun and planet that the third particle, for example spacecraft navigates near it. The following two subsections describe the computation of the position of the Lagrange points and their stability respectively [60, 63, 64].

2.3.1. Computation of the Libration Points locations

The force equation can be rewritten as follows by considering that the force acting on a third body at libration points is zeros. Let M_1 and M_2 are two primary masses, m is the mass of the third body, $\vec{r}_1$ and $\vec{r}_2$ are their position vector, and $\vec{r}$ is the position vector of the third body with respect to center of mass. So, the total force exerted on the third body is:

$$\vec{F} = -\frac{GM_1 m}{|\vec{r} - \vec{r}_1|^3}(\vec{r} - \vec{r}_1) - \frac{GM_2 m}{|\vec{r} - \vec{r}_2|^3}(\vec{r} - \vec{r}_2) \qquad \text{Eq. 2-67}$$

Here, the position vector $\vec{r}_1$ and $\vec{r}_2$ are the function of time due to M_1 and M_2 are orbiting around their center of mass. As seen from the previous sub-section, the straightforward way of finding libration points and computing force acting on the third body is to transform rotating frame to a non-rotating frame that two primary bodies have fixed positions, in our case is synodic reference frame. So, angular rate of the system given by Kepler's law is:

$$\omega = \sqrt{\frac{G(M_1 + M_2)}{R^3}} \rightarrow G = \frac{\omega^2 R^3}{(M_1 + M_2)} \qquad \text{Eq. 2-68}$$

And from the restricted three body dynamics, we know that:

$$\vec{F_x} = M_3 \ddot{\vec{x}} = \omega^2 x - \frac{GM_1(x + x_1)}{r_1^3} - \frac{GM_2(x - x_2)}{r_2^3} \qquad \text{Eq. 2-69}$$

$$M_3 \ddot{\vec{x}} = \omega^2 x - \frac{\omega^2 R^3}{(M_1 + M_2)} \frac{M_1(x + x_1)}{r_1^3} - \frac{\omega^2 R^3}{(M_1 + M_2)} \frac{M_2(x - x_2)}{r_2^3} \qquad \text{Eq. 2-70}$$

$$M_3 \ddot{\vec{x}} = \omega^2 \left(x - \frac{M_1}{(M_1 + M_2)} \frac{R^3(x + x_1)}{r_1^3} - \frac{M_2}{(M_1 + M_2)} \frac{R^3(x - x_2)}{r_2^3} \right)$$ Eq. 2-71

Let define;

$$\alpha = \frac{M_2}{(M_1 + M_2)}, \quad \text{and} \quad \beta = \frac{M_1}{(M_1 + M_2)}$$

$$x_1 = \frac{M_2}{(M_1 + M_2)} R = \alpha R, \quad \text{and} \quad x_2 = \frac{M_1}{(M_1 + M_2)} R = \beta R$$

So finally we have;

$$\left| \vec{F_x} \right| = \omega^2 \left(x - \frac{\beta R^3 (x + \alpha R)}{[(x + \alpha R)^2 + y^2]^{3/2}} - \frac{\alpha R^3 (x - \beta R)}{[(x - \beta R)^2 + y^2]^{3/2}} \right)$$ Eq. 2-72

$$\left| \vec{F_y} \right| = \omega^2 \left(y - \frac{\beta R^3 (y)}{[(x + \alpha R)^2 + y^2]^{3/2}} - \frac{\alpha R^3 (y)}{[(x - \beta R)^2 + y^2]^{3/2}} \right)$$ Eq. 2-73

$$\left| \vec{F} \right| = \sqrt{\left| \vec{F_x} \right|^2 + \left| \vec{F_y} \right|^2}$$ Eq. 2-74

A two-dimensional force map can be obtained by computing force for an interval of x and y coordinates respectively.
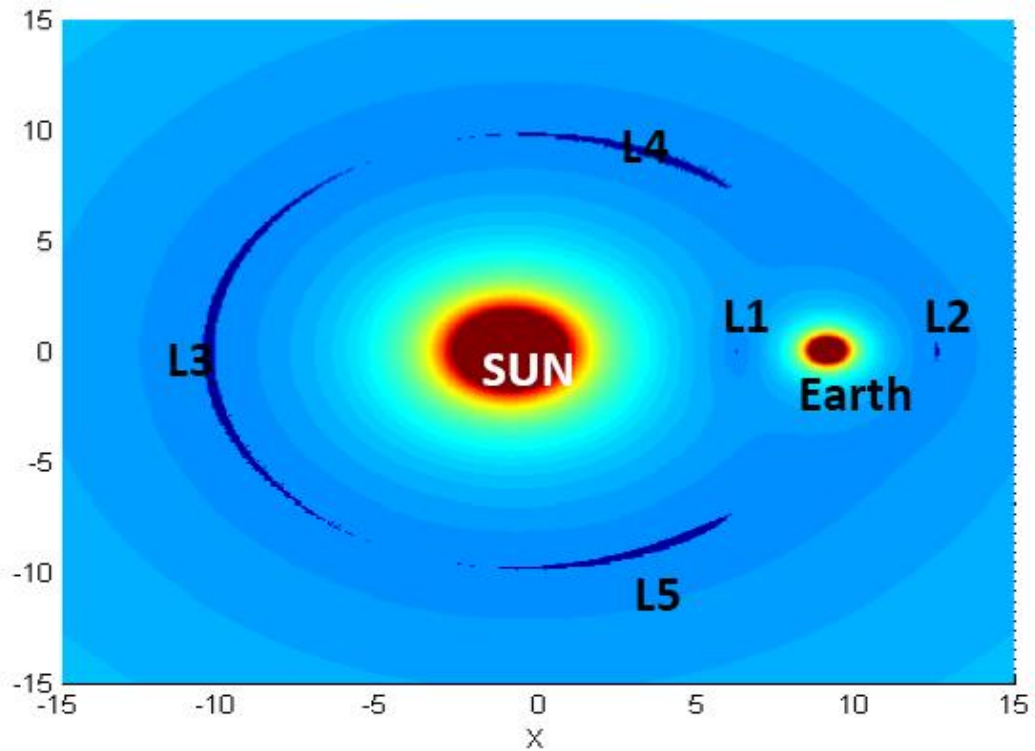
Figure 2-20. 2D force map of Sun-Earth system

Now, it is so straightforward to compute the coordinates of the collinear libration points by taking the roots of the equation of motion as follows. First, take the mass of the Sun and Earth, and define the constants:

$$\boldsymbol{m_{SUN}} = 1.9886294261178590 \times 10^{30}\ kg$$

$$\boldsymbol{m_{BARY}} = 6.045476730900739 \times 10^{24}\ kg$$

$$\mu = \frac{m_{BARY}}{m_{SUN} + m_{BARY}} = 3.040012519674380e\text{-}006$$

$$G = 6.67408*1e\text{-}11 \quad \frac{m^3}{kg\ s^2}$$

$$R = 149.59787066*1e6\ km$$

From the restricted three body dynamics, it is already stated that the dimensionless equation of motion for x axis:

$$\ddot{x} = x + 2\dot{y} - \frac{1-\mu}{((x+\mu)^2 + y^2 + z^2)^{3/2}}(x+\mu)$$

$$- \frac{\mu}{\left((x-(1-\mu))^2 + y^2 + z^2\right)^{3/2}}(x-(1-\mu)) \qquad \text{Eq. 2-75}$$

This equality is taken because the collinear libration points lies on this x axis. So, it is needed to consider that the velocities and the y, z coordinates are zeros at these the collinear libration points. It means that the total force on x axis is null.

$$\dot{x} = \dot{y} = \dot{z} = 0$$

$$y = z = 0$$

So, the equation reduces to:

$$x - \frac{1-\mu}{(x+\mu)^3}(x+\mu) - \frac{\mu}{(x-(1-\mu))^3}(x-(1-\mu)) = 0$$

$$\Rightarrow$$

$$\frac{x(x+\mu)^2(x-(1-\mu))^2 + (1-\mu)(x-(1-\mu))^2 + \mu(x+\mu)^2}{(x+\mu)^2(x-(1-\mu))^2} \qquad \text{Eq. 2-76}$$

$$= 0$$

Here, three different cases must be considered for three collinear points. The positions of the x coordinate according to the two massive bodies describe the position of L1, L2 and L3 respectively. So, for L1 x coordinate must be between Sun and Earth, L2 lies on the axis from Sun to Earth, and towards deep space, the L3 is behind the sun:

$$for \;\; L_1 \Rightarrow -\mu < x < (1-\mu) \;\; ;$$
$$for \;\; L_2 \Rightarrow -\mu < (1-\mu) < x \;\; ;$$
$$for \;\; L_3 \Rightarrow x < -\mu < (1-\mu) \;\; ;$$

This equality can be written in polynomial form:

$$a_5 x^5 + a_4 x^4 + a_3 x^3 + a_2 x^2 + a_1 x + a_0 = 0 \qquad \text{Eq. 2-77}$$

The values of the polynomial according to the L1, L2, and L3 are given in the following table:

Table 2.1. The values of the constant of the polynomial for L1, L2, L3

a_i	For L1	For L2	For L3
$a_5 =$	1		
$a_4 =$	$2(2\mu - 1)$		
$a_3 =$	$(1 - \mu)^2 - 4\mu(1 - \mu) + \mu^2$		
$a_2 =$	$2\mu(1 - \mu)(1 - 2\mu)$ $-1 + 2\mu$	$2\mu(1 - \mu)(1 - 2\mu) - 1$	$2\mu(1 - \mu)(1 - 2\mu) + 1$
$a_1 =$	$\mu^2(1 - \mu)^2 +$ $2(\mu^2 + (1 - \mu)^2)$	$\mu^2(1 - \mu)^2 +$ $2(-\mu^2 + (1 - \mu)^2)$	$\mu^2(1 - \mu)^2 +$ $2(\mu^2 - (1 - \mu)^2)$
$a_0 =$	$-(1 - \mu)^3 + \mu^3$	$-(1 - \mu)^3 - \mu^3$	$(1 - \mu)^3 + \mu^3$

The roots of this polynomial give the location of the collinear libration points. The position of the triangular libration points can be computed using the equilateral triangle which its base lies between two massive body. The distance from L4 (and L5) to the primary bodies is equal to the unit distance, the distance between two primaries. So, the x and y coordinates will be:

$$x = -\mu + 1/2$$
$$y = \pm\sqrt{3}/2$$

Table 2.2. The position of the libration points

	Distance from CM in unit value	Distance from Center of Mass in km	Distance from Earth in km
L1	X= 0.98998643221187	X= 148.0998622411871e+06	De=1.497553639413139e+006
L2	X= 1.01007474491390	X= 151.1050310465624e+06	De= 1.507615165962172e+006
L3	X=-1.00000126667188	X=-149.5980601514165e+06	De= 299.1954760320168e+006
L4	X=0.499996959987480 Y= 0.86602540378444	X= 074.7984805506003e+06 Y= 129.5555563436187e+06 D= 149.5976432708186e+06	De= 149.59787066000e+006
L5	X= 0.499996959987480 Y=-0.86602540378444	X= 074.7984805506003e+06 Y= 129.5555563436187e+06 D = 149.5976432708186e+06	De= 149.59787066000e+006

The Table 2.2 presents the coordinates calculated for the libration points of the Sun-Bary system. As seen, L1 and L2 are approximately 1.5 million kilometers far from Earth. The details about the orbit design at these points are presented in the chapter-3. The stability characteristic of these locations is another important issue to be analyzed and it is given in the following subchapter.

2.3.2. Stability of the Libration Points

Five equilibrium points are computed for Sun-Bary system in the previous section. Here, the stability of these points is analyzed. Linear stability analysis for each libration point is carried out by linearizing the equation of motion about each libration point [61, 63]. So, recall the equation of motion of the third body for the three-body system:

$$f(x, y, z, \dot{x}, \dot{y}, \dot{z}, t) = \dot{X} = \begin{bmatrix} \dot{x} \\ \dot{y} \\ \dot{z} \\ \ddot{x} \\ \ddot{y} \\ \ddot{z} \end{bmatrix}$$

$$= \begin{bmatrix} u \\ v \\ w \\ x + 2\dot{y} - \dfrac{(1-\mu)(x-\mu)}{r_1^3} - \dfrac{\mu(x-(1-\mu))}{r_2^3} \\ y - 2\dot{x} - \dfrac{(1-\mu)y}{r_1^3} - \dfrac{\mu y}{r_2^3} \\ -\dfrac{(1-\mu)z}{r_1^3} - \dfrac{\mu z}{r_2^3} \end{bmatrix}$$
Eq. 2-78

where;

$$r_1 = \sqrt{(x+\mu)^2 + y^2 + z^2} \quad \text{and} \quad r_2 = \sqrt{(x-(1-\mu))^2 + y^2 + z^2}$$

And state vector is $\quad X = [x\ y\ z\ \dot{x}\ \dot{y}\ \dot{z}]^T$

Partial derivatives of differential equation set can be written as:

$$F_{ij} = \frac{\partial f_i}{\partial X_j}$$

So, the partial derivative matrix of the first three equations with respect to position is a 3x3 zeros matrix, and velocity derivative matrix is a 3x3 unit matrix.

$$F_{ij} = \begin{bmatrix} 0 & 0 & 0 \\ 0 & 0 & 0 \\ 0 & 0 & 0 \end{bmatrix} \text{ for } i = 1 to 3 \quad \text{and } j = 1 to 3 \qquad \text{Eq. 2-79}$$

$$F_{ij} = \begin{bmatrix} 1 & 0 & 0 \\ 0 & 1 & 0 \\ 0 & 0 & 1 \end{bmatrix} \text{ for } i = 1 to 3 \quad \text{and } j = 4 to 6 \qquad \text{Eq. 2-80}$$

The partial derivatives for last three equations with respect to position and velocity components can be written as below:

$$F_{41} = 1 - \frac{(1-\mu)}{r_1^3} - \frac{3(1-\mu)(x+\mu)^2}{r_1^5} - \frac{\mu}{r_2^3} - \frac{3\mu\big(x-(1-\mu)\big)^2}{r_2^5}$$

$$F_{42} = \frac{3(1-\mu)(x+\mu)y}{r_1^5} + \frac{3\mu\big(x-(1-\mu)\big)y}{r_2^5}$$

$$F_{43} = \frac{3(1-\mu)(x+\mu)z}{r_1^5} + \frac{3\mu\big(x-(1-\mu)\big)z}{r_2^5}$$

$$F_{51} = \frac{3(1-\mu)(x+\mu)y}{r_1^5} + \frac{3\mu\big(x-(1-\mu)\big)y}{r_2^5}$$

$$F_{52} = 1 - \frac{(1-\mu)}{r_1^3} - \frac{3(1-\mu)(y)^2}{r_1^5} - \frac{\mu}{r_2^3} - \frac{3\mu(y)^2}{r_2^5} \qquad \text{Eq. 2-81}$$

$$F_{53} = \frac{3(1-\mu)yz}{r_1^5} + \frac{3\mu yz}{r_2^5}$$

$$F_{61} = \frac{3(1-\mu)(x+\mu)z}{r_1^5} + \frac{3\mu\big(x-(1-\mu)\big)z}{r_2^5}$$

$$F_{62} = \frac{3(1-\mu)yz}{r_1^5} + \frac{3\mu yz}{r_2^5}$$

$$F_{63} = -\frac{(1-\mu)}{r_1^3} - \frac{3(1-\mu)(z)^2}{r_1^5} - \frac{\mu}{r_2^3} - \frac{3\mu(z)^2}{r_2^5}$$

Here F can be called as state propagation matrix. State transition matrix Φ for linearized system can be written as $\Phi(t) = e^{Ft}$ for continuous time. So; Taylor series expansion of Φ will give the $x(t)$ state values for specified time. $x(t)$ can be written as below:

$$x(t) = \Phi(\text{t})x(0) = e^{Ft}\,x(0) \qquad \text{Eq. 2-82}$$

$$x(t) = (I + Ft + F^2 t^2/2! + F^3 t^3/3! + \ldots + F^n t^n/n!)\,x(0) \qquad \text{Eq. 2-83}$$

In this thesis, the simulation is run in discrete time. So, the state vector $X,$ and the linearized simplified equations can be written in discrete form as below:

$$X = [x \quad y \quad z \quad \dot{x} \quad \dot{y} \quad \dot{z} \;]^T \qquad\qquad \text{Eq. 2-84}$$

$$X_{k+1} = (I + F\Delta t)\, X_k = \Phi X_k \qquad\qquad \text{Eq. 2-85}$$

Then, the eigenvalues of the linearized state transition matrix give the information about the stability of the libration points, when this linearization is done about the point interested. It is well known that the collinear point L1, L2, and L3 with the Sun and Planet are unstable points. Small differences caused by perturbations from the equilibrium points will grow dramatically over a time. On the other hand, triangular points L4 and L5 are stable for a special condition. Here, the mass ratio of the primary bodies is critical. If this mass ratio is less than 0.0385 the stable condition is obtained. The Coriolis force provides their stability. An asteroid situated near L4 or L5 tends to decrease the potential, as a consequence its speed increases. Thanks to this speed Coriolis force create the force that keep into its orbit around the L4 (or L5) point. The stable areas of the L4 and L5 are called as Trojan, after the three asteroids Agamemnon, Achilles and Hector are located at the L4 and L5 points of Sun-Jupiter system [62]. At July 2011, a total number of asteroids found in Sun-Jupiter system are approximately between 3168 - 4917around L4 and 1645 around L5 point. An enormous spread is seen, a distance of more than 500 million km [63]. The details on the stability computations are given in the following two subsections.

2.3.2.1. Stability of the collinear L1, L2, and L3 libration points

In order to analyze the stability of the collinear points, the state transition matrix is rewritten by adding the state properties of these points; as; $y = 0$; $z = 0$; and $\dot{y} = \dot{z} = 0$.

So, state propagation matrix F become:

$$F_{41} = 1 - \frac{(1-\mu)}{r_1^3} - \frac{3(1-\mu)(x+\mu)^2}{r_1^5} - \frac{\mu}{r_2^3} - \frac{3\mu\big(x-(1-\mu)\big)^2}{r_2^5} \qquad \text{Eq. 2-86}$$

$$F_{42} = 0$$

$$F_{43} = 0$$

$$F_{51} = 0$$

$$F_{52} = 1 - \frac{(1-\mu)}{r_1^3} - \frac{\mu}{r_2^3}$$

$$F_{53} = 0$$

$$F_{61} = 0$$

$$F_{62} = 0$$

$$F_{63} = -\frac{(1-\mu)}{r_1^3} - \frac{\mu}{r_2^3}$$

where;

$$r_1 = \sqrt{(x+\mu)^2} \qquad \text{and} \qquad r_2 = \sqrt{\left(x - (1-\mu)\right)^2}$$

So, by substituting r1 and r2 in to F:

$$F_{41} = 1 + \frac{2(1-\mu)}{(x+\mu)^3} + \frac{2\mu}{\left(x - (1-\mu)\right)^3}$$

$$F_{52} = 1 - \frac{(1-\mu)}{(x+\mu)^3} - \frac{\mu}{\left(x - (1-\mu)\right)^3} \qquad \text{Eq. 2-87}$$

$$F_{63} = -\frac{(1-\mu)}{(x+\mu)^3} - \frac{\mu}{\left(x - (1-\mu)\right)^3}$$

Let define γ in order to simplify the notation:

$$\gamma = \frac{(1-\mu)}{(x+\mu)^3} + \frac{\mu}{\left(x - (1-\mu)\right)^3} \qquad \text{Eq. 2-88}$$

So, we have;

$$F_{41} = 1 + 2\gamma$$

$$F_{52} = 1 - \gamma$$

$$F_{63} = -\gamma$$

and

$$F_{44} = 0; \quad F_{45} = 2; \quad F_{46} = 0;$$

$$F_{54} = -2; \quad F_{55} = 0; \quad F_{56} = 0;$$

$$F_{64} = 0; \quad F_{65} = 0; \quad F_{66} = 0;$$

Then, the matrix F for collinear points is:

$$F = \begin{bmatrix} F_a & F_b \\ F_c & F_d \end{bmatrix}$$

where

$$F_a = \begin{bmatrix} 0 & 0 & 0 \\ 0 & 0 & 0 \\ 0 & 0 & 0 \end{bmatrix} \quad ; \quad F_b = \begin{bmatrix} 1 & 0 & 0 \\ 0 & 1 & 0 \\ 0 & 0 & 1 \end{bmatrix}$$

$$F_c = \begin{bmatrix} 1 + 2\gamma & 0 & 0 \\ 0 & 1 - \gamma & 0 \\ 0 & 0 & -\gamma \end{bmatrix} \quad ; F_d = \begin{bmatrix} 0 & 2 & 0 \\ -2 & 0 & 0 \\ 0 & 0 & 0 \end{bmatrix}$$

To find the eigenvalues, it is necessary to solve the following equation that gives the characteristic equation of the system:

$$det(F - \lambda I) = 0 \text{ where } \lambda \text{ are the eigenvalues.}$$

$$
\begin{vmatrix}
-\lambda & 0 & 0 & 1 & 0 & 0 \\
0 & -\lambda & 0 & 0 & 1 & 0 \\
0 & 0 & -\lambda & 0 & 0 & 1 \\
1+2\gamma & 0 & 0 & -\lambda & 2 & 0 \\
0 & 1-\gamma & 0 & -2 & -\lambda & 0 \\
0 & 0 & -\gamma & 0 & 0 & -\lambda
\end{vmatrix}
$$

$$
= (\lambda^2 + \gamma)(-2\gamma^2 - \gamma\lambda^2 + \gamma + \lambda^4 + 2\lambda^2 + 1) = 0
$$

Eq. 2-92

$$
\Rightarrow \lambda^6 + 2\lambda^4 + \lambda^2(-3\gamma^2 + 2\gamma + 1) + \gamma(1 + \gamma - 2\gamma^2) = 0
$$

Eq. 2-93

The roots of the equation above give the eigenvalues:

The first two roots are:

$$
\lambda_{1,2} = \pm\sqrt{-\gamma}
$$

Eq. 2-94

The second two roots:

$$
\lambda_{3,4} = \pm\sqrt{\frac{\gamma}{2} + \frac{\sqrt{\gamma(9\gamma - 8)}}{2} - 1}
$$

Eq. 2-95

The third two roots:

$$
\lambda_{5,6} = \pm\sqrt{\frac{\gamma}{2} - \frac{\sqrt{\gamma(9\gamma - 8)}}{2} - 1}
$$

Eq. 2-96

So, if γ is negative the first two roots $\lambda_{1,2}$ are real numbers, one positive, one is negative. This means that the system is unstable.

For $\lambda_{3,4}$, the inner of the square root must be negative in order to not have a real root, means an unstable condition, so;

$\frac{\gamma}{2} + \frac{\sqrt{\gamma(9\gamma-8)}}{2} - 1 < 0$ must be

After some rearrangement, it gives:

If $\gamma^2 < \frac{\gamma+1}{2}$ we have imaginary roots

For $\lambda_{5,6}$ the inner of the square root must be negative in order to not have a real root, means an unstable condition, so;

$\frac{\gamma}{2} - \frac{\sqrt{\gamma(9\gamma-8)}}{2} - 1 < 0$ must be

If $\gamma^2 > \frac{\gamma+1}{2}$ we have imaginary roots

So, it shows that at least two of the roots will be real numbers.

In our case, Sun-Earth/Moon(Bary) system is considered. The results obtained are given in the following table:

Table 2.3. The stability criteria of the collinear libration points

for stability (for imaginary roots), the conditions	For L1	For L2	For L3
$\gamma > 0$?	-1.9998 > 0 ? No, we have two real roots	3.9405 > 0 ? Yes, two imaginary roots	-1 > 0 ? No, two real roots
$\gamma^2 < \frac{\gamma+1}{2}$?	3.9992 < -0.4999 ? No, we have two more real roots	15.5277 < 2.4703 ? No, two real roots	1< 0 No, two real roots
$\gamma^2 > \frac{\gamma+1}{2}$?	3.9992 > -0.4999? Yes, two imaginary roots	15.5277 > 2.4703 ? Yes, two imaginary roots	1> 0 Yes, two imaginary roots
$\begin{bmatrix} \lambda_1 \\ \lambda_2 \\ \lambda_3 \\ \lambda_4 \\ \lambda_5 \\ \lambda_6 \end{bmatrix} =$	1.4141 -1.4141 1.2670 -1.2670 + 2.3675i -2.3675i	+ 1.9851i -1.9851i 2.4843 -2.4843 +2.0570i -2.0570i	1.0000 -1.0000 0.7494 -0.7494 +1.8872i -1.8872i
Stable ?	NO	NO	NO

2.3.2.2. Stability of the Triangular L4 and L5 libration points

It is more difficult to write the stability conditions for L4 and L5 points. Here, the state transition matrix is rewritten by adding the state properties of these points; as; $z = 0$; and $\dot{y} = \dot{z} = 0$. (Not that: $y \neq 0$). After a lot of mathematical operations, the following equations are obtained. First let define:

$$\alpha = \frac{(1 - \mu)}{r_1^3} + \frac{\mu}{r_2^3} \qquad\qquad \text{Eq. 2-97}$$

$$\beta_1 = \frac{3(1 - \mu)}{r_1^5} \qquad\qquad \text{Eq. 2-98}$$

$$\beta_2 = \frac{3\mu}{r_2^5} \qquad\qquad \text{Eq. 2-99}$$

where; $r_1 = \sqrt{(x + \mu)^2 + y^2}$ $\qquad$ and $\qquad$ $r_2 = \sqrt{\left(x - (1 - \mu)\right)^2 + y^2}$

So, state propagation matrix F become:

$$F_{41} = 1 - \alpha + \beta_1(x + \mu)^2 + \beta_2\left(x - (1 - \mu)\right)^2$$

$$F_{42} = \beta_1(x + \mu)y + \beta_2\left(x - (1 - \mu)\right)y$$

$$F_{43} = 0$$

$$F_{51} = \beta_1(x + \mu)y + \beta_2\left(x - (1 - \mu)\right)y$$

$$F_{52} = 1 - \alpha + \beta_1 y^2 + \beta_2 y^2 \qquad\qquad \text{Eq. 2-100}$$

$$F_{53} = 0$$

$$F_{61} = 0$$

$$F_{62} = 0$$

$$F_{63} = -\alpha$$

To find the eigenvalues:

$det(F - \lambda I) = 0$ where λ are the eigenvalues.

$$det(F - \lambda I) = \begin{vmatrix} A_1 & A_2 \\ A_3 & A_4 \end{vmatrix} = 0 \qquad \text{Eq. 2-101}$$

$$A_1 = \begin{bmatrix} -\lambda & 0 & 0 \\ 0 & -\lambda & 0 \\ 0 & 0 & -\lambda \end{bmatrix} \qquad \text{Eq. 2-102}$$

$$A_2 = \begin{bmatrix} 1 & 0 & 0 \\ 0 & 1 & 0 \\ 0 & 0 & 1 \end{bmatrix} \qquad \text{Eq. 2-103}$$

$$A_3 = \begin{bmatrix} a_{11} & a_{12} & a_{13} \\ a_{21} & a_{22} & a_{23} \\ a_{31} & a_{32} & a_{33} \end{bmatrix} \qquad \text{Eq. 2-104}$$

$$A_4 = \begin{bmatrix} -\lambda & 2 & 0 \\ -2 & -\lambda & 0 \\ 0 & 0 & -\lambda \end{bmatrix} \qquad \text{Eq. 2-105}$$

where;

$$a_{11} = 1 - \alpha + \beta_1(x + \mu)^2 + \beta_2\big(x - (1 - \mu)\big)^2$$

$$a_{12} = \beta_1(x + \mu)y + \beta_2\big(x - (1 - \mu)\big)y$$

$$a_{13} = 0$$

$$a_{21} = \beta_1(x + \mu)y + \beta_2\big(x - (1 - \mu)\big)y$$

$$a_{22} = 1 - \alpha + \beta_1 y^2 + \beta_2 y^2 \qquad \text{Eq. 2-106}$$

$$a_{23} = 0$$

$$a_{31} = 0$$

$$a_{32} = 0$$

$$a_{33} = -\alpha$$

Then, the following equation is obtained:

$$\lambda^6 + \lambda^4\{3\alpha - \beta_2 + 2 + 2\beta_2(x + \mu) - (\beta_1 + \beta_2)r_1^2\}$$
$$+ \lambda^2\{(\beta_1 + \beta_2)(r_1^2 - 2\alpha r_1^2) + \beta_1\beta_2 y^2 + \beta_2 + 1 + 3\alpha^2$$
$$- 2\beta_2(x + \mu) - 2\alpha\beta_2(1 - 2(x + \mu))\}$$
$$+ \{(\beta_1 + \beta_2)[\alpha r_1^2 - \alpha^2 r_1^2] + 2\alpha\beta_2(x + \mu)(\alpha - 1)$$
$$+ \alpha\beta_1\beta_2 y^2 + \alpha(1 + \beta_2 - \alpha(\beta_2 + 2) + \alpha^2)\} = 0$$

Eq. 2-107

The roots of the equation above give the eigenvalues:

The first two roots are:

$\lambda_{1,2} = \pm\sqrt{-\alpha}$, so α>0 to obtain imaginary roots.

The second two roots, let define $\sigma = \beta_1 r_1^2 + \beta_2 r_2^2$. Then;

$$\lambda_{3,4} = \pm\sqrt{\begin{array}{c}\dfrac{\beta_2}{2} - \alpha - \beta_2\mu - \beta_2 x + \dfrac{\sqrt{\sigma^2 - 8\sigma + 16\alpha}}{2}\\[3mm] +\dfrac{1}{2}(\beta_1 + \beta_2)(x^2 + \mu^2 + y^2) + (\beta_1 + \beta_2)\mu x - 1\end{array}}$$

Eq. 2-108

So, to obtain stable roots:

$$\frac{\beta_2}{2} - \alpha - \beta_2\mu - \beta_2 x <$$

Eq. 2-109

$$-\frac{\sqrt{\sigma^2 - 8\sigma + 16\alpha}}{2} - \frac{1}{2}(\beta_1 + \beta_2)(x^2 + \mu^2 + y^2) - (\beta_1 + \beta_2)\mu x + 1$$

must be

The third two roots:

$$\lambda_{5,6} = \pm\sqrt{\begin{array}{c}\dfrac{\beta_2}{2} - \alpha - \beta_2\mu - \beta_2 x - \dfrac{\sqrt{\sigma^2 - 8\sigma + 16\alpha}}{2}\\[3mm] +\dfrac{1}{2}(\beta_1 + \beta_2)(x^2 + \mu^2 + y^2) + (\beta_1 + \beta_2)\mu x - 1\end{array}}$$

Eq. 2-110

So, to obtain stable roots, the following condition is necessary:

$$\frac{\beta_2}{2} - \alpha - \beta_2\mu - \beta_2 x <$$

<div align="right">Eq. 2-111</div>

$$\frac{\sqrt{\sigma^2 - 8\sigma + 16\alpha}}{2} - \frac{1}{2}(\beta_1 + \beta_2)(x^2 + \mu^2 + y^2) - (\beta_1 + \beta_2)\mu x + 1$$

Table 2.4. The stability criteria of the triangular libration points

for stability (for imaginary roots), the conditions	For L4	For L5
$\begin{bmatrix} \lambda_1 \\ \lambda_2 \\ \lambda_3 \\ \lambda_4 \\ \lambda_5 \\ \lambda_6 \end{bmatrix} =$	0.0000 - 1.0000i 0.0000 + 1.0000i -0.0000 - 1.0000i -0.0000 + 1.0000i 0.0000 - 0.0045i 0.0000 + 0.0045i All roots have imaginary parts	-0.0000 - 1.0000i -0.0000 + 1.0000i 0.0000 - 1.0000i 0.0000 + 1.0000i -0.0000 - 0.0045i -0.0000 + 0.0045i All roots have imaginary parts
Stable ?	YES	YES

In this section, the stability characteristics of the libration points are examined and numerical results for the Sun-Bary system are given. As seen, the numerical results obtained are consistent with the algebraic stability conditions presented.

2.4. Zero Velocity (Maximum Potential Energy) boundary

The total energy value of the third body in Restricted Three Body Dynamics is a main key which gives an idea about the boundary of its motion. Regarding to the law of conservation of the energy, it is well known that when the maximum potential energy is reached, the kinetic energy is zeros, velocity is zeros – in ideal case, without any unexpected effect such as disturbance, friction, etc. –. This boundary can be defined using energy level of the third body. Jocabi Integral equation is used to plot

this boundary by putting zeros to all velocities terms, and finding implicitly the x and y coordinates for a selected energy level C, called Jacobi Energy constant.

For a preselected C Jacobi constant, when an initial position and velocity values are determined for the third particle, the trajectory of this particle will be always inside of the boundary obtained by this C constant. It will never pass the boundary since maximum potential energy level is reached. In this way, these Jacobi curves define the allowable regions of the motion and these regions also are called as Hill's Regions.

Recall that Jacobi integral equation for zeros velocity and for planar motion is:

$$x^2 + y^2 + 2\frac{1-\mu}{r_1} + 2\frac{\mu}{r_2} = C \qquad\qquad \text{Eq. 2-112}$$

The following table lists the Jacobi constants values computed for each libration point of the Sun-Bary system.

Table 2.5. Jacobi constants values of libration points

For L1:	CL1 = 3.000897861039225
For L2:	CL2 = 3.000893807647872
For L3:	CL3 = 3.000003040012327
For L4 & L5:	CL4_5 = 2.999996959996722

Firstly; let see the zero-velocity curve obtained for first libration point, L1, in the following plots. Actually, four different zones are obtained. It is zoomed around L1, Earth, L2 zone to see the shape of the curve.
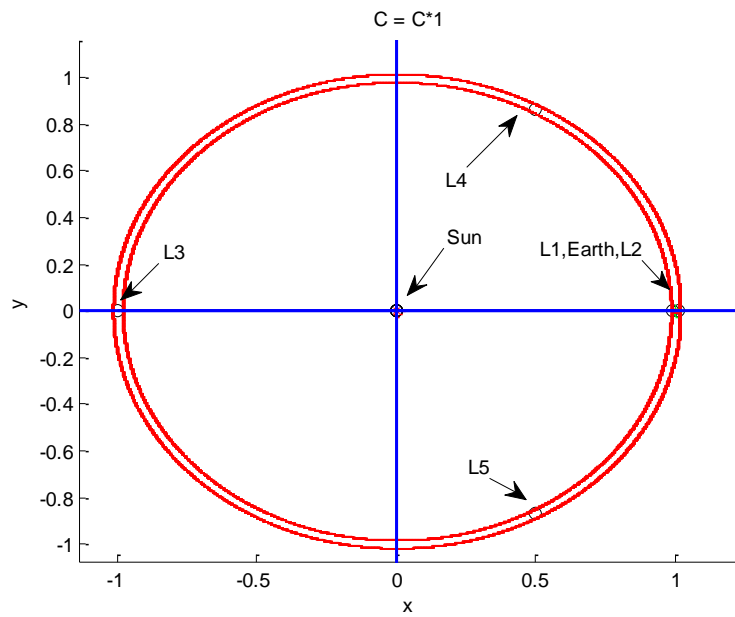
Figure 2-21. Zeros velocity curve
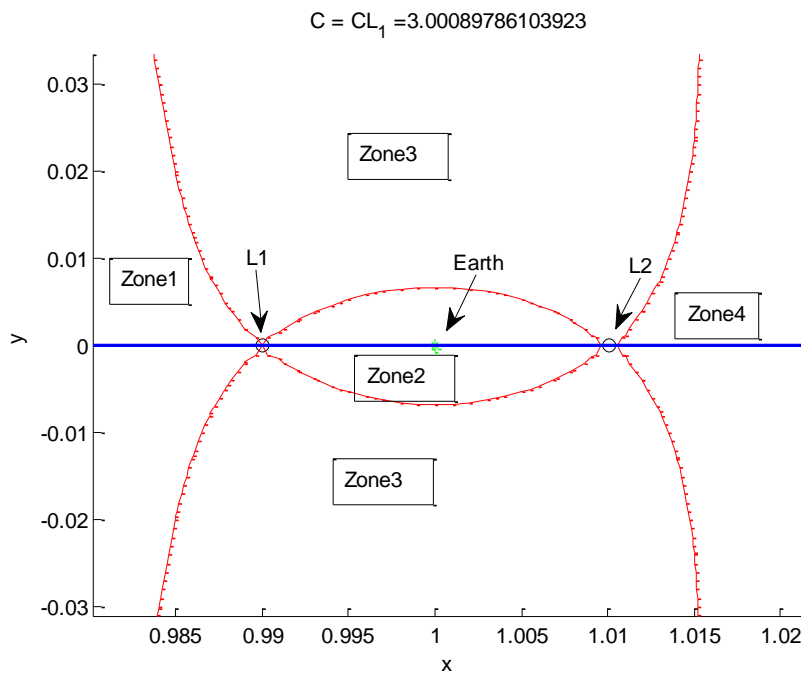
Figure 2-22. Zeros velocity curve at L1 and L2 for C = C of L1

Here, at this L1 energy level, four distinct zones are obtained. The first zone is the area around Sun until the boundary limited and shaped around L1, just left side of L1. Second zone is the zone limited between L1 and L2, around the Earth. Third zone is the area having a bagel shape between outside part of L1 and L2. And fourth zone is the outside zone, towards deep space. So, it shows that a body navigating around Sun with this energy level can never reach Earth; it cannot pass to the right side of the L1 point. One the other hand, if a particle starts its motion in Zone2, for instance near Earth, it will never reach Sun, or never goes to the deep space.

For the L2 energy level, see Figure 2-23, three distinct zones are formed. But, at this time, the boundary between the Sun and Earth disappears, and a passage appears near L1. It means that it is possible to have a trajectory between Sun and Earth, in Zone1. And a body in Zone1 will never go towards deep space, there is no gate to Zone3, and as well as Zone2. The existence of the gate around L1 means that it is also possible to have a periodic orbit around L1, in this gate.
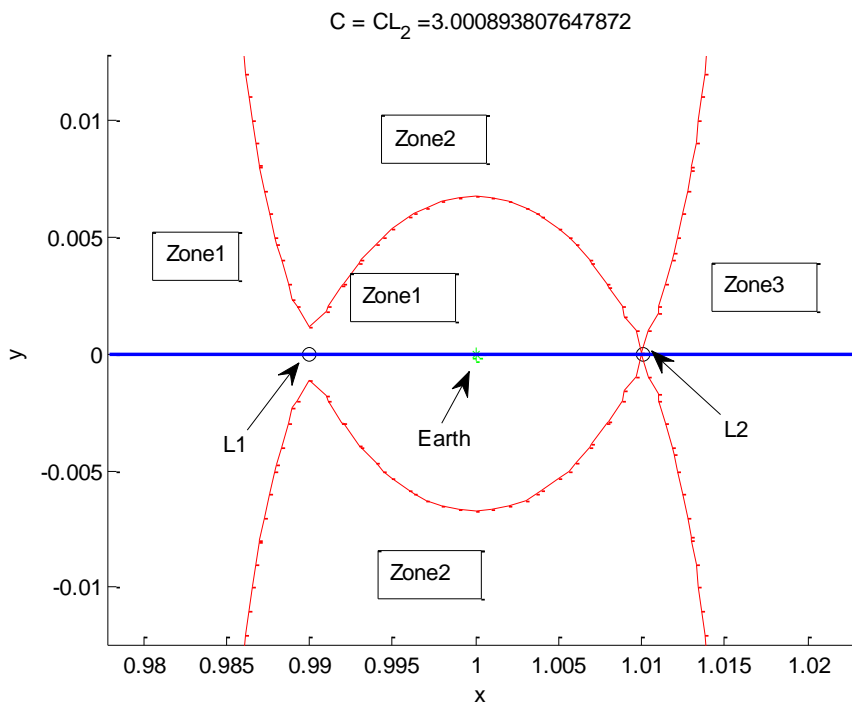
Figure 2-23. Zeros velocity curve at L1 and L2 for C = C of L2

For L3 energy level, it is not possible to have distinct zone like the case of L1 and L2, as seen in Figure 2-24. Here, two boundaries are obtained, one at the upper side and one symmetric of the first according to the x axis. For L4 energy level, no boundary is formed, as seen in Figure 2-25.
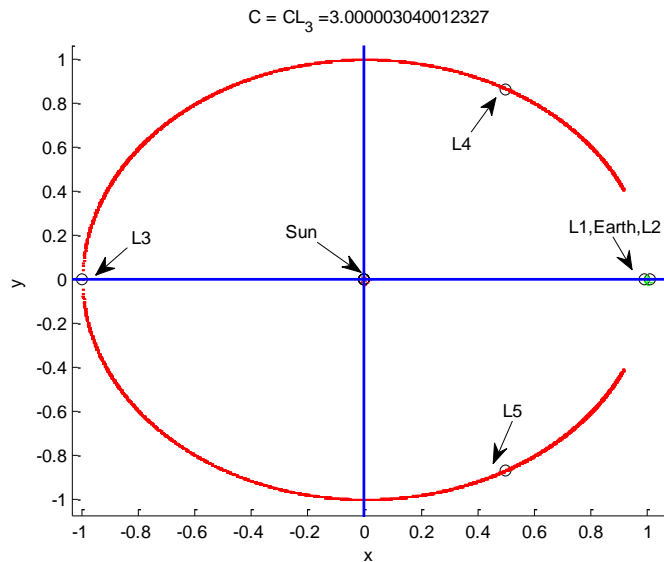
Figure 2-24. Zeros velocity curve at L1 and L2 for C = C of L3
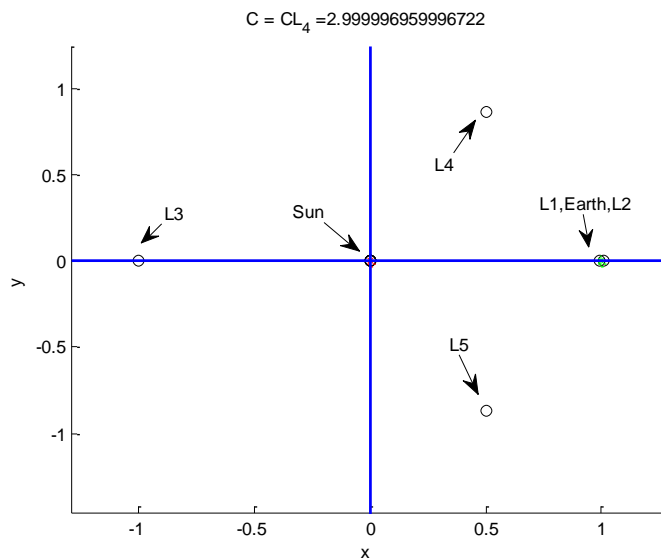
Figure 2-25. Zeros velocity curve at L1 and L2 for C = C of L4

It is possible to form the shape of the boundary L1 and L2, by increasing or decreasing the energy level around L1 and L2. So, this kind of manipulation provides to obtain more narrow or wide passages at L1 and L2. For instance, let C = CL1*0.999998; at this energy level the passage is formed at both point L1 and L2. So, a body having this energy level can navigate between Sun and Earth and can also escape toward deep space. But it is possible to have a periodic orbit around both L1 and L2.
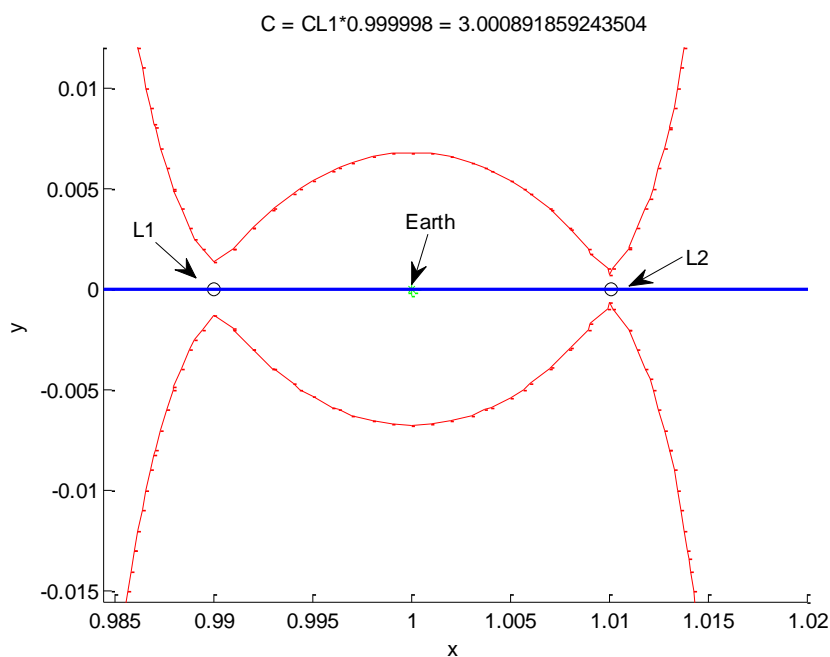
Figure 2-26. Zeros velocity curve at L1 and L2 for C = 0.999998xCL1

Now, in Figure 2-27 and Figure 2-28, the trajectory of a body is presented for several initial conditions providing the energy level given above. First, L1 energy level is selected:

C = CL1 = 3.000897861039225

Initial position and velocities =

$X_0 = [0.985 \quad 0 \quad 0 \quad 0 \quad 0.013302997062443 \quad 0]$
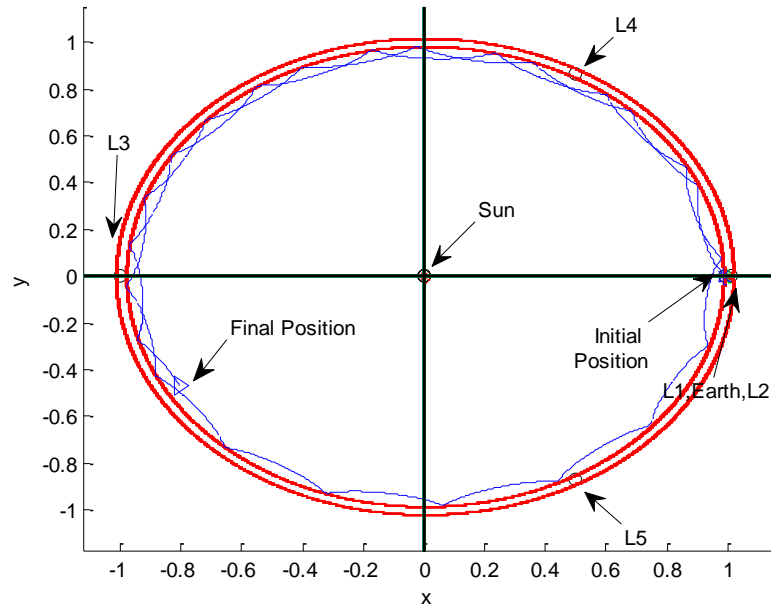
Figure 2-27. Trajectory of a body for C = CL1
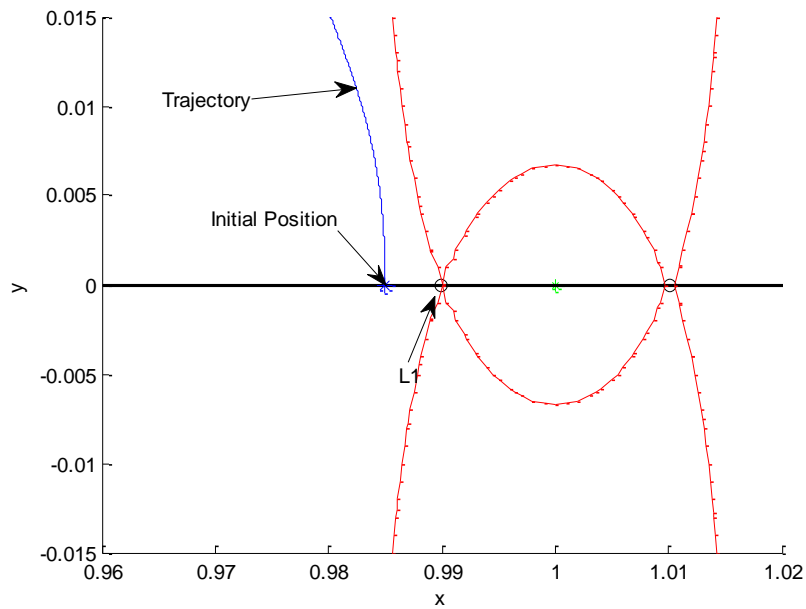
Figure 2-28. Trajectory of a body for C = CL1, Zoomed view

When an initial position which is between L1 and Earth position is selected, it is seen that the body navigates in the middle zone, around Earth:

C = CL1 = 3.000897861039225

Initial position and velocities =

$$X_0 = [0.992 \quad 0 \quad 0 \quad 0 \quad 0.006569304054335 \quad 0]$$
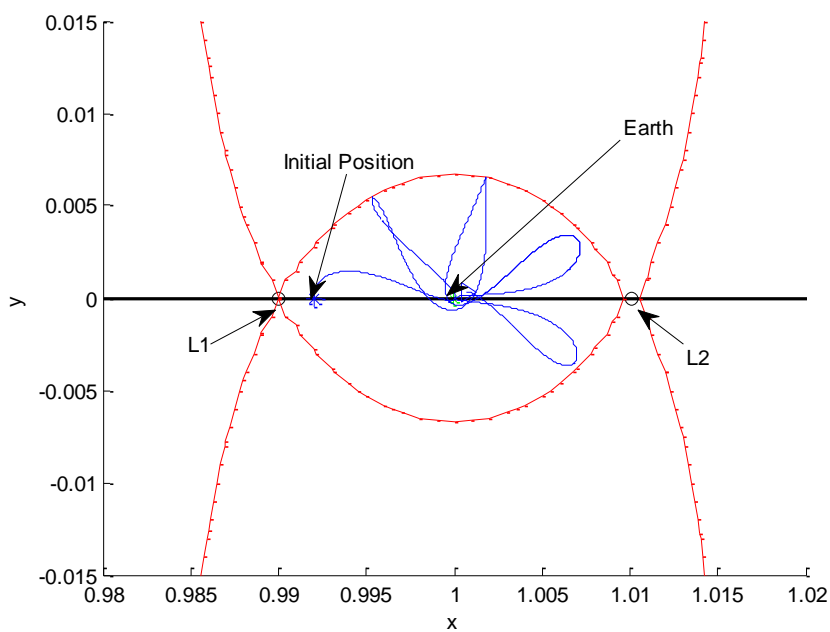
Figure 2-29. Trajectory for C = CL1, initial position between Earth and L1

For an energy level which is less than both L1 and L2, passages are obtained both around L1 and L2. Let an initial condition having an energy level C = 3.000795757023590, such that initial position and velocities are:

$$X_0$$
$$= [0.991975555663567 \quad 0 \quad -0.001885662044598 \quad 0 \quad -0.010971356910053 \quad 0]$$

So, a trajectory around L1, passing from right side to left of L1 and vice versa. Figure 2-30 presents the trajectory obtained for this case.
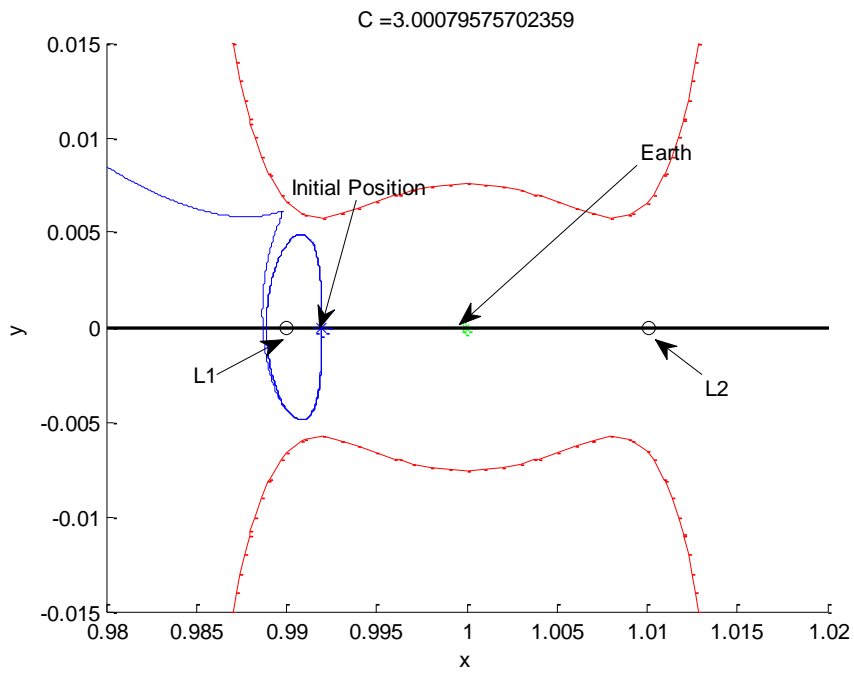
Figure 2-30. Trajectory of a body for C is between L1 and L2

The different trajectories obtained regarding to the energy levels are presented in this chapter and the importance of energy level is highlighted. Following sections give the details on orbit design around collinear libration points.

CHAPTER 3

ORBIT DESIGN AT COLLINEAR LIBRATION POINTS

3.1. Orbit types

Three different types of orbit can be defined according their trajectory characteristic: A *Lyapunov orbit* is a periodic orbit in the orbital plane of the primary bodies. A *Lissajous orbit* is a periodic orbit in which there is a combination of planar and out of plane (vertical) components. *Halo orbits* are special cases of Lissajous orbits where the in-plane and out-of-plane frequencies are the same [64]. The trajectory analyses around the collinear libration points of a three-body system show these three different types of motion depending on the energy level. The computation of two-dimensional tori around halo orbits that the motion is quasi-periodic is done by Lindstedt-Poincaré Method [65]. The definition of Poincaré Method is given in Appendix-G. The following sub-chapters present the details on the Halo orbit computation performed in this thesis.

3.2. Halo orbit design

The methodology used for computing a periodic orbit in Restricted Three Body (RTB) problem is presented in this chapter. The concept behind this method is based on the symmetry property of the RTB dynamic. With the aim of acquiring symmetrical orbit, appropriate initial positions and velocities can be computed using the differential corrections method with the advantage proposed by the symmetry property. Here the Newton's iteration method is basically used to obtain initial condition values. A technique for analyzing the stability of the periodic orbits is presented as well. It is important to notice that these methods are valid for orbit types having symmetry and periodicity as Halo, Lyapunov and Lissajous orbits [66].

3.2.1. Symmetry in the RTB dynamics

In synodic reference frame, two primaries and collinear libration points lie along x axis and this configuration of the RTBP has symmetry with respect to the x-axis [60]. First, this statement can be seen on the positions of the two triangular libration points L4 and L5, which are symmetric with respect to x axis. The real reason behind this is the potential function of the RTB dynamics that depends on the distance of the third body from the two primaries.

A periodic orbit can be defined mathematically as follows: the trajectory curve obtained by initial conditions X_0 will provide same conditions after a T period time in forward dynamic, as well, a $-T$ period time in backward dynamic [66].

Let $\dot{X} = f(X, t)$; and

$$X(t) = e^{Ft}X_0 = \Phi(t)X_0 \qquad \text{Eq. 3-1}$$

Considering the first expansion of Taylor series of e^{Ft}, the X values at time t is approximately can be written as:

$$X(t) = (I + Ft)X_0 \qquad \text{Eq. 3-2}$$

So, the final states obtained for a time T and $-T$

$$X_f(T) = (I + FT)X_0 \qquad \text{Eq. 3-3}$$

$$X_f(-T) = (I + F(-T))X_0 \qquad \text{Eq. 3-4}$$

Let take the state vector as:

$$X = [x \quad y \quad z \quad \dot{x} \quad \dot{y} \quad \dot{z}]^T = [x_1 \quad x_2 \quad x_3 \quad x_4 \quad x_5 \quad x_6]^T$$

Let take dimensionless equations of motion set for RTB dynamics:
Forward dynamics:

$$
\begin{bmatrix} \dot{x}_1 \\ \dot{x}_2 \\ \dot{x}_3 \\ \dot{x}_4 \\ \dot{x}_5 \\ \dot{x}_6 \end{bmatrix} = \dot{X}_{f\_forward} = f(X, T)
$$

$$
= \begin{bmatrix} x_4 \\ x_5 \\ x_6 \\ x_1 + 2x_5 - \dfrac{(1-\mu)(x_1+\mu)}{r_1^3} - \dfrac{\mu(x_1-(1-\mu))}{r_2^3} \\ x_2 - 2x_4 - \dfrac{(1-\mu)x_2}{r_1^3} - \dfrac{\mu x_2}{r_2^3} \\ -\dfrac{(1-\mu)x_3}{r_1^3} - \dfrac{\mu x_3}{r_2^3} \end{bmatrix}
\qquad \text{Eq. 3-5}
$$

Backward dynamics:

$$
\dot{X}_{f\_backward} = f(X, -T) =
$$

$$
\begin{bmatrix} -x_4 \\ -x_5 \\ -x_6 \\ -\left\{ x_1 + 2x_5 - \dfrac{(1-\mu)(x_1+\mu)}{r_1^3} - \dfrac{\mu(x_1-(1-\mu))}{r_2^3} \right\} \\ -\left\{ (x_2) - 2(x_4) - \dfrac{(1-\mu)(x_2)}{r_1^3} - \dfrac{\mu(x_2)}{r_2^3} \right\} \\ -\left\{ -\dfrac{(1-\mu)x_3}{r_1^3} - \dfrac{\mu x_3}{r_2^3} \right\} \end{bmatrix}
\qquad \text{Eq. 3-6}
$$

And finally, due to the symmetry with respect to the x axis, after a time T and –T, the third body must have an opposite the y coordinate; $y(T) = -y(-T)$. For the velocity components, the distance took for a time T and –T can be written as:

$\dot{x} = dx/dT$, and x will be in the same direction but time is reversed:

$\dot{x}(T) = dx/dT$, and $\dot{x}(-T) = \frac{dx}{-dT} = -\dot{x}(T)$

For $\dot{y} = dy/dT$, y distances are in opposite direction and time as well:

$\dot{y}(T) = dy/dT$, and $\dot{y}(-T) = \frac{-dy}{-dT} = \dot{y}(T)$

$\dot{z} = dz/dT$, and z will be in the same direction but time is reversed:

$\dot{z}(T) = dz/dT$, and $\dot{z}(-T) = \frac{dz}{-dT} = -\dot{z}(T)$

So, finally, we obtain the final states as:

$$\begin{bmatrix} x \\ y \\ z \\ \dot{x} \\ \dot{y} \\ \dot{z} \end{bmatrix}_{f\_forward} = \begin{bmatrix} x \\ -y \\ z \\ -\dot{x} \\ \dot{y} \\ -\dot{z} \end{bmatrix}_{f\_backward} \qquad \text{Eq. 3-7}$$

Table 3.1 gives the results of the final states obtained for both forward and backward dynamics for final times quarter, third, half, and full period. Next, figures show the trajectory obtained for forward and backward dynamics.

Figure 3-1 presents the forward and backward trajectories for t=T/3. The third body is initiated from the same initial coordinates and velocities, and the final states obtained satisfy the symmetry property of the orbit, it is totally symmetric with respect to x axis.

Table 3.1. ICs of forward and backward dynamics

time	X_final	
T/4	$\begin{bmatrix} 0.990744452492618 \\ -0.004918736621312 \\ 0.000518887478346 \\ -0.003361097580437 \\ 0.000557837344515 \\ 0.004329445168714 \end{bmatrix}_{f\_forward}$;	$\begin{bmatrix} 0.990744452492618 \\ 0.004918736621312 \\ 0.000518887478346 \\ 0.003361097580437 \\ 0.000557837344515 \\ -0.004329445168714 \end{bmatrix}_{f\_backward}$
T/3	$\begin{bmatrix} 0.989863808092535 \\ -0.004162743056771 \\ 0.001522587646915 \\ -0.003340473490557 \\ 0.005224669303005 \\ 0.003422848465568 \end{bmatrix}_{f\_forward}$;	$\begin{bmatrix} 0.989863808092535 \\ 0.004162743056771 \\ 0.001522587646915 \\ 0.003340473490557 \\ 0.005224669303005 \\ -0.003422848465568 \end{bmatrix}_{f\_backward}$
T/2	$\begin{bmatrix} 0.988877149288380 \\ 0.000000000001388 \\ 0.002450740009211 \\ -0.000000000008314 \\ 0.009728312882062 \\ 0.000000000001511 \end{bmatrix}_{f\_forward}$;	$\begin{bmatrix} 0.988877149288380 \\ -0.000000000001388 \\ 0.002450740009211 \\ 0.000000000008314 \\ 0.009728312882062 \\ -0.000000000001511 \end{bmatrix}_{f\_bakcward}$
T	$\begin{bmatrix} 0.991975555532526 \\ 0.000000000119871 \\ -0.001916554249932 \\ -0.000000000400615 \\ -0.011028335778654 \\ -0.000000000108102 \end{bmatrix}_{f\_forward}$;	$\begin{bmatrix} 0.991975555532526 \\ -0.000000000119871 \\ -0.001916554249932 \\ 0.000000000400615 \\ -0.011028335778654 \\ 0.000000000108102 \end{bmatrix}_{f\_bakcward}$

From the values given in the table it is seen that for t=T/2 trajectory pass the y axis, half period reach y axis. It means that the orbit is a symmetric periodic orbit. Figure 3-2 shows the trajectory obtained for t=T/2. For full orbital period the same final position is obtained. The trajectories obtained are overlapping. Figure 3-3 shows final trajectories for t=T.
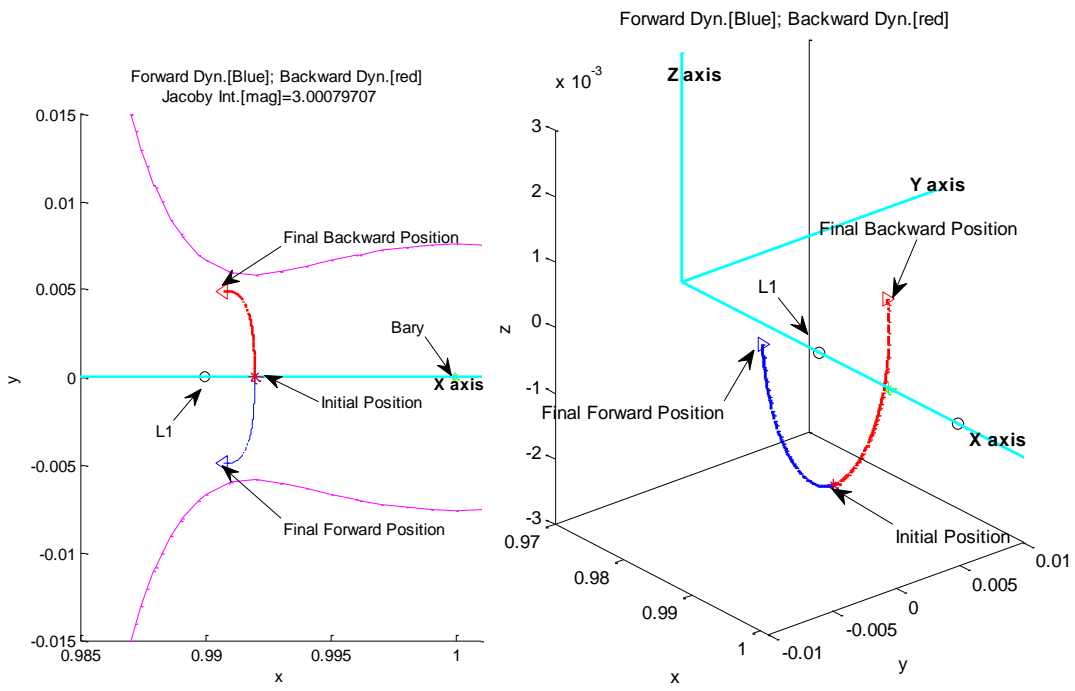
Figure 3-1. Forward and backward trajectories for t=T/3
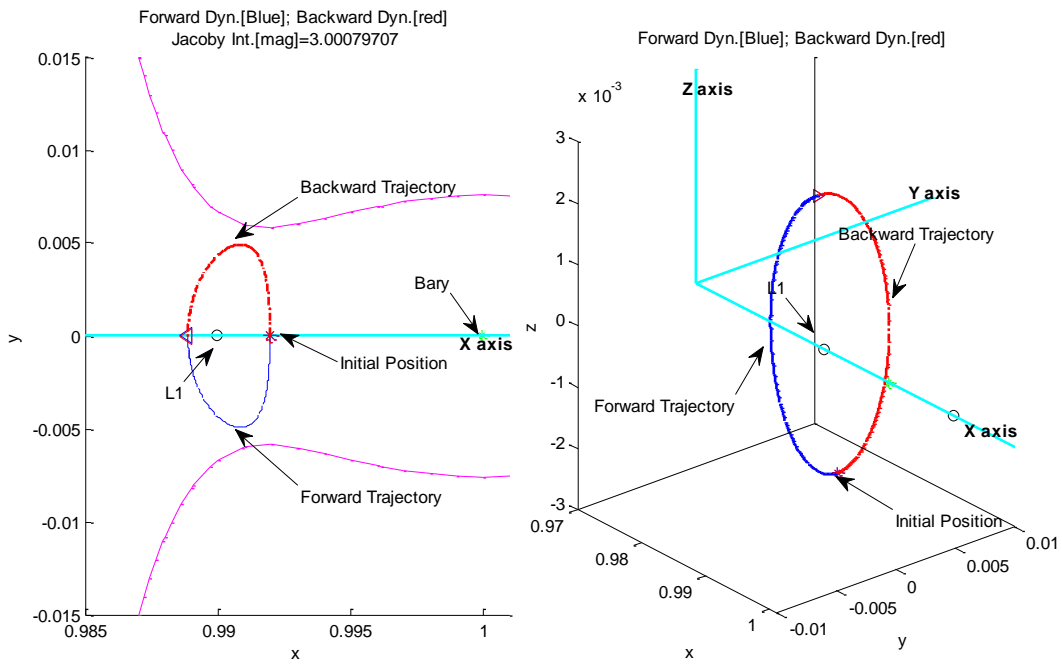
Figure 3-2. Forward and backward trajectories for t=T/2
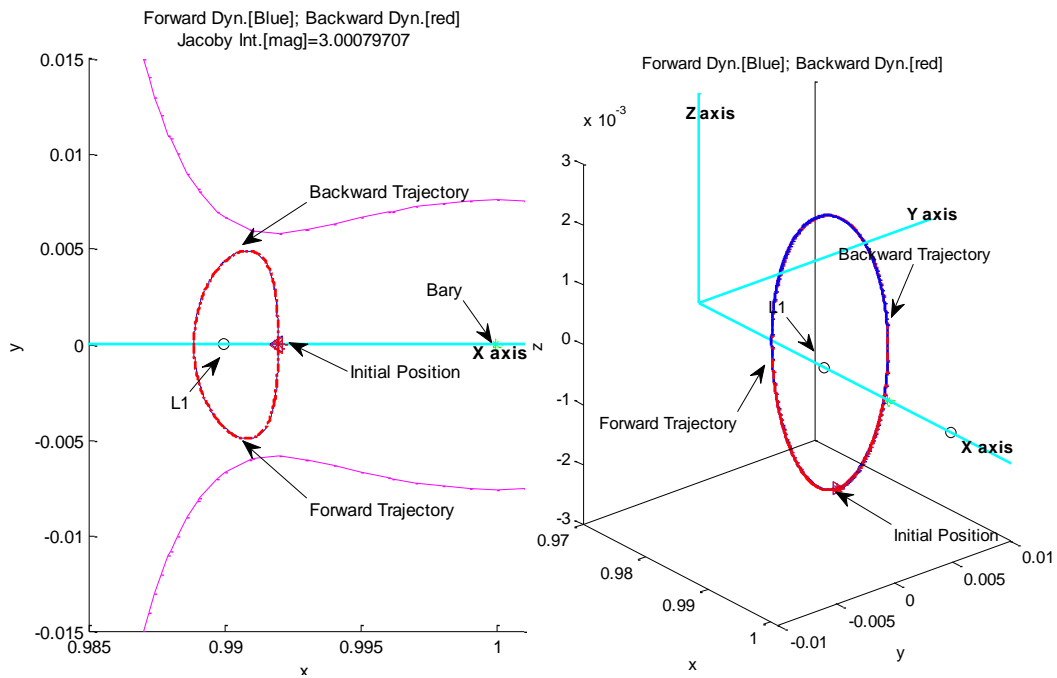
Figure 3-3. Forward and backward trajectories for t=T

The next subsection presents how to compute proper initial conditions that satisfy periodic Halo orbit using the symmetry property given here.

3.2.2. Halo orbit design methods

A halo orbit is a periodic orbit and every periodic motion has a symmetrical geometry with respect to the axis defined. So, the symmetry property of the RTB problem is used to design Halo orbit. According to the definition of the Halo orbit, this orbit has out of plane motion, symmetric with respect to the x axis, near the libration points L1 and L2. The main target is to find initial states in the xz plane ($y(0) = 0$) that satisfy periodic motion. The initial velocity components are taken as $\dot{x} = \dot{z} = 0$, so we have only a velocity on y axis.

The Initial guess for X_0 is based on the results obtained from Poincare Map (Appendix-G). However, this X_0 does not guarantee to have a periodic orbit. Here

two main methods are presented that gives a procedure to compute appropriate initial state for Halo orbit [66, 68].

The first method state that; if the orbit is periodic, after a half period of time the final positions and velocities must satisfy the symmetry [66]. So, when the initial positions taken in xz plane and velocities as well, the following relation must be obtained:

$$
\begin{bmatrix} x \\ y \\ z \\ \dot{x} \\ \dot{y} \\ \dot{z} \end{bmatrix}_{t=0} \rightarrow \begin{bmatrix} x_0 \\ 0 \\ z_0 \\ 0 \\ \dot{y}_0 \\ 0 \end{bmatrix}_{t=0} \rightarrow \begin{bmatrix} x_f \\ 0 \\ z_f \\ 0 \\ \dot{y}_f \\ 0 \end{bmatrix}_{t=\frac{T}{2}=\tau} = \begin{bmatrix} x_f \\ 0 \\ z_f \\ 0 \\ -\dot{y}_f \\ 0 \end{bmatrix}_{t=-\frac{T}{2}=-\tau}
$$

Now, the question formed as: what are the values of x, z and $\dot{y}$ that ensure that $y = \dot{x} = \dot{z} = 0$ when time is half orbital period $\tau = T/2$. Actually, the orbital period is not known exactly true from the initial guess. For that reason, it is needed to modify the problem like that: what are the values of τ, z and $\dot{y}$ that ensure that $y = \dot{x} = \dot{z} = 0$ for a given fixed x value.

Newton iteration method is used to solve this problem. State transition matrix is also needed in Newton method. First, dimensionless equations of motion are taken as (the bar sign indicates dimensionless states):

$$
\dot{X} = f(X) = \begin{bmatrix} \dot{\bar{x}} \\ \dot{\bar{y}} \\ \dot{\bar{z}} \\ \ddot{\bar{x}} \\ \ddot{\bar{y}} \\ \ddot{\bar{z}} \end{bmatrix} = \begin{bmatrix} u \\ v \\ w \\ \bar{x} + 2\dot{\bar{y}} - \dfrac{(1-\mu)(\bar{x}+\mu)}{\bar{r}_1^3} - \dfrac{\mu(\bar{x}-(1-\mu))}{\bar{r}_2^3} \\ \bar{y} - 2\dot{\bar{x}} - \dfrac{(1-\mu)\bar{y}}{\bar{r}_1^3} - \dfrac{\mu\bar{y}}{\bar{r}_2^3} \\ -\dfrac{(1-\mu)\bar{z}}{\bar{r}_1^3} - \dfrac{\mu\bar{z}}{\bar{r}_2^3} \end{bmatrix} \quad \text{Eq. 3-8}
$$

Newton's method using the first Taylor series approximation gives the following expression:

$$X_{k+1} = X_k - \begin{bmatrix} \dfrac{\partial f_1}{\partial x_1} & \cdots & \dfrac{\partial f_1}{\partial x_n} \\ \vdots & \ddots & \vdots \\ \dfrac{\partial f_n}{\partial x_1} & \cdots & \dfrac{\partial f_n}{\partial x_n} \end{bmatrix}^{-1} f(X) \qquad \text{Eq. 3-9}$$

Here, the minimization function selected to solve the problem is $\bar{y} = \dot{x} = \dot{z} = 0$:

$$f(X_{sub}) = \begin{bmatrix} \dot{\bar{x}} \\ \dot{\bar{z}} \\ \bar{y} \end{bmatrix} = \begin{bmatrix} 0 \\ 0 \\ 0 \end{bmatrix} \qquad \text{Eq. 3-10}$$

As the set searching is x, z and $\dot{y}$ that ensure minimization function, the differential variation of $f(X_{sub})$ with respect to searching set is called D_f matrix:

$$D_f = \begin{bmatrix} \dfrac{\partial f_4}{\partial \bar{z}} & \dfrac{\partial f_4}{\partial \dot{\bar{y}}} & \dfrac{\partial f_4}{\partial \tau} \\ \dfrac{\partial f_6}{\partial \bar{z}} & \dfrac{\partial f_6}{\partial \dot{\bar{y}}} & \dfrac{\partial f_6}{\partial \tau} \\ \dfrac{\partial f_2}{\partial \bar{z}} & \dfrac{\partial f_2}{\partial \dot{\bar{y}}} & \dfrac{\partial f_2}{\partial \tau} \end{bmatrix} \qquad \text{Eq. 3-11}$$

We know that:

$$X(t) = e^{Ft}X_0 = \Phi(t)X_0 \rightarrow \dot{X} = \dot{\Phi}(t)X_0$$

$$\text{Eq. 3-12}$$

And

$$\dot{\Phi}(t) = F\Phi(t) = D_f\Phi(t) \text{ where } \Phi(0) = I \text{ is an identity matrix}$$

$$D_f = \begin{bmatrix} \Phi_{4,3} & \Phi_{4,5} & f_4 \\ \Phi_{6,3} & \Phi_{6,5} & f_6 \\ \Phi_{2,3} & \Phi_{2,5} & f_2 \end{bmatrix}$$

Eq. 3-13

Finally, Newton iteration can be rewritten as:

$$\begin{bmatrix} \bar{z}^* \\ \dot{\bar{y}}^* \\ \tau^* \end{bmatrix}_{k+1} = \begin{bmatrix} \bar{z}^* \\ \dot{\bar{y}}^* \\ \tau^* \end{bmatrix}_k - (D_f)^{-1} \begin{bmatrix} \dot{x} \\ \dot{z} \\ \bar{y} \end{bmatrix}$$

Eq. 3-14

This iteration gives the initial condition set as:

$$\begin{bmatrix} x \\ y \\ z \\ \dot{x} \\ \dot{y} \\ \dot{z} \end{bmatrix}_{t=0} = \begin{bmatrix} \bar{x}_{fixed} \\ 0 \\ \bar{z}^* \\ 0 \\ \dot{\bar{y}}^* \\ 0 \end{bmatrix}$$ and the orbital period will be: $T = 2\tau^*$.

The iteration is terminated when a predefined error between successive results is reached, this iteration stopping parameter is denoted as ϵ, and it is computed as:

$$\epsilon = \begin{bmatrix} \bar{z}^* \\ \dot{\bar{y}}^* \\ \tau^* \end{bmatrix}_{k+1} - \begin{bmatrix} \bar{z}^* \\ \dot{\bar{y}}^* \\ \tau^* \end{bmatrix}_k$$

Eq. 3-15

The second method also uses the symmetry of the RTB problem [67]. As done in the first method, the initial conditions are taken as $y = \dot{x} = \dot{z} = 0$ and expected final conditions are $y = \dot{x} = \dot{z} = 0$ since we aim to have a periodic orbit. Here; $y_f = 0$ is taken as the first intersection of the orbit which passes through $y = 0$ point, by initial state X_0 . Then minimization function is defined again as:

$$f(X_{sub}) = \begin{bmatrix} \dot{x} \\ \dot{z} \end{bmatrix}_f = \begin{bmatrix} 0 \\ 0 \end{bmatrix}$$

Eq. 3-16

It is possible to take the initial guess for X_0 from Poincare mapping, as done in the first method. However, here, the integrations on the curve "s" is done using Adams predictor. The differential equations of the curve integration are:

$$\frac{dx}{ds} = \frac{K_1}{K_0} \quad ; \frac{dz}{ds} = \frac{K_2}{K_0} \quad ; \quad \frac{d\dot{y}}{ds} = \frac{K_3}{K_0}$$

Eq. 3-17

where

$$K_1 = \frac{\partial f_1}{\partial z}\frac{\partial f_2}{\partial \dot{y}} - \frac{\partial f_1}{\partial \dot{y}}\frac{\partial f_2}{\partial z}$$

$$K_2 = -\frac{\partial f_1}{\partial x}\frac{\partial f_2}{\partial \dot{y}} + \frac{\partial f_1}{\partial \dot{y}}\frac{\partial f_2}{\partial x}$$

$$K_3 = -\frac{\partial f_1}{\partial x}\frac{\partial f_2}{\partial z} + \frac{\partial f_1}{\partial z}\frac{\partial f_2}{\partial x}$$

$$K_0 = \sqrt{K_1^2 + K_2^2 + K_3^2}$$

Eq. 3-18

Adam's predictor (Adams Bashforth method):

According to the order selected the constant of the formulas changes with the values given in the following table.

Adam's prediction:

$$X_{i+1} = X_i + h \sum_{k=1}^{n} \alpha_{nk}\, f_{i-k+1}$$

Eq. 3-19

Table 3-2 Adams Bashforth coefficients

n \ k	1	2	3	4	5
1	1	–	–	–	–
2	3/2	-1/2	–	–	–
3	23/12	-16/12	5/12	–	–
4	55/24	-59/24	37/24	-9/24	–
5	190/720	-2774/720	2616/720	-1274/720	251/720

$$X_1 = X_0 + h\left(\frac{\partial x}{\partial s}\right)_0$$

$$X_2 = X_1 + \frac{3}{2}h\left(\frac{\partial x}{\partial s}\right)_1 - \frac{1}{2}h\left(\frac{\partial x}{\partial s}\right)_0 \qquad \text{Eq. 3-20}$$

$$X_3 = X_2 + \cdots$$

Performing this method gives the proper initial values of $x, z, \dot{y}$. This is an approximation for periodic orbit; it is needed to refine it. This refinement is done using Newton method.

$$\begin{bmatrix} \bar{x}^* \\ \bar{z}^* \\ \dot{\bar{y}}^* \end{bmatrix}_{k+1} = \begin{bmatrix} \bar{x}^* \\ \bar{z}^* \\ \dot{\bar{y}}^* \end{bmatrix}_k - \left(D_f\right)^{-1}\begin{bmatrix} \dot{\bar{x}} \\ \dot{\bar{z}} \\ \bar{y} \end{bmatrix} \qquad \text{Eq. 3-21}$$

Where D_f :

$$D_f = \begin{bmatrix} \Phi_{4,1} & \Phi_{4,3} & \Phi_{4,5} \\ \Phi_{6,1} & \Phi_{6,3} & \Phi_{6,5} \\ \Phi_{2,1} & \Phi_{2,3} & \Phi_{2,5} \end{bmatrix} \qquad \text{Eq. 3-22}$$

Actually the main structure of the Newton method is:

$$[X]_{k+1} = [X]_k + \Delta X_k \qquad \text{Eq. 3-23}$$

The iteration is terminated based on the value of ϵ, as given in Eq. 3-15. In reference [61], a modified Newton method is used by adding a positive definite weight matrix.

Where; ΔX_k satisfy that: $G(\Delta X_k) = -F(X_k)$

Minimize the $\Delta X_k{}^T Q \Delta X_k$

So ΔX_k is taken as:

$$\Delta X_k = -Q^{-1}G^T(GQ^{-1}G^T)^{-1}F(X_k) = -Q^{-1}D_f{}^T\left(D_f Q^{-1}D_f{}^T\right)^{-1}\begin{bmatrix}\dot{x}\\\dot{z}\\\bar{y}\end{bmatrix} \qquad \text{Eq. 3-24}$$

If $Q = I$, unmodified Newton Method:

$$\Delta X_k = -G^T F(X_k) = -\left(D_f\right)^{T=-1}F(X_k) = -\left(D_f\right)^{-1}\begin{bmatrix}\dot{x}\\\dot{z}\\\bar{y}\end{bmatrix} \qquad \text{Eq. 3-25}$$

This iteration gives the initial condition set as:

$$\begin{bmatrix}x\\y\\z\\\dot{x}\\\dot{y}\\\dot{z}\end{bmatrix}_{t=0} = \begin{bmatrix}\bar{x}^*\\0\\\bar{z}^*\\0\\\dot{\bar{y}}^*\\0\end{bmatrix} \qquad \text{Eq. 3-26}$$

In this thesis, Newton method is used to obtain a Halo orbit for chief satellite. The codes are prepared using Matlab and Simulink 2012a version. The execution time spent to compute Chief's halo orbit and the performance of the codes are given in details in Appendix-I, with the benchmark test of the computer used. For instance, in the computation of the chief's halo orbit, the time spent for one iteration is approximately 4 seconds with simulation having a sampling time that is equal to 3600 sec. In simulation, one iteration is the half period time of the chief's orbit, and it is approximately equal to 0.23 year.

3.2.3. Halo orbit design near L1

The methods described in preceding sub-chapters are used in this section to design a Halo orbit around L1 point.

3.2.3.1. Computation of Halo orbit near L1

As an initial guess for the X_0 state vector, the coordinates of the fixed point of the Poincare section is taken. After that RTB dynamics is run the see the trend of the trajectory with these initial coordinates. Then, Newton Method is implemented to find initial conditions that ensure periodic orbit. x position is chosen as 1.22 million kilometers away from Earth toward Sun, and z position is 0.28 million km. this z distance is selected according to the roughly orbital radius of a Halo orbit at this x coordinate, considering SOHO satellite. The distance from Earth to initial position is approximately 1.25 million kilometers. The orbit velocity in y direction is taken as 0.35 km/s as SOHO satellite [68]. As an initial guess, the following dimensionless values are taken:

$$\begin{bmatrix} \bar{x} \\ \bar{y} \\ \bar{z} \\ \dot{\bar{x}} \\ \dot{\bar{y}} \\ \dot{\bar{z}} \end{bmatrix}_{t=0} = \begin{bmatrix} 0.991841763696132 \\ 0 \\ -0.001871684394736 \\ 0 \\ -0.011750780966904 \\ 0 \end{bmatrix}$$

The gravitational constant and mass values of the primaries are taken as follows:

$$Gm_{SUN} = 1.327227188067 * 10^{11} \ \frac{\text{km}^3}{\text{s}^2};$$

$$Gm_{BARY} = 4.034799534017 * 10^5 \ \frac{\text{km}^3}{\text{s}^2}$$

Gm_{BARY} is the Gravitational constant and mass value of the Earth added Moon:

$$Gm_{BARY} = Gm_{Earth} + Gm_{Moon}$$

The parameter μ used in the dimensionless equations of motion is the proportion of the Bary mass to the total mass.

$$\mu = \frac{Gm_{BARY}}{Gm_{SUN} + Gm_{BARY}}$$

The astronomic unit distance, the distance between bary and sun is taken as:

$$au = 149.597.87066 * 10^6 \text{km}$$

The iteration for the Newton method is initiated with the initial guess X_0, and then Newton method gives new state values X_{i+1} that try to ensure the periodic orbit. The iteration is continued until acquiring a position error 0.748 meter (5*1e-12unit distance) between two successive iteration steps. Figure 3-4 shows the results obtained on Newton method for each of the iteration steps. This figure is obtained by running the RTB dynamics for half period of time. The aim is to obtain a passage at y axis, after a half period time. It is seen that at 8th step, the required convergence is reached. And the final step is around y=0 value. This final trajectory is the first half of the computed Halo orbit.
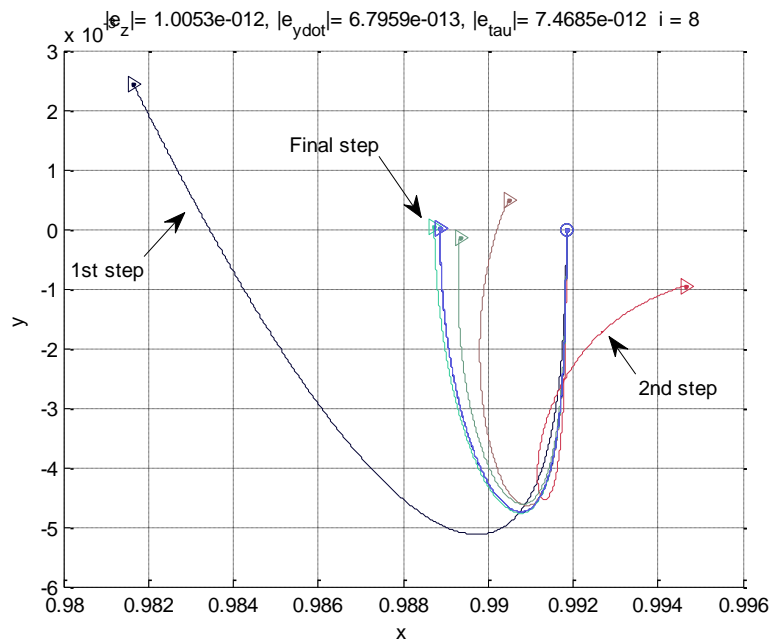
Figure 3-4. Trajectories obtained at L1 for each step of iteration

The following 2 dimensional and 3 dimensional plots given in Figure 3-5 present the trajectories obtained using initial state X_0 coming from initial guess (called 1st trajectory), and using X_0 obtained from Newton iterations (called 2nd trajectory).
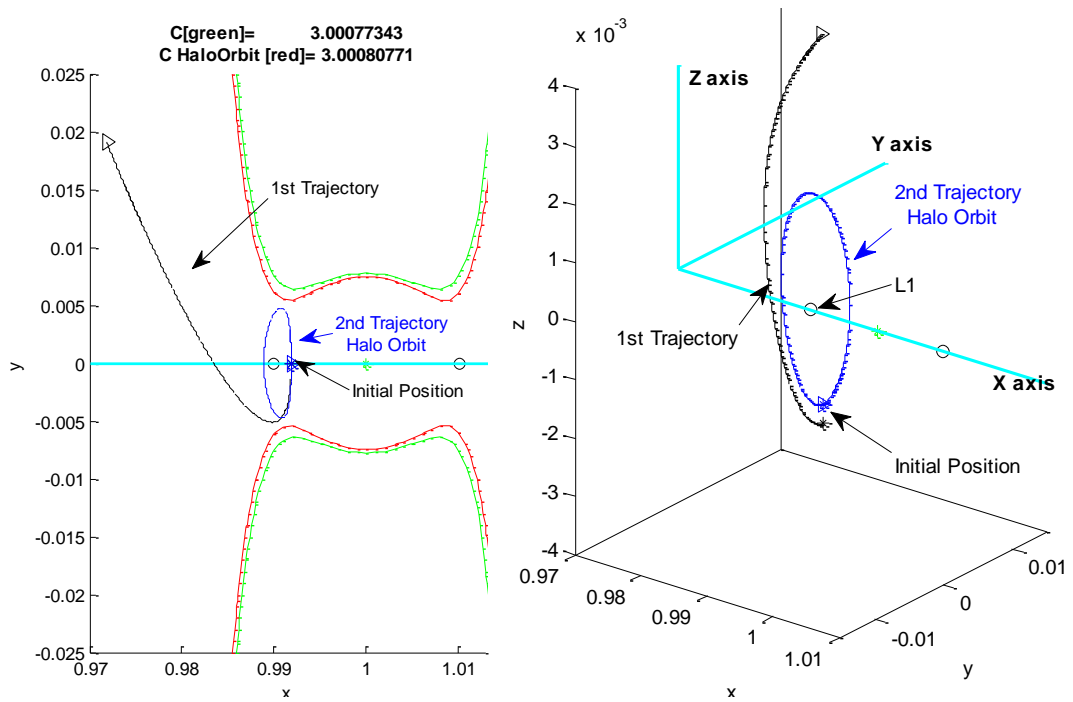
Figure 3-5. Trajectories obtained using initial state X_0

Table *3.3* gives the initial states comparison. In order to obtain a halo orbit for this fixed x coordinate, it is seen that the z value is decreased.

Table 3.3. Initial states

Guessed initial state vector X_0 [unit]	Computed initial state vector X_0 for Halo [unit]	Difference in [km] and [m/s]
$\begin{bmatrix} 0.991841763696132 \\ 0 \\ -0.001871684394736 \\ 0 \\ -0.011750780966904 \\ 0 \end{bmatrix}$	$\begin{bmatrix} 0.991841763696132 \\ 0 \\ -0.001543996135220 \\ 0 \\ -0.010527737547337 \\ 0 \end{bmatrix}$	$\begin{bmatrix} 0\,km \\ 0\,km \\ 49021.5\,\text{km} \\ 0\,m/s \\ 36.43\,m/s \\ 0\,m/s \end{bmatrix}$
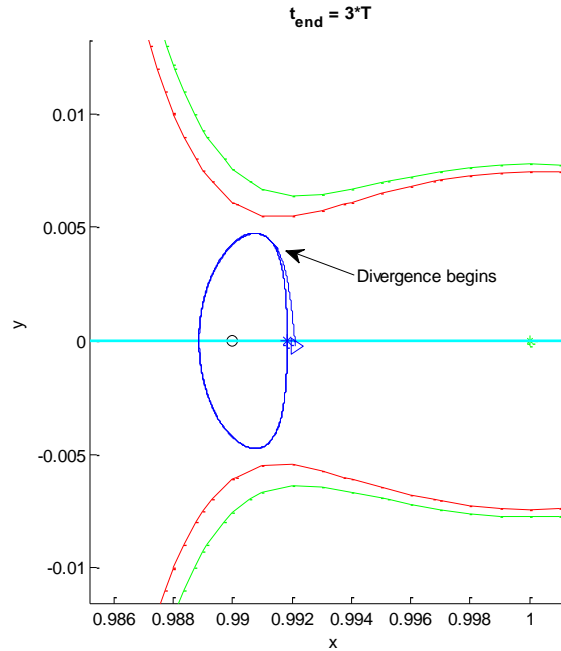
Figure 3-6. Divergence at trajectory

It is seen that periodic orbit is obtained. Now, the main question is about the stability and continuity of this orbit. It should be noted that, here all procedure is run under undisturbed environment. If the trajectory starts to diverge, the main reasons of this divergence, are the differential matrix used in Newton since it takes the first order Taylor series expansion (Eq. 3-9) and the iteration stopping criteria (Eq. 3-15). So, the initial conditions computed using symmetry property for half orbital period of time does not provide a periodic orbit for long time, since the nature of collinear libration points is unstable. Figure 3-6 presents the trajectory obtained for three orbital periods in non-disturbed case, and it is noticed that after 2.5 periods the divergence begins, the periodicity cannot be sustained. The method used to validate the computation done on the inhouse prepared software are shared in Chapter 2. In addition, the simulation is re-run using inertial frame mechanization to have an idea on the computation accuracy and the results are presented in Appendix-J. The stability analyses method and the stability figure of the Halo orbit family for different fixed x coordinates are discussed in the next sections.

92

3.2.3.2. Stability of the Halo orbit near L1

In Halo orbit design, the equations of motion are propagated using discrete model, so the stability analysis can be done using discrete-time system. It is already stated that $\dot{X} = f(X, t)$ and using first order expansion of e^{Ft} can be written in continuous form as $X(t) = (I + Ft)X(0) = \Phi(t)X(0)$. The time derivative of Φ is rewritten as $\dot{\Phi}(t) = F\Phi(t)$ where F is the state propagation matrix. The discrete form can be rewritten as: $X_{k+1} = (I + Fdt)X_k$ where dt is the sampling rate.

For discrete-time system, the state transition matrix Φ gives the information about stability of the system. For a Φ square matrix, it is called "Lyapunov" when spectral radius is less and equal to one and the modulus of every eigenvalue of Φ are equal to one has equal algebraic and geometric multiplicity; and it is called "Schur" when spectral radius is less than one [69]. So, a discrete time linear system, here it is represented by Φ, is asymptotically stable if and only if all the eigenvalues of state transition matrix Φ are inside the unit circle.

For a periodic motion, the state transition matrix Φ has always two eigenvalues equal to unity, because having a periodic motion means that there is always an oscillation with constant amplitude and frequency. The first unity eigenvalue is related to the eigenvector that indicates the direction of the flow; it is tangent to the trajectory. The second unity is related to the energy, it indicates the direction of change in energy. The rest four eigenvalues describe the dynamics near the orbit. Two of them have both real and imaginary part, conjugate to each other, they present to the center direction of the orbit. These eigenvalues have modulus equal to one, so they lie on the unit circle. It indicates that the orbit is near Halo and will remain near Halo for all time. The last two eigenvalues are real and reciprocal to each other, it means that one is too large, the other is too small. They show the stable and unstable manifolds of the orbit [66]. The determinant value of Φ is also a parameter that must be checked, it should be equal to one.

Finally, it can be stated that the orbit is unstable if one of the eigenvalues is outside of the unit circle. A stability parameter v_i is also defined in Ref.[67], to see the characteristic of the system: $v_i = 0.5(\lambda_i + 1/\lambda_i)$, orbit is stable if both $|v_1| < 1$ and $|v_2| < 1$.

Here, Halo orbit found in the previous section is taken as example to see its stability. The dynamic is run for one orbital time, tend = T, and Φ is computed for this end time.

Table 3.4. ICs for halo orbit

X_0 for Halo [unit]	$X_{final} = X(T)$ for Halo [unit]	Difference
X_0 $= \begin{bmatrix} 0.991841763696132 \\ 0 \\ -0.001543996135220 \\ 0 \\ -0.010527737547337 \\ 0 \end{bmatrix}$	X_0 $= \begin{bmatrix} \mathbf{0.991841763}803963 \\ -\mathbf{0.000000000}97927 \\ -\mathbf{0.001543996}125539 \\ \mathbf{0.000000000}328306 \\ -\mathbf{0.010527737}745419 \\ 0.000000000068948 \end{bmatrix}$	ΔX $= \begin{bmatrix} 16.13 \text{ m} \\ -14.65 \text{ m} \\ 1.45\text{m} \\ 0.978 * 10^{-5} \text{ m/s} \\ -0.590 * 10^{-5} \text{ m/s} \\ 0.205 * 10^{-5} \text{ m/s} \end{bmatrix}$

It is seen that the difference between initial and final states is around 15 m for distances and negligible for velocities. The determinant of Φ is approximately one: $|\Phi| = 1.000000000360359$, and eigenvalues are:

$$\lambda = \begin{bmatrix} 1593.639 \\ 1.000003938283 \\ 0.980248301428 - 0.197770744924\text{i} \\ 0.980248301428 + 0.197770744924\text{i} \\ 0.999996061732 \\ 0.000627494557 \end{bmatrix}$$

Here the first eigenvalue λ_1 is outside of the unit circle and it shows that the orbit is not stable. As described above, first eigenvalue is very large and the last one is too small, and they are reciprocal: $1/\lambda_6 = \frac{1}{0.000627494557} = 1593.639 = \lambda_1$.

These reciprocal eigenvectors correspond to the unstable (λ_1) and stable (λ_6) manifolds of the orbit. The unity eigenvalues are obtained: $\lambda_2\ and\ \lambda_5$, they are on unit circle, they correspond to the center manifolds. The last two $\lambda_3\ and\ \lambda_4$ have real and imaginary parts. The modulus: $|\lambda_3| = |\lambda_4| = 1$, they are inside unit circle [61].

The stability parameter v_i shows also that orbit is unstable.

$$|v| = \begin{bmatrix} 796.82 > 1 \\ 1.000000000007755 > 1 \\ 0.980248 < 1 \\ 0.980248 < 1 \\ 1.000000000007755 > 1 \\ 796.82 > 1 \end{bmatrix}$$

Manifolds can be defined as the interplanetary superhighways formed by the gravitational pull between celestial bodies. Manifolds are the corridors where spacecraft can travel using little amount of fuel. The existence of stable, unstable, and center manifolds indicates that it is possible to find special solutions which converge to libration point, diverge from libration point, or periodically orbit around libration point [60]. There are orbits which converge to the halo orbit in positive time, and orbits which converge to them in backward time. The small enough neighborhoods of the halo orbit make the stable and unstable manifolds. The stable and unstable manifolds are the trajectories which flow in either positive or negative time [61]. For instance, Figure 3-7 shows the trajectories obtained in forward dynamics (in positive time) and backward dynamics (in negative time) and these trajectories make two tubes symmetrical in xy plane.
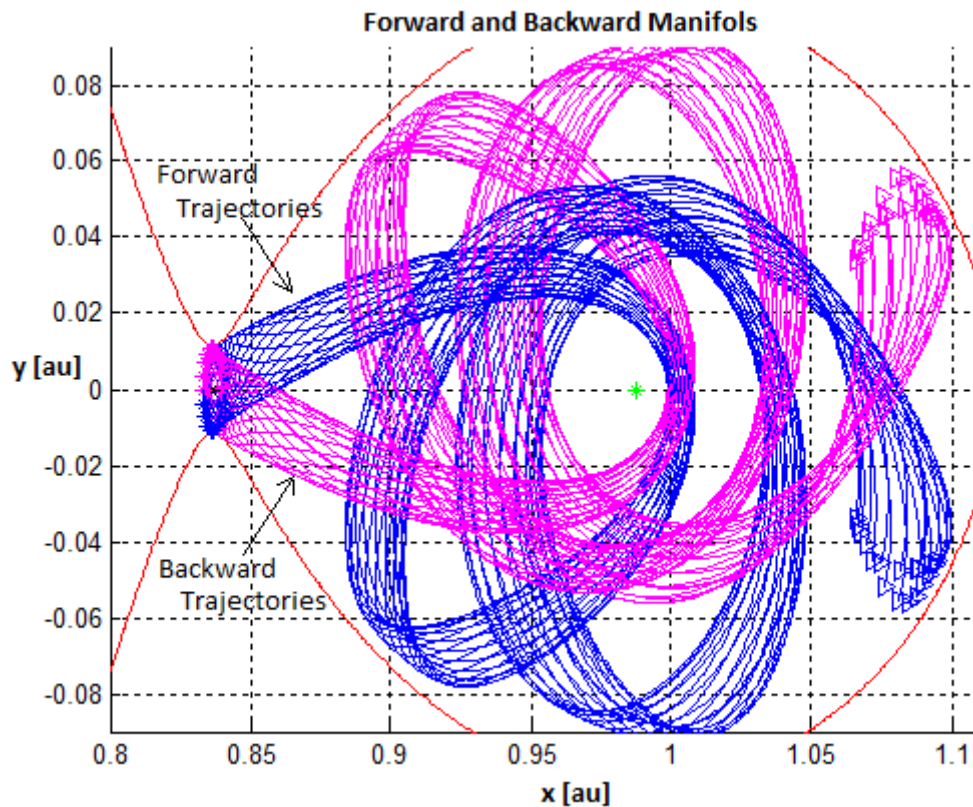
Figure 3-7. Stable and unstable manifolds

3.2.3.3. Halo orbit family for L1 and their stability

In this section, a set of orbits composed of several Halo orbits are taken into consideration in order to see how the orbital characteristic changes depending on their initial coordinates. First, the Halo orbit computed in the previous section is taken as the starting case. Then, the initial x position is increased; the orbit is brought close to the Earth. And the iteration procedure given above is performed for every new x coordinate. Then, the eigenvalues of new orbit are checked to see if the orbit is stable or not. Figure 3-8 presents the Halo orbits obtained for different x values which approaches to the Earth. Here, the increment given to x coordinate for each step is approximately 2992 km (unit increment is 2e-5). The initial conditions computed for the Halo orbit feed the next iteration for new Halo orbit computation, in this IC set, only the x value is augmented for one step of increment.

96
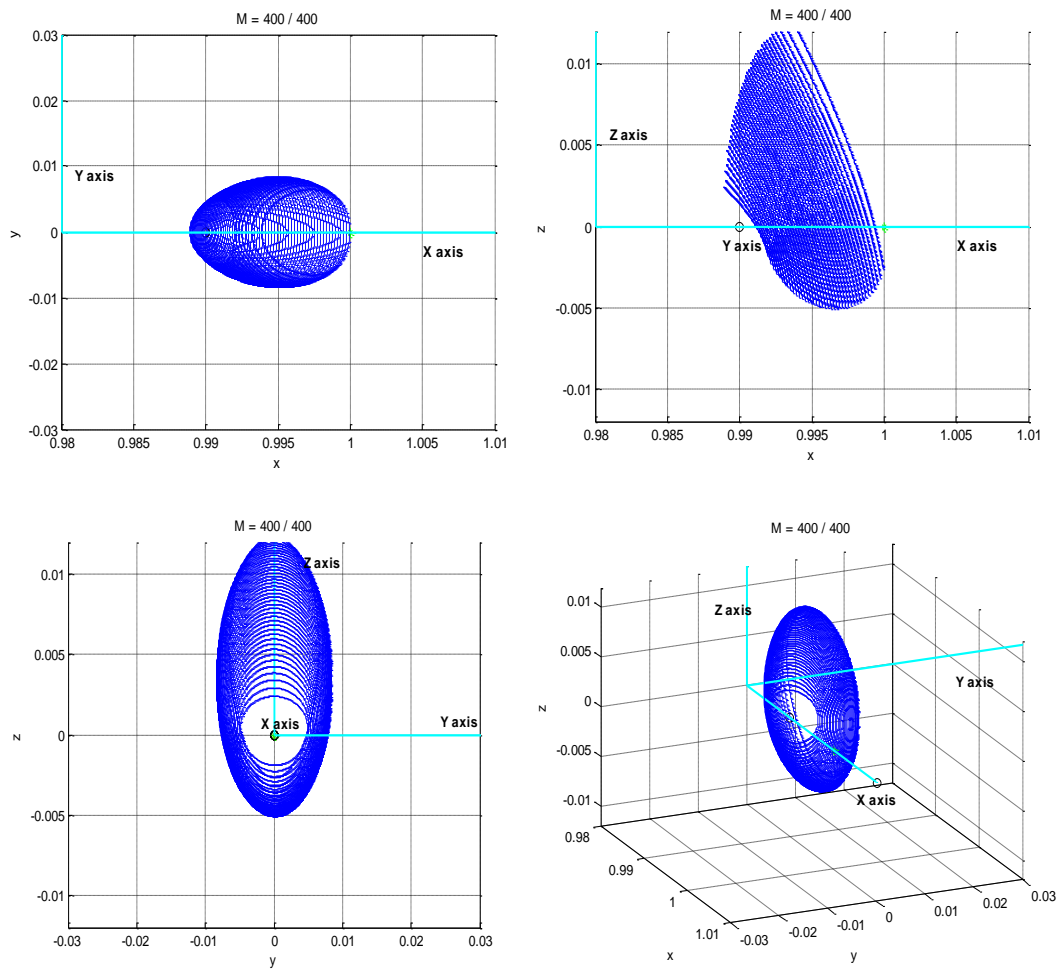
Figure 3-8. Halo orbits family for L1

It is seen that the orbit diameter enlarges as it gets close to the Earth, and orbital period decreases. The shape formed is like a cone growing towards Earth. So, the orbital velocities are higher for the orbits near the Earth. Figure 3-9 and Figure 3-10 plot the modulus of every six eigenvalues computed for each of the halo orbit in the family.
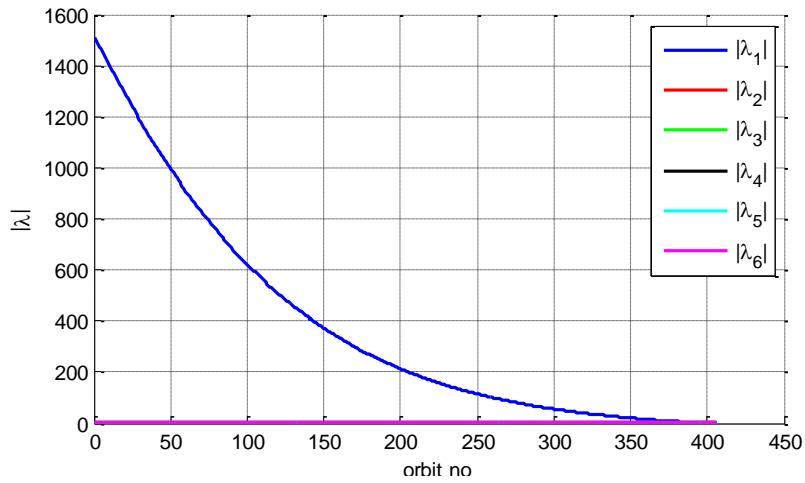
Figure 3-9. Eigenvalues for halo orbit family of L1
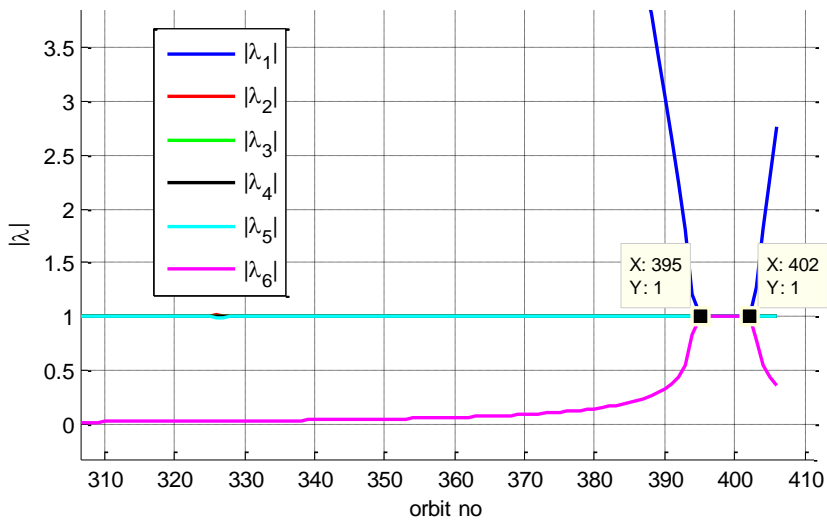
Figure 3-10. Eigenvalues for halo orbit family of L, zoomed view

For the orbit near L1, first eigenvalues have a large value, and it indicates the unstability, and it decrease when orbit get closer the Earth. The sixth eigenvalue of each orbit is near zeros as it is reciprocal of the first one. Other eigenvalues have modulus one. For the orbits numbered between 395 and 402, it is seen that the stability is reached, all eigenvalues has modulus equal to one. After that, the results

start to increase. At 402th orbit, the initial x position coincides with the Earth x coordinate. So, the stable region is the orbit interval numbered 395-402 and it is roughly between 0.999855 – 0 .999995 unit x distance, which is 21623.55 km – 679.86 km away from the Earth. One more consequence obtained from the results: the orbital speed increase when the orbit gets closer to the Earth and the orbital period decrease as well despite to the increase on orbit perimeter.
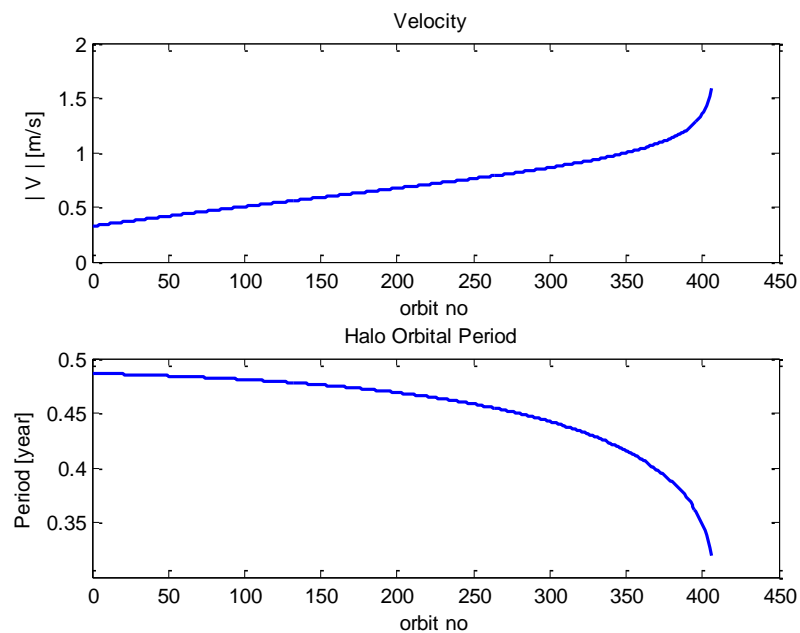
Figure 3-11. Orbital velocity and periods depending on family orbits

One more test is run by adjusting x coordinate increment to 14960 km (unit increment is 10e-5). In that case, Halo orbit is not obtained after 10th increment. The second set of orbits is on the XY plane, so they are Lyapunov orbits. As the initial conditions for the next orbit computation is feed from the previous one, the value of the increment effects the performance of finding Halo orbit. When increment is large, the accuracy become weak, it is gone away from the initial guess provided by Poincare mapping. Figure 3-12 presents the results. The same behavior is obtained

as the previous case: when it is approached to Earth, the orbit radius increase, for both Halo and Lyapunov orbits.
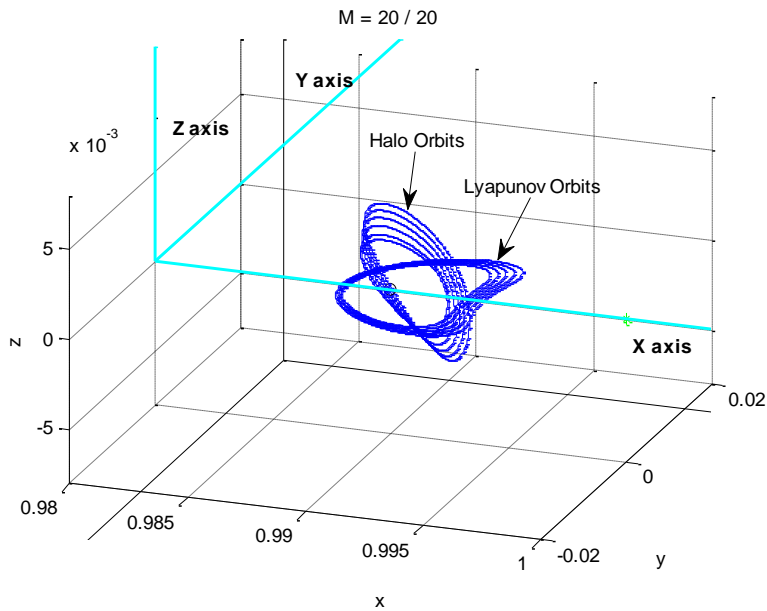
Figure 3-12. Halo and Lyapunov orbits

The modulus of the eigenvalues, velocity and orbital period are given respectively in Figure 3-13.
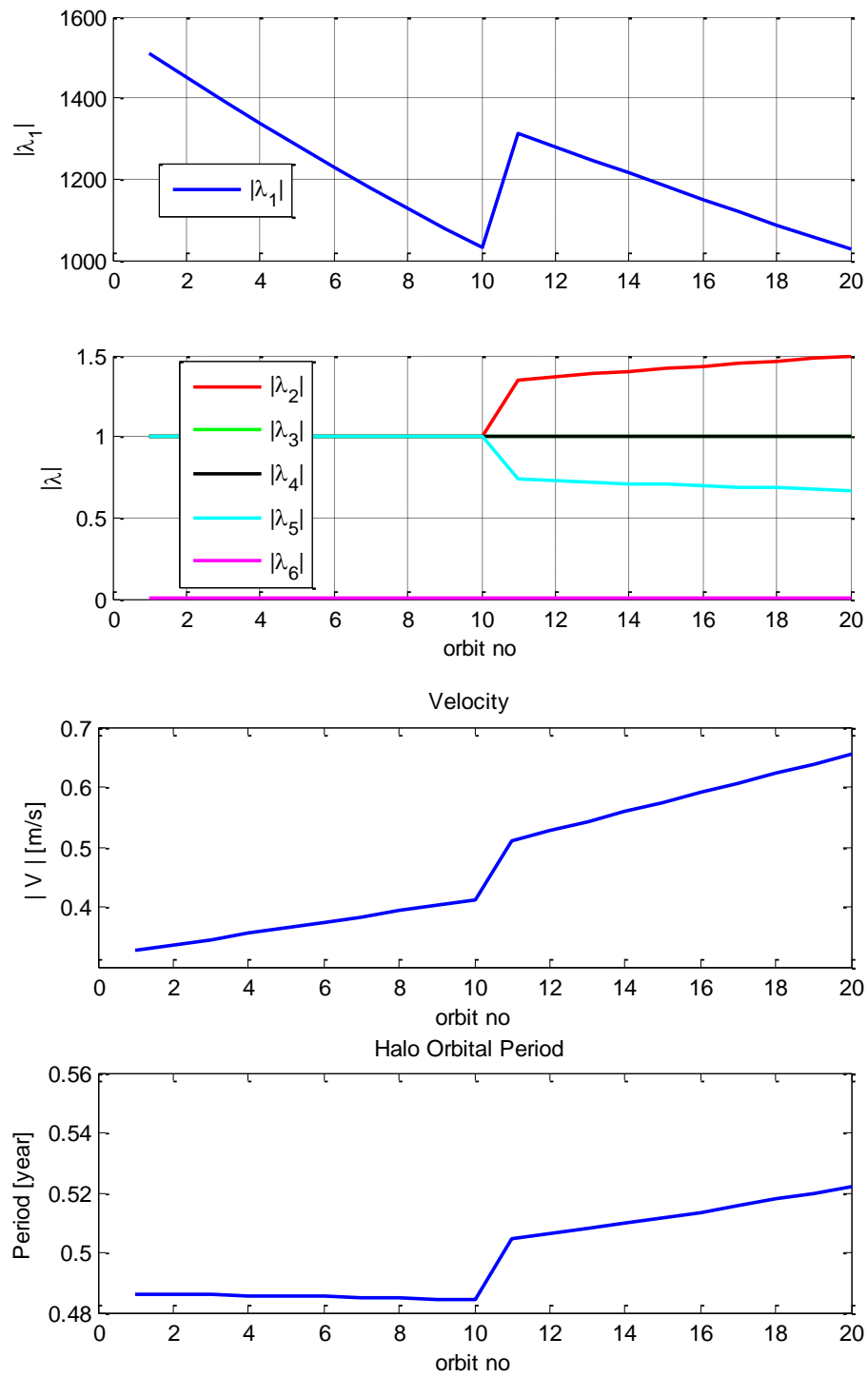
Figure 3-13. The modulus of the eigenvalues, velocity and orbital period

From those figures, it is clearly seen that a jump occurred after 10th orbit, it means that manifold is changed. The orbits are unstable but, as the previous case, the unstability loses its force when orbit is getting closer to the Earth. Again, the orbit velocity increase near Earth. However, different results are obtained for the orbit period values. As seen in the previous case, the orbit period decreases for Halo orbit, but period is increasing for Lyapunov orbit when it is getting close to the Earth. This may also be observed from Figure 3-14, where amplitude along Z direction becomes zero after the 11th orbit.
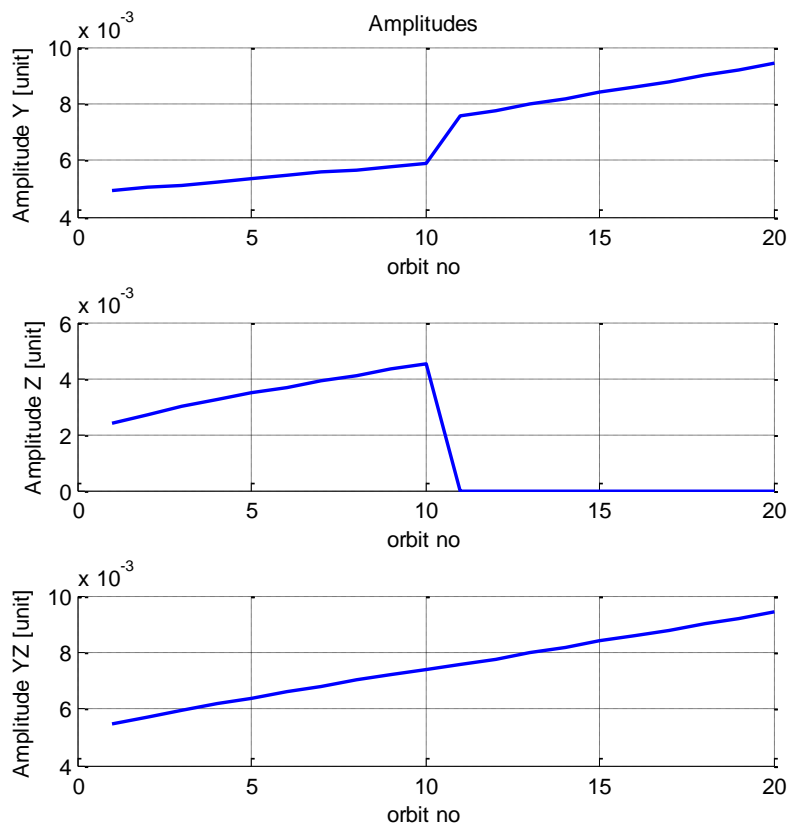
Figure 3-14. Amplitude of the orbits

It is not very useful to define this kind of orbits using the orbit radius parameter, since their shape is not perfectly a circle, or an ellipse (Figure 3-12). For that reason,

the maximum amplitude obtained on Y and Z axis can be used as a parameter to make comments about the shape of the orbit [67]. Figure 3-14 above indicates the change on the amplitudes of the orbit. It is seen that the amplitudes are increasing towards Earth, even if orbit type is converted to Lyapunov from Halo.

3.2.4. Halo orbit design near L2

In this section, Halo orbit design for L2 point is explained in details. The state vector used in the Newton method is changed to obtain Halo orbit, the process modified is given in the following sub-sections.

3.2.4.1. Computation of Halo orbit near L2

The process followed is the same as done for L1 point. The position vector of the fixed point of the Poincare section is again taken for L2 as an initial guess for the initial conditions X_0. Then RTB is run, Newton method is implemented with same manner as done for L1 and the trajectories obtained presented below. Initial x position is between Earth and L2, and it is roughly 1.26 million kilometers away from Earth and z position is 0.29 million km. The initial orbit velocity in y direction is 0.29 km/s. As an initial guess, the following dimensionless values are taken:

$$\begin{bmatrix} \bar{x} \\ \bar{y} \\ \bar{z} \\ \dot{\bar{x}} \\ \dot{\bar{y}} \\ \dot{\bar{z}} \end{bmatrix}_{t=0} = \begin{bmatrix} 1.00842815565444 \\ 0 \\ 0.002 \\ 0 \\ 0.009810393065200 \\ 0 \end{bmatrix}$$

The Newton method iteration is used to find Halo orbit for L1. Figure 3-15 shows the results obtained on Newton method for each of the iteration step. This figure is obtained by running the RTB dynamics for half period of time. Final trajectory is the

first half of our Halo orbit. Here, the main difference from the case of L1 is to have an initial velocity in positive y direction. That's why the trajectory first has a motion towards +y direction then its turn to complete one-half period.
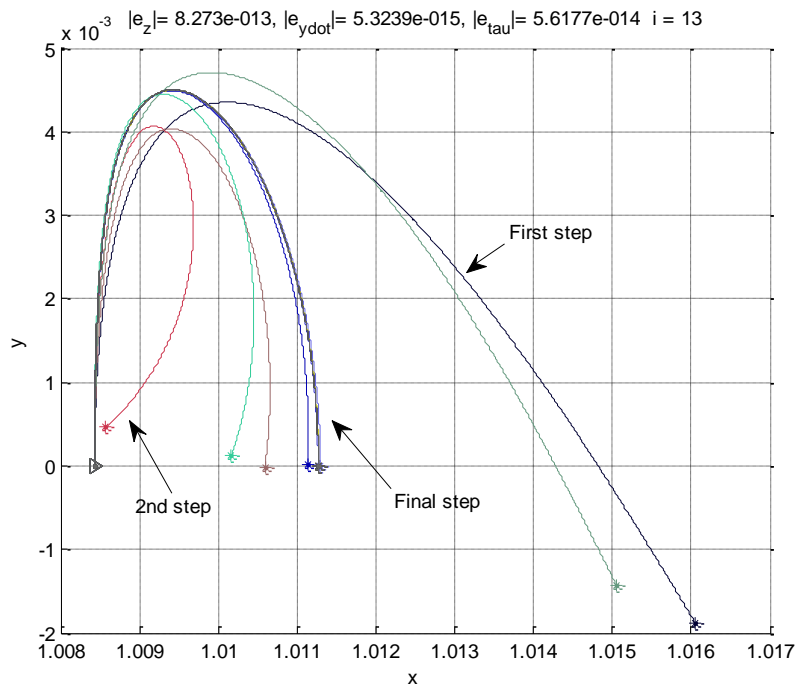
Figure 3-15. Trajectories obtained at L2 for each step of iteration

The following 2 and 3 dimensional figures present the trajectories obtained using initial state X_0 coming from initial guess (called 1st trajectory), and using X_0 obtained from Newton iterations (called 2nd trajectory). Here it is noticed that Newton optimization gives a Lyapunov orbit, an orbit on the XY plane.
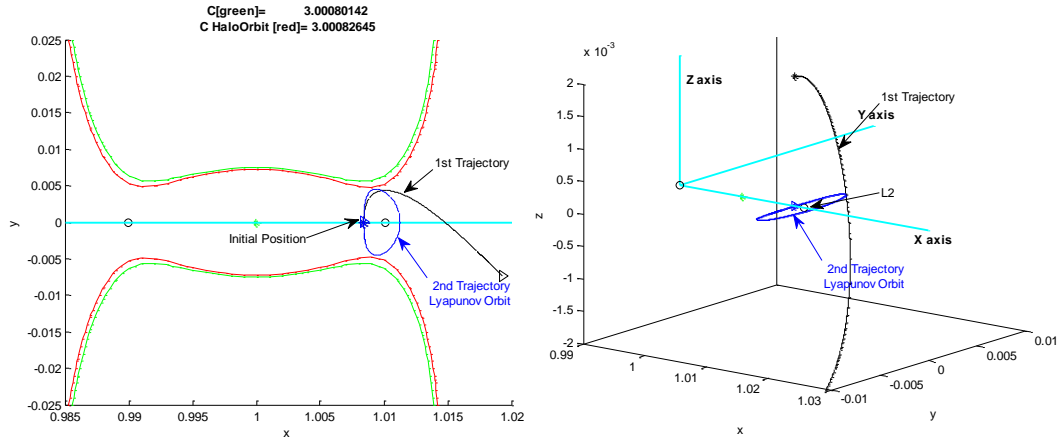
Figure 3-16. Trajectories obtained using initial state X_0

In order to find Halo orbit near L2, it is needed to change the state vector used in Newton method. This time, the z coordinate is taken as a given fixed value and τ, x and $\dot{y}$ that ensure that $y = \dot{x} = \dot{z} = 0$ are searched.

$$\begin{bmatrix} \bar{x}^* \\ \dot{\bar{y}}^* \\ \tau^* \end{bmatrix}_{k+1} = \begin{bmatrix} \bar{x}^* \\ \dot{\bar{y}}^* \\ \tau^* \end{bmatrix}_k - \left(D_f\right)^{-1} \begin{bmatrix} \dot{x} \\ \dot{z} \\ \bar{y} \end{bmatrix} \qquad \text{Eq. 3-27}$$

This iteration gives the initial condition set as:

$$\begin{bmatrix} x \\ y \\ z \\ \dot{x} \\ \dot{y} \\ \dot{z} \end{bmatrix}_{t=0} = \begin{bmatrix} \bar{x} \\ 0 \\ \bar{z}_{fixed} \\ 0 \\ \dot{\bar{y}}^* \\ 0 \end{bmatrix} \qquad \text{Eq. 3-28}$$

and the orbital period will be: $T = 2\tau^*$.

Figure 3-17 and Figure 3-18 present the Halo orbit found using this new iteration set. Table 3.5 gives the comparison of initial states guessed and optimized.
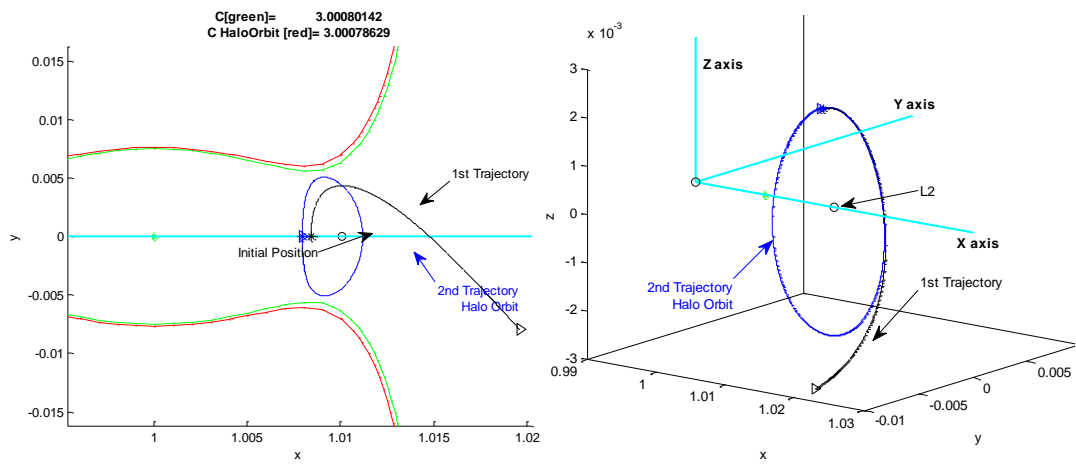
Figure 3-17. Trajectory obtained for L2
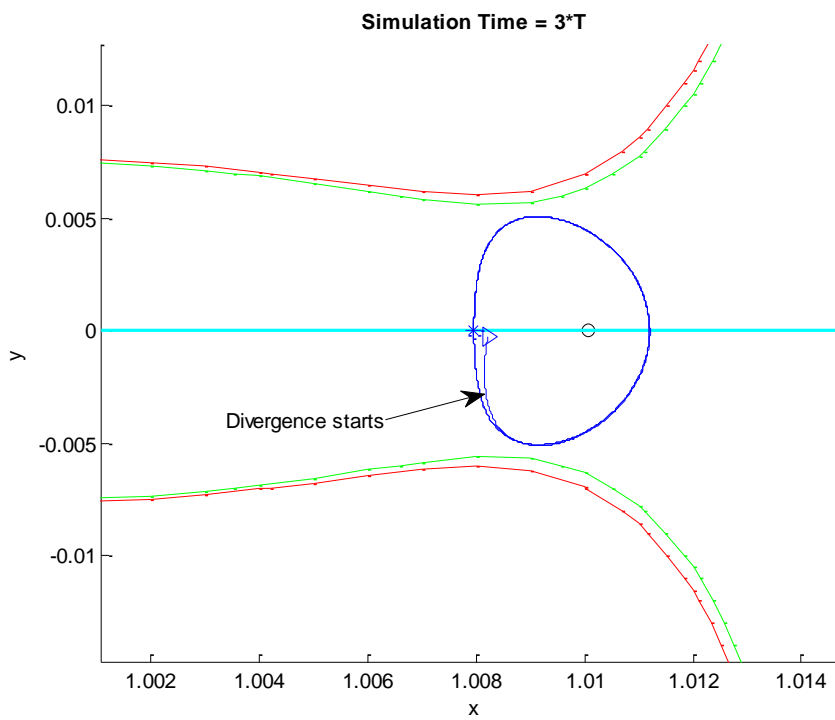
Figure 3-18. Divergence at trajectory for L2

Table 3.5. ICs guess for L2

Guessed initial state vector X_0 [unit]	Computed initial state vector X_0 for Halo [unit]	Difference in [km] and [m/s]
$\begin{bmatrix} 1.00842815565444 \\ 0 \\ 0.002 \\ 0 \\ 0.009810393065200 \\ 0 \end{bmatrix}$	$\begin{bmatrix} 1.007962094945760 \\ 0 \\ 0.002 \\ 0 \\ 0.011283741292199 \\ 0 \end{bmatrix}$	$\begin{bmatrix} 69721.69\ km \\ 0\ km \\ 0\ km \\ 0\ m/s \\ 43.88\ m/s \\ 0\ m/s \end{bmatrix}$

Finally, a periodic orbit is obtained by modifying the Newton states; however, it is not possible to maintain this periodicity. Figure 3-18 plots the trajectory obtained for three orbital periods in non-disturbed case, and it is noticed that near time=2.5 periods the divergence begins, the periodicity cannot be sustained. The stability analyses tell us the characteristic of this orbit. The eigenvalues belonging to this orbit are listed as follows:

$$\lambda = \begin{bmatrix} 1423.44 \\ 0.999999999985 - 0.000005539455i \\ 0.999999999985 + 0.000005539455i \\ 0.962496910519 - 0.271292641333i \\ 0.962496910519 - 0.271292641333i \\ 0.000702522840 \end{bmatrix}$$

As described in the section of L1, first eigenvalue is very large and the last one is too small, and they are reciprocal: $1/\lambda_6 = \frac{1}{0.000702522840} = 1423.44 = \lambda_1$

The unity eigenvalues are obtained: $\lambda_2\ \lambda_3$, and $\lambda_4\ \lambda_5$ they are on unit circle. In this L2 case, the unity eigenvalues are not obtained very clearly. The set of $\lambda_2\ \lambda_3$ are very close to the unity. Here the first eigenvalue λ_1 is outside of the unit circle and it shows that the orbit is not stable. The stability parameter ν_i shows also that orbit is unstable.

$$|v| = \begin{bmatrix} 711.72 > 1 \\ 0.9999999999847 < 1 \\ 0.9999999999847 < 1 \\ 0.9624969105189 < 1 \\ 0.9624969105189 < 1 \\ 711.72 > 1 \end{bmatrix}$$

However, since $\lambda_1 \ and \ \lambda_6$ are real reciprocal, the volume of the flow is preserved. It means that this halo orbit has stable and unstable directions. It is possible to obtain stable or unstable trajectories when the initial position is selected as a small enough neighborhood of this halo orbit. Eigenvalues $\lambda_3 \ and \ \lambda_4$ ensure that the orbit remain near Halo.

3.2.4.2. Halo orbit family for L2 and their stability

In this section, a set of orbits composed of several Halo types is considered to analyze the changes on orbital shape depending on their initial coordinates. The process used for L1 points is implemented, so, the initial x position is increased. The trajectories obtained by applying the Newton method are presented in Figure 3-19. For this case the orbits computed are all Lyapunov orbits, on XY plane.

In order to find Halo orbits for L2, the modified Newton iteration presented in the previous section is used. Figure 3-19 and Figure 3-20 contain the Halo orbits obtained for different z value which decrease toward to z=0 and increasing in the negative direction by passing the z axis. It is expected to obtain a symmetric profile formed by the Halo orbit family. Here, the decrement given to z coordinate for each step is approximately 2992 km (unit increment is 2e-5). Then the eigenvalues of new orbits are checked to see their stability.
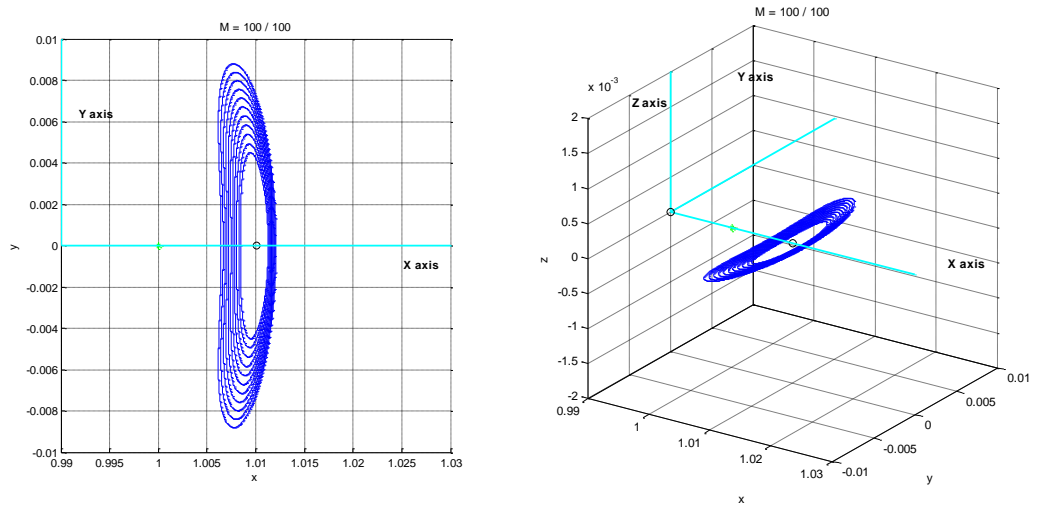
Figure 3-19. Lyapunov orbit family for L2
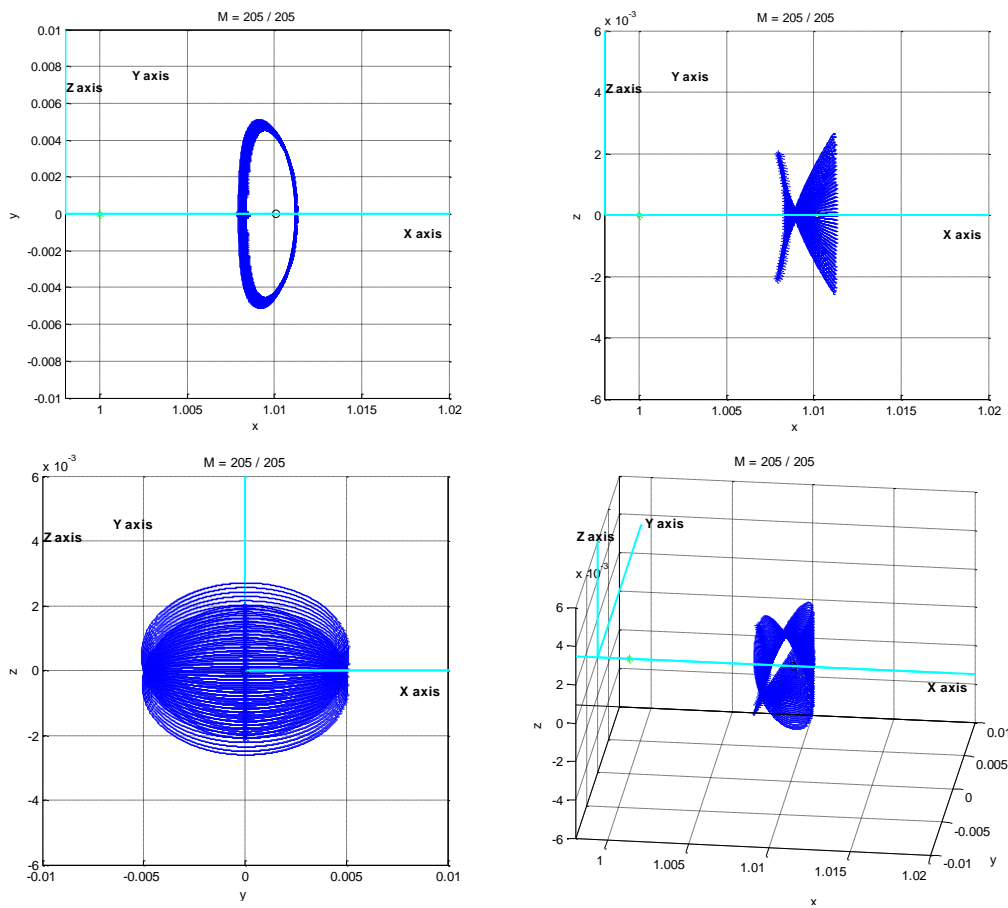
Figure 3-20. Halo orbits family for L2

In this case, the computed x position, for given z, increase slightly towards L2 points and it come back, get close to the Earth after passing z=0 position. So, the eigenvalue which indicates the unstability also first increases then decreases, symmetrically (Figure 3-21). The amplitude of the orbits also behaves accordingly to this symmetrical case.
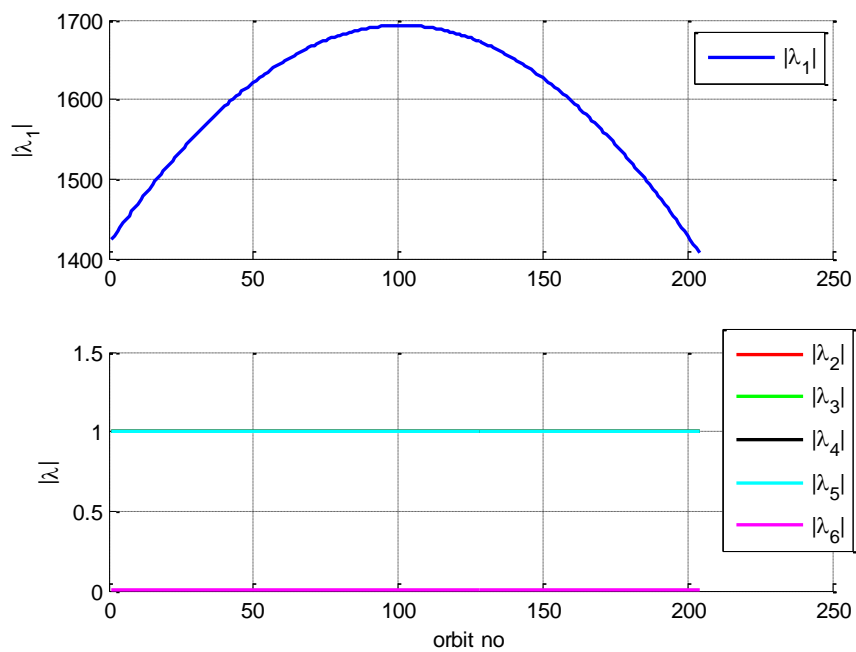
Figure 3-21. Eigenvalues for halo orbit family of L2
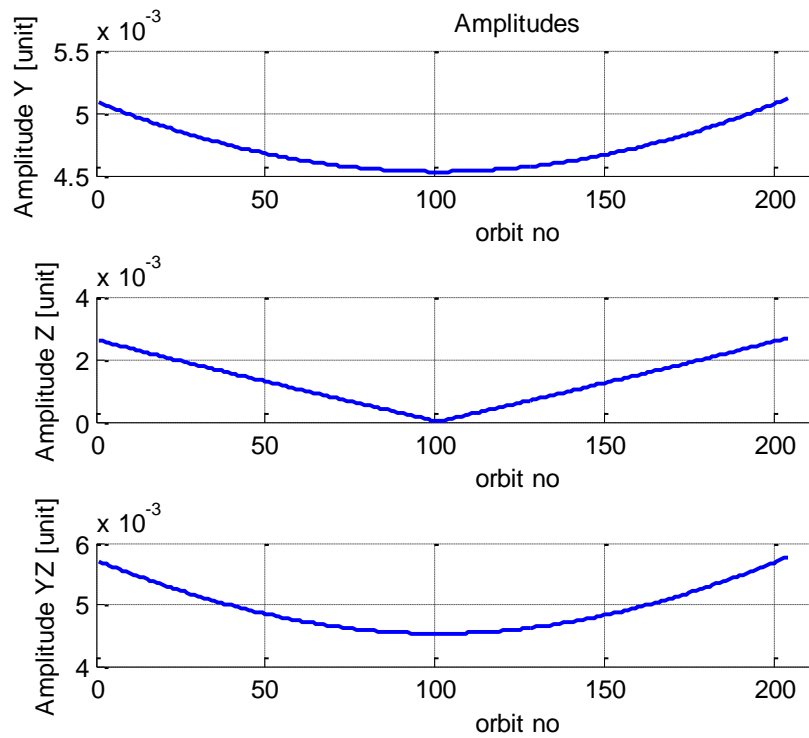
Figure 3-22. Amplitude values of halo orbit family of L2

From the results above, it is seen that a stable orbit near L2 is not found, but it can be stated that the stability may be reached for higher initial z position, because the value of first eigenvalues become larger for small initial z positions. So, the process is rerun and the following results are obtained.
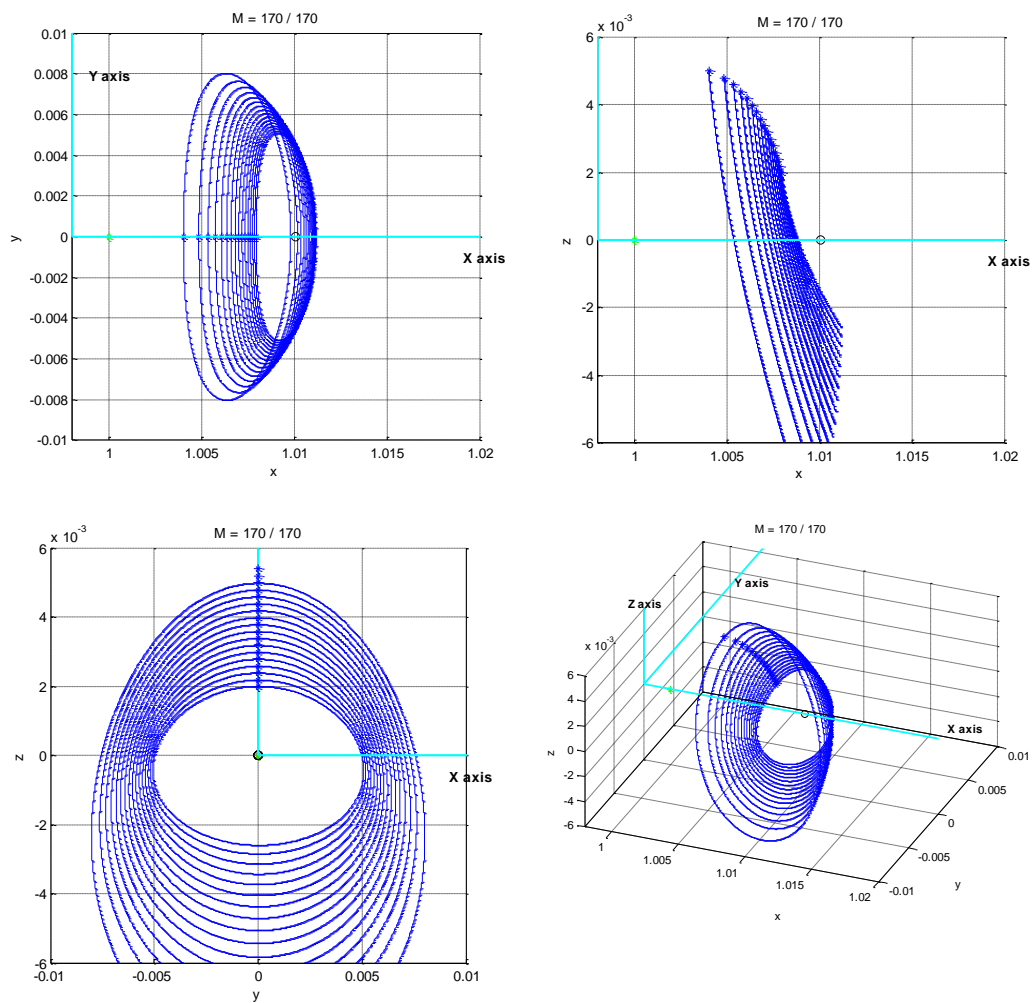
Figure 3-23. Recomputed halo orbits family for L2 by z increment

It is seen that first eigenvalue decreases for the larger initial z, since the x position computed to have Halo orbit is closer to Earth. As seen in the case of L1, stable orbits are obtained near Earth. The orbits unstability is strong when it is getting close to the libration point. Figure 3-24, Figure 3-25 and Figure 3-26 show the changes of eigenvalues and orbital amplitude regarding to the z, and x positions.
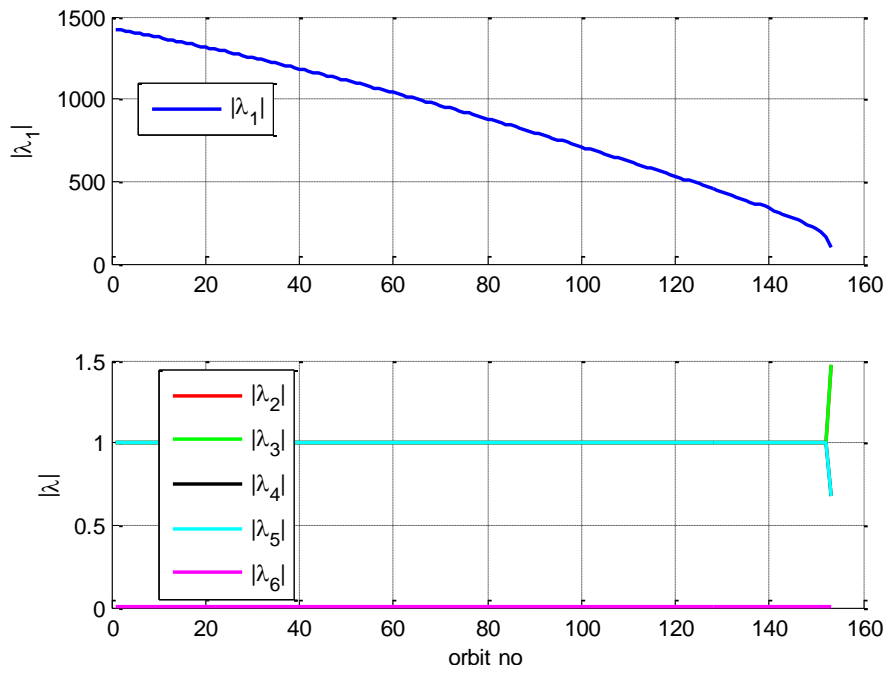
Figure 3-24. Eigenvalues of New Halo Orbits Family for L2
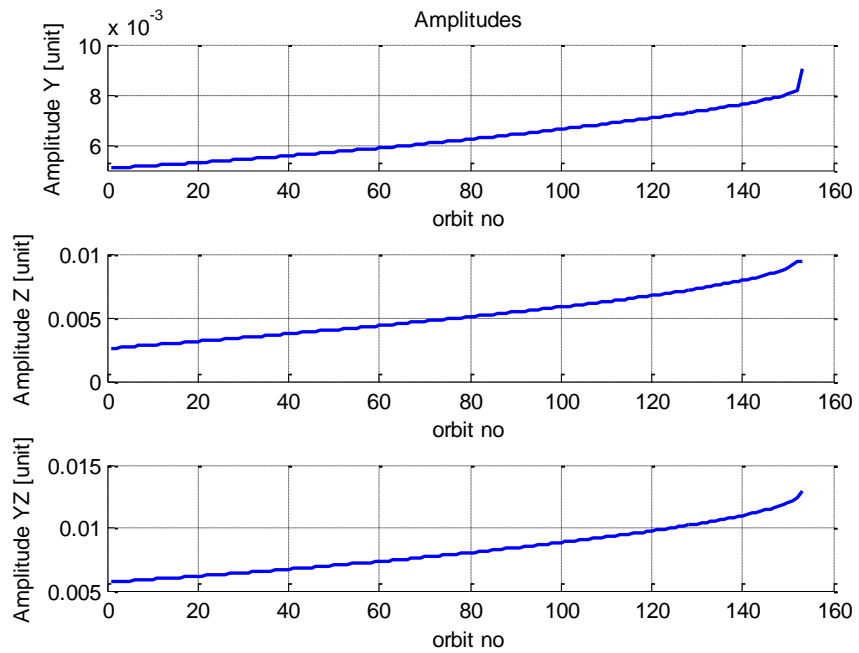
Figure 3-25. Amplitude of new halo orbits family for L2

113
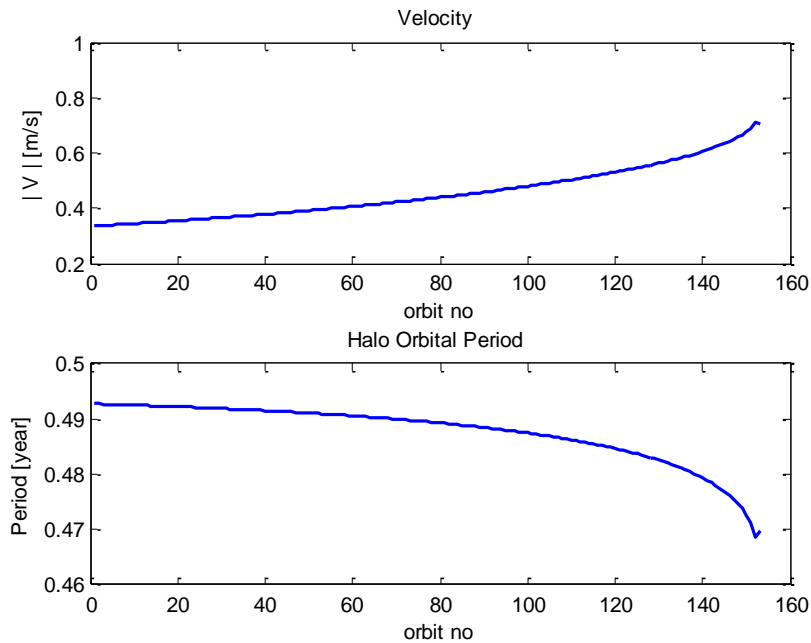
Figure 3-26. Orbital velocity and periods of new halo orbits family for L2

The analyses indicate that the periodicity in orbit is acquired for large initial z position. When the initial position is close to the Earth, the halo orbits computed has much larger amplitude. The orbital velocity increases and orbit period decreases when the orbit is getting closer the Earth.

3.3. Halo orbit design with disturbance sources

The studied presented above are based on circular restricted three body dynamics for the Sun-Earth/Moon system and the equations of motion derived for a spacecraft navigating around libration points are ideal equations, they do not contain perturbation. In this section the perturbation sources and their effects on the trajectory of the orbit and on the stability of the orbit are elaborated.

3.3.1. Disturbance sources

The disturbance sources that effect the trajectory of the spacecraft, navigating around libration points, are presented in this section.

The third body motion is mechanized using the assumption that the Bary (center of mass of the Earth+Moon) has a circular orbit around Sun, so, circular restricted equation of motion is used. In the real-world Earth has noncircular motion around Sun and Moon has a noncircular motion around Earth. However, the noncircular motion effect will be taken as negligible in the studies performed here [25]. The second perturbation source is the solar radiation pressure (SRP). The intensity of the SRP on the spacecraft depends on the cross-sectional area of the spacecraft and on its reflectivity. The main perturbation source is the solar system planets. The effects of their gravitational forces have also to be added on the trajectory computations, since Jupiter has a major effect on the solar system, as it is so massive compared to the other planets.

The actions taken in the simulation model in order to constitute the disturbed environment can be listed as follows:

- The sum of the mass of the Earth and Moon are taken in the codes to simulate the motion of the Bary around the Sun.
- The solar radiation pressure is computed recursively in the simulation regarding to the position of the satellite with respect to Sun.
- The ephemeris model is constituted to obtain the positions of the planets regarding to the Sun in synodic reference frame according to the Julian Date.
- The position of each Planet is calculated with respect to spacecraft.
- Finally, all of those disturbances are added to the ideal equations of motion and disturbance equations of motion are obtained, as given in the following section 3.3.2.

3.3.1.1. Solar radiation pressure

Solar radiation pressure is basically defined as a function of solar pressure, cross sectional area of the satellite exposed to the sun S and the mass of the satellite m_{SAT}. The acceleration occurred due to SRP can be formulized as [70]:

$$a_{SRP} = \frac{P_{SR} C_R S}{m_{SAT}} \frac{\bar{r}_{SAT}}{|\bar{r}_{SAT}|} \qquad \text{Eq. 3-29}$$

where; C_R is the spacecraft reflectivity. It is taken zeros for transparent body, 1 for black body (all radiation is absorbed), and 2 for white body (all radiation is reflected). P_{SR} is the solar pressure and it is mean solar flux over light speed. Solar flux is a function of the distance from the sun, so for L1 and L2 different values are computed.

$$P_{SR} = \frac{L}{4\pi R^2 c} \qquad \text{Eq. 3-30}$$

where $L = 3.828 \times 10^{26} \, Watt$ the intensity of the Sun light is, R is the distance from Sun and c is the speed of light. So, solar radiation pressure computed for L1 and L2 positions is:

$$P_{SR}|_{L1} = 4.63267 \times 10^{-6} \frac{N}{m^2}$$

$$P_{SR}|_{L2} = 4.45054 \times 10^{-6} \frac{N}{m^2}$$

In this study S is taken 30 m2 and mass of the satellite is 1800 kg. Figure 3-27 and Figure 3-28 show SRP acceleration acting on a satellite moving on Halo orbit near L1 and L2 respectively with its trajectory.
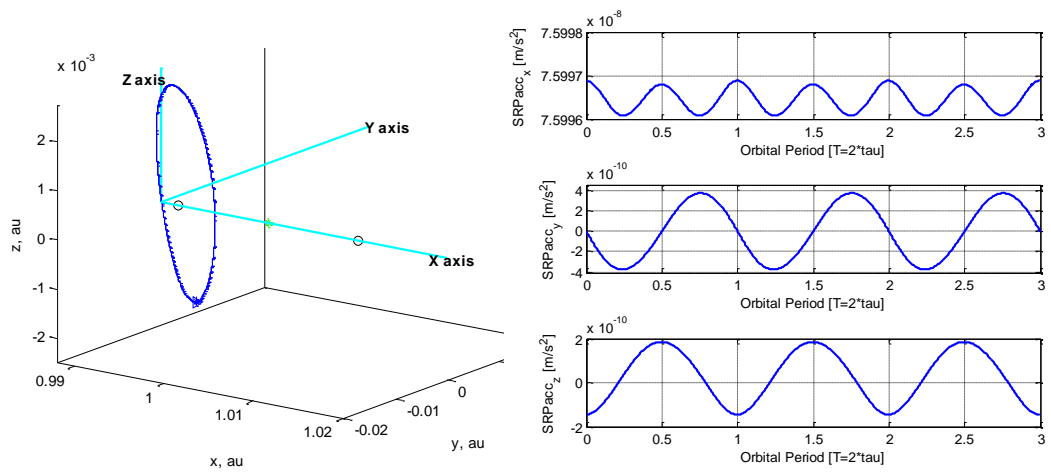
Figure 3-27. Solar radiation pressure for L1
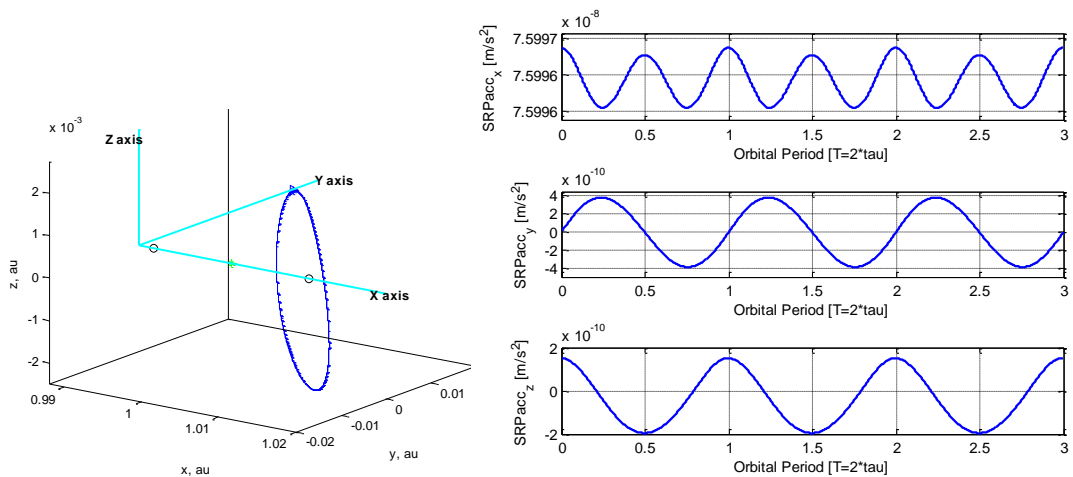
Figure 3-28. Solar radiation pressure for L2

Form the results it is seen that SRP has an order 10^{-8} m/s^2 for x axis and 10^{-10} m/s^2 for y and z axes. The SRP x component oscillates around 7.5996×10^{-8} m/s^2 and the two other SRP components y and z have mean zeros with amplitude of 4×10^{-10} m/s^2 of 2×10^{-10} m/s^2 respectively. Consequently, the SRP disturbance have an effect on the periodicity of the orbit, orbit life time and on orbit design. These will be given in Section 4.

117

3.3.1.2. Gravitational Disturbances due to the Solar System Planets

The effect of a planet is defined as a function of the distance between satellite and planet and the gravitational force of the planet. The ephemeris model is constituted to obtain the positions of the planets regarding to the sun in synodic reference frame according to the Julian Date in order to compute the accelerations caused by the gravitational forces of the planets. The details on ephemeris models are given in the Appendix-H.

Figure 3-29 illustrates the position of the planet, satellite and two primary bodies in synodic reference frame. The position vector of spacecraft with respect to the Sun is r_1, the position of the planet with respect to the Sun is named as R_{Pi} and the position of the planet with respect to the spacecraft is noticed as R_{P_SC} which is equal to the difference of the planet position and spacecraft position with respect to the Sun. So, it can be formulated as:

$$R_{P\_SC} = R_{Pi} - r_1 = \begin{bmatrix} R_{Px} - (x + x_1) \\ R_{Py} - y \\ R_{Pz} - z \end{bmatrix} \qquad \text{Eq. 3-31}$$
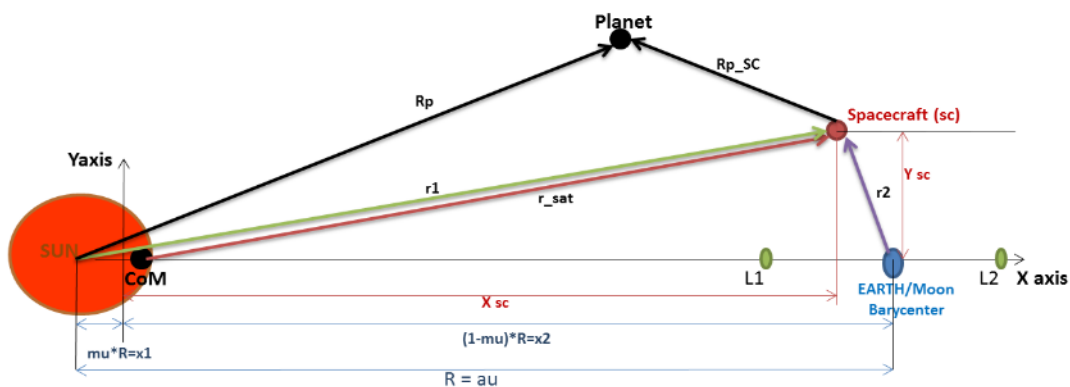
Figure 3-29. Distance between bodies in synodic reference frame

In the model, all the sun system's planets are taken into consideration except Pluto. As known, there is an argument between astronomers whether Pluto was a planet, in the late 1990s. At the end, in 2006 the International Astronomical Union ultimately decided to call Pluto a "dwarf planet", and the list of "real planets" is reduced to 8 from 9. But it is sure that it is not the reason not to add Pluto in the computation done here, the main reason is its mass and its distance from Sun compared to eight other planets; mass is negligible and distance is too far, so pull of Pluto is negligible. One more interesting item, The Planet-Nine is not also added: On 20 January 2016 astronomers found another planet in our solar system, which is about ten times the mass of our planet and 5000 times to mass of Pluto, so-called as "Planet Nine" [71]. So, the sum of the acceleration caused by the seven Planets is formulated as follows:

$$acc_{Planets} = \sum_{i=1}^{7} acc_{Pi} = \sum_{i=1}^{7} \frac{Gm_{Pi}}{|R_{Pi} - r_1|^3} \begin{bmatrix} R_{Pxi} - (x + x_1) \\ R_{Pyi} - y \\ R_{Pzi} - z \end{bmatrix} \qquad \text{Eq. 3-32}$$

As defined above in section 2.2, the Sun-Earth/Moon system is studied in RTB dynamics. It is also possible to add the Earth/Moon acceleration to the formulas given above in order to collect all planets caused forces, or as done in this thesis, Earth/Moon is taken separately and the other 7 planets make another group.

The following figures (Figure 3-30 to Figure 3-36) present the magnitude and the shape of the acceleration caused by each of the planets to satellite moving around L1. Here, a periodical Halo orbit around L1 is taken as example and simulation is run for 25 Halo periods (approximately 12 Earth's year) to cover one revolution of the Jupiter, to see its effects as it is the massive planet of the solar system. Julian Date is selected 01 June 2012, as starting date of the simulation. Orbital periods of the planets are:

119

Table 3.6. Orbital periods of planets

Planet	Period
Mercury	~0.24 years (~87.97 days)
Venus	~0.616 years (~224.70 days)
Earth	1 year (~365.25 days)
Mars	~1.88 years (~686.98 days)
Jupiter	~11.86 years (~4332.82 days)
Saturn	~29.45 years (~10755.70 days)
Uranus	~84 years (~30687.15 days)
Neptune	~164.79 years (~60190.03 days)
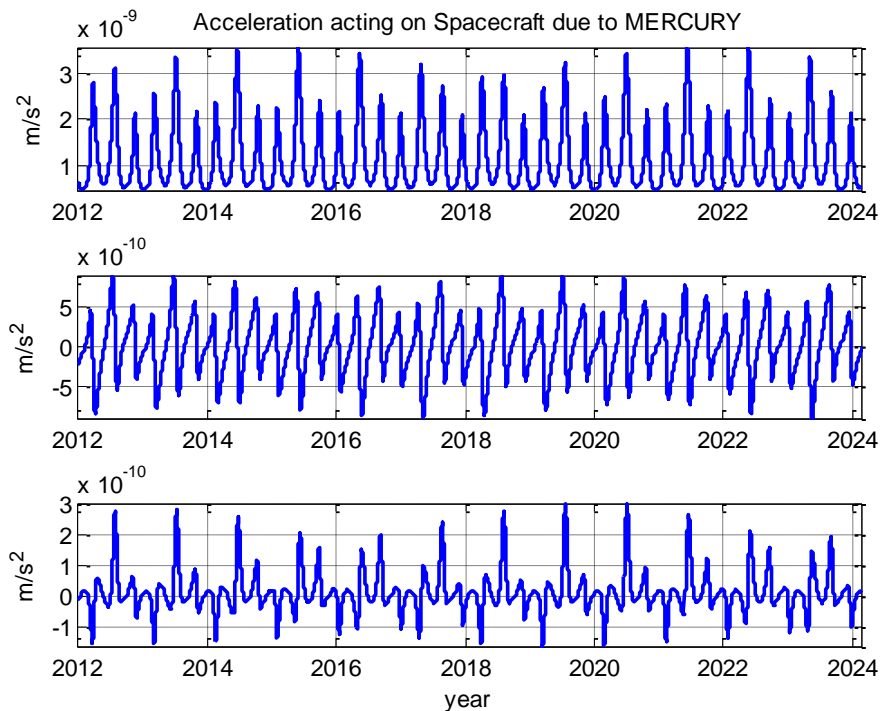
Figure 3-30. Gravitational pulls of Mercury

120
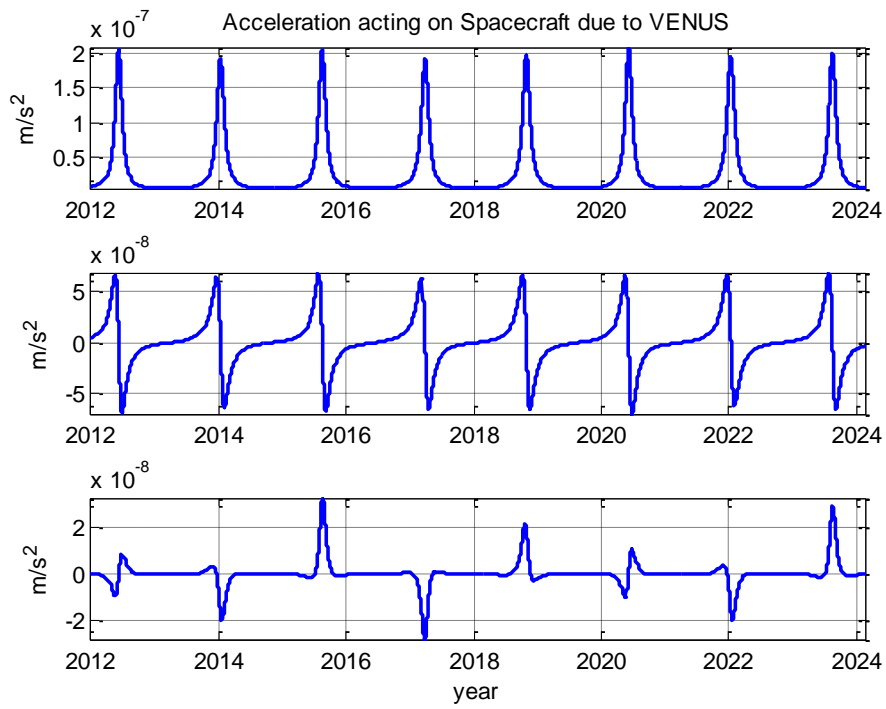
Figure 3-31. Gravitational pulls of Venus
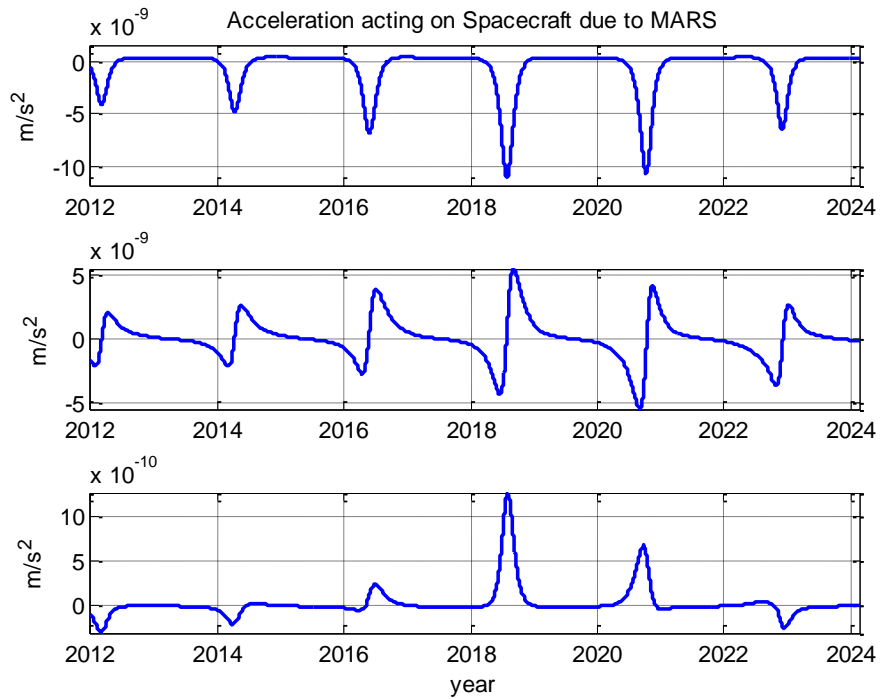
Figure 3-32. Gravitational pulls of Mars

121
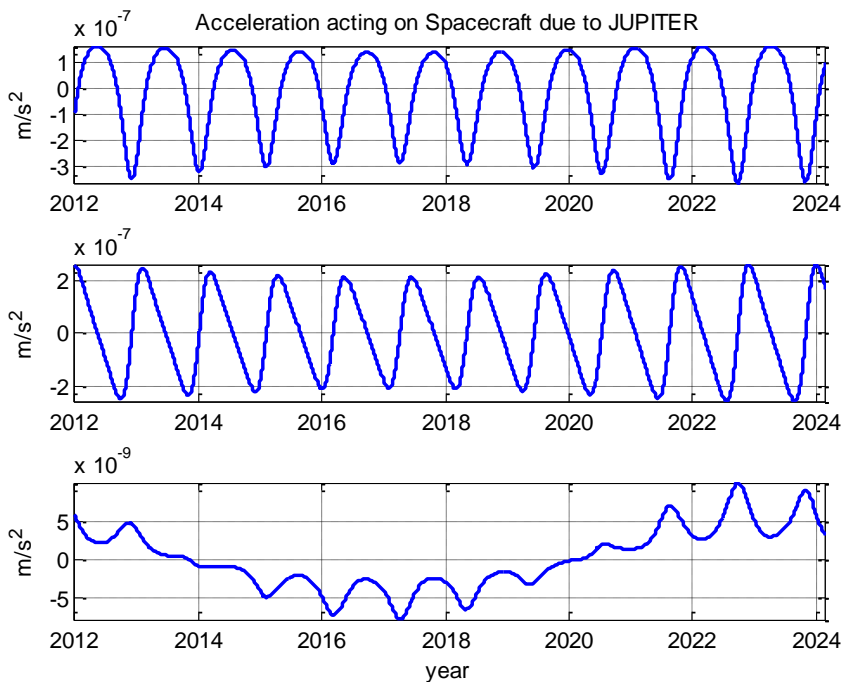
Figure 3-33. Gravitational pulls of Jupiter
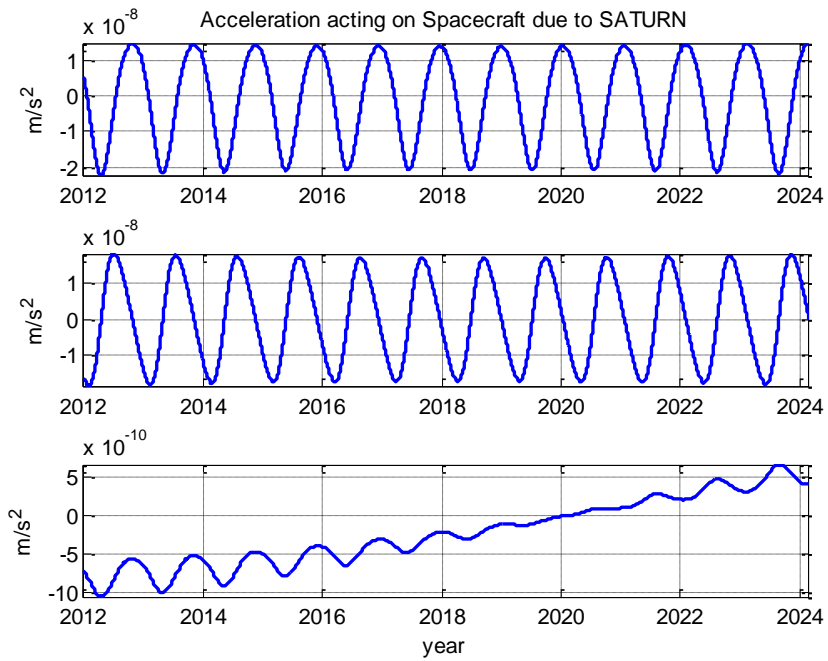
Figure 3-34. Gravitational pulls of Saturn

122
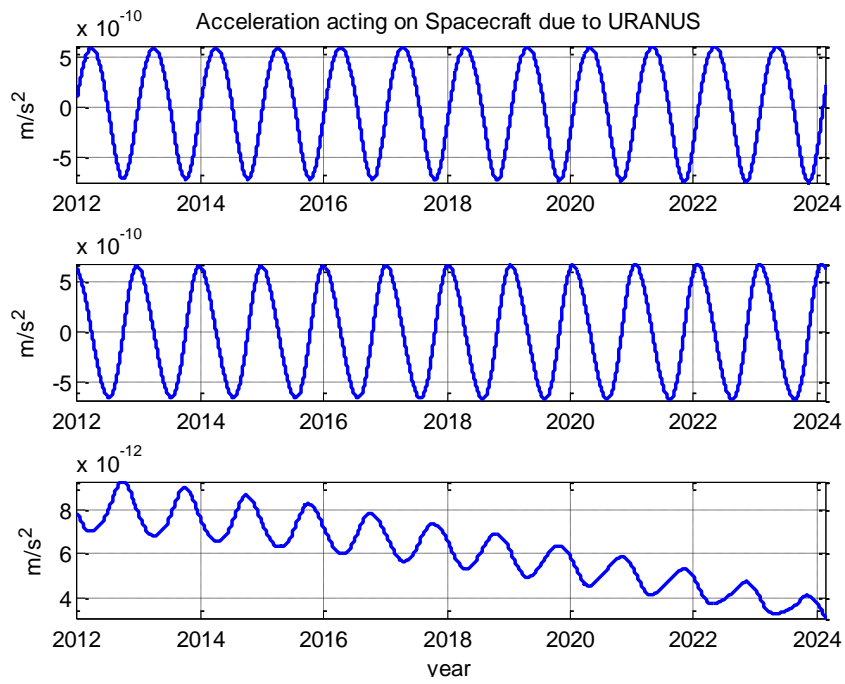
Figure 3-35. Gravitational pulls of Uranus
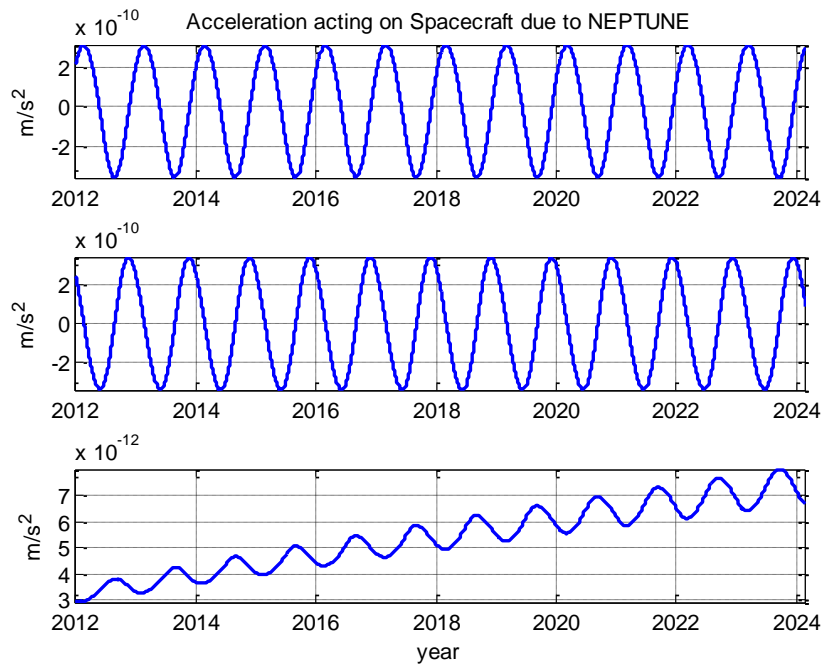
Figure 3-36. Gravitational pulls of Neptune

123

Effects of gravitational pulls of planets on a satellite at L1 are calculated and plotted in Figure 3-30 - Figure 3-36 for each of the planets. The gravitational pull of the Mercury has a periodic motion and it has a high frequency since the orbital period is one fifth of the Earth, and its magnitude is about $3.5 \times 10^{-9} \, m/s^2$ in x direction (Figure 3-30). The acceleration due to Venus has a pick values every 1.6 year and it is about $2 \times 10^{-7} \, m/s^2$, as seen in Figure 3-31. Mars shows very interesting behavior. The maximum gravitational pull of Mars is seen at half of the year 2018 in $-x$ direction and it is approximately $1 \times 10^{-8} \, m/s^2$. At the third quarter of the 2020, one more pick is seen, but after that it decrease again. Mars gets closer to spacecraft approximately every 2.20 years and maximum pick values occurs (Figure 3-32). Jupiter, the biggest planet, it has a periodic gravitational pull on the spacecraft and its magnitude is about $3 \times 10^{-7} \, m/s^2$ in $-x \, and - y$ directions (Figure 3-33). Saturn's pull has an order of $2 \times 10^{-8} m/s^2$ (Figure 3-34). Uranus and Neptune effects are about $3 \times 10^{-10} \, m/s^2$ orders (Figure 3-35 and Figure 3-36). As a consequence, it is seen that the most disturbance sources are Venus and Jupiter; Venus due to its distance which is close to the Earth and spacecraft, and Jupiter due to its huge mass. And the interesting point was the Mars case, for the date 2018 and 2020 it shows the maximum disturbance level. The position of the Mars in synodic references frame is investigated to understand this effect. It is noticed that, on 2018 June, the minimum distance with respect to the Sun is reached with having near zeros in y axis, and maximums in $x, and \, z$ axis. So, Mars is nearly aligned to Earth in that dates and it shows maximum effect on this line, to the spacecraft also.

The similar gravitational pulls are obtained for a trajectory on L2. The effects of Mercury, Venus reduce slightly since the distance between spacecraft and planets increase about 3 million km for the dates run in the simulation. The pulls of the other planets do not change a lot because the distance from L1 to L2 (approx. 3 million km) do not have an importance compared to the distance between planets and spacecraft.

3.3.2. Equations of motion with disturbances

The acceleration terms occurred due to disturbances based on the solar radiation pressure and on the gravitational forces of the solar system planets are added to the equations of motion, and finally the following set of equations is obtained.

$$\ddot{x} = \omega^2 x + 2\omega\dot{y} - \frac{Gm_{SUN}(x + x_1)}{r_1^3} - \frac{Gm_{BARY}(x - x_2)}{r_2^3} + \frac{\tilde{\alpha}(x + x_1)}{r_1}$$

$$- \sum_{i=1}^{7} \frac{Gm_{PLANETi}(R_{Pix} - (x + x_1))}{|R_{Pi} - r_1|^3}$$

$$\ddot{y} = \omega^2 y - 2\omega\dot{x} - \frac{Gm_{SUN}y}{r_1^3} - \frac{Gm_{BARY}y}{r_2^3} + \frac{\tilde{\alpha}y}{r_1} \qquad\qquad \text{Eq. 3-33}$$

$$- \sum_{i=1}^{7} \frac{Gm_{PLANETi}(R_{Piy} - y)}{|R_{Pi} - r_1|^3}$$

$$\ddot{z} = - \frac{Gm_{SUN}z}{r_1^3} - \frac{Gm_{BARY}z}{r_2^3} + \frac{\tilde{\alpha}z}{r_1} - \sum_{i=1}^{7} \frac{Gm_{PLANETi}(R_{Piz} - z)}{|R_{Pi} - r_1|^3}$$

where,

$$r_1 = \sqrt{(x + x_1)^2 + y^2 + z^2}$$

$$r_2 = \sqrt{(x - x_2)^2 + y^2 + z^2}$$

$\tilde{\alpha} = P_{SR}AC_R/(m_{sat})$ and

R_{Pi} is the position of the planet with respect to Sun in synodic reference frame, as defined in the previous sections.

The dimensionless form of this set can be rewritten as follows:

$$\ddot{\bar{x}} = \bar{x} + 2\dot{\bar{y}} - \frac{(1-\mu)(\bar{x}+\mu)}{\bar{r}_1^3} - \frac{\mu(\bar{x}-(1-\mu))}{\bar{r}_2^3} + \frac{\tilde{\alpha}(\bar{x}+\mu)}{\omega^2 R \bar{r}_1}$$
$$- \sum_{i=1}^{7} \left(\frac{m_{PLANETi}}{m_{BARY}}\right) \frac{\mu(\bar{R}_{Pix}-(\bar{x}+\mu))}{|\bar{R}_{P\_Sc}|^3}$$

$$\ddot{\bar{y}} = \bar{y} - 2\dot{\bar{x}} - \frac{(1-\mu)\bar{y}}{\bar{r}_1^3} - \frac{\mu\bar{y}}{\bar{r}_2^3} + \frac{\tilde{\alpha}\bar{y}}{\omega^2 R \bar{r}_1} \qquad\qquad \text{Eq. 3-34}$$
$$- \sum_{i=1}^{7} \left(\frac{m_{PLANETi}}{m_{BARY}}\right) \frac{\mu(\bar{R}_{Piy}-\bar{y})}{|\bar{R}_{P\_Sc}|^3}$$

$$\ddot{\bar{z}} = - \frac{(1-\mu)z}{\bar{r}_1^3} - \frac{\mu\bar{z}}{\bar{r}_2^3} + \frac{\tilde{\alpha}\bar{z}}{\omega^2 R \bar{r}_1} - \sum_{i=1}^{7} \left(\frac{m_{PLANETi}}{m_{BARY}}\right) \frac{\mu(\bar{R}_{Piz}-\bar{z})}{|\bar{R}_{P\_Sc}|^3}$$

where,

$$\bar{r}_1 = \sqrt{(\bar{x}+\mu)^2 + \bar{y}^2 + \bar{z}^2}$$

$$\bar{r}_2 = \sqrt{\left(\bar{x}-(1-\mu)\right)^2 + \bar{y}^2 + \bar{z}^2}$$

$$|\bar{R}_{P\_SC}| = \sqrt{\left(\bar{R}_{Pix}-(\bar{x}+\mu)\right)^2 + \left(\bar{R}_{Piy}-\bar{y}\right)^2 + (\bar{R}_{Piz}-\bar{z})^2}$$

The following section presents the details on the effect of the disturbances on the Halo orbit design. The lifetime of the periodic orbit is critically dependent on the consideration of the disturbances while computation is made. The process is performed for L1 and L2 libration points in order to see and compare the computation contents.

3.3.3. The Effects of the disturbances on Halo orbit computation

Naturally it is not possible to have a stable orbit at collinear libration points L1 and L2, as mentioned in the previous sections. However, the objective is to obtain a Halo orbit with a trajectory and an energy level that satisfy the periodicity. As seen above, this aim is achieved by computing the proper initial positions and velocities of the third body using symmetry property of the dynamics and Newton's iteration method by running the RTB dynamics.

Initial conditions can be computed for undisturbed equations of motion, but it is obvious that the trajectory will not satisfy a periodic orbit when the disturbances are added to the simulation code. For that reason, disturbed equations are used in all computations, with solar radiation pressure and gravitational forces of the other planets are added. And the process presented above to compute proper initial conditions are performed.

Figure 3-37 and Figure 3-38 give the comparison between undisturbed and disturbed motions for both L1 and L2 libration points. When the initial conditions computed with undisturbed dynamics are used in perturbed environment, the blue colored motion is obtained for L1 (The trajectory colored cyan is the case obtained for undisturbed RTB). In the same manner, for L2 the computations are also performed. The red colored trajectory is the trajectory obtained for disturbed dynamics, the magenta one is for undisturbed environment.
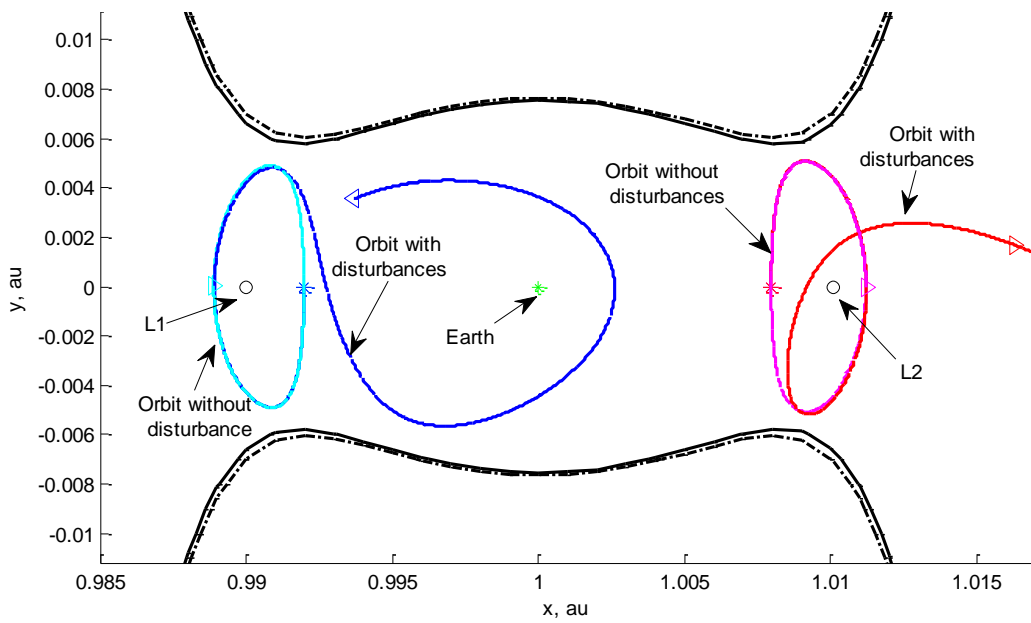
Figure 3-37. Comparison between undisturbed and disturbed motions-2D view
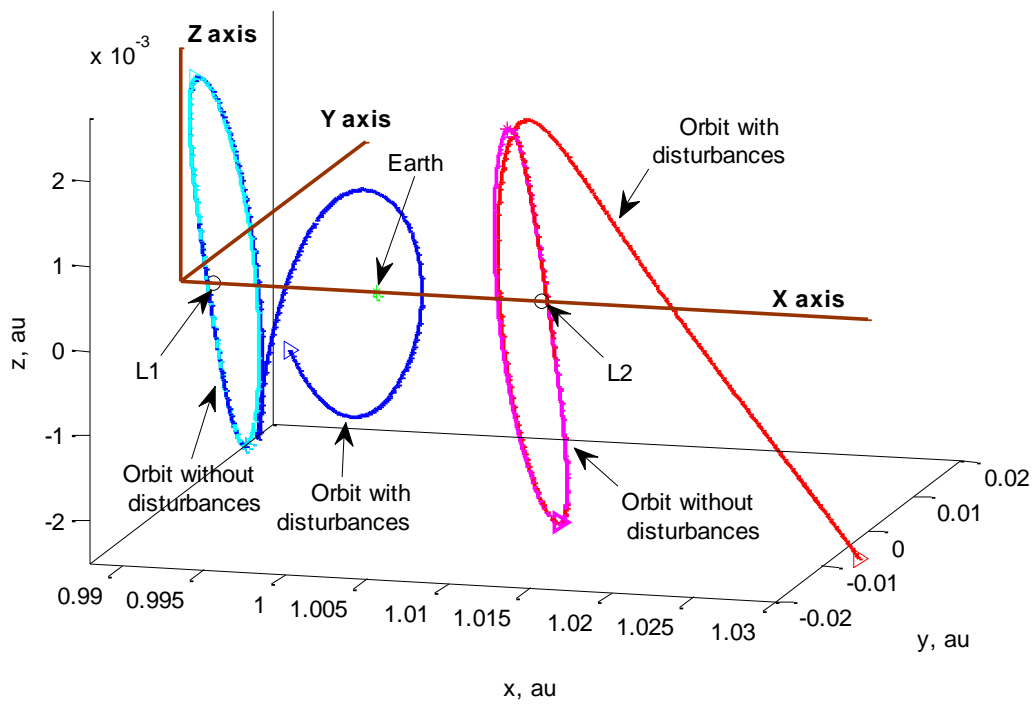
Figure 3-38. Comparison between undisturbed and disturbed motions-3D view

128

The Halo orbit design results and orbit family behaviors and analyses for L1 and L2 are given in the next sub sections.

3.3.3.1. Halo Orbit Design near L1 and L2 under Disturbances

Trajectories for L1 and L2 are given in Figure 3-39 and Figure 3-40 respectively. These orbits are computed using both undisturbed and disturbed RTB dynamics. For undisturbed case, the ICs are computed using undisturbed model and the simulation is run with the undisturbed EoM. For disturbed case, the model with the solar radiation as well as the disturbances due to the pulls of the other planets is used in computation iteratively searching the proper initial conditions. The orbits computed for undisturbed RTB are given in colors cyan for L1, and magenta for L2. The orbits colored in blue and red are the orbits computed for disturbed RTB respectively.
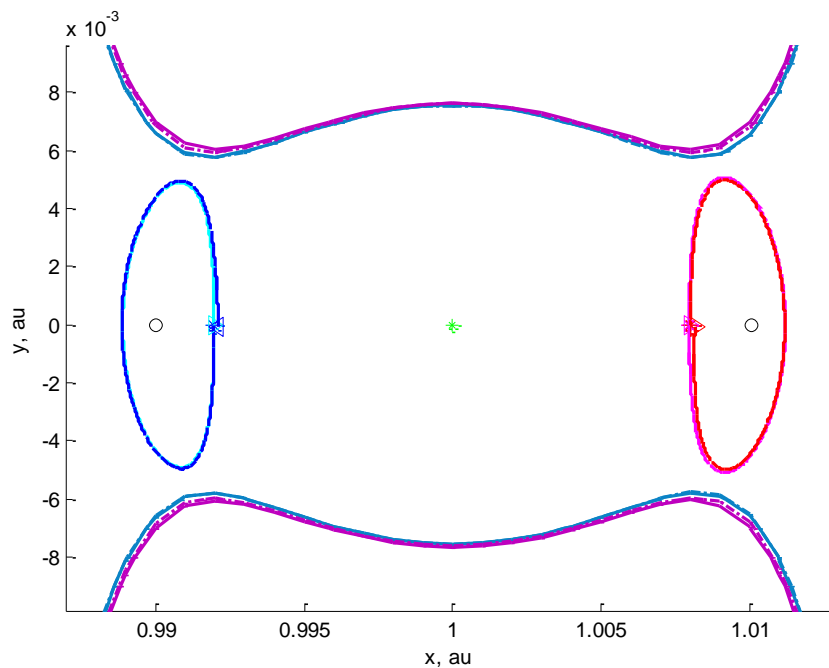
Figure 3-39. Orbits computed using RTB with and without disturbances – 2D view
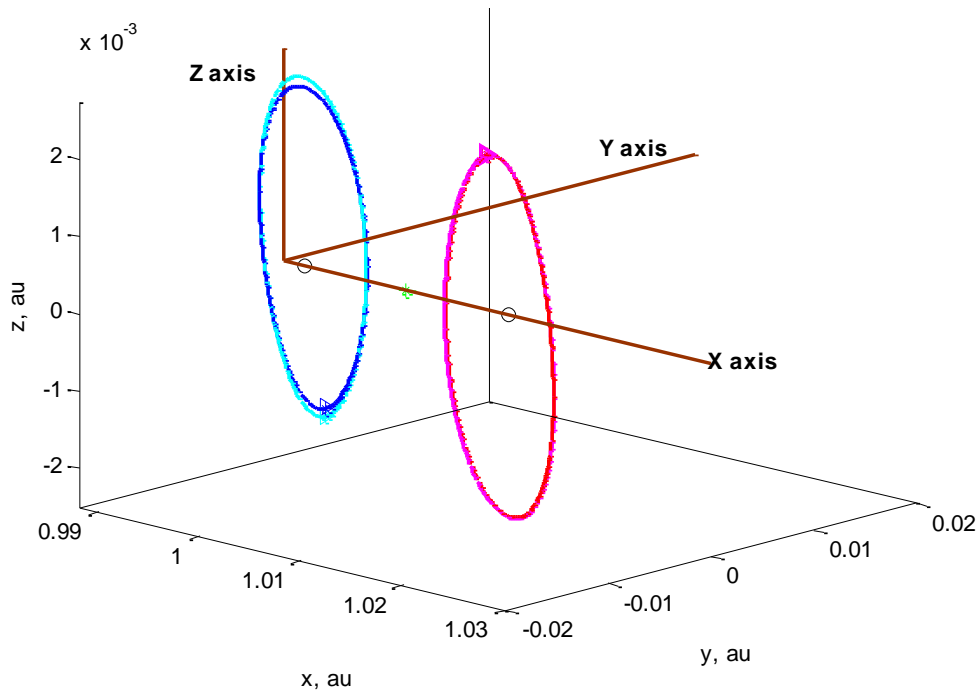
Figure 3-40. Orbits computed using RTB with and without disturbances – 3D view

Table 3.7. ICs comparison: Undisturbed-disturbed motions for L1

Initial Date taken is: 1/ 6/2018 (dd/mm/yyyy) at 12:00:00 (hh:mm:ss)		
Results for L1		
Nondimensional ICs of Undisturbed motion	**Nondimensional ICs of Disturbed motion**	**Differences in km and m/s**
x_u = 0. 9919754554386 y_u = 0.00 z_u = -0. 001885431277	x_u = 0. 9919754554386 y_u = 0.00 z_u = -0. 001782835456	Δx = 0.00 km Δy = 0.00 km Δz = 15348.1km
V_{xu} = 0.0 V_{yu} = -0.01097102715 V_{zu} = 0.0	V_{xu} = 0.0 V_{yu} = -0.01106286967 V_{zu} = 0.0	ΔV_x = 0.0 m/s ΔV_y = -2.73m/s ΔV_z = 0.0 m/s
Orbital Period in year: T=0. 4863107460643	Orbital Period in year: T=0. 4859685147159	Difference in orbital periods: -3 Hours

Table 3.8. ICs comparison: Undisturbed- disturbed motions for L2

Initial Date taken is: 1/ 6/2018 (dd/mm/yyyy) at 12:00:00 (hh:mm:ss)		
Results for L2		
Nondimensional ICs of Undisturbed motion	Nondimensional ICs of Disturbed motion	Differences in km and m/s
$x_u = 1.007962094945$ $y_u = 0.00$ $z_u = 0.002$	$x_u = 1.008007907715$ $y_u = 0.00$ $z_u = 0.002$	$\Delta x = 6853.5$ km $\Delta y = 0.00$ km $\Delta z = 0.00$ km
$V_{xu} = 0.0$ $V_{yu} = 0.01128374129$ $V_{zu} = 0.0$	$V_{xu} = 0.0$ $V_{yu} = 0.01104182302$ $V_{zu} = 0.0$	$\Delta V_x = 0.0$ $\Delta V_y = -7.206$ m/s $\Delta V_z = 0.0$
Orbital Period in year: T=0.4926990645676	Orbital Period in year: T=0.4932694501483	Orbital period difference: 5 Hours

The Table 3.7 and Table 3.8 give the difference of the initial conditions computed with and without disturbances for L1 and L2 halo orbits. The first two columns give the dimensionless distances and dimensionless velocities computed using astronomical unit au and angular velocity of the Bary around the Sun $\boldsymbol{\omega}$ as: $x_u = x/au$ and $V_{xu} = V_x/(au.\omega)$. Third column gives distance difference in kilometers and velocity difference in meter per second. From the results it may be observed that the radius of the orbit obtained for disturbed motion is less than undisturbed for L1 case. And the absolute velocity y component is higher and the orbital period is about 3 hours lower. For L2 the case, the orbit radius is approximately 6850 km further from the Earth and the initial velocity in the y direction lower, and while the orbital period is higher.

The projected amplitudes A_{YZ} for L1 and L2 trajectories are given in Figure 3-41 and Figure 3-42. Here, A_{YZ} is the projected distance of the satellite on YZ plane in synodic reference frame ($A_{YZ} = \sqrt{A_Y^2 + A_Z^2}$). For disturbed case, it is seen that initial amplitude is about 15000 km less then undisturbed case for L1 (see in Figure 3-42. as L1 ΔA_{YZ}), while at the quarter orbital period disturbed orbital amplitude is greater than undisturbed about 5000 km, changing in an oscillating fashion. In L2 case, the

initial amplitude is always less than the undisturbed case (L2 ΔA_{YZ}). Due to this difference, equations containing solar radiation pressure and gravitational forces of the other planets are used in the computations.
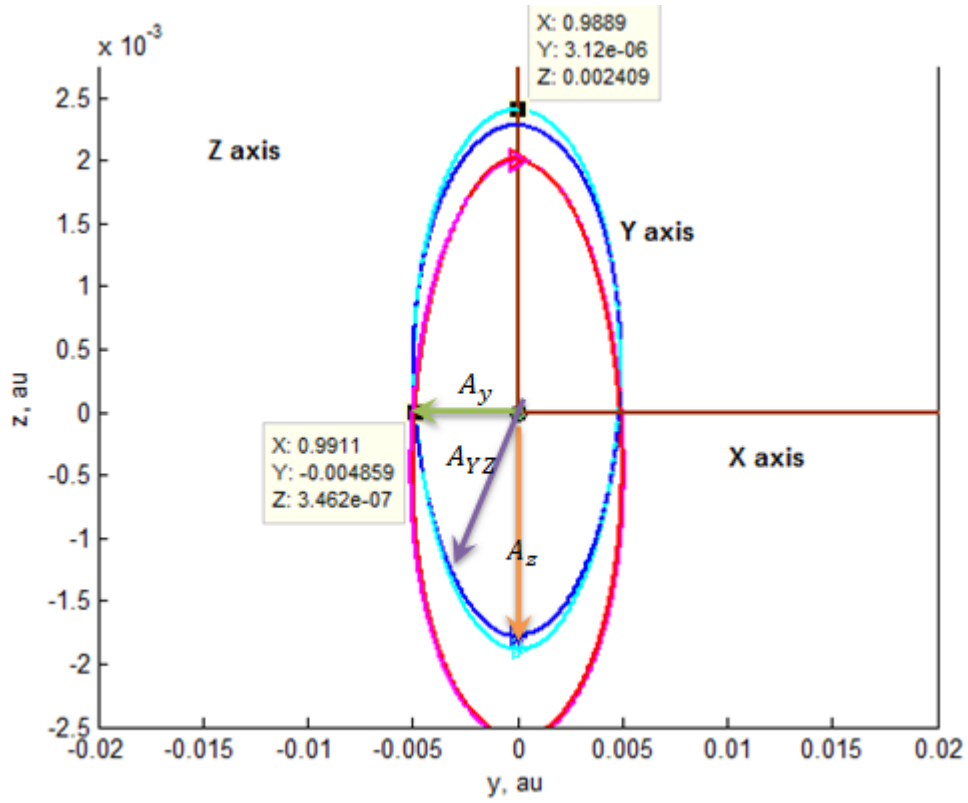
Figure 3-41. Representation of the amplitude of the orbit
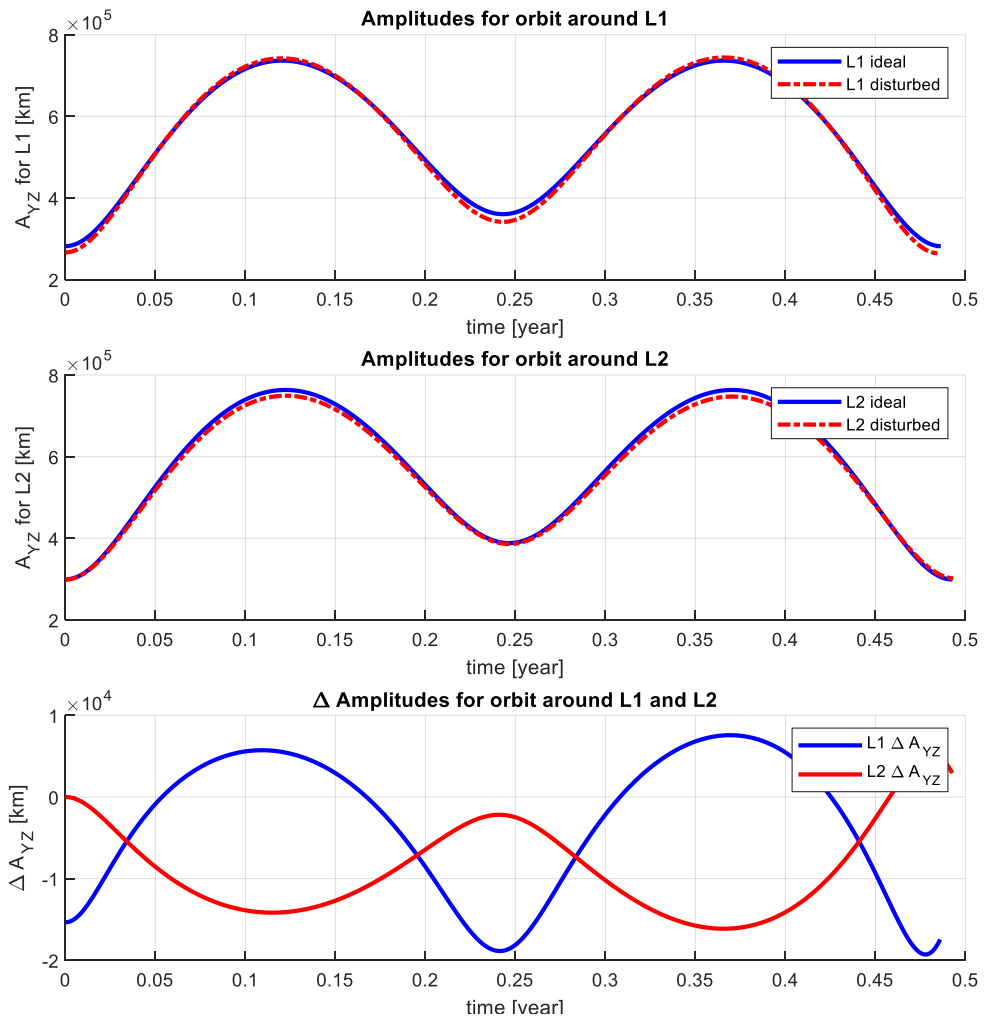
Figure 3-42. Amplitudes of the orbits for L1 and L2, undisturbed-disturbed case for L1 and L2

3.3.3.2. Keeping Halo orbit and orbital corrections

Actually, the effects of the disturbance are clearly seen in the periodicity of the Halo orbit. It is noticed that even if Halo orbit design process is performed, it is not possible obtain periodicity even for one orbital period. The initial and final positions are given in following Figure 3-43:
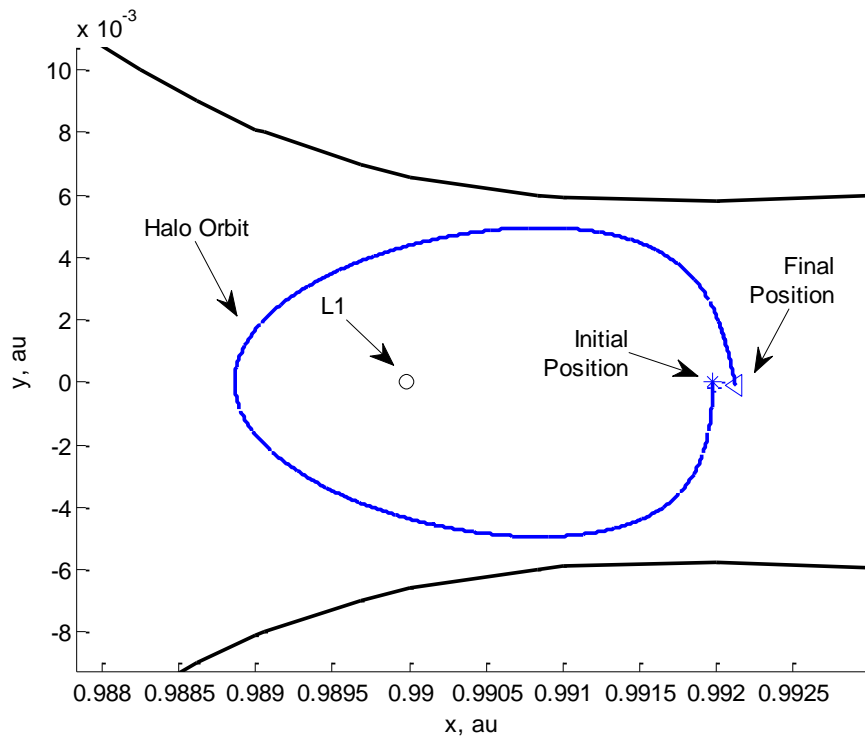
Figure 3-43. Initial and Final positions of the satellite
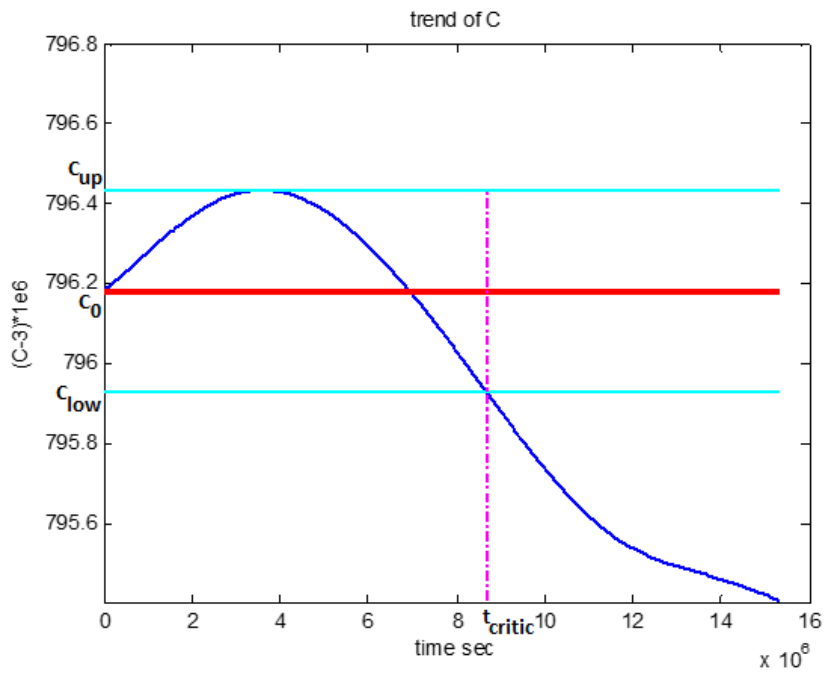
Figure 3-44. Jacobi energy value

134

It is clear that an orbit correction is necessary but it is also needed to define criteria to determine the maneuver implementation time; when and how? The changes on the value of the Jacobi energy may give an information about the orbit correction need. Figure 3-44 gives the Jacobi energy values of the orbit given above.

The y axis label presents the value of the C, Jacobi energy and it is given as $Cn = (C - 3) \times 10^6$ to make it readable the decimal part of the value. The red line indicates the initial C value which is the energy level of the initial conditions, it is denoted as C_0. The upper straight line shows the maximum value reached. The lower straight line is the symmetry of the maximum reached value with respect to the C_0, and these upper and lower boundaries are indicated as C_{up} and C_{low}. The vertical straight dashed line shows the critical time, it is the time that energy starts to diverge from the area determined by extramums, and it is nearly half period time. So, it is possible to state at this is the time that a maneuver is needed. The Jacobi integral value (let's say energy value) is taken into consideration for making a decision to do orbital correction. After analyzing of the several scenarios, it is obtained that a periodically orbit correction can provide continuous Halo orbit. One period is nearly six earth's months, so if every six months (full period) maneuver is performed, it is possible to keep Halo orbit. Only the first maneuver is done at 3rd moths (half period). The first maneuver is done at half period time. And the maneuver quantity, delta_V is computed like that: As a first step, the positions and velocity obtained at half period is taken. These coordinates are taken as the initial values of the process used for find Halo orbit. The Newton's iteration method is used to find initial velocity components with these positions which ensure periodic orbit. So, the difference between computed velocity and old velocity is the maneuver quantity delta_V to be performed. After one orbital period the same process is followed to find delta_V for second maneuver; take positions as initial, perform iteration to find correct velocity and computed velocity difference. The results with used scenarios are given in the following figures (Figure 3-45 to Figure 3-47): the orbits end energy obtained with maneuvers, and delta_V budget.
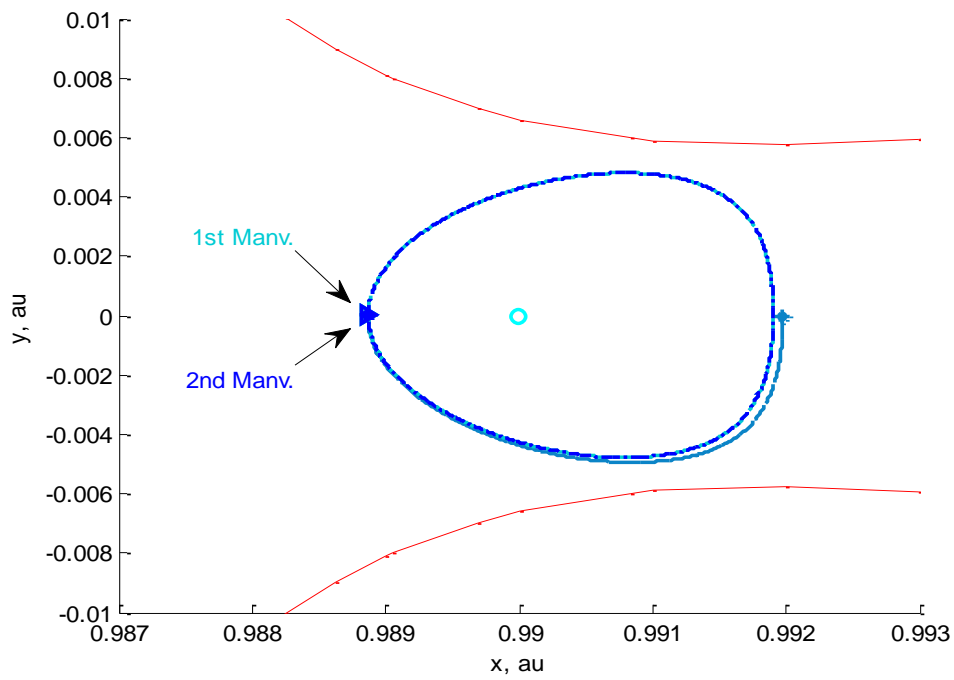
Figure 3-45. Orbital correction maneuvers
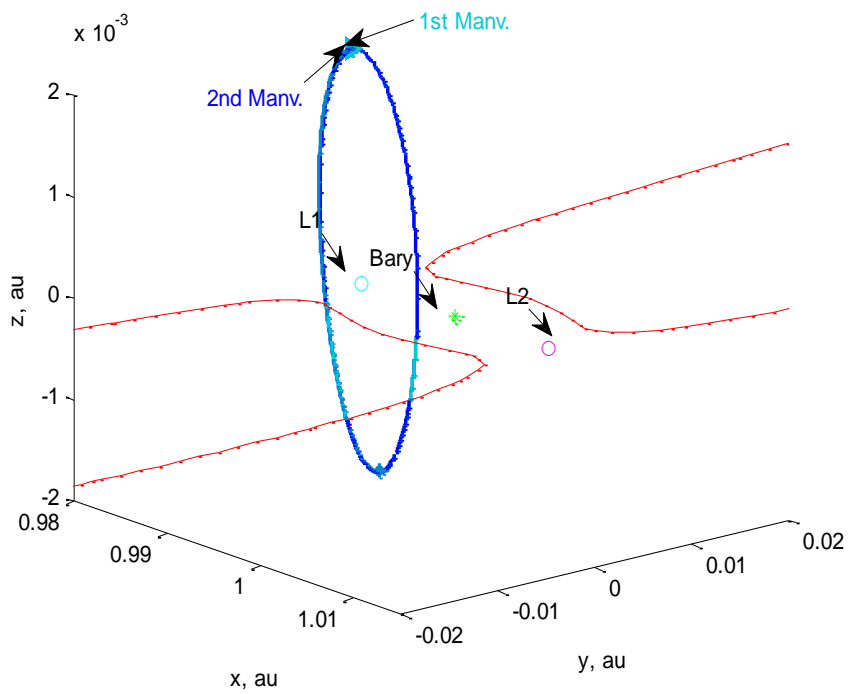
Figure 3-46. Orbital correction maneuvers – 3D view

136
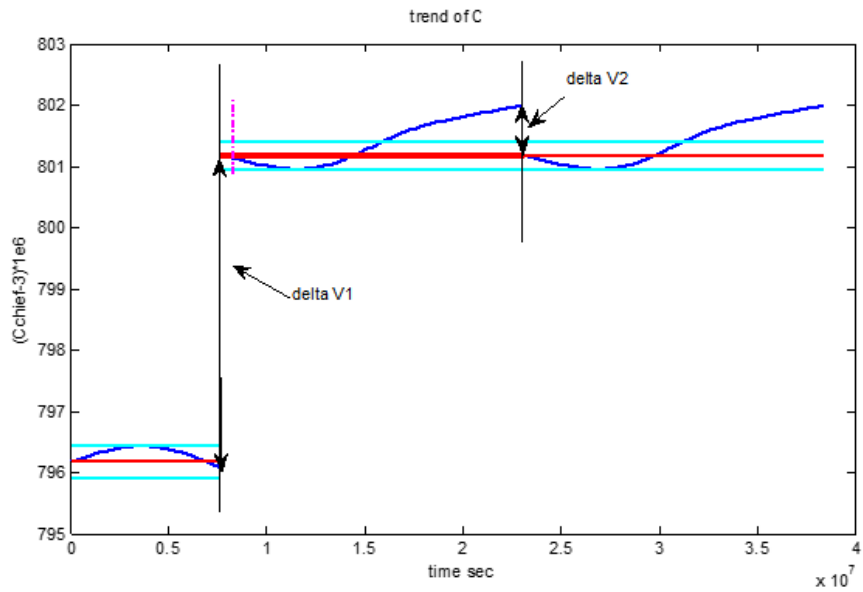
Figure 3-47. Orbital deltaV implementation

Table 3.9. DeltaV values of the maneuvers

Maneuvers	Unit DeltaV values	DeltaV values in m/s
First Maneuver, DeltaV1:	0.000279072	~ 8.3124 m/s
Second Maneuver, DeltaV2:	0.000175115	~ 5.21596 m/s

So, finally all the process followed can be summarized as: first maneuver is made at the half period, the next maneuvers are performed every one full period and such a maneuvering strategy ensures to have a periodic Halo orbit.

CHAPTER 4

FORMATION FLIGHT DESIGN NEAR L1 AND L2 POINTS

This chapter presents a design methodology for a formation flight near Sun-Earth collinear libration points. The satellites operating at L1 and L2 are presented briefly in the first section. The next section describes the design method used for each of the deputy satellites to form the formation flight scheme. Finally, simulation results are given and inferences are shared regarding to the result obtained for different formation flight configurations.

4.1. Spacecraft at libration points and formation flight concept

There exist many satellites navigating near Sun-Earth collinear libration point and their missions are composed of observations and researches on our Sun, studies on star formation, the detection of Earth-like planets and understanding the conditions of early Earth-like planets. For instance, SOHO is one of the most famous satellites moving near L1 on Lissajous orbit, it is launched in 1995 [60]. Before SOHO, there was WIND at L1 Lissajous orbit and launched 1994 [58]. GENESIS, TRIANA, MAXIM and DARWIN are the other projects for dedicated to L1 missions. ISEE-3, launched at 1978, it is one of the very interesting; it navigated around L1, then around L2 and finally it is directed to a Comet. The satellites MAP (L2- Lissajous), NGST (L2- Quasi Periodic Lissajous), SPECs (L2- Lissajous), Constellation-X (L2-Lissajous), STELLAR IMAGER and TPS are the projects planned for L2. The formation flight concept is started to be considered for L1 and L2 missions. SPECs is planned to have tethered formation, MAXIM and Constellation-X also contains the formation. DARWIN is also another formation concept and STELLAR IMAGER is one of the biggest formation family having roughly 30 satellites [19].

Among them, DARWIN constellation is taken one of the motivation sources of this thesis study. It has three to four free-flying spacecraft that will be at the L2. This is an European mission aims to characterize Earth-like planets. And the project called ESPRIT also has a formation flight scheme, it will carry subarcseconds far infrared observatory payload. The trade-off report of ESPRIT notice that it has a loose formation flying constraints [4], so this also is a motivation source. For future plans, PLATO and ATHENA are the projects developed by ESA for the years 2024 and 2028. The formation flight can be a reasonable solution for their mission.

All of these projects, which are completed, ongoing, and planned for the future, all of point out that the formation flight capability is a need for them, formation flight present abilities in terms of mission redundancy, mission capability, flexibility and so on.

4.2. Relative equations of motion with disturbances

This section defines the motion of the deputy satellite with respect to the chief satellite for the formation flight at libration points. First, the relative equations of motion are written without adding the disturbances. As given in the section 2.2.1, the differential equations of the chief and deputy satellites described in synodic reference frame can be rewritten as follows:

$$
\begin{aligned}
\ddot{x}_{chief}\big|_{syn} = {}& \omega^2 x_{chief} + 2\omega \dot{y}_{chief} - \frac{Gm_{SUN}(x_{chief} + x_1)}{\left|r_{1_{chief}}\right|^3} \\
& - \frac{Gm_{BARY}(x_{chief} - x_2)}{\left|r_{2_{chief}}\right|^3} + \frac{\tilde{\alpha}(x_{chief} + x_1)}{\left|r_{1_{chief}}\right|} \\
& - \sum_{i=1}^{7} \frac{Gm_{PLANETi}\left(R_{Pix} - (x_{chief} + x_1)\right)}{\left|R_{Pi} - r_{1_{chief}}\right|^3}
\end{aligned}
\qquad \text{Eq. 4-1a}
$$

140

$$\ddot{y}_{chief}\big|_{syn} = \omega^2 y_{chief} - 2\omega \dot{x}_{chief} - \frac{Gm_{SUN}\, y_{chief}}{\left|r_{1_{chief}}\right|^3}$$

$$- \frac{Gm_{BARY}\, y_{chief}}{\left|r_{2_{chief}}\right|^3} + \frac{\tilde{\alpha}\, y_{chief}}{\left|r_{1_{chief}}\right|}$$

$$- \sum_{i=1}^{7} \frac{Gm_{PLANETi}\left(R_{Piy} - y_{chief}\right)}{\left|R_{Pi} - r_{1_{chief}}\right|^3}$$

Eq. 4-1b

$$\ddot{z}_{chief}\big|_{syn} = - \frac{Gm_{SUN}\, z_{chief}}{\left|r_{1_{chief}}\right|^3} - \frac{Gm_{BARY}\, z_{chief}}{\left|r_{2_{chief}}\right|^3} + \frac{\tilde{\alpha}\, z_{chief}}{\left|r_{1_{chief}}\right|}$$

$$- \sum_{i=1}^{7} \frac{Gm_{PLANETi}\left(R_{Piz} - z_{chief}\right)}{\left|R_{Pi} - r_{1_{chief}}\right|^3}$$

Eq. 4-1c

$$\ddot{x}_{dept}\big|_{syn} = \omega^2 x_{dept} + 2\omega \dot{y}_{dept} - \frac{Gm_{SUN}\left(x_{dept} + x_1\right)}{\left|r_{1_{dept}}\right|^3}$$

$$- \frac{Gm_{BARY}\left(x_{dept} - x_2\right)}{\left|r_{2_{dept}}\right|^3} + \frac{\tilde{\alpha}\left(x_{dept} + x_1\right)}{\left|r_{1_{dept}}\right|}$$

$$- \sum_{i=1}^{7} \frac{Gm_{PLANETi}\left(R_{Pix} - \left(x_{dept} + x_1\right)\right)}{\left|R_{Pi} - r_{1_{dept}}\right|^3}$$

Eq. 4-2a

$$\ddot{y}_{dept}\big|_{syn} = \omega^2 y_{dept} - 2\omega \dot{x}_{dept} - \frac{Gm_{SUN}\, y_{dept}}{\left|r_{1_{dept}}\right|^3} - \frac{Gm_{BARY}\, y_{dept}}{\left|r_{2_{dept}}\right|^3}$$

$$+ \frac{\tilde{\alpha} y_{dept}}{\left|r_{1_{dept}}\right|} - \sum_{i=1}^{7} \frac{Gm_{PLANETi}\left(R_{Piy} - y_{dept}\right)}{\left|R_{Pi} - r_{1_{dept}}\right|^3}$$

Eq. 4-2b

$$\ddot{z}_{dept}\Big|_{syn} = -\frac{Gm_{SUN}\,z_{dept}}{\left|r_{1_{dept}}\right|^3} - \frac{Gm_{BARY}\,z_{dept}}{\left|r_{2_{dept}}\right|^3} + \frac{\tilde{\alpha}z_{dept}}{\left|r_{1_{dept}}\right|}$$
$$-\sum_{i=1}^{7}\frac{Gm_{PLANETi}\left(R_{Piz} - z_{dept}\right)}{\left|R_{Pi} - r_{1_{dept}}\right|^3}$$

Eq. 4-2c

Recall that:

$$r_{1_{chief}} = \sqrt{\left(x_{chief} + x_1\right)^2 + y_{chief}^2 + z_{chief}^2}$$

Eq. 4-3

$$r_{2_{chief}} = \sqrt{\left(x_{chief} - x_2\right)^2 + y_{chief}^2 + z_{chief}^2}$$

Eq. 4-4

$$r_{1_{dept}} = \sqrt{\left(x_{dept} + x_1\right)^2 + y_{dept}^2 + z_{dept}^2}$$

Eq. 4-5

$$r_{2_{dept}} = \sqrt{\left(x_{dept} - x_2\right)^2 + y_{dept}^2 + z_{dept}^2}$$

Eq. 4-6

Here, $r_{1_{chief}}$ is the distance between chief satellite and Sun, $r_{2_{chief}}$ is the distance between chief satellite and Bary, and similarly, $r_{1_{dept}}$ distance between deputy satellite and Sun, $r_{2_{dept}}$ distance between deputy satellite and Bary. Here the suffix syn denotes that equation is expressed in synodic reference frame. And ω is the angular rate of synodic reference frame with respect to the inertial reference frame:

$$\boldsymbol{\omega} = \sqrt{\frac{G(m_{SUN} + m_{BARY})}{\boldsymbol{R}^3}}$$

Eq. 4-7

Where m_{sun} is the mass of the Sun, m_{earth} is the mass of the Earth, and R is the distance between Sun and Bary, called astronomic unit – au –, and G is the gravitational constant. Let ρ is the distance between deputy and chief satellite, relative distance of the deputy satellite with respect to the chief.

$$\vec{\rho} = \vec{r}_{deputy} - \vec{r}_{chief}$$ Eq. 4-8

In matrix form deputy position can be define as:

$$\bar{r}_{deputy} = \bar{\rho} + \bar{r}_{chief}$$ Eq. 4-9

In synodic reference frame, the relative differential equation can be described in matrix form as the following equation:

$$\ddot{\rho}|_{syn} = \begin{bmatrix} \ddot{x}_{dept} \\ \ddot{y}_{dept} \\ \ddot{z}_{dept} \end{bmatrix}_{syn} - \begin{bmatrix} \ddot{x}_{chief} \\ \ddot{y}_{chief} \\ \ddot{z}_{chief} \end{bmatrix}_{syn}$$ Eq. 4-10

The visualization of the chief and the deputy satellite is given in Figure 4-1 and Figure 4-2. Here, the orbital reference frame defined for chief satellite is shown. The unit vector of x is aligned toward r position vector of the chief satellite. The position and velocity vector are known, and it is known that X position vector and V velocity vector make a plane, so the y axis also is on that plane and y is perpendicular to x. Secondly z axis is defined and it is perpendicular to the plane defined by X and V. after obtaining z, the y axis is computed using x and z in order to get orthonormal axis frame according to the right hand system:
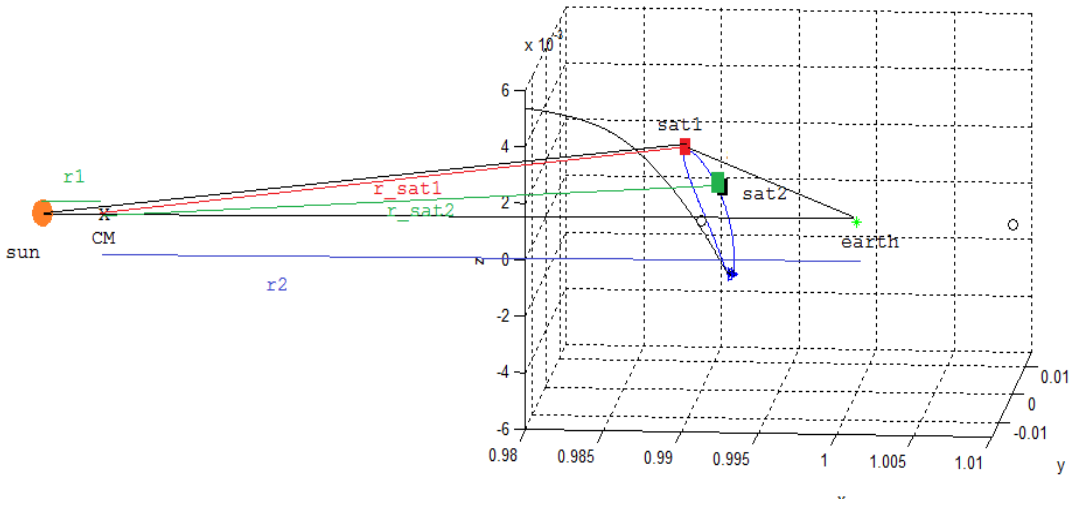
Figure 4-1. Relative position of deputy satellite with respect chief satellite
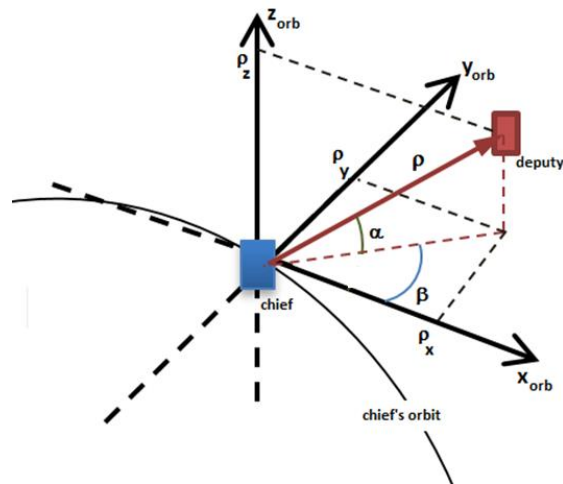
Figure 4-2. Relative position expresses in chief's orbital frame

The unit vectors of the chief's orbital reference frame are computed using following equations:

$$\vec{e}_x = \vec{r}_{chief}/|\vec{r}_{chief}|$$

Eq. 4-11

144

$$\vec{e}_z = (\vec{r}_{chief} \times \vec{V}_{chief})/|\vec{r}_{chief} \times \vec{V}_{chief}| \qquad \text{Eq. 4-12}$$

$$\vec{e}_y = \vec{e}_z \times \vec{e}_x \qquad \text{Eq. 4-13}$$

Orbital reference frame of the chief is illustrated in
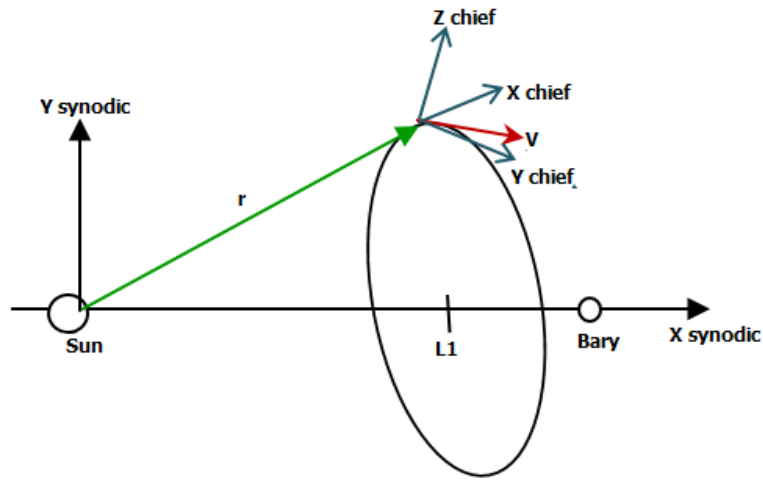
Figure 4-3. Orbital reference frame of the chief satellite

Here, it is needed to describe the relative motion with respect to the chief satellite's orbital frame. So, the angular rate of the chief's orbital frame with respect to synodic reference frame, denoted as Ω , it will be computed using Direction Cosine Matrix (DCM) between synodic and chief's orbital frames. Let define unit vectors of the synodic frame as I, J, K respectively. DCM can be written using dot product; it means angular relations between I, J, K and $\vec{e}_x, \vec{e}_y, \vec{e}_z$ as:

$$C = C_{orb}^{syn} = \begin{bmatrix} I \cdot \vec{e}_x & I \cdot \vec{e}_y & I \cdot \vec{e}_z \\ J \cdot \vec{e}_x & J \cdot \vec{e}_y & J \cdot \vec{e}_z \\ K \cdot \vec{e}_x & K \cdot \vec{e}_y & K \cdot \vec{e}_z \end{bmatrix} \qquad \text{Eq. 4-14}$$

And the angular velocity $\Omega = [\Omega_1 \quad \Omega_2 \quad \Omega_3]^T$ can be computed using following equation:

$$\tilde{\Omega} = \begin{bmatrix} 0 & -\Omega_3 & \Omega_2 \\ \Omega_3 & 0 & -\Omega_1 \\ -\Omega_2 & \Omega_1 & 0 \end{bmatrix} = C^T \dot{C} \qquad \text{Eq. 4-15}$$

So, the relative acceleration of the deputy in chief's orbital reference frame can be written in matrix form as follows:

$$\ddot{\rho}|_{orb} = C^T \left(\begin{bmatrix} \ddot{x}_{dept} \\ \ddot{y}_{dept} \\ \ddot{z}_{dept} \end{bmatrix}_{syn} - \begin{bmatrix} \ddot{x}_{chief} \\ \ddot{y}_{chief} \\ \ddot{z}_{chief} \end{bmatrix}_{syn} \right) \\ - \left(2\tilde{\Omega}\,\dot{\rho}|_{orb} + \dot{\tilde{\Omega}}\,\rho|_{orb} + \tilde{\Omega}^2 \rho|_{orb} \right) \qquad \text{Eq. 4-16}$$

In the same manner, the relative velocity can be described as follows:

$$\dot{\rho}|_{orb} = C^T \left(\begin{bmatrix} \dot{x}_{dept} \\ \dot{y}_{dept} \\ \dot{z}_{dept} \end{bmatrix}_{syn} - \begin{bmatrix} \dot{x}_{chief} \\ \dot{y}_{chief} \\ \dot{z}_{chief} \end{bmatrix}_{syn} \right) - \left(\tilde{\Omega}\,\rho|_{orb} \right) \qquad \text{Eq. 4-17}$$

The final equation, relative equation of motion expressed in chief's orbital frame, it is obtained by subtracting the first two Eq 4-1 and Eq.4-2 in to last Eq 4-16:

$$\ddot{\rho} = \left\{ -2\omega\left(\dot{\rho} + \widetilde{\Omega}\,\rho\right) - \omega^2\rho - Gm_{sun}\left[\frac{r_{1c} + \rho}{|r_{1c} + \rho|^3} - \frac{r_{1c}}{|r_{1c}|^3}\right]\right.$$

$$- Gm_{earth}\left[\frac{r_{2c} + \rho}{|r_{2c} + \rho|^3} - \frac{r_{2c}}{|r_{2c}|^3}\right] + \tilde{\alpha}\left[\frac{r_{1c} + \rho}{|r_{1c} + \rho|} - \frac{r_{1c}}{|r_{1c}|}\right]$$

$$- \sum_{i=1}^{7} Gm_{PLANETi}\left[\frac{\left(R_{Pix} - (r_{1c} + \rho)\right)}{|R_{Pi} - (r_{1c} + \rho)|^3}\right.$$

$$\left.\left. - \frac{\left(R_{Pix} - (r_{1c})\right)}{|R_{Pi} - (r_{1c})|^3}\right]\right\} - \left(2\widetilde{\Omega}\,\dot{\rho} + \dot{\widetilde{\Omega}}\,\rho + \widetilde{\Omega}^2\rho\right) \qquad \text{Eq. 4-18}$$

where ω is expressed in the orbital reference frame, so:

$$\omega = C^T\overline{\omega}_{syn} = C^T[0 \quad 0 \quad \omega_{syn}]^T$$

$$\text{Eq. 4-19}$$

$$r_{1c} = r_{1c_{orb}} = \left(r_{chief} + x_1\right)_{orb} = \left(r_{chief}\right)_{orb} + C^T[x_1 \quad 0 \quad 0]^T \qquad \text{Eq. 4-20}$$

$$r_{2c} = r_{2c_{orb}} = \left(r_{chief} - x_2\right)_{orb} = \left(r_{chief}\right)_{orb} - C^T[x_2 \quad 0 \quad 0]^T \qquad \text{Eq. 4-21}$$

$$\left(r_{chief}\right)_{orb} = C^T\left(r_{chief}\right)_{syn} \qquad \text{Eq. 4-22}$$

Finally, relative equations of motion of the deputy satellite with respect to chief satellite expressed in chief's orbital reference frame are derived.

4.3. Formation flight design near L1

Formation flight concept is mainly based on keeping and controlling the relative distance between each members of the formation. Some propose to control relative distance with respect to a selected chief satellite (some references called it as leader satellite), others intend to control the relative position of satellite with respect to the each of the members which are close to it. In latter approach formation is kept by following all the neighborhood satellites' relative positions.

In this section it is aimed to find an orbit for deputy satellite which ensures naturally long-term formation flight for a desired chief/deputy formation configuration without need of formation correction maneuver. The meaning of the configuration is the selection of the relative initial position of the deputy satellite with respect to the chief. So, the desired relative distance ρ, the desired relative elevation angle, α and azimuth angle, β are the parameters that indicate the relative initial position (see Figure 4-2). Here, the main assumption is that; chief and deputies have periodic orbits. So, it is expected to be at the same position as the initial position after passing one orbital period of time. It can be stated that the formation is achieved when the deputy satellite reaches the same initial relative position after one orbital period. The infrastructure of the methodology presented here is based on this idea.

In this way, the problem is reduced to find a proper initial velocity that ensures the final position is equal to the initial desired one. So, the problem may be redefined as: What is the initial velocity that satisfies the same position at the end of the one orbital period? As a starting point of the formation design, the main items to be considered can be listed as follows:
- The initial x coordinate of the deputy satellite will be taken same as the chief satellite. So, azimuth angle, β is taken constant and it is equal to 90 degrees.
- The initial $y\ and\ z$ coordinates will be desirable which are dependent on ρ and elevation angle α ($\rho = 1\ km$ and $\alpha = -30\ degrees$ at Figure 4-4).
- The orbital period of the deputy must be the same as the chief's period.

- The convenient velocities $\dot{x}, y, \dot{z}$ that satisfy formation flight will be computed.
- The Newton's iteration method is used to find optimal initial velocity components. The minimization function is: after one orbital period the final positions must be same as the initial positions

Remembering the equations of motion of the satellite in matrix form with velocity and acceleration components (Eq. 2-39):

$$f(X) = [\dot{x}, \dot{y}, \dot{z}, \ddot{x}, \ddot{y}, \ddot{z}]^T$$ Eq. 4-23

The equation set of $\ddot{x}, \ddot{y}, \ddot{z}$ are given in Eq.4-1 and Eq.4-2.

The minimization function is:

$$f(X_{sub}) = \begin{bmatrix} x_{final} - x_{initial} \\ y_{final} - y_{initial} \\ z_{final} - z_{initial} \end{bmatrix} = \begin{bmatrix} \Delta\bar{x} \\ \Delta\bar{y} \\ \Delta\bar{z} \end{bmatrix} = \begin{bmatrix} 0 \\ 0 \\ 0 \end{bmatrix}$$ Eq. 4-24

Here initial coordinates are the sum of the chief's positions and desired relative positions.

$$\begin{bmatrix} x_{initial} \\ y_{initial} \\ z_{initial} \end{bmatrix} = \begin{bmatrix} x_{chief} + dx_{desired} \\ y_{chief} + dy_{desired} \\ z_{chief} + dz_{desired} \end{bmatrix}$$ Eq. 4-25

where;

$$\begin{bmatrix} dx_{desired} \\ dy_{desired} \\ dz_{desired} \end{bmatrix} = \begin{bmatrix} \rho_{desired} \cos(\alpha_{desired}) \cos(\beta_{desired}) \\ \rho_{desired} \cos(\alpha_{desired}) \sin(\beta_{desired}) \\ \rho_{desired} \sin(\alpha_{desired}) \end{bmatrix}$$ Eq. 4-26

And the iteration process is:

$$
\begin{bmatrix} \dot{\bar{x}}^* \\ \dot{\bar{y}}^* \\ \dot{\bar{z}}^* \end{bmatrix}_{k+1} = \begin{bmatrix} \dot{\bar{x}}^* \\ \dot{\bar{y}}^* \\ \dot{\bar{z}}^* \end{bmatrix}_k - \left(D_f\right)^{-1} \begin{bmatrix} \Delta\bar{x} \\ \Delta\bar{y} \\ \Delta\bar{z} \end{bmatrix}
$$

Eq. 4-27

$$
D_f = \begin{bmatrix} \Phi_{1,4} & \Phi_{1,5} & \Phi_{1,6} \\ \Phi_{2,4} & \Phi_{2,5} & \Phi_{2,6} \\ \Phi_{3,4} & \Phi_{3,5} & \Phi_{3,6} \end{bmatrix}
$$

Eq. 4-28

The iteration is continued until the error between successive results is reached predefined iteration stopping parameter, it is denoted as ϵ. This process gives the optimal initial conditions, for that reason it is called as OPTICs that stands ***Optimal Initial Conditions***.

$$
\begin{bmatrix} \epsilon_x \\ \epsilon_y \\ \epsilon_z \end{bmatrix} = \begin{bmatrix} \dot{\bar{x}}^* \\ \dot{\bar{y}}^* \\ \dot{\bar{z}}^* \end{bmatrix}_{k+1} - \begin{bmatrix} \dot{\bar{x}}^* \\ \dot{\bar{y}}^* \\ \dot{\bar{z}}^* \end{bmatrix}_k
$$

Eq. 4-29

This iteration process is coded using Matlab and Simulink 2012a version. The execution time spent for computing the initial conditions of the deputy satellite is analyzed. For instance, the time spent for one iteration is approximately 5 seconds with a simulation having sampling time that is equal to 1 hour. The details are given in Appendix-I.

In section 3.3.3.2, the effects of disturbances in Halo orbit design was given. It was shown that for some of the cases presented the orbit computed using symmetry property did not give a perfect periodic orbit due to the gravitational pulls of the planets and solar radiation pressure. For that reason, the initial conditions were recomputed at the half period in order to ensure periodic orbit (it was the value of the 1st maneuver). In this section the initial conditions are taken for chief satellite since periodic orbit is achieved for full period. Initial position for the deputy satellite is taken as the desired relative distance and angles are given, and velocities are computed by

the process described above. So, the initial conditions, orbit trajectories and the relative positions are given in the following table and figures respectively.

Figure 4-4 shows the relative trajectory of the deputy with respect to the chief in three-dimensional view. The following three figures, Figure 4-5, Figure 4-6 and Figure 4-7, they show the projection of this relative trajectory respectively on xy, xz, yz planes.

Table 4.1. Initial conditions and periodicity check for chief and deputy satellites

Initial conditions of chief before Newton iteration	Initial conditions of chief after Newton iteration	Initial conditions of deputy before Newton iteration	Initial conditions of deputy after Newton iteration
0.988863916985417 0.000000190354307 0.002283164826074 0.000000173093585 0.009797574474637 -0.000000137742170	0.988863916985417 0.000000190354307 0.002283164826074 0.000079282180680 0.009561450590853 -0.000003813751236	0.988863916985417 0.000000196143330 0.002283161483781 0.000079282180680 0.009561450590853 -0.000003813751236	0.988863916985417 0.000000196143330 0.002283161483781 0.000079287255726 0.009561447356541 -0.000003817998113
Period of chief's Orbit in Earth's day:	177.5833 days	**Period of deputy's Orbit in Earth's day:**	177.5833 days
Jacobi constant C of chief:	3.000800635360898	**Jacobi constant C of deputy:**	3.000800635469296
Periodicity Check of Chief:	0.2126376620 meter	**Periodicity Check of deputy:**	0.18595558333 meter
Test: Determinant of chief's Φ:	1.000000000754795	**Test: Determinant of deputy's Φ**	0.999999999375502
EigenValues of chief's Φ:		**EigenValues of deputy's Φ:**	
1529.423095479949 1.014054183326 0.969308034388 - 0.245868259983i 0.969308034388 + 0.245868259983i 0.986173253860 0.00653813601		1529.423802360684 1.014054141623 0.969308134143 - 0.245867866800i 0.969308134143 + 0.245867866800i 0.986173294363 0.000653813298	
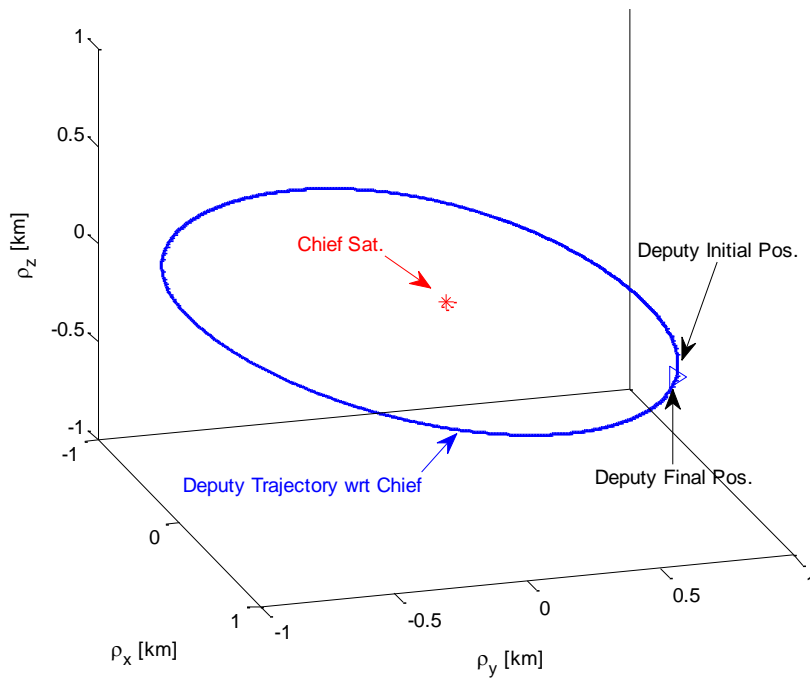
Figure 4-4. Relative trajectory of the deputy with respect to the chief
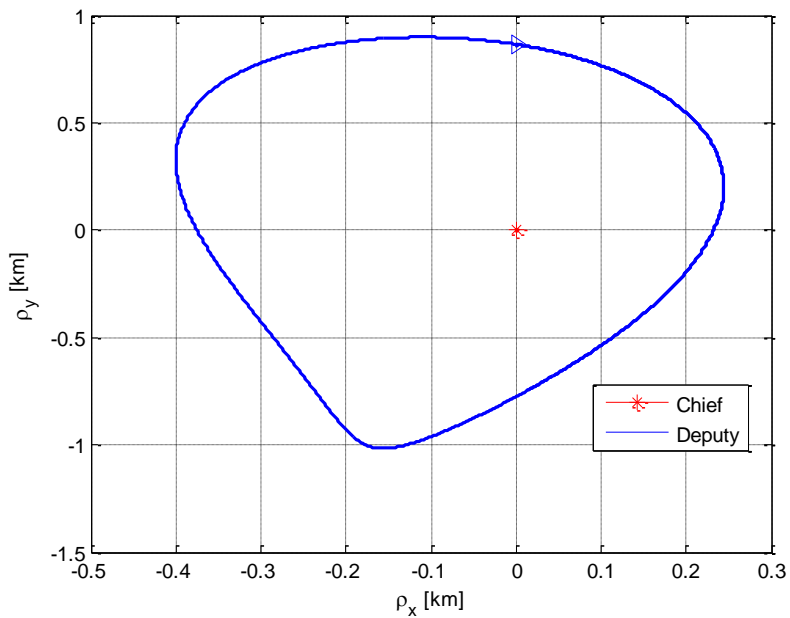
Figure 4-5. XY projection of the relative trajectory

152
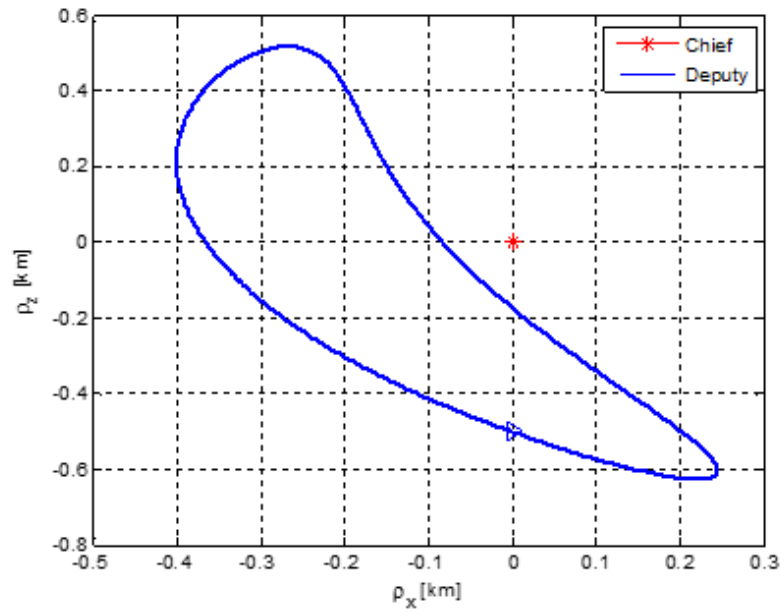
Figure 4-6. XZ projection of the relative trajectory
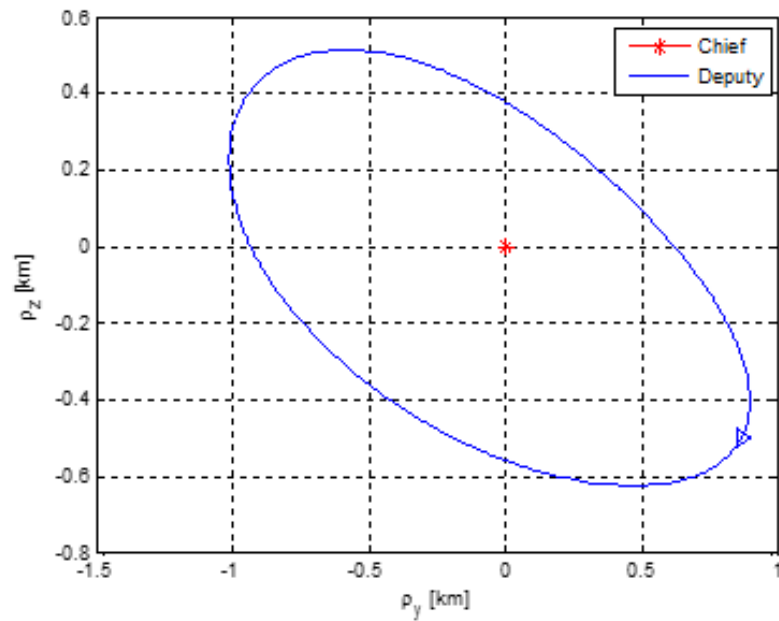
Figure 4-7. YZ projection of the relative trajectory

Figure 4-8 gives the relative position and its components with respect to the time. Here it is seen that x component of relative distance ρ_x varies between 0.25km - 0.4km.

Actually, it is not a symmetric. The regular motion, under the effects of gravitational pulls of planets orbiting, changes positions with respect to the chief satellite. For example, ρ_y the relative position changes from 1 km to -1 km. However, it may still be stated that the motion is nearly periodic along the y axis. This kind of harmonic motion is also seen in z component. Thus, a quasi-harmonic motion is obtained.
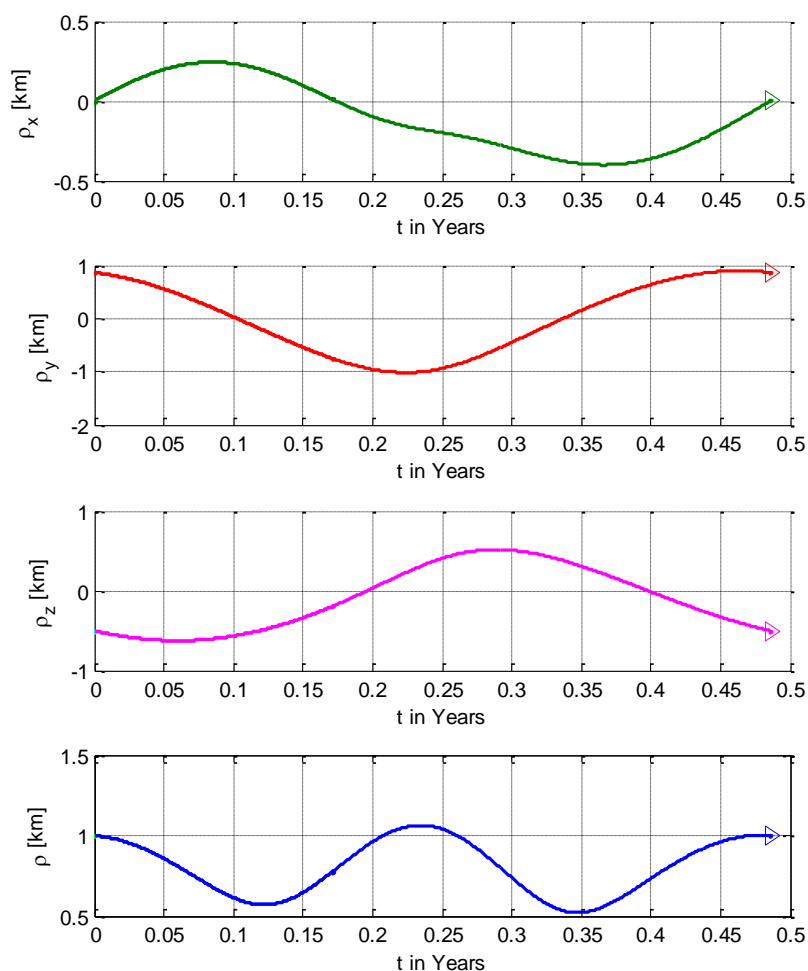
Figure 4-8. Relative position and its components with respect to the time

Required formation is kept during one orbital period of time. It is seen that relative distance has a periodic motion and formation periodically narrows and expands around the required relative distance. As a result, it may be stated that it is not possible to obtain a constant relative distance for this type of formation configurations where the

154

relative position varies between 1 km-0.5 km. It is also interesting to note that the required ρ is reached at every half period and this is the maximum limit obtained, then it decreases up to 0.5 km, at odd quarter periods, and then it goes back to 1 km at half period again.

The following section contains three different formation schemas in order to analyze the relation between the initial relative position and the shape of the relative trajectory obtained. It is intended to obtain an idea on how to obtain nearly constant relative distance by examining these various configurations.

4.3.1. Different formation clusters and simulation results

In this section different formation clusters are analyzed in order to understand the effect of the initial relative position to the relative trajectory. The first example is composed of three deputy satellites forming an equilateral triangle; the second cluster has four deputies with a planar square shape, and the third one has also same form as second but in this case the plane has an inclination with respect to the yz plane.

4.3.1.1. Equilateral triangle formation (ETF)

The first formation cluster is motivated from the DARWIN and ESPRIT projects, a cluster having three to four flying satellites. The three satellites positioned on the corner of an equilateral triangle and the chief satellite is on the center of this triangle. This chief satellite can be considered as a hypothetical satellite for a formation of three satellites. Figure 4-9 shows the deputy satellites and chief (hypothetical) is located on the center.
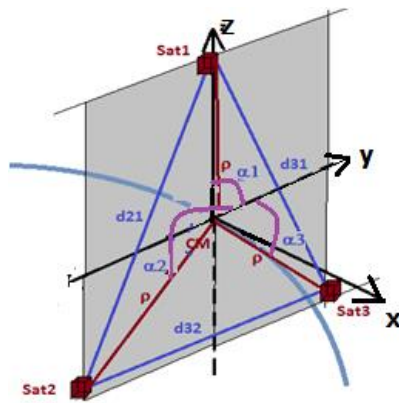
Figure 4-9. Equilateral triangle shape formation

The desired relative distance ρ between deputy satellites and chief is 1 km. and the relative initial positions with respect to the chief are:

Table 4.2. Relative positions of the deputies for ETF around L1

Deputy Satellite 1	Deputy Satellite 2	Deputy Satellite 3
$\rho = 1\ km$	$\rho = 1\ km$	$\rho = 1\ km$
$\beta = 90^0$	$\beta = 90^0$	$\beta = 90^0$
$\alpha = 90^0$	$\alpha = 210^0$	$\alpha = -30^0$

The chief's orbit has already computed in previous section. In fact, the initial values and trajectory for third satellite is also already computed in the previous section. Now the initial velocities and trajectory for the first and second satellites will be computed.

Table 4.3. ICs and periodicity checks for ETF around L1

Initial conditions of chief	Initial conditions of deputy_1	Initial conditions of deputy_2	Initial conditions of deputy_3
0.988863916985417 0.000000190354307 0.002283164826074 0.000079282180680 0.009561450590853 -0.000003813751236	0.988863916985417 0.000000190354307 0.002283171510662 0.000079282450908 0.009561457021163 -0.000003813623039	0.988863916985417 0.000000184565285 0.002283161483781 0.000079276835433 0.009561447394770 -0.000003809632559	0.988863916985417 0.000000196143330 0.002283161483781 0.000079287255726 0.009561447356541 -0.000003817998113
Period of chief's Orbit in Earth's day: 177.5833 days	**Period of deputy_1 Orbit in Earth's day:** 177.5833 days	**Period of deputy_2 Orbit in Earth's day:** 177.5833 days	**Period of deputy_3 Orbit in Earth's day:** 177.5833 days
Chief's Jacobi Constant: 3.000800635360898	**deputy_1's Jacobi Constant:** 3.000800635143107	**deputy_2's Jacobi Constant:** 3.000800635470291	**deputy_3's Jacobi Constant:** 3.000800635469296
Periodicity Check of chief: 0.2126 meter	**Periodicity Check of deputy_1:** 0.5332 meter	**Periodicity Check of deputy_2:** 0.1550 meter	**Periodicity Check of deputy_3:** 0.18595 meter
Test: Determinant of chief's Φ: 1.000000000754795	**Test: Determinant of deputy_1's Φ:** 1.000000000555292	**test Test: Determinant of deputy_2's Φ:** 1.000000000286739	**Test: Determinant of deputy_3's Φ:** 0.999999999375502
EigenValues of chief's Φ:	**EigenValues of deputy_1's Φ:**	**EigenValues of deputy_2's Φ:**	**EigenValues of deputy_3's Φ:**
1529.42309 1.01405 0.96931- 0.245868i 0.96931+ 0.245868i 0.986173 0.006538	1529.42168 1.014054 0.969308- 0.2458690i 0.969308+0.2458690i 0.986173171 0.000653814	1529.42379 1.014054 0.969308- 0.24586787i 0.969308+0.24586787i 0.986173295 0.000653813	1529.42380 1.0140541 0.969308- 0.24586787i 0.969308+0.24586787i 0.986173294 0.000653813

157
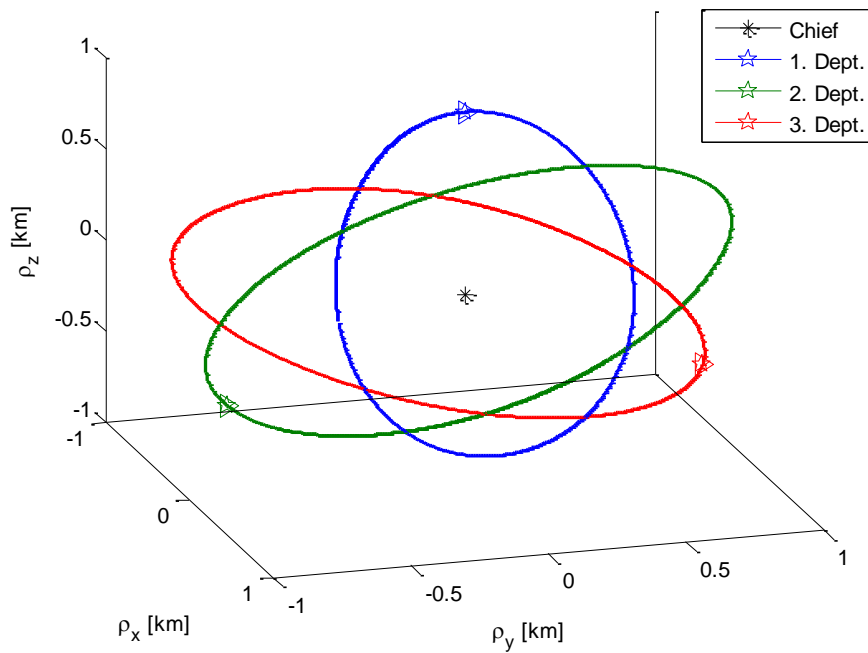
Figure 4-10. Trajectories of the deputies with respect to chief for ETF around L1

The trajectory of each deputy satellite with respect to chief is given in Figure 4-10. Following Figure 4-11, Figure 4-12 and Figure 4-13 are the set of multiple sub-figures. The left part contains three sub-figures showing the projection of the trajectory respectively in xy, xz, yz planes. The first three figures of the right part present the components of relative distance change with time. The last figure of the right part contains the resultant relative distance, the distance between deputy and chief satellites.

Figure 4-11. ETF-L1, Deputy #1: Projected and time dependent views

Figure 4-12. ETF-L1, Deputy #2: Projected and time dependent views

Figure 4-13. ETF-L1, Deputy #3: Projected and time dependent views

From the results, it is seen that the relative trajectory of the first deputy has a different characteristic from the two others. In xz plane it has quasi one-dimensional motion, and it has a quasi-elliptical motion in yz plane. However, the second and the third deputy satellites has symmetric relative trajectory with respect to the y axis and their motion has non-regular motion on projection. For all of them, the relative distances are not constant, they oscillate between 1 km and 0.5 km, narrowing and expanding, although the periodic relative motion is obtained for one orbital period time.
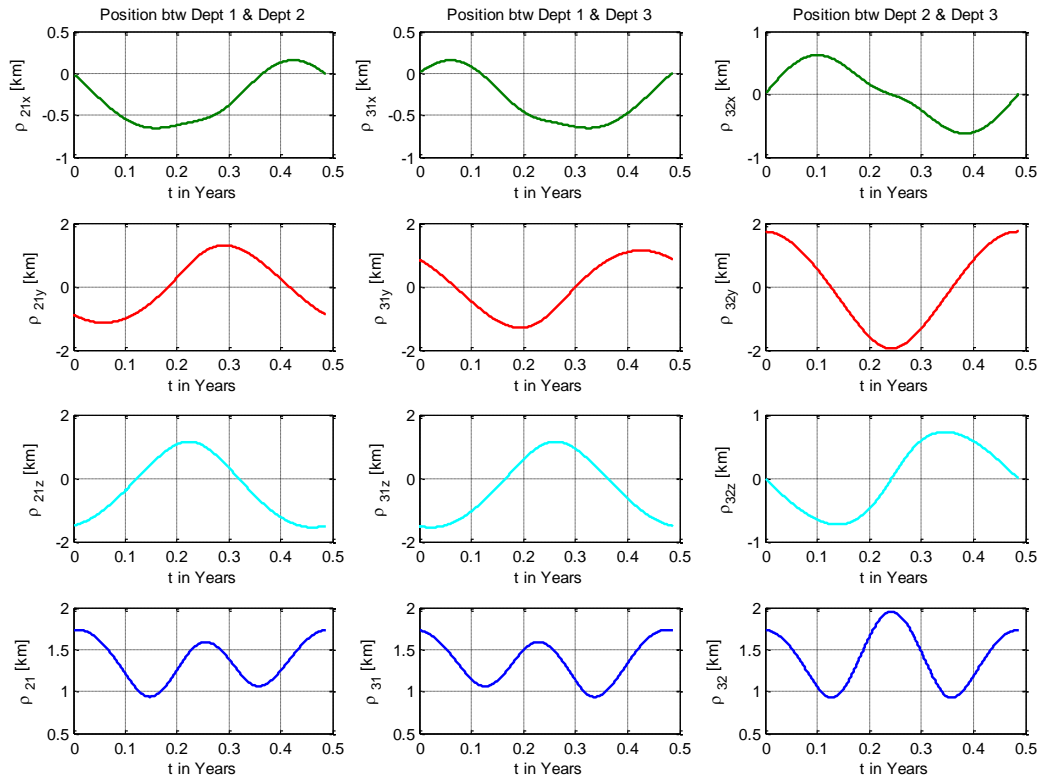
Figure 4-14. ETF-L1: The relative distances between deputies

The relative distances between deputies are given in Figure 4-14. The objective distance between them is $\sqrt{3}\rho = 1.732\ km$. An oscillating relative motion is obtained; the acquired formation shape shrinks and expands between aimed distances which is roughly 1.732 km and 1 km. The shape change of the triangle is illustrated in the following Figure 4-15. The bold green colored triangle is the starting configuration, the bold blue one is the last positions. The plane is colored from green to blues according to the time changes. The inclination angle of the plane formed by deputy satellites varies and the distance between them start narrowing until 1st and third quarter period then it expands at half and full period; last plane and 1st plane coincide since motion is periodic.
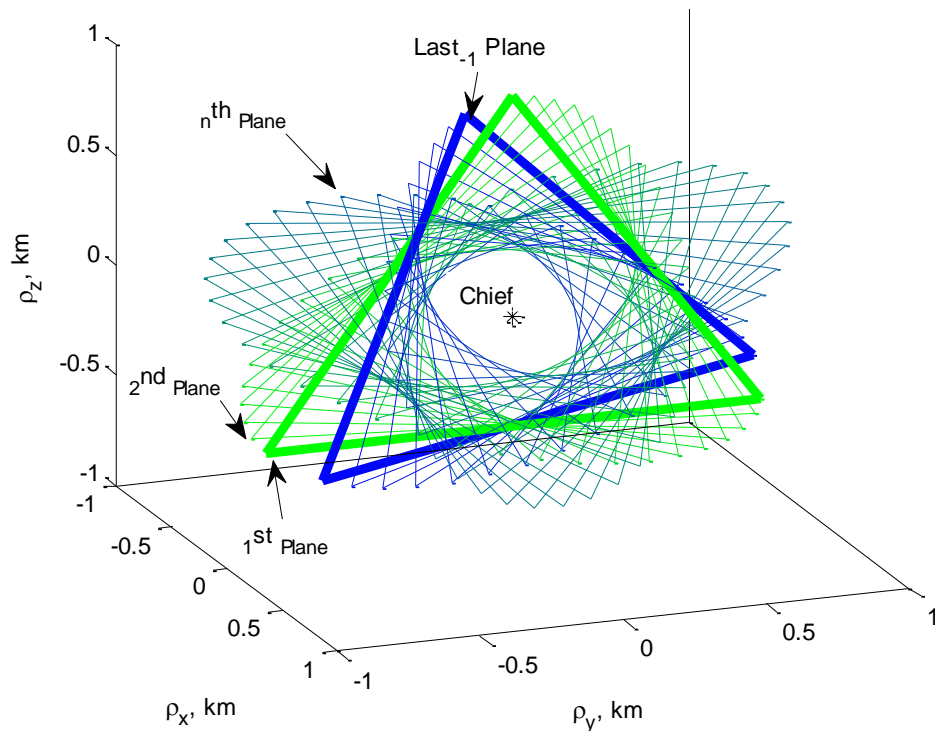
Figure 4-15. ETF-L1: The plane formed by deputies

The results obtained for this kind of triangular shape configuration shows that the deputy located at the top of the Chief (1st deputy) does not have a harmonious motion compared to the two other members of the formation. The other two deputies have symmetric motion with respect to y axis, so Chief, 2nd and 3rd satellites make a harmonic formation flight configuration. So, a question has occurred for the deputies located at just left/right/top and down of the chief. For that reason, the next formation configuration focuses on this kind of schema.

4.3.1.2. Square formation (SF)

This section presents the results obtained for a formation flight cluster composed of four deputy satellites having a square shaped configuration, as given in Figure 4-16; four deputy satellites are located at the corners of the square and chief is located on the center. Here too, the chief can be thought as a hypothetical satellite.
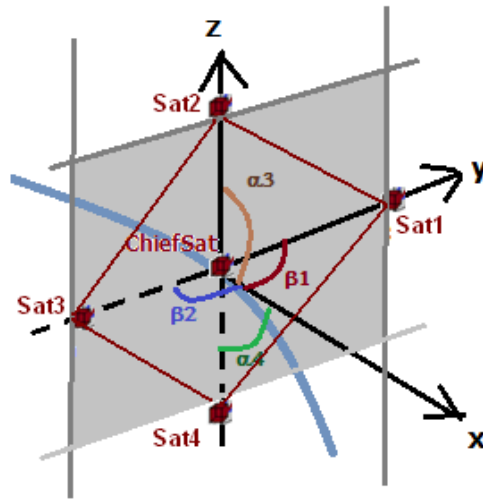
Figure 4-16. Square shape formation

The desired relative distance ρ between deputy satellites and chief and the relative initial azimuth and elevation angles with respect to the chief are listed in the following table.

Table 4.4. Relative positions of the four deputies, SF around L1

Deputy Satellite 1	Deputy Satellite 2	Deputy Satellite 3	Deputy Satellite 4
$\rho = 1\ km$	$\rho = 1\ km$	$\rho = 1\ km$	$\rho = 1\ km$
$\beta = 90^0$	$\beta = 0^0$	$\beta = -90^0$	$\beta = 0^0$
$\alpha = 0^0$	$\alpha = 90^0$	$\alpha = 0^0$	$\alpha = -90^0$

The chief's orbit is the same as used in the precedent section. The initial velocities and trajectory for the deputies are computed and given in the following Table 4.5 and figures from Figure 4-18 to Figure 4-21.

Table 4.5. ICs and periodicity checks, SF around L1

| Initial conditions of chief	Initial conditions of deputy_1	Initial conditions of deputy_2	Initial conditions of deputy_3	Initial conditions of deputy_4
0.988863916 0.000000190 0.002283164 0.000079282 0.009561451 -0.000003813	0.988863916985 0.000000197038 0.002283164826 0.000079288196 0.009561450568 -0.000003818581	0.988863916985 0.000000190354 0.002283171510 0.000079282450 0.009561457021 -0.000003813623	0.988863916985 0.000000183669 0.002283164826 0.000079276164 0.009561450612 -0.000003808921	0.988863916985 0.000000190354 0.002283158141 0.000079281910 0.009561444160 -0.000003813879
Period of chief's Orbit in Earth's day: 177.5833 days	**Period of deputy_1 Orbit in Earth's day:** 177.5833 days	**Period of deputy_2 Orbit in Earth's day:** 177.5833 days	**Period of deputy_3 Orbit in Earth's day:** 177.5833 days	**Period of deputy_4 Orbit in Earth's day:** 177.5833 days
Chief's Jacobi Constant: 3.0008006353	**deputy_1's Jacobi Constant:** 3.0008006353603	**deputy_2's Jacobi Constant:** 3.0008006351431	**deputy_3's Jacobi Constant:** 3.0008006353614	**deputy_4's Jacobi Constant:** 3.00080063557869
Periodicity Check of chief: 0.2126 meter	**Periodicity Check of deputy_1:** 0.1965 meter	**Periodicity Check of deputy_2:** 0.53326 meter	**Periodicity Check of deputy_3:** 0.025213 meter	**Periodicity Check of deputy_4:** 0.31738 meter
Test: Determinant of chief's Φ: 1.000000000755	**Test: Determinant of deputy_1's Φ:** 0.99999999949297	**Test: Determinant of deputy_2's Φ:** 1.00000000055529	**Test: Determinant of deputy_3's Φ:** 1.00000000000331	**Test: Determinant of deputy_4's Φ:** 1.00000000044442
EigenValues of chief's Φ:	**EigenValues of deputy_1's Φ:**	**EigenValues of deputy_2's Φ:**	**EigenValues of deputy_3's Φ:**	**EigenValues of deputy_4's Φ:**
1529.42309 1.01405 0.96931-0.24587i 0.96931+0.24587i 0.986173 0.006538	1529.4231 1.0140542 0.96931-0.245868i 0.96931+0.245868i 0.9861732 0.0006538	1529.4216852 1.014054268 0.96931-0.245869i 0.96931+0.2458i 0.9861732 0.0006538	1529.423093 1.0140542 0.96931-0.245868i 0.96931+0.24586i 0.9861732 0.0006538	1529.424505 1.0140541 0.96931-0.245867i 0.96931+0.2458i 0.9861732 0.0006538

The trajectory of each deputy satellite with respect to chief is given in the figures below. Figure 4-18 to Figure 4-21, they are composed of multiple sub-figures. The left part has three sub-figures showing the projection of the trajectory. The right part has four figures; the first three of them present the components of relative distance change with time, the fourth one gives the resultant relative distance.
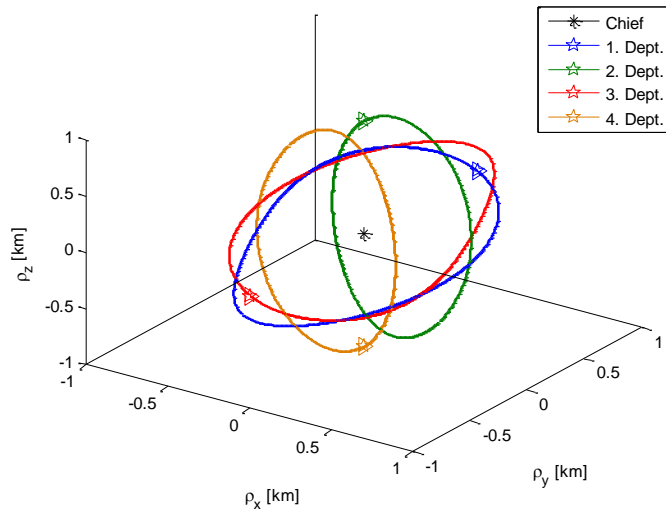
Figure 4-17. SF-L1, The trajectory of the deputy satellites with respect to chief
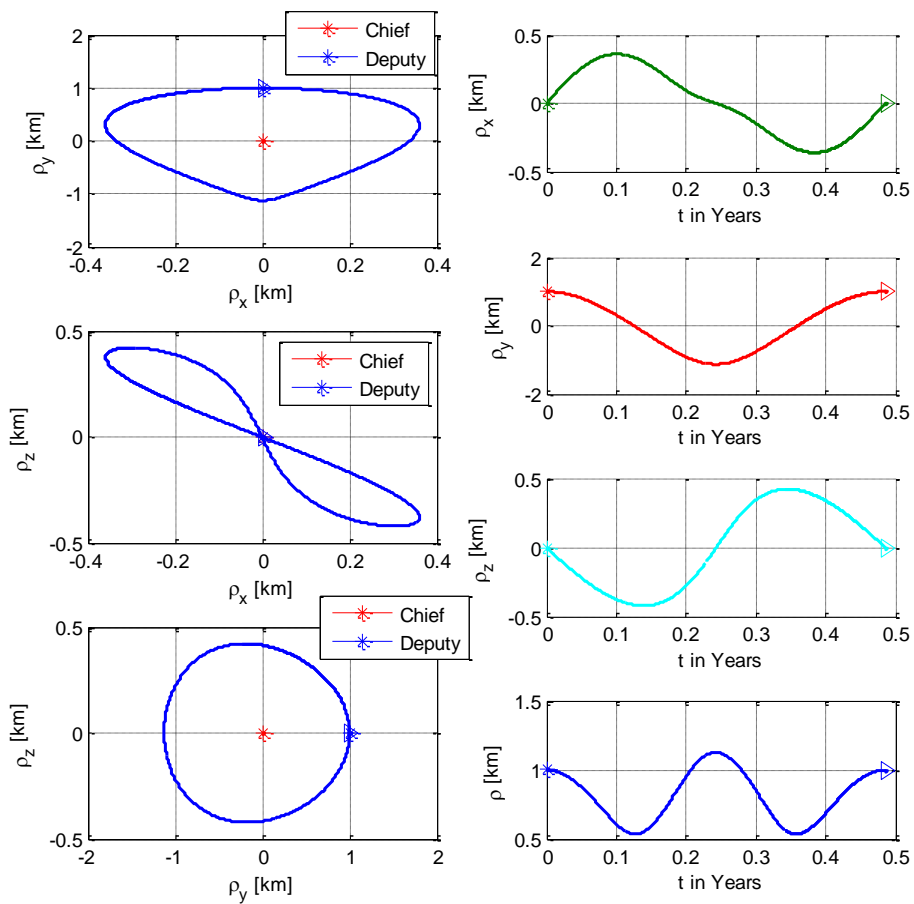
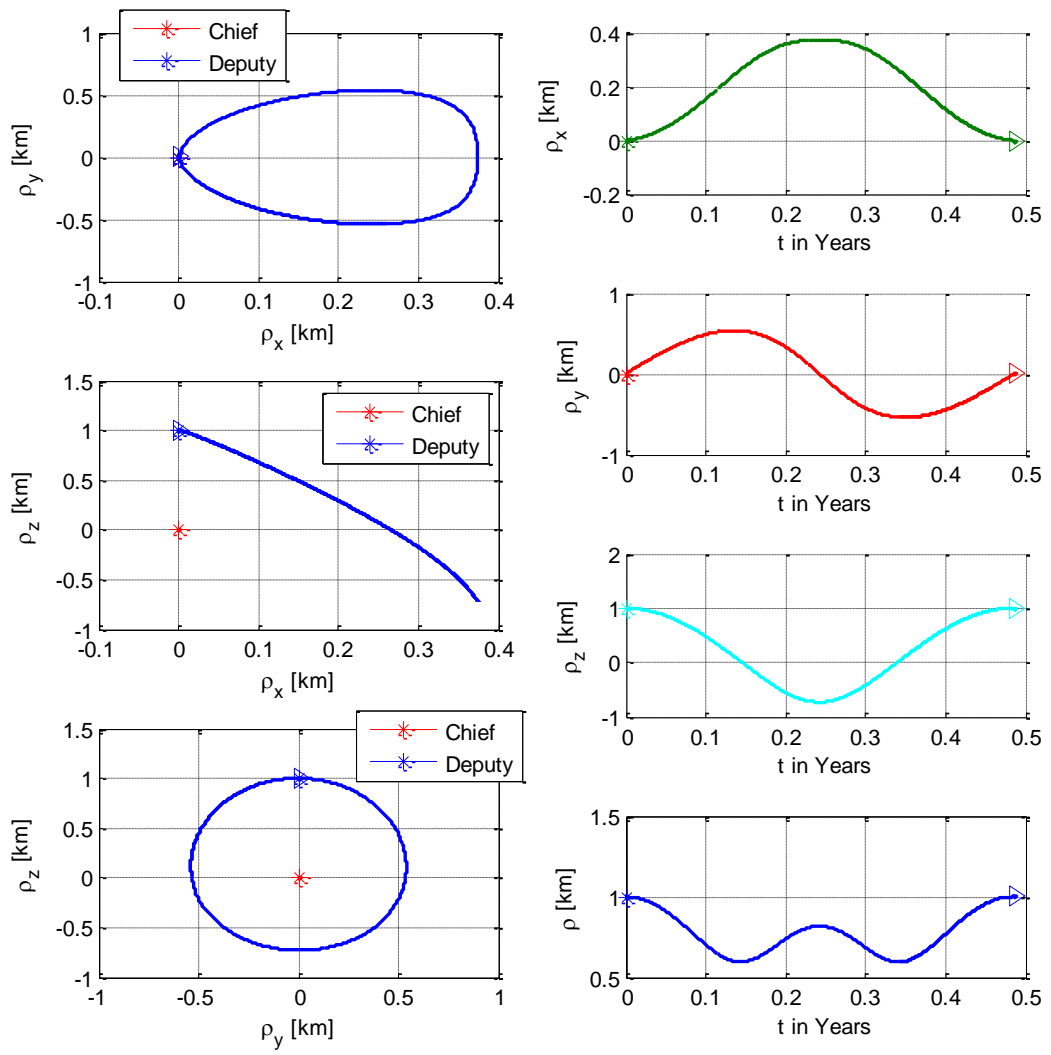Figure 4-18. SF-L1, Deputy #1: Projected and time dependent views

166
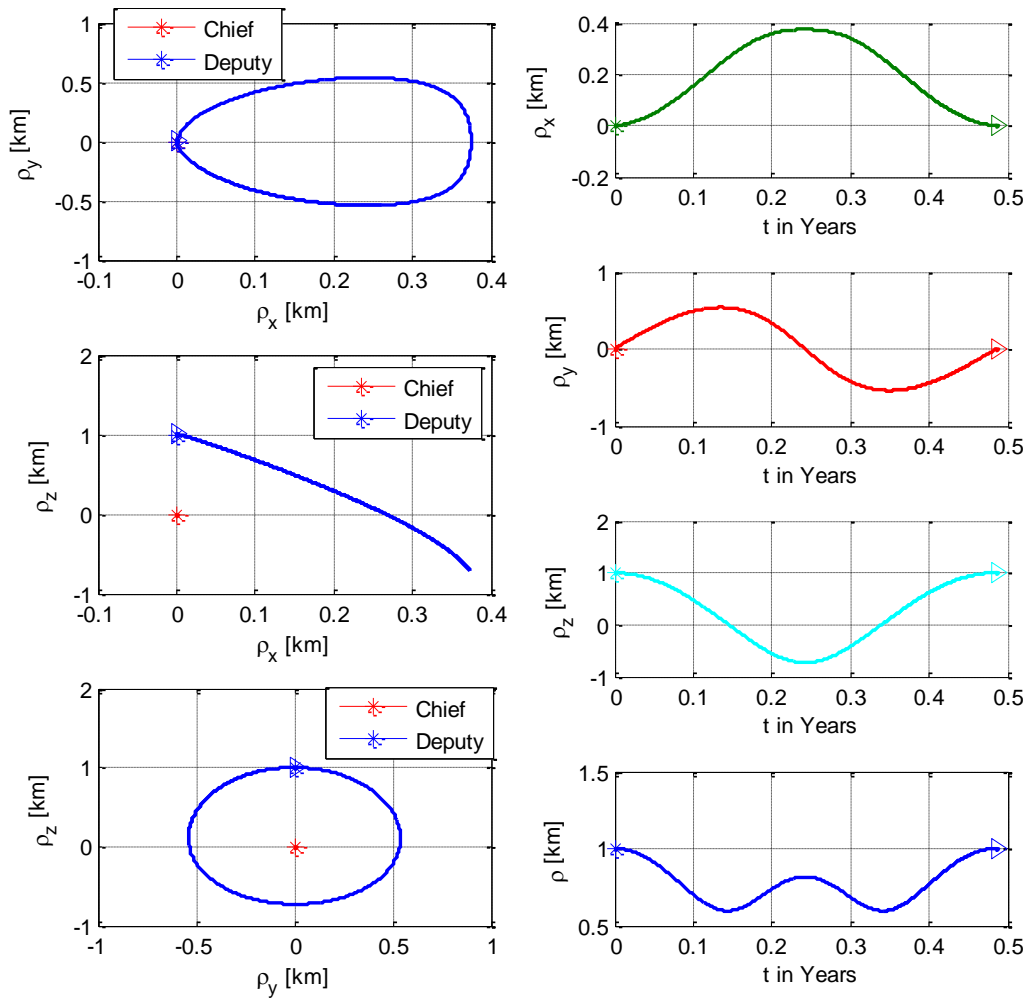
Figure 4-19. SF-L1, Deputy #2: Projected and time dependent views

167
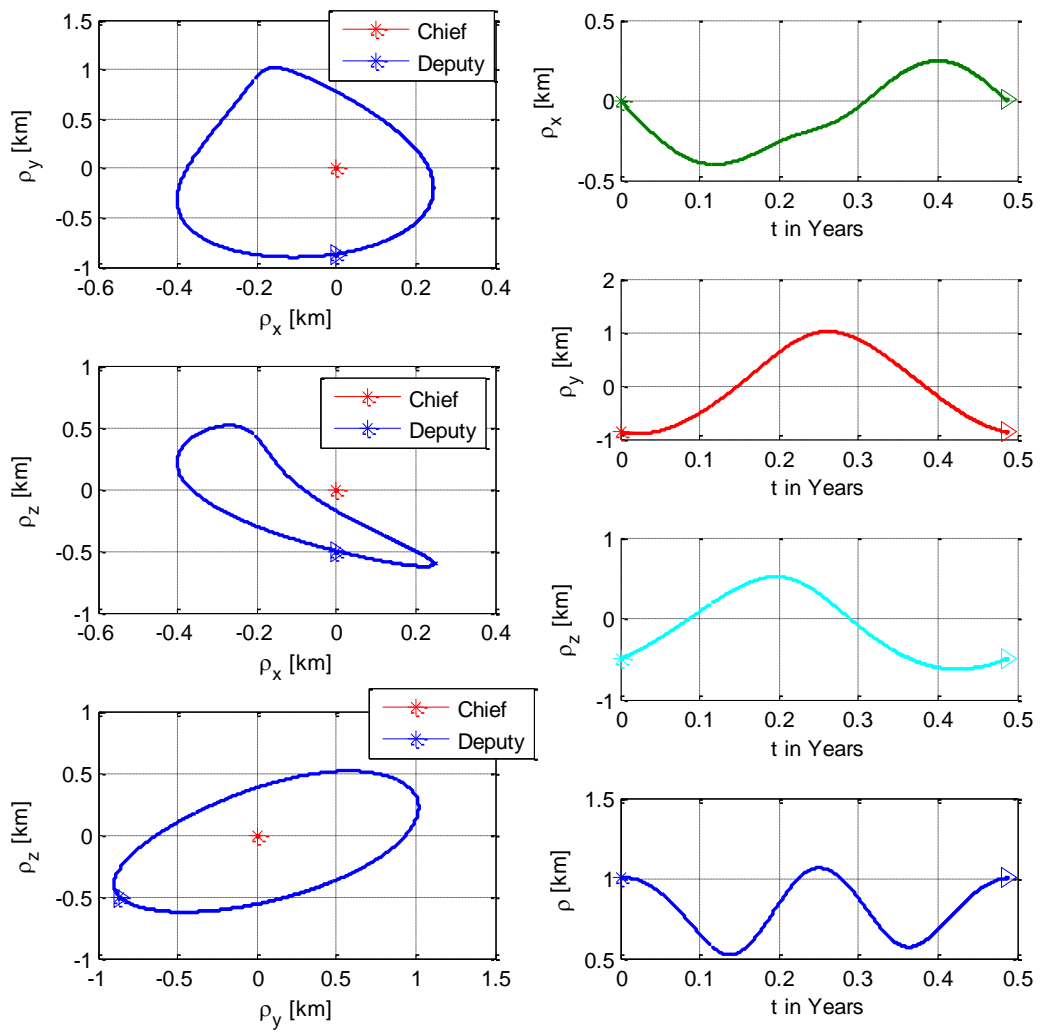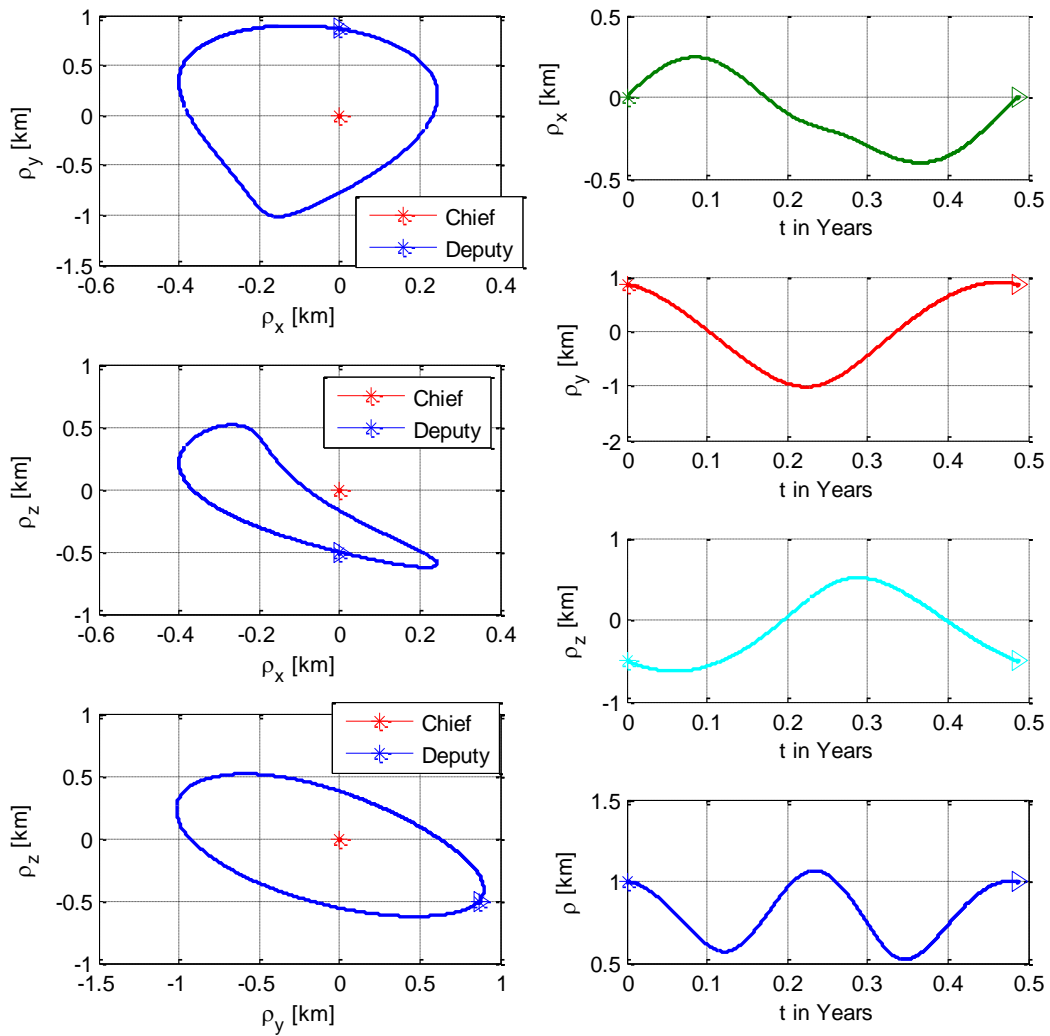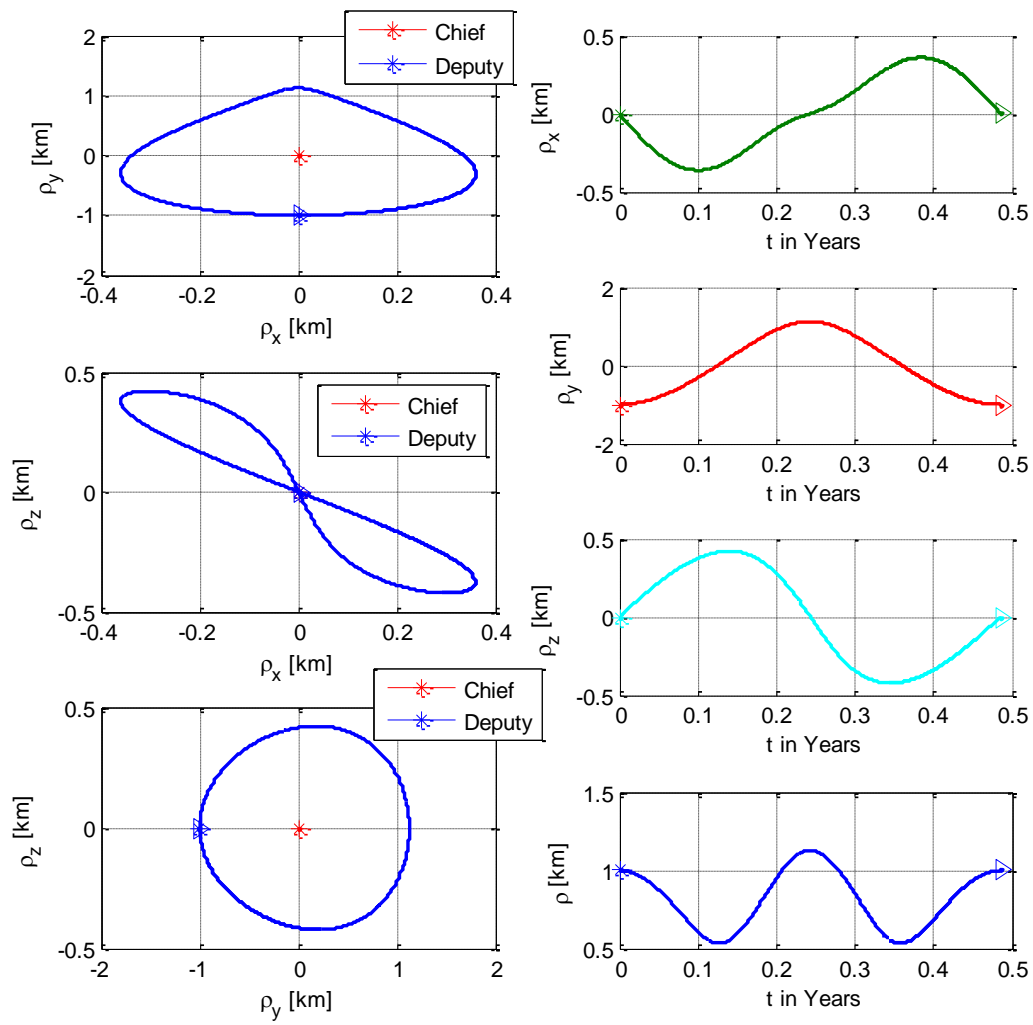
Figure 4-20. SF-L1, Deputy #3: Projected and time dependent views
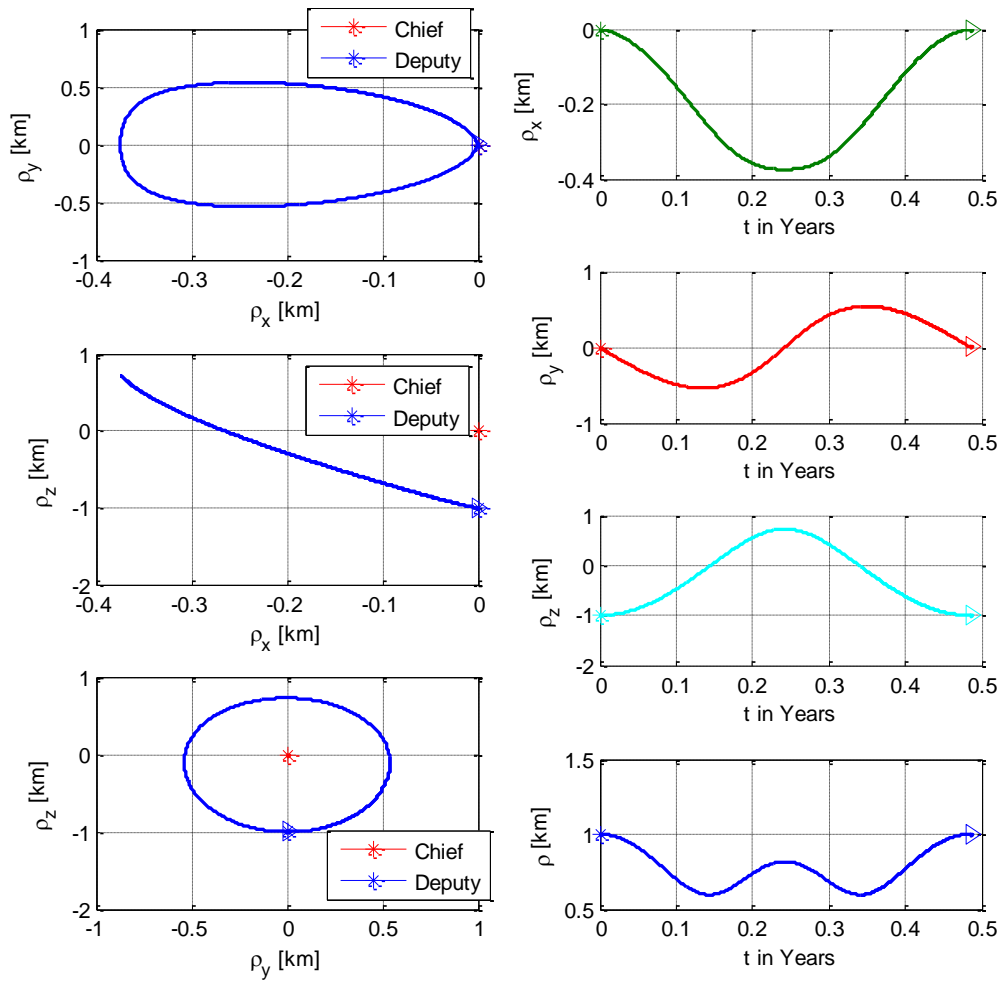
Figure 4-21. SF-L1, Deputy #4: Projected and time dependent views

Regarding to the results, it can be stated that the deputies initially located at y axis ($+y$ and $-y$ with equally distancing), the 1st and 3rd satellites, has a symmetrical trajectory with respect to the xz plane located at Chief position, it can be called skew-symmetric or diagonal symmetric. The 2nd and 4th satellites, initially located at z axis ($+z$ and $-z$ with equally distancing) also form different types of symmetry with respect to the xz plane fixed on Chief position. In xz plane they have quasi one-dimensional motion, and it has a quasi-elliptical motion in yz plane.

For all of them, the relative distances between deputies are not constant; they are given in Figure 4-22. The objective distance from 1st to 2nd, 2nd to 3rd, 3rd to 4th and 4th to 1st

deputy is $\sqrt{2}\rho = 1.414\ km$. The objective relative distance between 1st and 3rd deputies is $2\rho = 2\ km$, same for 2nd and 4th ones. The acquired formation shape narrows and expands between this distance which is roughly 1.414 km and 0.75 km. this numbers are between 2 km to 1 km for the relative distance between 1st and 3rd (2nd and 4th). The constant relative motion is not obtained; however, a harmony is acquired between the deputies and Chief; a stable formation flight is made for one orbital period, which is approximately 0.5 Earth's Year for L1 point.
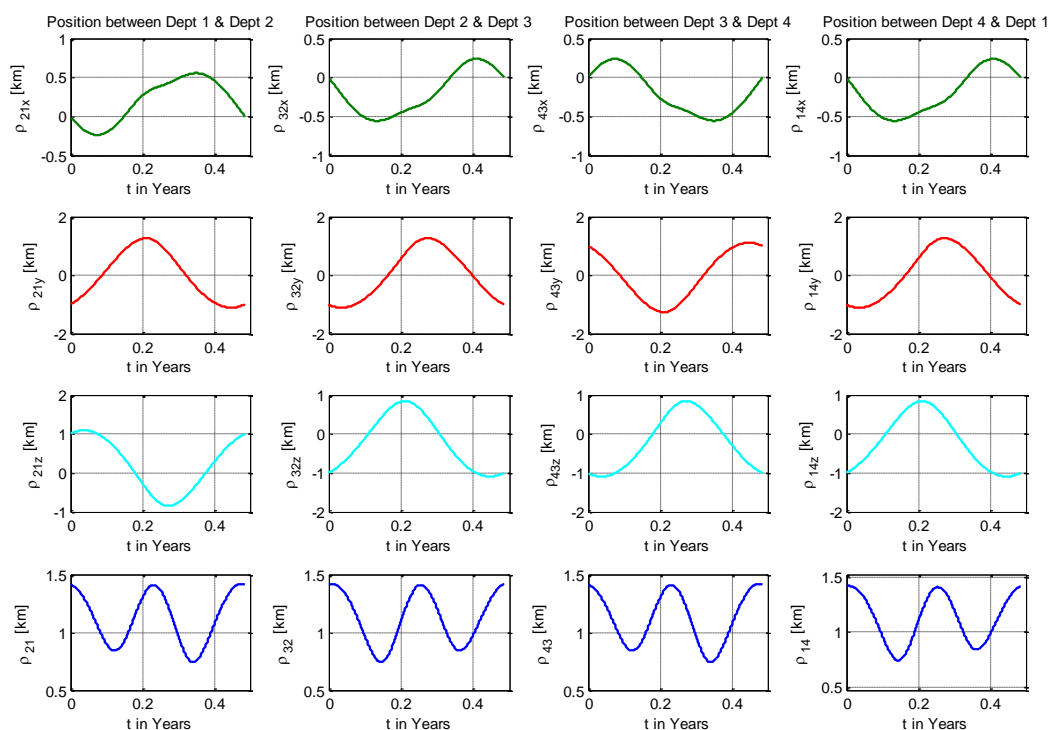
Figure 4-22. SF-L1: The relative distances between deputies
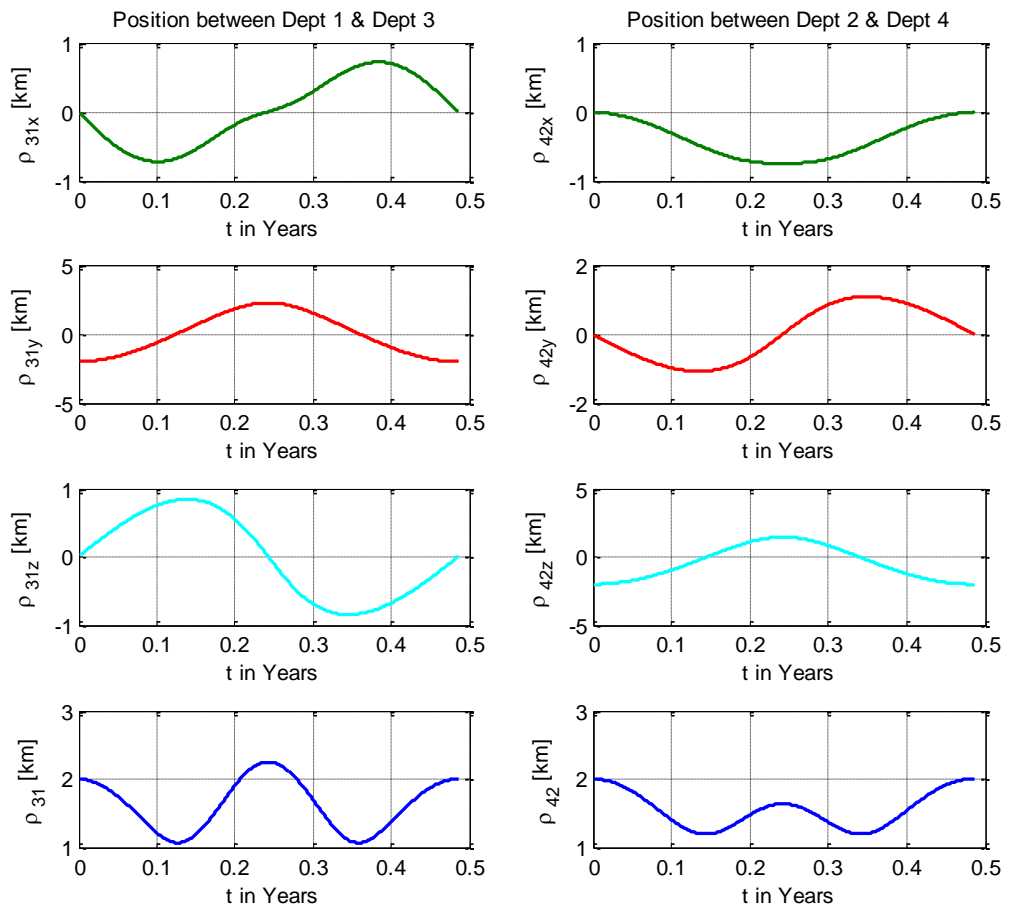
Figure 4-23. SF-L1: The relative distances between deputies-2
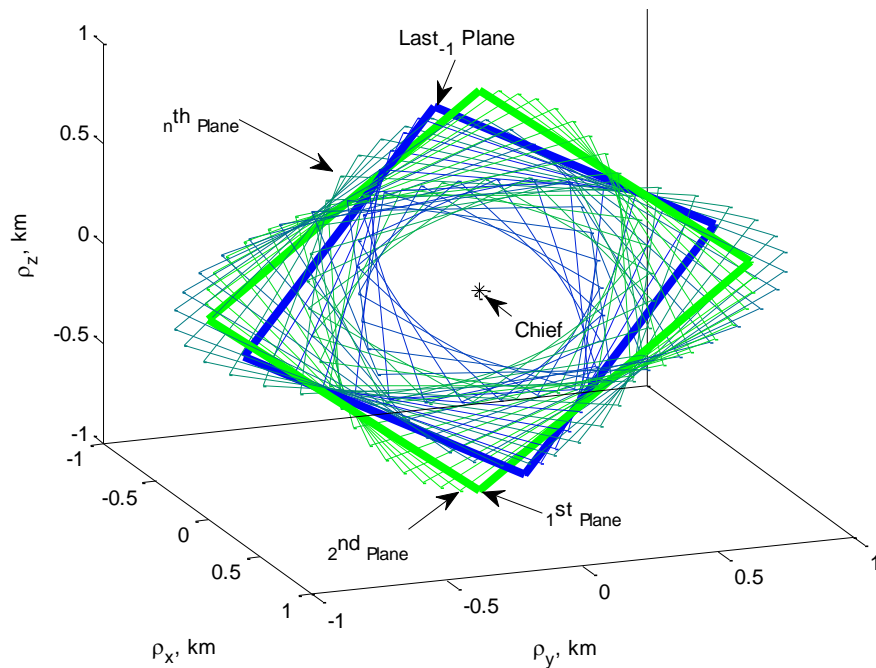
Figure 4-24. SF-L1: The plane formed by deputies

The shape change of this square formation schema is illustrated in Figure 4-24. The bold green colored square is the starting configuration, the bold blue one is the near last positions. The plane is colored from green to blues according to the time changes. The inclination angle and the size of the plane formed by deputy satellites varies; it is narrowing until first and third quarter period, then it expands at the half and full period; last plane and first plane coincide since motion is periodic. The results for this kind of square shape configuration shows that the deputy initially located at y axis and at z axis form different type of formation trajectory. If it is required not to transverse the xz plane located at Chief position; on the other words, when it is not required to pass from the left side of the Chief to its right side, the deputies must be initially located on z axis. If it is required to transverse xz Chief's plane, according to the mission, it is necessary to initially locate the deputies on y axis. According to the mission requirements and needs, a formation cluster can be formed by initially locating the deputies only on y axis or on z axis. Finally, a question about the possibility to have constant relative distance by natural way (without performing any control maneuver)

172

for a special initial relative position is occurred. Next formation configuration focuses on this kind of formation cluster.

4.3.1.3. Inclined square formation (ISF)

The formation cluster presented in this section has also four deputy satellites with on Chiefs on its center. However, in this case, unlike from the previous cluster, the deputies on z axis are initially located with an inclination angle: The 2nd and 4th satellites are placed on a plane defined with an inclination angle (Figure 4-25). Here this inclination angle is computed regarding to the quasi-plane formed by Chief's orbit. It is called quasi-plane because the shape occurred in not perfectly planar. The inclination angle of this quasi-plane with respect o the xy plane is computed by the initial and half orbital position values, indicated in Figure 4-26, as 1st and 2nd points. This inclination angle is $\alpha_2 = 126.7775^0$ regarding to the xy plane, and this number will be taken as the elevation angle of the 2nd deputy. The complement of this angle to 180^0 is $\alpha_4 = 53.2225^0$ is the elevation angle for 4th deputy.
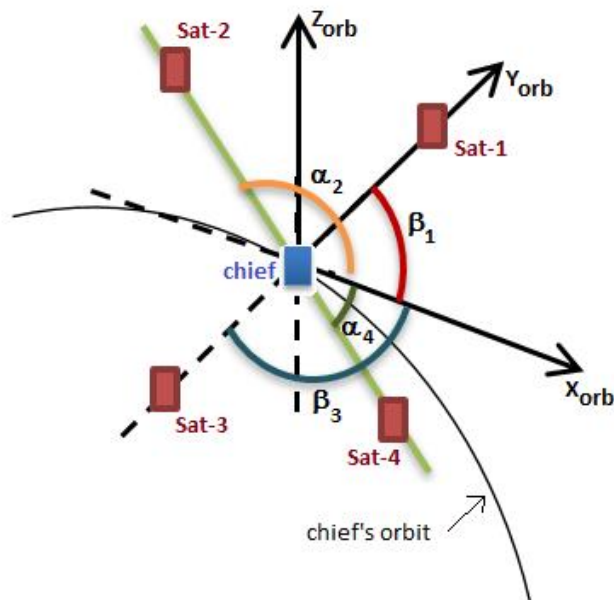
Figure 4-25. Inclined shape formation

173
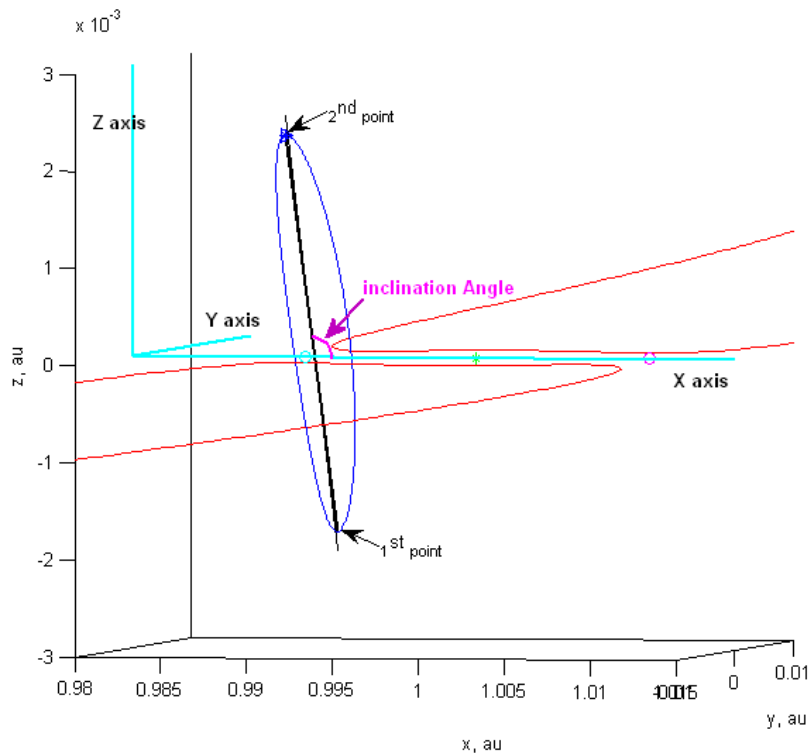
Figure 4-26. Orbital plane inclination angle representation

The desired relative distance ρ between deputy satellites and chief is taken $\rho = 1\ km$, and the relative initial azimuth and elevation angles with respect to the chief are listed in the following Table 4.6.

Table 4.6. Relative positions of the four deputies, ISF at L1

Deputy Satellite 1	Deputy Satellite 2	Deputy Satellite 3	Deputy Satellite 4
$\rho = 1\ km$	$\rho = 1\ km$	$\rho = 1\ km$	$\rho = 1\ km$
$\beta = 90^0$	$\beta = 0^0$	$\beta = -90^0$	$\beta = 0^0$
$\alpha = 0^0$	$\alpha = 126.7775^0$	$\alpha = 0^0$	$\alpha = -53.2225^0$

The chief's orbit is the same as used in the precedent section. The initial velocities and trajectory for the deputies are computed and given in the following table and figures. Notice that the values for the chief, 1st and 3rd deputies are the values computed on the

174

previous formation cluster, they are taken exactly same. The trajectory of the 2nd and 4th deputy satellites with respect to chief, the projection views of the trajectories, the components of relative distance change with time, and the resultant relative distances are presented respectively in the following figures, Figure 4-27, Figure 4-28 and Figure 4-29.

Table 4.7. ICs and periodicity checks, ISF at L1

Initial conditions of chief	Initial conditions of deputy_1	Initial conditions of deputy_2	Initial conditions of deputy_3	Initial conditions of deputy_4
0.988863916 0.000000190 0.002283164 0.000079282 0.009561451 -0.000003813	0.988863916985 0.000000197038 0.002283164826 0.000079288196 0.009561450568 -0.000003818581	0.988863912983 0.000000190354 0.002283170180 0.000079289072 0.009561470652 -0.000003813831	0.988863916985 0.000000183669 0.002283164826 0.000079276164 0.009561450612 -0.000003808921	0.988863920987 0.000000190354 0.002283159471 0.000079275289 0.009561430528 -0.000003813670
Period of chief's Orbit: 177.5833 days	**Period of deputy_1's Orbit:** 177.5833 days	**Period of deputy_2's Orbit:** 177.5833 days	**Period of deputy_3's Orbit:** 177.5833 days	**Period of deputy_4's Orbit:** 177.5833 days
Chief's Jacobi Constant: 3.0008006353	**deputy_1's Jacobi Constant:** 3.0008006353603	**deputy_2's Jacobi Constant:** 3.0008006349859	**deputy_3's Jacobi Constant:** 3.0008006353614	**deputy_4's Jacobi Constant:** 3.0008006357358
Periodicity Check of chief: 0.2126 meter	**Periodicity Check of deputy_1:** 0.1965 meter	**Periodicity Check of deputy_2:** 0.3724 meter	**Periodicity Check of deputy_3:** 0.025213 meter	**Periodicity Check of deputy_4:** 0.4302 meter
Test: Determinant of chief's Φ: 1.000000000755	**Test: Determinant of deputy_1's Φ:** 0.99999999949297	**Test: Determinant of deputy_2's Φ:** 0.99999999988630	**Test: Determinant of deputy_3's Φ:** 1.00000000000331	**Test: Determinant of deputy_4's Φ:** 1.00000000100169
EigenValues of chief's Φ:	**EigenValues of deputy_1's Φ:**	**EigenValues of deputy_2's Φ:**	**EigenValues of deputy_3's Φ:**	**EigenValues of deputy_4's Φ:**
1529.42309 1.01405 0.96931-0.245868i 0.96931+0.245868i 0.986173 0.006538	1529.4231 1.0140542 0.969308-0.2458682i 0.969308+0.2458682i 0.9861732 0.0006538	1529.42001 1.01405486 0.969307-0.245869i 0.969307+0.245869i 0.98617259 0.00065381	1529.423093 1.0140542 0.969308-0.2458682i 0.969308+0.2458682i 0.9861732 0.0006538	1529.426181 1.014053506 0.969308-0.24586i 0.969308+0.24586i 0.9861744 0.0006538
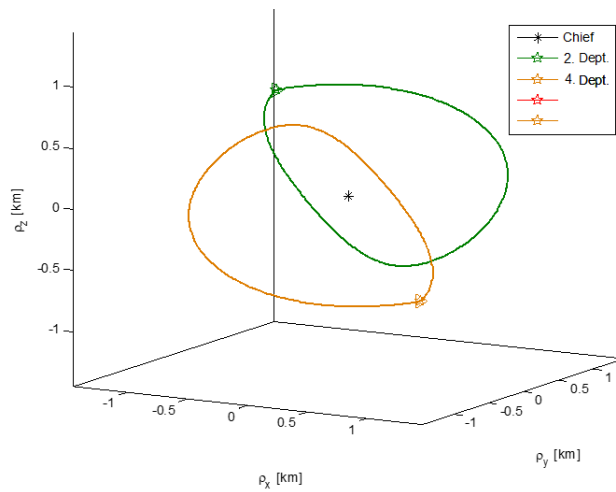
Figure 4-27. ISF-L1, Trajectory of 2nd and 4th deputies with respect to chief
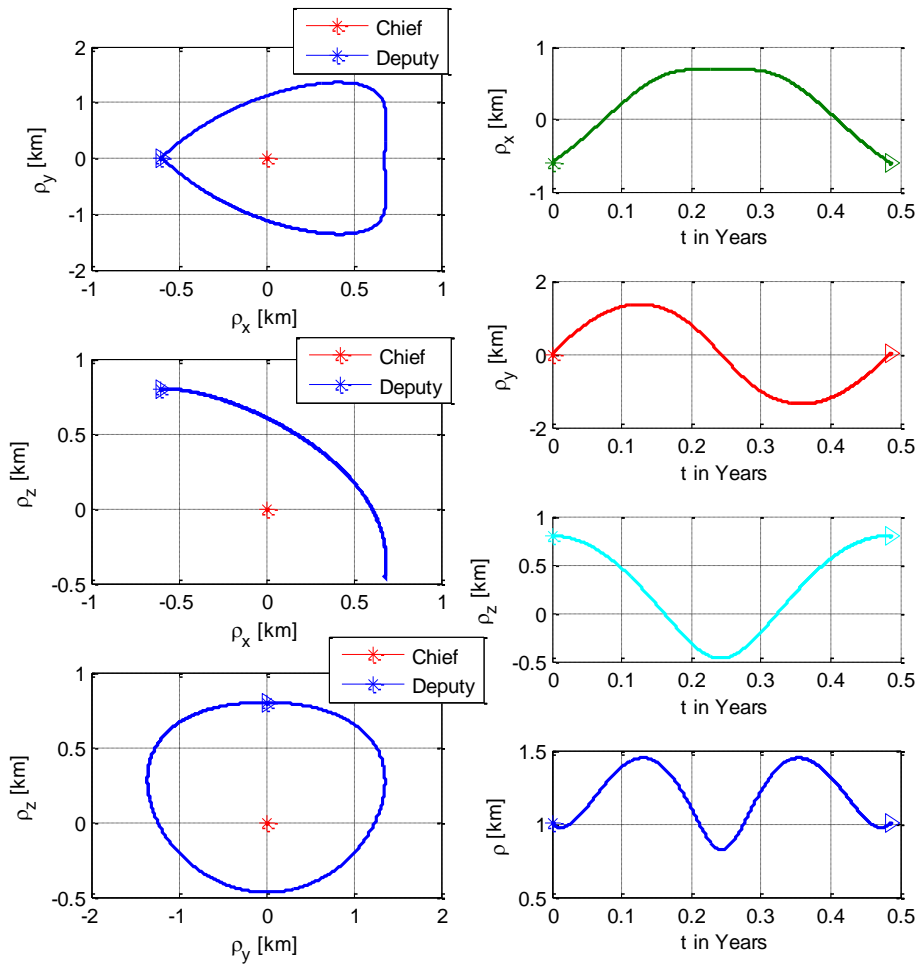
Figure 4-28. ISF-L1, Deputy #2: Projected and time dependent views

176
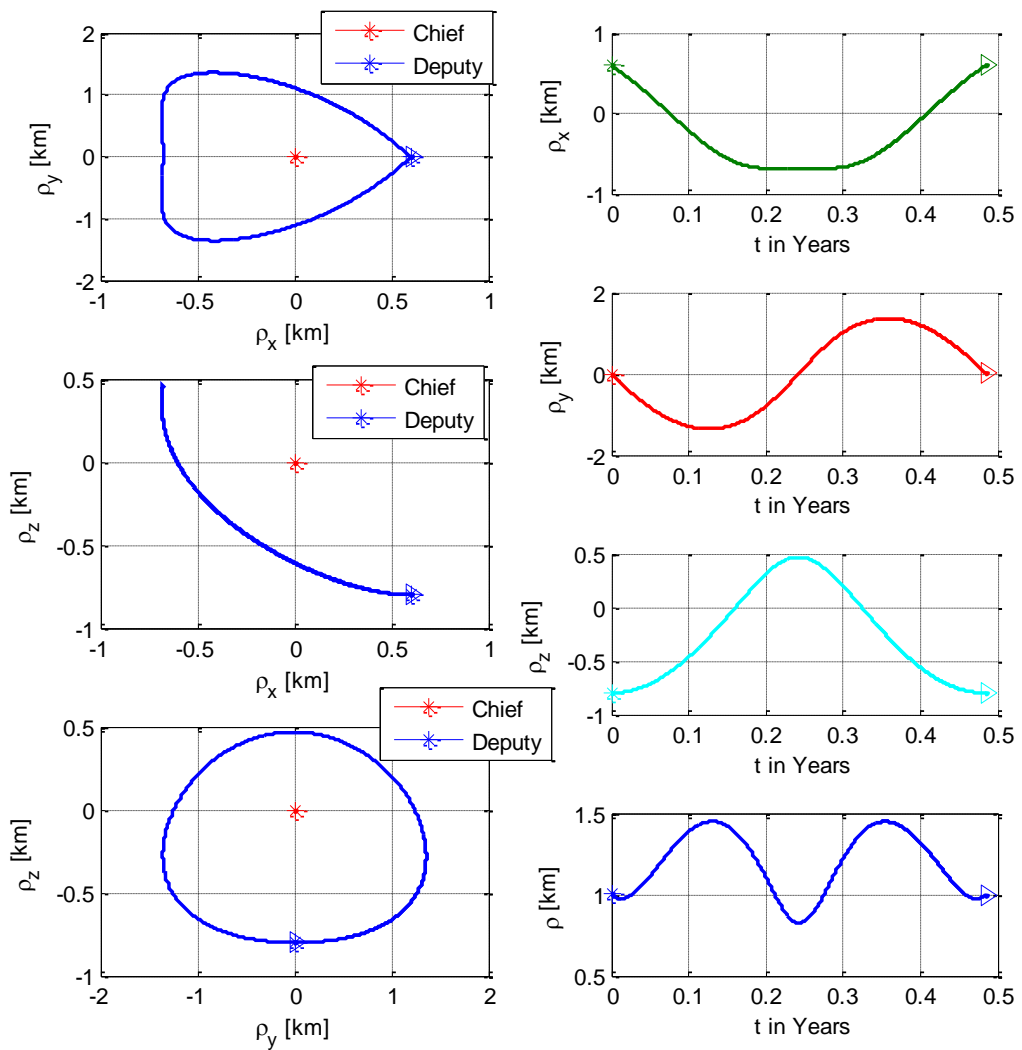
Figure 4-29. ISF-L1, Deputy #4: Projected and time dependent views

The symmetric relative trajectories are obtained for 2nd and 4th deputies. However, in that case the relative distance obtained enlarges compared to the results obtained in the precious section. Here, the relative distance varies between 1 km to 1.45 km with a sinusoidal form. The relative distance behaviors, and the planed behaviors formed by those 4 deputies are given in Figure 4-30. It is seen that, the spaced area between satellites are wider regarding to previous case. Two cases are shared in order to notice the difference, as follows:
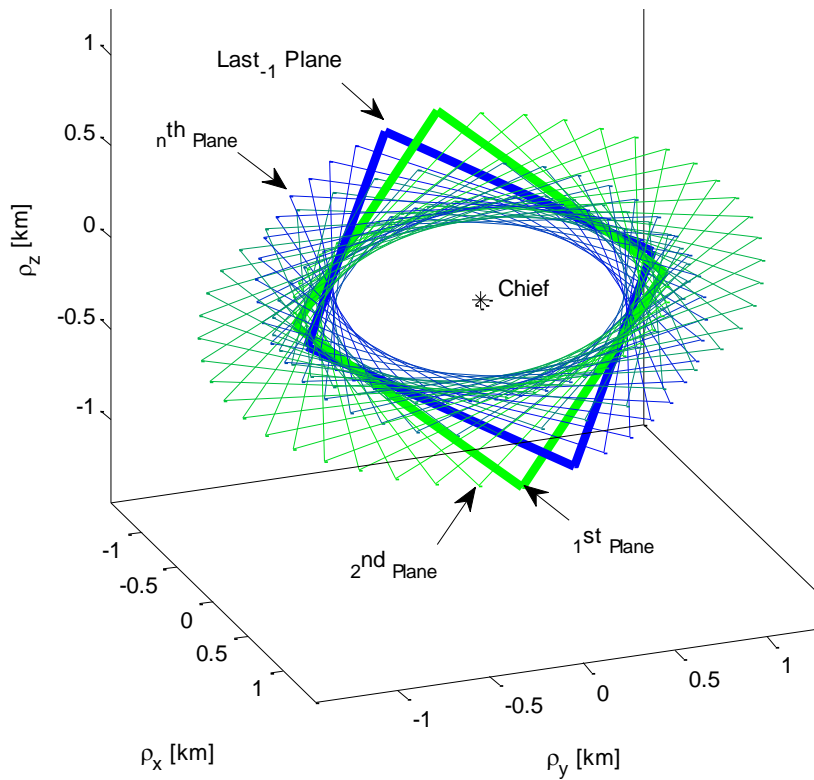
Figure 4-30. ISF-L1: The plane formed by deputies

The acquired formation shape expands and narrows within those numbers, $1\ km$ to $1.45\ km$. Still, the constant relative motion is not obtained, but it is seen that for a given inclination value to the initial plane, the relative distance increases compared to the decreasing results obtained in the previous sections. In that case next question occurred is: how the relative distance change according to the initial inclination given to the plane? Is there any fixed inclination value that provides nearly constant relative distance? Here, the plane inclination is given by the initial elevation angle of the deputy. So, the next subsection presents the relation between initial elevation angle and relative distance.

4.3.2. Optimum formation clusters and simulation results

This section contains the results of the analyses performed to find optimum relative initial position of the deputy that provide the minimum deviation on relative distance ρ defined with respect to the chief satellite. As a first step, both elevation angle α and azimuth angle β are scanned from 0^0 to 180^0 with 10^0 increments, and the relative distance plots are given in the following figures for each of β with changes of α ($\alpha = [0^0 : 10^0 : 180^0]$, and $\beta = [0^0 : 10^0 : 180^0]$).
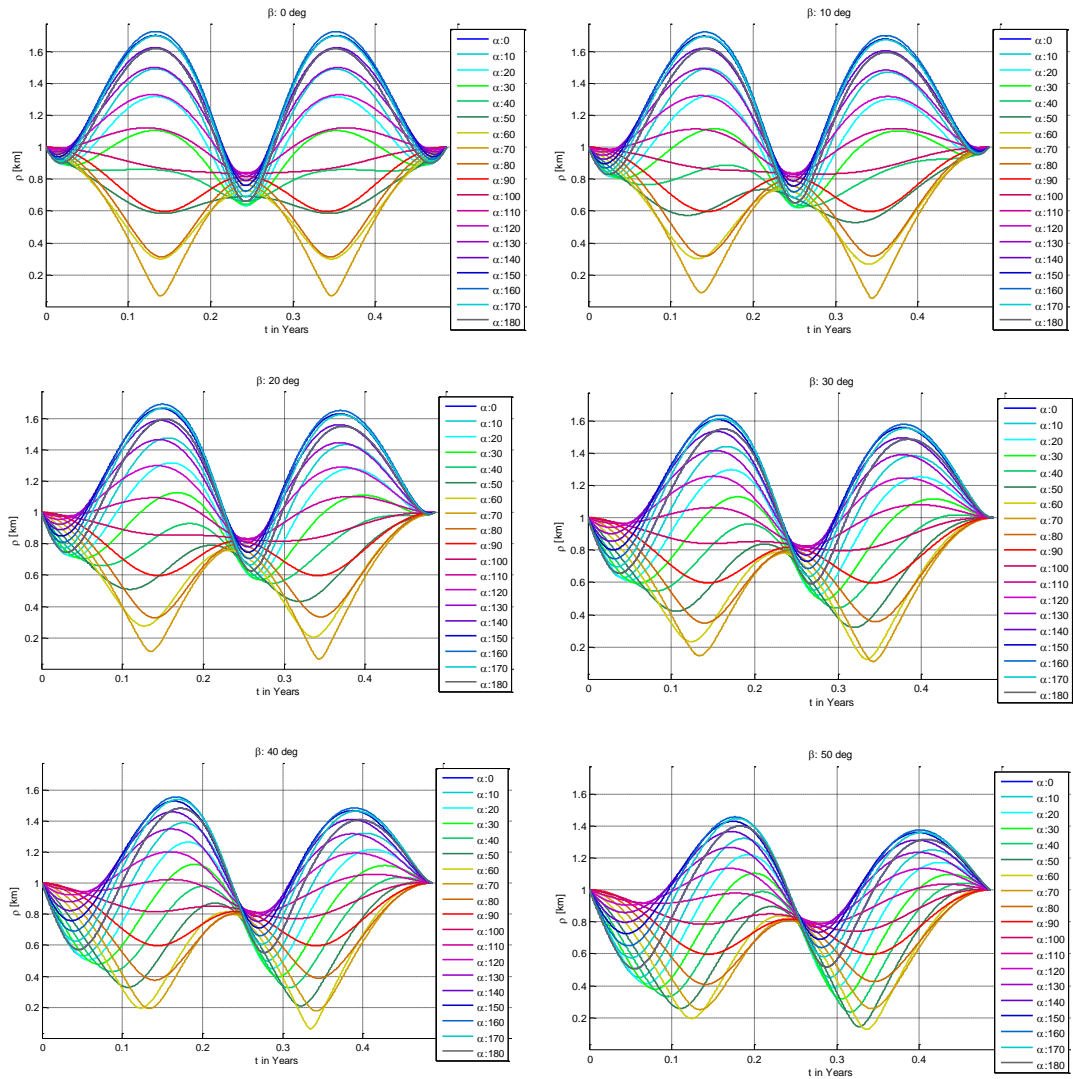
Figure 4-31. Relative positions depending on ICs, α and β angles for L1
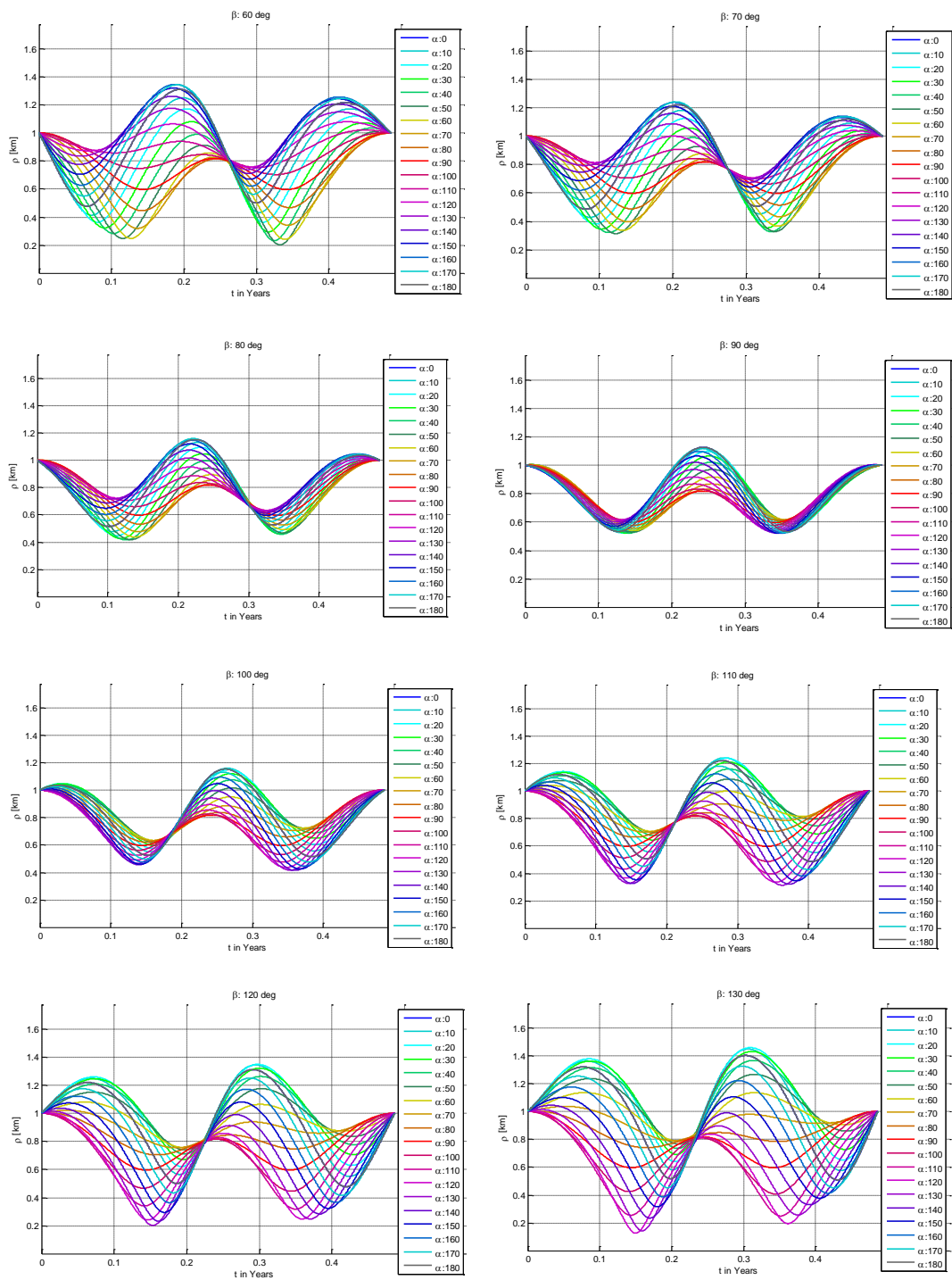
Figure 4.31. Relative positions depending on ICs, α and β angles for L1 (cont'd)
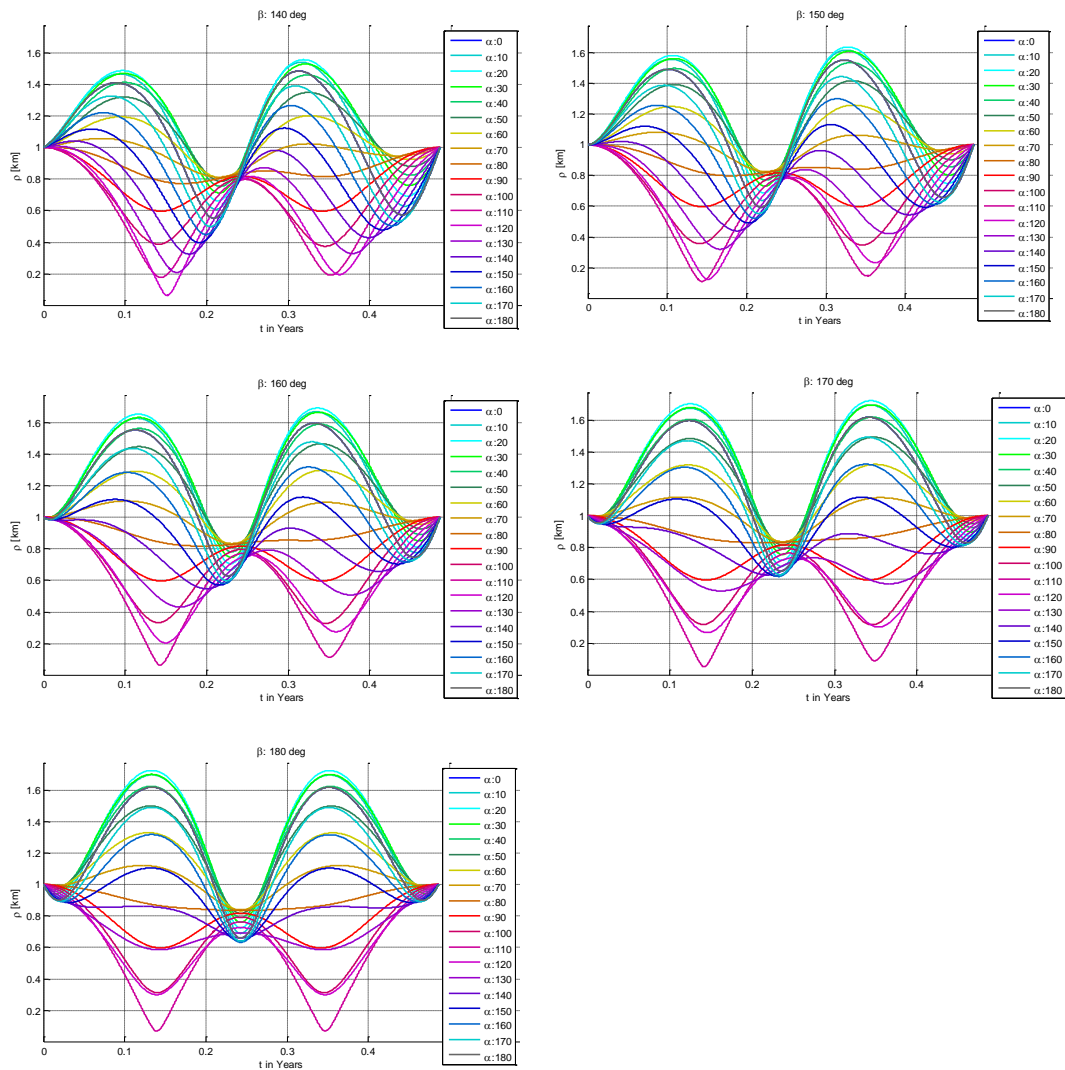
Figure 4.31. Relative positions depending on ICs, α and β angles for L1 (cont'd)

Regarding to the results, as first impression, an α between 100^0 and 110^0 gives minimum deviation in ρ for a β between 0^0 to 90^0. And for β less than 40^0 , α = $100^0 - 110^0$ gives a one minimum point is seen at half period. But when β greater than 40^0 and less than 160^0, two minimum points are seen in first and third quarter orbital period as minimum ρ , and one maximum point at half period.

These results are re-evaluated statistically. So, in that case, it is needed to obtain a statistical parameter to choose suitable β and α. One method to qualify the orbit is to compute standard deviation σ of the relative distance ρ for all of the α, β set. This σ gives an idea about how the ρ oscillates around its mean value. The second computation is to calculate the standard deviation from required relative distance, which is 1 km for the cases considered here; It is denoted as $\sigma_{\rho Req}$. As a third orbit qualification parameter, the maximum value of ρ during one orbit may be used (A_{Max}). Figure 4-32 presents the three deviation qualification parameters defined above. It shows that minimum deviation is obtained for $\beta = 0^0$ (with $\alpha = 100^0 - 110^0$), and for $\beta = 180^0$ (with $\alpha = 70^0 - 80^0$). This result is also valid for σ computation. But, $\sigma_{\rho Req}$ statistic gives different results for some cases: $\beta = 30^0$ (with $\alpha = 100^0 - 110^0$) and $\beta = 150^0$ (with $\alpha = 70^0 - 80^0$). The summary of the results is given in Figure 4-32 and Table 4.8. Figure 4-32 gives minimum deviation obtained in ρ for a given β value, and Table 4.8 indicates the corresponding α value for this minimum deviation. For that reason, it is needed to make more fine analyses between those angle values, they are given as follows.
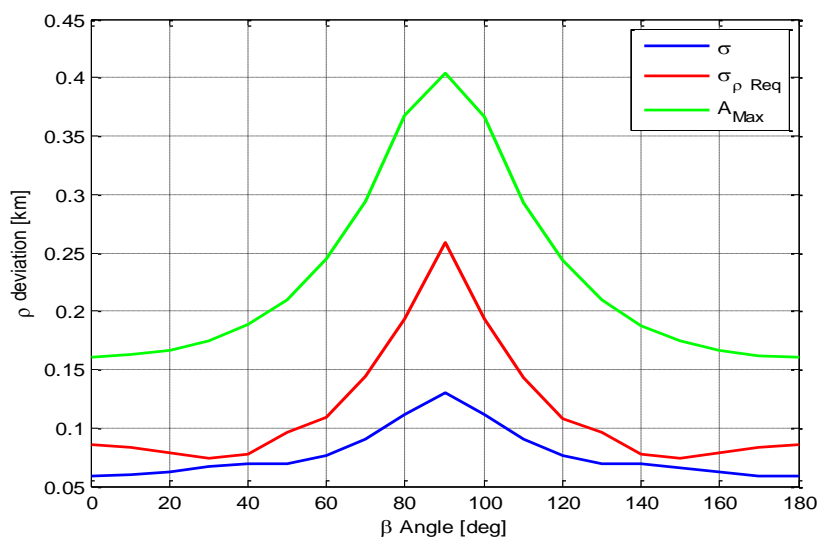
Figure 4-32. Statistical results of the relative position for β values around L1

Table 4.8. α that statistically provide minimum deviation for given β at L1

alpha values\ for beta:	0	10	20	30	40	50	60	70	80	90	100	110	120	130	140	150	160	170	180
sigma results STD:	100	100	100	100	110	110	110	110	110	90	70	70	70	70	70	80	80	80	80
sigma to rhoReq :	110	110	110	110	110	110	120	120	130	50	50	60	60	70	70	70	70	70	70
dA(rho-rhoReq):	110	110	110	110	110	110	120	120	120	90	60	60	60	70	70	70	70	70	70

Table 4.9. Selected cases of β's for fine analyses around L1

Case-1:	$\beta = [0^0 : 1^0 : 10^0]$ $with$ $\alpha = [100^0 : 1^0 : 110^0]$
Case-2:	$\beta = [170^0 : 1^0 : 180^0]$ $with$ $\alpha = [70^0 : 1^0 : 80^0]$

For case-1 the minimum value of ρ is obtained for $\beta = 0^0$, and the α values that gives the minimum deviation is $\alpha = 102^0 - 104^0$, as seen in Figure 4-33 and Figure 4-34:
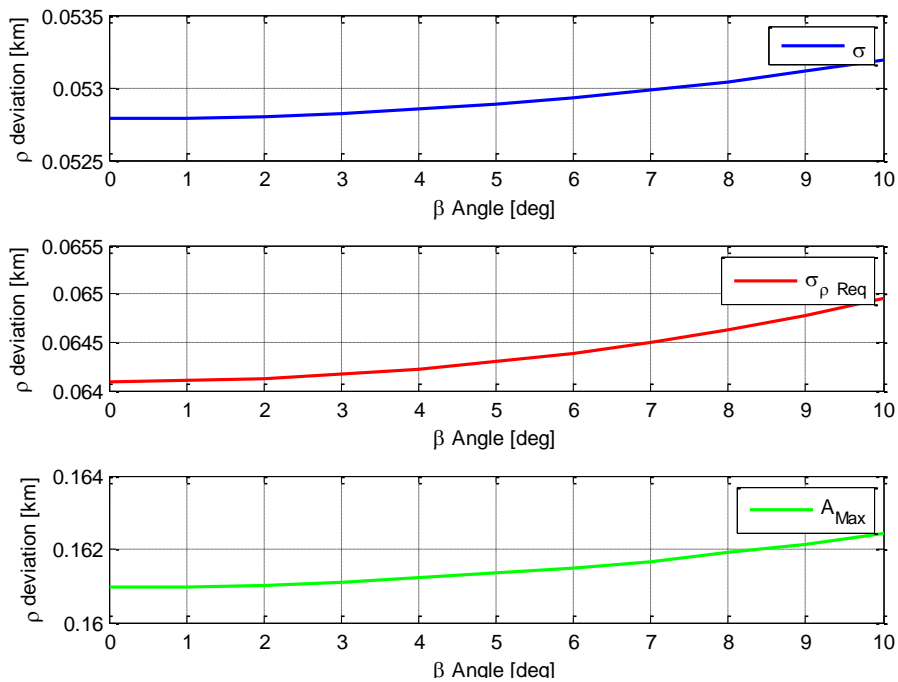
Figure 4-33. Deviation statistics for different β 0 to 10 degree for L1
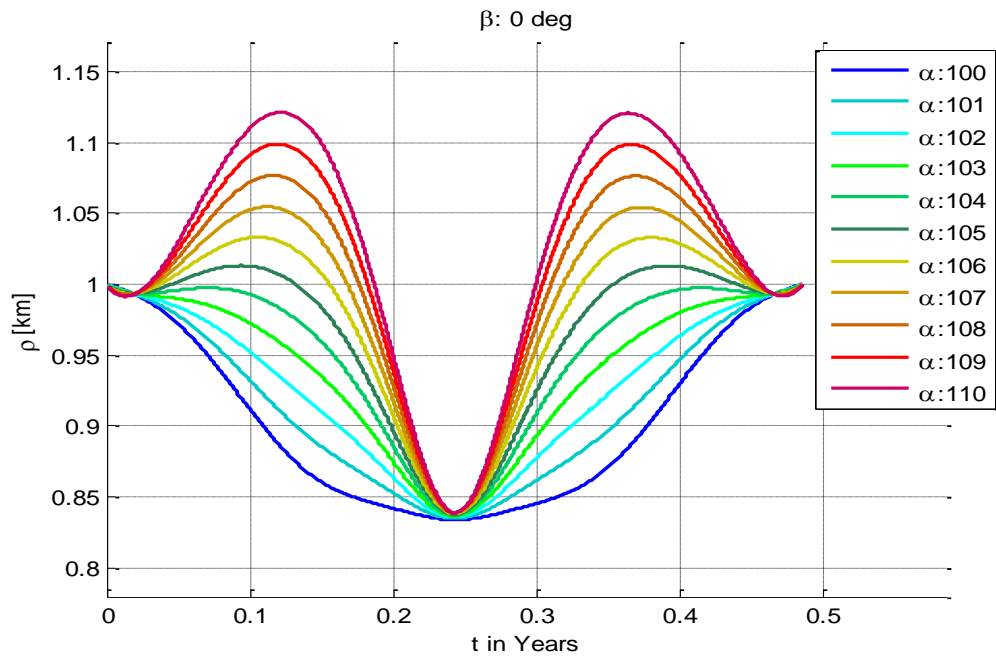
Figure 4-34. Deviation for zero β and α 100 to 110 degree for L1

For case-2 the minimum value of ρ is obtained for $\beta = 180^0$, and the α values that gives the minimum deviation is $\alpha = 76^0 - 78^0$, as seen in the following figures, Figure 4-35 and Figure 4-36:
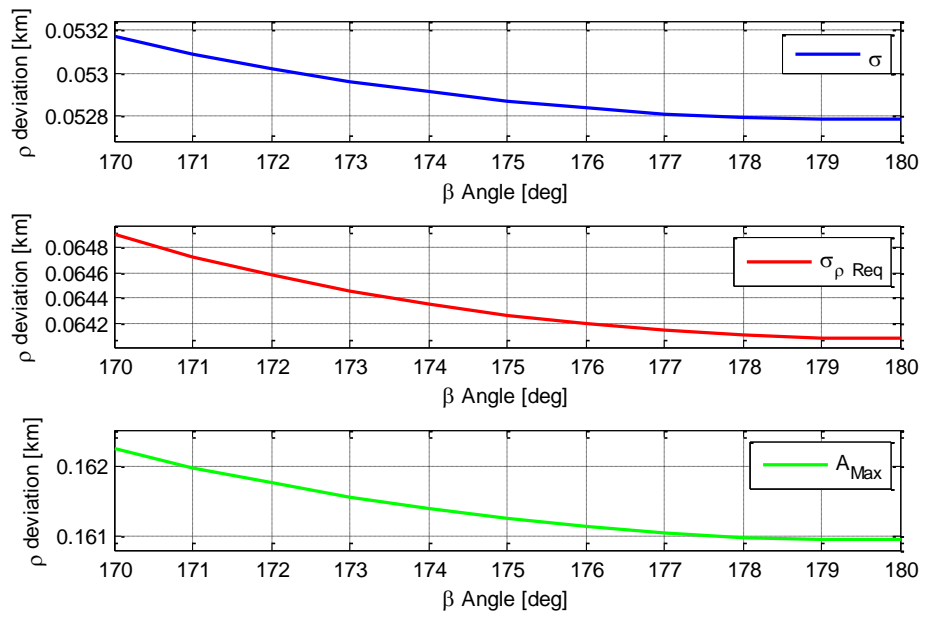
Figure 4-35. Deviation statistics for different β 170 to 180 degree for L1
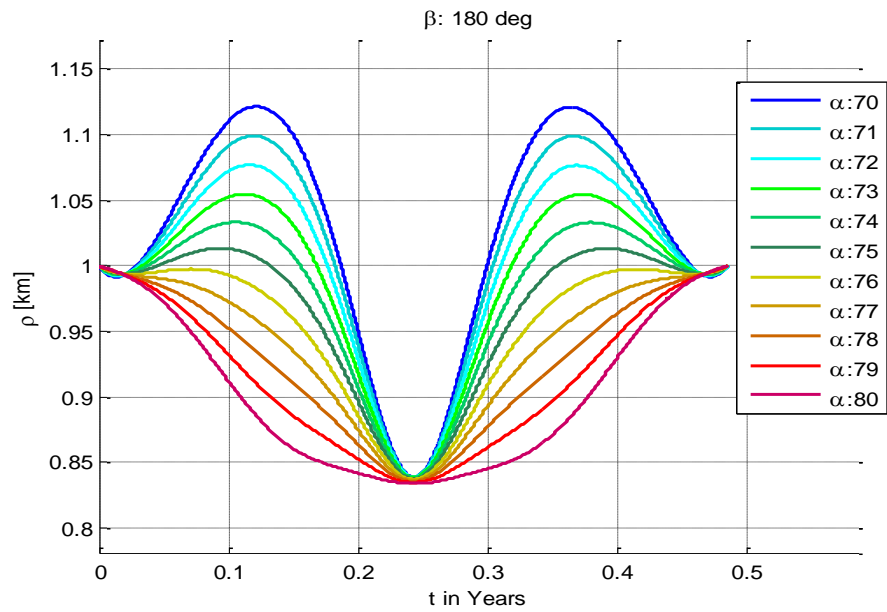
Figure 4-36. Deviation for 180 β and α 70 to 80 degrees for L1

It is obvious that the results obtained for the Case-1 and Case-2 are symmetric, in other words they are geometrically the same positions. For formation clusters having more than two deputies, it is also possible to choose a location near $\beta = 90^0$ and near $\beta = -90^0$ to have quasi constant relative distance between all deputies.

4.3.2.1. Inclined square shape formation with optimum elevation and azimuth

The initially inclined plane formed by deputies can be defined as a plane which is not on yz plane. It means that deputies are initially located at z axis. So, the inclined plane is obtained by giving an elevation angle different from 90^0 degree for the initial position of the deputies. First, an interval from 0^0 to 180^0 with 10^0 increments is given to the simulation to see the trajectories and relative distance obtained with respect to the chief. So, for $\alpha = [0^0 : 10^0 : 180^0]$, we have 19 different cases. The trajectories obtained are shown in the following Figure 4-37, in 3-dimensional view, and the projected views in Figure 4-38, relative distances with its components in Figure 4-39 and Figure 4-40Figure 4-38.
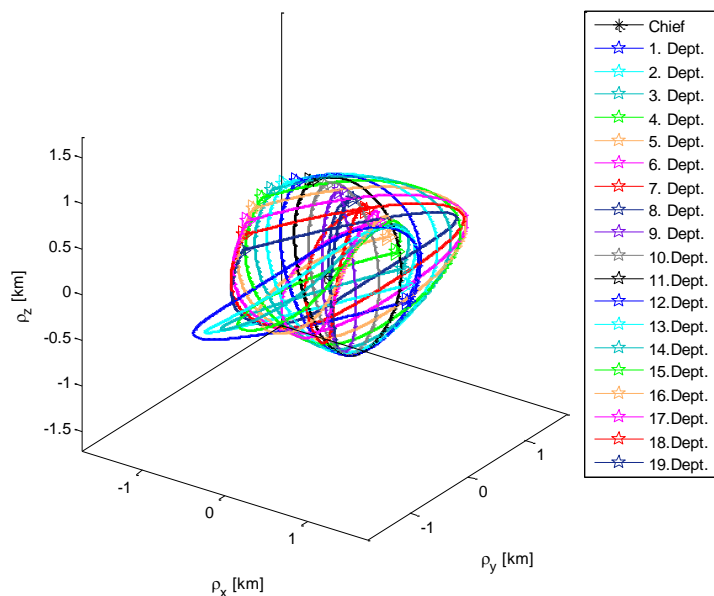
Figure 4-37. 3D view of 19 different cases for L1: α from zeros to 180 degree
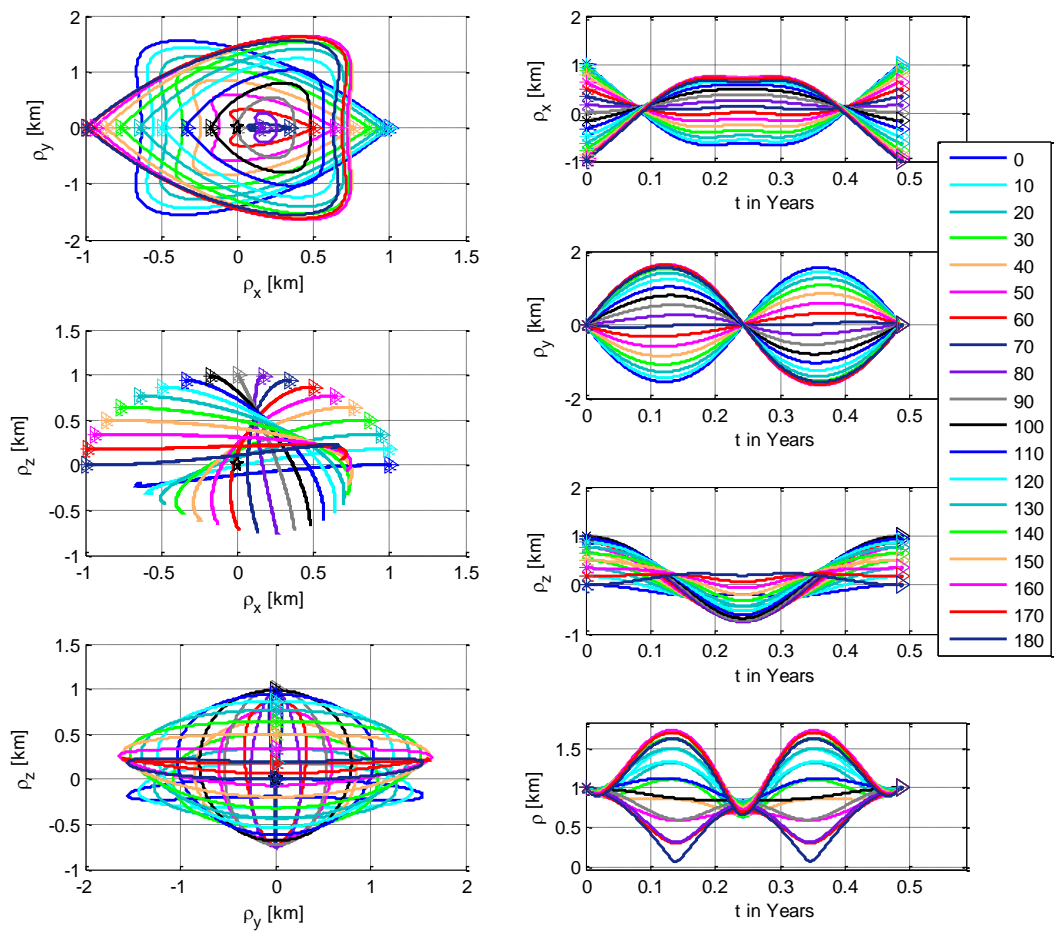
Figure 4-38. 2D view of 19 different cases for L1: α from zeros to 180 degree

187
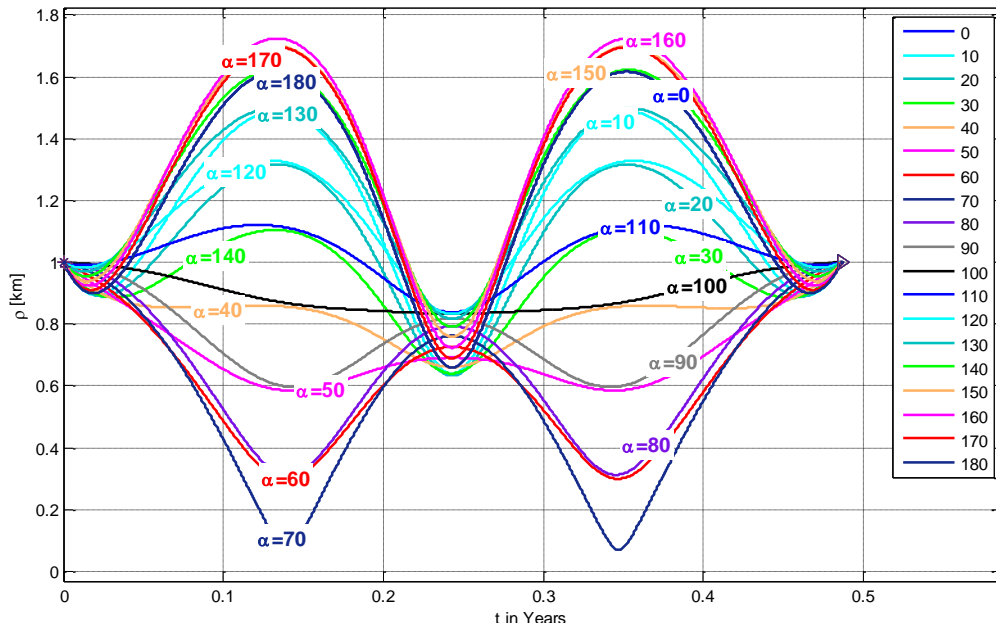
Figure 4-39. Relative position for α zeros to 180 degree around L1
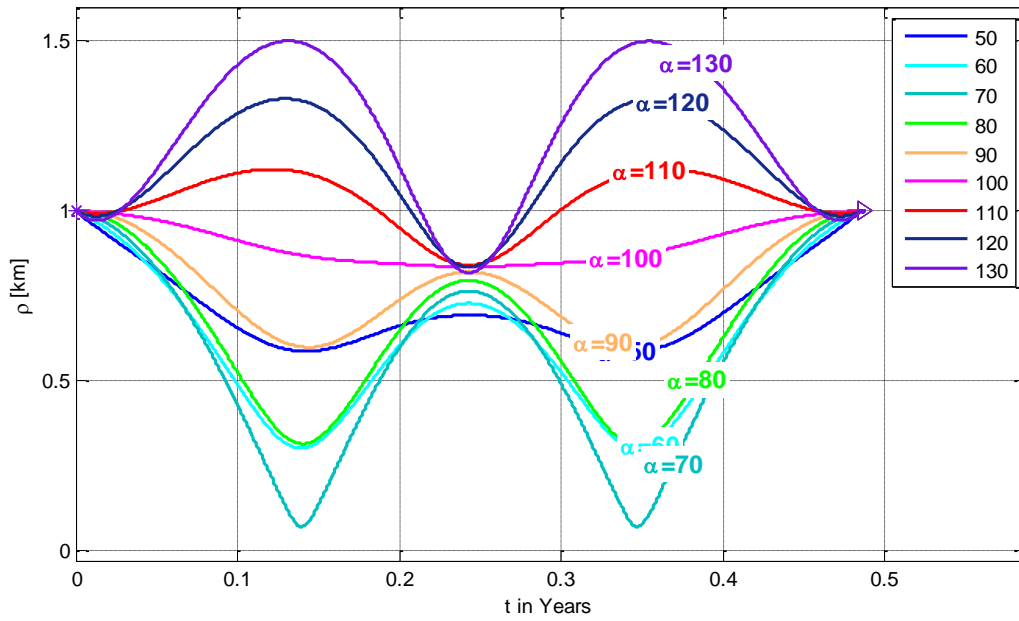
Figure 4-40. Relative position for α 80 to 130 degree around L1

188

Here, it is obviously seen that the inclination of the plane affects the deviation of the relative distances. As seen in Figure 4-40 showing the resultant relative distances, the less deviation is obtained around $\alpha = 100^0$, ρ changes between $1\ km$ to $0.85\ km$. All ρ coincides around $0.60\ km - 0.85\ km$ at half period, and forms extrama at 1st quarters and 3rd quarters, in positive and negative direction depending on the α value. But, around $\alpha = 100^0$ the extrama disappear and smoothest deviations are acquired at half period, maximum deviation is about $0.15\ km$.
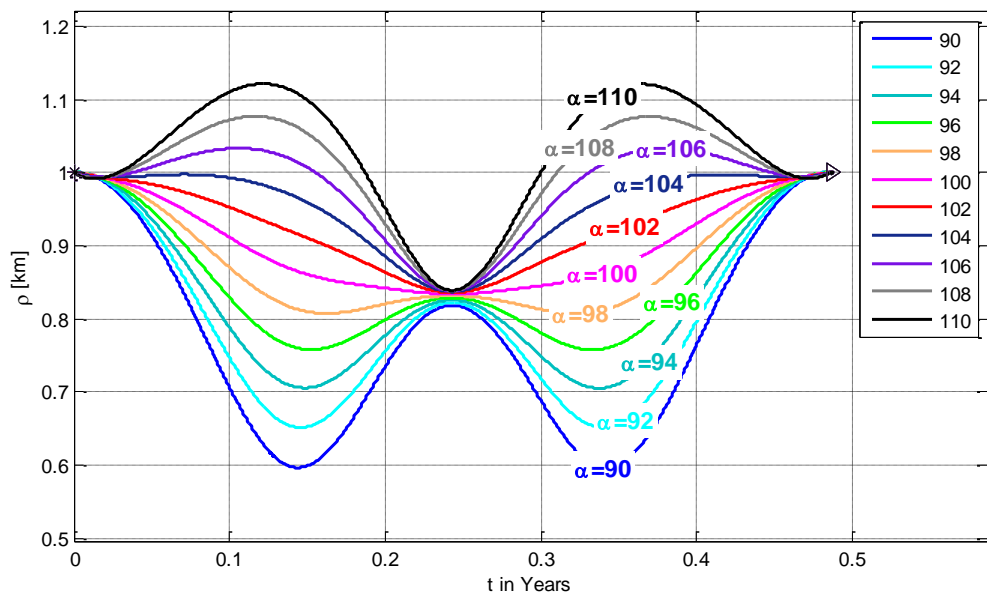
Figure 4-41. Relative position for α 90 to 110 degree around L1

As a second step around $\alpha = 100^0$ is refined and analyzed by an interval from 90^0 to 110^0 with 2^0 increments. Here it is seen that for the α greater than 104^0 the relative distance has an value greater than required distance ρ. it can be stated that ρ has only one extremum point just only at half period for an α between $98^0 and\ 104^0$. the only difference among them is the change of ρ towards this extramum. For instance, when $\alpha = 104^0$ ρ begins to deviate from required value at 0.1 years' time. Approximately linear changes before and after half period is obtained around $\alpha = 102^0$. The

deviation starts rapidly and downsizing for $\alpha < 100^0$ and rapidly growth for $\alpha > 104^0$.
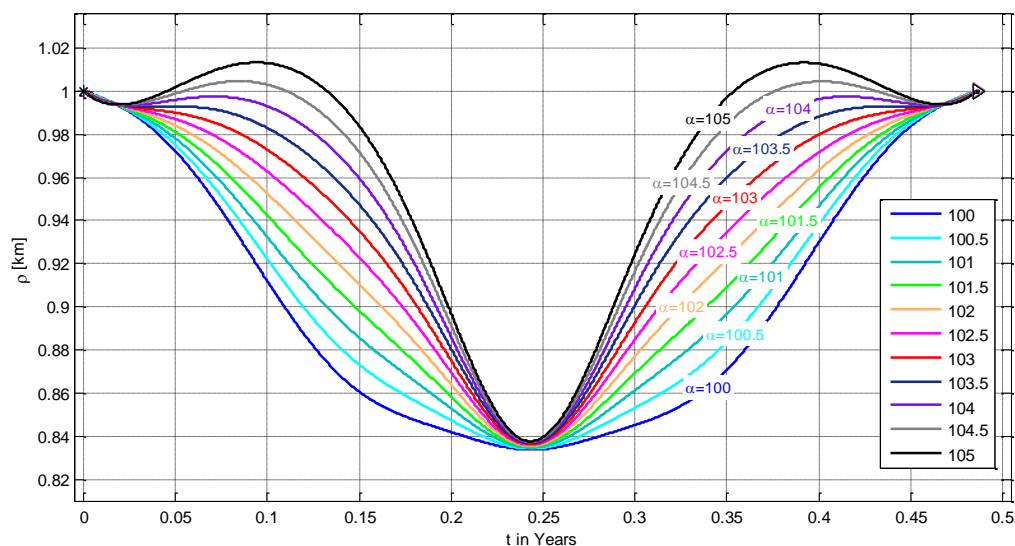
Figure 4-42. Relative position for α 100 to 105 degree around L1

From this refined analyze, it is seen that the most resistant result is get for $\alpha = 104^0$, but the rate of change toward minimum point $\rho = 0.84\ km$ is high. The most uniformly change is obtained for $\alpha = 102.5^0$, decreasing rate to minimum and increasing rate form minimum distance are nearly linear. Here after, for the formation clusters given in the next subsections, the elevation angle is taken as $\alpha = 102.5^0$ and its complement to $180^0\ \alpha = -77.5^0$ for a constant azimuth $\beta = 0^0$. So, two deputies with these initial conditions form a formation flight as presented in the following figures.

The 3D view of the deputies' trajectory:
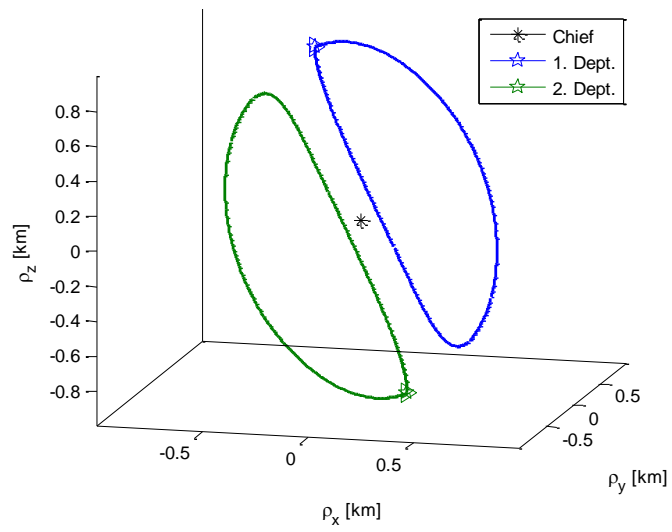
Figure 4-43. 3D Trajectory of 1st and 2nd deputies for Optimum ISF around L1
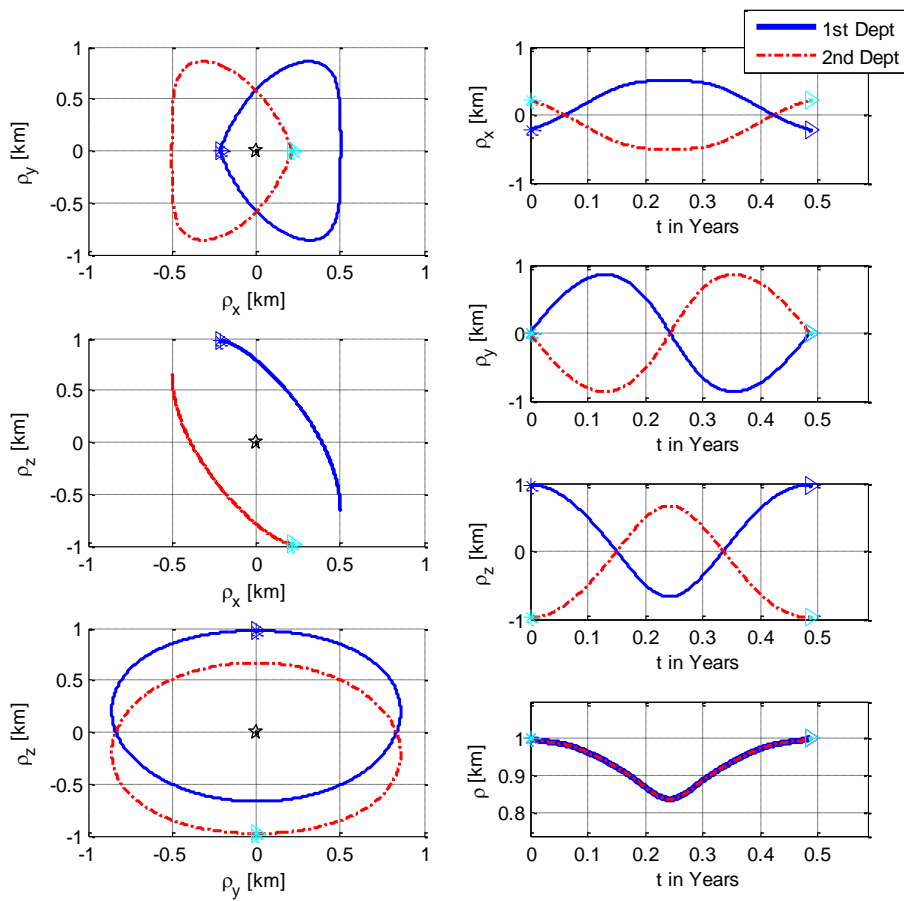
Figure 4-44. Relative position of 1st and 2nd deputies, optimum ISF around L1

191

It can be stated that the minimum relative distance deviation for one deputy that can be obtained is approximately 0.16 km for the formation designed at L1.

Finally, it is possible to obtain a formation having four deputies by adding two more satellites on y axis ($\beta = 90^0$ and $\beta = -90^0$), as done in the previous sections. The dynamics of the plane formed by these 4 deputies is shared in Figure 4-45. The distances between deputies can be seen in Figure 4-45 and in following Figure 4-46 and Figure 4-47 as well, that time dependent values are given.
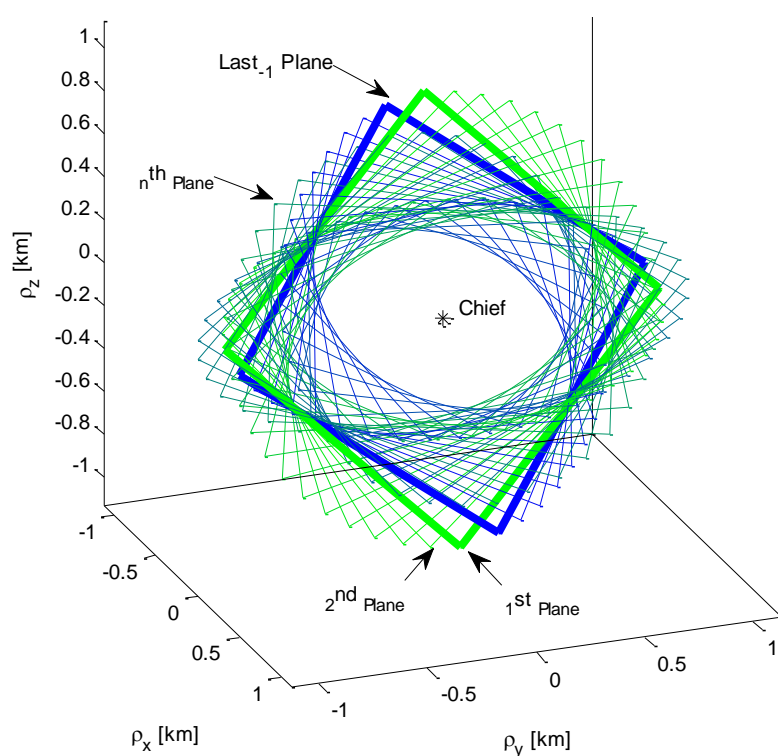
Figure 4-45. Plane formed by four deputies for optimum ISF around L1
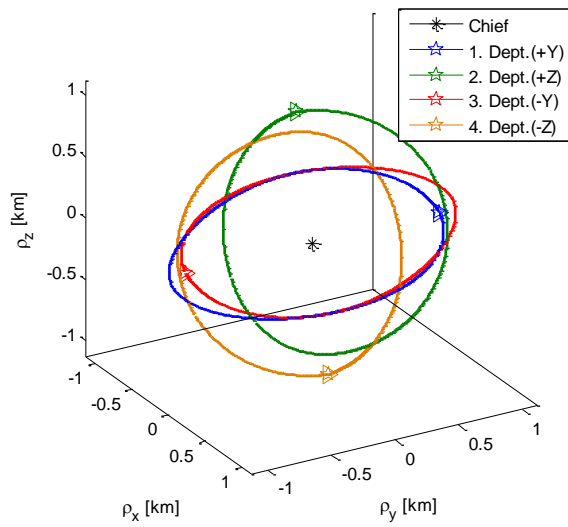
Figure 4-46. Relative trajectories for optimum ISF around L1
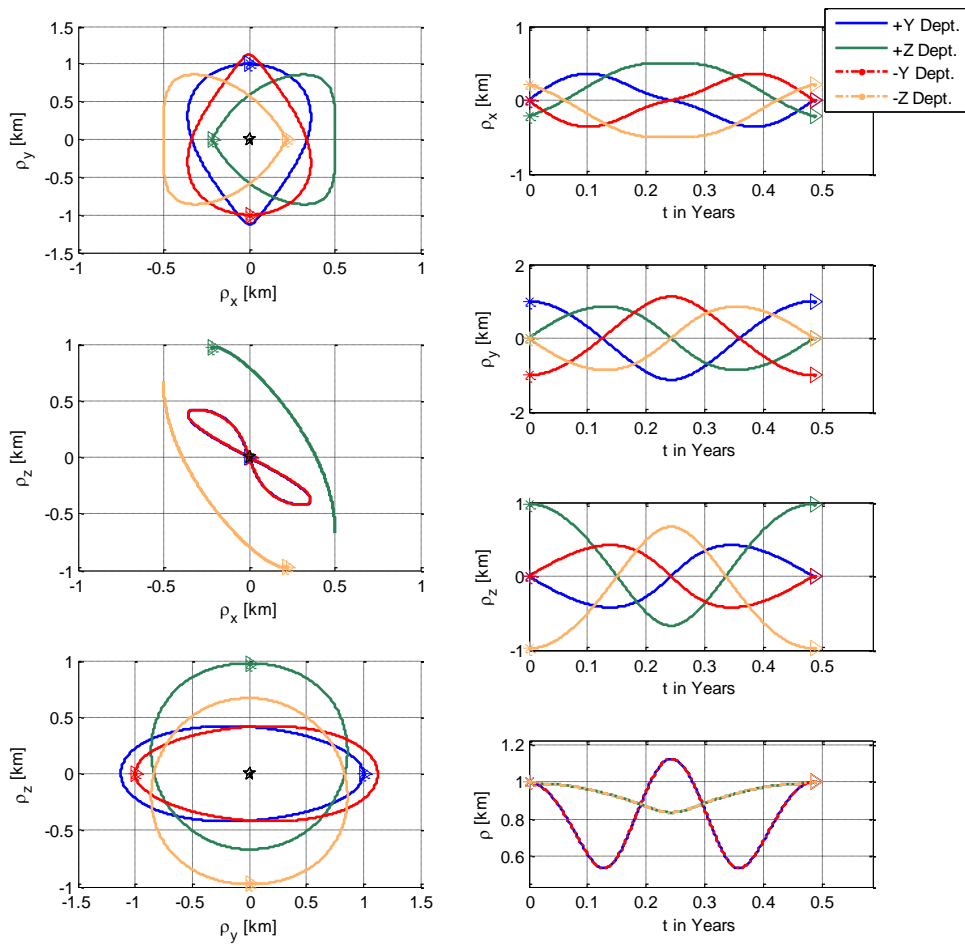
Figure 4-47. Projected and time dependent views for optimum ISF around L1

193
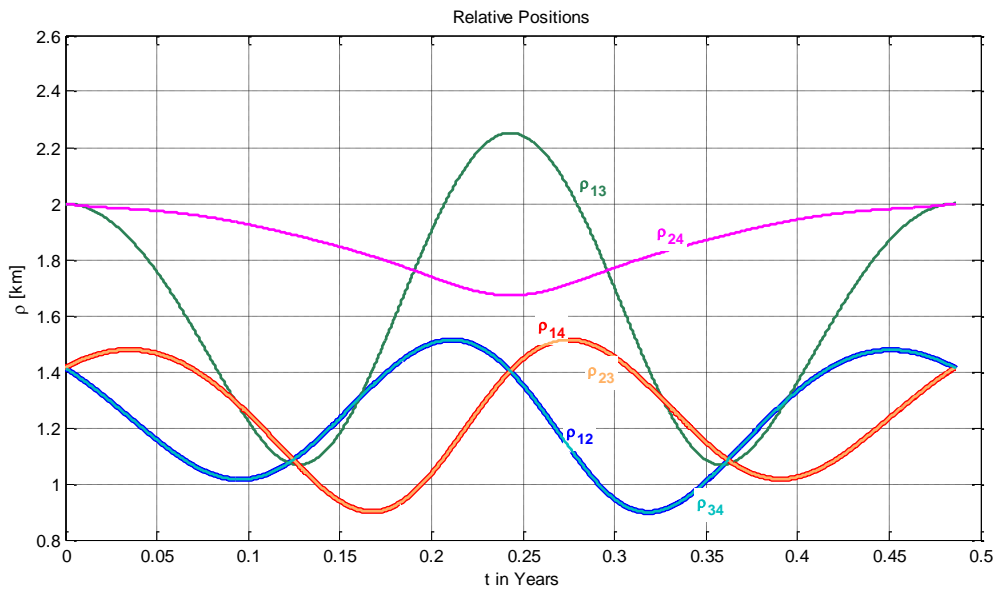
Figure 4-48. The relative distances between deputies for optimum ISF around L1

The relative distances between deputies are given in Figure 4-48, it changes between $1.5\ km$ to $1.0\ km$. Geometrical initial relative distance is $\sqrt{2}\rho = 1.414\ km$. Compared to the results obtained at previous formations, the previous formation varies between $2.0\ km$ to $1.0\ km$. So, thanks to the optimum elevation angle $0.5\ km$ is corrected.

Same scanning method is used for β azimuth angle and in first step it is seen that minimum deviation for relative distance is get at near $\beta = 90^0$ for $\alpha = 0^0$. It is shown in bold green line in Figure 4-49.
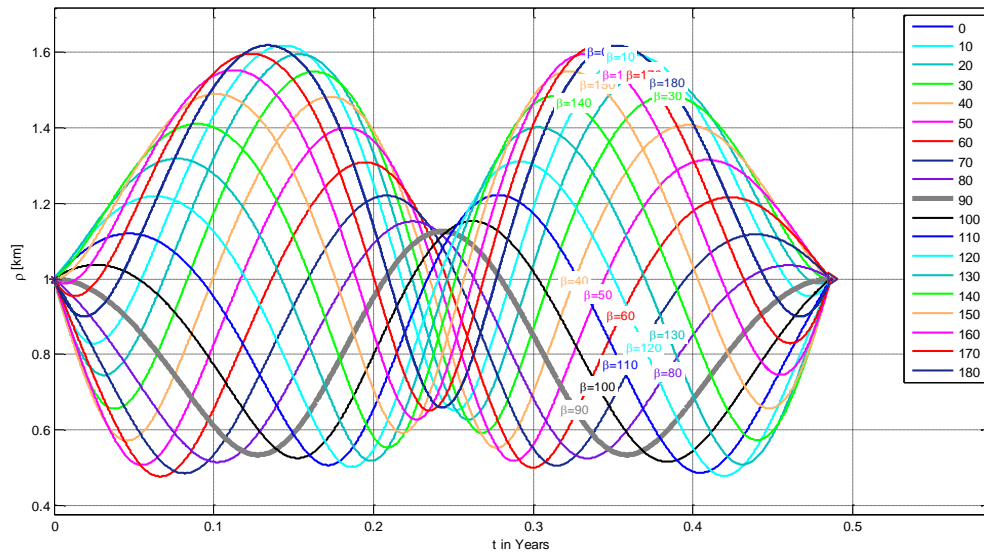
Figure 4-49. Relative distance changes for β scanning around L1

A complete scanning for both β and α to find optimum relative distance is also performed. In this section an optimal elevation angle for deputy satellite is computed and as a consequence of this, the next section proposes the formation schema composed of multiple satellites initially located at this elevation angle with different initial relative distances.

4.3.2.2. Aligned and uniformly equally separated formation

In that part, a formation composed of again four deputy satellites, but aligned and initially positioned at $1.0 \, km$ distance from each other successively, is given. The initial desired elevation angle is taken optimum elevation angle with zeros degree azimuth angle. So, the formation configuration is given in the following Table 4.10. hereafter uniformly aligned formation is denoted as UAF.

Table 4.10. Relative positions of the four deputies, UAF around L1

Deputy Satellite 1	Deputy Satellite 2	Deputy Satellite 3	Deputy Satellite 4
$\rho = 1\ km$	$\rho = 2\ km$	$\rho = 3\ km$	$\rho = 4\ km$
$\beta = 0^0$	$\beta = 0^0$	$\beta = 0^0$	$\beta = 0^0$
$\alpha = 102.5^0$	$\alpha = 102.5^0$	$\alpha = 102.5^0$	$\alpha = 102.5^0$

The trajectories obtained are:
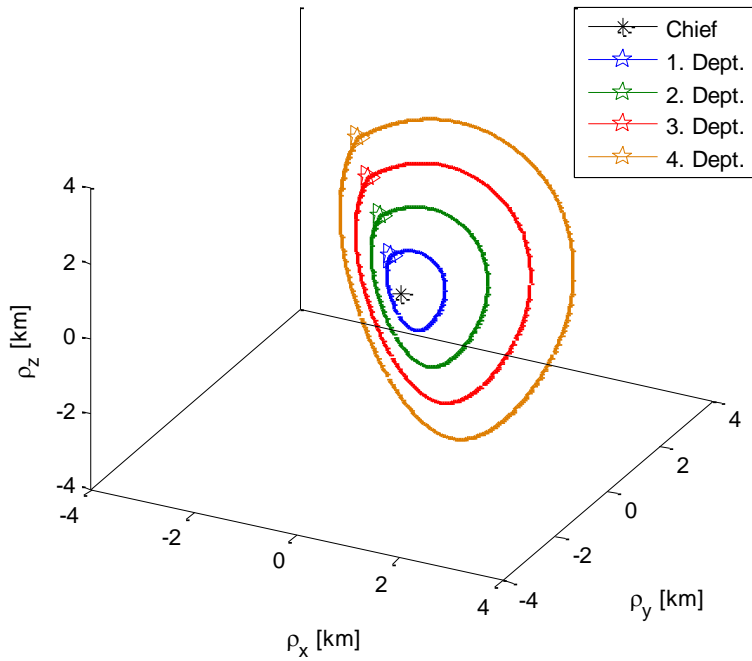
Figure 4-50. Trajectory of the deputies with respect to chief for UAF around L1

The relative distances:
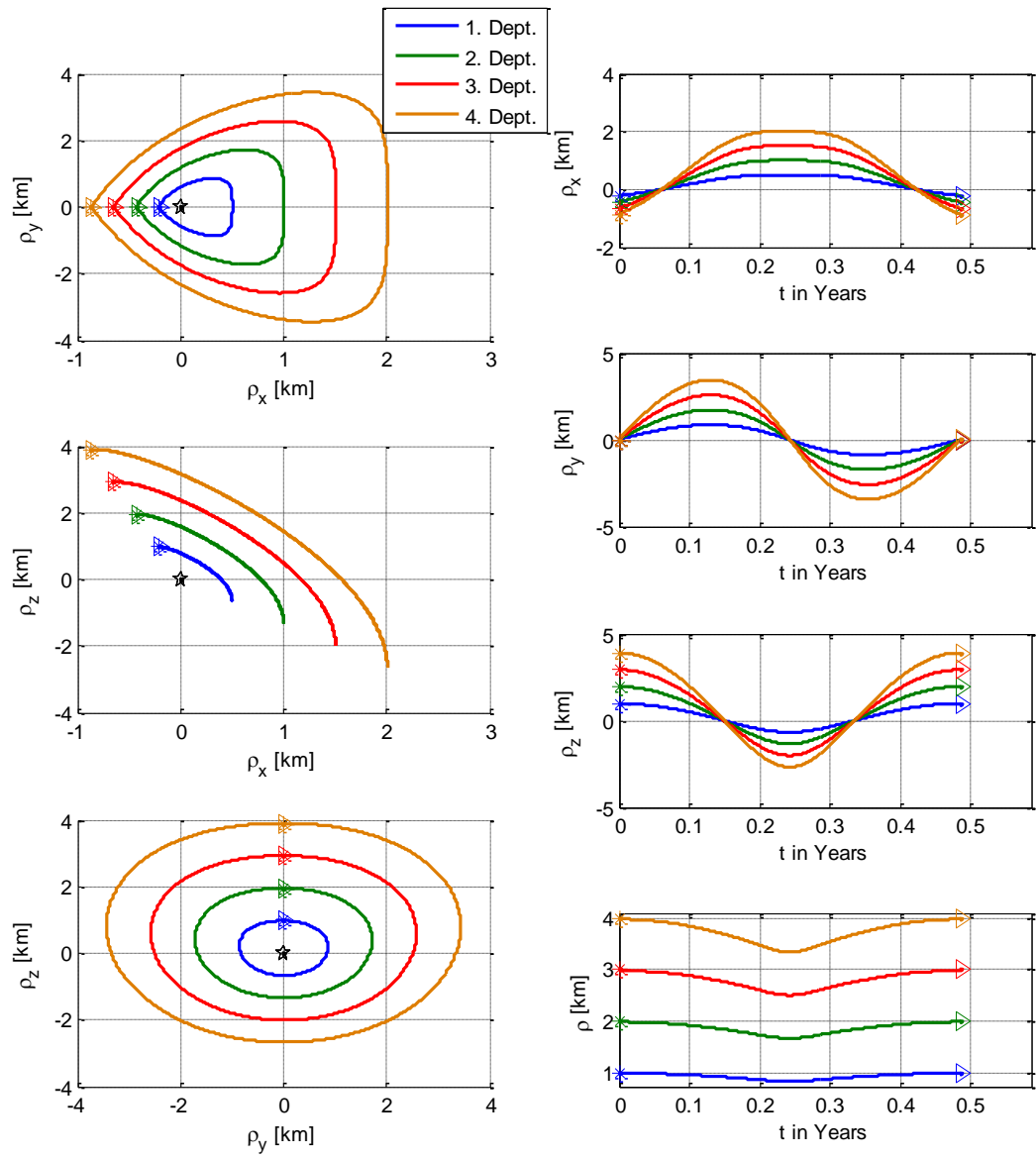
Figure 4-51. Projected and time dependent views for UAF around L1

197
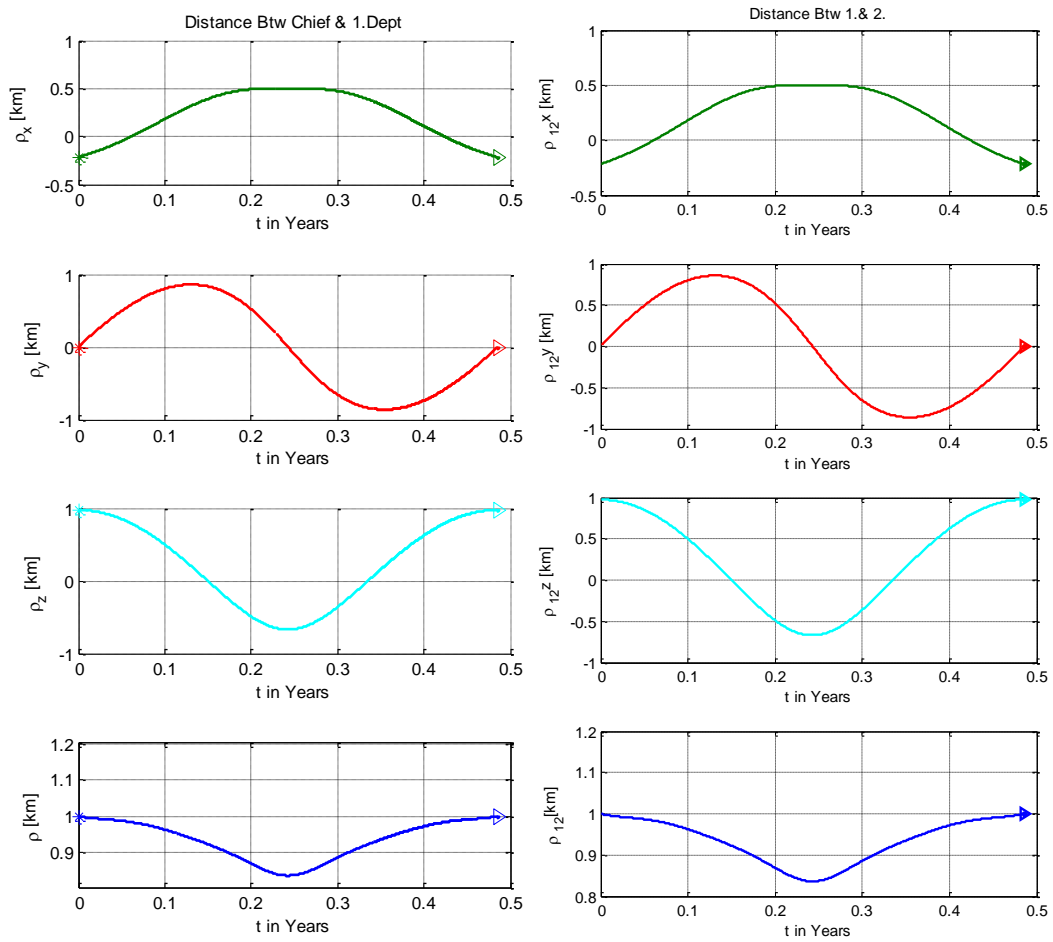
Figure 4-52. Relative distances between deputies for UAF around L1
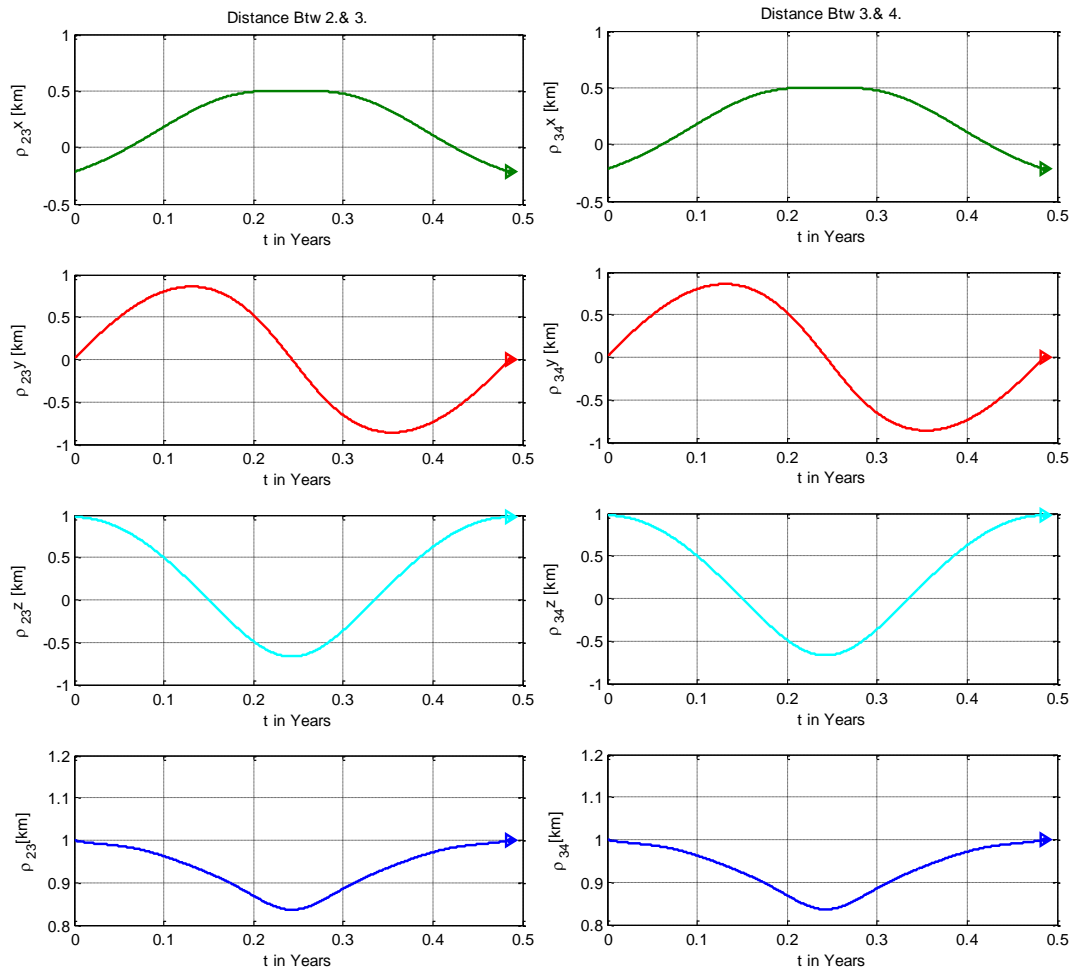
Figure 4-53. Relative distances between deputies for UAF around L1-2

Here, the relative distance changes between satellites that are positioned consecutively are similar, and these changes are between $1.0\ km$ to $0.85\ km$ as the optimum elevation angle is selected as initial relative position. This kind of formation cluster is really very useful for missions required a constant distance changes between each successive satellite, for each member of formation, as well as for chief satellite.

As seen above, the minimum changes on relative distance is acquired for a formation having a plane with an inclination angle defined by elevation angles equal to the $\alpha = 102.5^0\ and\ \alpha = -77.5^0$ for L1 point. For missions that requires to maintain the relative distance between satellites consecutively, the formation given above is ideal,

and the same number of satellites can be positioned symmetrically at $\alpha = -77.5^0$. For example, the results obtained for a formation cluster having 6 satellites, three of them initially located at $\alpha = 102.5^0$ and the last three $\alpha = -77.5^0$ gives a formation as presented in the following figures. This kind of formation can be called as formation with successive pairs.
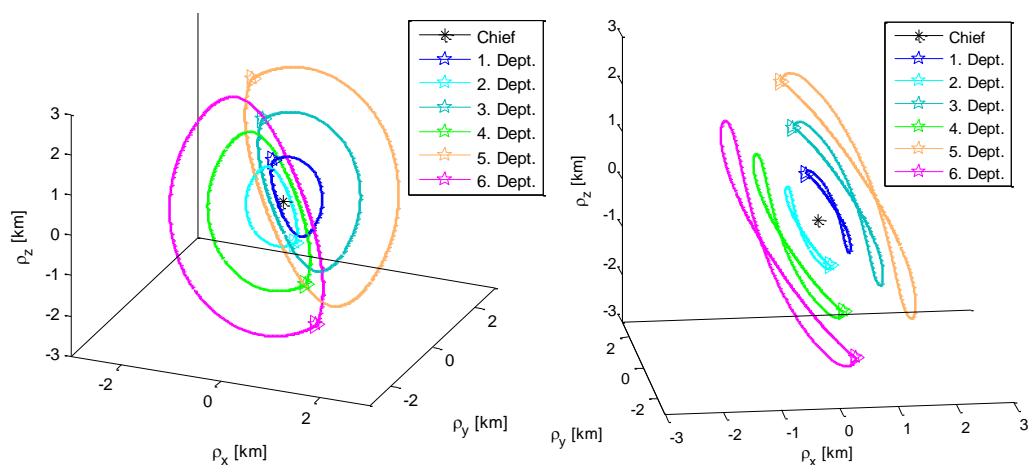
Figure 4-54. Trajectories of deputies for UAF-L1
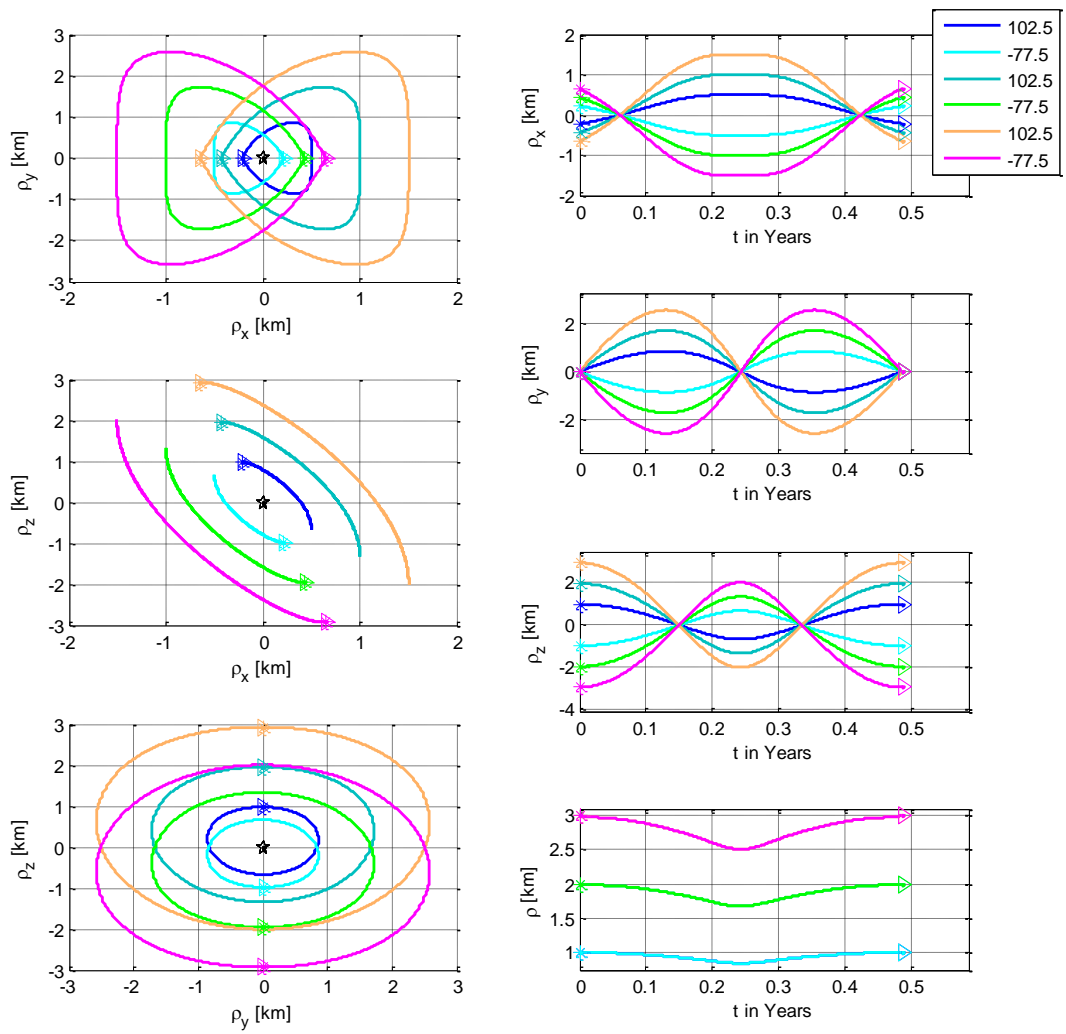
Figure 4-55. Projected and time dependent views for UAF-L1
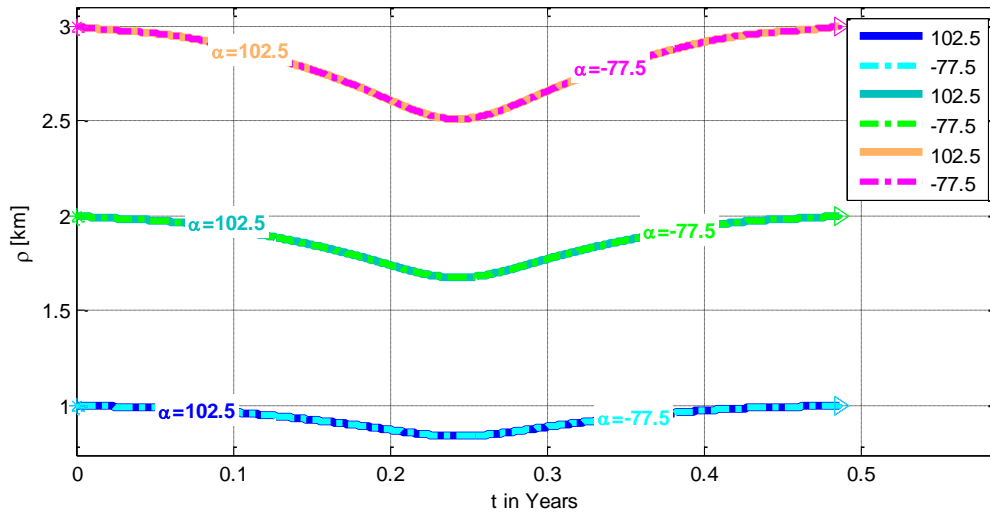
Figure 4-56. Relative distance between satellites for UAF-L1

In this case, the minimum relative distance between each satellite is different, regarding to the distance step given for each successive satellite. It is clear that, it is useful to use this kind of formation schema for a mission that requires quasi-constant relative distance with respect to the chief, for each pairs of formation.

4.4. Formation flight design near L2

This section contains the explanations about the design of formation around L2 and the analyses of several types of formation configuration, as given in case of formation design around L1. The same purpose is still valid: find an orbit for deputy satellite which ensures naturally long-term formation flight without need of control maneuver. The OPTICs method given in section 4.3 is used to find proper initial velocity that satisfies the formation for the desired position.

The formation dynamics and relative positions of the deputies with respect to chief and with respect to each other are given in the following sections for several types of formation configurations as done for L1 case.

4.4.1. Different formation clusters and simulation results

This section presents analyses of different formation configurations in order to see the effect of formation schema for L2 case. The chief's orbit is computed regarding to the remarks given in the previous section 3.2.4 and section 3.3.4, so in a first step, a periodic Halo orbit is designed for Chief. The following figures, Figure 4-57 and Figure 4-58, give the Chief's orbit around L2.
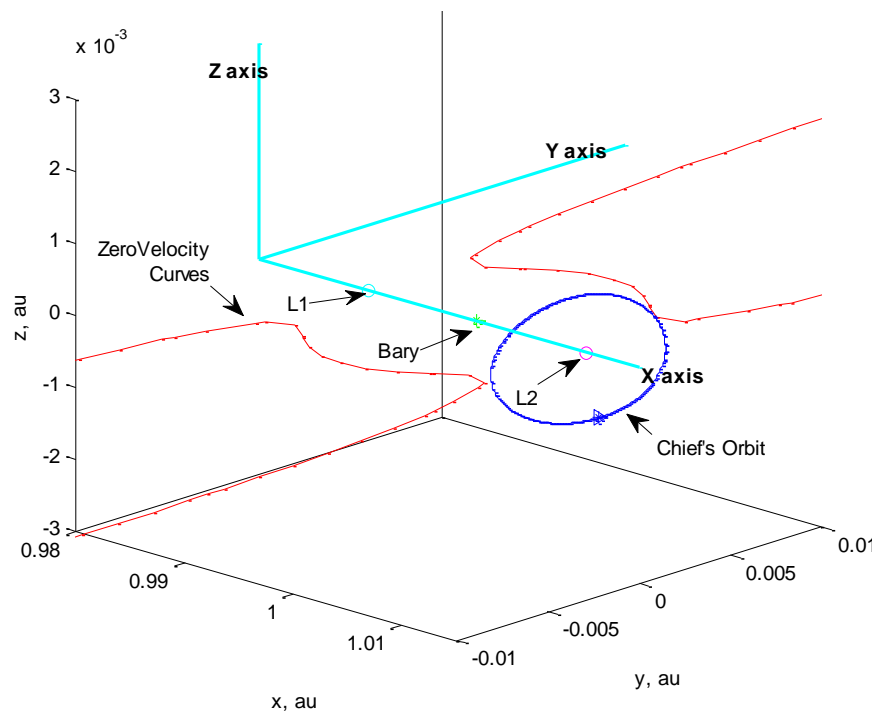
Figure 4-57. Orbit obtained for L2 – 3D view
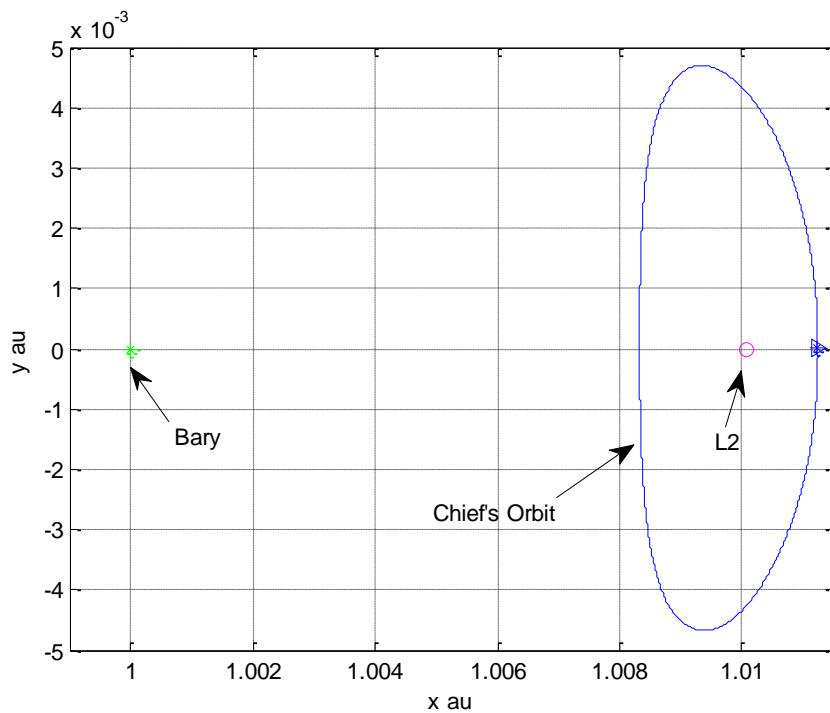
Figure 4-58. Orbit obtained for L2 – 2D view

The following subsections present several formation configurations. The first example analyzes a formation having an equilateral triangle; the second has four deputy satellites forming square shape, and the third has a modified form of the second, with an inclined plane, as done for L1 case.

4.4.1.1. Equilateral triangle formation (ETF)

This formation configuration has four satellites. The three satellites positioned on the corner of an equilateral triangle and the chief satellite is on the center of this triangle. The desired relative distance ρ between deputy satellites and chief is 1 km. and the relative initial positions with respect to the chief are given Table 4.11. The initial conditions for the Chief and deputies are given in the following Table 4.12.

Table 4.11. Relative positions of deputies for ETF around L2

Deputy Satellite 1	Deputy Satellite 2	Deputy Satellite 3
$\rho = 1\ km$ $\beta = 90^0$ $\alpha = 90^0$	$\rho = 1\ km$ $\beta = 90^0$ $\alpha = 210^0$	$\rho = 1\ km$ $\beta = 90^0$ $\alpha = -30^0$

The trajectory of each deputy satellite with respect to chief is given in the following figures (Figure 4-59 to Figure 4-63). The second and third deputies are symmetrical to each other trajectory with respect to the xz plane. The following figures are the set of multiple sub-figures. The left part contains the projection of the trajectory respectively in xy, xz, yz planes. The first three figures of the right part show the components of relative distance depending on time. The last figure of the right part contains the resultant relative distance, the distance between deputy and chief satellites.
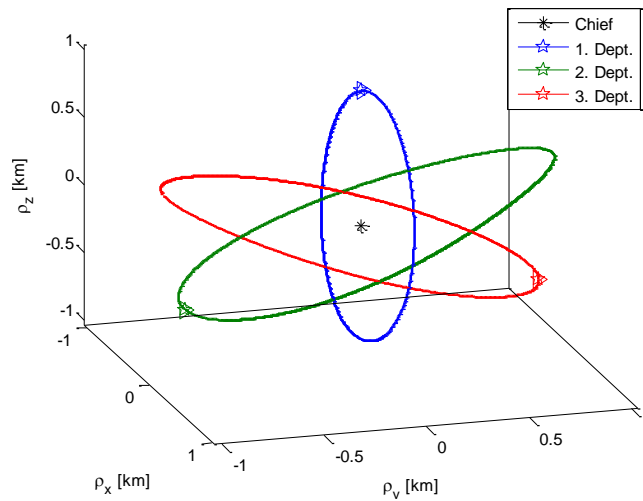
Figure 4-59. Trajectories of the deputies with respect to chief for ETF around L2

Table 4.12. ICs and periodicity checks for ETF around L2

Initial conditions of chief	Initial conditions of deputy_1	Initial conditions of deputy_2	Initial conditions of deputy_3
1.011239967214949 0.000000255658354 -0.000850376654007 0.000122281872260 -0.009166722628605 -0.000000965801832	1.011239967214949 0.000000255658354 -0.000850369969420 0.000122281899255 -0.009166719971525 -0.000000965672931	1.011239967214949 0.000000249869332 -0.000850379996301 0.000122276470366 -0.009166723990221 -0.000000964111545	1.011239967214949 0.000000261447376 -0.000850379996301 0.000122287247118 -0.009166723923963 -0.000000967621020
Period of chief's Orbit in Earth's day: 180.5000 days	**Period of deputy_1 Orbit in Earth's day:** 180.5000 days	**Period of deputy_2 Orbit in Earth's day:** 180.5000 days	**Period of deputy_3 Orbit in Earth's day:** 180.5000 days
Chief's Jacobi Constant: 3.000818743599308	**deputy_1's Jacobi Constant:** 3.000818743683121	**deputy_2's Jacobi Constant:** 3.000818743558123	**deputy_3's Jacobi Constant:** 3.000818743556683
Periodicity Check of chief: 0.193 meter	**Periodicity Check of deputy_1:** 0.099 meter	**Periodicity Check of deputy_2:** 0.357 meter	**Periodicity Check of deputy_3:** 0.02812 meter
Test: Determinant of chief's Φ: 1.000000001863806	**Test: Determinant of deputy_1's Φ:** 0.999999999124470	**Test: Determinant of deputy_2's Φ:** 1.000000000751922	**Test: Determinant of deputy_3's Φ:** 0.999999999495909
EigenValues of chief's Φ:	**EigenValues of deputy_1's Φ:**	**EigenValues of deputy_2's Φ:**	**EigenValues of deputy_2's Φ:**
1673.1903149 1.0457613- 0.0446915i 1.0457613+ 0.0446915i 0.9545161- 0.0407903i 0.954516+ 0.040790i 0.000597637836	1673.19088 1.04576159-0.0446911i 1.04576159+0.0446911i 0.95451595-0.0407900i 0.95451595+0.0407900i 0.00059763	1673.19003043 1.04576128-0.0446916i 1.04576128+0.0446916i 0.95451620-0.0407905i 0.95451620+0.0407905i 0.00059763	1673.19003217 1.04576128-0.0446916i 1.04576128+0.0446916i 0.95451619- 0.0407905i 0.95451619+ 0.0407905i 0.00059763

Figure 4-60. ETF-L2, Deputy #1: Projected and time dependent

Figure 4-61. ETF-L2, Deputy #2: Projected and time dependent views

208

Figure 4-62. ETF-L2, Deputy #3: Projected and time dependent views

The results show that the first relative trajectory has a different characteristic from the two others. In xz plane it has quasi one-dimensional motion, and it has a quasi elliptical motion in yz plane. However, the second and the third deputy satellites has symmetric relative trajectory with respect to the y axis and their motion has non-regular motion on projection. For all of them, the relative distances are not constant, they oscillate between 1 km and 0.25 km for the first deputy and, 1 km to 0.35 km for the second and third one. Relative distance is narrowing and expanding, although the periodic relative motion is obtained for one orbital period time.

The relative distances between deputies are given in Figure 4-63. The aimed relative distance between deputies is $\sqrt{3}\rho = 1.732\ km$. The acquired formation shape shrinks and extends between aimed distance which is roughly 1.732 km and 0.5 km, an oscillating relative motion.
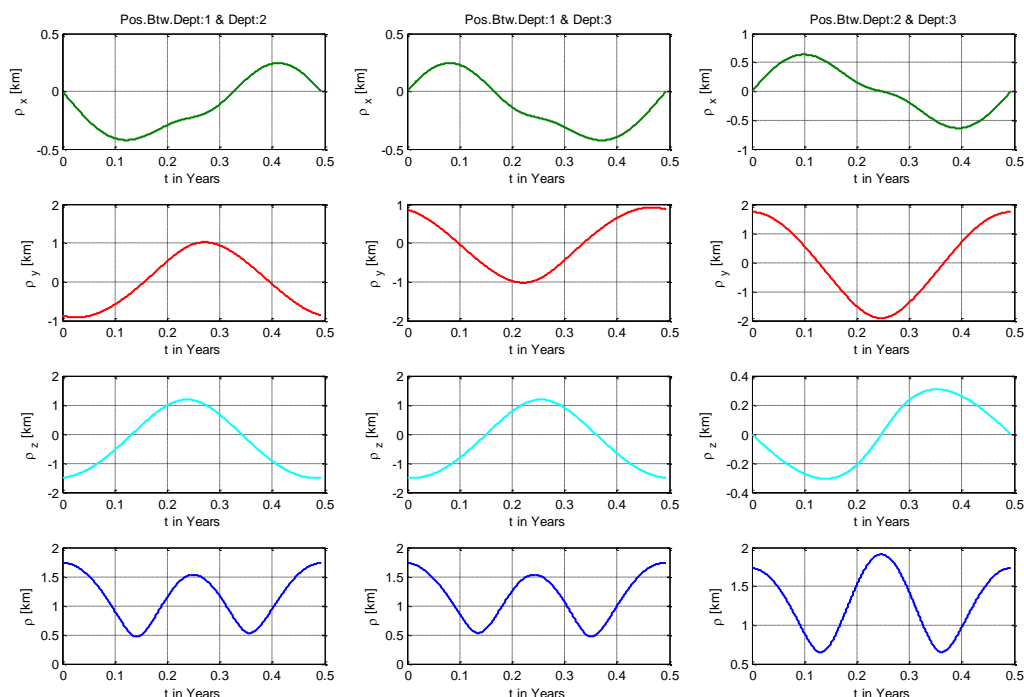
Figure 4-63. ETF-L2: The relative distances between deputies

The shape change of the triangle is illustrated in Figure 4-64; bold green colored triangle is the starting positions; bold blue one is the last configuration. The plane is colored from green to blues according to the time changes. The inclination angle of the plane formed by deputy satellites varies and the distance between them start narrowing until 1st and third quarter period then it expands at half and full period; last plane and 1st plane coincide since motion is periodic.
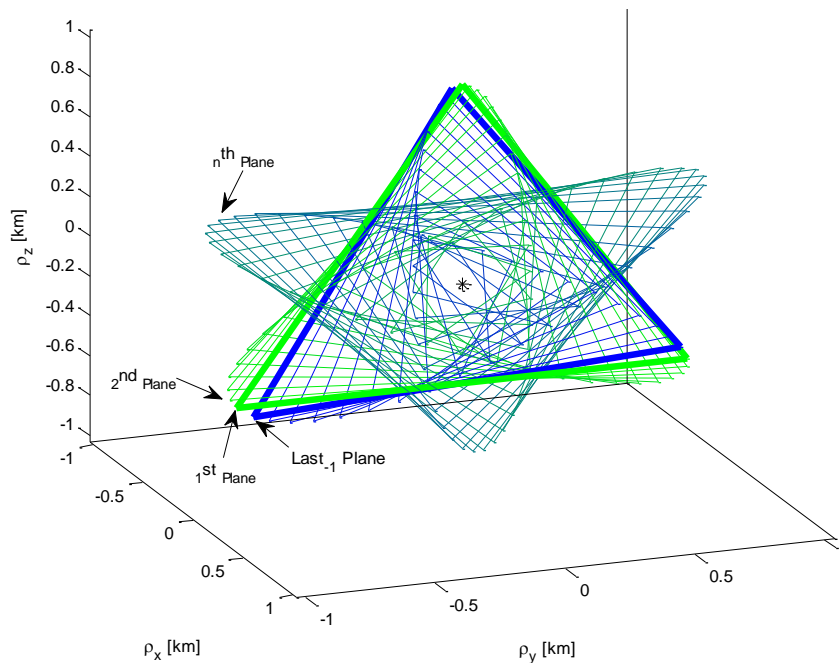
Figure 4-64. ETF-L2: The plane formed by deputies

For this kind of equilateral triangular shape configuration, the deputy located at the top of the Chief (1st deputy) does not have a harmonious motion compared to the two other members of the formation. The other two deputies have symmetric motion with respect to y axis, so Chief, 2nd and 3rd satellites make a harmonic formation flight configuration. For that reason, the next subsection contains the analyses for the deputies located at just left/right/top and down of the chief.

4.4.1.2. Square formation (SF)

The results obtained for a formation flight cluster composed of four deputy satellites around L2 and having a square shaped configuration are presented in this section. Four deputy satellites are located at the corners of the square and chief is located on the center. The desired relative distance ρ between deputy satellites and chief and the relative initial azimuth and elevation angles with respect to the chief are listed in the following Table 4.13.

Table 4.13. Relative positions of the four deputies, SF around L2

Deputy Satellite 1	Deputy Satellite 2	Deputy Satellite 3	Deputy Satellite 4
$\rho = 1\ km$	$\rho = 1\ km$	$\rho = 1\ km$	$\rho = 1\ km$
$\beta = 90^0$	$\beta = 0^0$	$\beta = -90^0$	$\beta = 0^0$
$\alpha = 0^0$	$\alpha = 90^0$	$\alpha = 0^0$	$\alpha = -90^0$

The chief's orbit is the same as used in the precedent section. The initial velocities and trajectory for the deputies are computed and given in the following Table 4.14 and Figure 4-66 to Figure 4-69.
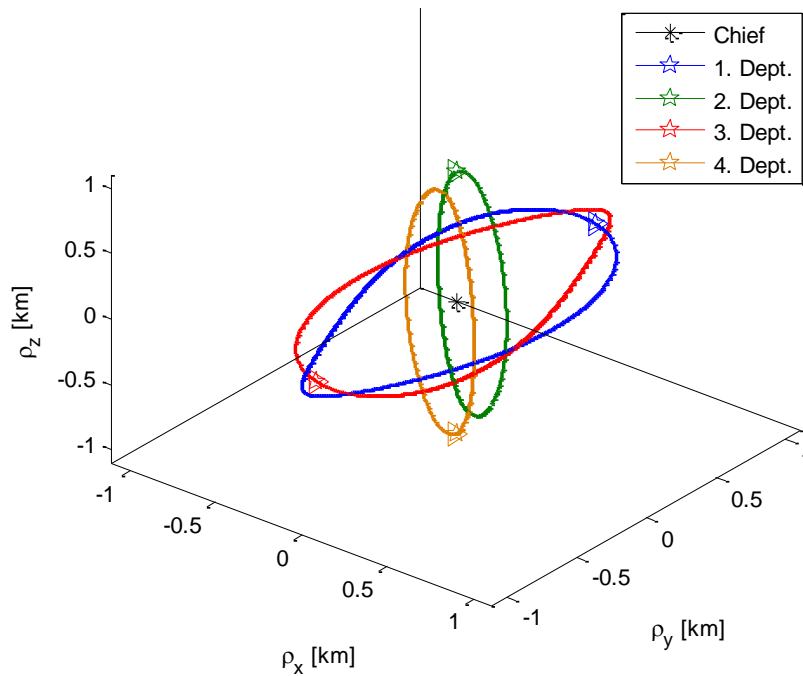
Figure 4-65. SF-L2, The trajectory of the deputies with respect to chief

Table 4.14. ICs and periodicity checks, SF around L2

Initial conditions of chief	Initial conditions of deputy_1	Initial conditions of deputy_2	Initial conditions of deputy_3	Initial conditions of deputy_4
1.011239967214 0.000000255658 -0.000850376654 0.000122281872 -0.009166722628 -0.000000965801	1.01123996721 0.00000026234 -0.00085037665 0.00012228809 -0.00916672259 -0.00000096782	1.01123996721 0.00000025565 -0.00085036996 0.00012228189 -0.00916671997 -0.00000096567	1.01123996721 0.00000024897 -0.00085037665 0.00012227565 -0.00916672266 -0.00000096377	1.01123996721 0.00000025565 -0.00085038333 0.00012228184 -0.00916672528 -0.00000096593
Period of chief's Orbit in Earth's day: 180.5 days	**Period of deputy_1 Orbit in Earth's day:** 180.5 days	**Period of deputy_2 Orbit in Earth's day:** 180.5 days	**Period of deputy_3 Orbit in Earth's day:** 180.5 days	**Period of deputy_4 Orbit in Earth's day:** 180.5 days
Chief's Jacobi Constant: 3.00081874359930	**deputy_1's Jacobi Constant:** 3.00081874359847	**deputy_2's Jacobi Constant:** 3.00081874368312	**deputy_3's Jacobi Constant:** 3.00081874360014	**deputy_4's Jacobi Constant:** 3.00081874351549
Periodicity Check of chief: 0.193 meter	**Periodicity Check of deputy_1:** 0.421 meter	**Periodicity Check of deputy_2:** 0.099 meter	**Periodicity Check of deputy_3:** 0.125 meter	**Periodicity Check of deputy_4:** 0.093 meter
Test: Determinant of chief's Φ: 1.00000000186380	**Test: Determinant of deputy_1's Φ:** 1.00000000054402	**Test: Determinant of deputy_2's Φ:** 0.99999999912447	**Test: Determinant of deputy_3's Φ:** 1.00000000203944	**Test: Determinant of deputy_4's Φ:** 1.00000000088200
EigenValues of chief's Φ:	**EigenValues of deputy_1's Φ:**	**EigenValues of deputy_2's Φ:**	**EigenValues of deputy_3's Φ:**	**EigenValues of deputy_4's Φ:**
1673.1903149 1.04576-0.04469i 1.04576+0.04469i 0.95451-0.04079i 0.95451+0.04079i 0.000597637836	1673.19031550 1.04576-0.04469i 1.04576+0.04469i 0.95451-0.04079i 0.95451+0.04079i 0.0005976	1673.1908822 1.04576-0.04469i 1.04576+0.04469i 0.95451-0.04079i 0.95451+0.04079i 0.0005976	1673.1903141 1.04576-0.04469i 1.04576+0.04469i 0.95451-0.04079i 0.95451+0.04079i 0.0005976	1673.1897479 1.04576-0.04469i 1.04576+0.04469i 0.95451-0.04079i 0.95451+0.04079i 0.0005976
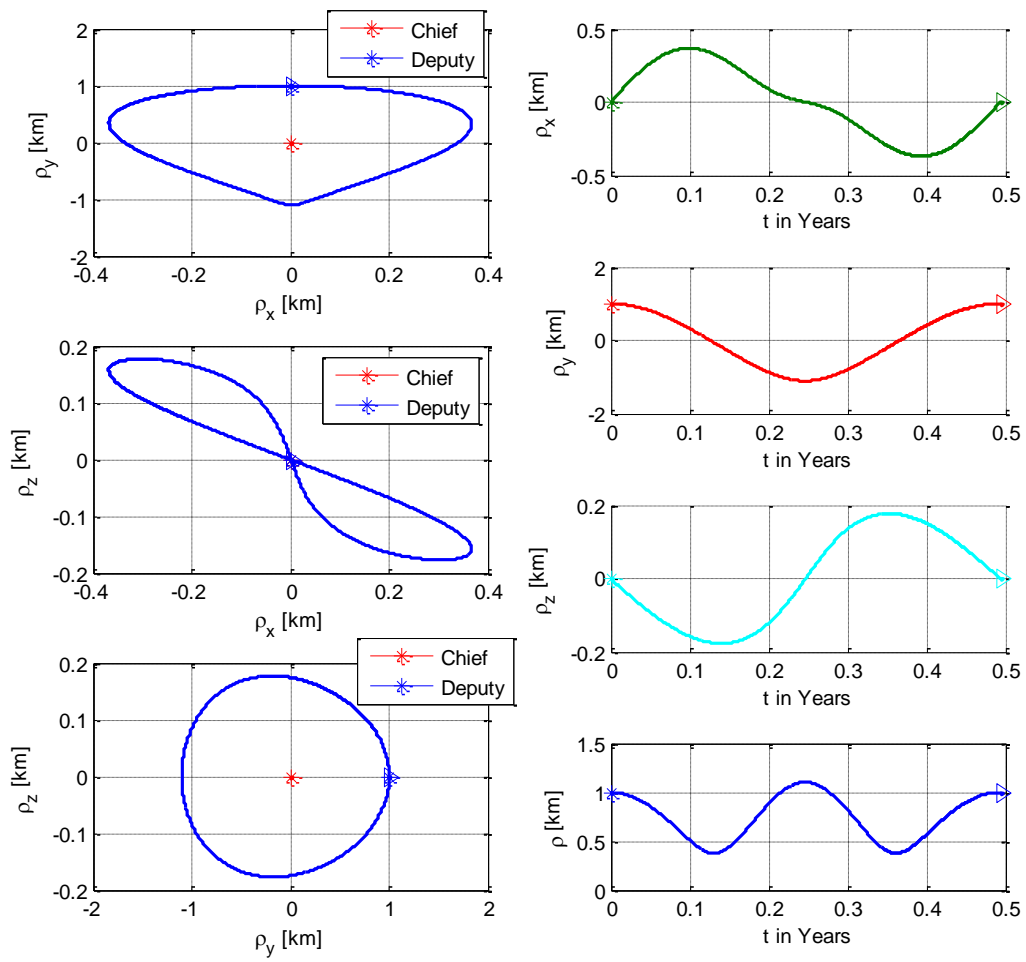
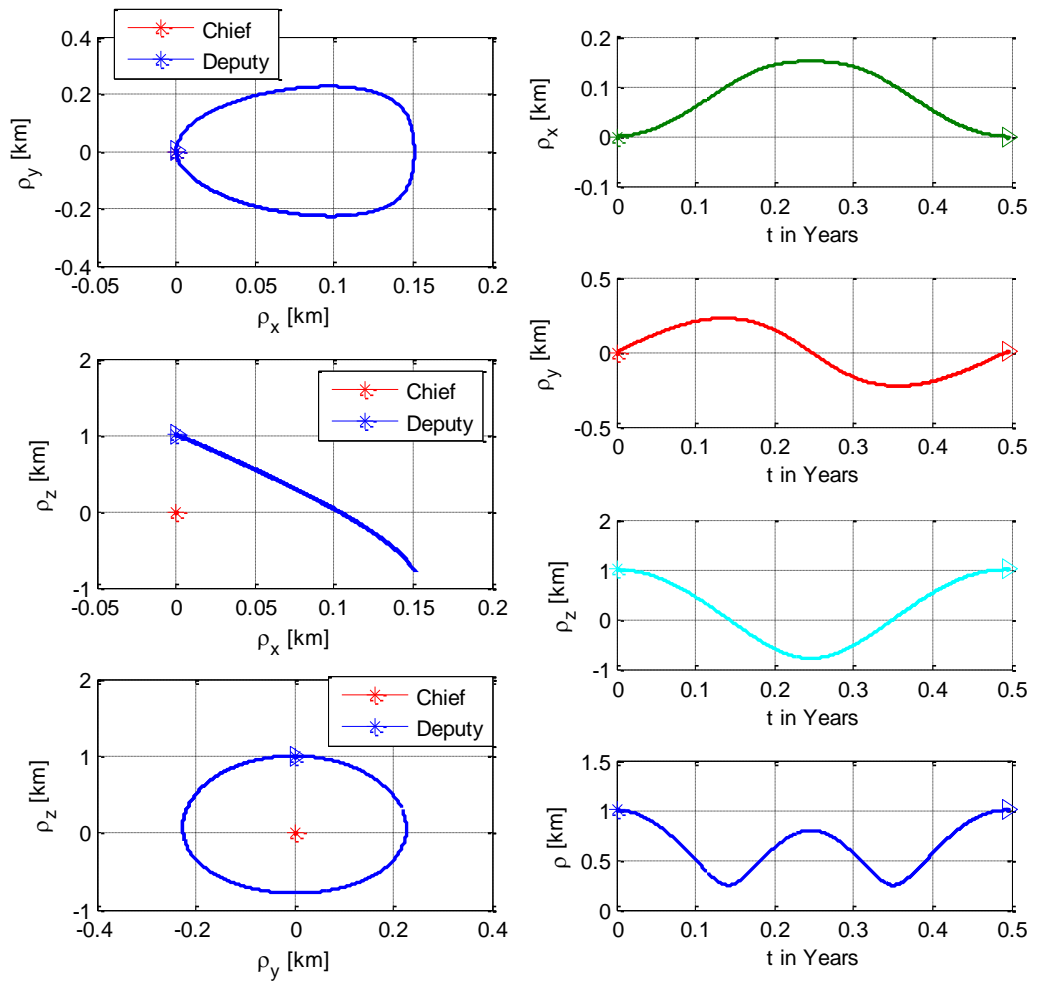Figure 4-66. SF-L2, Deputy #1: Projected and time dependent views

214
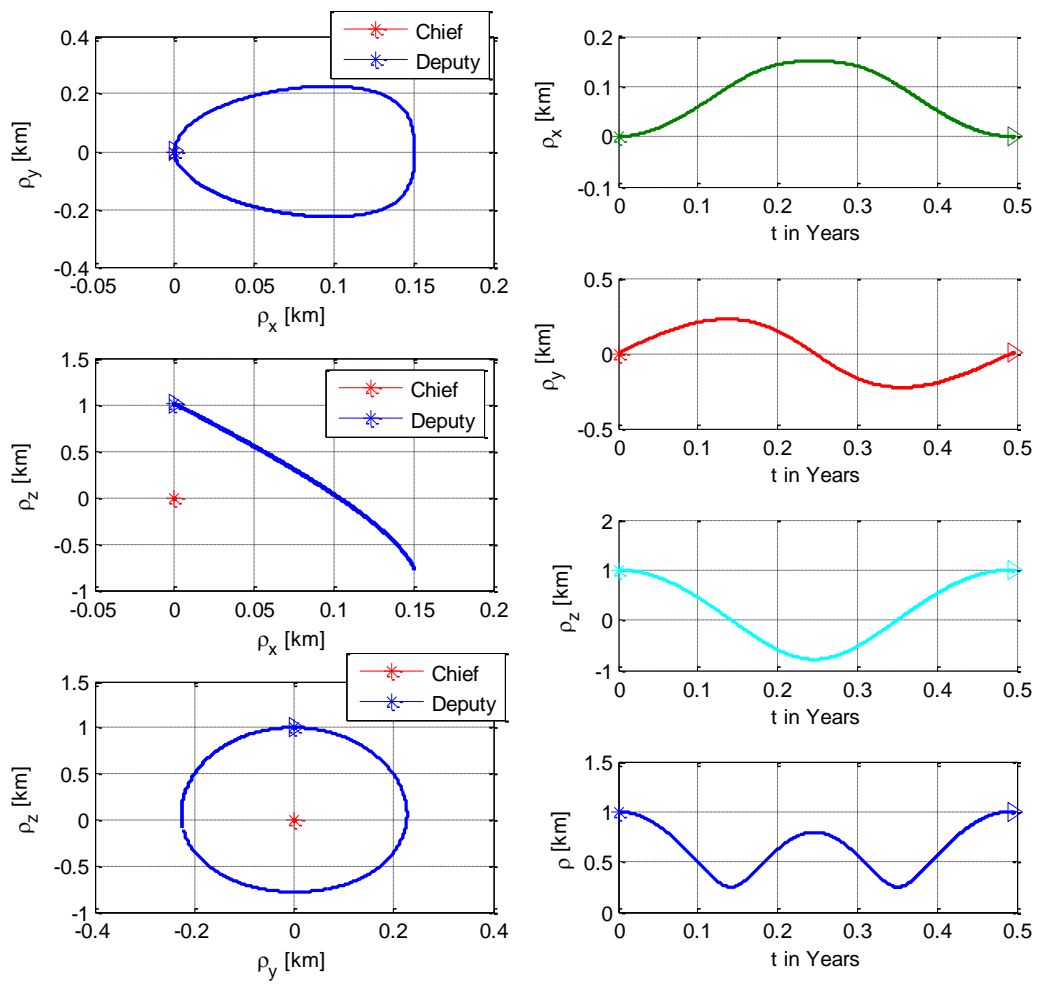
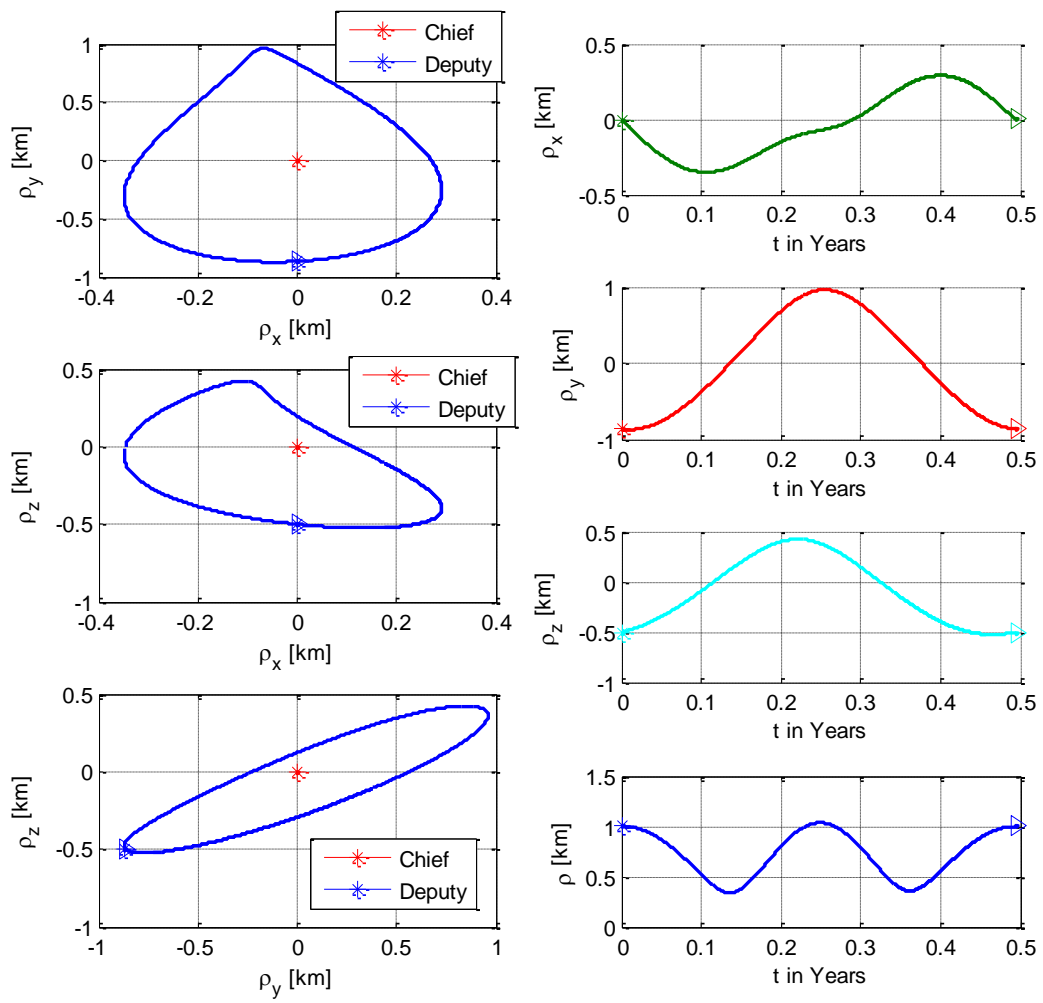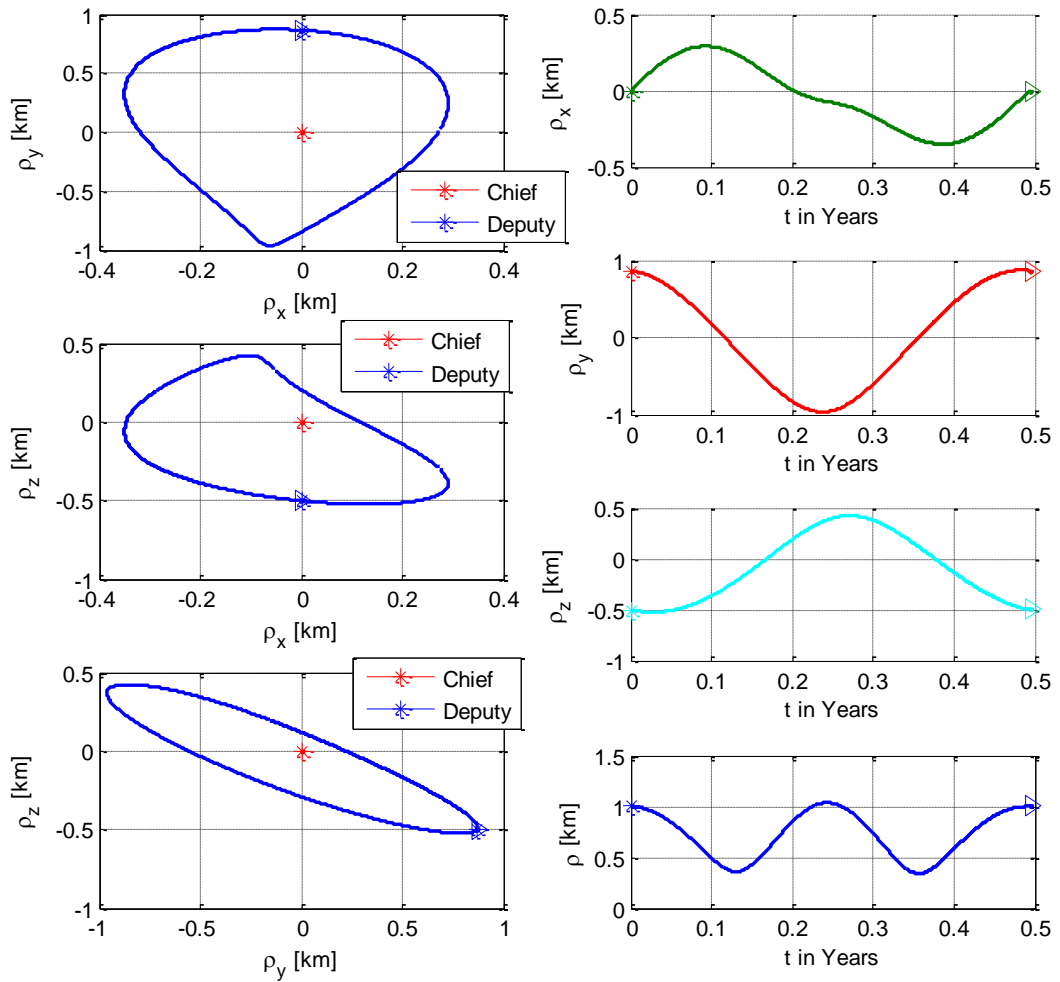Figure 4-67. SF-L2, Deputy #2: Projected and time dependent views
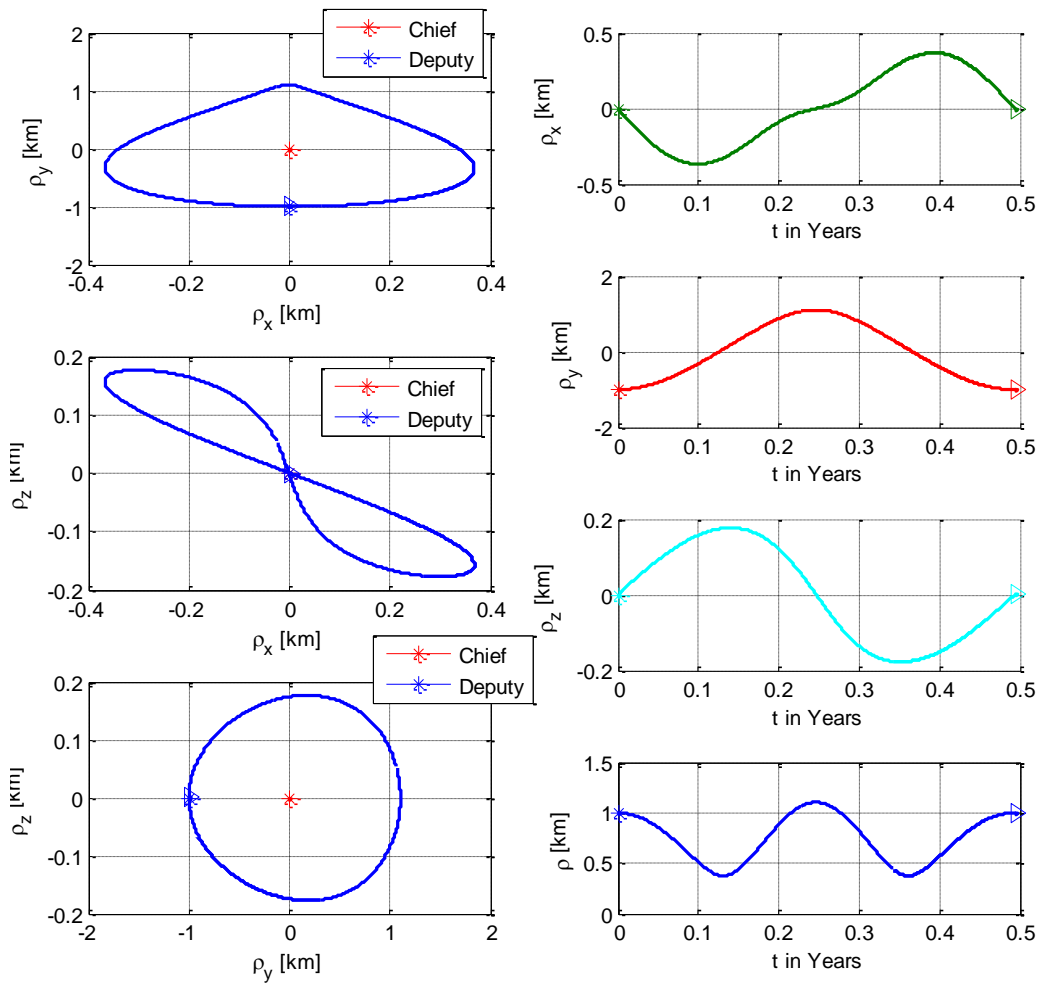
Figure 4-68. SF-L2, Deputy #3: Projected and time dependent views
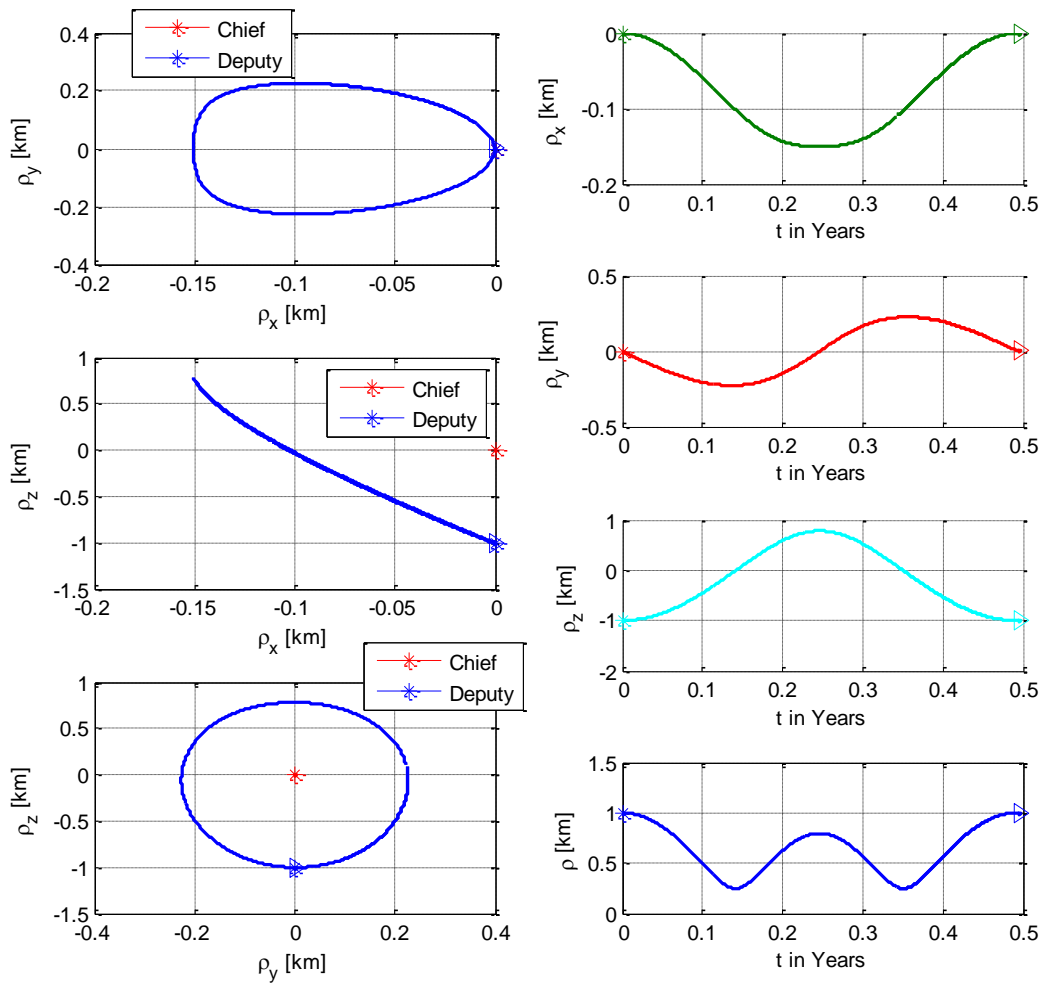
Figure 4-69. SF-L2, Deputy #4: Projected and time dependent views

The results show that the deputies initially located at y axis ($+y$ and $-y$ with equally distancing), the 1st and 3rd satellites, has a symmetrical trajectory with respect to the xz plane. It can be called skew-symmetric or diagonal symmetric. The 2nd and 4th satellites, initially located at z axis ($+z$ and $-z$ with equally distancing) have different types of symmetry with respect to the xz plane. In xz plane they have quasi one-dimensional motion, and there is a quasi-elliptical motion in yz plane.

The relative distances between deputies are not constant; they are given in Figure 4-70 and Figure 4-71. The objective distance from 1st to 2nd, 2nd to 3rd, 3rd to 4th and 4th to 1st deputy is $\sqrt{2}\rho = 1.414\ km$. The objective relative distance between 1st and 3rd deputies is $2\rho = 2\ km$, same for 2nd and 4th ones. The acquired formation shape

narrows and expands between this distance which is roughly 1.414 km and 0.50 km. This numbers are between 2 km to 0.75 km for the relative distance between 1st and 3rd, and from 2 km to 0.50 km for the 2nd and 4th deputies. This indicates that deputies located on y axis provide more acceptable formation flight behavior; they have less amplitude on relative distance oscillation. The constant relative motion is not obtained; however, a harmony is acquired between the deputies and Chief; a stable formation flight is made for one orbital period, which is approximately 0.5 Earth's Year for L2 point.
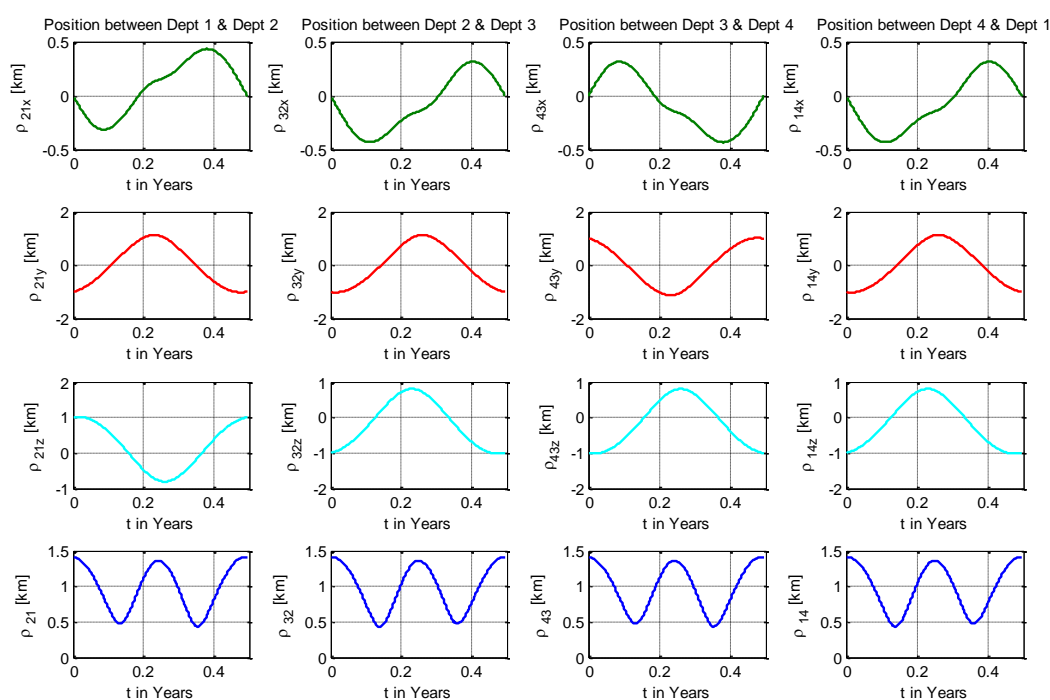
Figure 4-70. SF-L2: The relative distances between deputies
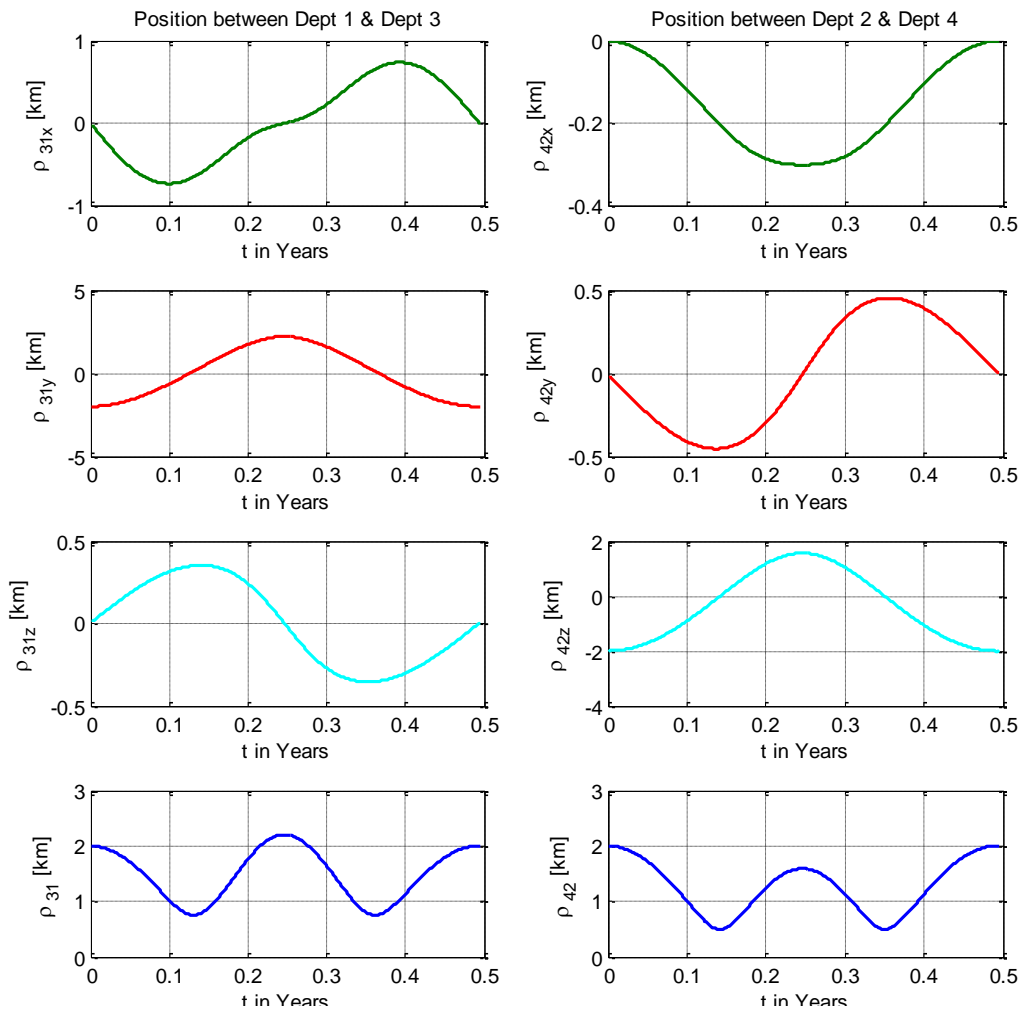
Figure 4-71. SF-L2: The relative distances between deputies-2
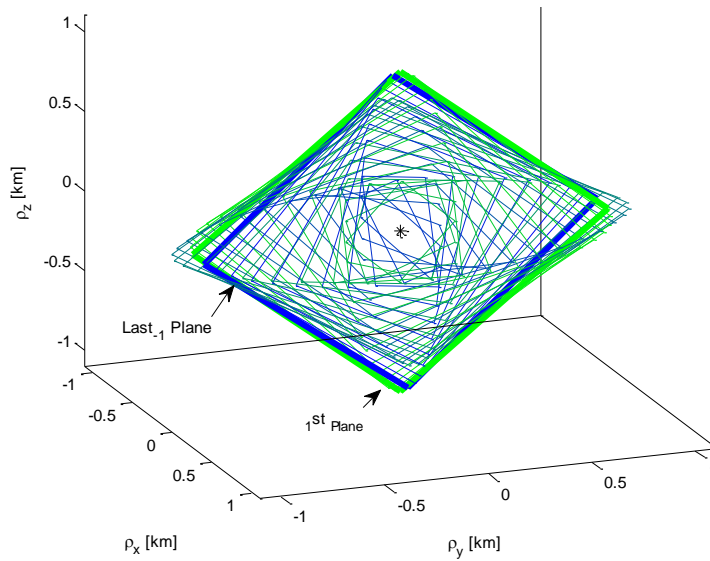
Figure 4-72. SF-L2: The plane formed by deputies

Figure 4-72 illustrates the change of the square formation schema. The bold green colored square is the starting and the bold blue one is the near last positions. The plane is colored from green to blue depending on time. This plane is narrowing until first and third quarter period, then it expands at the half and full period; last plane and first plane coincide since motion is periodic. A square shape configuration shows that the deputies initially located at y axis and at z axis provide different type of formation flight. For a mission that it is not required to transverse the xz plane located at Chief position; the deputies must be initially located on z axis. If the mission requirements force to transverse xz Chief's plane, it is necessary to initially locate the deputies on y axis. So, a formation cluster can be formed according to the mission needs by initially locating the deputies only on y axis or on z axis.

The next section contains the studies on finding the optimum initial elevation and azimuth angles; it presents the analyses about the relation between relative distance and optimum angle sets. For that reason, in this section, inclined square shape formation analysis for a constant inclination angle is not considered for formation around L2 as done for L1 case.

4.4.2. Optimum formation clusters and simulation results

This section presents the analyses carried out in order to find optimum relative initial position of the deputy; initial position that ensure the minimum deviation on relative distance ρ with respect to the chief satellite. First step, both elevation angle α and azimuth angle β are scanned from 0^0 to 180^0 with 10^0 increments, and the relative distance plots are given in Figure 4-73 for each of β with changes of α ($\alpha = [0^0: 10^0: 180^0]$, $and\ \beta = [0^0: 10^0: 180^0]$).
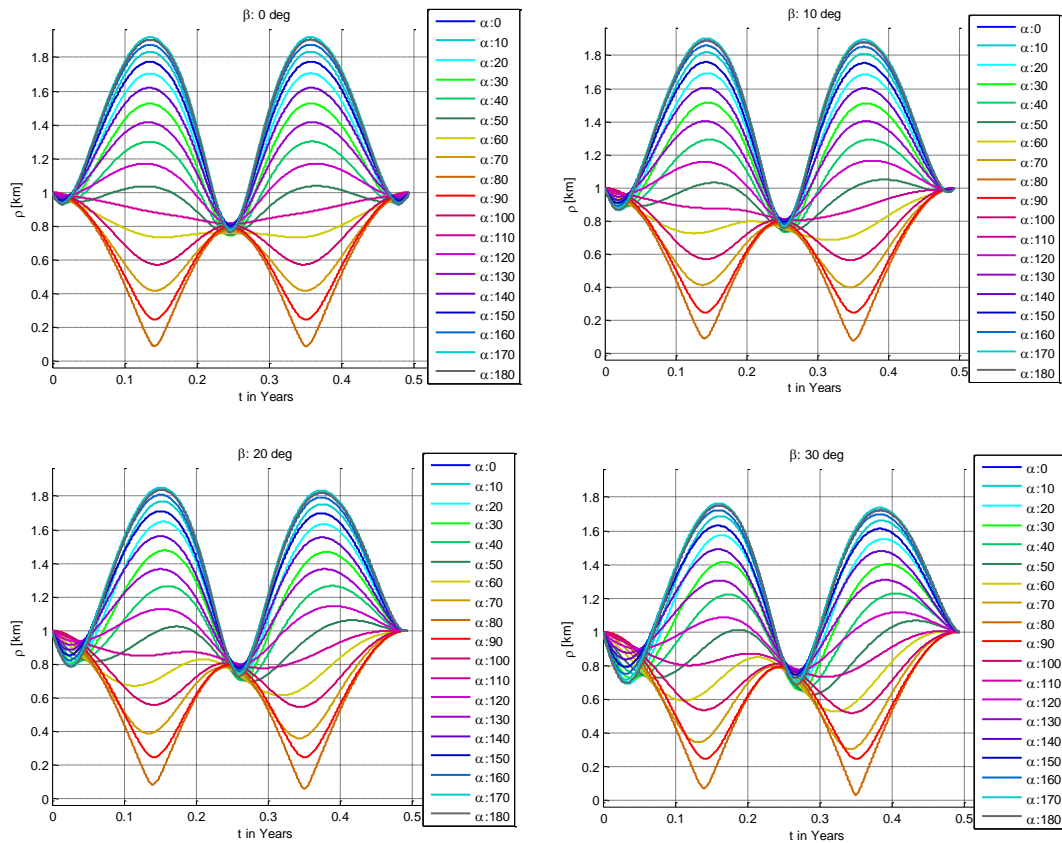
Figure 4-73. Relative positions depending on ICs, α and β angles, around L2
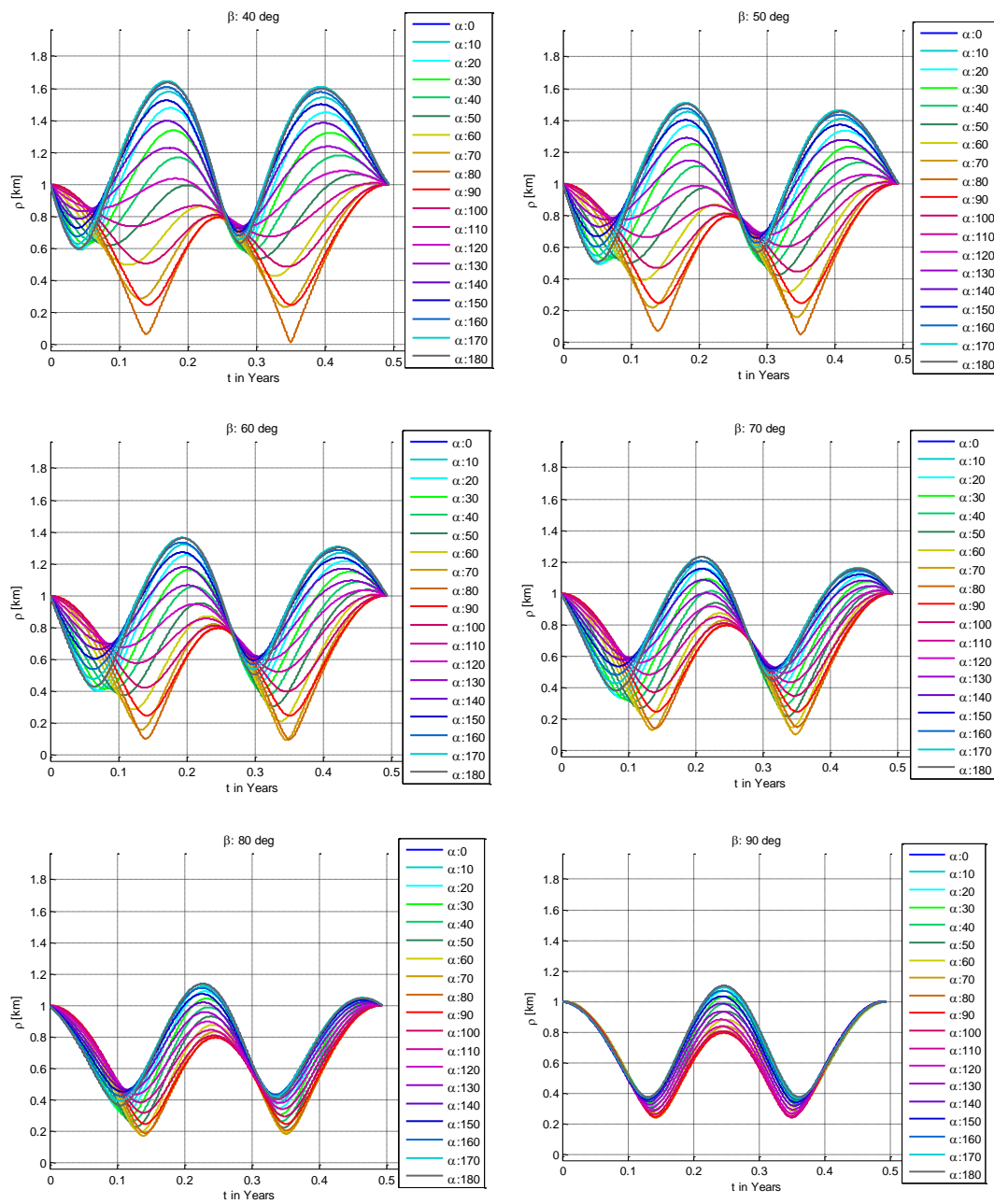
Figure 4.73. Relative positions depending on ICs, α and β angles, around L2 (cont'd)
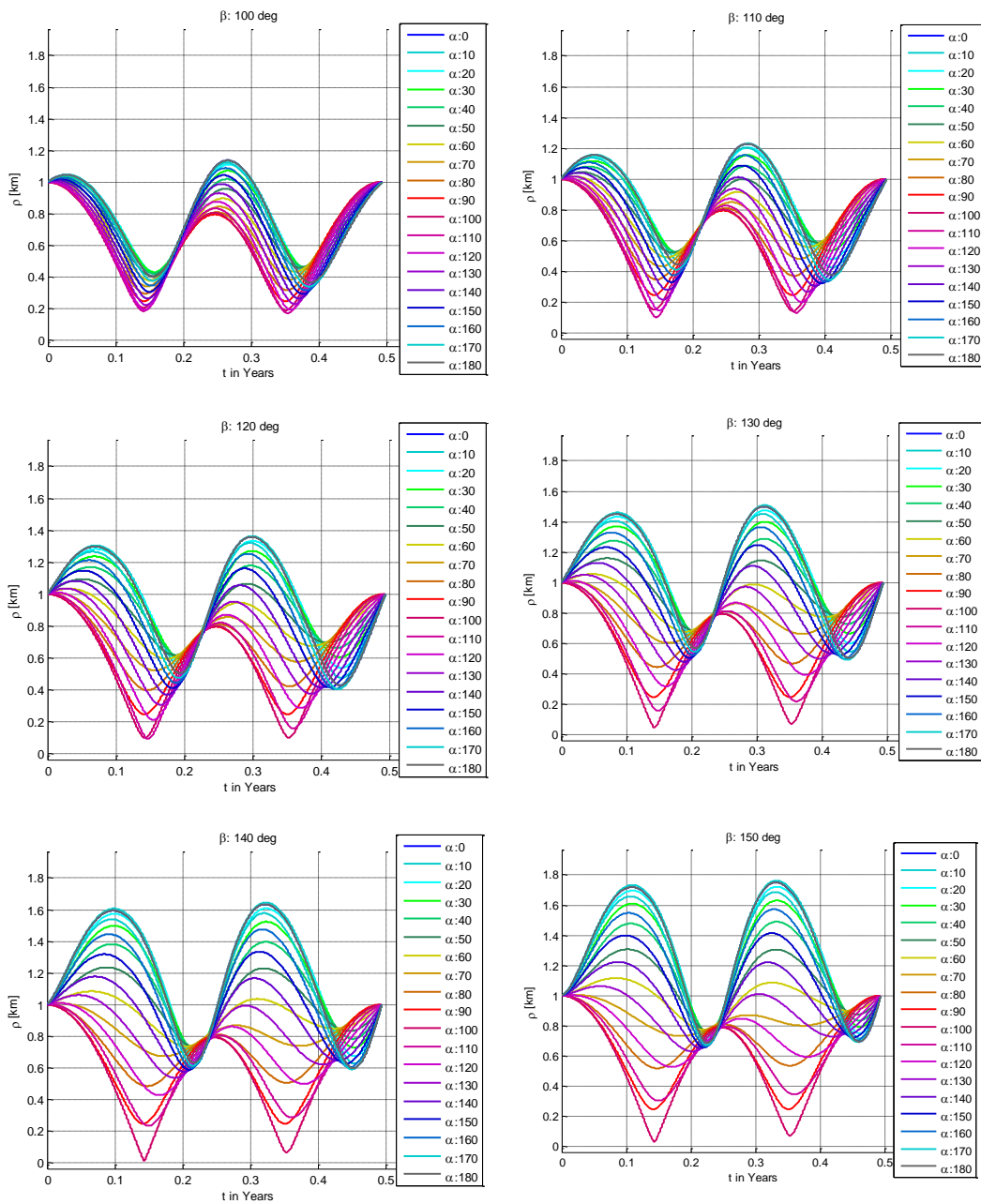
Figure 4.73. Relative positions depending on ICs, α and β angles, around L2 (cont'd)
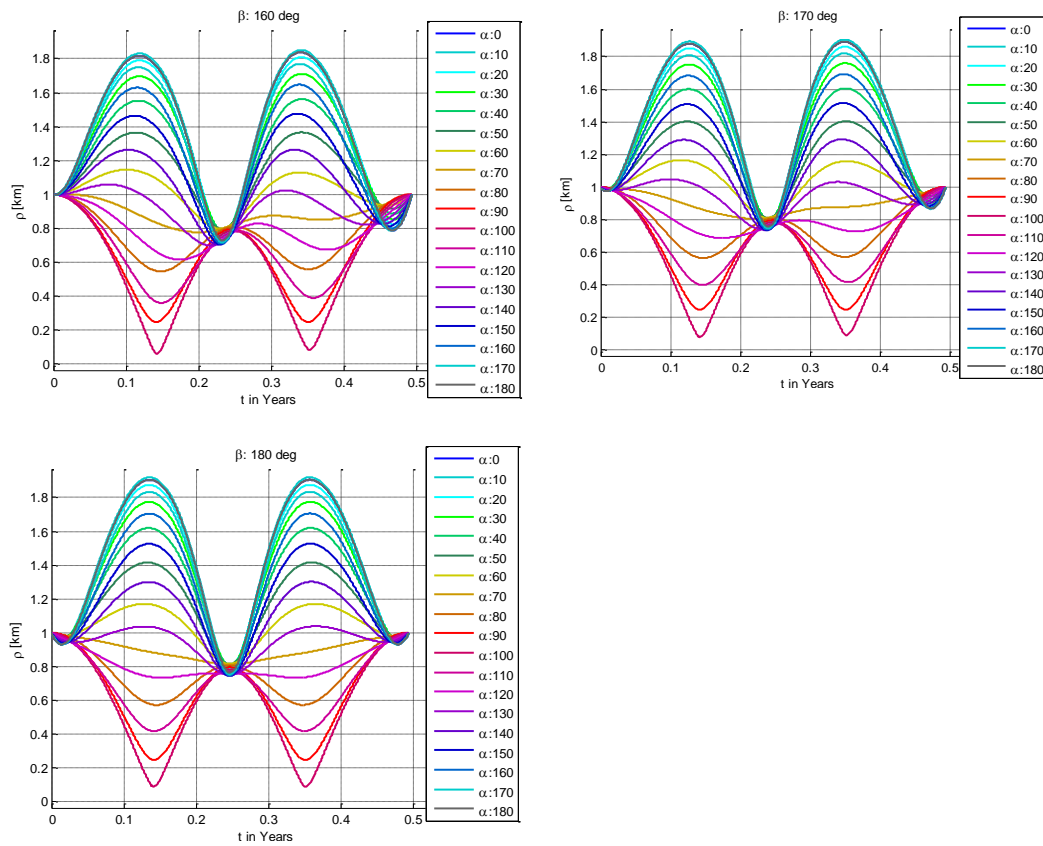
Figure 4.73. Relative positions depending on ICs, α and β angles, around L2 (cont'd)

First impression gets from the results, α between 110^0 and 130^0 gives minimum deviation in ρ for a β between 0^0 to 90^0. For β less than 30^0, $α = 110^0 - 120^0$ gives a one minimum point is seen at half period. However, for β greater than 30^0 and less than 160^0 two minimum points are seen in first and third quarter orbital period as minimum ρ, and one maximum point at half period. Again, one minimum point at half period is obtained for β greater than 160^0 and for $α = 70^0$. These results are re-evaluated statistically, as done in L1 case. For β less than 30^0, $α = 110^0 - 120^0$ gives a one minimum point, it is seen at half period. However, for β greater than 30^0 and less than 160^0 two minimum points are seen in first and third quarter orbital period as minimum ρ, and one maximum point at half period. Again, one minimum point at half period is obtained for β greater than 160^0 and for $α = 70^0$. The following

Figure 4-74 and Table 4.15 summarizes results obtained using those statistical parameters.
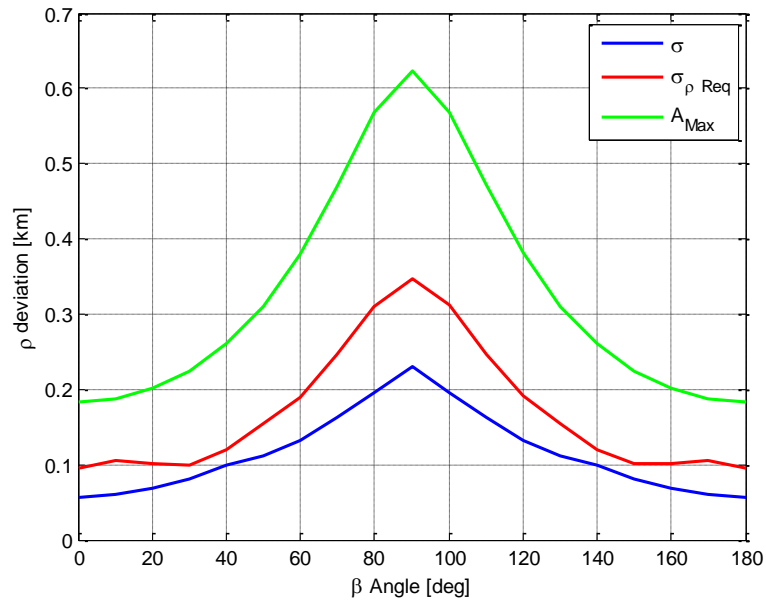
Figure 4-74. Statistical results of the relative position for β values around L2

Table 4.15. α that statistically provide minimum deviation for given β at L2

alpha values\ for beta:	0	10	20	30	40	50	60	70	80	90	100	110	120	130	140	150	160	170	180
sigma results STD:	110	110	110	110	110	120	120	120	130	140	50	60	60	60	70	70	70	70	70
sigma to rhoReq :	50	50	120	120	120	130	130	140	150	180	30	40	50	50	60	60	60	130	130
dA(rho-rhoReq):	120	120	120	120	130	130	130	140	150	0	30	40	50	50	50	60	60	60	60

Results shows that minimum amplitude is obtained for $\beta = 0^0$ (with $\alpha = 110^0 - 120^0$)and for $\beta = 180^0$ (with $\alpha = 70^0$). This result is also valid for standard deviation σ computation. But, $\sigma_{\rho Req}$ statistic gives different results for some cases: $\beta = 0^0 - 10^0$(with $\alpha = 50^0$)and for $\beta = 170^0 - 180^0$ (with $\alpha = 130^0$). For that reason it is necessary to perform more fine analyses between those angle values, they are given as follows.

Table 4.16. Selected cases of β's for fine analyses for L2

Case-1:	$\beta = [0^0 : 1^0 : 10^0] \ with \ \alpha = [105^0 : 1^0 : 115^0]$
Case-2:	$\beta = [170^0 : 1^0 : 180^0] \ with \ \alpha = [65^0 : 1^0 : 75^0]$

For case-1 the minimum value of ρ is obtained for $\beta = 0^0$, and the α values that gives the minimum deviation is $\alpha = 110^0 - 112^0$, as seen in Figure 4-75 and Figure 4-76:
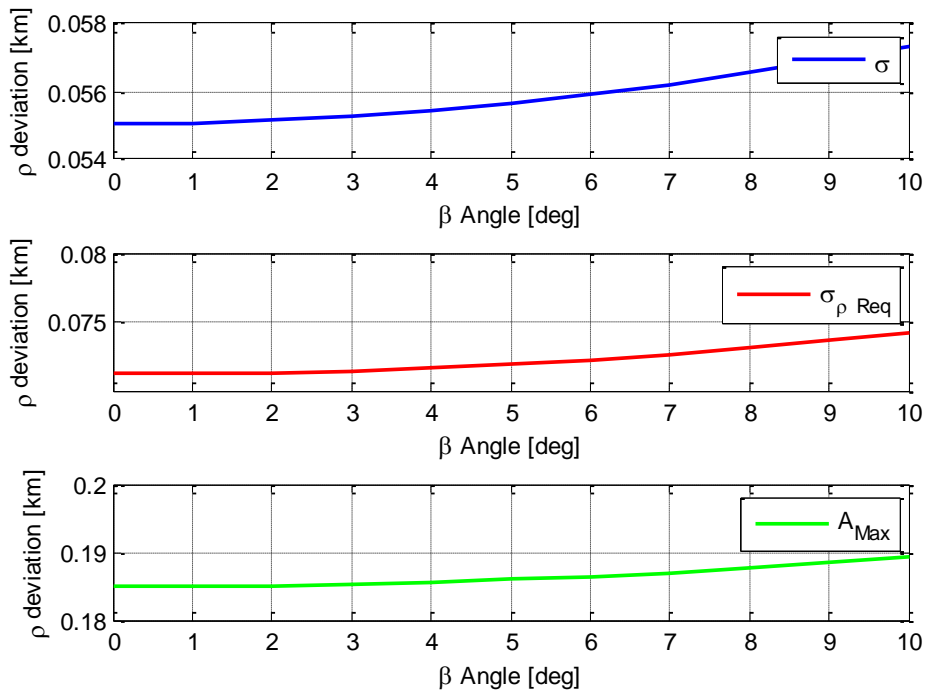
Figure 4-75. Deviation statistics for different β 0 to 10 degree for L2
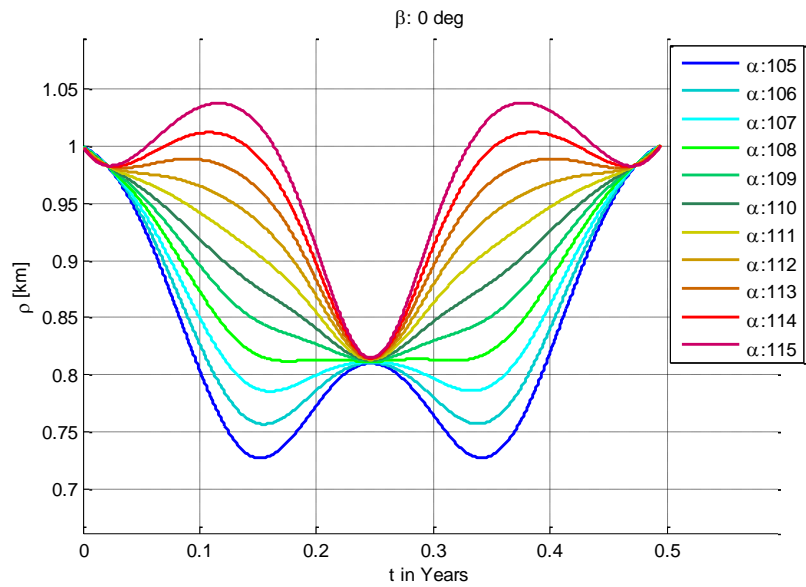
Figure 4-76. Deviation for zero β and α 105 to 115 degree for L2

For case-2 the minimum value of ρ is obtained for $\beta = 180^0$, and the α values that gives the minimum deviation is $\alpha=68^0 - 70^0$, as seen in Figure 4-77 and Figure 4-78:
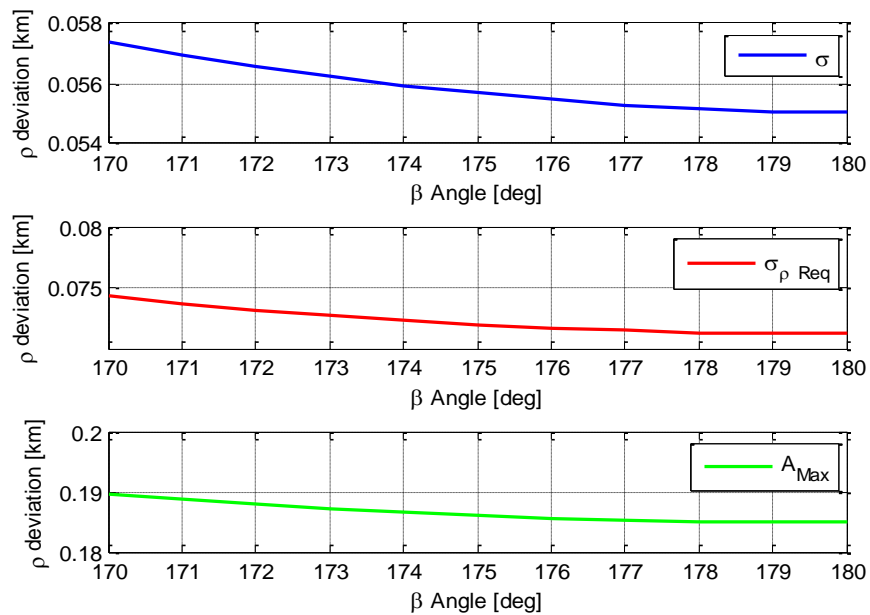
Figure 4-77. Deviation statistics for different β 170 to 180 degree for L2
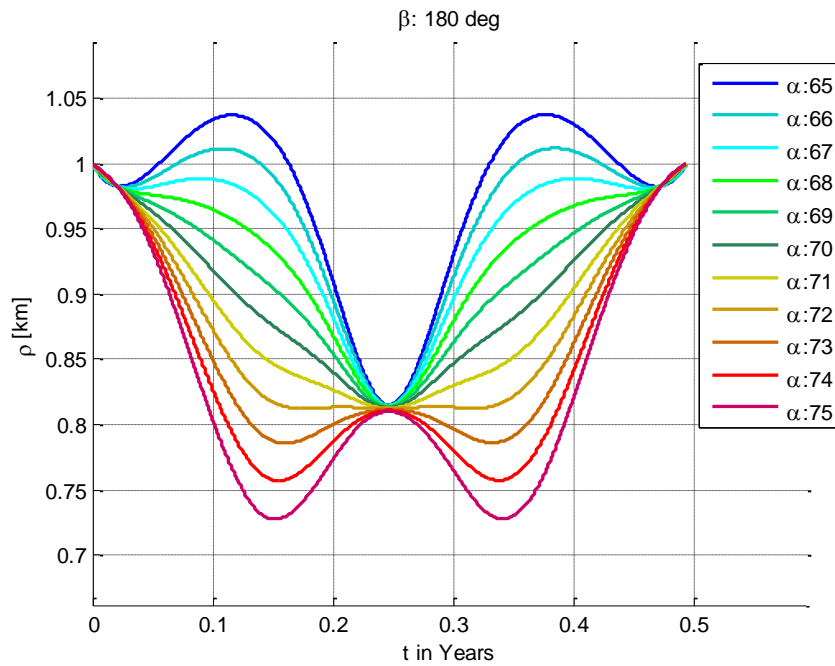
Figure 4-78. Deviation for zero β and α 65 to 75 degree for L2

As indicated in L1 case, for L2 also the results obtained for the Case-1 and Case-2 are symmetric, in other words they are geometrically the reciprocal points on the same plane.

4.4.2.1. Inclined square shape formation with optimum elevation and azimuth angles

This section presents the result obtained for a formation schema having inclined plane with an elevation angle regarding to the xy plane. Here, firstly, elevation angle from 0^0 to 180^0 with 10^0 increments is analyzed to examine the relative distance obtained with respect to the chief. There exist 19 different cases for $\alpha = [0^0: 10^0: 180^0]$ with $\beta = 0^0$. The trajectories obtained in three dimensional views are shown in the following figures, and the projected views, relative distances with its components.
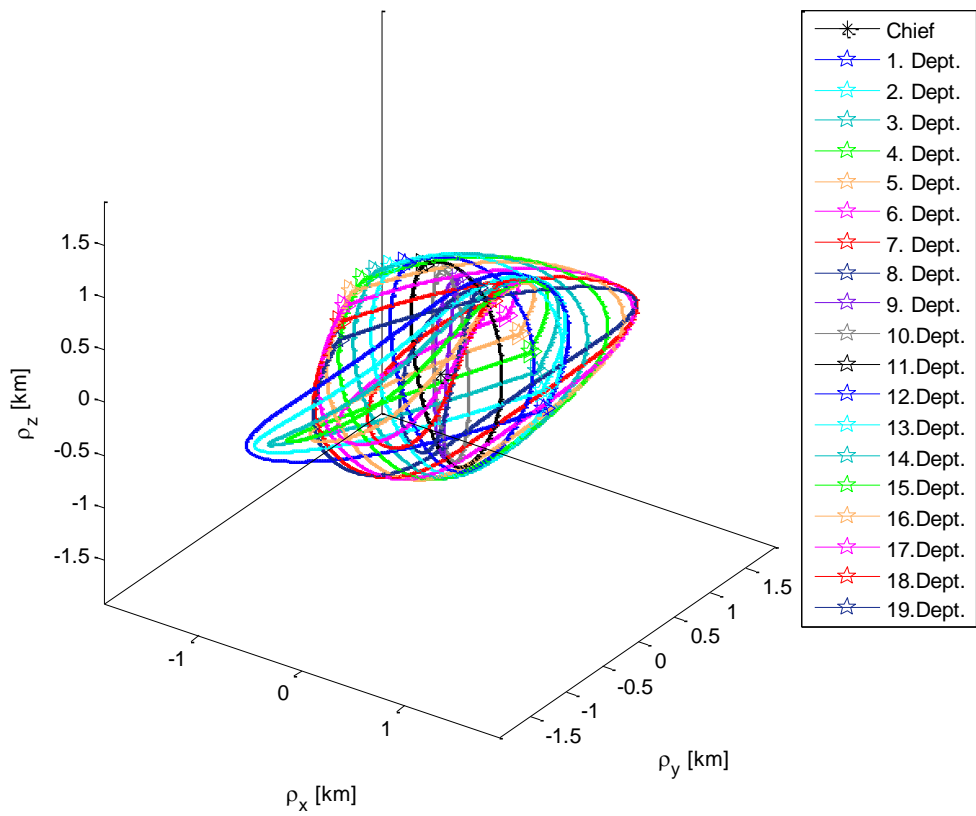
Figure 4-79. 3D view of 19 different cases for L2: α from zeros to 180 degree
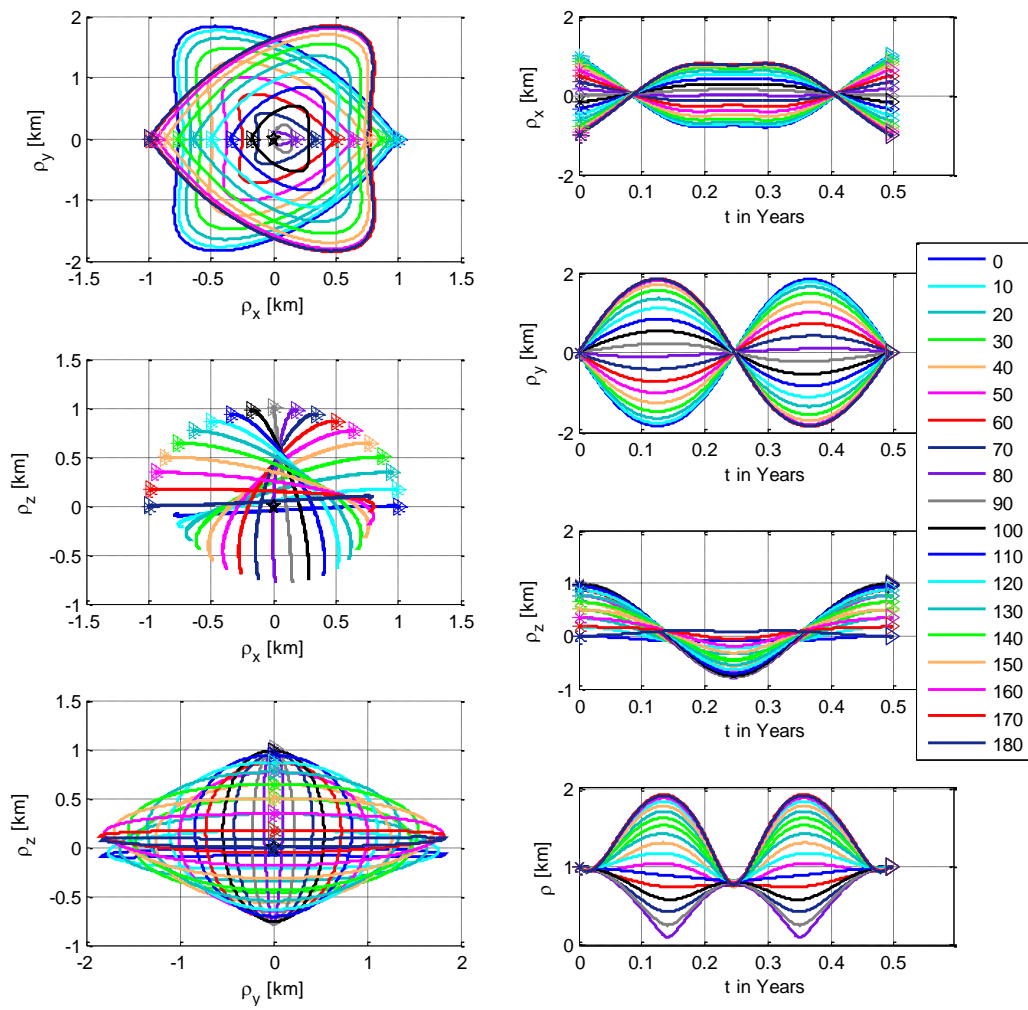
Figure 4-80. 2D view of 19 different cases for L2: α from zeros to 180 degree
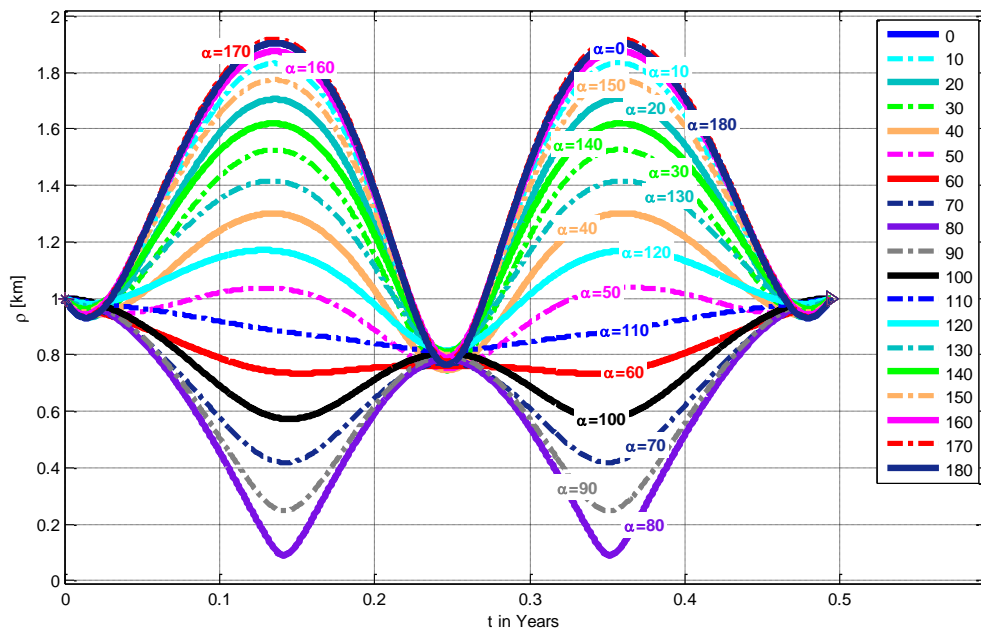
Figure 4-81. Relative position for α zeros to 180 degree around L2
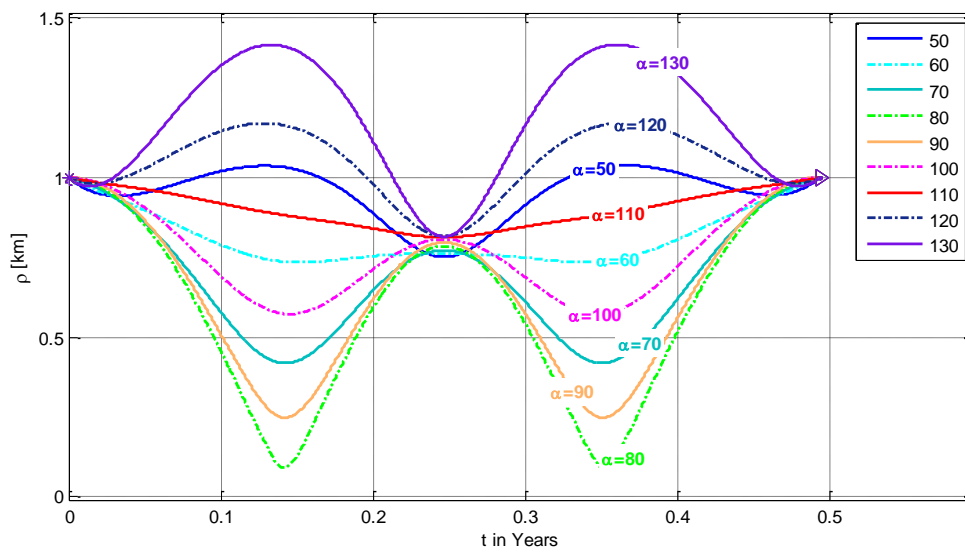
Figure 4-82. Relative position for α from 50 to 130 degree around L2

Figure 4-82 shows that the inclination of the plane affects the deviation of the relative distances, less deviation is obtained around $\alpha = 110^0$, ρ changes between $1\ km$

to $0.82\ km$. All ρ coincides around $0.75\ km - 0.82\ km$ at half period, and forms extrama at 1ˢᵗ quarters and 3ʳᵈ quarters, in positive and negative direction depending on the α value. Around $\alpha = 110^0$ the extrama disappear and smoothest deviations are acquired at half period, maximum deviation is about $0.2\ km$ for this elevation value.
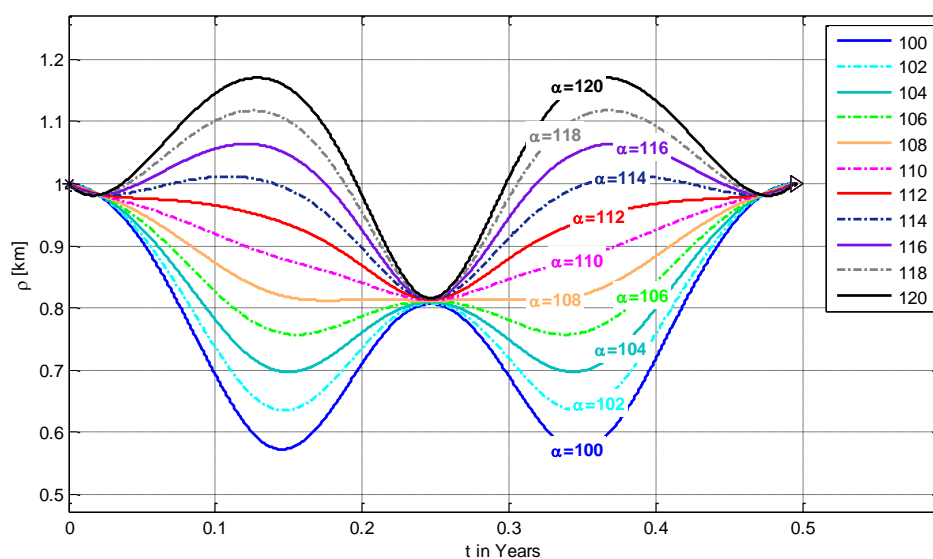
Figure 4-83. Relative position for α from 100 to 120 degree around L2

As a second step, $\alpha = 110^0$ is refined and for an interval from 100^0 to 120^0 with 2^0 increments. Here, it can be stated that ρ has only one extramum point just only at half period for an α between $108^0 and\ 114^0$. The only difference among them is the change of ρ towards this extramum. For instance, when $\alpha = 114^0$ ρ begins to deviate from required value at 0.1 years. Approximately linear changes before and after half period is obtained around $\alpha = 110^0 - 112^0$. The deviation starts rapidly and downsizing for $\alpha < 110^0$ and rapidly growth for $\alpha > 114^0$. The relative distance has a value greater than required distance ρ for α greater than 114^0 .
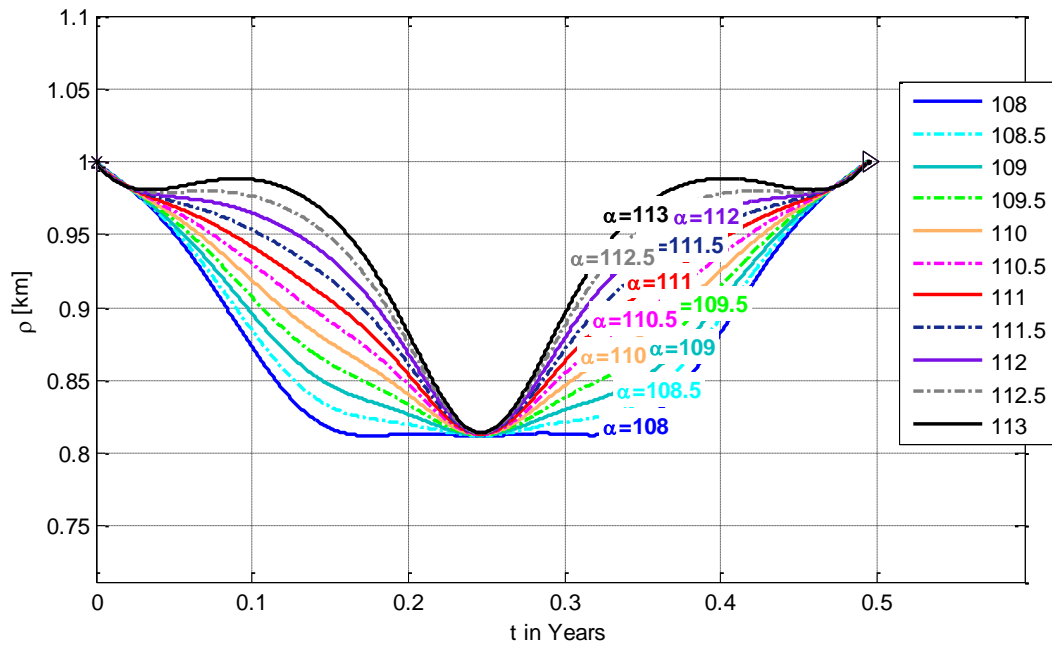
Figure 4-84. Relative position for α from 108 to 113 degree around L2

This refined analyze shows that the most resistant result is get for $\alpha = 113^0$, but the rate of change toward minimum point $\rho = 0.82\ km$ is high. The most uniformly change is obtained for $\alpha = 110.5^0$, decreasing rate to minimum and increasing rate form minimum distance are nearly linear.

Here after, for the formation clusters given in the next subsections, the elevation angle is taken as $\alpha = 110.5^0$ and its complement to 180^0 $\alpha = -69.5^0$ for a constant azimuth $\beta = 0^0$. So, two deputies with these initial conditions form a formation flight as presented in Figure 4-85 and Figure 4-86.

The 3D view of the deputies' trajectory:
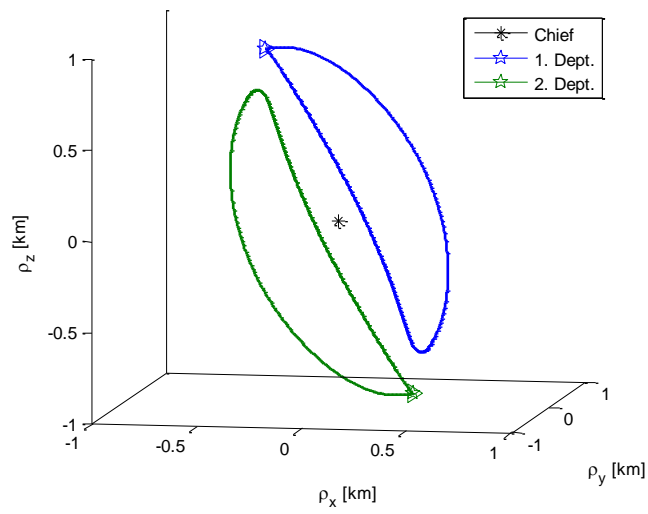
Figure 4-85. 3D Trajectory of 1st and 2nd deputies for Optimum ISF around L2
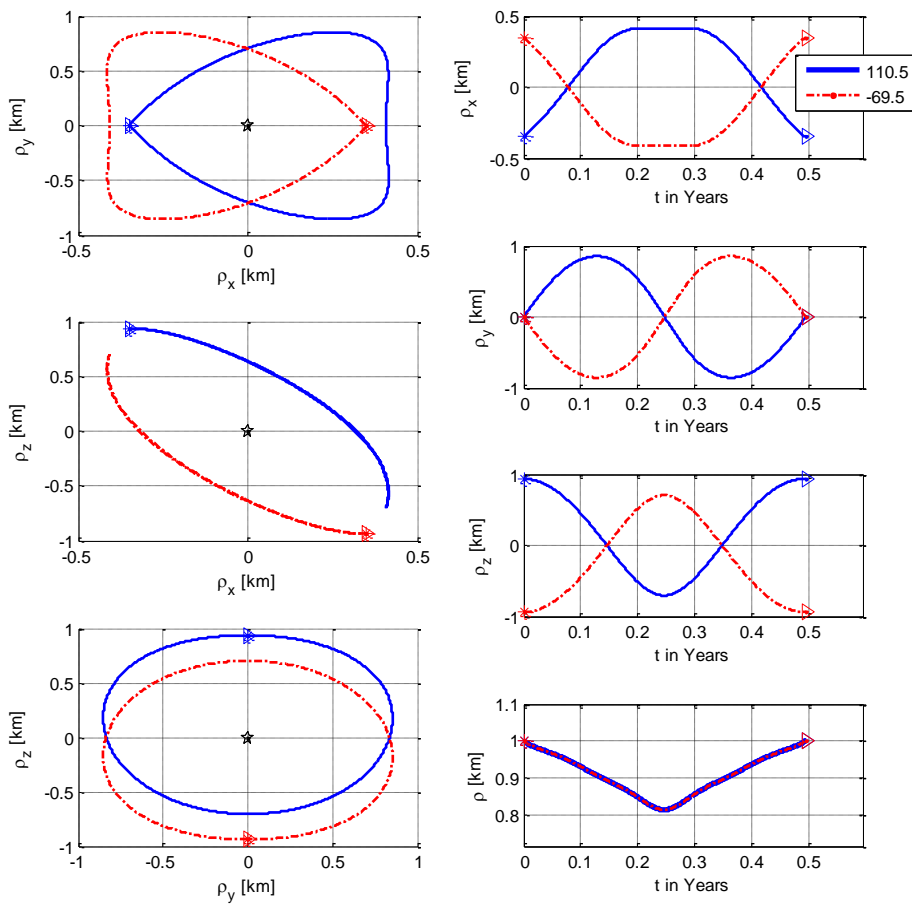
Figure 4-86. Relative position of 1st and 2nd deputies, optimum ISF around L2

234

For the formation designed at L2, it can be stated that the minimum relative distance deviation for one deputy that can be obtained is approximately 0.20 km. Finally, it is an option to add two more satellites on y axis in order to form a formation configuration having four deputies, as done in the previous sections. The behavior of the plane formed by these 4 deputies is given in Figure 4-87. The distances between deputies can be seen in Figure 4-87 and in Figure 4-88 to Figure 4-90 as well, that time dependent values are given.
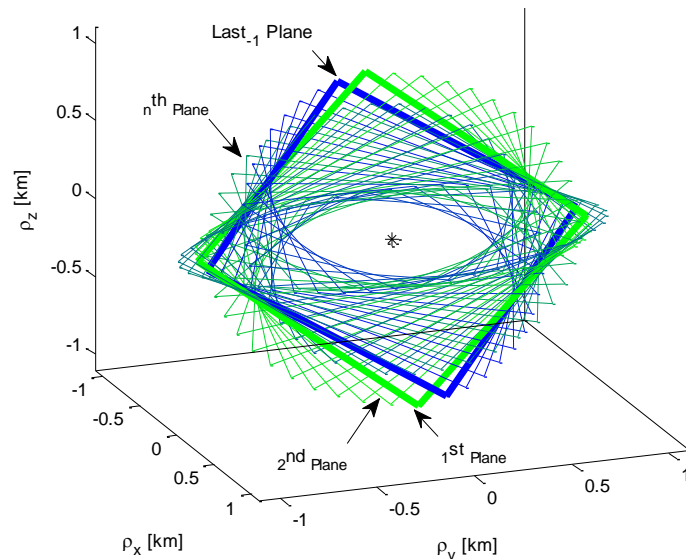
Figure 4-87. Plane formed by four deputies for optimum ISF around L2
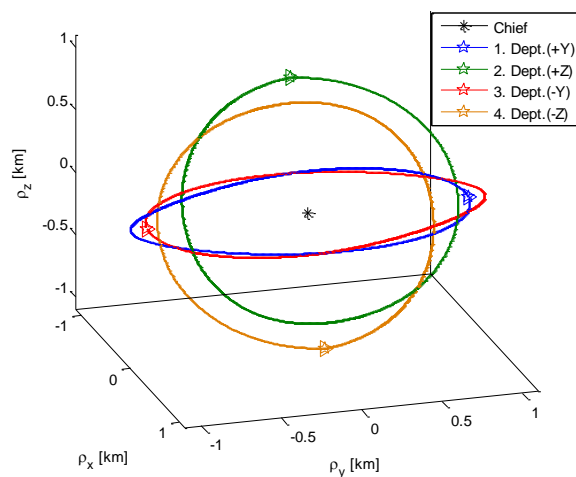
Figure 4-88. Relative trajectories for optimum ISF around L2
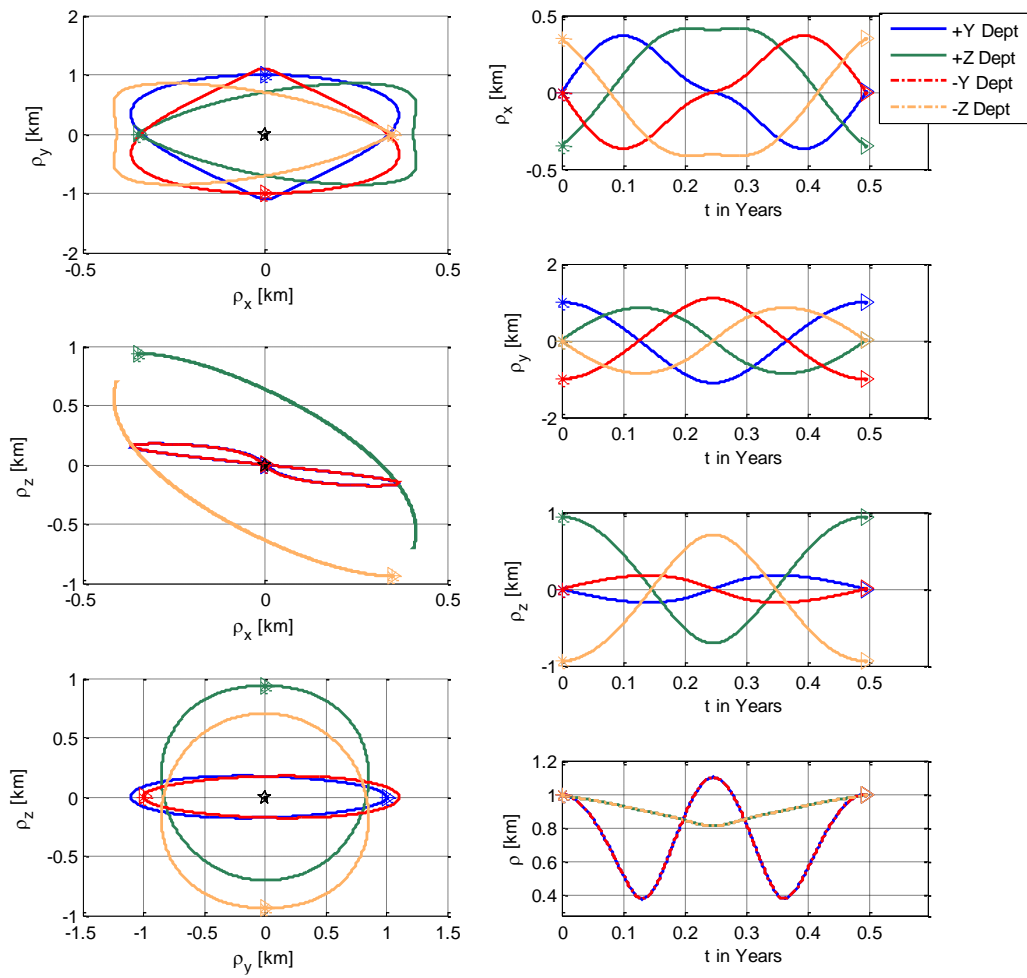
Figure 4-89. Projected and time dependent views for optimum ISF around L2
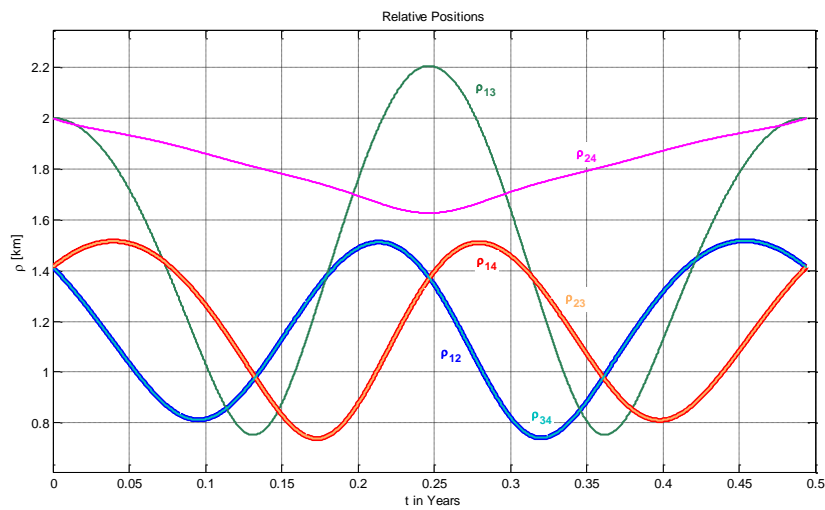
Figure 4-90. The relative distances between deputies for optimum ISF around L2

236

The relative distances between deputies are given in Figure 4-90, distances between neighborhood deputies (1-2, 2-3, 3-4 and 4-1). Neighborhood distances vary between $1.5\ km$ to $0.75\ km$. Geometrical initial relative distance is $\sqrt{2}\rho = 1.414\ km$. Scanning method is used for β azimuth angle and it is obvious that minimum deviation on relative distance is get at near $\beta = 90^0$ for $\alpha = 0^0$. It is shown in bold gray line in Figure 4-91.
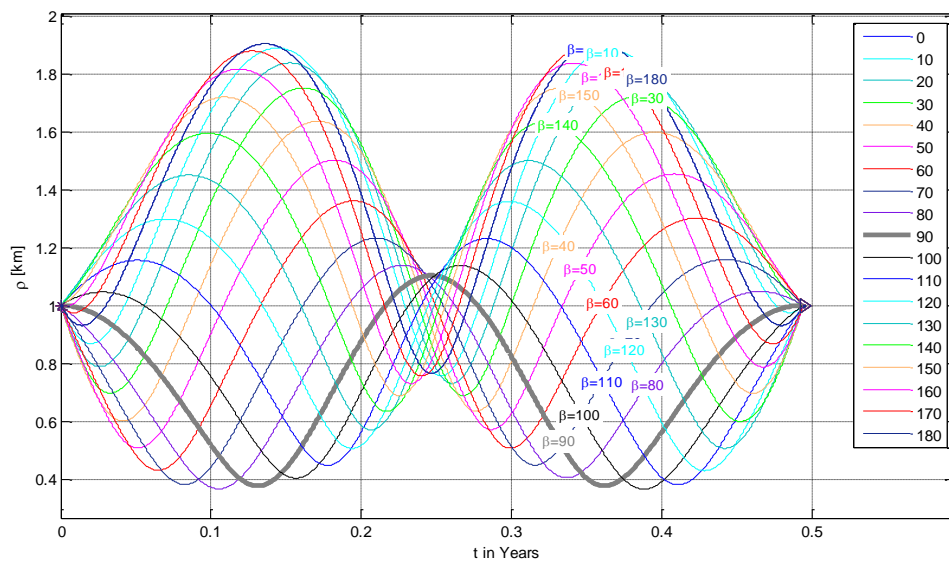
Figure 4-91. Relative distance changes for β scanning around L2

A complete scanning for both β and α to find optimum relative distance is also performed. This section has presented the studies performed to find an optimal elevation angle for deputy satellite and as a consequently, the next section proposes the formation schema composed of multiple satellites initially located at this elevation angle with different initial relative distances.

4.4.2.2. Aligned and uniformly equally separated formation

This part presents a formation composed of four deputy satellites, but aligned and initially positioned at $1.0\ km$ distance from each other successively. The initial desired elevation angle is taken optimum elevation angle with zeros degree azimuth angle. So, the formation configuration is given in the following Table 4.17. Again, the abbreviation UAF is used for uniformly aligned formation.

Table 4.17. Relative positions of deputies, UAF around L2

Deputy Satellite 1	Deputy Satellite 2	Deputy Satellite 3	Deputy Satellite 4
$\rho = 1\ km$	$\rho = 2\ km$	$\rho = 3\ km$	$\rho = 4\ km$
$\beta = 0^0$	$\beta = 0^0$	$\beta = 0^0$	$\beta = 0^0$
$\alpha = 110.5^0$	$\alpha = 110.5^0$	$\alpha = 110.5^0$	$\alpha = 110.5^0$

The trajectories obtained and relative distances are given in Figure 4-92 to Figure 4-95:
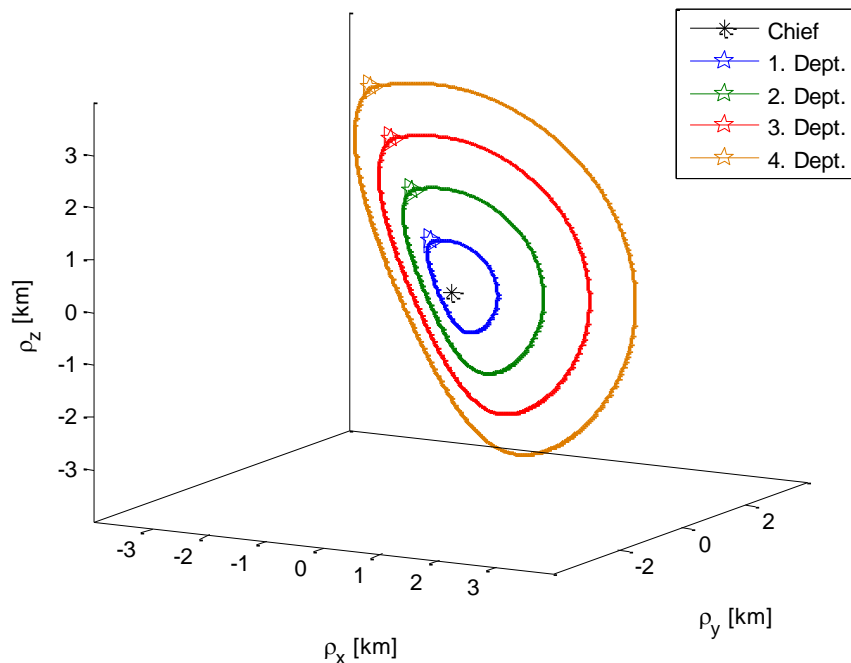
Figure 4-92. Trajectory of the deputies with respect to chief for UAF around L2
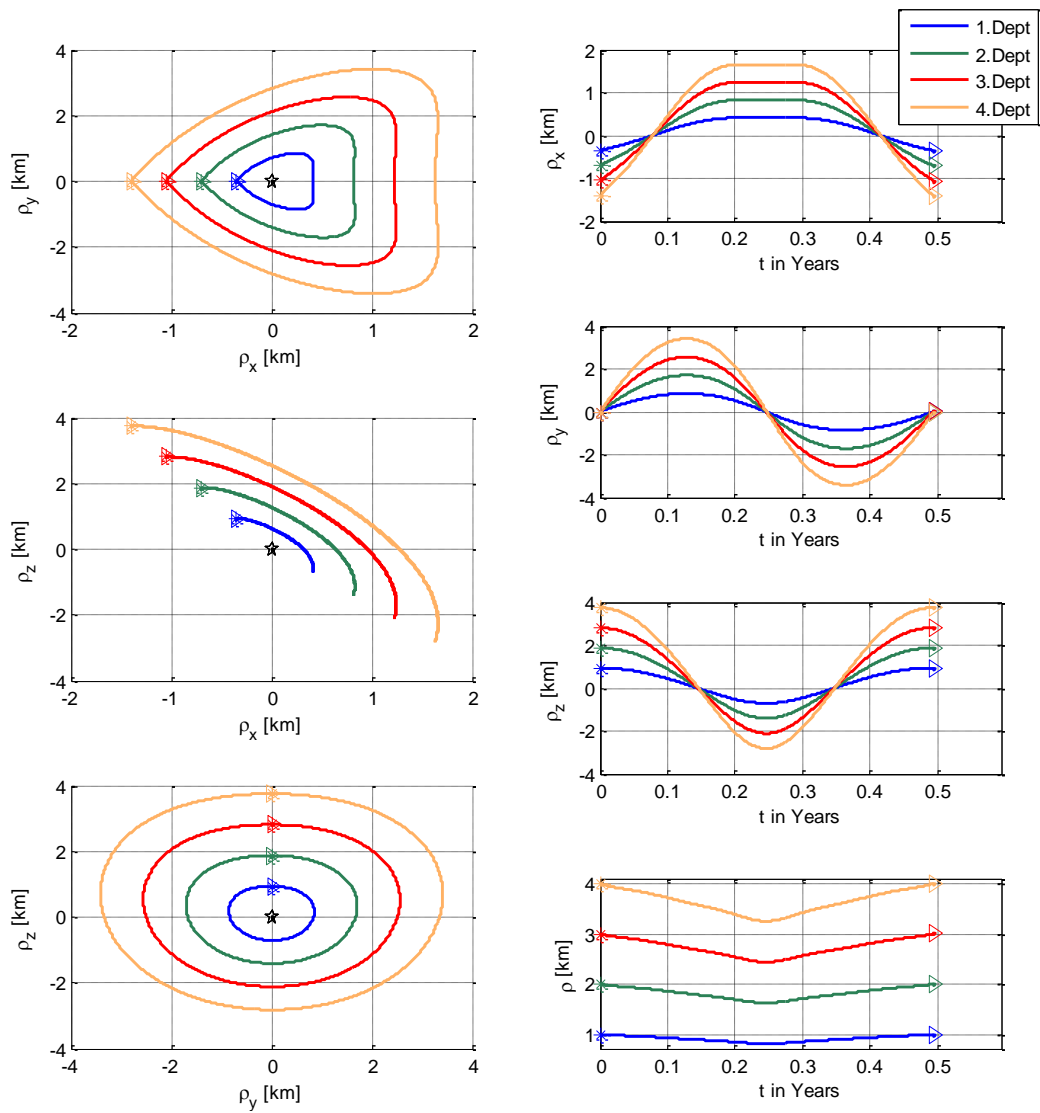
Figure 4-93. Projected and time dependent views for UAF around L2
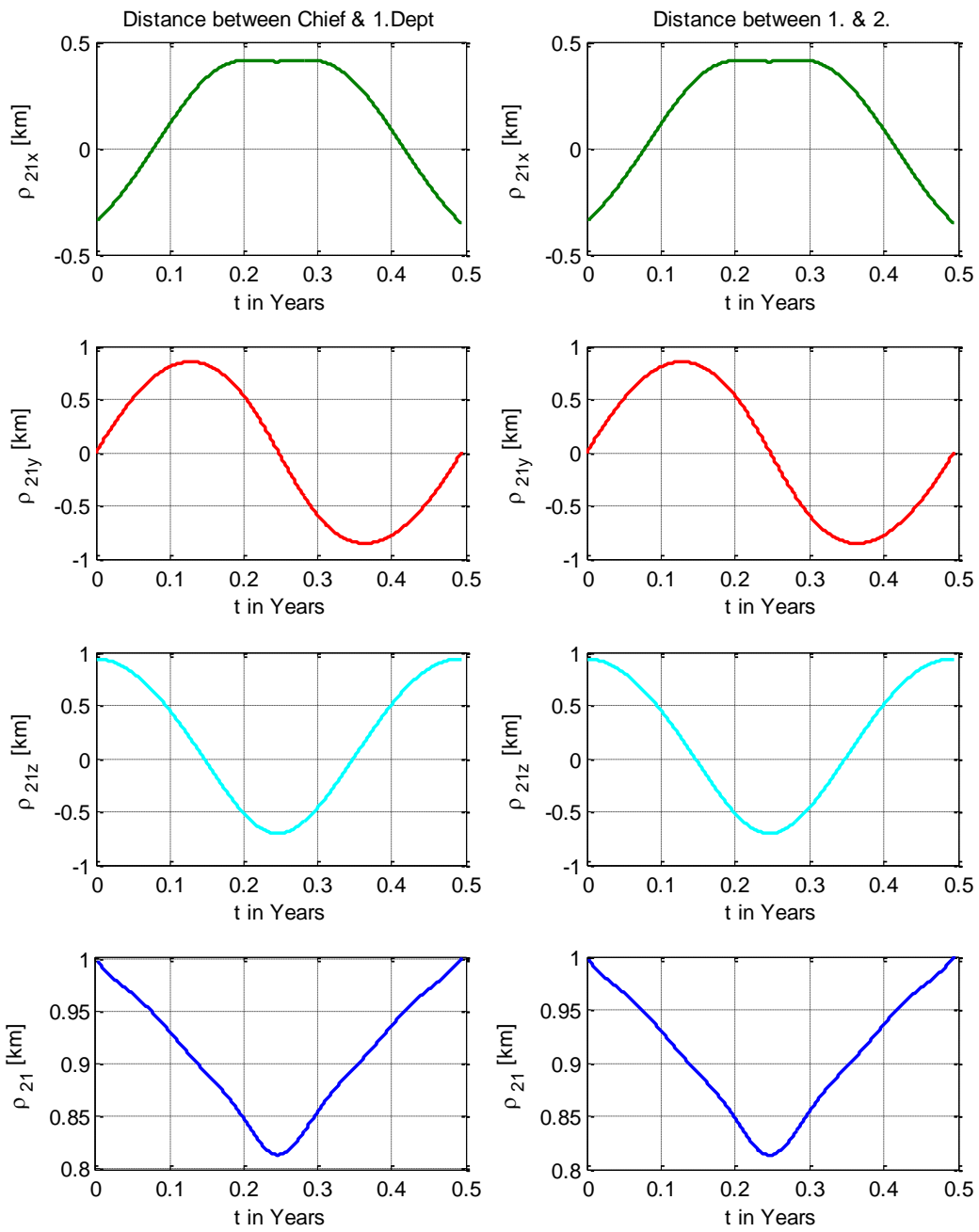
Figure 4-94. Relative distances between deputies for UAF around L2
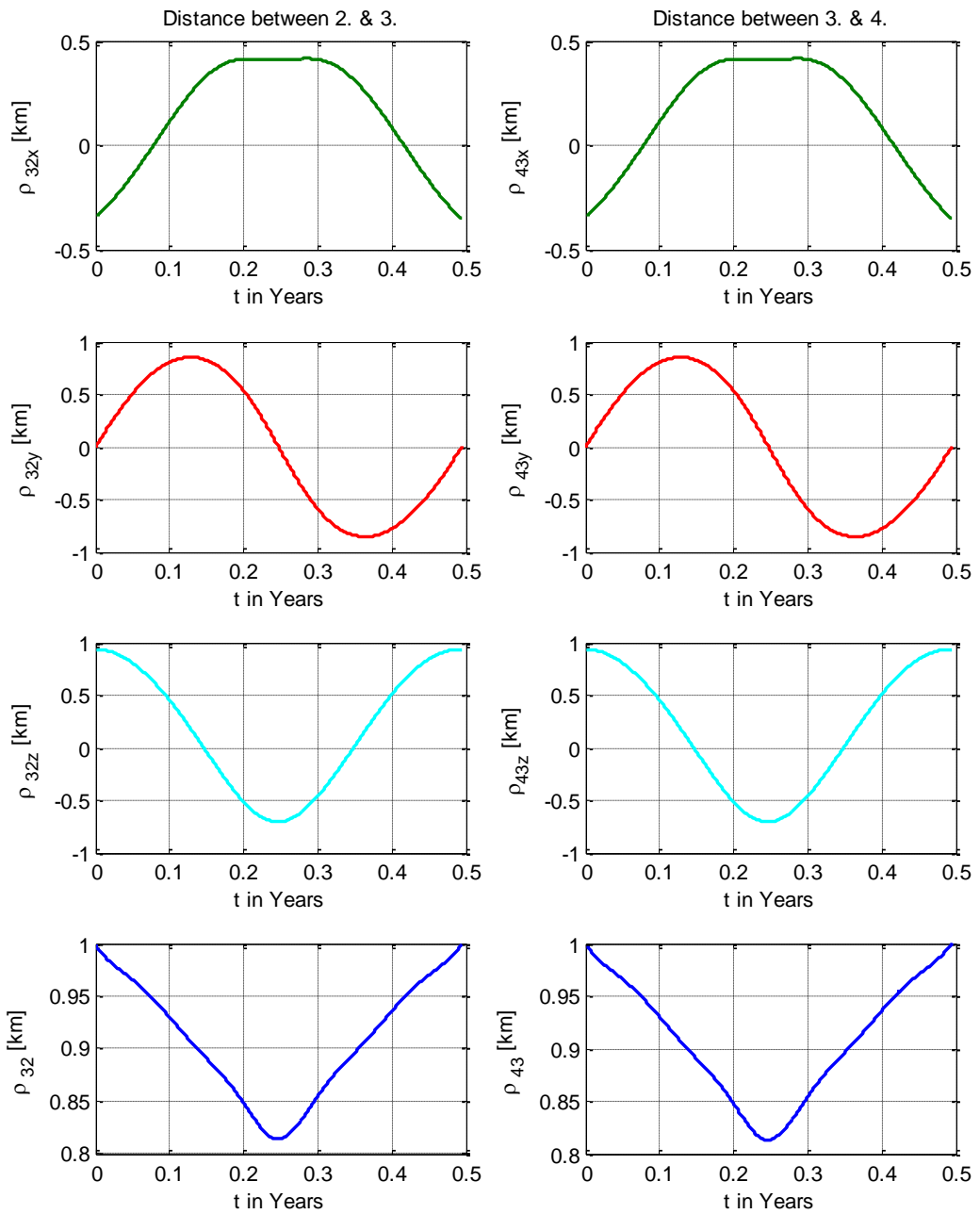
Figure 4-95. Relative distances between deputies for UAF around L2 - 2

As seen from the results, the relative distance behavior of the satellites positioned consecutively are similar, and the drifts are between $1.0\ km$ to $0.80\ km$ as the optimum elevation angle is selected as initial relative position. This kind of formation

cluster is really very powerful for the missions aimed a constant distance changes between each successive satellite.

In this section it is obtained that minimum changes on relative distance is acquired for a formation having a plane with an inclination angle defined by elevation angles equal to the $\alpha = 110.5^0$ and $\alpha = -69.5^0$ for L2 point. For missions that requires to maintain the relative distance between satellites consecutively, the formation given above is a ideal solution, and the same number of satellites can be positioned symmetrically at $\alpha = -69.5^0$. For instance, for a formation cluster having 6 satellites, three of them initially located at $\alpha = 110.5^0$ and the last three $\alpha = -69.5^0$ gives a formation as presented in Figure 4-96 to Figure 4-98. This kind of formation can be called as formation with successive pairs.
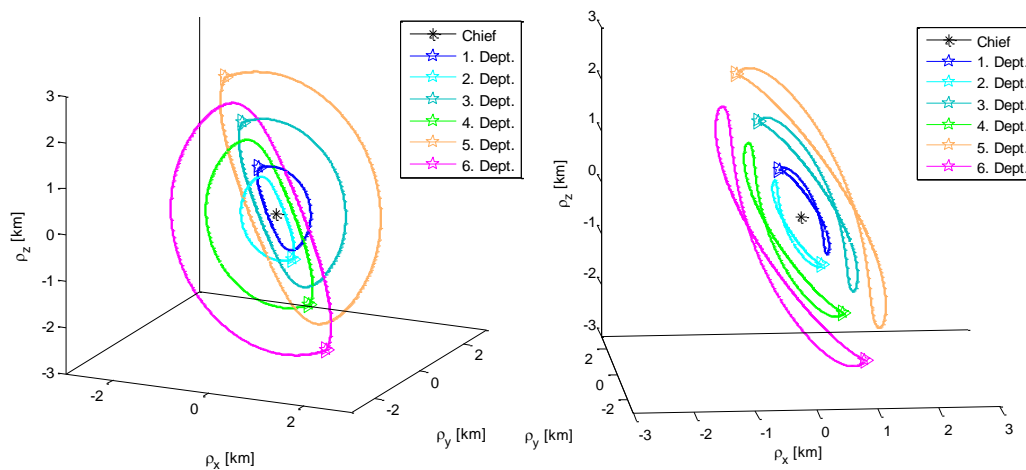
Figure 4-96. Trajectory of deputies for UAF-L2
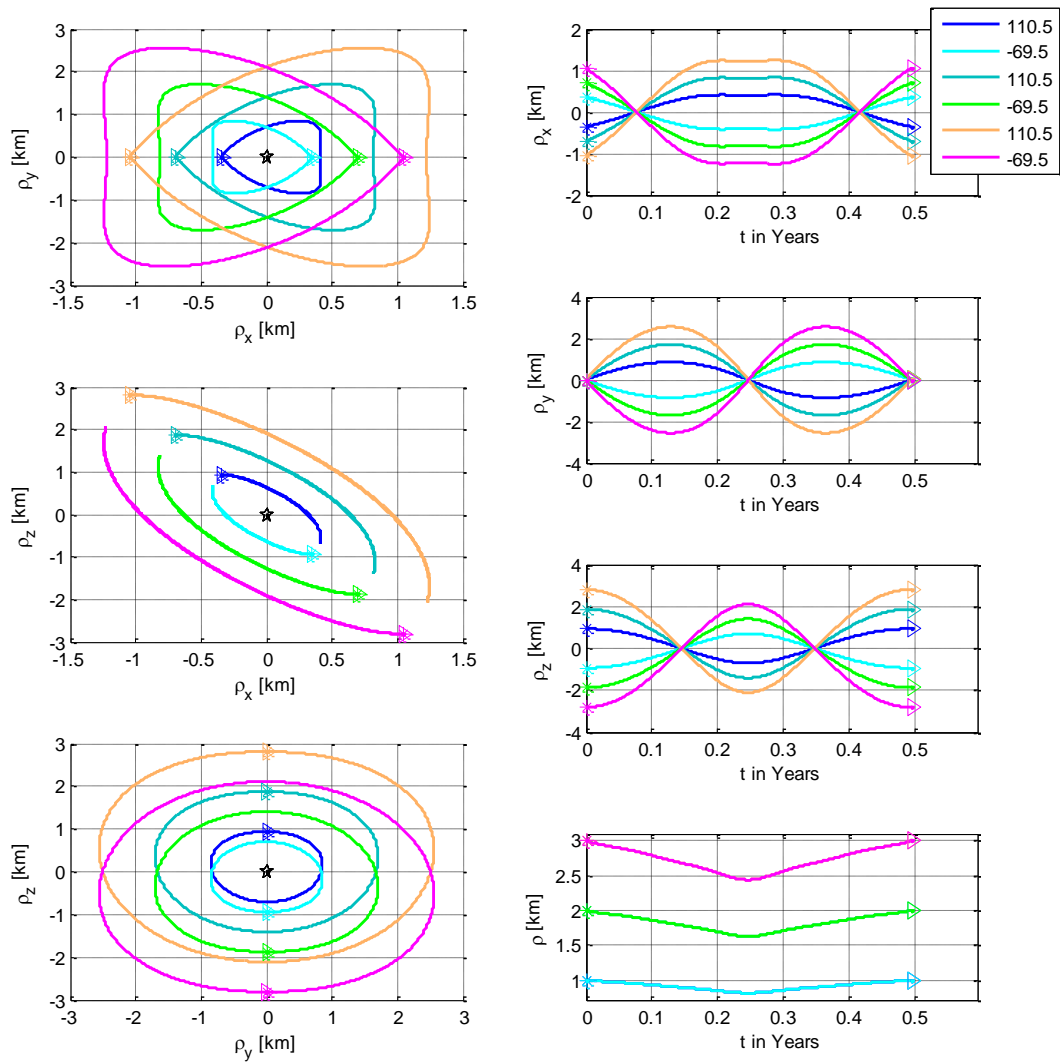
Figure 4-97. Projected and time dependent views for UAF-L2

243
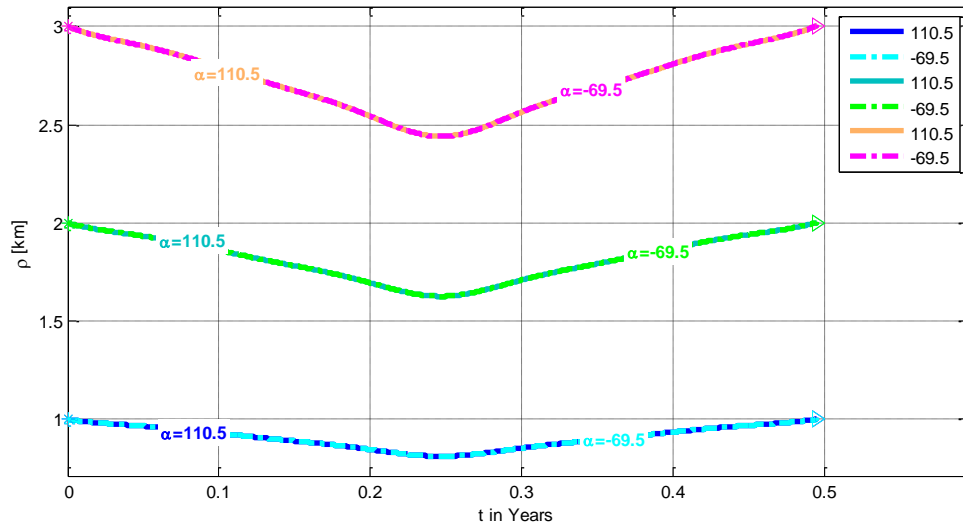
Figure 4-98. Relative distance between satellites for UAF-L2

Here, the minimum relative distance obtained for each satellite varies regarding to the distance step given for each successive satellite. It is seen that, this is a useful formation schema for a mission that requires quasi-constant relative distance with respect to the chief, for each pairs of formation.

CHAPTER 5

SUMMARY OF L1 AND L2 FORMATION FLIGHT DESIGN

This first part of this thesis contains the studies performed for the formation flight design near Sun-Earth collinear libration points L1 and L2. The main objective is to compute an orbit for deputy satellite which ensures naturally long-term formation flight without need of orbital maneuver to achieve desired formation configuration.

Several formation clusters are analyzed in order to understand the effect of the initial relative position to the relative trajectory. Equilateral triangle shape, square shape, inclined square shape formation schemes are obtained. At the end, an initial condition set that provide minimum deviation is found. For instance, for a formation around L1, the minimum deviation on relative distance is obtained for azimuth angle of $\beta = 0^0$, and the elevation angle $\alpha = 102^0 - 104^0$. Furthermore, it is seen that the inclination of the plane, formed by the relative position vector between deputy and chief, affects the deviation of the relative distances. Minimum deviation is obtained for $\alpha = 100^0$, ρ is $1\ km$ to $0.85\ km$. All ρ coincides at half period, and at 1st quarters and 3rd quarters extrama are formed. However, around $\alpha = 100^0$ the extrama disappear and smoothest deviations are acquired at half period, maximum deviation is about $0.15\ km$. Fine analyses around $\alpha = 100^0$ shows that the best result is for $\alpha = 104^0$, but the rate of change toward minimum point $\rho = 0.84\ km$ is very high. Most uniform change in the relative deputy distance is obtained for $\alpha = 102.5^0$, decreasing and increasing rates has a linear form.

Same procedure is applied to the formation design around L2 and similar results are obtained. Minimum deviation in ρ is obtained for elevation angles α between 110^0 and 130^0. For $\beta = 0^0$, and the α values that gives the minimum deviation is $\alpha = 110^0 - 112^0$: around $\alpha = 110^0$, ρ changes between $1\ km$ to $0.82\ km$. All ρ coincides at half period, and reaches extramum values at 1st quarters

and 3rd quarters. Around $\alpha = 110^0$ smoothest deviations are acquired at half period; maximum deviation is about $0.2\ km$ for this elevation value. This refined analyze for L2 shows that the most resistant result is get for $\alpha = 113^0$. However, the rate of change toward minimum point $\rho = 0.82\ km$ is high. The most uniformly change is obtained for $\alpha = 110.5^0$, decreasing and increasing rates are nearly linear.

After computing optimal elevation angle for the deputy satellite, it is also a possible to create a formation schema having multiple satellite aligned and uniformly equally separated, namely a rectilinear formation. For this kind of formation, it is seen that the relative distances between successive deputies remain constant and this may be a good property depending on the mission that requires quasi-constant relative distance with respect to the chief, for each pairs of formation.

All different formation schemas given here indicate that it is possible to modify and /or create a formation regarding to the mission need and payload capabilities. The method presented in this thesis will provide a reasonable formation flight by computing convenient initial velocities for desired initial relative positions, that is mean designing a convenient orbit for formation structure.

CHAPTER 6

MODELING RELATIVE MOTION OF THE LEO FORMATION FLYING SATELLITES

The second part of this thesis includes the formation flight design and analyses for the Low Earth Orbit satellites. This section includes the details on the modeling of the relative motion of the low Earth orbit satellites on formation flight. First formulation gives the nonlinear equation of motion by using Keplerian two body dynamics and the second formulation use orbital elements of the satellites to obtain the relative position.

6.1. Modeling Relative Motion Using the Keplerian Formulation

In this section, two coordinate systems are used in order to define the motion of the Chief satellite. First one is the **perifocal coordinate system**; centered at the Earth, x axis points to the perigee of the Chef's orbit, z is normal to the orbital plane and it is positive in the direction of the orbital angular momentum vector and y axis completed the set according to the right hand rule. The second coordinate system used is **orbital coordinate system**; it is also called as Local Vertical Local Horizontal (LVLH) reference frame. Orbital coordinate system is centered at the satellite, x axis is aligned radially form Earth to the satellite and it is directed from satellite outward, z axis is normal to the orbital plane, positive in the direction of the angular momentum vector, and y axis completes the set via right hand rule. The following figure illustrates these coordinate systems and shows the relative distance according the Chief's orbital frame. In Figure 6-1 the perifocal frame is denoted by x, y, z unit vectors centered at the Earth and orbital frame is defined by Xo, Yo, Zo unit vectors centered at the satellite. Here, $\vec{r}_{chief}$ is position vector of the chief satellite from Earth, and $\vec{r}_{deputy}$

is the deputy satellite position, $\vec{\rho}$ is the relative distance of the deputy with respect to chief expressed in orbital reference frame.
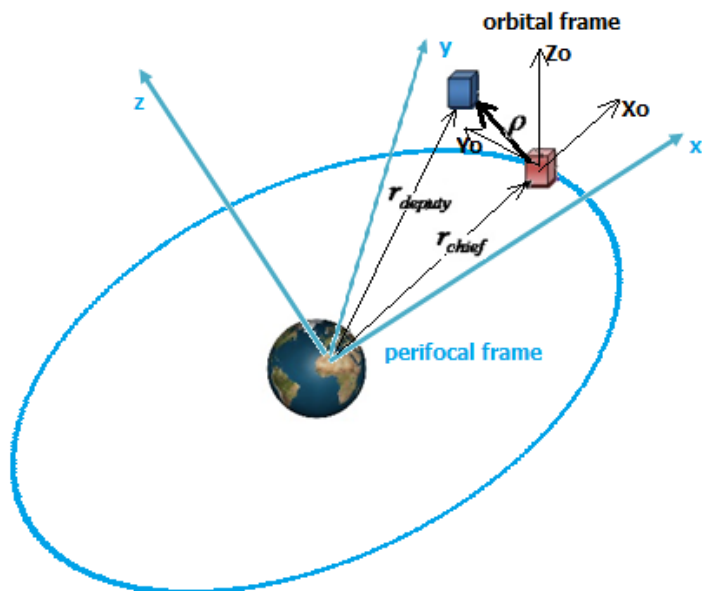
Figure 6-1. Perifocal and orbital coordinate systems

First, the chief's position is computed using an orbit propagator including the variation of the mean classical orbital elements. The perturbations due to non-spherical Earth (J2), due to Moon and Sun are included on the computations. The details on orbit propagator are presented in Appendix-D. As known, Kepler's equation states that [72]:

$$M = M_0 + n(t - t_0) = E - e\sin(E) \qquad \text{Eq. 6-1}$$

where, M is the mean anomaly, E is the eccentric anomaly, $n = \sqrt{\mu/a^3}$ is the orbital mean motion, t_0 is the epoch and M_0 is the mean anomaly at epoch. After solving this equation, the perifocal position vector of the chief satellite written in terms of the eccentric anomaly is:

$$[r_{chief}]_P = \begin{bmatrix} a(\cos(E) - e) \\ a\sqrt{1 - e^2}\sin(E) \\ 0 \end{bmatrix} \qquad \text{Eq. 6-2}$$

The relative motion of the deputy is derived using the equations of motion of the chief and deputy satellites that are defined by Keplerian two-body problem:

$$\ddot{\vec{r}}_{chief} = -\frac{\mu \vec{r}_{chief}}{\left| \vec{r}_{chief} \right|^3} \qquad \text{Eq. 6-3}$$

$$\ddot{\vec{r}}_{deputy} = -\frac{\mu \vec{r}_{deputy}}{\left| \vec{r}_{deputy} \right|^3} \qquad \text{Eq. 6-4}$$

The position of the deputy relative to the chief is denoted as $\vec{\rho}$, and it is obtained by using Eq. 6-3 and Eq. 6-4 that are written for chief and deputy satellites.

$$\vec{\rho} = \vec{r}_{deputy} - \vec{r}_{chief} \qquad \text{Eq. 6-5}$$

$$\ddot{\vec{\rho}}\Big|_{Prf} = -\frac{\mu(\vec{r}_{chief} + \vec{\rho})}{\left| \vec{r}_{chief} + \vec{\rho} \right|^3} + \frac{\mu \vec{r}_{chief}}{\left| \vec{r}_{chief} \right|^3} \qquad \text{Eq. 6-6}$$

The Eq. 6-6 is expressed in chief's perifocal frame. However, Chief's orbital frame has an angular motion with respect to perifocal frame. So, the relative acceleration in the orbital frame can be expressed as [73]:

$$\ddot{\vec{\rho}}|_{Orb} = \frac{d^2\vec{\rho}}{dt^2}\bigg|_{Prf}$$

<div style="text-align:right">Eq. 6-7</div>

$$- \left(2\vec{\omega} \times \frac{d\vec{\rho}}{dt}\bigg|_{Orb} + \frac{d\vec{\omega}}{dt} \times \vec{\rho}|_{Orb} + \vec{\omega} \times (\vec{\omega} \times \vec{\rho}|_{Orb})\right)$$

where, suffix *Orb* denotes orbital frame and *Prf* denotes perifocal frame, and $\vec{\omega}$ orbital angular velocity of the chief satellite expressed in orbital frame and it is normal to the orbital plane. It can be expressed in matrix form as $\omega = \begin{bmatrix} 0 & 0 & \dot{\theta}_{chief} \end{bmatrix}^T$. In vector form Eq. 6-7 can be written as follows:

$$\ddot{\rho}|_{Orb} = C^T \left[-\frac{\mu(r_{chief} + \rho)}{|r_{chief} + \rho|^3} + \frac{\mu r_{chief}}{|r_{chief}|^3} \right]_{Prf}$$

<div style="text-align:right">Eq. 6-8</div>

$$- \left(2\tilde{\omega}\,\dot{\rho}|_{Orb} + \dot{\tilde{\omega}}\,\rho|_{Orb} + \tilde{\omega}^2\,\rho|_{Orb}\right)$$

where, C is the transformation matrix from orbital frame to perifocal frame, and $\tilde{\omega}$ is dyadic form of the angular rate. So, Eq. 6-8 is in matrix form and it is expressed at orbital reference frame. The following component wise relative motion equations in the orbital frame may be written as,

$$\ddot{x} = -\frac{\mu(r_{chief\_Orb} + x)}{\left[(r_{chief\_Orb} + x)^2 + y^2 + z^2\right]^{3/2}} + \frac{\mu}{r^2_{chief\_Orb}} + 2\dot{\theta}_{chief}\dot{y}$$
$$+ \ddot{\theta}_{chief}y + \dot{\theta}^2{}_{chief}x + d_x + u_x$$

$$\ddot{y} = -\frac{\mu y}{\left[(r_{chief\_Orb} + x)^2 + y^2 + z^2\right]^{3/2}} - 2\dot{\theta}_{chief}\dot{x} - \ddot{\theta}_{chief}x$$
$$+ \dot{\theta}^2{}_{chief}y + d_y + u_y$$

<div style="text-align:right">Eq. 6-9</div>

$$\ddot{z} = -\frac{\mu z}{\left[\left(r_{chief\_Orb} + x\right)^2 + y^2 + z^2\right]^{3/2}} + d_z + u_z$$

In the above equation $r_{chief\_Orb} = r_{chief}\big|_{Orb}$ chief position expressed in chief's orbital frame, $\rho\big|_{Orb} = \begin{bmatrix} x & y & z \end{bmatrix}^T$, d_i are the disturbance vector components and u_i are the control forces. The orbital disturbances are given in Appendix-D as they are added on the orbit propagator model. Appendix-E contains the equations with disturbances for a special case of J2 effects. The computation of the control inputs in order to keep satellite on formation is presented in Appendix-F.

The block diagram of the model developed to simulate the relative motion using Keplerian formulation is given in Figure 6-2:
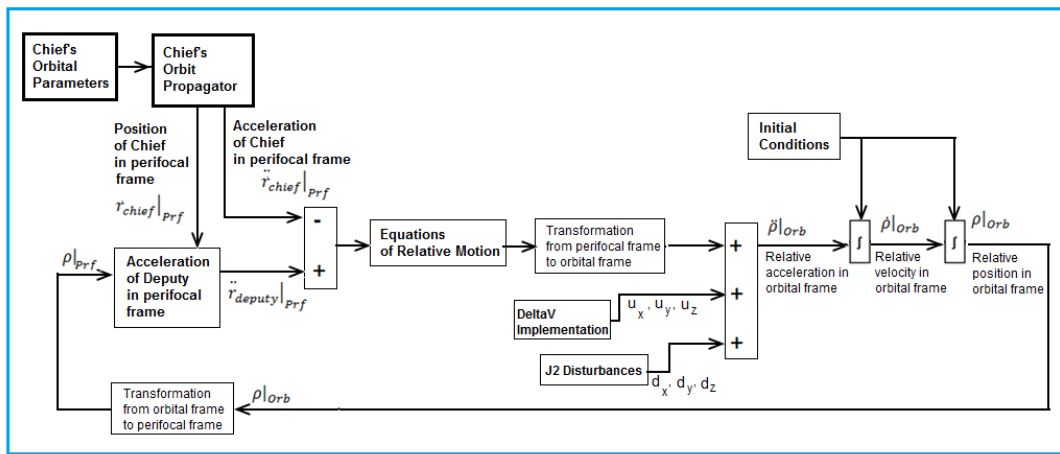
Figure 6-2. Block diagram of model that use the Keplerian equations of motion

In this model, the orbital parameters of the chief satellite are selected and are given to the model as input. Orbit propagator is used to compute the chief's position depending on time. After those equations of motion given in Eq. 6-7 is used to obtain the deputy relative position and velocity for a given relative initial position and velocity. The

disturbances and control forces, if there exist, are also given as input. So, the component wise velocity and position elements are computed by integrating the acceleration obtained from Eq. 6-7. Finally, the orbital parameters of the deputy satellites are calculated in order to compare the orbits of chief and deputy satellites. The formulas used to compute orbital parameters are presented in Appendix-B.

6.2. Modeling Relative Motion Using Orbital Elements

The relative position of the deputy may also be expressed using orbital elements. This method, originally suggested by G.W. Hill [74], and it has been widely used in the analysis of relative satellite motion. One of the main advantages of the orbital elements approach is to obtain a non-differential relative position equation and incorporate straightforwardly the orbital perturbations. The relative deputy's position, defined using orbital elements, is obtained (subscript x_c denotes x_{chief} and x_d denotes x_{deputy}).

$$\rho = C(f_c)T^T(\omega_c, i_c, \Omega_c)T(\omega_d, i_d, \Omega_d)[r_d]_{P_d} - \begin{bmatrix} r_c \\ 0 \\ 0 \end{bmatrix} \qquad \text{Eq. 6-10}$$
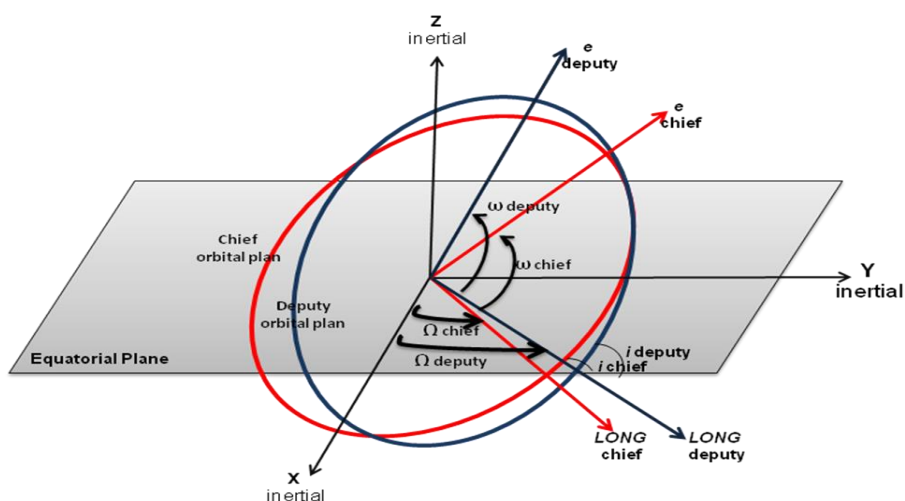
Figure 6-3. Orbital elements

252

The block diagram of the model developed to simulate the relative motion using Orbital Elements formulation is given in Figure 6-4:
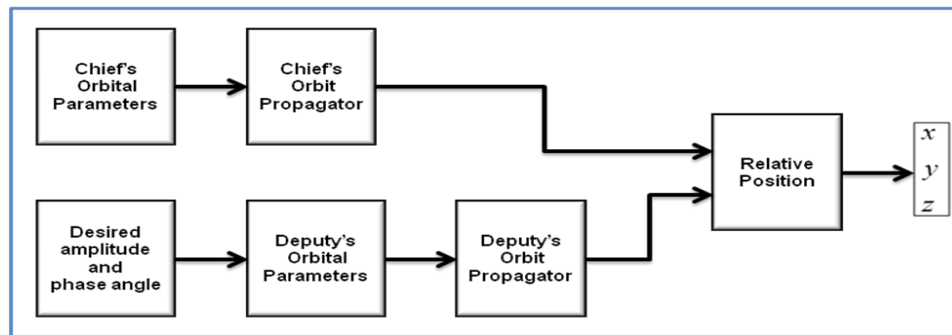
Figure 6-4. Block diagram of model with orbital elements.

In this model, the orbital parameters of the both chief and deputy satellites are given as input to the model. Orbit propagator is run for both of satellites to compute the time dependent position of the satellites. After that, relative position of the deputy with respect to the chief perifocal frame is calculated using Eq. 6-10.

CHAPTER 7

MODELING FORMATION FLIGHT ORBITS FOR LEO SATELLITES

This section contains the methods used to design the orbit of the deputy satellite that provides the formation flight around the chief. The main subject on orbit design for a formation flight is the selection of the initial condition of the deputy satellite. In this section, two main approaches existing in the literature are briefly given and offered approach here is presented. Those methods based on the energy matching approach. The main requirement for formation flight is that: the energy level of the chief and deputy satellite must be equal; it means that their semi-major axis must be equal [73]. So, it is possible to compute directly the velocity and position components of the deputy satellite with matched energy by using the following equality:

$$\varepsilon_{chief} - \varepsilon_{deputy} = 0 \qquad\qquad \text{Eq. 7-1}$$

where;

$$\varepsilon_{deputy} = \frac{1}{2}\left\{ \left(\dot{x} - \dot{\theta}_{chief}y + \dot{r}_{chief}\right)^2 + \left[\dot{y} + \dot{\theta}_{chief}\left(x + r_{chief}\right)\right]^2 \right. $$
$$\left. + \dot{z}^2 \right\} - \frac{\mu}{\sqrt{\left(r_{chief} + x\right)^2 + y^2 + z^2}} \qquad\qquad \text{Eq. 7-2}$$

and

$$\varepsilon_{chief} = -\frac{\mu}{2a_{chief}} \qquad\qquad \text{Eq. 7-3}$$

This equation has six unknowns, with five of them must be known to solve for the unknown parameter. Let, as initial positions, the desired relative position components $x, y\ and\ z$ are taken. And the two of the velocity components $\dot{x}\ and\ \dot{z}$ are taken as zeros. Then, it is now possible to compute analytically initial velocity component $\dot{y}$. The straightforward computations are given in detail at Appendix-C.

These two methods in the literature, they have computation techniques with some assumptions and constraints: small formations are considered, semimajor axis are taken equal, projected motion is considered, it is focused on initial position, not on the initial velocities, etc. Here, the method proposed in section 4.3 is used to design long-term formation flight for LEO satellites. So, those three methods can be listed as follows:

- Along Track and Cross Track ICs for Projected Circular Orbit (PCO-ICs) [62]
- Geometrical Relative Orbit Modelling (GROM) [75]
- Optimal ICs, performs optimization to determine the Initial Conditions (OPTICs) (See section 4.3)

The following subchapters give the details about these three methods.

7.1. PCO-ICs

This technique is based on the linear equations of motion written by Clohessy-Wiltshire (CW). It is also known as Hill's equations. CW equations describe a simplified model of orbital relative motion assuming that motion is circular. This model is a first-order approximation of the motion [76]. In the previous section, the component wise equation of motion is given in Eq. 6-9. By considering that angular rate of the orbital frame with respect to perifocal frame is constant, $\begin{bmatrix} 0 & 0 & \dot{\theta}_{chief} \end{bmatrix}^T = \begin{bmatrix} 0 & 0 & n \end{bmatrix}^T$, $\ddot{\theta}_{chief} = 0$; assuming that chief's orbit is circular and position vector of the chief is equal to the semimajor axis value, and ignoring the disturbances and control inputs, this equation set can be rewritten as:

$$\ddot{x} = 2n\dot{y} + n^2 x - \frac{\mu(a_{chief} + x)}{\left[(a_{chief} + x)^2 + y^2 + z^2\right]^{3/2}} + \frac{\mu}{a_{chief}^2}$$

$$\ddot{y} = -2n\dot{x} + n^2 y - \frac{\mu y}{\left[(a_{chief} + x)^2 + y^2 + z^2\right]^{3/2}} \qquad \text{Eq. 7-4}$$

$$\ddot{z} = -\frac{\mu z}{\left[(a_{chief} + x)^2 + y^2 + z^2\right]^{3/2}} + d_z + u_z$$

Clohessy-Wiltshire equations are derived by expanding the right side of the Eq. 7-4 set in to first order Taylor series about the origin. This gives:

$$\ddot{x} = 2n\dot{y} + 3n^2 x$$

$$\ddot{y} = -2n\dot{x} \qquad \text{Eq. 7-5}$$

$$\ddot{z} = -n^2 z$$

For a state vector $X = \begin{bmatrix} x & y & z & \dot{x} & \dot{y} & \dot{x} \end{bmatrix}^T$;

$$\dot{X}(t) = AX(t) \qquad \text{Eq. 7-6}$$

with:

$$A = \begin{bmatrix} zeros(3x3) & I(3x3) \\ A21 & A22 \end{bmatrix} \qquad \text{Eq. 7-7}$$

$$A21 = \begin{bmatrix} 3n^2 & 0 & 0 \\ 0 & 0 & 0 \\ 0 & 0 & -n^2 \end{bmatrix} \quad and \; A22 = \begin{bmatrix} 0 & 2n & 0 \\ -2n & 0 & 0 \\ 0 & 0 & 0 \end{bmatrix} \qquad \text{Eq. 7-8}$$

The solution of this above set can be written in form of the transition matrix as follows:

$$X(t) = e^{A(t-t_0)} X(t_0) \qquad \text{Eq. 7-9}$$

And the following component wise expression is obtained [77]:

$$x(t) = \left(4x_0 + \frac{2\dot{y}_0}{n}\right) + \frac{\dot{x}_0}{n}\sin(nt) - \left(3x_0 + \frac{2\dot{y}_0}{n}\right)\cos(nt)$$

$$y(t) = -(6nx_0 + 3\dot{y}_0)\, t + \left(y_0 - \frac{2\dot{x}_0}{n}\right) + \left(6x_0 + \frac{4\dot{y}_0}{n}\right)\sin(nt)$$
$$+ \frac{2\dot{x}_0}{n}\cos(nt)$$

<div style="text-align:right">Eq. 7-10</div>

$$z(t) = \frac{\dot{z}_0}{n}\sin(nt) - z_0\cos(nt)$$

Here, it is seen that $y(t)$ has time depending drift component, it is required to select as initial condition $\dot{y}_0 = -2nx_0$ in order to prevent this drift. So, the new set is:

$$x(t) = \rho_x \sin(nt + \alpha_x)$$

$$y(t) = \rho_y + 2\rho_x\cos(nt + \alpha_x)$$

<div style="text-align:right">Eq. 7-11</div>

$$z(t) = \rho_z\sin(nt + \alpha_z)$$

where;

$$\rho_x = \left(\sqrt{\dot{x}_0{}^2 + x_0^2 n^2}\right)/n$$

$$\rho_y = y_0 - 2\dot{x}_0/n$$

$$\rho_z = \left(\sqrt{\dot{z}_0{}^2 + z_0^2 n^2}\right)/n$$

<div style="text-align:right">Eq. 7-12</div>

$$\alpha_x = atan(nx_0/\dot{x}_0)$$

$$\alpha_z = atan(nz_0/\dot{z}_0)$$

Here, ρ_x is the amplitude of the along track motion, α_x is the in-plane phase angle, ρ_z is the amplitude of the cross-track motion and α_z is the cross-track phase angle. The illustration is given in Figure 7-1 for initial case where $t = 0$.
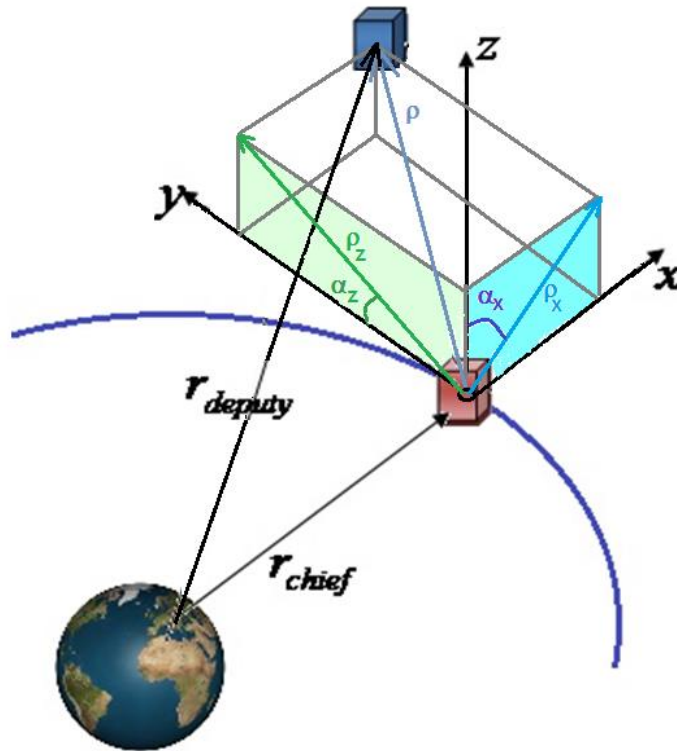
Figure 7-1. Along track, cross track amplitudes and phase angles.

This gives a three-dimensional ellipse centered at $(0, \rho_y, 0)$. The following conditions can be defined [73]:

- when $\alpha_z = \frac{\pi}{2} + \alpha_x$ it gives elliptic projection on xz plane.

- when $\alpha_z = \frac{\pi}{2} + \alpha_x$ and $\rho_z = \rho_x$: it gives circular projection on xz plane.

This is called as General Circular Orbit (GCO) conditions.

On the other hand:

- when $\alpha_z = \alpha_x$ and $\rho_z = 2\rho_x$: it gives circular projection on yz plane. This is called as Projected Circular Orbit (PCO)

The following formulas are given in order to compute the proper initial condition for the relative motion is based on PCO approach. For instance;

- let $x_0 = \dot{z}_0 = 0$ and $\dot{x}_0 = nz_0$, this yields **circular xz** projection and **linear yz** projection
- let $\dot{x}_0 = \dot{z}_0 = 0$ and $z_0 = 2x_0$, this yields **circular yz** projection and **linear xz** projection

An approximate solution to determine the initial conditions for near circular orbit is derived using Eq. 7-11. So, the component wise equations may be rewritten as follows to define the amplitudes and phase angles of the along track and cross track motion (subscript x_c denotes x_{chief} and x_d denotes x_{deputy}):

$$x \cong \delta a + \rho_x sin(M_c + \alpha_x)$$

$$y \cong a_c[(\delta M + \delta\omega) + \delta\Omega \cos i_c]$$
$$- a_c[e_d e_c \sin \delta M_0 + 2\rho_x cos(M_c + \alpha_x)] \qquad \text{Eq. 7-13}$$

$$z \cong \rho_z \sin(M_c + \omega_c + \alpha_z) - \frac{3}{2}\rho_z e_c \sin(\omega_c + \alpha_z)$$

Here, in order to define the initial conditions of the deputy orbit regarding a desired formation flight scheme, the approximate solution given in Eq. 7-13 is considered and it is assumed that the change in the semimajor axis δa does not impact on the formation design for near circular orbit and for the formations having small relative distance. In this way, the along track and the cross track initial condition may be obtained as:

$$y_0 = \rho_0 \cos\left(M_{chief_0} + \omega_{chief_0} + \alpha_0\right) \qquad \text{Eq. 7-14}$$

$$z_0 = \rho_0 \left[\sin\left(M_{chief_0} + \omega_{chief_0} + \alpha_0\right) \right.$$
$$\left. - \frac{3}{2} e_{chief_0} \sin\left(\omega_{chief_0} + \alpha_0\right) \right]$$

where, ρ_0 is the desired initial distance between two satellite and α_0 is the desired initial phase angle in the yz plane. The related equations and the computation derived for the initial values of the deputy's orbital elements are given in details by Alfriend K.T., Vadali S.R et al,as [73]. So, the initial values of the deputy's orbital elements can be computed for the desired ρ_0 and α_0 using the following set of equations:

$$i_{deputy_0} = i_{chief_0} + \frac{\rho_0}{a_{chief}} \cos\alpha_0$$

$$\Omega_{deputy_0} = \Omega_{chief_0} - \frac{\rho_0}{a_{chief_0} \sin i_{chief_0}} \sin\alpha_0$$

$$M_{deputy_0} = M_{chief_0}$$
$$+ atan\left[\frac{\frac{\rho_0}{2a_{chief_0}} \cos\left(\omega_{chief_0} + \alpha_0\right)}{e_{chief_0} - \frac{\rho_0}{2a_{chief_0}} \sin\left(\omega_{chief_0} + \alpha_0\right)}\right]$$

$$e_{deputy_0} = \frac{\frac{\rho_0}{2a_{chief_0}} \cos\left(\omega_{chief_0} + \alpha_0\right)}{\sin(\delta M_0)}$$

$$\omega_{deputy_0} = \omega_{chief_0} - \delta M + \frac{\rho_0}{2a_{chief_0}} \cos\left(\omega_{chief_0} + \alpha_0\right)$$

$$a_{deputy} = a_{chief} + 0.5\, a_{chief} \left(\frac{R_{earth}}{a_{chief}}\right)^2 \left(\frac{3\eta_{chief} + 4}{\eta_{chief}^5}\right)$$
$$\times \left[\left(1 - 3\cos^2\left(i_{chief}\right)\right) \delta\eta - \eta_{chief} \sin\left(2i_{chief}\right)\delta i\right]$$

$$where;\ \eta = \sqrt{1 - e^2_{chief}}$$

At the end the initial relative distance values are obtained using Eq. 7-14 and Eq. 7-15. These values can be used in the first model given in section 6.1 to get the relative dynamics between chief and deputy satellite. Furthermore, the orbital parameters of the deputy satellite are obtained using Eq. 7-16 to Eq. 7-21. So, the second model given in section 6.2 can be used directly in order to get relative motion.

7.2. GROM

This approach, by S.S. Lee [75], is based on the spherical coordinates representation of the relative motion and compute initial orbital elements for a desired initial relative position. The main assumptions in this method are that the semimajor axes of the both satellites are equal, both orbits are circular (eccentricities are zeros) and mean anomalies are equal. The following figures and equations are taken from Ref.[75]. The spherical coordinates are given in Figure 7-2.
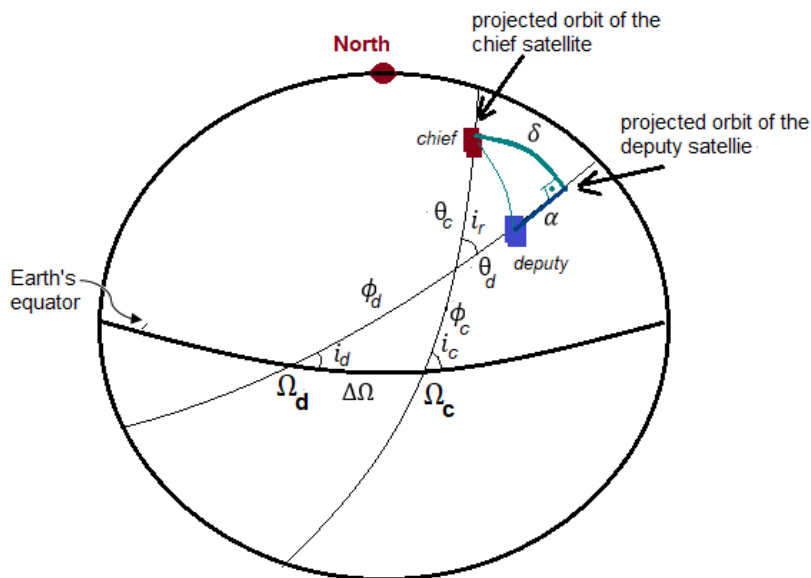
Figure 7-2. Geometrical relative orbit modeling [75]

Here chief satellite is denoted by suffix "c" and deputy by suffix "d". Regarding to the figure above, the relative position of the deputy satellite with respect to chief satellite is written as:

$$\bar{r} = \begin{bmatrix} r\ cos\delta\ cos\alpha \\ r\ cos\delta\ sin\alpha \\ r\ sin\delta \end{bmatrix}$$

Eq. 7-22

The spherical triangle formed by $\Delta\Omega_d\Omega_cI_P$ is used to calculate the angle i_r, showed in following Figure 7-3:
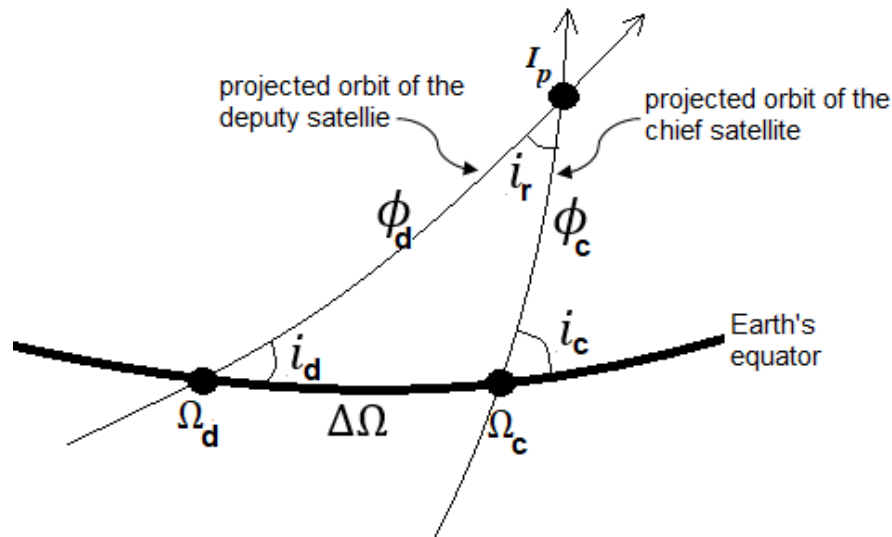
Figure 7-3. Projected orbits

Here, note that i_r is not equal to the difference of i_c and i_d, since spherical coordinates are used. So, the i_r can be computed using following equation:

$$\cos(i_r) = \cos(i_d)\cos(i_c) + \sin(i_d)\sin(i_c)\cos(\Delta\Omega)$$

Eq. 7-23

where

$$\Delta\Omega = -\Omega_d + \Omega_c$$

Eq. 7-24

So, along track and cross track distances can be written using follwoing equations:

$$\alpha = \phi_d - \omega_d - v_d + \mathrm{atan}(cos(i_r)\, tan(-\phi_c + \omega_c + v_c))\,; 0^o \leq \alpha$$
$$< 360^o \qquad\qquad \text{Eq. 7-25}$$

$$\delta = \mathrm{asin}(sin(i_r)\, sin(-\phi_c + \omega_c + v_c))\,; -90^o \leq \delta < 90^o \qquad \text{Eq. 7-26}$$

Then, the relative position and velocity can be written in matrix form as follows:

$$\bar{r} = \begin{bmatrix} r_c\, cos\delta\, cos\alpha - r_d \\ r_c\, cos\delta\, sin\alpha \\ r_c\, sin\delta \end{bmatrix} \qquad\qquad \text{Eq. 7-27}$$

$$\bar{V} = \begin{bmatrix} \dot{r}_c\, cos\delta\, cos\alpha - r_c\, \dot{\delta} sin\delta\, cos\alpha - r_c\, \dot{\alpha} cos\delta\, sin\alpha - \dot{r}_d \\ \dot{r}_c\, cos\delta\, sin\alpha - r_c\, \dot{\delta} sin\delta\, sin\alpha + r_c\, \dot{\alpha} cos\delta\, cos\alpha \\ \dot{r}_c\, sin\delta + r_c \dot{\delta} cos\delta \end{bmatrix} \qquad \text{Eq. 7-28}$$

So, finally a set of equation is obtained to determine the orbital parameters of the deputy satellite for the desired relative orbit size (along track (Ay) and cross track (Az) distance) and the relative phase angle ψ. Note here the assumption is semimajor axis, eccentricity and mean anomaly of both satellites are equal; $\Delta a = \Delta e = \Delta M = 0$.

$$\delta i = A_z\, cos(\omega_c + \psi)/\, a_c \qquad\qquad \text{Eq. 7-29}$$

$$\delta\Omega = A_z\, sin(\omega_c + \psi)/\, (a_c\, sin(i_c)) \qquad\qquad \text{Eq. 7-30}$$

$$\delta\omega = -\frac{A_y}{(a_c e_c)} - \frac{A_z\, sin(\omega_c + \psi)}{(a_c\, tan(i_c))} \qquad\qquad \text{Eq. 7-31}$$

The second model given in Section 6.2 can be run by using those initial orbital elements to get relative motion.

7.3. OPTICs for LEO Formation Design

Methods presented in the previous subsections propose a computation technique with some assumptions and constraints (formations having small relative distance are considered, semimajor axes are taken equal, projected motion is considered, near circular orbit is assumed, etc.). At the end of analyses performed, it is seen that these methods give reasonable results for some specific conditions. For that reason, an optimization method is proposed with a suitable minimization function in order to find a formation flight solution without considering any assumption and constraint. The OPTICs method is implemented for the LEO formation flight design. The definition and details of OPTICs are given in chapter 4.3. In the examples given in chapter 4.3 and chapter 4.4, recall the main assumption: Chief and deputy satellites have periodic orbit. So, it is expected to reach same orbital position after passing one orbital period of time. It may also be expected that the deputy satellite will have the same relative position after one orbital period. Desired relative position is illustrated in Figure 7-4.
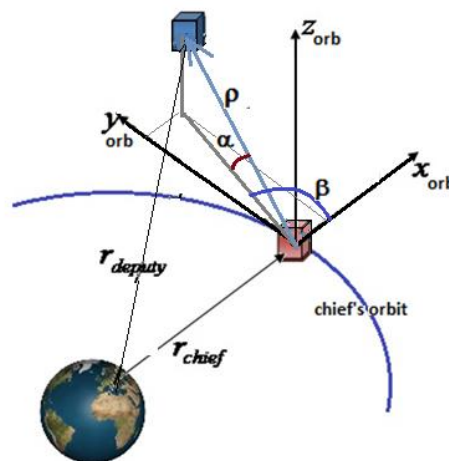
Figure 7-4. Relative desired position of deputy with respect to chief

Finally, the optimal initial velocity is computed for desired initial relative position. The minimization function can be rewritten as follows (subscript x_c for x_{chief} and x_d for x_{deputy}):

$$\dot{X} = f(X) = \begin{bmatrix} \dot{x} \\ \dot{y} \\ \dot{z} \\ \ddot{x} \\ \ddot{y} \\ \ddot{z} \end{bmatrix}$$

$$= \begin{bmatrix} \dot{x} \\ \dot{y} \\ \dot{z} \\ 2\dot{\theta}_c\dot{y} + \ddot{\theta}_c y + \dot{\theta}^2{}_c x - \dfrac{\mu(r_c + x)}{[(r_c + x)^2 + y^2 + z^2]^{3/2}} + \dfrac{\mu}{r_c^2} \\ -2\dot{\theta}_c\dot{x} - \ddot{\theta}_c x + \dot{\theta}^2{}_c y - \dfrac{\mu y}{[(r_c + x)^2 + y^2 + z^2]^{3/2}} \\ -\dfrac{\mu z}{[(r_c + x)^2 + y^2 + z^2]^{3/2}} \end{bmatrix} \qquad \text{Eq. 7-32}$$

$$f(X_{sub}) = \begin{bmatrix} x_{final} - x_{initial} \\ y_{final} - y_{initial} \\ z_{final} - z_{initial} \end{bmatrix} = \begin{bmatrix} \Delta\bar{x} \\ \Delta\bar{y} \\ \Delta\bar{z} \end{bmatrix} = \begin{bmatrix} 0 \\ 0 \\ 0 \end{bmatrix} \qquad \text{Eq. 7-33}$$

where;

$$\begin{bmatrix} x_{initial} \\ y_{initial} \\ z_{initial} \end{bmatrix} = \begin{bmatrix} x_c \\ y_c \\ z_c \end{bmatrix} + \begin{bmatrix} \rho_{desired}\cos(\alpha_{desired})\cos(\beta_{desired}) \\ \rho_{desired}\cos(\alpha_{desired})\sin(\beta_{desired}) \\ \rho_{desired}\sin(\alpha_{desired}) \end{bmatrix} \qquad \text{Eq. 7-34}$$

And the iteration process is:

$$\begin{bmatrix} \dot{x}^* \\ \dot{y}^* \\ \dot{z}^* \end{bmatrix}_{k+1} = \begin{bmatrix} \dot{x}^* \\ \dot{y}^* \\ \dot{z}^* \end{bmatrix}_k - (D_f)^{-1}\begin{bmatrix} \Delta\bar{x} \\ \Delta\bar{y} \\ \Delta\bar{z} \end{bmatrix} \qquad \text{Eq. 7-35}$$

$$D_f = \begin{bmatrix} \dfrac{\partial f_1}{\partial \dot{x}} & \dfrac{\partial f_1}{\partial \dot{y}} & \dfrac{\partial f_1}{\partial \dot{z}} \\[2mm] \dfrac{\partial f_2}{\partial \dot{x}} & \dfrac{\partial f_2}{\partial \dot{y}} & \dfrac{\partial f_2}{\partial \dot{z}} \\[2mm] \dfrac{\partial f_3}{\partial \dot{x}} & \dfrac{\partial f_3}{\partial \dot{y}} & \dfrac{\partial f_3}{\partial \dot{z}} \end{bmatrix} = \begin{bmatrix} \Phi_{1,4} & \Phi_{1,5} & \Phi_{1,6} \\ \Phi_{2,4} & \Phi_{2,5} & \Phi_{2,6} \\ \Phi_{3,4} & \Phi_{3,5} & \Phi_{3,6} \end{bmatrix} \qquad \text{Eq. 7-36}$$

Unlike the first two methods, this approach provides this initial position values and velocities. The positive effects of this method are seen at the simulation results given in the next sections.

The execution time of the code prepared for LEO formation flight design is examined. Here, the sampling time of the simulation is taken as 1 second. Simulation time is taken as 1 orbital period and it is approximately equal to the 99 minutes. The execution time of one iteration is approximately 8 seconds. The details are given Appendix-I.

CHAPTER 8

SIMULATION AND RESULTS FOR LEO FORMATION FLIGHT

This section contains the results of the methods presented in the previous section and the comparisons between them are presented. The advantage of the third method is seen very clearly in the following detailed results.

Here, the orbit given in the [73] is selected for the chief's orbit in order to make a good comparison environment. The orbital parameters of chief satellite are given in the following table:

Table 8.1. Orbital parameters of the chief satellite

Chief Satellite:	
Altitude (km):	713.863 km
Semimajor axis (km):	7092 km
RAAN (deg):	45°
Inclination (deg):	70°
Argument of Perigee (deg):	0.00°
Initial Mean Anomaly (deg):	0.00°
Eccentricity:	0.00

The orbital parameters of the deputy satellite, in other words its initial position and velocity, are computed by the PCO, GROM and OPTICs methods. The following results contain four different cases based on the PCO method: the phase angles

(azimuth angle on projected yz plane) selected are respectively $90^o, 60^o, 30^o$ and 0°. The simulation is run for 30 chief satellite's orbital period in order to sense the drift in time. As given in Ref.[73], PCO gives the best solution for a phase angle that is equal to 90°. However, thanks to the method presented in this thesis, by combining with some inference given in Ref.[73], it is possible to obtain stable formation flight for different phase angles unlike the PCO and GROM method.

In the first subsection, the PCO and GROM results are shared for 90 degree phase angle case. And it is seen that GROM is not very successful for J2 added cases. So, the main purpose of this section is to present the performance of the OPTICs method, for that reason, the following subsections (written for $60^o, 30^o$ and 0° phase angles) contains only the results of PCO and OPTICs.

8.1. Design with 90 degree phase angle

The results obtained for a phase angle equal to the 90° are given in this section. First PCO results are presented in Figure 8-1 to Figure 8-4, for both undisturbed and disturbed (J2 added) environment. Note that the disturbance model used is shared in Appendix-E. Figure 8-1 indicates the relative distance of the deputy satellite with respect to the chief. Here, the requirement for the relative distance is taken as 1 km. The second figure, Figure 8-2, it gives projected view on XY, YZ, and XZ plane of the relative motion around chief satellite. The last subfigure of Figure 8-2 (right-down) is the three-dimensional vision of the relative motion.

Results without adding J2 to the simulation:
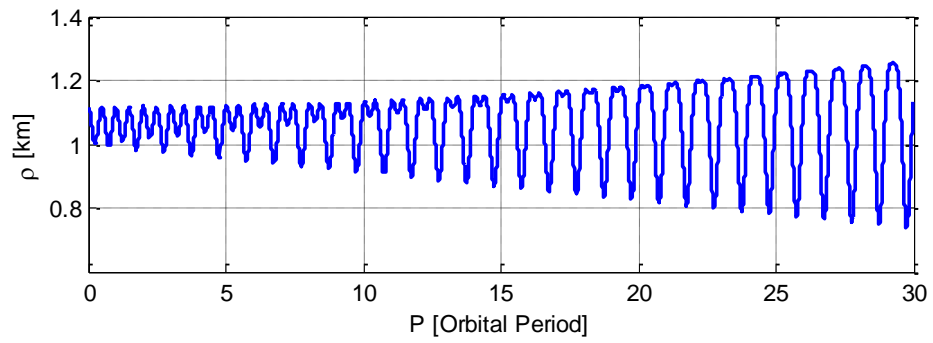
Figure 8-1. PCO: Relative distance, phase 90 deg. without disturbance
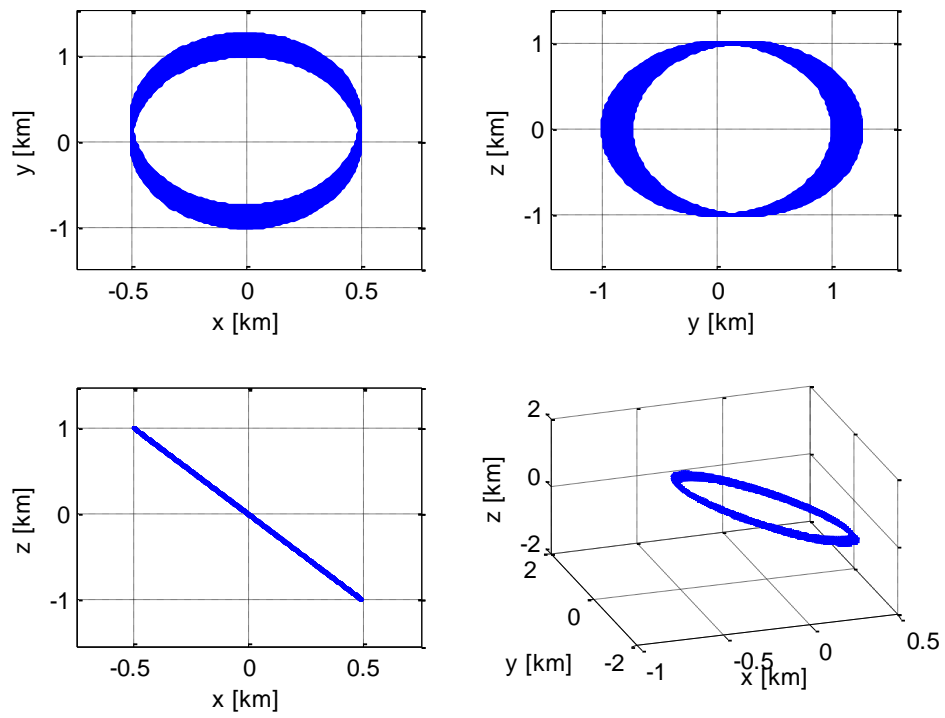
Figure 8-2. PCO: Projected views for phase 90 deg. without disturbance

Simulation results with J2 effect added:
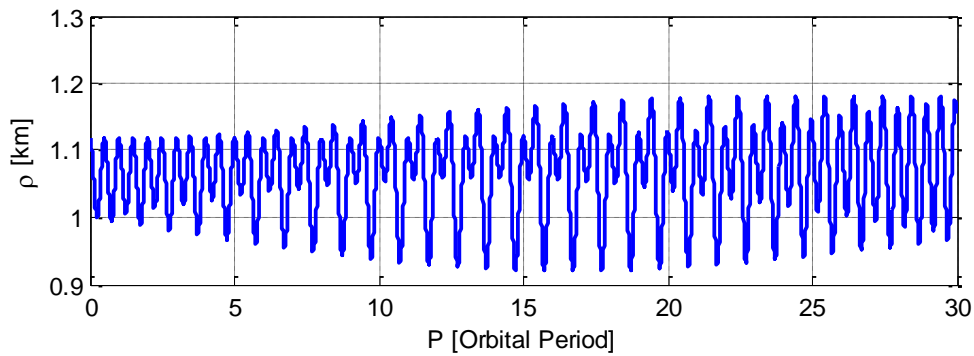
Figure 8-3. PCO: Relative distance for phase 90 degree with J2
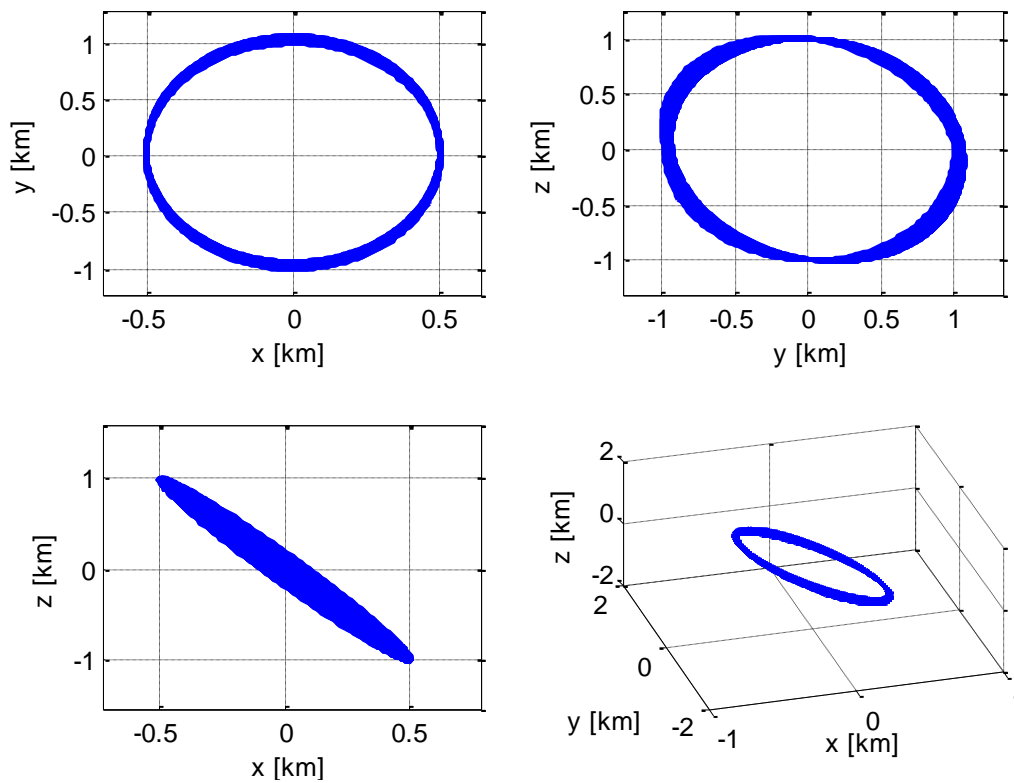
Figure 8-4. PCO: Projected views for phase 90 deg., with J2

Results show that PCO provides a good formation flight for 90 degree phase angle. As mentioned in the related previous section (Section 3.1) PCO is based on the design

on YZ plane. Here, relative distance has an oscillation and it diverges slightly depending on time. The oscillation amplitude is between 0.9 km to 1.2 km.

Unlike PCO, the GROM method gives more stable result for the case without J2 disturbance, but J2 added results shows that the deputy satellite gets very closer to the chief and it has an oscillated relative motion. The comparison of PCO and GROM is given in Figure 8-5 to Figure 8-8.

Simulation results without J2 effect:
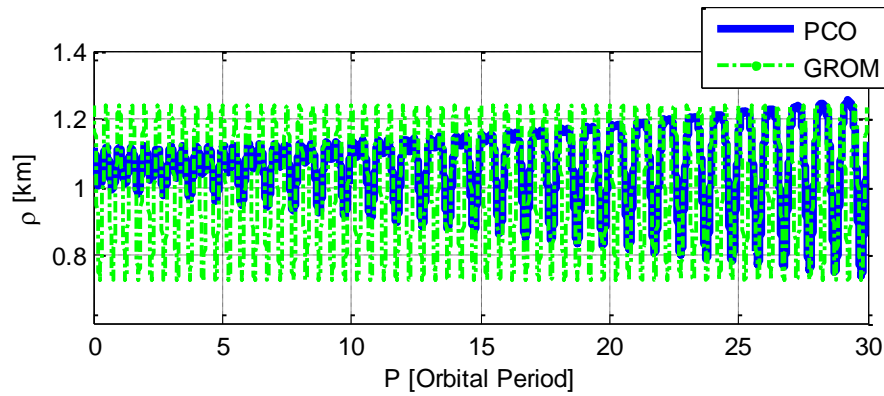
Figure 8-5. PCO/GROM: Relative distance, phase 90 deg. without disturbance
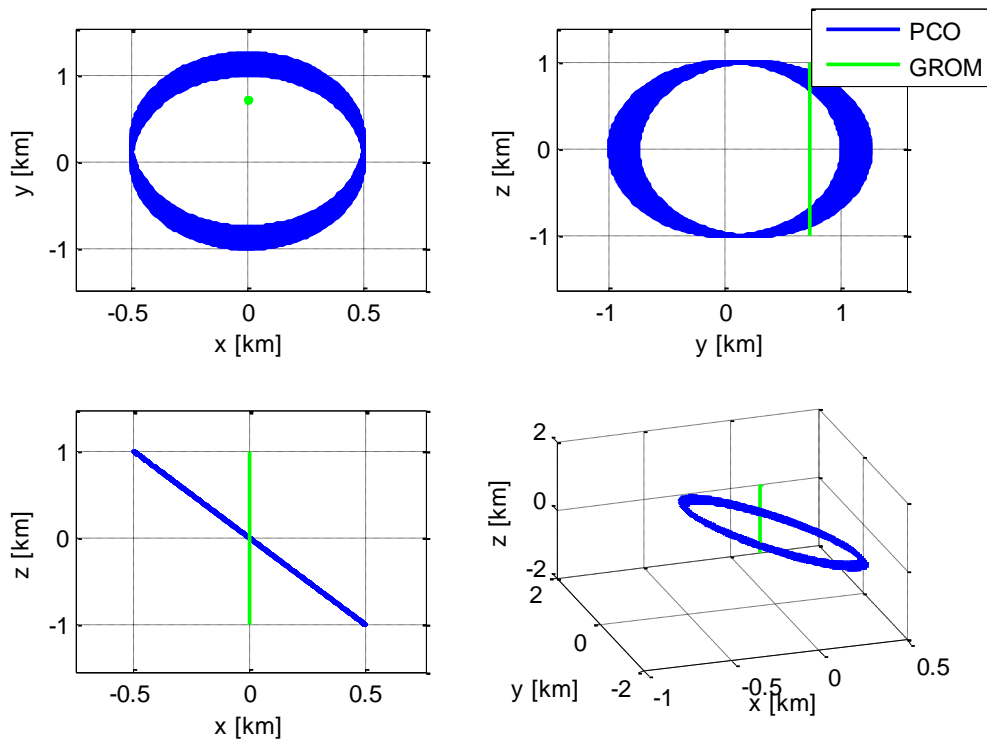
Figure 8-6. PCO/GROM: Projected views, phase 90 deg. without disturbance

Simulation results with J2 effect added:
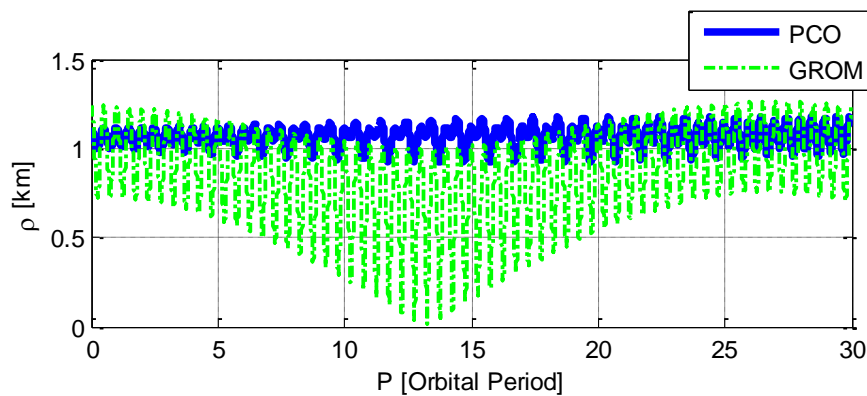
Figure 8-7. PCO/GROM: Relative distance, phase 90 deg. with J2
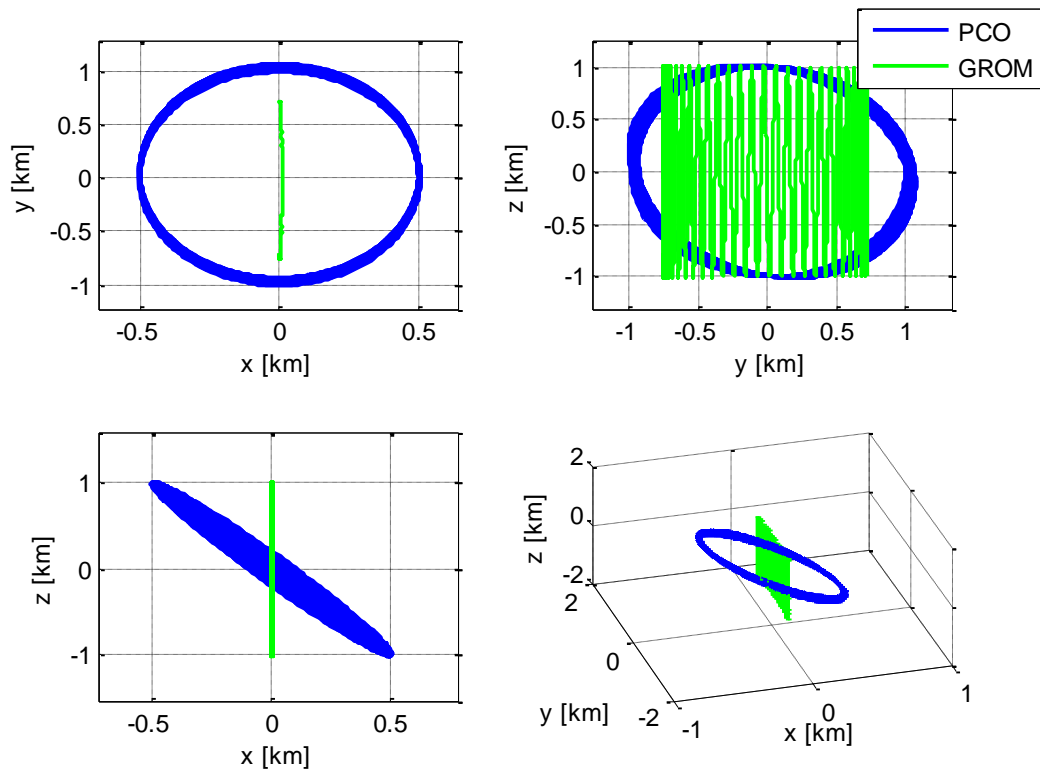
Figure 8-8. PCO/GROM: Projected views, phase 90 deg. with J2

According to the results, it is obvious that GROM does not provide a good formation flight when J2 is added. At 12th – 13th period, deputy satellite is very close the chief, it is not possible to obtain a stable and constant relative distance with initial conditions computed using GROM.

Figure 8-9 and Figure 8-10 present the results of the OPTICs compared to the PCO. Here, the initial relative position is selected according to the desired phase angle 90° and $\rho = 1\ km$ and the initial relative position is forced to obtain circular motion on YZ plane: $\dot{x}_0 = \dot{z}_0 = 0$ and $z_0 = 2x_0$, this yields **circular yz** projection and **linear xz** projection The initial position and computed velocity component values obtained by OPTICs are :

$x_0 = -500\ m, y_0 = 0\ m, z_0 = 1000\ m,$

$$\dot{x}_0 = \dot{z}_0 = 0 \; m/s \; , \dot{y}_0 = 1.057 \; m/s$$

And the initial elevation and azimuth angle computed form these initial positions:

$$\alpha_0 = 63.4351^o, \qquad \beta_0 = 180^o \; or \; 0^o$$

The iteration process given in section 7.3, called as OPTICs, it is initiated with these values and the computed results are given in Table 8.2. These values force to start the relative motion on xz plane, having no component on y axis, and it gives best formation flight scheme, similar to PCO case. Figure 8-9 and Figure 8-10 show the comparison of PCO and OPTICs forced to have circular relative motion on YZ plane, with J2 disturbance added.
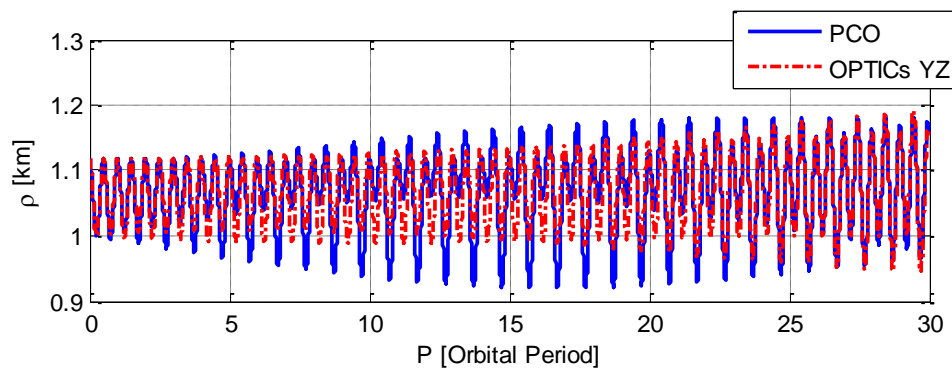
Figure 8-9. PCO/OPTICs YZ: Relative distance, phase 90 deg. with J2
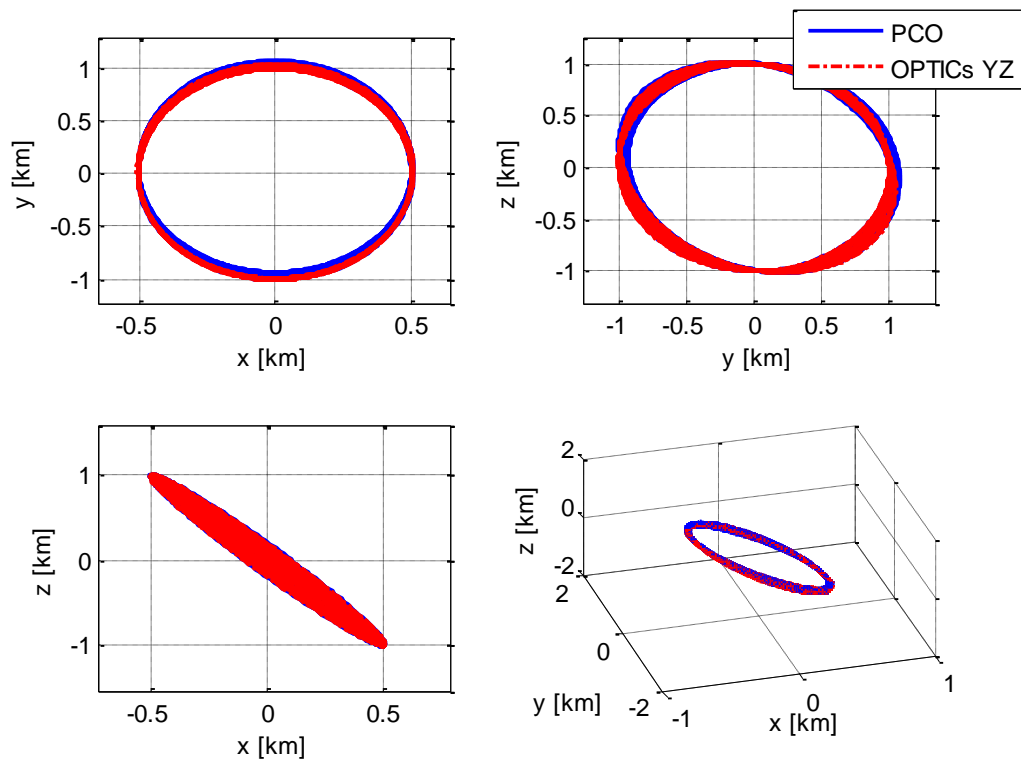
Figure 8-10. PCO/OPTICs YZ: Projected views, phase 90 deg. with J2

These results prove that OPTICs method which is based on well-known Newton's iteration method is consistent and gives approximately similar results; obtained with PCO method for 90 degree phase angle. This is a good verification of the OPTICs. The following Table 8.2 contains the initial conditions values computed by PCO and OPTICs. There exist very small differences between PCO and OPTICs initial conditions. On the other hand, OPTICs provides less deviation on oscillation between 10th and 20th orbits. Regarding to those differences, it can be stated that the relative motion is really dramatically sensitive to the small differences on the initial conditions, especially on initial velocities.

Table 8.2. ICs of PCO and OPTICs YZ for 90 degree phase angle

PHI=90	PCO	OPTICS force circular YZ
x_0 [m]	-500.0705	-499.9978
y_0 [m]	-0.021394	0
z_0 [m]	999.9611	1000
$\dot{x}_0$[m/s]	8.38E-06	0
$\dot{y}_0$[m/s]	1.0567	1.057
$\dot{z}_0$[m/s]	-4.38E-05	0
α_0 [deg]	63.4308	63.4351
β_0 [deg]	180 or 0	180 or 0

Unlike the PCO method, OPTICs will provide a formation scheme having circular XZ projection and YZ projection. However in that case, even if a non-diverged relative motion is achieved, it is not possible to get nearly constant relative motion; an oscillation from 1 km to 4km is obtained (Figure 8-11) Recall that for **circular xz** projection and **linear yz** projection it is required to set initial conditions as: $x_0 = \dot{z}_0 = 0$ and $\dot{x}_0 = nz_0$. Results indicated that it is possible to achieve circular motion in XZ plane with J2 disturbance added. However, the linear motion obtained on the YZ plane is oscillatory. The relative motion component ρ_y changes from -4 km to 4 km. The initial position and velocity components computed by OPTICs method for circular XZ are:

$$x_0 = 0 \, m, y_0 = 0 \, m, z_0 = 1000 \, m, \qquad \dot{x}_0 = 1.057 \, m/s, \, \dot{y}_0 = \dot{z}_0 = 0 \, m/s$$

And the initial elevation and azimuth angle computed form these initial positions:

$$\alpha_0 = 90^o, \qquad \beta_0 = 180^o \, or \, 0^o$$
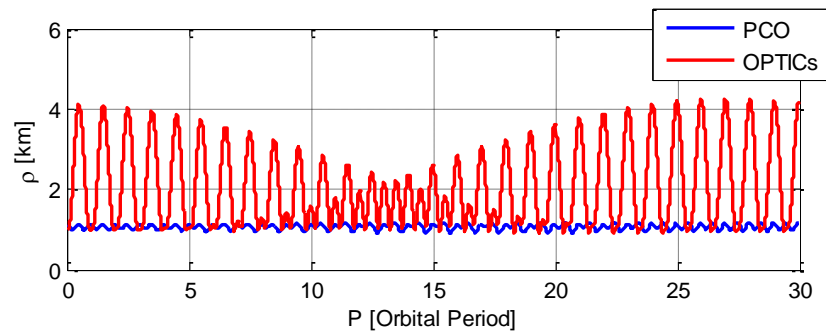
Figure 8-11. PCO/OPTICs XZ: Relative distance, phase 90 deg. with J2
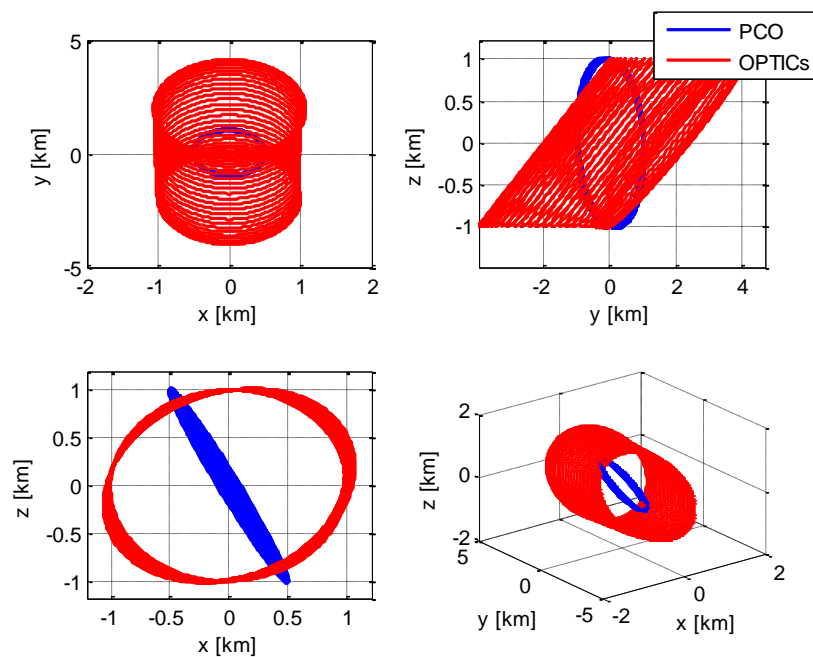
Figure 8-12. PCO/OPTICs XZ: Projected views, phase 90 deg. with J2

According to the results obtained it can be stated that PCO and OPTICs forced for circular YZ motion give approximately similar results, i.e., a stable formation flight. This verifies the success of OPTICs. Moreover, OPTICs helps to design another type of formation having circular motion on XZ plane. However, this formation may not be acceptable for the missions requiring constant relative motion. This design flexibility of the OPTICs will provide advantages for the phase angles different then 90°. These cases are considered in the following subsections.

8.2. Design with 60 degree phase angle

This section contains the results for a phase angle 60° obtained using PCO and OPTICs methods. First part presents the comparison between PCO and OPTICs force for YZ circular motion. The second part gives PCO versus OPTICs force for XZ circular motion.

Results without J2 disturbance:
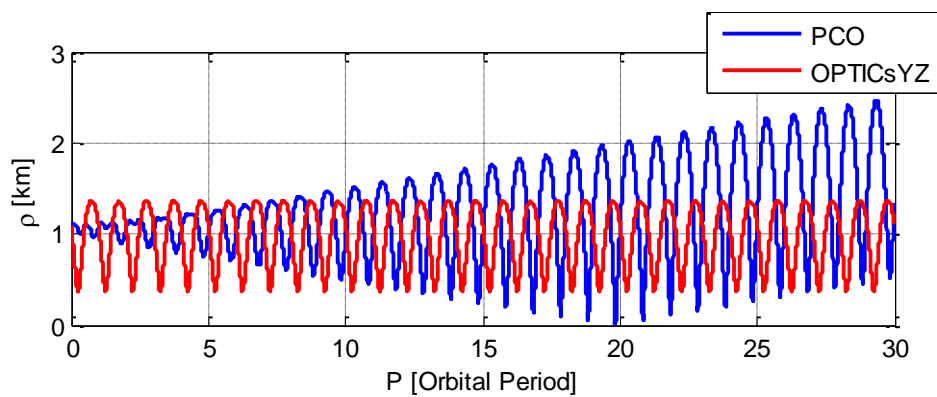
Figure 8-13. PCO/OPTICs YZ: Relative distance, phase 60 deg. without J2
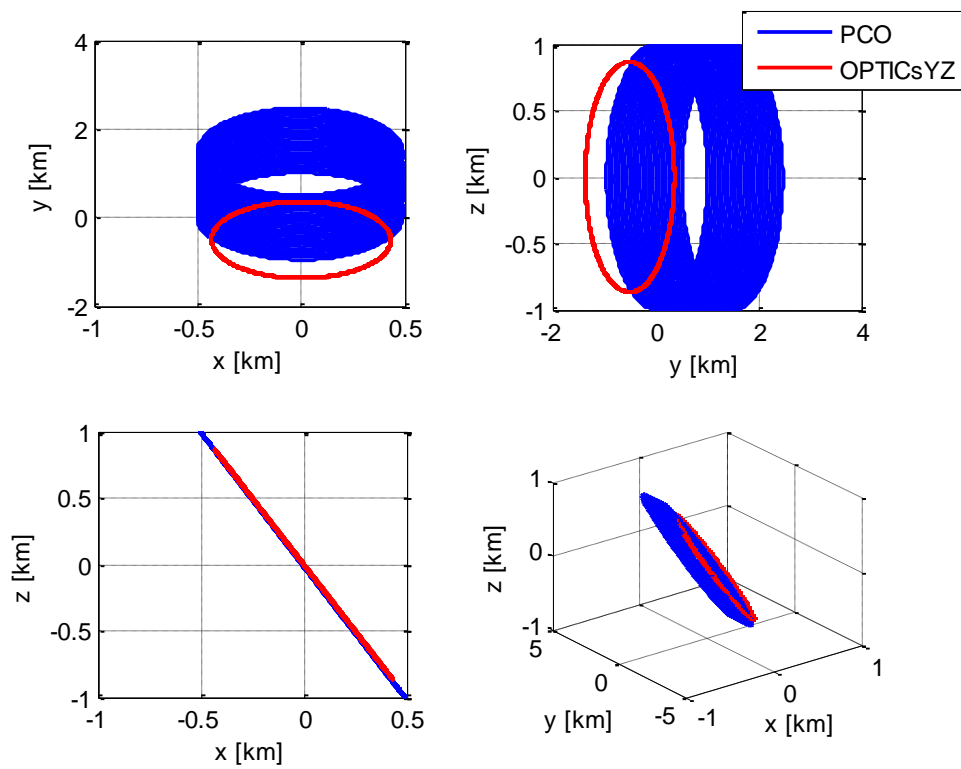
Figure 8-14. PCO/OPTICs YZ: Projected views, phase 60 deg. without J2

Results with J2 disturbance added:
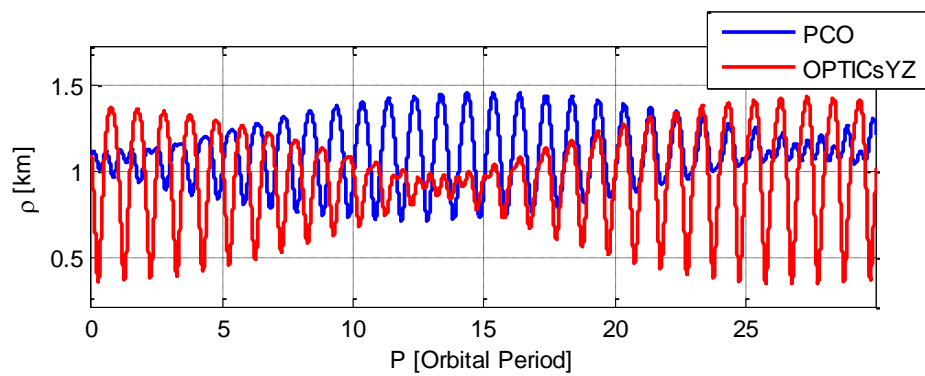
Figure 8-15. PCO/OPTICs YZ: Relative distance, phase 60 deg. with J2
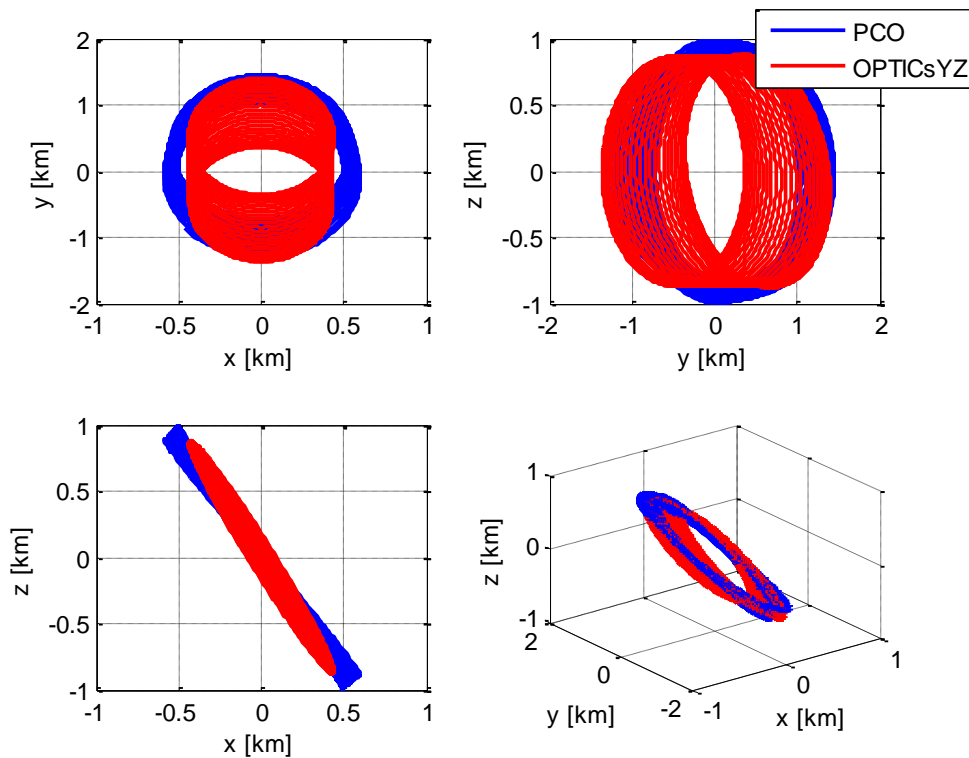
Figure 8-16. PCO/OPTICs YZ: Projected views, phase 60 deg. with J2

Figure 8-13 and Figure 8-14 show that undisturbed results are obviously very different and OPTICs give better formation performance. After 15th orbit the divergence starts for PCO, but OPTICs stay stable. The drift seen on y axis for PCO is not present for the orbits obtained by OPTICs. However, the performance difference between PCO and OPTICs is not as much pronounced when J2 disturbance is added (Figure 8-15 and Figure 8-16). The changes on amplitude of the oscillation of the relative motion are observable for both propagated orbits of PCO and OPTICs. The simulation is re-run for 90 orbits, in order to see the difference. Figure 8-17 gives the answer for this question.
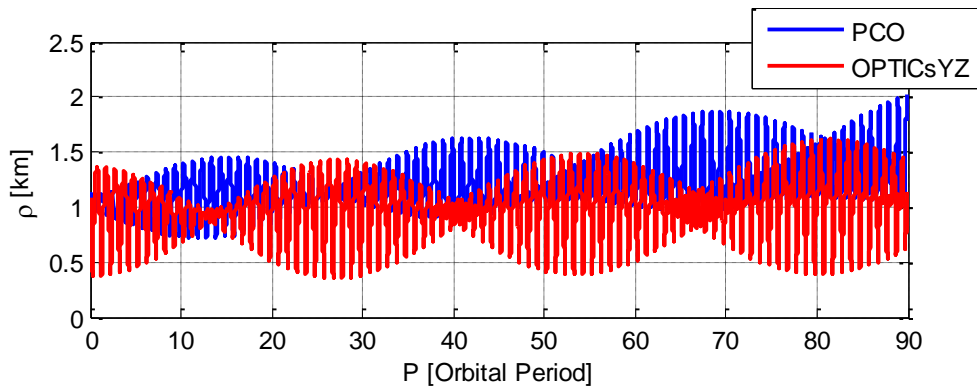
Figure 8-17. PCO/OPTICsYZ: ρ for 90 Orbits, phase 60 deg. with J2

The initial conditions computed by the two methods are presented in Table 8.3. From Figure 8-17, it is seen that the relative error has an oscillating behavior with increasing and decreasing amplitude for both of the methods. But, the amplitude of the PCO increase substantially with time, as opposed to OPTICs results. Consequently, it can be stated that OPTICs provide more resistant results in the long term as compared with the PCO results.

Table 8.3. ICs of PCO and OPTICs YZ for 60 degree phase angle

PHI=60	PCO	OPTICS force circular YZ
x_0 [m]	-434.7454	-433.0108
y_0 [m]	-500.0303	-500
z_0 [m]	865.9962	866.0254
$\dot{x}_0$[m/s]	-0.26419	6.11E-05
$\dot{y}_0$[m/s]	0.91622	0.91555
$\dot{z}_0$[m/s]	0.5276	0
α_0 [deg]	52.5795	52.6288
β_0 [deg]	-131.0049	-130.8934

When the phase angle is equal to 60 degree, the OPTICs give an opportunity to design a formation for 60 degree phase angle having a circular XZ motion. But in that case, the relative distance obtained has an osculating motion with varying amplitude from 1 km to 3 km. the results are given in the following figures:
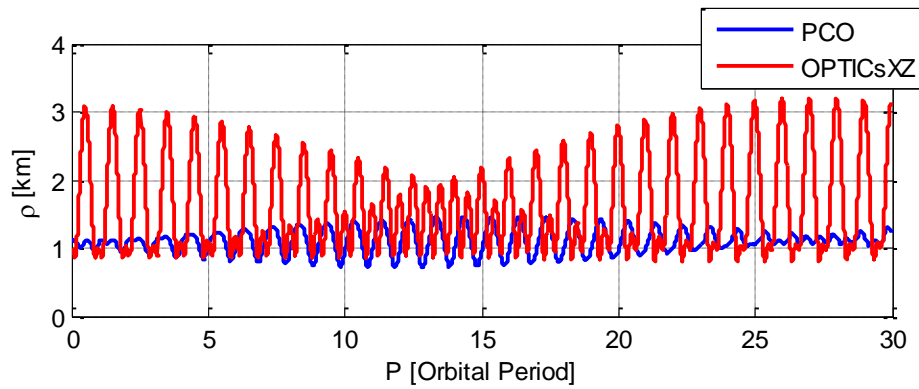
Figure 8-18. PCO/OPTICs XZ: ρ for phase 60 deg. with J2
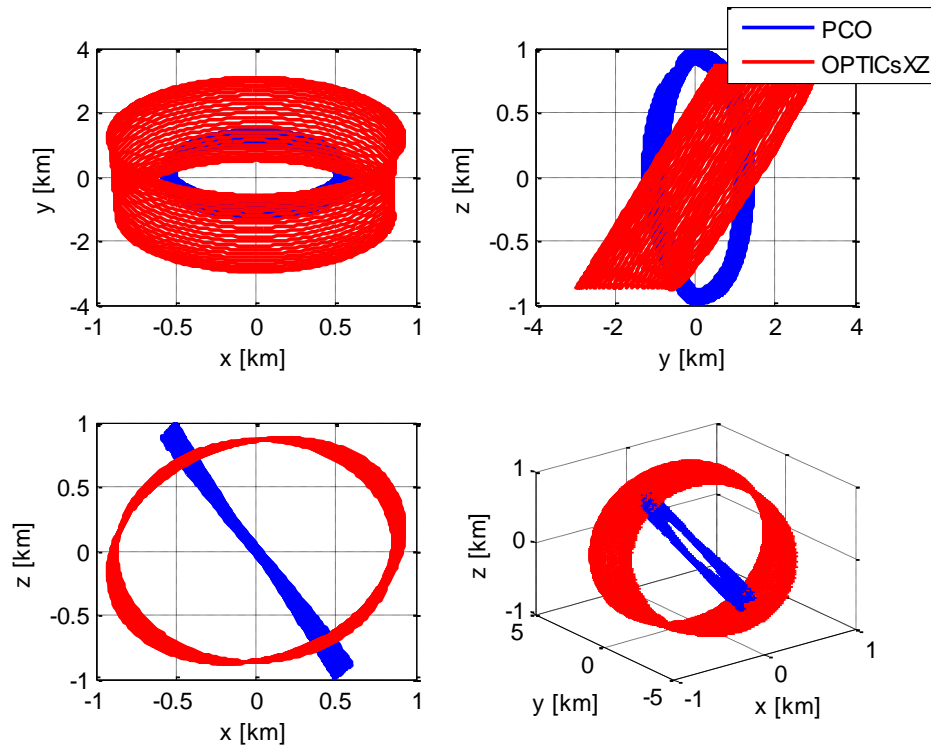
Figure 8-19. PCO/OPTICs XZ: Projected views of ρ, phase 60 deg. with J2

OPTICs force for XZ circular motion successively provide this relative motion, but in y axis the position changes are between +/- 3 km, Y axis has an osculation with an amplitude of 2 km. despite to this osculation the relative motion is stable, no divergence is seen. The initial conditions are:

$$x_0 = 0 \, m, y_0 = 433.0127 \, m, z_0 = 866.0254 \, m,$$

$$\dot{x}_0 = 0.91547 \, m/s, \, \dot{y}_0 = \dot{z}_0 = 0 \, m/s$$

And the initial elevation and azimuth angle computed form these initial positions:

$$\alpha_0 = 63.4349^o, \qquad \beta_0 = 90^o$$

So, it can be stated that, here, OPTICs propose to design two different type of formation; 1st: a formation having circular motion on YZ plane like PCO, and OPTICs is more stable to the time depended drifts. 2nd: a stable formation having circular motion on XZ plane is also achieved.

8.3. Design with 30 degree phase angle

The results obtained for the 30° phase angle is different from the cases presented in the preceding sections. Here it is seen that OPTICs is forced for circular XZ motion gives the best solution. The following figures gives respectively the results obtained from pure OPTICs (without modifying the initial position, the position is taken from desired phase angle and velocities are computed), OPTICs YZ (circular YZ motion is forced), OPTICs XZ (circular XZ motion is forced).
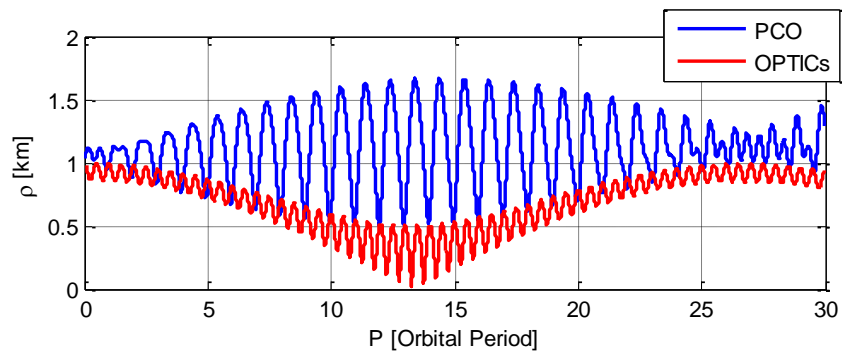
Figure 8-20. PCO/OPTICs for 30 deg. phase angle
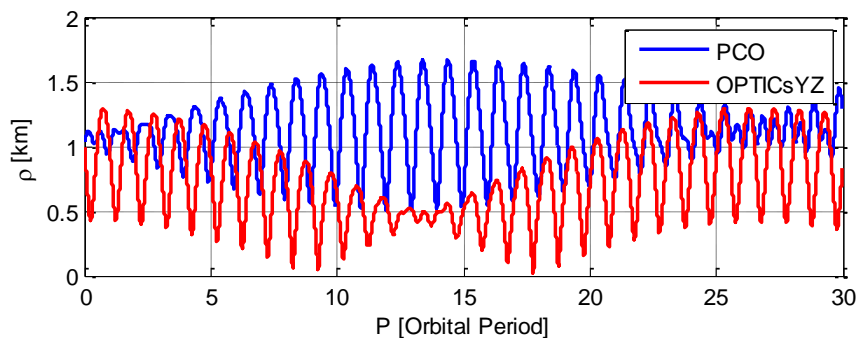
Figure 8-21. PCO/OPTICsYZ for 30 deg. phase angle
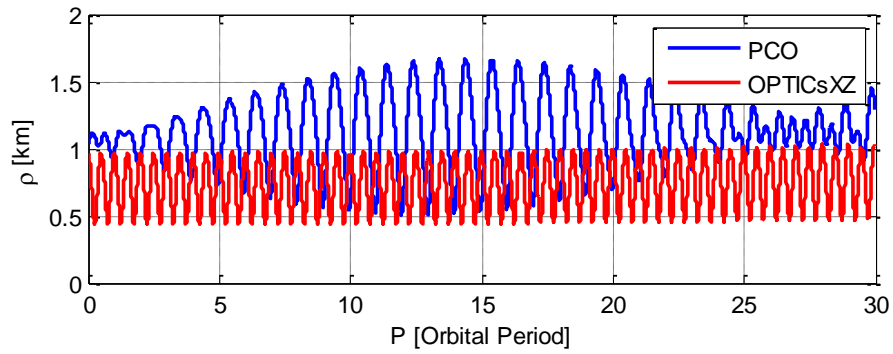
Figure 8-22. PCO/OPTICsXZ for 30 deg. phase angle

The initial conditions computed using the methods are given in the Table 8.4.

Table 8.4. Initial condition for 30 degree phase angle

PHI=30	PCO	OPTICS force circular YZ	OPTICS force circular XZ
x_0 [m]	-252.9385	216.5054	0.00E+00
y_0 [m]	-866.0593	866.0254	866.0254
z_0 [m]	499.9394	433.0127	433.0127
$\dot{x}_0$[m/s]	-0.45757	0	0.45774
$\dot{y}_0$[m/s]	0.53016	-0.45786	0
$\dot{z}_0$[m/s]	0.91382	0	0
α_0 [deg]	28.9912	25.8767	26.5651
β_0 [deg]	-106.2808	75.9638	90

OPTICs which is not forced for obtaining any circular planar relative motion, is called "Pure OPTICs" in the following. It does not provide a good formation flight; the deputy gets closer to the chief satellite at approximately 13th orbit (Figure 8-20). OPTICs forced for circular planar relative motion in YZ plane, it is not successful to

287

have an acceptable formation (Figure 8-21). However, OPTICs forced for circular planar relative motion in XZ plane, it gives stable motion for this phase (Figure 8-22). The constant relative distance is not achieved, the relative distance changes between 0.5 km and 1 km like a sinusoidal signal, but the stability is obtained. Figure 8-23 presents projected views of PCO and OPTICsXZ in order to compare them. Here, simulation time is 30 orbital period.
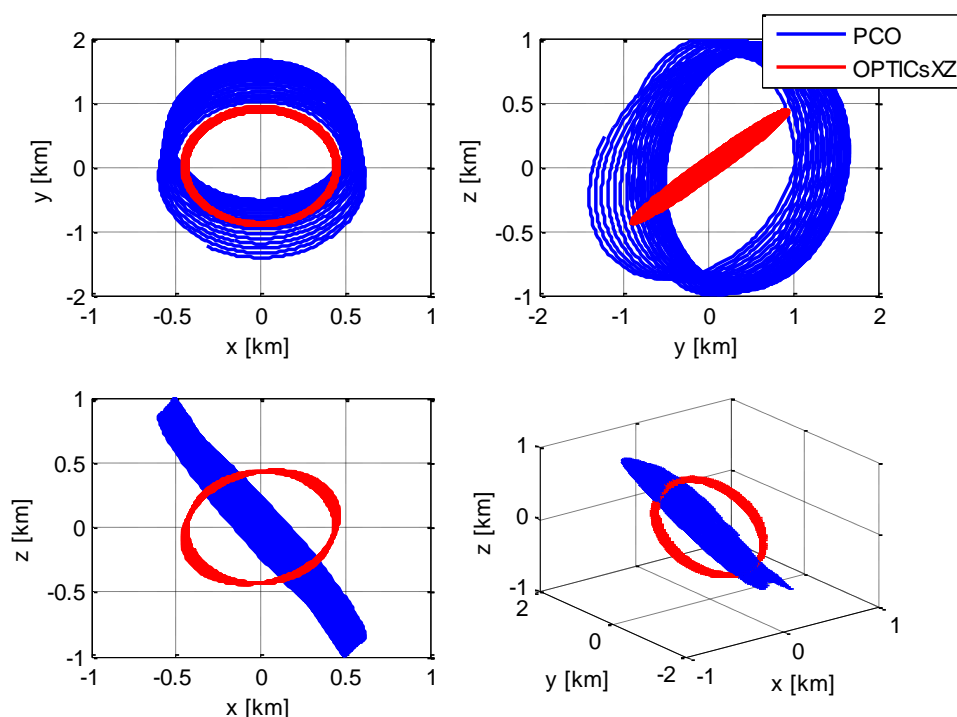
Figure 8-23. PCO/OPTICs XZ: Projected views of ρ, phase 30 deg. with J2

A long term simulation is also run for 90 orbital periods in order to have a good comparison based on the divergence characteristic of the relative motion, as seen in Figure 8-24. PCO divergence can be seen very clearly, unlike PCO, the time drift of the OPTICs XZ is more reasonable. The only disadvantage of these results, constant relative distance is not achieved, it varies between 0.5 km – 1 km, but it is stable, more robust to time drifts.
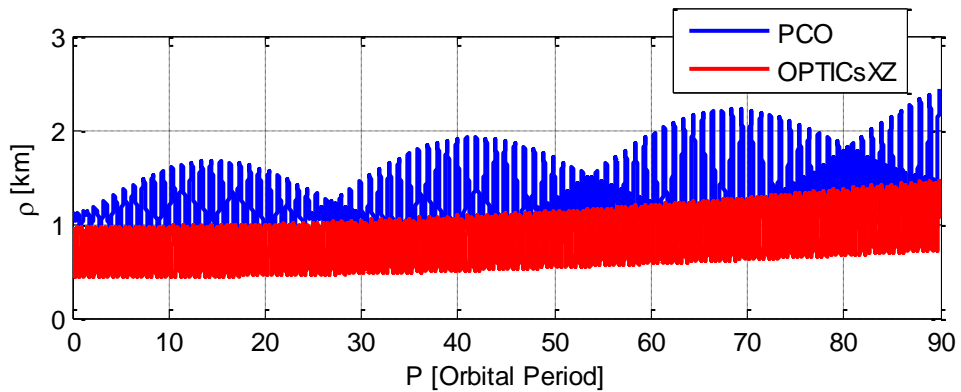
Figure 8-24. PCO/OPTICs XZ: 90 Orbits, ρ for phase 30 deg. with J2

Finally, it may be stated that OPTICS method forced for XZ circular relative motion gives the best formation flight scheme if a 30 degree phase angle is required. It is seen that when the magnitude of the y component of the relative motion is increase, the circular XZ motion forced formation design gives the better solution. This will be seen more clearly for zero phase angle, in the following section.

8.4. Design with Zero degree phase angle

The results obtained for the 0° phase angle is given in the following figures. Like the phase angle 30 degree case, here OPTICs forced for circular XZ motion gives the best solution. Pure OPTICs, OPTICs YZ, OPTICs XZ results are given respectively by comparing them with PCO.
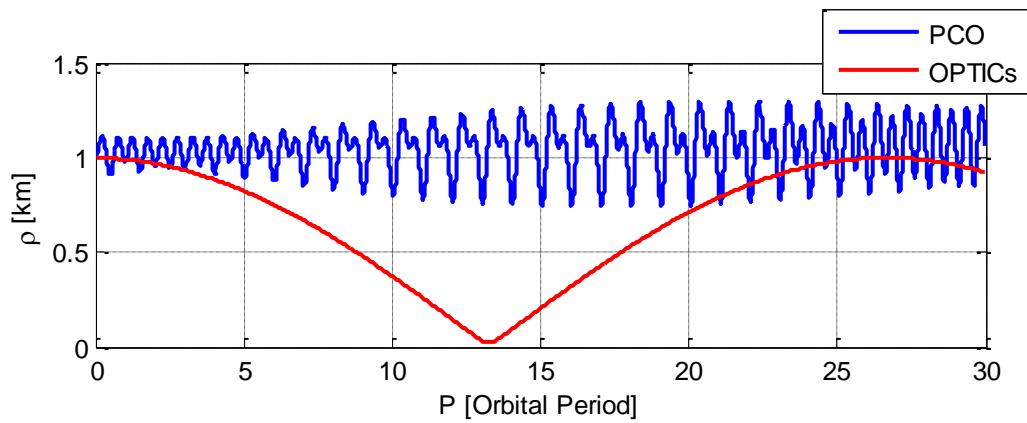
Figure 8-25. PCO/OPTICs: ρ for 0 deg. phase angle
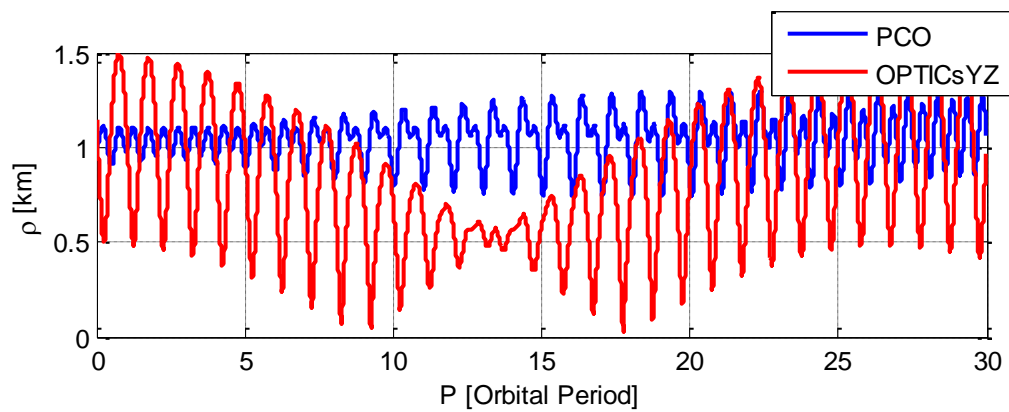
Figure 8-26. PCO/OPTICsYZ: ρ for 0 deg. phase angle
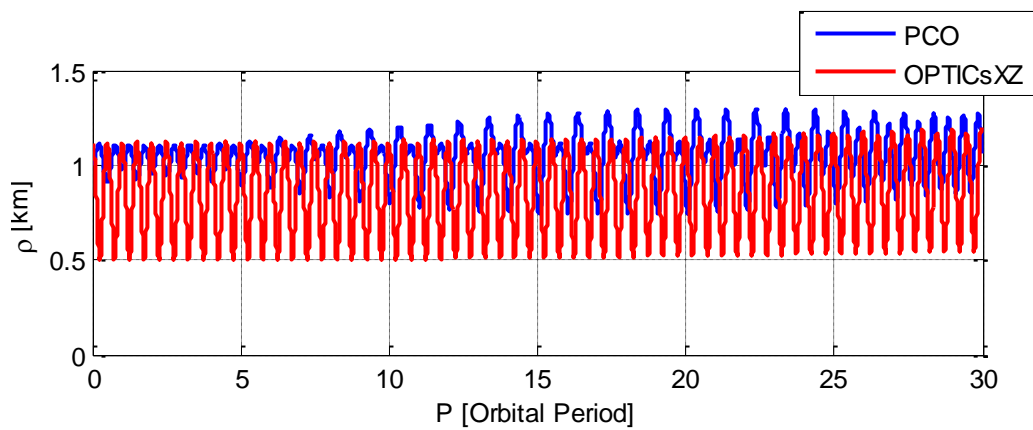
Figure 8-27. PCO/OPTICsXZ: ρ for 0 deg. phase angle

Table 8.5. Initial conditions for 0 degree phase angle

PHI=0	PCO	OPTICS force circular YZ	OPTICS force circular XZ
x_0 [m]	0	250	0
y_0 [m]	1000	1000	1000
z_0 [m]	0	500	500
$\dot{x}_0$[m/s]	0.52832	0	0.52855
$\dot{y}_0$[m/s]	0	-0.52871	-0.00011179
$\dot{z}_0$[m/s]	1.0551	0	0
α_0 [deg]	0	25.8767	26.5651
β_0 [deg]	90	75.9638	90
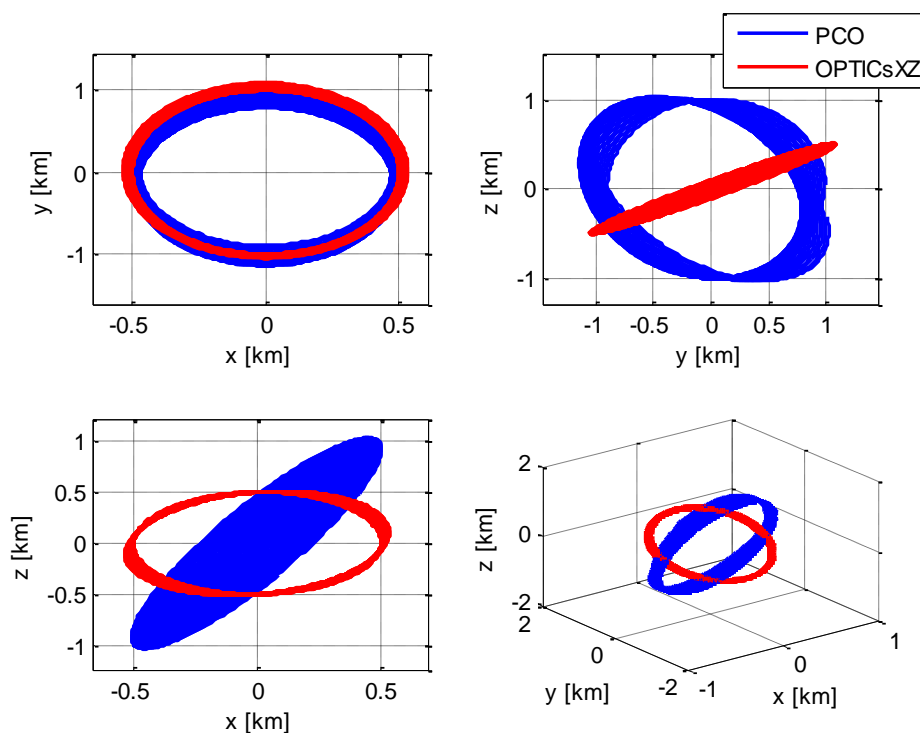
Figure 8-28. PCO/OPTICs XZ: Projected views of ρ, phase 0 deg. with J2
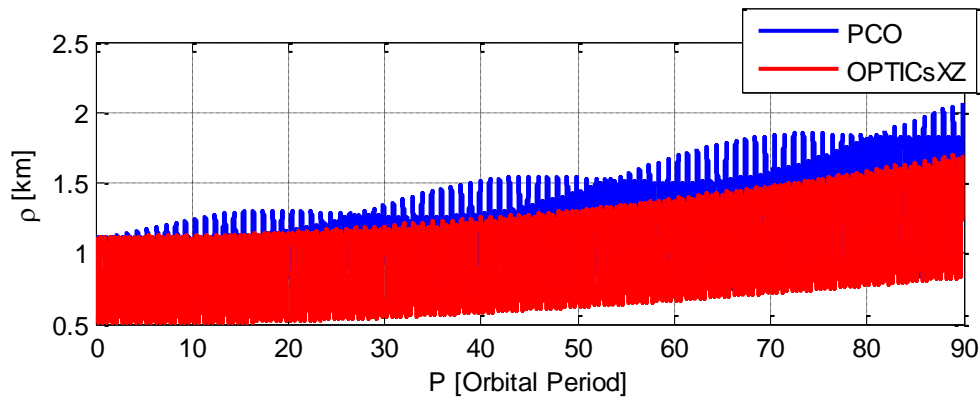
Figure 8-29. PCO/OPTICs XZ: 90 Orbits, ρ for phase 0 deg. with J2

A long-term simulation (for 90 orbital periods) is also run to see the divergence of the relative motion (Figure 8-29). Drift of PCO can be seen very clearly. Unlike PCO, the drift of the OPTICs XZ is smaller. The only disadvantage of this result, constant relative distance is not achieved, it varies between 0.5 km and 1 km, but it is more robust to time drifts.

8.5. Comparison for an arbitrary phase angle, initial position

In that case, an arbitrary initial formation position is selected in order to analyze the performance of PCO versus OPTICs. The phase angle is chosen as 70 degree. Actually, the computed phase angle is approximately 75 degree, the initial position obtained from PCO and OPTICs computation gives this value. The selected elevation angle and azimuth angle of the relative position and the initial position and velocity values computed by PCO and OPTICs are given in the Table 8.6.

Table 8.6. ICs for arbitrary selected phase angle

PHI=70	PCO	OPTICS force circular YZ	OPTICS force circular XZ
x_0 [m]	-485.1216	-262.0015	-469.8442
y_0 [m]	-249.2703	-219.8463	-219.8463
z_0 [m]	968.4123	939.6926	939.6926
$\dot{x}_0$[m/s]	-0.13169	0	0
$\dot{y}_0$[m/s]	1.0239	0.55399	0.99329
$\dot{z}_0$[m/s]	0.26298	0	0
α_0 [deg]	60.6115	70	61.1002
β_0 [deg]	27.1955	40.0001	25.0755
x_0 [m]	75.56	76.8	76.8

The results obtained are given in Figure 8-30 - Figure 8-34: Pure OPTICs, OPTICs YZ are given respectively by comparing them with PCO.
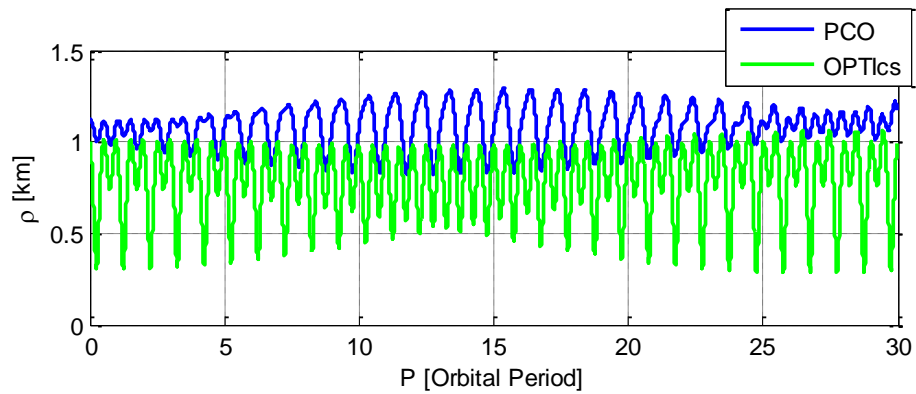
Figure 8-30. PCO/OPTICs: ρ for 75 deg. phase angle with J2
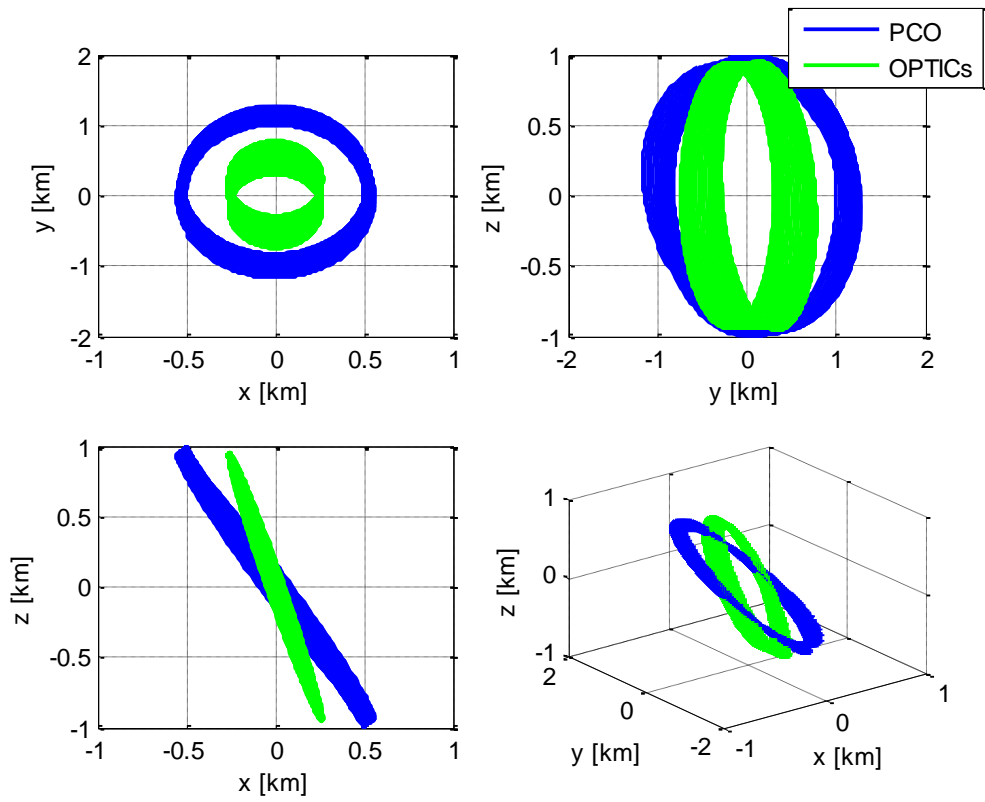
Figure 8-31. PCO/OPTICs: Projected views of ρ, phase 75 deg. with J2
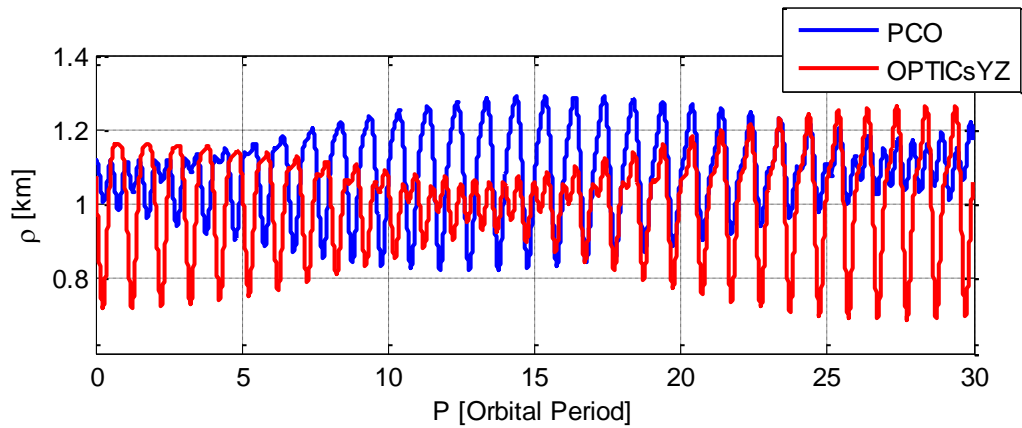
Figure 8-32. PCO/OPTICsYZ: ρ for 75 deg. phase angle with J2
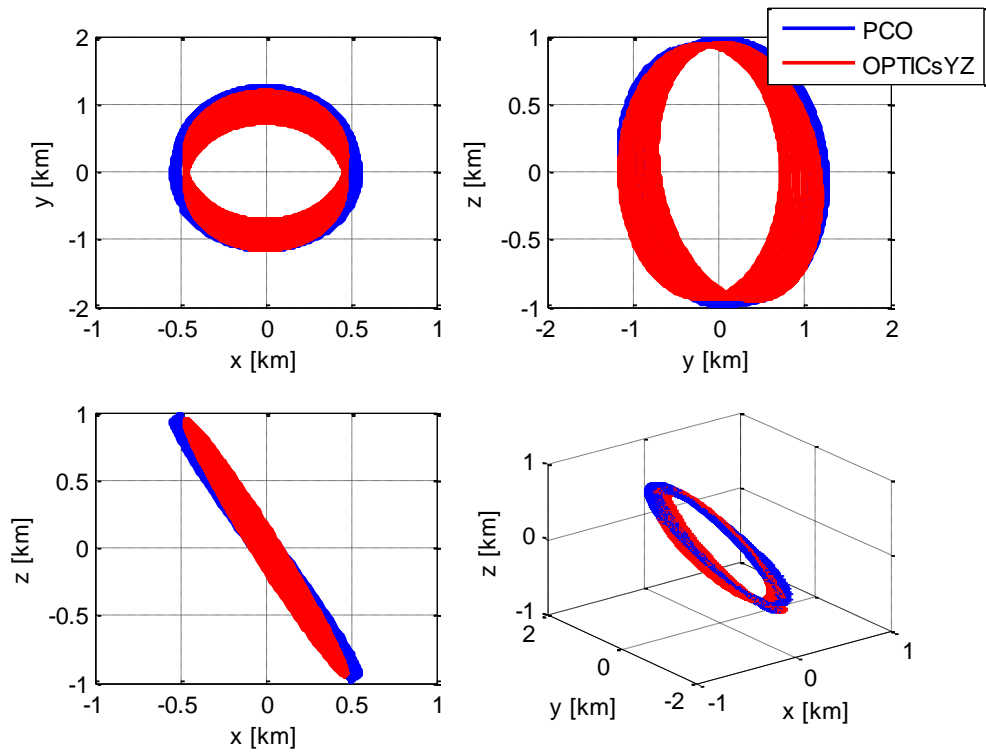
Figure 8-33. PCO/OPTICsYZ: Projected views of ρ, phase 75 deg. with J2
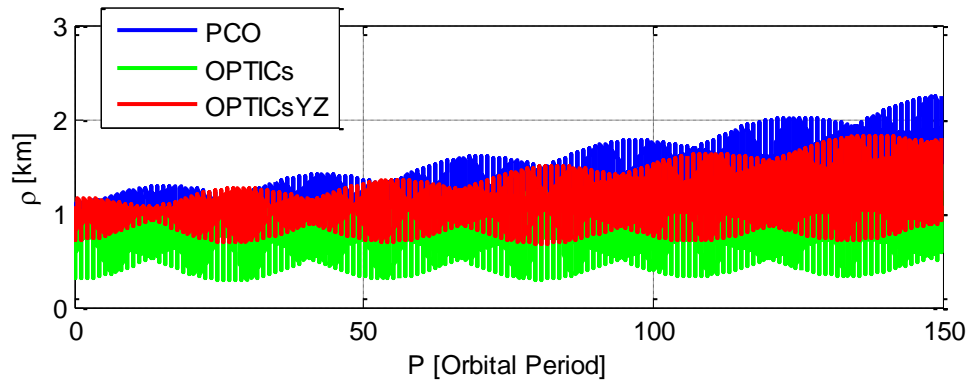
Figure 8-34. Long-term simulation, ρ for 150 orbital periods

A long-term simulation is also run for 150 orbital periods in order to compare the divergence characteristic of the relative motion, as shown in Figure 8-34. PCO

divergence can be seen very clearly, unlike PCO, the time drift of the OPTICs YZ is smaller. And pure OPTICs nearly does not have a divergence but in that case the relative motion has osculation between 0.5 km and 1 km. Depending on the mission requirements, if less deviation is required, OPTICs YZ results can be selected. On the other hand, if the long-term stability is important for the mission in order to not spend fuel to correct orbit, the pure OPTICs results can be used.

8.6. Orbit corrections and Maneuver Budgets Comparison

In this section, one of the conditions mentioned above is used in order to compare orbit correction budgets for PCO and OPTICs cases. The condition with a phase angle of 30 degree and PCO versus OPTICsXZ results are selected.

Figure 8-35 and Figure 8-36 show deltaV values required for the formation correction, for both propagated orbits of PCO and OPTICs XZ. For instance, for the orbit obtained using PCO method, the magnitude of deltaV needed is roughly 5e-3 m/s when the formation correction is done at 20th orbit. But, for the orbit obtained using OPTICs XZ method, the deltaV needed doesn't vary a lot, it can be considered as a constant value. Maximum magnitude of deltaV required is about 5e-3 m/s for PCO and 1e-3 m/s for OPTICs. The dominant component for orbital correction is on Y axis for both cases (Figure 8-35).

Figure 8-36 gives only OPTICs deltaV values in order to display clearly the values computed, since those values are not clearly visible in the first part of the figure when they are compared with PCO. The ratio between PCO and OPTICs is around 1/5 to 1/10.
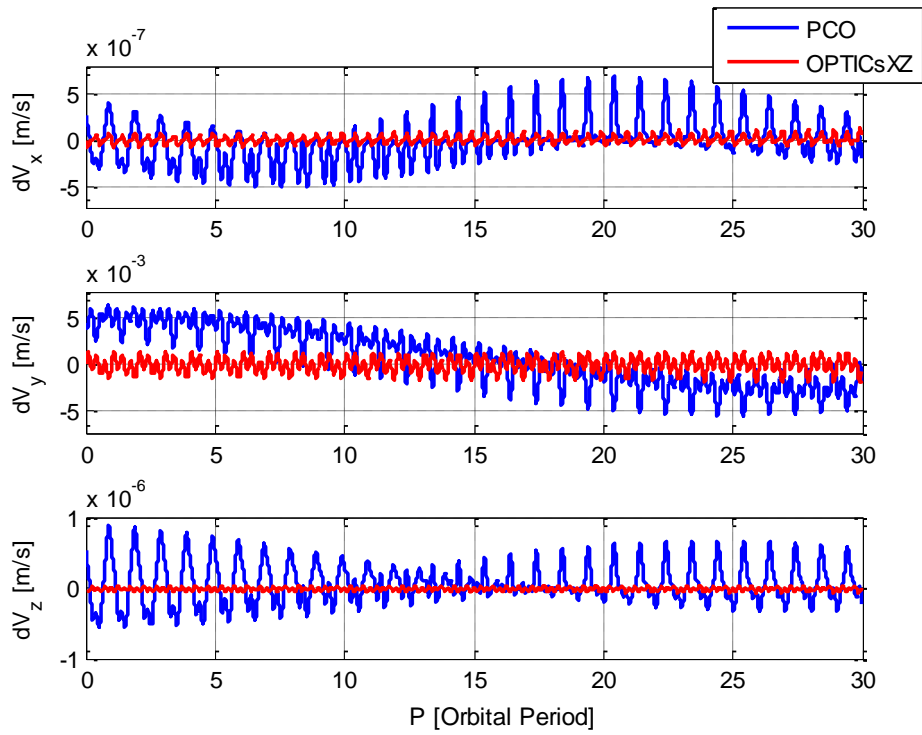
Figure 8-35. Required deltaV for PCO and OPTICS XZ, phase angle 30 deg.
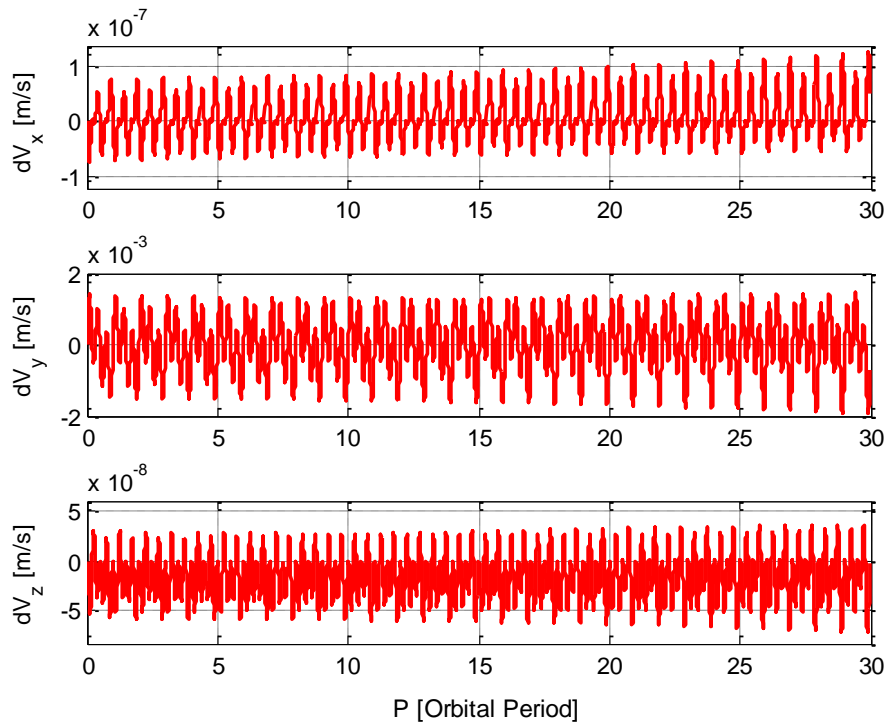
Figure 8-36. Required deltaV for OPTICs XZ - 2

297

Figure 8-37 and in Figure 8-38 present the relative distance for 30 orbital periods when periodic firing is applied, it means that in every orbital period required deltaV is applied. The required deltaV computation is based on the energy matching approach. The details on this computation are given in the Appendix-F. The following figures give the comparison of uncorrected and periodically corrected formation for PCO and OPTICs respectively. The deviation which is about 0.5 km decreases to the 0.25 km due to periodic deltaV correction. Figure 8-39 presents the consumed deltaV in each orbital period and the total consumed deltaV. Here, it is seen that total deltaV is about 0.0402 m/s for the PCO case.
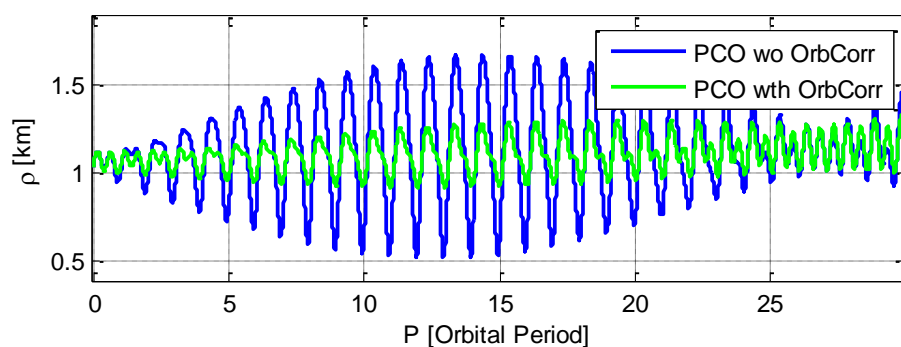
Figure 8-37. ρ without/with periodically formation correction for PCO
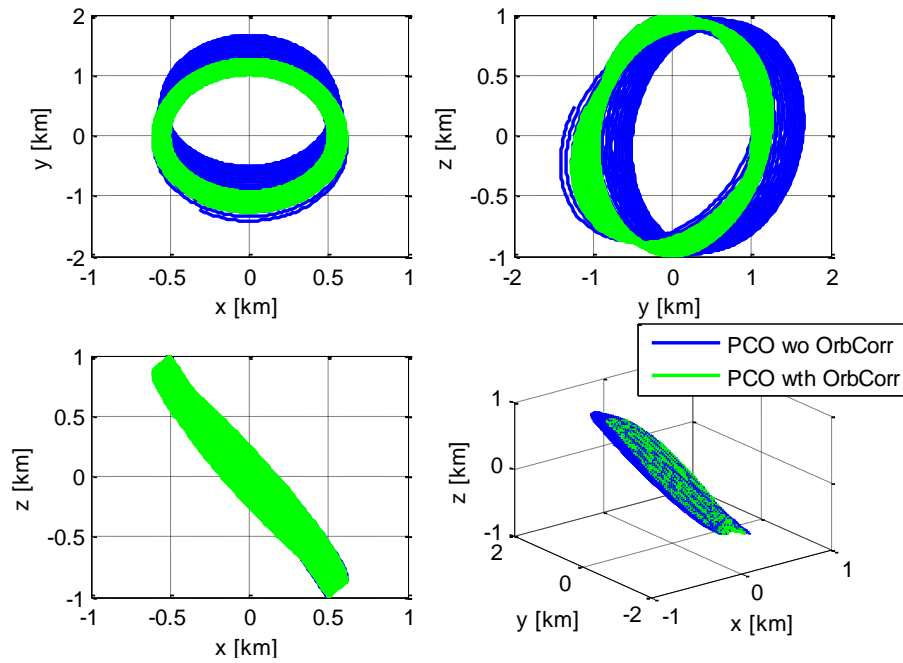
Figure 8-38. Projection views of ρ without/with periodically formation correction for PCO
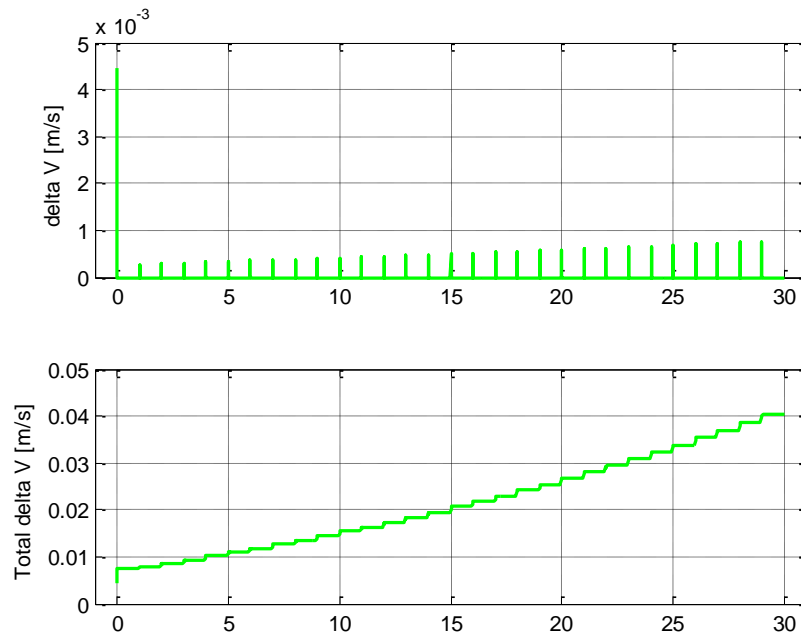
Figure 8-39. DeltaV budget for periodically formation corrections in PCO

Figure 8-40, Figure 8-41 and Figure 8-42 present the results obtained for OPTICs case. The first figure gives the relative distance behavior during 30 orbital periods. The projected views of relative distance show that there is no significant difference between uncorrected and corrected formation, it means that it is not actually very critical to implement any control input to keep the formation for the OPTICs case.
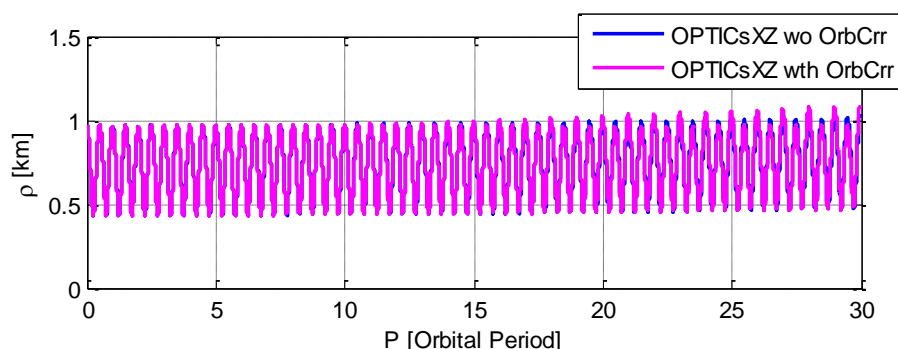
Figure 8-40. ρ without/with periodically formation correction for OPTICs XZ
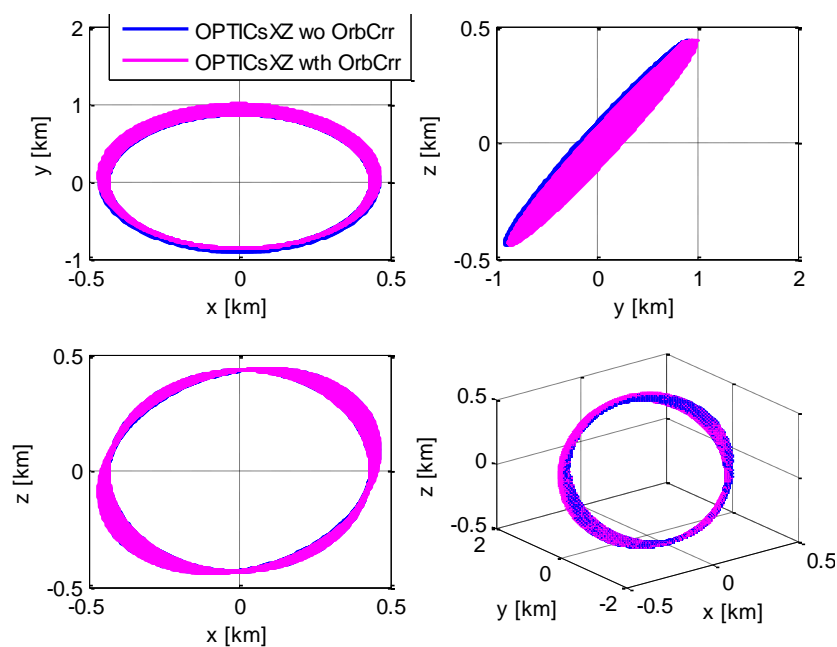
Figure 8-41. Projection views of ρ without/with periodically formation correction for OPTICs
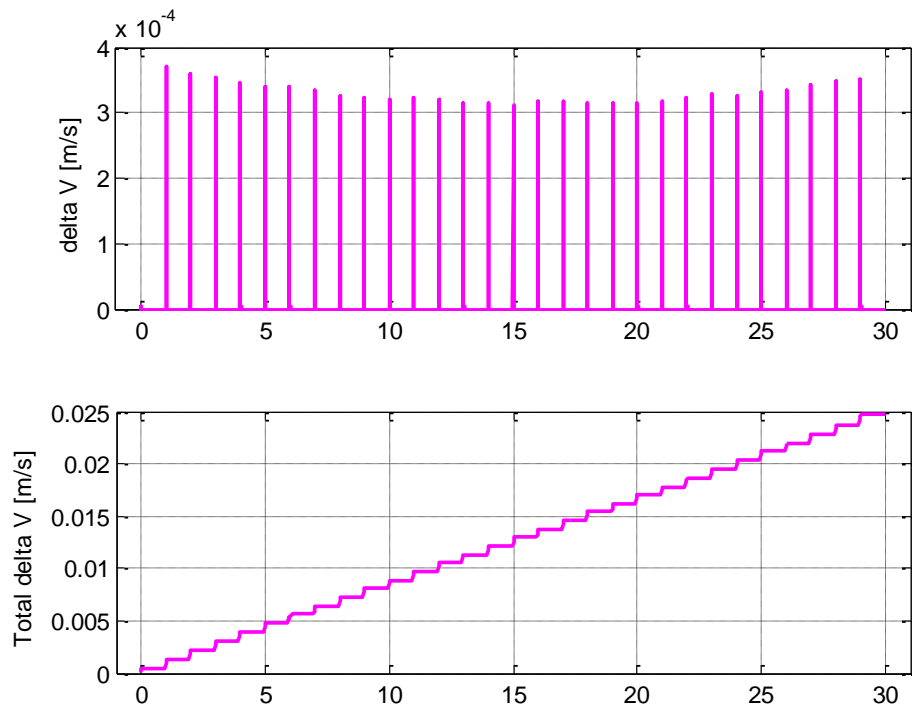
Figure 8-42. DeltaV budget for periodically formation correction in OPTICs XZ

The consumed deltaV for each orbital period is about 4e-4 magnitude and the total consumed deltaV is roughly 0.02465 m/s for OPTICs case and it is approximately half of the PCO case (Figure 8-42). Furthermore, the relative distance does not change substantially. Consequently, the implementation of the correction may be ignored regarding to the mission requirements.

CHAPTER 9

SUMMARY OF LEO FORMATION FLIGHT DESIGN

Studies performed for LEO formation flight design are presented in the second main part of this thesis. The existing methods and the method presented in this thesis are compared in detailed. According to the results obtained it may be stated that the presented method, called OPTICs, it provides much better formation flight performance in terms of formation duration and fuel consumption as well, and it provides flexibility on the orbit design for formation flight.

The simulations are run for different phase angles. As a first step, the simulations performed with both unperturbed and perturbed case (J2 disturbance added models) for 90 degree phase angle. Here, these results prove that the method presented in this thesis is consistent and gives approximately the similar results with the method proposed in literature, called PCO. Then, several phase angle conditions are examined to see the performance of the proposed method, OPTICs. According to the results, it can be stated that OPTICs provides several types of design and offer more stable solutions for a lot of cases, as shared in the previous sections. However, for some of the cases, it is seen that PCO is more successful, but by changing the initial position set of OPTICs, it means forcing for a selected plane, OPTICs gives more stable solutions compared to the PCO. Long term simulations are also run (90 or 150 orbital periods) in order to examine the divergence characteristic of the relative motion. Finally, fuel consumption budget used for formation keeping presents a good performance index to compare the methods. It is seen that the fuel consumption value computed for every orbital period in usage of OPTICs case is approximately half of the PCO case and the implementation of those corrections may be canceled since the relative motion is not disturbed a lot. Here, the deviation obtained on relative distance is in an acceptable interval thanks to the initial conditions computed by the OPTICs.

CHAPTER 10

CONCLUSION

Designing formation configuration that guarantees long-term formation flight with minimum or without correction maneuvers to maintain the formation is addressed. Two different formation cases are examined: trajectories near Sun-Earth system libration points and orbits around Earth. Therefore, this thesis consists of two major parts. The first main part contains the explanations on the three body dynamics, libration points of Sun-Bary system, Halo orbit computation and finally formation flight design near collinear libration points L1 and L2. The second main part is dedicated to the formation flight design for LEO satellites, the orbital dynamics around Earth.

In first part, the main goal is to design halo orbits for each of the formation fleet members by computing the proper relative initial conditions between chief and deputy satellites, such that the computed orbits ensure naturally long-term formation flight without need of orbit correction maneuvers to maintain the desired formation configuration. For this reason, the main disturbances sources are added on the discrete model: solar radiation pressure and gravitational force due to the solar system planets. In first step, it is seen that the gravitational forces due to planets have a significant effect on the spacecraft trajectory near L1 and L2 and it depends on the periodic orbital motion of the planet, as expected.

Differently shaped formation clusters are analyzed in order to understand the effect of the initial relative position on the relative trajectory. The results show that the relative initial condition set creates different relative distance characteristic. Some results have high deviation from desired relative distance, some results have peaks and valleys like a sinusoidal motion, some of them have high deviation rate while other have low, some of them have only one summit or bottom, etc. Finally, an initial

condition set that provide minimum deviation is found for both near L1 and L2 trajectories. It is noticed that various type of formation schema can be formed using computed optimal relative initial conditions. Minimum deviation obtained for both L1 and L2 is around 0.15 km for a desired relative distance of 1 km. All formation configurations given in this thesis show that it is possible to modify or create a formation cluster according to the mission requirements. The method presented in this thesis, named OPTICs, makes it possible to obtain an effective formation flight by computing convenient initial velocities for desired initial relative positions. In summary, square shaped planar and rectilinear formations are generated and investigated. Inclined square shaped planar formation may be useful for the mission requiring quasi-constant relative distance with respect to the chief since deputy pairs make periodic relative trajectory around chief. This formation configuration may be considered for the concepts similar to those of DARWIN and ESPRIT projects. Rectilinear formation on the other hand may be good for mission that requires aligned multiple satellites since identical relative motion is obtained for each successive deputy satellite. For instance, this may offer great advantages for the post-processing operations done on the payload measurements. Furthermore, this rectilinear formation is more flexible in terms of multiplying the number of satellites, it allows to expand the formation fleet. In terms of performance, it is seen that computed formations are maintained roughly for one orbital period of time, approximately half Earth's year, without the need for any correction maneuvers for formation keeping.

The second main part of this thesis contains the formation flight design and analyses for the LEO satellites. OPTICs is reconfigured for LEO dynamic. OPTICs, PCO and GROM methods are compared. It is observed that OPTICs gives consistent results and provides flexibility on the orbit design for formation.

Fuel consumption is a critical issue for LEO formations. Therefore, long term simulations are run (90 and 150 orbital periods) to examine the divergence characteristic of the relative motion. So, fuel consumption budget used for formation keeping is a good performance index to compare the methods. Results indicate that

fuel consumed for formation maintenance is almost halved by the OPTICs method compared to the implementation of the PCO method. Furthermore, the formation corrections may be canceled since the deviation of the relative motion is not at a critical level, it is in an acceptable interval due to the initial conditions computed by the OPTICs.

Finally, it may be stated that the trajectory and orbit computation done using the method given in this thesis provide long term formation flight. For L1 and L2 mission cases, the important parts of this method are the usage of all disturbance sources in the time variant discrete time model for different Julian date intervals and find the initial condition set iteratively that ensure the periodic trajectory. For LEO mission case, the usage of time variant discrete time model to obtain periodic relative motion is a feature that distinguishes it from the existing methods.

Possible future studies that can be performed may be listed as follows: The disturbance characteristic of the solar system planets may be defined as a polynomial in trigonometric form, using Fourier series, depending on the Julian date and they can be added on the equation of motion in this form. In this way, it may be possible to compute analytically the initial conditions ensuring less deviated relative distance between chief and deputy satellites. Proposed procedure may be used for triangular libration points L4 and L5. Formation flight fleets can be design for different three-body systems, for instance Sun-Jupiter-Spacecraft using the methodology given in this thesis.

REFERENCES

[1] Alfriend K.T., Vadali S.R., Gurfil P., Jonatan P.H., Breger L.S., Spacecraft Formation Flying, Dynamics, Control and Navigation, chapter-1, Elsevier, Bulrington, MA, USA, 2010.

[2] Spinoglio L., Schito D., Pezzuto S., Holland W., "Far Infrared Space Intereferometer Critical Assessment", FISICA D1.1SPA.2012.2.2-01: Key technologies enabling observations in and from space, FISICA, October 2014

[3] M. Sauvage, R. J. Ivison, F. Helmich, "Sub-arcsecond far-infrared space observatory: a science imperative", submitted in response to the ESA's call for Science White Papers for the L2 and L3 L-class missions, May 2013

[4] Wallner, O., Ergenzinger, K., Flatscher, R., Johann, U., "DARWIN Mission and Configuration Trade-Off", EADS Astrium GmbH, 88039 Friedrichshafen, Germany, doi: 10.1117/12.671658, June 2006

[5] Fridlund M., "The Darwin Mission", Scientific Frontiers in Research on Extrasolar Planets ASP Conference Series, Vol. 294, 2003

[6] Wilda W., de Graauw Th., Baryshev A., Baselmans J, Bos A. , Gao J.R., Gunst A., Helmich F., ter Horst R. , Jackson B. , Koshelets V.P., Maat P. , Noordam J., Roelfsema P., Venema L., Whyborn N., Yagoubov P., "ESPRIT – A Far-Infrared Space Interferometer", 18th International Symposium on Space Terahertz Technology, 2007

[7] Dr. F. Helmich, Prof. R. Ivison, "FIRI – a Far-InfraRed Interferometer for ESA", Proposal for Cosmic Vision 2015-2025, July 2007

[8] A. Lyngvi, M. Bandecchi, "FIRI – a Far-InfraRed Interferometer ", FIRI, CDF Study Report: CDF-49(A), June 2006

[9] M. Sauvage, G. Durand, "TALC: a Thinned Aperture Light Collector for space far-infrared studies", Seminair de Prospective Scientifique, 2014

[10] ESA eoportal Directory Website, https://earth.esa.int/web/eoportal/satellite-missions/v-w-x-y-z/wind (accessed 11/06/2019)

[11] F.C. Vandenbussche, "SOHO's Recovery– An Unprecedented Success Story", ESA bulletin 97, March 1999

[12] C. E. Roberts, "The SOHO Mission L1 Halo Orbit Recovery From the Attitude Control Anomalies of 1998", June 2002

[13] ESA eoportal Directory Website, https://directory.eoportal.org/web/eoportal/satellite-missions/s/soho (accessed 12/06/2019)

[14] NASA, WMAP Mission Overview Website, https://wmap.gsfc.nasa.gov/mission/ (accessed 02/07/2019)

[15] NASA, WMAP Website, https://map.gsfc.nasa.gov (accessed 03/06/2019)

[16] NASA, NSSDCA Master Catalog Search, Spacecraft, Genesis, https://nsdc.gsfc.nasa.gov/nmc/spacecraft/diplay.action?id=2001-034A (accessed 15/06/2019)

[17] Spaceflights-101, Space News and Beyond, https://spaceflight101.com/dscovr (accessed 15/06/2019)

[18] S. Jung, S.Y. Park, H. Park, C.D. Park, S.W. Kim, Y.S. Jang, "Real-Time Determination of Relative Position Between Satellites Using Laser Ranging", Journal of Astronomy and Space Sciences, 29(4), 351-362, 2012

[19] D. Folta, M. Beckman, "Libration Orbit Mission Design: Applications of Numerical And Dynamical Methods" Libration Point Orbits and Applications, Girona, Spain, June 10-14,2002

[20] J. Leitner, "Formation Flying - The Future of Remote Sensing from Space" 18th International Symposium on Space Flight Dynamics, Munich; Germany, 11 October 2004

[21] E. Canalias, G. Gomez, M. Marcote, J. J. Masdemont, "Assessment of Mission Design Including Utilization of Libration Points and Weak Stability Boundaries", Department de Matematica Aplicada, Universitat Politecnica de Catalunya and Department de Matematica Aplicada, Universitat de Barcellona, 2008

[22] K. C. Howell, B. G. Marchand, "Natural and non-natural spacecraft formations near the L1 and L2 libration points in the Sun–Earth/Moon ephemeris system", Dynamical Systems: An International Journal, Vol. 20, No. 1, 149–173, March 2005

[23] P. Chidambararaj, R.K. Sharma, "Halo Orbits around Sun-Earth L1 in Photogravitational Restricted Three-Body Problem with Oblateness of Smaller Primary", International Journal of Astronomy and Astrophysics, 6, 293-311, 2016

[24] T.Flinois, M.Bottom, S.Martin, D.Scharf, M.C.Davis, S. Shaklan, "Starshade technology to TRL5 Milestone 4 Final Report: Lateral formation sensing and control", JPL CL 19-0503, California Institute of Technology, 2018

[25] M. Bando, A. Ichikawa, "Formation Flying near the Libration Points in the Elliptic Restricted Three-Body Problem", Research paper supported by the Ministry of Education, Sports, Science and Technology of Japan under Grant-in-Aid for Young Scientists, 2013

[26] M. Beckman, "Orbit Determination Issues for Libration Point Orbits", Parador d'Aiguablava, Girona, Spain, June, 2002

[27] T. Luo, M. Xu, Y. Dong, "Natural formation flying on quasi-halo orbits in the photogravitational circular restricted three-body problem", Acta Astronautica 149 (2018) 35–46, https://doi.org/10.1016/j.actaastro.2018.05.027

[28] A. Héritier, K. C. Howell, "Regions near the libration points suitable to maintain multiple spacecraft", AIAA 2012-4666, AIAA/AAS Astrodynamics Specialist Conference, Minneapolis, Minnesota, August 2012

[29] A. Héritier, K. C. Howell, "Dynamical evolution of natural formations in libration point orbits in a multi-body regime", Acta Astronautica 102 (2014) 332 – 340, http://dx.doi.org/10.1016/j.actaastro.2013.10.017

[30] K. Shahid, K. D. Kumar, "Multiple spacecraft formation reconfiguration using solar radiation pressure", Acta Astronautica 103 (2014) 269 – 281, http://dx.doi.org/10.1016/j.actaastro.2014.05.021

[31] S. Jung, Y. Kim, "Formation flying along unstable Libration Point Orbits using switching Hamiltonian structure-preserving control", Acta Astronautica 158(2019) 1-11, 2019, https://doi.org/10.1016/j.actastro.2018.07.020

[32] J. Zhao, Z. Cai, "Nonlinear dynamics and simulation of multi-tethered satellite formations in Halo orbits", Acta Astronautica 63 (2008) 673–681, doi:10.1016/j.actaastro.2008.04.007

[33] I. S. Ilyin, V. V. Sazonov, A. G. Tuchin, "Halo Orbits in the Vicinity of the L2 Libration Point in the Sun–Earth System", ISSN 0010 9525, Cosmic Research, 2014, Vol. 52, No. 3, pp. 189–204

[34] S. Gong, J. Li,H. Baoyin, Y. Gao, "Formation reconfiguration in restricted three body problem", Acta Mech Sin (2007) 23:321–328, DOI 10.1007/s10409-007-0074-5

[35] S. Gong, J. Li,H. Baoyin, "Solar radiation pressure used for formation flying control around the Sun-E arth libration point", Appl . Math. Mech.-Engl .Ed. 30(8) , 1009–1016 (2009), DOI: 10.1007/s10483- 009- 080 7- z

[36] L. G. Taberner, J. J. Masdemont, "FEFF methodology for spacecraft formations reconfiguration in the vicinity of libration points", Acta Astronautica 67 (2010) 810 –817, doi:10.1016/j.actaastro.2010.05.007

[37] H. Peng, J. Zhao, Z. Wu, W. Zhong, "Optimal periodic controller for formation flying on libration point orbits", Acta Astronautica 69 (2011) 537 –550, doi:10.1016/j.actaastro.2011.04.020

[38] H. Zhanga, S. Li, "Station-keeping of libration point orbits by means of projecting to the manifolds", Acta Astronautica 163 (2019) 38–44, https://doi.org/10.1016/j.actaastro.2018.12.002

[39] M. YunHe, Z. YueDong, D. JinHai, "Floquet-based design and control approach to spacecraft formation flying in libration point orbits", Science China Technological Sciences, March 2011 Vol.54 No.3: 758–766, doi: 10.1007/s11431-010-4250-7

[40] L. Jing, L. QiShao, W. Qi, "Orbit control strategy for Lagrange point orbits based on an analytical method", Science China Physics, Mechanics & Astronomy , April 2013 Vol.56   No.4: 830–839, doi: 10.1007/s11433-013-5051-3

[41] M. Martin, P. Klupar, S. Kilberg, j.Winter, "Techsat 21 and Revolutionizing Space Missions Using Microsatellites", American Institute of Aeronautics and Astronautics, SSC01-1-3, January 2001

[42] ESA, Science and Exploration, Space Science, Cluster Overview Website, https://www.esa.int/Science_Exploration/Space_Science/Cluster_overview2 (accessed 15/06/2019)

[43] C. P. Escoubet, M. Fehringer, M. Goldstein, "The Cluster Mission", Annales Geophysicae, 19:1197-1200, 2001

[44] ESA eoportal Directory Website, https://directory.eoportal.org/web/eoportal/satellite-missions/p/proba-3 (accessed 16/06/2019)

[45] L.T. Castellani, J.S. Llorente, J.M.F. Ibarz, M. Ruiz, "PROBA-3 mission", Int. J. Space Science and Engineering, Vol.1, No. 4, 2013

[46] ESA eoportal Directory Website, https://earth.esa.int/web/eoportal/satellite-missions/g/grace (accessed 17/06/2019)

[47] G. Joodaki, "Earth Mass Change Tracking Using Grace Satellite Gravity Data", Thesis for the degree of Philosophiae Doctor, Norwegian University of Science and Technology, Faculty of Engineering Science and Technology, Department of Civil and Transport Engineering, Trondheim, January 2014

[48] NASA, Prolific Earth Gravity Satellites End Science Mission Website, https://www.nasa.gov/press-release/prolific-earth-gravity-satellites-end-science-mission (accessed 18/06/2019)

[49] D. Folta, J. Bristow, "Enhanced Formation Flying (GSFC Algorithm) Summary", Maryland, 2002

[50] D. Folta, "Enhanced Formation Flying for The New Millennium and Mission to Planet Earth Programs", Mission Design and Implementation of Satellite Constellations International Workshop, Toulouse; France, November 1997

[51] D. Folta, J. Bristow, A. Hawkins, G. Dell, "NASA's Autonomous Formation Flying Technology Demonstration, Earth Observing-1 (EO-1), Proceedings of International Symposium Formation Flying, Toulouse; France, 29-31 October 2002

[52] D.Folta, L.K. Newman, D.Quinn, "Design and Implementation of Satellite Formations and Constellations", AAS 98-304, 13th International Symposium on Space Flight Dynamics, Greenbelt, MD; United States, 11-15 May 1998

[53] C.S. Arnot, C.R. McInnes,"Low Thrust Augmented Spacecraft Formation-Flying", 25th International Symposium on Space Flight Dynamics: ISSFD 2015, Munich; Germany, 19-23 October 2015

[54] L.F. Peñín, J.C. Bastante and J.L. Cano, "Formation Flying Mission Analysis for Proba-3", IAC-07-C1.7.02September 2007

[55] J.S. Llorente, A. Agenjo, C. Carrascosa, C. de Negueruela, A. Mestreau-Garreau, A. Cropp, A. Santovincenzo, "PROBA-3: Precise formation flying demonstration mission", Acta Astronautica 82 (2013) 38–46, 2013

[56] M. Martin, S. Kilberg,"TECHSAT 21 And Revolutionizing Space Missions Using Microsatellites" American Institute of Aeronautics and Astronautics, SSC01-1-3, 2001

[57] J. P. Vinti, Edited by G.J. Der, N.L. Bonavito, "Orbital and Celestial Mechanics", Volume 177 Progress in Astronautics and Aeronautics. AIAA, USA,1998

[58] James, J.D.M., "Celestial Mechanics Notes Set 1: Introduction to the N-Body Problem", Florida Atlantic University, Department of Mathematical Sciences, January 3,2007, http://cosweb1.fau.edu/~jmirelesjames/notes.html (accessed 02.04.2018)

[59] ESA ATHENA Study Team, ESTEC document unclassified - for official use, Athena - Coordinate System document, 2015

[60] Gomez, G., Llibre, J., Martinez, R., Simó, C., Dynamics and Mission Design Near Libration Points Vol. l Fundamentals: The Case of Collinear Libration Points, World Scientific Publishing Co. Pte. Ltd., Chapter 1, 2001

[61] James, J.D.M., "Celestial Mechanics Notes Set 4: The Circular Restricted Three Body Problem", Florida Atlantic University, Department of Mathematical Sciences, December 19,2006, http://cosweb1.fau.edu/~jmirelesjames/notes.html (accessed 01.05.2018)

[62] Neil J. The Lagrange Points, Cornish Document Created for WMAP Education and Outreach, 1998

[63] Australian Space Academy Library Website, http://www.spaceacademy.net.au/library/notes/lagrangp.htm (accessed 21/09/2018)

[64] A. K. Pal, B.S. Kushvah, "Geometry of Halo and Lissajous orbits in the circular restricted three-body problem with drag forces", MNRAS 446.959-972(2015), doi: 10.1093/mnras/stu2100

[65] G. Gómez, J. Masdemon, C. Simó, "Lissajous Orbits Around Halo Orbits", AAS 97-106, AAS/AIAA Space Flight Mechanics Meeting, January, 1997

[66] James J.D.M., "Celestial Mechanics Notes Set 5: Symmetric Periodic Orbits of the Circular Restricted Three Body Problem and their Stable and Unstable Manifolds", Florida Atlantic University, Department of Mathematical Sciences, December 22, 2006, http://cosweb1.fau.edu/~jmirelesjames/notes.html (accessed 01.05.2018)

[67] Gomez, G., Jorba, À., Simó, C., Masdemont, J., Dynamics and Mission Design Near Libration Points Vol. Ill Advanced Methods for Collinear Points, World Scientific Publishing Co. Pte. Ltd., Appendix B, 2001

[68] SOHO Community-Local Information Website, https://soho.nascom.nasa.gov/about/orbit.html (accessed 10/08/2019)

[69] H. Halikas, L. Dritsas, A. Pantelus, V. Tsoulkas, Strong Stability of Discrete-Time Systems, Linear Algebra and its Applications 436 (2012) 1890-1908, 2012

[70] I. Reda, A. Andreas, "Solar Position Algorithm for Solar Radiation Applications", National Renewable Energy Laboratory, Technical Report, NREL/TP-560-34302, Revised January 2008

[71] The Planets Today Website, https://www.theplanetstoday.com/planet_nine.html (accessed 05/09/2018)

[72] M.H. Kaplan, "Modern Spacecraft Dynamics and Control", Wiley, Published October 19th 1976

[73] Alfriend K.T., Vadali S.R., Gurfil P., Jonatan P.H., Breger L.S., Spacecraft Formation Flying, Dynamics, Control and Navigation, chapter-4-8, Elsevier, Bulrington, MA, USA, 2010

[74] Hill, G. W., "Researches in Lunar Theory", American Journal of Mathematics, Vol.1, 1878, pp.5-26.

[75] S. Sub Lee, Dynamics and Control of Satellite Relative Motion: Designs and Applications, PhD. Dissertation, Blacksburg, Virginia March 20, 2009

[76] The University of Texas at Austin, Aerospace Engineering and Engineering Mechanics, Courses Notes, Website, http://www.ae.utexas.edu/courses/ase366k/cw_equations.pdf (accessed 04/03/2018)

[77] Chris Sabol, Rich Burns, and Craig A. McLaughlin., "Satellite Formation Flying Design and Evolution", Journal of Spacecraft and Rockets, Vol. 38, No. 2, March–April 2001

[78] H.Cui, J.Li, Y.Gao. (2006), "An Orbital Design Method for Satellite Formation Flying", Journal of Mechanical Science and Technology, Vol.20, No.2, pp177-184,2006

[79] Mark B. Milam, Nicolas Petit, and Richard M. Murray., "Constrained Trajectory Generation for Micro-Satellite Formation Flying", AIAA 2001 -4030, California Institute of Technology, 2001

[80] S.S. Ose, "Attitude Determination for the Norwegian Student Satellite nCube", Master's Thesis, Department of Engineering Cybernetics, Norwegian University of Science and Technology, Norway, June 2004

[81] M. J. Sidi, "Spacecraft Dynamics and Control, A Practical Engineering Approach", Cambridge University Press, 1997

[82] K. Svartveit, "Attitude Determination of nCube Satellite" Master's Thesis, Department of Engineering Cybernetics, Norwegian University of Science and Technology, Norway, June 2003

[83] C. Robinson, Dynamical Systems: Stability, Symbolic Dynamics and Chaos, Second Edition, CRC Press, Boca Raton Florida, 1999

[84] H. Poincare. Les Methodes Nouvelles de la Mecanique Celeste. Gauthier-Villars, 1892, 1893, 1899

[85] NASA, Jet Propulsion Laboratory, Solar System Dynamics Website, https://ssd.jpl.nasa.gov/?planet_eph_export (accessed 15/04/2018)

[86] Rocket and Space Technology, Basic of Space Flight, Planet Positions Website, http://www.braeunig.us/space/plntpos.htm (accessed 15/04/2018)

[87] Meeus, J., Astronomical Formulae for Calculators, Fourth Edition, Willmann-Bell Inc., 1988

[88] Franz, M., Harper, D., "Heliospheric Coordinate Systems", Corrected Version of Planetary and Space Science, 50, 217ff. (2002), March 12, 2002

[89] MIT web course notes, Website, http://web.mit.edu/8.01t/www/materials/modules/chapter25.pdf (accessed 11/06/2017)

A. Reference Frames

i. Heliocentric Coordinate System

In Heliocentric system, since the Helios was the personification of the Sun in Greek mythology, the sun is at the center of the system. The unit vector x is directed from Sun's center towards vernal equinox, the unit vector z is the normal of the fundamental plane named as ecliptic plane and it is directed towards celestial north positively. The unit y vector completes the setup according to the right-hand rule.
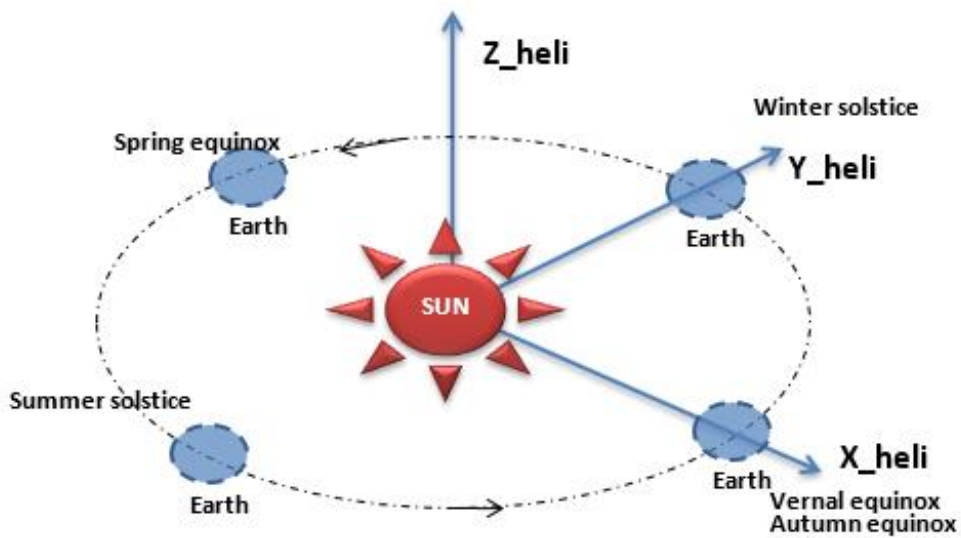
Figure A.1. Heliocentric Coordinate System

ii. Synodic Reference Frame

Synodic reference frame is defined for two massive primaries, for example for the Sun and Earth-Moon Bary. The center of mass of those primaries is the center of the synodic reference frame. The x axis is passing through the Sun and Bary (Earth + Moon), it is aligned towards the Bary. The z axis is perpendicular to the ecliptic plane. The y-axis completes the right-hand Cartesian coordinate system. The main property of this frame is that: This frame has a same angular velocity as that of the primaries. For that reason, it is this very useful for three-body dynamics studies: The primaries are fixed, and additionally Lagrange points of this three-body system is also fixed, since they rotate with same angular velocity of the second primary around the main primary regarding to the inertial reference frame. And the motion of the third body can be easily defined using this fixed reference frame regarding to the primaries. The following figure illustrates the synodic reference frame.
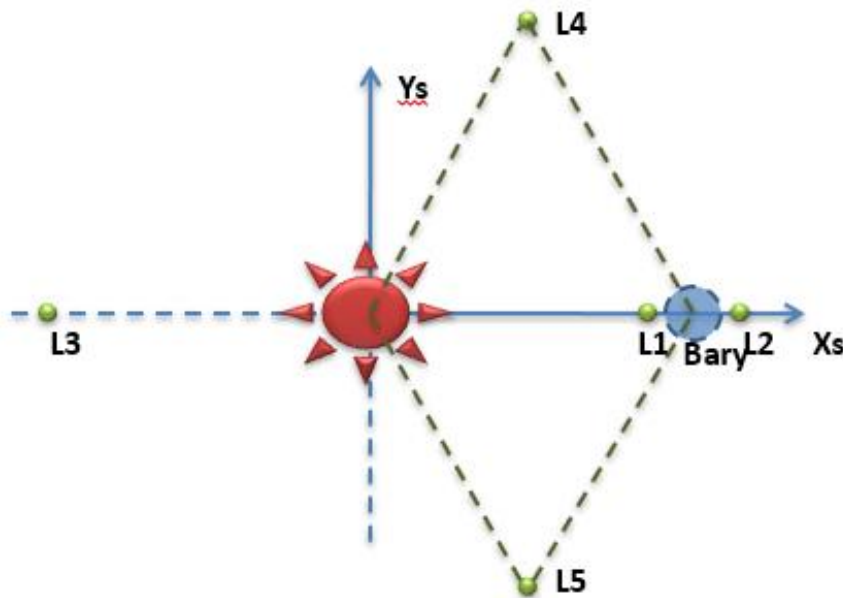
Figure A.2. Synodic Reference Frame

.

iii. Earth-Centered Inertial (ECI) Reference Frame

The ECI frame is assumed to be a non-accelerated frame used for navigation, which is fixed in space with respect to the fixed star defined by the axes X_i, Y_i, Z_i. The origin of the ECI is located at the center of the Earth with the *z-axis* pointing towards the North Pole. The *x-axis* is in the vernal equinox direction, the point where the plane of the Earth's orbit about the Sun, crosses the Equator going from south to north. The *y-axis* completes the right-hand Cartesian coordinate system. The motions of the satellite, the velocity of the Orbit frame and the motion of the Sun is directly compared to this frame. This reference frame is sometimes called as Geocentric Reference Frame.
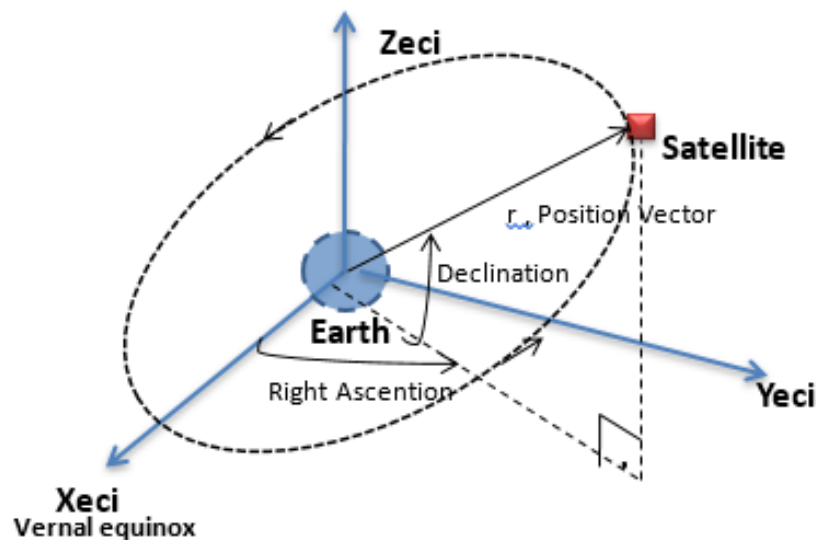
Figure A.3. Earth-Centered Inertial (ECI) Reference Frame

iv. Earth-Centered Earth Fixed (ECEF) Reference Frame

The ECEF frame has its origin at the center of the Earth and axes which are fixed with respect to the Earth (X_e, Y_e, Z_e). The *x-axis* lies along the intersection of the plane of the Greenwich meridian with the Earth's equatorial plane. The *y-axis* completes the right hand system. The earth frame rotates, with respect to the inertial frame, at a rate $\omega_e = 7.2921 \times 10^{-5} rad/s$ (15.0417 °/h) about the *z-axis*. The ECEF frame can be used to express the geomagnetic field around the Earth, along with an orbit estimator to create a reference model.
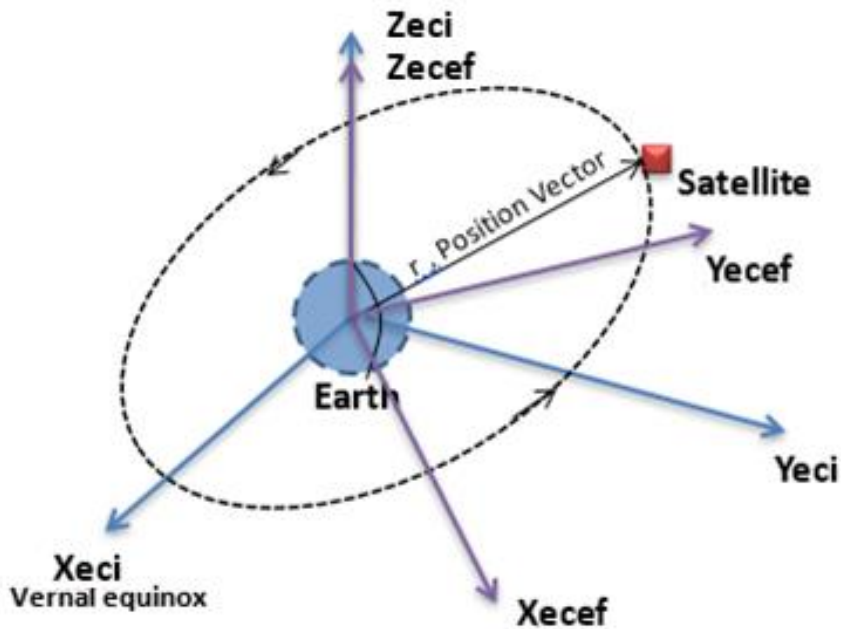
Figure A.4. Earth -Centered Earth Fixed (ECEF) Reference Frame

v. Perifocal Reference Frame

Perifocal reference frame is centered at the Primary bodies of two (or three) body system. The fundamental plane is the orbital plane. The *x-axis* lies along the periapsis form the center of the Primary. The z unit vector is normal to the plane and y completes the right-hand system.
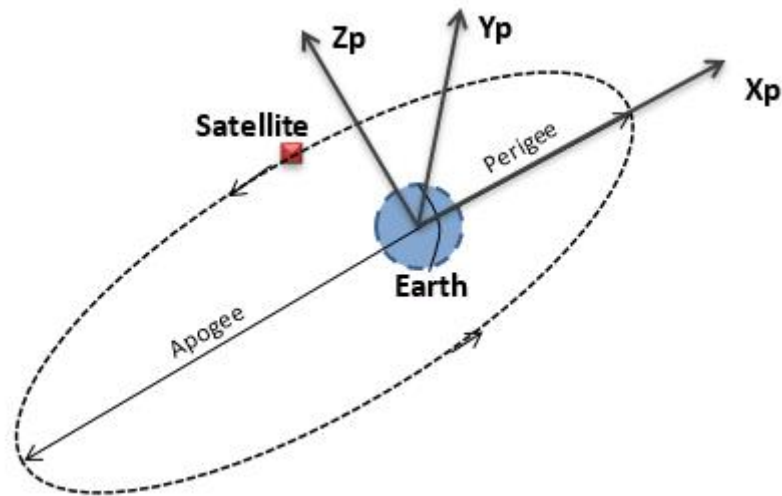
Figure A.5. Perifocal Reference Frame

vi. Orbit (ORB) Reference Frame

The ORB frame has its origin at the mass center the satellite, defined by the axes $X_{orb}, Y_{orb}, Z_{orb}$. This origin rotates relative to the ECI frame, with a rate of ω_{orb} depending on the altitude of the orbit. The *z-axis* lies towards the center of the Earth. The *x-axis* points in the direction of motion tangentially to the orbit. It is important to note that the *tangent* is perpendicular to the radius vector only in case of a circular orbit. In case of a elliptic orbits, the *x-axis* does not align with the satellite's velocity vector. The *y-axis* completes the right hand system. The satellite attitude is described in this frame. This frames is also called as Local vertical Local horizontal (LVLH) frame is some references.
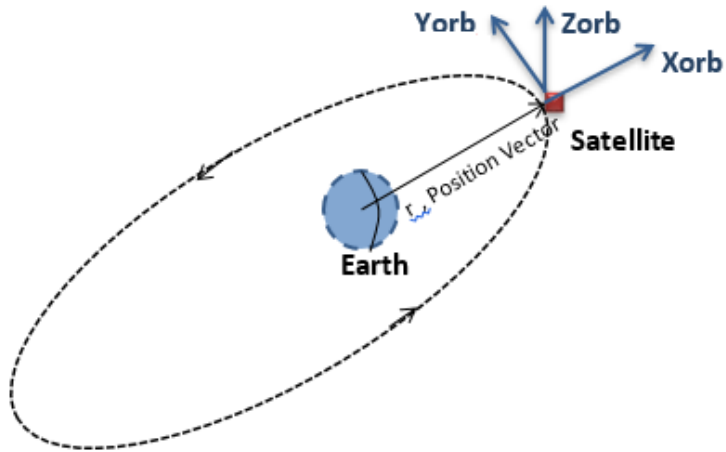
Figure A.6. Orbit (ORB) Reference Frame

vii. Polar Rotating Reference Frame

It is centered at the primary and the plane is the orbital plane. The unit vector r is directed radially towards out from center of the primary. The angle θ is the angular position from perigee to the secondary (satellite) position, this is the angular path and its direction is counterclockwise.
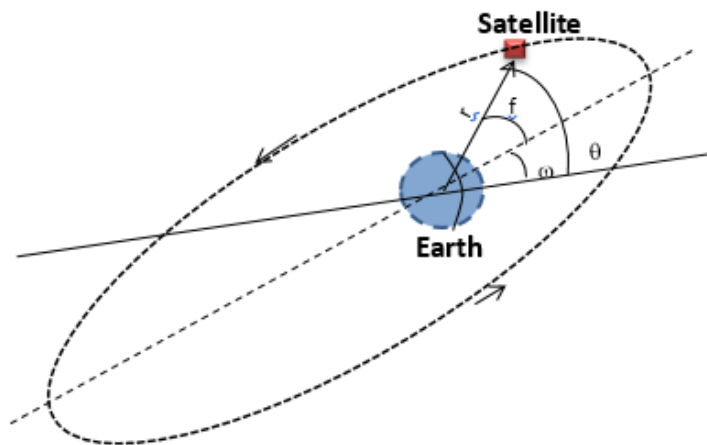
Figure A.7. Polar Rotating Reference Frame

B. Orbital Parameter Computation

The position and the position change of the deputy expressed in ECI reference frame is needed to determine orbit parameters. The deputy position in ECI is computed as follows:

Position vector of the deputy expressed in chief LVLH frame.

$$r_{deputy_{LVLH}} = \rho + \begin{bmatrix} r_{chief} \\ 0 \\ 0 \end{bmatrix} \qquad \text{Eq. A-1}$$

Finally, the deputy's position vector that is expressed in LVLH frame of the chief satellite is transferred to the ECI frame:

$$r_{deputy_{ECI}} \equiv r_{d_{ECI}} = T_{ChiefLVLH}^{ECI} \; r_{deputy_{LVLH}} \qquad \text{Eq. A-2}$$

And;

$$\dot{r}_{deputy_{ECI}} \equiv \dot{r}_{d_{ECI}} = \left(r_{d_{ECI_{t+\Delta t}}} - r_{d_{ECI_t}} \right) / \Delta t \qquad \text{Eq. A-3}$$

Latitude and Longitude of the deputy:

$$longitude_{deputy} \equiv \lambda = \tan^{-1}\left(r_{y\_d_{ECI}} / r_{x\_d_{ECI}} \right) \qquad \text{Eq. A-4}$$

$$latitude_{deputy} \equiv \gamma = \sin^{-1}\left(r_{z\_d_{ECI}} / |r_{d_{ECI}}| \right) \qquad \text{Eq. A-5}$$

    a.   semi-major (a) axis computation:

$$Energy \equiv \varepsilon_{deputy} = \frac{1}{2}|\dot{r}_{d_{ECI}}|^2 - \frac{\mu}{|r_{d_{ECI}}|} \qquad \text{Eq. A-6}$$

$$a_{deputy} = -\frac{\mu}{2\,\varepsilon_{deputy}} \qquad \text{Eq. A-7}$$

$$R_{Earth} = \frac{6378137}{\sqrt{1 + 0.0818191908426^2 \sin^2(\gamma)}} \qquad \text{Eq. A-8}$$

$$Altitude_{deputy} \equiv H = a_{deputy} - R_{Earth} \qquad \text{Eq. A-9}$$

b. Right Ascension of Ascending Node (Ω) computation:

$$K_{ECI} = \begin{bmatrix} 0 \\ 0 \\ 1 \end{bmatrix} \qquad \text{Eq. A-10}$$

$$h = r_{deputy_{ECI}} \times \dot{r}_{deputy_{ECI}} \qquad \text{Eq. A-11}$$

$$Ip = \frac{K_{ECI} \times \frac{h}{|h|}}{\left| K_{ECI} \times \frac{h}{|h|} \right|} \qquad \text{Eq. A-12}$$

$$\Omega = \tan^{-1}\left(\frac{Ip_2}{Ip_1}\right) \qquad \text{Eq. A-13}$$

c. Inclination (i) computation:

$$i = \cos^{-1}\left(K_{ECI}{}^{T} \frac{h}{|h|}\right) \qquad \text{Eq. A-14}$$

d. Argument of perigee (ω) computation:

$$e_v = \frac{1}{\mu}\left(\left(|\dot{r}_{d_{ECI}}|^2 - \frac{\mu}{|r_{d_{ECI}}|} \right) r_{d_{ECI}} - \left(r_{d_{ECI}} \cdot r_{d_{ECI}} \right) \dot{r}_{d_{ECI}} \right) \qquad \text{Eq. A-15}$$

$$e = -|e_v| \qquad \text{Eq. A-16}$$

$$\omega = \cos^{-1}(\text{sign}(e_v{}^{T} K_{ECI})\, Ip^{T}\, e_v) - \pi/2 \qquad \text{Eq. A-17}$$

e. True anomaly (f) computation:

$$\theta = \cos^{-1}\left(\text{Ip}^{\text{T}}\left(\frac{r_{d\text{ECI}}}{|r_{d\text{ECI}}|} \right) \right) \qquad \text{Eq. A-18}$$

$$f = \theta - \omega \qquad \text{Eq. A-19}$$

f. Eccentric anomaly (E) computation:

$$E = 2\tan^{-1}\left(\sqrt{\frac{1-e}{1+e}}\ \tan\left(\frac{f}{2}\right) \right) \qquad \text{Eq. A-20}$$

g. Mean anomaly (M) computation:

$$M = E - e\sin(E) \qquad \text{Eq. A-21}$$

C. Initial Condition Computation via Energy Matching

Here, there are 6 unknowns for initial condition computation; 3 position components and 3 velocity components. It is possible to make equal chief and deputy energy by taking five of six unknowns as given and computing one unknown using the following equation.

$$\varepsilon_{chief} - \varepsilon_{deputy} = 0 \qquad \text{Eq. A-22}$$

$$-\frac{1}{2}\left\{\left(\dot{x} - \dot{\theta}_{chief}y + \dot{r}_{chief}\right)^2 + \left[\dot{y} + \dot{\theta}_{chief}\left(x + r_{chief}\right)\right]^2 + \dot{z}^2\right\}$$

$$-\frac{\mu}{\sqrt{\left(r_{chief} + x\right)^2 + y^2 + z^2}} + \frac{\mu}{2a_{chief}} = 0 \qquad \text{Eq. A-23}$$

a. For $\dot{x}, \dot{y}, \dot{z}, y, z$ are given, x is computed using following equations:

Let:

$$r \equiv r_{chief}$$

$$X = x + r$$

$$A = \left(\dot{x} - \dot{\theta}y + \dot{r}\right)^2$$

$$B = \dot{z}^2 \qquad \text{Eq. A-24}$$

$$E = \mu/a_0$$

$$D = y^2 + z^2$$

$$\xrightarrow{yields} A + B + \left[\dot{y} + \dot{\theta}X\right]^2 + E - \frac{2\mu}{\sqrt{X^2 + D}} = 0 \qquad \text{Eq. A-25}$$

$$\xrightarrow{yields} X^6\left(\dot{\theta}^4\right) + X^5\left(4\,\dot{y}\,\dot{\theta}^3\right) + X^4\left(6\dot{y}^2\dot{\theta} + D\dot{\theta}^4 + 2F\dot{\theta}^2\right)$$

$$+ X^3\left(4\dot{y}^3\dot{\theta} + 4D\dot{y}\dot{\theta}^3 + 4F\dot{y}\dot{\theta}\right)$$

$$+ X^2\left(F^2 + \dot{y}^4 + 6D\dot{y}^2\dot{\theta} + 2F\dot{y}^2 + 2FD\dot{\theta}^2\right) \quad \text{Eq. A-26}$$

$$+ X\left(4D\,\dot{y}^{\,3} + 4FD\dot{y}\dot{\theta}\;\right)$$

$$+ \left(DF^2 + D\dot{y}^4 + 2FD\dot{y}^2 - 4\mu^2\right) = 0$$

Solution of this 6th order equation gives the value of X

b. For $\dot{x}, \dot{y}, \dot{z}, x, z$ are given, y is computed using following equations:

Let:

$$r \equiv r_{chief}$$

$$A = \left(\dot{y} + \dot{\theta}(x + r)\right)^2 \qquad \text{Eq. A-27}$$

$$B = \dot{z}^2$$

326

$$E = \mu/a_0$$
$$C = \dot{x} + \dot{r}$$
$$D = (x + r)^2 + z^2$$

$$\xrightarrow{yields} (C - \dot{\theta}y)^2 A + B - \frac{2\mu}{\sqrt{y^2 + D}} + E = 0 \qquad \text{Eq. A-28}$$

$$\xrightarrow{yields} y^6(\dot{\theta}^4) + y^5(-4C\dot{\theta}^3) + y^4(2F\dot{\theta}^2 + 6C^2\dot{\theta}^2 + D\dot{\theta}^4)$$
$$+ y^3(-4FC\dot{\theta} - 4C^3\dot{\theta} - 4CD\dot{\theta}^3)$$
$$+ y^2(F^2 + 2FC^2 + 2FD\dot{\theta}^2 + C^4 \qquad \text{Eq. A-29}$$
$$+ 6DC^2\dot{\theta}^2) + y(-4DFC\dot{\theta} - 4DC^3\dot{\theta} \ )$$
$$+ (DF^2 + 2FDC^2 + DC^4 - 4\mu^2) = 0$$

Solution of this 6th order equation gives the value of y

c. For $\dot{x}, \dot{y}, \dot{z}, x, y$ are given, z is computed using following equations:
Let:

$$r \equiv r_{chief}$$
$$A = (\dot{x} - \dot{\theta}y + \dot{r})^2$$
$$B = (\dot{y} + \dot{\theta}(x + r))^2 \qquad \text{Eq. A-30}$$
$$E = \mu/a_0$$
$$C = \dot{z}^2$$
$$D = (x + r)^2 + y^2$$

$$\xrightarrow{yields} F^2 - \frac{4\mu^2}{z^2 + D^2} = 0 \qquad \text{Eq. A-31}$$

$$\xrightarrow{yields} z = \pm\sqrt{\frac{4\mu^2}{F^2} - D} \qquad \text{Eq. A-32}$$

Solution of this equation gives the value of z

d. For $\dot{y}, \dot{z}, x, y, z$ are given, $\dot{x}$ is computed using following equations:

Let:

$$r \equiv r_{chief}$$

$$A = \left(\dot{y} + \dot{\theta}(x + r)\right)^2$$

$$B = \dot{z}^2$$

$$C = \frac{2\mu}{\sqrt{(x + r)^2 + y^2 + z^2}}$$
Eq. A-33

$$D = r - \dot{\theta}y$$

$$E = \mu/a_0$$

$$F = A + B - C + E$$

$$\xrightarrow{yields} (\dot{x} + D)^2 + A + B - C + E = 0$$
Eq. A-34

$$\xrightarrow{yields} \dot{x}^2 + \dot{x}2D + (D^2 + F) = 0$$
Eq. A-35

Solution of this equation gives the value of $\dot{x}$

e. For $\dot{x}, \dot{z}, x, y, z$ are given, $\dot{y}$ is computed using following equations:

Let:

$$r \equiv r_{chief}$$

$$A = \left(\dot{x} - \dot{\theta}y + \dot{r}\right)^2$$

$$B = \dot{z}^2$$

$$C = \frac{2\mu}{\sqrt{(x + r)^2 + y^2 + z^2}}$$
Eq. A-36

$$D = \theta(x + r)$$

$$E = \frac{\mu}{a_0}$$

$$F = A + B - C + E$$

$$\xrightarrow{yields} \dot{y}^2 + \dot{y}2D + (D^2 + F) = 0$$
Eq. A-37

Solution of this equation gives the value of $\dot{y}$

f. For $\dot{x}, \dot{y}, x, y, z$ are given, $\dot{z}$ is computed using following equations:

Let:

$$r \equiv r_{chief}$$

$$A = \left(\dot{x} - \dot{\theta}y + \dot{r}\right)^2$$

$$B = \left(\dot{y} + \dot{\theta}(x + r)\right)^2$$

$$C = \frac{2\mu}{\sqrt{(x+r)^2 + y^2 + z^2}}$$

$$E = \mu/a_0$$

$$F = A + B - C + E$$

Eq. A-38

$$\xrightarrow{yields} \dot{z}^2 + F = 0$$

Eq. A-39

Solution of this equation gives the value of $\dot{z}$

$$\dot{z} = \pm\sqrt{F}$$

Eq. A-40

D. Orbit Propagator Model

Keplerian orbit, in other word Kepler's equation is used to model the orbital motion of the LEO satellites. As known; the physical laws describing the motion of planets were first described by Johann Kepler. Kepler's three laws state that:

1. The orbit of each planet is an ellipse, with the Sun at one of the foci.
2. The line joining the planet to the Sun sweeps out equal areas in equal times.
3. The square of the period of a planet is proportional to the cube of its mean distance from the Sun.

Kepler's laws are the basis for the Keplerian elements, called also orbital elements, which are used in predicting a satellite's orbit and position. The Earth is at one focus of the ellipse. The two foci coincide with the center in the case of the circular orbit and as a result, the Earth takes its place at the center of the ellipse [80]. The Orbit Propagator Model used in the simulation is given in Keplerian elements. See Figure A.8 and Figure A.9 for visual description of all the Keplerian elements [81]:

1. Orbital Inclination
2. Right Ascension of Ascending Node (R.A.A.N.)
3. Argument of Perigee
4. Eccentricity
5. Mean Motion
6. Mean Anomaly
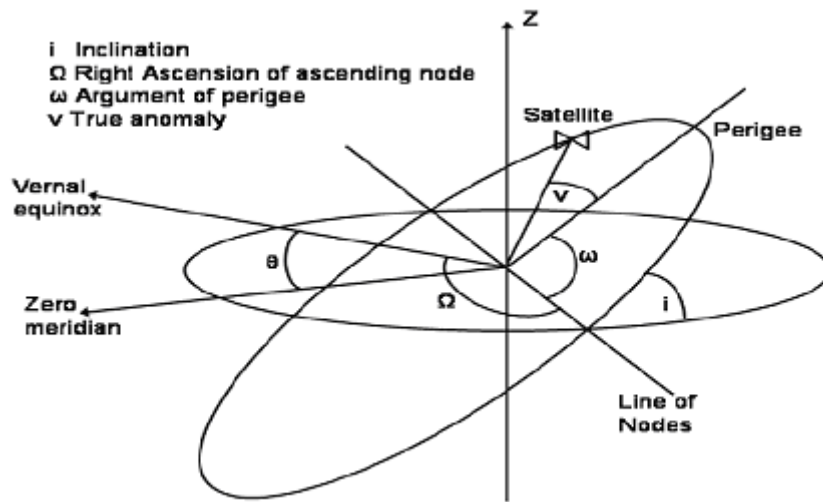
Figure A.8. The Keplerian Elements [80]
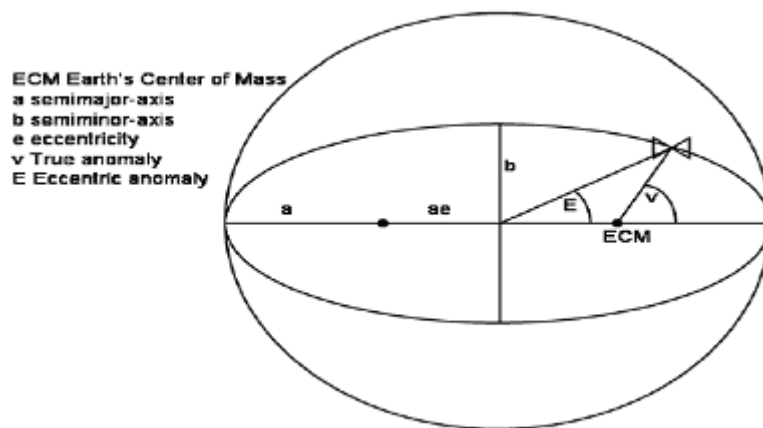
Figure A.9. The Keplerian Elements in plane [80]

These elements describe the position of the satellite at a specific time. The most widely used format for this time is called epoch (Julian Date) that gives the year and day of the year as a decimal number. Based on this time, the ascension of the zero

331

meridians (θ), can also be calculated. The rotation between ECI and ECEF reference frame given by:

$$C_E^I = C_{z_I, \theta} = \begin{bmatrix} \cos\theta & \sin\theta & 0 \\ -\sin\theta & \cos\theta & 0 \\ 0 & 0 & 1 \end{bmatrix} \qquad \text{Eq. A-41}$$

The following four Keplerian elements specify the orientation of the orbital plane, the orientation of the orbit ellipse in the orbital plane, and the shape of the orbit ellipse [80]:

Orbital Inclination (i):
The inclination is the angle between the orbital and equatorial plane. By convention, inclination is a number between 0 and 180 degrees. Orbits with inclination near 0 degrees are called equatorial orbits and orbits with inclination near 90 degrees are called polar. The intersection of the equatorial plane and the orbital plane is a line which is called the line of nodes. The line of nodes is more thoroughly described below.

Right Ascension of Ascending Node (Ω):
The line of nodes intersects the equatorial plane two places: One of them the satellite passes from south to north, this is called the ascending node and the other node where the satellite passes from north to south is called the descending node. The angle between the ascending node and the vernal equinox is called the right ascension of ascending node. By convention, the right ascension of ascending node is between 0 and 360 degrees. The combination of the right ascension of ascending node and the inclination defines the orbital plane in which the elliptic orbit lies.

Argument of Perigee (ω):

In the ellipse, the closest point to the focus point, in which the earth lies, is called *perigee*, and the farthest point from the earth is called *apogee*. The angle between the line from perigee through the center of the earth to the apogee and the line of nodes is the argument of perigee. This angle is defined as the angle from the ascending node and by convention it is between 0 and 360 degrees.

Eccentricity (e):

The eccentricity is given as

$$e = \sqrt{1 - \frac{b^2}{a^2}}$$ Eq. A-42

where a is the semimajor-axis and b is the semiminor-axis. The semimajor-axis is half the distance between the apogee and the perigee, and semiminor-axis half the length between the edges perpendicular to a. For an ellipse, e is between 0 and 1. For a perfect circle $a = b$ and thus $e = 0$.

The following Keplerian elements is time varying and specify the position of the satellite in orbit using the previous four elements describing above [78].

Mean Motion (n):

The mean motion is the average angular velocity describes the size of the ellipse. It is related to the semimajor-axis using Kepler's third law:

$$n = \sqrt{\frac{\mu_e}{a^3}}$$ Eq. A-43

where $\mu_e = G. M_e$, G is the Earth's gravitational constant and M_e is the mass of the Earth.

Mean Anomaly (M):

Mean Anomaly defines the position of the satellite in the ellipse. It is an angle that marches uniformly in time from 0 to 360 degrees during one revolution. It is defined to be 0 degrees at perigee and 180 degrees at apogee. There is an important point to note that in a non-circular ellipse, this angle does not give the direction towards the satellite except at perigee and apogee. This is because satellite does not have a constant angular velocity.

The direction from the earth center towards the satellite is called *true anomaly (v)* and the direction from the center of the ellipse towards the point on a circle is called *eccentric anomaly (E)*. The relationship between true anomaly and eccentric anomaly is:

$$\cos v = \frac{\cos E - e}{1 - e \cos E} \qquad \text{Eq. A-44}$$

$$\sin v = \frac{\sqrt{1 - e^2} \sin E}{1 - e \cos E} \qquad \text{Eq. A-45}$$

And the relationship between mean anomaly and eccentric anomaly is:

$$M = E - e \sin E \, (t) \qquad \text{Eq. A-46}$$

The orbit propagotor model can now be made by using the cahnge of the mean anomaly in time. The prediction of the future position becomes relatively straight forward tahnks to keplerian elements for a single point in time. Given the Keplerian elements for a time, t_0, a prediction of the orbit is:

$$M(t_0 + t) = M(t_0) + n \cdot t \qquad \text{Eq. A-47}$$

where t is the time passed since t_0. Eq.13-47 describes the motion of the spacecraft in ECOF, coordinates. To transform this to ECEF frame it is required to solve Kepler's equation which relates the eccentric anomaly to the mean anomaly.

$$E(t) = M(t) + e \cdot \sin E(t) \qquad\qquad \text{Eq. A-48}$$

This equation can be solved iteratively such as:

$$E_{i+1} = M + e \sin E_i \qquad\qquad \text{Eq. A-49}$$

It is taken $E_0 = 0$ for the initial condition as does Newton method and finally the following solution is obtained:

$$E_{i+1} = E_i + \frac{M + e \sin E_i - E_i}{1 - e \cos E_i} \qquad\qquad \text{Eq. A-50}$$

Finally, the vector from the center of the Earth to the satellite expressed in the ECOF is formulated by using the eccentric anomaly as follows:

$$r^{OC} = a \begin{bmatrix} \cos E - e \\ \sqrt{1 - e^2} \sin E \\ 0 \end{bmatrix} \qquad\qquad \text{Eq. A-51}$$

The orbit propagator can now be implemented in ECI frame and ECEF frame:

$$r^I = C^I_{OC} r^{OC} = C_z(-\Omega) \ C_x(-i) \ C_z(-\omega) \ r^{OC} \qquad \text{Eq. A-52}$$

$$r^E = C^E_{OC} r^{OC} = C_z(-\Omega + \theta) \ C_x(-i) \ C_z(-\omega) \ r^{OC} \qquad \text{Eq. A-53}$$

where Ω is the Right Ascension of Ascending Node, i is the inclination of the satellite, ω is Argument of Perigee and θ is the ascension of the zero meridians.

An orbit propagator based only on the Keplerian elements will degrade in accuracy over time. In order to prevent from this error, certain improvements utilizing known irregularities can be made. The biggest source of degradation is the nonspherical shape of the Earth. The deformation is often parameterized by the geopotential function as described in Wertz and Larson (1999), which uses the deformation coefficients J_i for i^{th} order deformations. The other error sources which are less influence on the perturbations of the spacecraft's orbit can be listed as gravitational forces from the sun and the moon, tidal earth and ocean, and different electromagnetic radiations [82]. In the following sub-sections, the descriptions of these perturbations are given respectively:

Perturbations due to the nonspherical Earth

The earth has not a perfect spherical shape; actually, it has a bulge at the equator, is flattened at the poles and is slightly pear-shaped. This imperfect form leads to perturbations in all Keplerian elements. In the second order deformation of the Earth it is considered that the Earth is partly flattened, and leads to the largest perturbations in the Keplerian elements. According to the Lagrange planetary equations, the flattening factor J_2 is governed by using the time derivatives functions of the right ascension of the ascending node and the argument of perigee:

$$\dot{\Omega}_{J2} = -\frac{3}{2}nR_{earth}^2 \frac{\cos i}{a^2(1-e^2)^2}J_2 \qquad \text{Eq. A-54}$$

$$\dot{\omega}_{J2} = \frac{3}{4}nR_{earth}^2 \frac{5\cos^2 i - 1}{a^2(1-e^2)^2}J_2 \qquad \text{Eq. A-55}$$

$$n = \bar{n} + \frac{3}{4}J_2 n \left(\frac{R_{earth}}{a(1-e^2)}\right)\sqrt{1-e^2}(2 - 3\sin^2(i)) \qquad \text{Eq. A-56}$$

where R_{earth} is the Earth radius, and the numerical value of J_2 for the Earth is $1.08284 \cdot 10^{-3}$.

Perturbations due to the sun and the moon

The Sun and the moon cause periodic variations in all Keplerian elements. There are only secular perturbations to the right ascension of the ascending node and the argument of perigee. An approximation is suggested by Wertz and Larson (1999) for nearly circular orbits as [82]:

$$\dot{\Omega}_{sun} = -0.00154 \frac{\cos i}{n} \qquad \text{Eq. A-57}$$

$$\dot{\Omega}_{moon} = -0.00338 \frac{\cos i}{n} \qquad \text{Eq. A-58}$$

And

$$\dot{\omega}_{sun} = 0.00077 \frac{5\cos^2 i - 1}{n} \qquad \text{Eq. A-59}$$

$$\dot{\omega}_{moon} = 0.00169 \frac{5\cos^2 i - 1}{n} \qquad \text{Eq. A-60}$$

where n is the number of the revolution per day and $\dot{\Omega}$ and $\dot{\omega}$ units are given in degree/day.

E. Equations of Motion Added J2 Effects

The perturbation model due to J2 is derived using the mean orbital elements. The following model gives a method to add J2 perturbation for the nearly circular orbit. The equation of the relative motion can be written in matrix form as follows [73]:

$$\ddot{\rho}|_{Orb} = C^T \left[-\frac{\mu(r_{chief} + \rho)}{|r_{chief} + \rho|^3} + \frac{\mu r_{chief}}{|r_{chief}|^3} \right]_{Prf}$$

Eq. A-61

$$-\left(2\widetilde{\omega}\,\dot{\rho}|_{Orb} + \dot{\widetilde{\omega}}\,\rho|_{Orb} + \widetilde{\omega}^2\,\rho|_{Orb} \right) + Acc_{J2}$$

where ρ is the relative position vector, ω is the angular velocity vector of the orbital frame with the component:

$$\omega = [\omega_x \quad \omega_y \quad \omega_z]$$

Eq. A-62

$$\omega_x = \dot{\Omega}_{chief} \sin(i_{chief}) \sin(\theta_{chief}) + i_{chief} \cos(\theta_{chief})$$

Eq. A-63

$$\omega_y = \dot{\Omega}_{chief} \sin(i_{chief}) \cos(\theta_{chief}) - i_{chief} \sin(\theta_{chief}) = 0$$

Eq. A-64

$$\omega_z = \dot{\Omega}_{chief} \cos(i_{chief})\, s + \dot{\theta}_{chief}$$

Eq. A-65

Here, θ_{chief} is the argument of latitude, i_{chief} is the inclination of the chief's orbit, Ω_{chief} is the longitude of the ascending node.

The acceleration due to J2 perturbation is denoted as Acc_{J2} and the Linearized differential acceleration vector of this can be written as follows:

$$Acc_{J2} = 6\Gamma \begin{bmatrix} 1 - 3\,s^2(i)\,s^2(\theta) & s^2(i)s(2\theta) & s(2i)s(\theta) \\ s^2(i)s(2\theta) & s^2(i)\left(\frac{7}{4}s^2(\theta) - \frac{1}{2}\right) - \frac{1}{4} & -0.25s(2i)s(\theta) \\ s(2i)s(\theta) & -0.25s(2i)s(\theta) & s^2(i)\left(\frac{5}{4}s^2(\theta) + \frac{1}{2}\right) - \frac{3}{4} \end{bmatrix} \rho$$

Eq. A-66

Where $\sin(x)$ is denoted by $s(x)$ and $\cos(x)$ is denoted by $c(x)$ and

$$\Gamma = J_2\mu\left(\frac{R_{earth}^2}{r_{chief}^5}\right)$$

Eq. A-67

On the other way, this J2 model added equations of motion can be written as follows [79]:

$$\ddot{x} = -\frac{\mu x}{m|x|^3}\left(1 - J_2\frac{3}{2}\frac{R_{earth}^2}{r_{chief}^2}\left(5\frac{z^2}{r_{chief}^2} - 1\right)\right)$$

$$\ddot{y} = -\frac{\mu y}{m|x|^3}\left(1 - J_2\frac{3}{2}\frac{R_{earth}^2}{r_{chief}^2}\left(5\frac{z^2}{r_{chief}^2} - 1\right)\right)$$

Eq. A-68

$$\ddot{z} = -\frac{\mu z}{m|x|^3}\left(1 - J_2\frac{3}{2}\frac{R_{earth}^2}{r_{chief}^2}\left(5\frac{z^2}{r_{chief}^2} - 3\right)\right)$$

This J2 model is added to the simulation in order to see relative motion characteristic under disturbed environment.

F. Control Force Computation to Keep LEO Formation

The computation of the control forces required for keeping formation is based on the energy matching approach: the energy of the chief and deputy satellites must be equal.

$$\frac{1}{2}\left\{(v_x + \Delta v_x)^2 + \left[v_y + \Delta v_y\right]^2 + [v_z + \Delta v_z]^2\right\}$$

$$-\frac{\mu}{\sqrt{\left(r_{chief} + x\right)^2 + y^2 + z^2}} - \frac{\mu}{2a_{chief}} = 0 \qquad \text{Eq. A-69}$$

Where; v_x, v_y, v_z are the current velocity components of the deputy satellite. And $\Delta v_x, \Delta v_y, \Delta v_z$ are the required deltaV values in order to keep the formation. The current velocity components of the deputy satellite can be written as follows:

$$\begin{bmatrix} v_x \\ v_y \\ v_z \end{bmatrix} = \begin{bmatrix} \dot{x} - \dot{\theta}_{chief}y + \dot{r}_{chief} \\ \dot{y} + \dot{\theta}_{chief}\left(x + r_{chief}\right) \\ \dot{z} \end{bmatrix} \qquad \text{Eq. A-70}$$

And finally, required deltaV is computed using following equation set:

$$\begin{bmatrix} \Delta v_x \\ \Delta v_y \\ \Delta v_z \end{bmatrix} = \begin{bmatrix} v_x \\ v_y \\ v_z \end{bmatrix} \Gamma \qquad \text{Eq. A-71}$$

where;

$$\Gamma = -1 \pm \frac{1}{v_{deputy}}\sqrt{\frac{\mu\left(2a_{chief} - r_{deputy}\right)}{a_{chief}\,r_{deputy}}} \qquad \text{Eq. A-72}$$

G. Poincaré Maps

Henri Poincaré invented a new mathematical method in order to answer the stability question using geometric arguments, rather than analytic methods [84]. This method produces the modern fields of differential geometry and topology. Poincaré prove that the three-body problem is stable due to the existence of periodic solutions [89]. So, Poincare maps are a fundamental tool for analyzing flows in the dynamical systems. This map gives much more global picture of the dynamics of a system than the linear analysis [83].

The choice of Poincare map can reduce the dimension of the system. The discrete dynamical system generated by the Poincare map gives a lower bound on the complexity of the dynamics of the flow. Period points in the Poincare map expose periodic orbits in the flow.
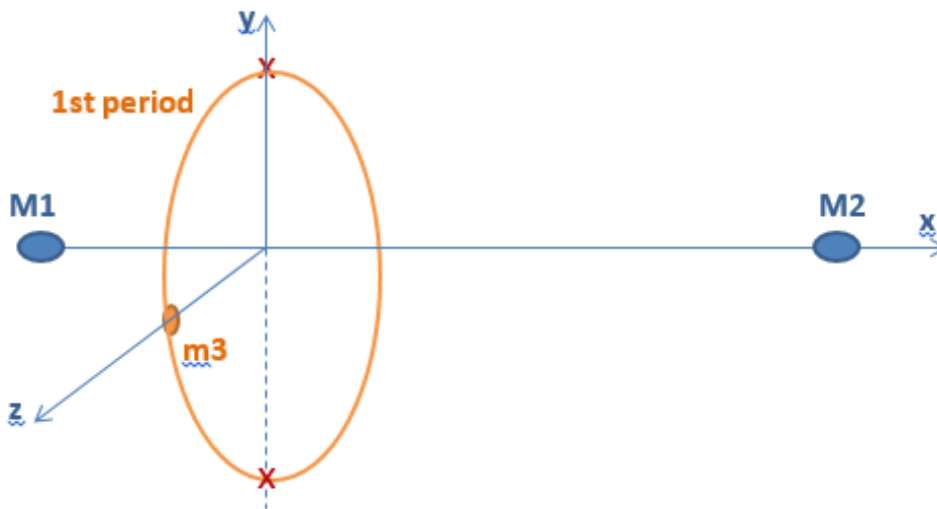
Figure A.10. One period run to visualize first period

The procedure to construct Poincare Map can be listed as follows:

- The mass of the third body is negligible compared to the primary bodies: M1>>m3 and M2>>m3
- The third body, m3 is placed on the z axis with the initial velocity parallel to the axis as well
- then, the motion of the third body will be restricted to the z axis
- It is needed to know the position of the primaries (r1 and r2) and the position and velocities of the third body (r3 and v3) in order to describe the states of the dynamical system
- For an Initial Condition of the system, the angular variable and the velocities of the third body every time it crosses xy plane is marked. An Initial Condition has to be integrated as long as necessary to find i number of intersections within the xy plane. Finally, the angle of the primaries and the magnitude of the velocities are plotted).
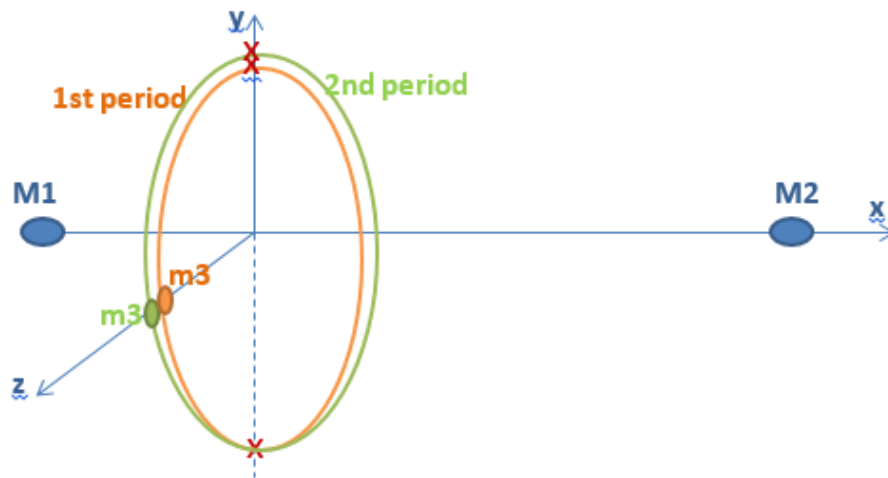
Figure A.11. Two periods run to see unperiodicity

- The intersection marks which seems to be filled densely correspond to periodic motion which is not a rational multiple of the period of the primaries,
- While "spotted" filling (every time the same location on xy plane is crossed) is periodic motion whose frequency is a rational multiple of the primary period.

Two examples with equal M1=M2 having an orbit with an eccentricity value 0.5 and 0:
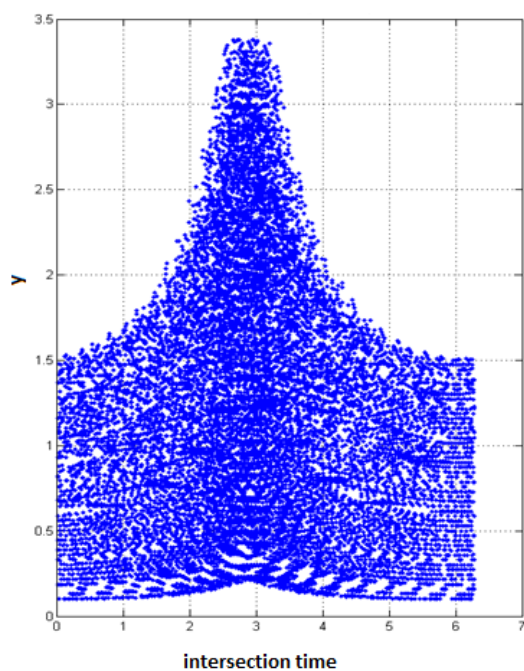
Figure A.12. Poincare map for primaries having equal mass with e=0.5
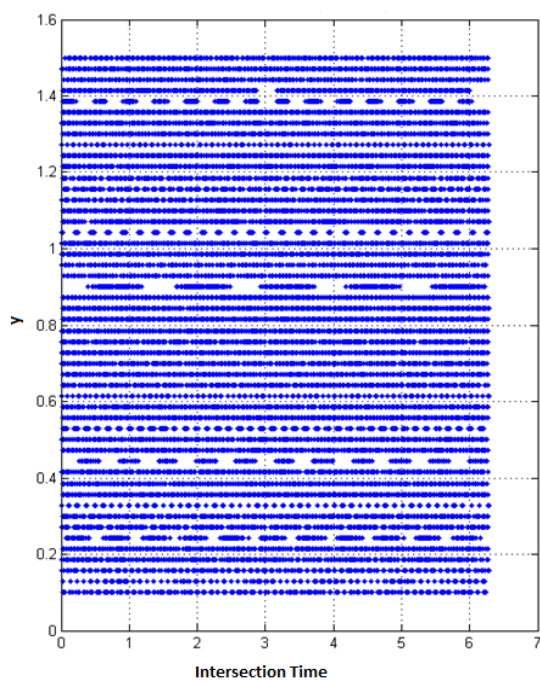
Figure A.13. Poincare map for primaries having equal mass with e=0

344

This methodology is used to get Poincare map for the primaries Sun and Bary (M1=Sun and M2=Bary), and the following results are obtained, given in Figure A.14, Figure A.15, and Figure A.16. Here the iteration process is run for an x interval 0.978au to 1.006au. the "dot" markers are obtained when the same position is obtained for every orbital time period. The lines formed by adjacent points shows that different positions are crossed every orbital time period.
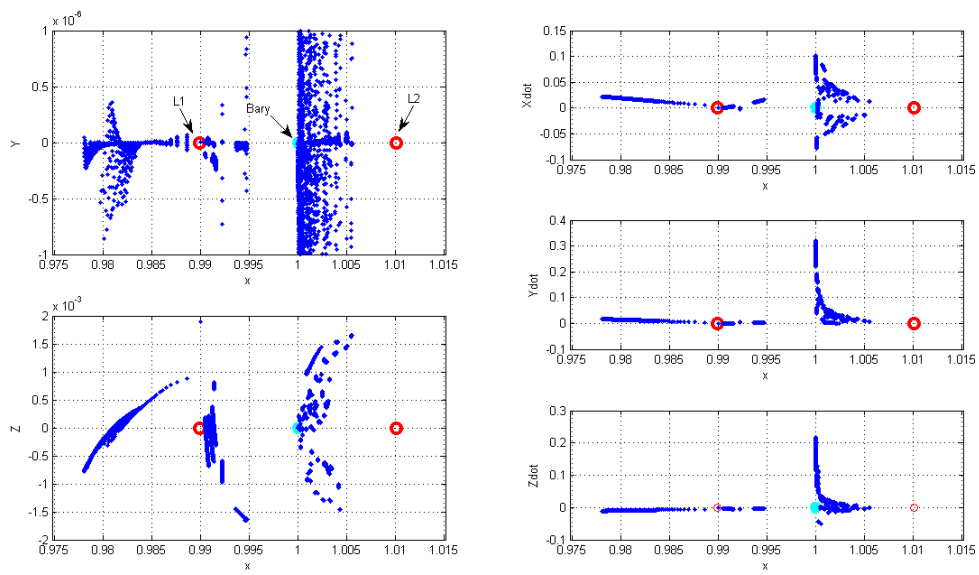
Figure A.14. Poincare map for L1 of Sun-Bary system
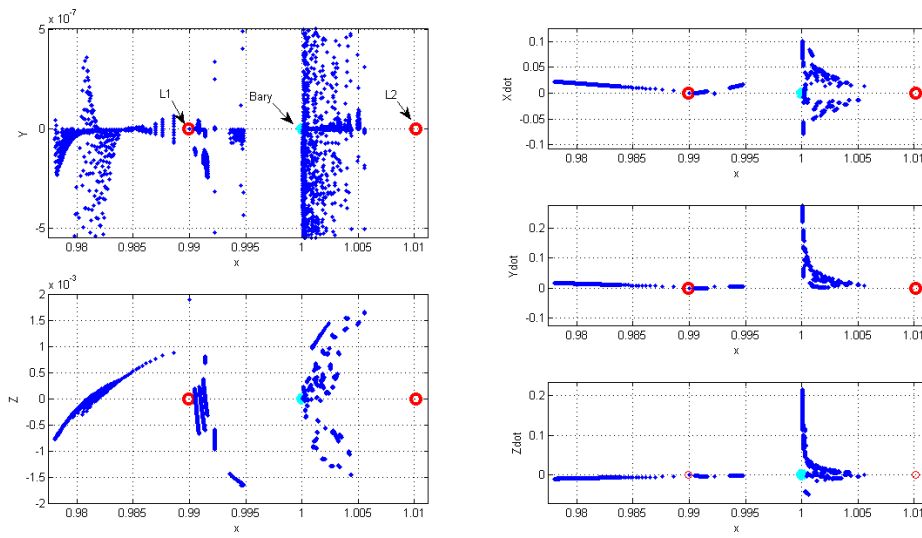
Figure A.15. Poincare map for L1 of Sun-Bary system- Zoomed view-1
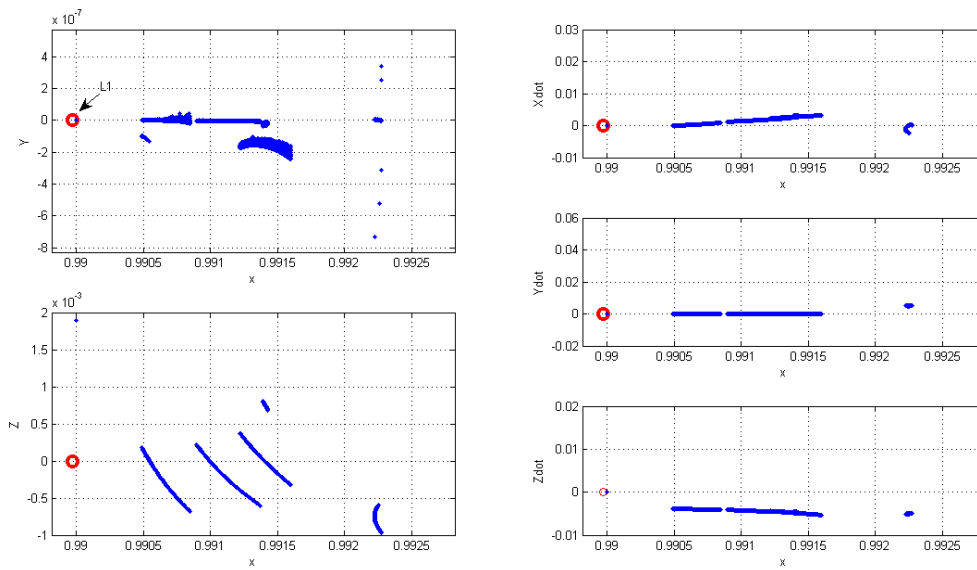
Figure A.16. Poincare map for L1 of Sun-Bary system- Zoomed view-2

H. Ephemeris Model

The ephemeris model is constituted to compute the positions of the planets regarding to the Sun in synodic reference frame by using Julian Date in order to computes the accelerations caused by the gravitational forces of the planets. Julian Date is a kind of time measurement system for scientific use by the astronomy community. It is the interval of time in days and fractions of a day since 4713 BC January-1 Greenwich noon, that is at 12:00 Universal Time [87]. In order to get the position of a planet for a specified date, it is needed to convert the calendar date to the Julian date. The following steps are done for this conversion:

$$JD = bias + 1720994.5 + day + int(30.6001 \times (month + 1))$$
$$+int(365.25 \times year)$$

Eq. A-73

Here, note that the value of year and month must be modified for January and February using the following equations:

$$if\ month = 1\ or\ month = 2$$
$$month = month + 12$$
$$year = year - 1$$

Eq. A-74

And if the date selected is equal of greater than 15 October 1582 (dates in Gregorian calendar) the bias must be calculated as ($bias = 0$ for the date before 15 October 1582):

$$bias = 2 - int\left(\frac{year}{100}\right) + int(\frac{year}{400})$$

Eq. A-75

This Julian date value is used to compute the time measured in Julian centuries of 36525 ephemeris days from the epoch January 1900, that is:

$$Time = (JD - 2415020)/36525$$

Eq. A-76

Here Time value is expressed in centuries, and it is negative for the dates before 1900.

The positions of the Planets are defined using its orbital elements and those orbital elements are expressed in time dependent polynomial form:

$$Orbital\ Element \equiv Orb_k = c_0 + c_1 t + c_2 t^2 + c_3 t^3 \qquad \text{Eq. A-77}$$

Orbital elements can be listed as:

L: mean longitude of the planet (deg)

a: semimajor axis in AU

e: eccentricity

i: inclination on the plane o f the ecliptic (deg)

ω: argument of perihelion (deg)

Ω: longitude of ascending node (deg)

The following table presents the values of the polynomial's constants for orbital elements for each of the planets [86]

Table A.1. Polynomials constants for orbital elements of planets

MERCURY	L	a	e	i	ω	Ω
c_0	178.179078	0.3870986	0.20561421	7.002881	28.753753	47.145944
c_1	149474.07078	0	2.046e-5	0.0018608	0.3702806	1.1852083
c_2	3.011e-4	0	-3.0e-8	−1.83e-5	1.208e-4	1.739e-4
c_3	0	0	0	0	0	0
VENUS	L	a	e	i	ω	Ω
c_0	342.767053	0.7233316	6.82069e-3	3.393631	54.384186	75.779647

348

Table A.1. Polynomials constants for orbital elements of planets (cont'd)

c_1	58519.21191	0	–4.774e-5	1.0058e-3	0.5081861	0.89985
c_2	3.097e-4	0	9.1e-8	–1.0e-6	–1.3864e-3	4.100e-4
c_3	0	0	0	0	0	0
EARTH (*)	L	a	e	i	$M^{(*)}$	$\pi^{(*)}$
c_0	99.69668	1.0000002	1.675104e-2	0	358.47583	L-M
c_1	36000.76892	0	-4.18e-5	0	35999.04975	L-M
c_2	3.025e-4	0	-1.26e-7	0	–1.5e-4	L-M
c_3	0	0	0	0	–3.3e-6	L-M
MARS	L	a	e	i	ω	Ω
c_0	293.737334	1.5236883	9.33129e-2	1.850333	285.431761	48.786442
c_1	19141.69551	0	9.2064e-5	–6.750e-4	1.0697667	0.7709917
c_2	3.107e-4	0	–7.7e-8	1.26e-5	1.313e-4	–1.4e-6
c_3	0	0	0	0	4.14e-6	–5.33e-6
JUPITER	L	a	e	i	ω	Ω
c_0	238.049257	5.202561	4.83347e-2	1.308736	273.277558	99.443414
c_1	3036.301986	0	1.64180e-4	–5.6961e-3	0.5594317	1.0105300
c_2	3.347e-4	0	–4.676e-7	3.9e-6	7.0405e-4	3.5222e-4
c_3	–1.65e-6	0	–1.7e-9	0	5.08e-6	–8.51e-6
SATURN	L	a	e	i	ω	Ω
c_0	266.564377	9.554747	5.58923e-2	2.492519	338.307800	112.790414
c_1	1223.509884	0	–3.4550e-4	–3.9189e-3	1.0852207	0.8731951
c_2	3.245e-4	0	–7.28e-7	–1.549e-5	9.7854e-4	–1.5218e-4
c_3	–5.8e-6	0	7.4e-10	4e-8	9.92e-6	–5.31e-6
URANUS	L	a	e	i	ω	Ω
c_0	244.197470	19.21814	4.63444e-2	0.772464	98.071581	73.477111

	L	a	e	i	ω	Ω
c_1	429.863546	0	–2.658e-5	6.253e-4	0.9857650	0.4986678
c_2	3.160e-4	0	7.7e-8	3.95e-5	–1.0745e-3	0.0013117
c_3	-6.0e-7	0	0	0	–6.1e-7	0
NEPTUNE	L	a	e	i	ω	Ω
c_0	84.457994	30.10957	8.99704e-3	1.779242	276.045975	130.681389
c_1	219.885914	0	6.330e-6	–9.5436e-3	0.3256394	1.0989350
c_2	3.205e-4	0	–2e-9	–9.1e-6	1.4095e-4	2.4987e-4
c_3	–6.0e-7	0	0	0	4.113e-6	–4.718e-6

(*) Earth's orbital elements is defined differently from the other solar system planets, because inclination of the Earth's orbital plane is taken zero as it is on the ecliptic plane. For this reason, the value of ω and Ω are not determined.

The initial position of the planets can be computed by using the equations and constants given above. Then orbit propagator can be run for each of the planets. The orbital period and the mass of the planets of the solar system is represented in the following table.

Table A.2. Period and mass of the solar system planets

Planet	Period	Mass
Mercury	~0.24 years (87.97 days)	3.3022x1e23 kg
Venus	~0.616 years (224.70 days)	48.685x1e23 kg
Earth	~1 year (365.25 days)	59.720x1e23 kg (60.455x1e23 with Moon)
Mars	~1.88 years (686.98 days)	6.4185x1e23 kg
Jupiter	~11.86 years (4332.82 days)	18986 x 1e23 kg
Saturn	~29.45 years (10755.70 days)	5684.6x1e23 kg
Uranus	~84 years (30687.15 days)	868.10x1e23 kg
Neptune	~164.79 years (60190.03 days)	1024.3x1e23 kg

In the Ref.[85] the list and the details about the dynamical model of planetary ephemeris model are shared.

The detailed equations and explanations on Hemispheric coordinate system are given in Ref.[88]. These references present Keplerian elements for planetary orbits and determine their precision for the dates from 1950 to 2050.

I. Execution Times of the Algorithms

Benchmark Tests:

The algorithms, models used in this thesis are coded using Matlab 2012a version. The simulation environment and graphics are constituted using   Matlab editor and Simulink. The following steps are performed in order to analyze the performance of the computer used and the codes prepared.

Benchmark test of the computer is done. This benchmark test is performed by "bench" command of the Matlab. The command "bench" run six different Matlab tasks and compares the execution speed with the speed of several other computers. The six tasks are listed in the Table A.3:

Table A.3. Tasks used in Matlab Benchmark test

LU:	LAPACK; Floating point, regular memory access.
FFT:	Fast Fourier Transform; Floating point, irregular memory access.
ODE:	Ordinary differential equation; Data structures and functions.
Sparse:	Solve sparse system; Sparse linear algebra.
2-D:	plot(fft(eye)); 2-D line drawing graphics.
3-D:	MathWorks logo; 3-D animated OpenGL graphics.

A bar chart is obtained and it shows speed. **Here, longer bars indicate faster machines, shorter bars indicate slower.**

The properties of the computer used:

System
Rating: System rating is not available
Processor: Intel(R) Core(TM) i5-2450M CPU @ 2.50GHz   2.50 GHz
Installed memory (RAM):   8.00 GB
System type: 64-bit Operating System

Figure A.17. Computer properties

The benchmark results of the computer are given in the Figure A.18 and Figure A.19.

Computer Type	LU	FFT	ODE	Sparse	2-D	3-D
Linux (64-bit) 3.47 GHz Intel Xeon	0.0582	0.0541	0.1468	0.1208	0.1969	0.0889
Windows 7 Enterprise (64-bit) 3.47 GHz Intel Xeon	0.0664	0.0722	0.1056	0.1305	0.2772	0.7000
Windows 7 Enterprise (64-bit) 2.7 GHz Intel Core i7	0.0834	0.1147	0.0902	0.1424	0.2927	0.6880
This machine	0.1037	0.1505	0.0972	0.1686	0.3847	0.7585
Mac OS X Lion (64-bit) 2.66 GHz Intel Xeon	0.0445	0.1251	0.1829	0.1858	0.6658	0.6193
Windows 7 Enterprise (64-bit) 2.66 GHz Intel Core 2 Quad	0.1201	0.2605	0.1493	0.2565	0.4723	0.7182
Windows XP (32-bit) 2.66 GHz Intel Core 2	0.2307	0.2666	0.1323	0.2341	0.3719	0.5556
Mac OS X Snow Leopard (64-bit) 2.66 GHz Intel Xeon	0.1395	0.3060	0.2042	0.2990	0.8073	0.9341

Figure A.18. Matlab benchmark test results-1
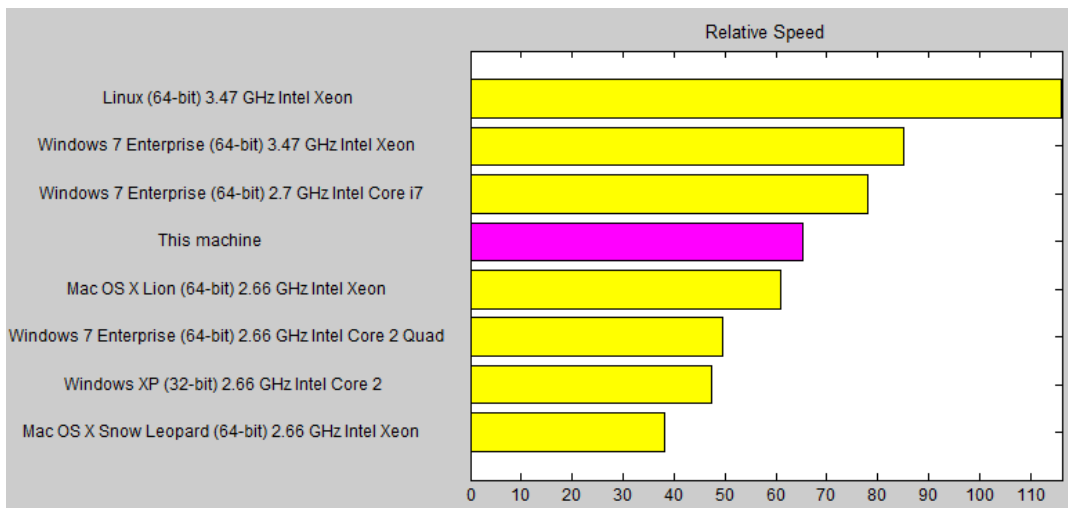
Figure A.19. Matlab benchmark test results-2

352

Execution time for halo orbit computation:

The execution time spent for the computation of the initial conditions of the chief's halo orbit is obtained. Simulation properties and the results are given in Table A.4.

Table A.4. Chief's halo orbit computation performance

Simulation sampling time:	1 hour = 3600 sec
Simulation time:	0.231 year
Elapsed time to run simulation:	32.75 sec
Number of iterations: (Newton method iteration)	9
Performance:	3.6 sec/iteration

Execution time for halo formation design computation:

The results obtained for the computation of the initial conditions of the deputy satellite's orbit is given Table A.5.

Table A.5. Deputy's halo orbit computation performance

Simulation sampling time:	1 hour = 3600 sec
Simulation time:	0.46 year
Elapsed time to run simulation:	19.25 sec
Number of iterations: (Newton method iteration)	4
Performance:	4.8 sec/iteration

Execution time for LEO formation design computation:

The simulation prepared in order to design formation flight for LEO satellite is analyzed. The execution time spent for the Newton method used to compute initial conditions for deputy is given in the Table A.6

Table A.6. Deputy's LEO orbit computation performance

Simulation sampling time:	1 sec
Simulation time:	99 min
Elapsed time to run simulation:	47.5 sec
Number of iterations: (Newton method iteration)	6
Performance:	7.9 sec/iteration

J. Synodic and Inertial Reference Frame Comparison

This section is prepared to give an idea on the consistency of the computations given in the thesis. This may be considered as a validation method of the computations. In chapter-2, the details of the dynamic model and the results obtained from simulations are presented to demonstrate the accuracy of the codes developed. In addition to this, this section gives the simulation results run in inertial reference frame.

The equations of motion expressed in inertial reference frame are coded for simulation and similar simulations are performed. The initial condition set used for synodic reference frame is converted to the inertial reference frame and simulations are carried out

Finally, synodic reference frame-based results are converted to the inertial reference frame by using Eq. A-78 and Eq. A-79 in order to compare with those of the inertial reference frame computations.

$$\overline{X}_{(t=0)}\Big|_i = C_s^i \, \overline{X}_{(t=0)}\Big|_s \qquad\qquad \text{Eq. A-78}$$

$$\dot{\overline{X}}_{(t=0)}\Big|_i = C_s^i \, \dot{\overline{X}}_{(t=0)}\Big|_s + C_s^i \, \widetilde{\omega} \, \dot{\overline{X}}_{(t=0)}\Big|_s \qquad\qquad \text{Eq. A-79}$$

Initial conditions computed for inertial reference frame-based simulation are:

$$\overline{X}_{(t=0)}\Big|_i = \begin{bmatrix} 0.988863916985417 \\ 0.000000190354307 \\ 0.002283164826074 \end{bmatrix} au$$

$$\dot{\overline{X}}_{(t=0)}\Big|_i = \begin{bmatrix} 0.052770697952 \\ 9.633777243277 \\ -0.004351902636 \end{bmatrix} \times 10^{-3} \; au \; \omega$$

Equation of motion of the spacecraft written in inertial reference frame where the origin is the center of mass of the Sun+Bary system:

$$
\begin{bmatrix} \ddot{x} \\ \ddot{y} \\ \ddot{z} \end{bmatrix}_i = \begin{bmatrix} -\dfrac{Gm_1(x+x_1)}{r_1^3} - \dfrac{Gm_2(x-x_2)}{r_2^3} \\[4mm] -\dfrac{Gm_1(y+y_1)}{r_1^3} - \dfrac{Gm_2(y-y_2)}{r_2^3} \\[4mm] -\dfrac{Gm_1(z+z_1)}{r_1^3} - \dfrac{Gm_2(z-z_2)}{r_2^3} \end{bmatrix}
\qquad\text{Eq. A-80}
$$

where; position of Sun with respect to center of mass of Sun+Bary system expressed in inertial reference frame is:

$$
\begin{bmatrix} x_1 \\ y_1 \\ z_1 \end{bmatrix}_i = C_s^i \begin{bmatrix} x_1 \\ 0 \\ 0 \end{bmatrix}_s
$$

Position of Bary with respect to center of mass Sun+Bary system expressed in inertial reference frame is:

$$
\begin{bmatrix} x_2 \\ y_2 \\ z_2 \end{bmatrix}_i = C_s^i \begin{bmatrix} x_2 \\ 0 \\ 0 \end{bmatrix}_s
$$

Following figures and table present the results obtained for the simulation run in inertial reference frame. $Xsat_{si}, Ysat_{si}, Zsat_{si}$ are the x, y, z position of the satellite computed at synodic reference frame and expressed in (converted to) the inertial reference frame by using the transformation given in Eq. A-78. $VXsat_{si}, VYsat_{si}, VZsat_{si}$ are the vx, vy, vz velocity of the satellite computed at synodic reference frame and expressed in (converted to) the inertial reference frame by using the transformation given in Eq. A-79.

$Xsat_i, Ysat_i, Zsat_i$ are the x, y, z position of the satellite computed at inertial reference frame and expressed in inertial reference frame by using Eq. A-80.
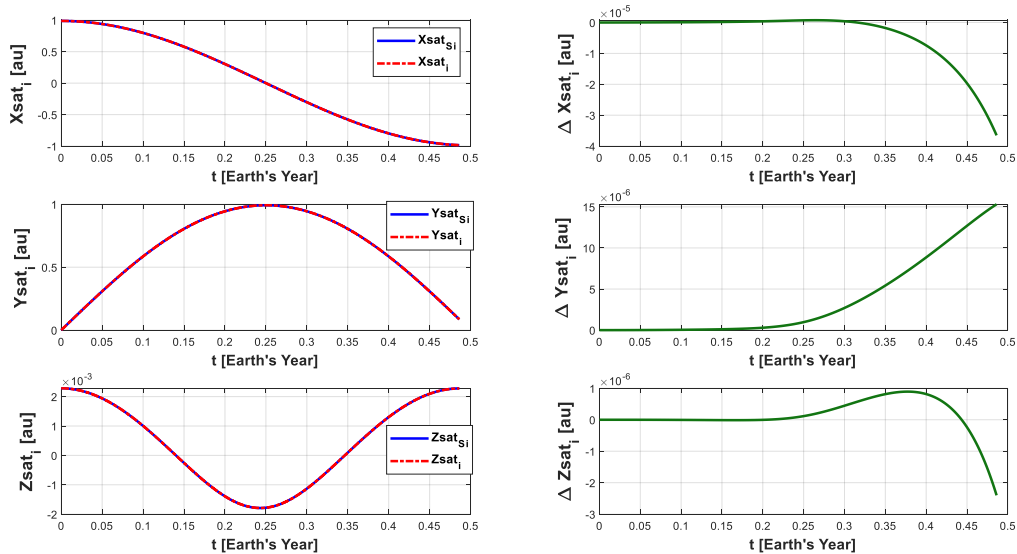
Figure A.20. Position Comparison

The divergence starts at the half period of the satellite orbit and this is due to computation performance of the discrete-time integration of the computer (i.e. sampling time is 1 s., integration method is RK 4th order).
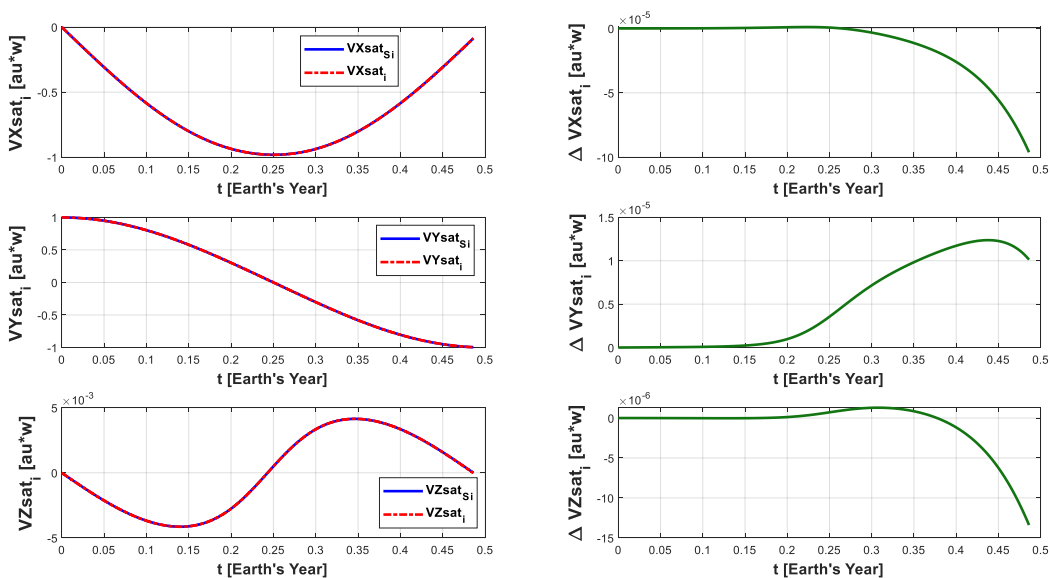

Figure A.21. Velocity Comparison

357

The position and velocity differences at quarter, half, third quarter and one orbital period are presented in Table A.7:

Table A.7. Difference between position and velocities

	At first quarter orbit	At half orbit	At third quarter orbit	At one orbit
$\Delta \bar{X}\|_i$ [au]	$\cong \begin{bmatrix} 0.11553 \\ 0.06203 \\ -0.00748 \end{bmatrix} 10^{-6}$	$\cong \begin{bmatrix} 0.67803 \\ 0.82594 \\ 0.08703 \end{bmatrix} 10^{-6}$	$\cong \begin{bmatrix} -2.9682 \\ 6.3639 \\ 0.8751 \end{bmatrix} 10^{-6}$	$\cong \begin{bmatrix} -36.519 \\ 15.314 \\ -2.400 \end{bmatrix} 10^{-6}$
$\Delta \dot{\bar{X}}\|_i$ [au ω]	$\cong \begin{bmatrix} 0.21149 \\ 0.11886 \\ -0.024084 \end{bmatrix} 10^{-6}$	$\cong \begin{bmatrix} 0.8812 \\ 3.07267 \\ 0.60770 \end{bmatrix} 10^{-6}$	$\cong \begin{bmatrix} -14.723 \\ 10.461 \\ 0.457 \end{bmatrix} 10^{-6}$	$\cong \begin{bmatrix} -96.162 \\ 10.128 \\ -13.393 \end{bmatrix} 10^{-6}$

From the results presented in the table, it may be stated that computation-based errors accumulate and start show itself up at the half period, in 0.25 Earth's year, for the simulation run with the parameters given above. It is obvious that sampling time of the integration is the dominant factor of this kind of error and shall improve with smaller integration time step. However, the difference between two simulations is quite small and negligible.

<h1 style="text-align:center">CURRICULUM VITAE</h1>

PERSONAL INFORMATION

Surname, Name: Kutlu, Aykut
Nationality: Turkish (TC)
Date and Place of Birth: 4 February 1980, Adana
Marital Status: Married
Phone: +90 536 325 47 33
email: e150515@metu.edu.tr; aykutkutlu@gmail.com; aykut.kutlu@esensi.com.tr

EDUCATION

Degree	Institution	Year of Graduation
MS	METU Aerospace Engineering	2008
BS	İTÜ Astronautical Engineering	2005
BS (Double Major)	İTÜ Aeronautical Engineering	2005
High School	Saint-Benoît French High School, İstanbul	1999

WORK EXPERIENCE

Year	Place	Enrollment
2020-Present	ESEN- UAV Systems	Leader System Engineer
2016-2020	TAI-UAV Systems Department	Senior Design Engineer
2005- 2015	TAI- Space Systems Department	
• 2012 – 2015	• Potential Indigenous Satellite Projects	System Engineer
• 2011 – 2012	• GOKTURK-1 Project, Direct participant work packages at France	Technical Leader, System Engineer

• 2010 – 2011	• GOKTURK-1 Project, Direct participant work packages at France	AOCS Design Engineer
• First half of 2010	• Sounding Rocket Project, Conceptual Design	System Engineer
• 2007 – 2010	• DÖNENCE Project, CMG Test Bed Development Work package	Design Engineer
• 2005 – 2007	• Pre-contractual phases for the potential project	Design Engineer
• 2005	• Training Aircraft Research and Design Project (HÜRKUŞ)	Research Assistant Engineer

FOREIGN LANGUAGES

English, French

PUBLICATIONS

1. A.Kutlu, O.Tekinalp, " Formation Flight Design near Sun-Earth Collinear Libration Points under the Effect of Disturbances", RAST Conference, March, 2019, İstanbul, TURKEY

2. A.Kutlu, O.Tekinalp, " A Simulation Tool to Design Satellite Formation Flight", ICATT 2016 March, 2016, Darmstadt, GERMANY

3. A.Kutlu, O.Tekinalp, "Development of A Simulation Tool for The Design of Spacecraft Formation Flight", AIAC, 8th Ankara International Aerospace Conference, September 10-12,2015, Ankara, TURKEY

4. A.Kutlu, O.Tekinalp, "Kalman Filter Based Multimode Attitude Determination Algorithms for A LEO Satellite", 19th Spaceflight Mechanics Conference, AAS09-205, February 2009, GA Savannah - USA.

5. A.Kutlu, Ch. Haciyev, O.Tekinalp, "Attitude Determination and Rotational Motion Parameters Identification of a LEO Satellite through Magnetometer and Sun Sensor Data", Third International Conference on Recent Advances in Space Technologies – RAST, June 2007, Istanbul TURKEY.

6. A.Kutlu, Ch. Haciyev, "Attitude Control of Leo Satellite via LQR and Linear Stochastic Estimator", Ankara International Aerospace Conference, August – 2005, Ankara TURKEY.

HOBBIES

Basketball, Cycling, Playing Guitar